ISSN 2518-1726 (Online),
ISSN 1991-346X (Print)

ҚАЗАҚСТАН РЕСПУБЛИКАСЫ
ҰЛТТЫҚ ҒЫЛЫМ АКАДЕМИЯСЫНЫҢ
әл-Фараби атындағы Қазақ ұлттық университетінің

Х А Б А Р Л А Р Ы

ИЗВЕСТИЯ

НАЦИОНАЛЬНОЙ АКАДЕМИИ НАУК
РЕСПУБЛИКИ КАЗАХСТАН
Казахский национальный университет
им. аль-Фараби

N E W S

OF THE NATIONAL ACADEMY OFSCIENCES
OF THE REPUBLIC OF KAZAKHSTAN
Al-Farabi Kazakh
National University

SERIES
PHYSICO-MATHEMATICAL

3 (331)

MAY – JUNE 2020

PUBLISHED SINCE JANUARY 1963

PUBLISHED 6 TIMES A YEAR

ALMATY, NAS RK

«ҚР ҰҒА Хабарлары. Физика-математикалық сериясы».
ISSN 2518-1726 (Online), ISSN 1991-346X (Print)
Меншіктенуші: «Қазақстан Республикасының Ұлттық ғылым академиясы» РҚБ (Алматы қ.).
Қазақстан республикасының Мәдениет пен ақпарат министрлігінің Ақпарат және мұрағат комитетінде 01.06.2006 ж. берілген **№5543-Ж** мерзімдік басылым тіркеуіне қойылу туралы куәлік.

Мерзімділігі: жылына 6 рет.
Тиражы: 300 дана.

Редакцияның мекенжайы: 050010, Алматы қ., Шевченко көш., 28; 219, 220 бөл.; тел.: 272-13-19; 272-13-18,
http://physics-mathematics.kz/index.php/en/archive

Типографияның мекенжайы: «NurNaz GRACE», Алматы қ., Рысқұлов көш., 103.

«Известия НАН РК. Серия физика-математическая».
ISSN 2518-1726 (Online), ISSN 1991-346X (Print)
Собственник: РОО «Национальная академия наук Республики Казахстан» (г. Алматы).
Свидетельство о постановке на учет периодического печатного издания в Комитете информации и архивов Министерства культуры и информации Республики Казахстан **№5543-Ж**, выданное 01.06.2006 г.

Периодичность: 6 раз в год.
Тираж: 300 экземпляров.

Адрес редакции: 050010, г. Алматы, ул. Шевченко, 28; ком. 219, 220; тел.: 272-13-19; 272-13-18,
http://physics-mathematics.kz/index.php/en/archive

Адрес типографии: «NurNaz GRACE», г. Алматы, ул. Рыскулова, 103.

News of the National Academy of Sciences of the Republic of Kazakhstan. Physical-mathematical series.
ISSN 2518-1726 (Online), ISSN 1991-346X (Print)
Owner: RPA "National Academy of Sciences of the Republic of Kazakhstan" (Almaty).
The certificate of registration of a periodic printed publication in the Committee of information and archives of the Ministry of culture and information of the Republic of Kazakhstan N 5543-Ж, issued 01.06.2006.

Periodicity: 6 times a year.
Circulation: 300 copies.

Editorial address: 28, Shevchenko str., of. 219, 220, Almaty, 050010, tel. 272-13-19; 272-13-18,
http://physics-mathematics.kz/index.php/en/archive

Address of printing house: «NurNaz GRACE», 103, Ryskulov str, Almaty.

Astrophysical research in Kazakhstan

NEWS
OF THENATIONAL ACADEMY OF SCIENCES OF THE REPUBLIC OF KAZAKHSTAN
PHYSICO-MATHEMATICAL SERIES
ISSN 1991-346X **https://doi.org/10.32014/2020.2518-1726.30**
Volume 3, Number 331 (2020), 5 – 14

UDK 524.6-8
МРНТИ 41.27.25

E. K. Denissyuk, A. V. Serebryanskiy

Fesenkov Astrophysical Institute, Almaty, Kazakhstan.
E-mail: eddenis@mail.ru, aserebryanskiy@yahoo.com

THE ORBIT OF THE STAR S2 ≡ S0-2 IN THE CENTER OF THE GALAXY

Abstract. The study of the center of the Galaxy in the IR wavelengths, using the largest telescopes, aloud us to obtain data on coordinates and radial velocities for several tens of stars located in the immediate vicinity of the supermassive central body of the Galaxy, hereinafter (CB) Such data for S2≡S0-2 –one of the brightest and closest to the center stars, were used by us to determine the parameters of its orbit. The method we proposed was used to calculate the positions and velocities of a star in its orbit with the parameters at which the calculated coordinates and velocities best coincided with those observed.

In order to estimate the errors of parameters, the Monte Carlo method was used. In this case, it was assumed that there was diffuse matter near the center of the Galaxy. An estimate of the average value of its density $(5.2 \pm 1.5) \times 106\ M_{\odot} / ps^3$ is obtained, which is comparable with the density of typical nebulae. The presence of such matter leads to the rotation of the orbit around the center of gravity. A full revolution of the orbit requires about 7760 years. In addition to the direct parameters of the star's orbit the parameters of the CB itself were found. The mass of the CB of the Galaxy turned out to be $(4034 \pm 13) \times 10^3 M_{\odot}$, and its distance from the Sun is 8333.0 ± 7.0 ps.

Key words: Galaxy: center - methods: data analysis - stars: kinematics and dynamics.

1. Introduction

The ultra-high angular resolution achieved in astronomy as a result of technological progress made it possible to study in detail in the IR range the Central region of the Galaxy shrouded by dust clouds. It turned out that there is a massive, almost invisible, Central Body (CB), in the gravitational field of which move dozens of stars. In about 20 years, we managed to build maps of the movement of such stars and for many of them to measure the radial velocities [1 – 6].

On the basis of this observational material, the search for parameters characterizing both the CB and the orbits of stars moving in its gravitational field is carried out. The most studied star turned out to be one of the closest to CB and the relatively bright star S2 ≡ S02. The results of determining the parameters of CB and the orbit of this star, obtained by different authors on the basis of almost the same observational data, are markedly different from each other [3-5, 7-9]. One of the reasons for this difference is the lack of data on the exact position of the CB in the images of the central region of the Galaxy, obtained with ultra-high angular resolution in the IR range [4]. The team of Fesenkov Astrophysical Institute (FAI) has developed a method for determining the orbits of emission objects moving in the gravitational field of the nuclei of Seyfert galaxies utilizing change of their radial velocities in time [10,11]. It was decided to apply this method to the region of the Galactic center using the published observational data for the star S2. The basis of the method is a recurrent method of constructing the orbit of the motion of the test body in the gravitational field of the central mass. At the same time, for any moment of time, it is possible to

determine the position and velocity of the motion of such body in the plane of an orbit. This allows us to find all parameters of motion of the star S2, which are in the best way consistent with the observations and to estimate the possible errors of these parameters.

The most important is to determine the mass of CB, its distance from the Sun, the density of diffuse matter in the vicinity of CB and the ability to determine CB location on IR images, which is poorly visible in such images and is usually taken as the center of the coordinate system. As observational data, the published tables of the dependence of the radial velocities and coordinates on time for the star S2 were used [9].

2 Method

2.1 Recurrent method for the construction of the orbit

Let us consider a rectangular coordinate system (X, Y, Z) where the Z-axis is directed along the view plane, (X,Y) orthogonal to the line of sight and the X-axis coincides with the line of nodes (line of nodes perpendicular to the line of sight). The observed radial velocities [12] at different times is a set of measurements of the projection of the velocity of the star S2 on Z-axis and denoted as Vr(t). The angle between the plane of the orbit and (X,Y) plane is denoted as i (i≠ 0, otherwise all Vr(t) = 0).

To account for mass of dispersed matter near the CB, it is necessary to add an additional mass $\Delta m=4/3\pi r_i^3\rho_0$ to the mass of the CB at each point along the orbit. To strictly take into account the influence of the mass of dispersed matter (hereinafter MDM), it is necessary to know the three-dimensional distribution of the density ρ_0. This function is unknown. Preliminary calculations have shown that the effect of MDM on the movement of stars is not very large and is comparable to the effect of observation uncertainties. A number of authors suggest that MDM has spherical symmetry distribution around the CB, and ρ_0 decreases from center to outer boundary according to the power law. However, a significant heterogeneity in the distribution of MDM is also possible. Given these circumstances, we decided to limit ourselves to finding the density ρ_0, which is constant in the volume where the star S2 moves.

The following method is used to calculate the motion of a star in its orbital plane. Let m_0 is the mass of CB (which can be a function of other parameters), g is the gravitational constant, r_i is the distance of the star from CB at the time t_i, q is the distance in the periapsis, V_i is the velocity vector module, ϕ_i is the angle between the X-axis and the radius vector $\boldsymbol{r}_i$, γ_i is the angle between velocity vector V_i and Y- axis, perpendicular to the X-axis and lying in the orbital plane. One has to set the time step, Δt, to move to the next position along the orbit and other parameters are obtained according to the formulas:

$$
\begin{aligned}
m_i &= m_0 + \frac{4}{3}\pi r_i^3 \rho_0 \\
\phi_{i+1} &= \phi_i + V_i \cdot \cos(\phi_i - \gamma_i) \cdot \Delta t / r_i \\
\gamma_{i+1} &= \phi_i - \arctan\left(\frac{V_i \cdot \sin(\phi_i - \gamma_i) - \Delta t \cdot m_i g / r_i^2}{V_i \cdot \cos(\phi_i - \gamma_i)}\right) \\
V_{i+1} &= ((V_i \cdot \cos(\phi_i - \gamma_i))^2 + (V_i \cdot \sin(\phi_i - \gamma_i) - \Delta t \cdot m_i g / r_i^2)^2)^{1/2} \\
r_{i+1} &= r_i + V_i \cdot \sin(\phi_i - \gamma_i) \cdot \Delta t \cdot \phi_i V_i
\end{aligned}
\tag{1}
$$

2.2 A search of the orbital parameters on the basis of the observed radial velocities

We begin with estimation of the orbital parameters and r(x;y;z) for which the observed and calculated values of V_r coincide in the best way.

Theoretical calculations of the orbit are started at the moment when the star passes of periapsis T_p. The search is performed by iterating through seven parameters: T_p – the moment of passage of the pericentre, M - CB mass, angles ϕ and γ which are equal to each other in the pericentre, V_p (velocity module in the pericentre), *e, i* and ρ_0. At t_i moments for which observations are available, theoretical values of V_r are calculated and χ^2 is calculated from the differences between these values and the observed values of V_r. [12].

It is obvious that the smaller the step *dt*, the less error accumulates in this method of orbit calculation. Check on the real orbit of the star S2 showed that at the apoapsis, where *r*~1950 AU, using *dt* = 10 sec for

one revolution the r is changed by 0:046 AU and if dt = 1000 sec is used the r changed by 4.5 AU. We decided to perform our calculations using dt = 10 sec. The orbital parameters obtained in this way can be considered as the most probable. The minimum χ^2 value in our calculations was equal to 0.6969. The result is shown in figure 1.

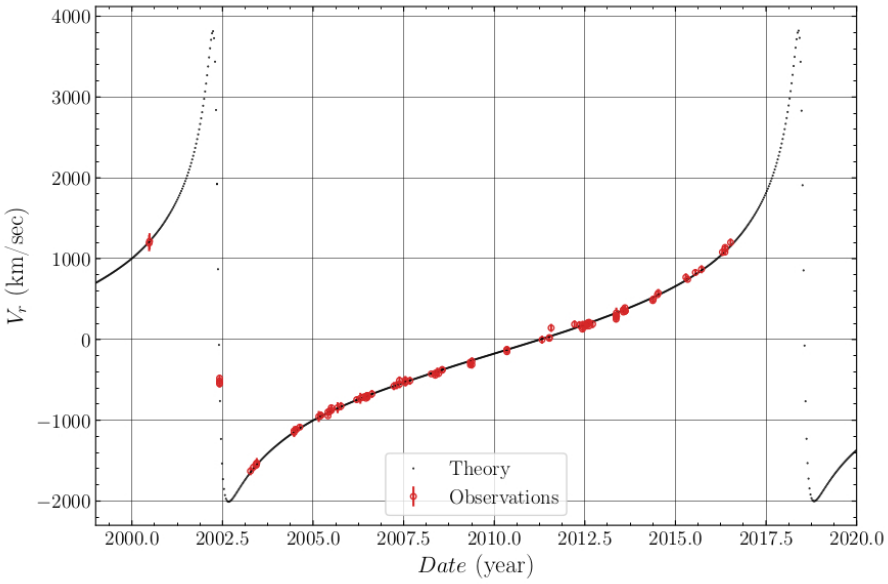

Figure 1 - Radial velocity of S2 star at different epochs. Symbols show observations [12] and dotted line shows our theoretical orbit

The mean square errors of these parameters were found by the Monte-Carlo method. The following orbital parameters were obtained: T_p = 2002.3482 ± 0.0009 year, q = (1.7416 ±0.0018)×10^{15} cm, ϕ_p = γ_p = $69^0.43\pm0^0.24$, M =(4034±13)×10^3 M_Θ, e = 0.88657±0.00011, ρ = (4.76± 1.5)×10^6 M_Θ/ps^3 ~3.5×10^{-16} g/cm^3, i = $133^0.83\pm0^0.067$.

The value ρ_0 ~ 3.5 x10^{-16} g/cm^3 corresponds to a high density nebula. However, the mass added by such nebula to the mass of CB in calculating the motion of the star S2 is small compared to the mass of CB. For instance, at the periapsis it is about 1.3 M_Θ, and in the apoapsis it is ~640 M_Θ, which is a very small fraction of the CB mass.

2.3 Determination of the orbital parameters of the star S2 using astrometric data.

In addition to observational data on the radial velocities Vr(t) [12] there was published the coordinates of S2 in the vicinity of CB for different moments in time [9]. The coordinates are given in milliseconds of the arc (mas). The observations were mainly obtained by Keck and VLT telescopes. For further analysis we utilize astrometric data obtained from these two telescopes. Only data for which the uncertainty of coordinates did not exceed 1 mas were taken into account and presented in table 1 and table 2.

Table 1 - Sample of S0-2 astrometric measurements obtained with KEK used in this work [9]

Epoch (year)	X (mas)	Y (mas)	σ_X (mas)	σ_Y (mas)	Epoch (year)	X (mas)	Y (mas)	σ_X (mas)	σ_Y (mas)
2003.554	38.63	84.30	0.89	0.82	2009.689	24.78	182.65	0.18	0.14
2004.327	35.95	115.39	0.76	0.62	2010.342	-31.94	180.59	0.12	0.12
2004.564	32.61	123.28	0.79	0.53	2010.511	-33.82	179.84	0.13	0.12
2004.660	31.37	125.84	0.69	0.60	2010.620	-35.01	179.31	0.16	0.13
2005.312	24.83	141.10	0.81	0.59	2011.401	-42.77	173.77	0.22	0.17
2005.566	20.84	149.20	0.83	1.10	2011.543	-44.23	171.96	0.14	0.14
2006.336	12.96	161.91	0.15	0.16	2011.642	-45.17	171.21	0.25	0.25
2008.371	-10.16	181.01	0.13	0.14	2012.371	-51.36	163.26	0.13	0.17
2008.562	-12.32	181.84	0.16	0.16	2012.562	-53.12	160.74	0.14	0.20
2009.340	-21.14	182.66	0.11	0.11	2013.318	-58.37	149.65	0.21	0.26
2009.561	-23.43	182.69.	0.13	0.20	2013.550	-59.79 -	145.41	0.14	0.21

Table 2 - Sample of S0-2 astrometric measurements obtained with VLT [2] used in this work

Epoch (year)	X (mas)	Y (mas)	σ_X (mas)	σ_Y (mas)	Epoch (year)	X (mas)	Y (mas)	σ_X (mas)	σ_Y (mas)
2003.214	41.1	66.6	0.3	0.4	2005.576	24.9	149.4	0.4	0.4
2003.351	41.4	75.0	0.3	0.3	2006.324	17.5	161.7	0.8	0.6
2003.356	40.7	74.8	0.4	0.4	2007.545	2.80	175.7	0.9	0.7
2003.446	40.6	79.8	0.5	0.5	2007.550	4.10	175.2	0.4	0.4
2003.451	41.3	80.4	0.4	0.4	2007.686	2.50	176.0	0.5	0.5
2003.452	41.5	80.5	0.3	0.3	2007.687	1.90	176.0	0.6	0.6
2003.453	40.9	80.6	0.3	0.3	2008.148	-4.60	179.0	0.4	0.4
2003.455	-41.3	81.8	0.4	0.4	2008.197	-5.20	179.0	0.3	0.3
2003.55	-40.9	85.3	0.3	0.3	2008.268	-6.10	180.0	0.3	0.3
2003.676	-40.6	91.8	0.3	0.3	2008.456	-8.40	180.2	0.3	0.3
2003.678	-41.1	91.6	0.6	0.6	2008.472	-8.10	180.7	0.4	0.4
2003.761	-40.2	96.6	0.4	0.4	2008.601	-10.60	180.3	0.3	0.3
2004.24	-37.2	113.2	0.9	0.9	2008.708	-11.40	181.2	0.3	0.3
2004.325	-36.9	116.2	0.3	0.3	2009.185	-17.30	181.1	0.7	0.7
2004.347	-36.1	117.6	0.3	0.3	2009.273	-18.00	181.2	0.3	0.3
2004.443	-36.0	120.4	0.3	0.3	2009.300	18.50	181.3	0.3	0.3
2004.513	-35.3	123.1	0.3	0.3	2009.303	-18.20	181.5	0.3	0.3
2004.516	-35.2	123.1	0.6	0.6	2009.335	-18.30	181.2	0.3	0.3
2004.573	-34.4	124.8	0.4	0.4	2009.337	-18.40	181.2	0.4	0.4
2004.575	-34.3	123.9	0.6	0.6	2009.371	-18.60	181.0	0.3	0.3
2004.664	-33.6	127.2	0.3	0.3	2009.505	-20.10	181.2	0.3	0.3
2004.730	-34.0	128.9	0.7	0.7	2009.556	-20.90	181.5	0.4	0.4
2005.270	28.1	143.0	0.3	0.3	2009.558	-20.20	181.4	0.3	0.3
2005.366	27.0	145.2	0.3	0.3	2009.606	-21.20	181.5	0.3	0.3
2005.467	26.3	146.9	0.4	0.4					

These observational data make it possible to determine the missing parameters, which allows to compare observations with the theoretical orbit. To compare the theoretical coordinates expressed in metric units of length with the angular coordinates, it is necessary to find the coefficient K of the transition from metric units of length to the angular (observed) units. The dimension of the parameter K is mas/m. The distance from the CB to the Sun is found as $R = 6.6845 \times 10^{-9}/K$ ps. The problem is solved by dividing the lengths of the segments measured from the observations between two positions of the star, expressed in mas, by the corresponding segments of the theoretical orbit, expressed in meters, for the same moments of time. Using vector radii for this purpose can lead to errors. The position of the CB, and hence the center of the coordinate system in the images is determined with some uncertainty [2,4,13]. This introduces errors in the length of the measured segments. Errors in the position of the CB, i.e. the origin of the coordinate system, may depends on both the epochs of the observations and the instruments on which the observations were carried out. Such errors can be evaluated separately for each instrument, assuming that the errors are not time-dependent, but are inherent only in the way the data is processed. If, at the same time, for different epochs of observations the coordinate systems with different positions of the origin is used, it will increase the errors given in the tables 1,2. In figure 3 it can be seen that there is a systematic difference between the positions of the star S2 obtained by the Keck and VLT telescopes for those measurements with errors less than 1 mas. In order to reduce the dependence on the position of CB, we used the ratios of the chord lengths of the observed star positions and the same chord lengths of the theoretical orbit projected on the sky plane at an angle i. There are many ways to choose these chords. The number of different chords is the number of combinations of 2 of the number of observations. We used two methods of choosing chords separately for the table 2 and table 1. From Table 1 the lengths of the chords for the first method were calculated between the positions of the stars 11 and 12, 10 and 13, 9 and 14 . . . , 1 and 22. For the second method, lengths of the chords were computed between stars 1 and 12, 2 and 13, 3 and 14 . . . , 11 and 22, in total for 11 chords in both cases.

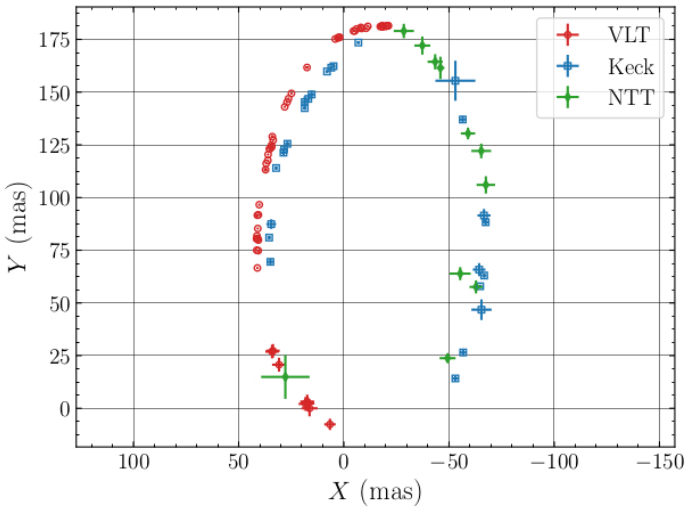

Figure 3 - (X,Y) coordinates of the star S2

The same two methods were used to calculate the lengths of the chords using data from table 2. For the first method, chords were chosen between locations 24 and 26, 23 and 27, 22 and 28 . . . , 1 and 49. For the second method between 1 and 26, 2 and 27, . . . , 24 and 49. In total 24 chords for each method. Next, for each pair of observed and theoretical chords, we calculated the ratio, i.e. the coefficient K had its uncertainty, taking into account error of measurement and weight proportional to the theoretical length of the chord. Calculations for the VLT data were carried out using the following formulas:

$$\sigma_i^2 = \frac{(X_i - X_{50-i})^2 \cdot (\Delta X_i^2 + \Delta X_{50-i}^2)}{(X_i - X_{50-i})^2 + (Y_i - Y_{50-i})^2} + \frac{(Y_i - Y_{50-i})^2 \cdot (\Delta Y_i^2 + \Delta Y_{50-i}^2)}{(X_i - X_{50-i})^2 + (Y_i - Y_{50-i})^2} \tag{2}$$

$$K = \frac{\sum_{i=1}^{24} \frac{1}{\sigma_i^2} \left(\frac{(X_i - X_{50-i})^2 + (Y_i - Y_{50-i})^2}{(x_i - x_{50-i})^2 + (y_i - y_{50-i})^2} \right)^{1/2}}{\sum_{i=1}^{24} \frac{1}{\sigma_i^2}}$$

The coefficient K and its uncertainty using Keck data were computed in similar way. The rotation angle w of the theoretical coordinate system in the sky projection to align with the observed orbit was determined by calculating the weighted average differences of angles between all selected observable and theoretical chords, separately for each pair of chords using the same weights as for the calculation of K.

$$\Omega_1 - \pi/2 = \frac{\sum_{i=1}^{24} \frac{1}{\sigma_i^2} \left[\arctan\left(\frac{X_i - X_{50-i}}{Y_i - Y_{50-i}} \right) - \arctan\left(\frac{x_i - x_{50-i}}{y_i - y_{50-i}} \right) \right]}{\sum_{i=1}^{24} \frac{1}{\sigma_i^2}} \tag{3}$$

The obtained values of K and Ω_1 for the two variants of chord selection are:
For Keck:
$K^{(1)} = (8.0005 \pm 0.0983) \times 10^{-13}$ mas/m
$\Omega_1^{(1)} = 37°.518 \pm 1°.084$
$K^{(2)} = (8.1070 \pm 0.0811) \times 10^{-13}$ mas/m
$\Omega_1^{(2)} = 39°.436 \pm 1°.084$

For VLT:
$K^{(1)} = (7.9804 \pm 0.0750) \times 10^{-13}$ mas/m
$\Omega_1^{(1)} = 38°.244 \pm 0°.496$
$K^{(2)} = (7.9956 \pm 0.0660) \times 10^{-13}$ mas/m
$\Omega_1^{(2)} = 38°.559 \pm 0°.553$

The upper index corresponds to the chord selection method.

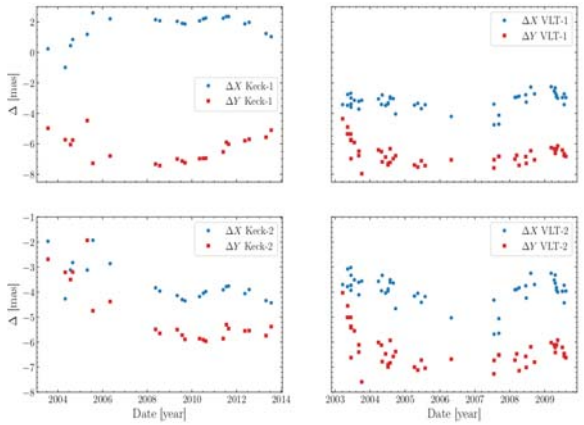

Figure 4 - Difference between observed and theoretical values of the Galactic center coordinates (X,Y) for VLT and Keck using two different sets of orbital parameters

Table 4 - Average values of differences between theoretical and observed coordinates (X,Y) of the Galactic center shown in Figure 4 for Keck and VLT

VLT		KECK	
Δ X(mas)	Δ Y(mas)	Δ X(mas)	Δ Y(mas)
(1) -3.21±0.22	-6.06±1.24	0.11±0.51	-4.65±1.12
(2) -3.37±0.04	-5.82±1.17	0.37±0.95	-3.41±1.71
mean: -3.37±0.04	-5.93±0.85	0.17±45	-4.28±0.94

For each of these set of parameters the differences between the observed (table 2 and table 1) and the theoretical values of the S2 coordinates are found. The results are shown in figure 4, where relatively large differences between theory and observations are seen. These differences cannot be explained by errors in the orbital parameters, because in this case these differences would have had a smooth rather than random appearance. These differences are far greater than the errors in the table 2 and table 1. Most likely, this is due to the uncertain determination of the position of the CB in the images. For the case (2) of Keck data fairly smooth variation of the deviations of the theory from observations is probably related to unaccounted proper motion of astrometric standard with respect to CB. In this case, the time related to the middle of the chords increases monotonically in one direction. The average values of ΔX and ΔY deviations are given in the table 3. Previously, similar values for both telescopes were obtained [14] : ΔX = -3.7±0.6 mas, ΔY = -4.1±0.6 mas. All values are given in milliseconds of arc.

Mean values of parameter K is $(8.018\pm0.039)\times10^{-13}$ mas/m and parameter Ω_1 is 38°.40±0.33°. In this case R = 8333.0±7.0 ps.

Knowing the parameters of the theoretical orbit in the projection onto the sky, it is possible to obtain the coordinates of the star S2 for any moment of time and thus use it as an astrometric standard to determine the position of CB in any image of this region of the sky, for which the scale and time of observation is known. The tabulated coordinates X and Y of the star S2 depending on time are provided online.

The mean square errors of these parameters were found by the Monte Carlo method. The following orbit parameters were obtained: T_p = 2002.3482 ± 0.0009 year, q = (1.74160 ± 0018)×10^{15} cm, $\phi = \gamma$ = 69°.43 ± 0°.24, M = (4034 ± 13)×10^3 $M_\odot$, e = 0.88657 ± 0.00011, ρ = (4.76 ± 1.5)×10^6 $M_\odot$/ps^3 ~ 3.5×10^{-16}g/cm^3, i = 133°.83±0°.067.

3 Conclusions

Among the parameters that determine the movement of stars in the gravitational field of CB, two require special attention. These are the dispersed mass at the center of the Galaxy and the position of the CB in the high angular resolution images. In such images, the background is very heterogeneous and is an overlap of radiation of nebulae that located are not only in the Galactic center but also in front and behind

of it. To accurately account for such a mass, it is necessary to know the its three-dimensional density distribution function which is not known with sufficient accuracy. When searching for the orbital parameters of the star S2 it was found that the addition of a diffuse mass to the parameters determining the motion of this star improves the agreement with the observations. For the simplest case, r_0 is assumed to be a constant. The best value was determined to be $r_0 = (5.2\pm1.5)\times10^6\ M_\odot/ps^3$. The presence of a dispersed mass causes the rotation of the apoapsis relative to the CB. After each revolution around CB there is rotation of the orbit to 0º.755. Full revolution of the orbit is made for 7760 years.

It is known that in IR images the position of CB is difficult to measure accurately. The origin of coordinate system in which the positions of the stars in the IR images are given must coincide with the CB position. Sometimes, other stars are used as astrometric standards to determine the position of CB, which may not have their proper motion known with sufficient precision. As a result, it turns out that the errors of coordinate can be an order of magnitude greater than indicated in the publications. We suggest to use the star S2 as an astrometric standard, the coordinates of which can be calculated with high accuracy or one can use data given in Appendix A. This star is one of the brightest and closest to the CB. It is clear that a similar study of other stars in the region of the center of the Galaxy will allow to obtain more accurate parameters. This requires high-precision observational data obtained over long time intervals.

ACKNOWLEDGMENTS

The work was carried out within the framework of Project No. BR05236322 “Studies of physical processes in extragalactic and galactic objects and their subsystems”, financed by the Ministry of Education and Science of the Republic of Kazakhstan.

Э.К. Денисюк, А.В. Серебрянский

Фесенков атындағы астрофизикалық институт, Алматы, Казақстан

ҒАЛАМНЫҢ ЦЕНТРІНДЕГІ S2≡S0-2 ЖҰЛДЫЗЫНЫҢ ОРБИТАСЫ

Аннотация. Әлемнің алып және массивті объектілері ғаламдар және квазарлар болып табылады. Олардың көбінің центрінде, яғни ядросында аса қуатты барлық толқын аумағында сәуле шығаратын үлкен масса орналасқан. Олардың ішінде болып жатқан физикалық процестерді зерттеу күрделі, себебі бұл объектілерге ара-қашықтық аса үлкен. Ең жақыны біздің Ғаламның ядросы. Бірақ, оны да зерттеудің үлкен қиындықтары бар. Ғаламның центрлік аймағының суретін алуға мыңдаған парсек қашықтық кедергі, тек қана бұрыштық секунттың мыңнан бірін бұрыштық шешу кезінде. Сонымен қатар, Ғаламның центрі тығыз шаң-тозаңды бұлттармен жабылған. Сондықтан, Ғаламның центрін бұлттан асып тек қана спектрдің инфрақызыл (ИҚ) аймағынан бақылай аламыз. Алып телескоптарды қолдану арқылы астрономияда интерферометрді жасау арқылы, өте жоғарғы бұрыштық рұқсатпен қол жетімді. Қабылдағыш ретінде жоғары тиімділіктегі ИҚ матрицалары қолданылады. Осы техникалық құралдардың арқасында Ғаламның центрлік аумағының және басқа да әртүрлі жеке объектілердің суретерін алдық. Центрінде көрінбейтін масситі центрлік дене бар болып шықты. Оның айналасында гравитациялық өрісте ондаған жұлдыздар айналуда. Шамамен 20 жылда осындай жұлдыздардың қозғалысының картасын құрып және көбінің спектрлік талдау әдісімен сәулелік жылдамдықтың уақыт бойынша өзгеру тәуелділігі анықталды. Бақылау мәліметтерінің негізінде центрлік денені (ЦД) сипаттайтын параметрлер, оның гравитациялық өрісінде қозғалатын жұлдыздардың орбиталары анықталды. ЦД жақын орналасқан, S2 жарық жұлдызы көбірек зертелген. Әртүрлі обсерваторияларда алынған нәтижелер, айтарлықтай өзгеше болып шықты. Оның бір себебі, ИҚ аумағында ультражоғарғы бұрыштық рұқсатпен, Ғаламның центрлік аумағының дәл орнын анықтайтын мәліметтердің жоқтығы. Сәулелік жылдамдықтың уақыт бойынша өзгеруі, сейферт ғаламдарының ядроларының гравитациялық өрісінде қозғалатын эмиссиялық объектілердің орбиталарын есептеудің әдісі ФАФИ өңделді. S2 жұлдызы үшін жарияланған бақылау мәліметтерін қолданып, Ғаламның центрлік аймағы үшін осы әдісті қолдану шешілді. Бұл жұлдыздың орбитасы кеплерлік, мүмкін қандайда да бір ауытқулармен.

Сәулелік жылдамдығының бақылау мәліметтерінен басқа ЦД маңындағы жұлдыздардың координаталары және әртүрлі дәуірлердегі бақылаулар жарияланды. Координаталары миллисекунтағы доғамен (ms) берілген. Бақылаулар KEK және VLT телескоптарының көмегімен алынды. Координаталарын анықтау қателігі 1 ms аспады, арықарай талдау жүргізуге осы екі телескоптан алған астрометрлік мәліметтер

қолданылды. ЦД гравитациалық өрісінде сынамалы дене қозғалысының орбитасын құру рекурренттік формула әдісіне негізделген. Орбита жазықтығында дененің жылдамдығын және орынын қандай да бір уақытқа анықтауға болады. S2 жұлдызының барлық орбиталық параметрлерін анықтауға, бақылау мәліметтерімен жақсы сәйкестендіруге және параметрлердің қателіктерін бағалауға мүмкіндік береді. Анықталған бақылау мәліметтері ЦД ден Жерге дейінгі қашықтықты анықтауға мүмкіндік береді. Теориялық координаталарды аспан жазықтығына і бұрышпен проекциялау арқылы табылған және ұзындықтың метрлік бірліктерімен бақылаулардан алынған бұрыштық координаттармен салыстыру үшін ұзындық метрлік бірліктерінен бұрыштыққа K өту коэффициентін табу керек. K параметрінің өлшем бірлігі – ms/м. ЦД ден Күнге дейінгі қашықтық R=6.6845×10-9/K пс өрнығімен анықталады. Бір уақытта екі жұлдыздың аралық бақыланатын бағытының теориялық орбита аспанына проекциясы екеуінің арасындағы қашықтықты бөлу арқылы шешіледі. Ол үшін радиус-векторды қолдансақ онда орталық нүктенің орналасуының белгісіздігі айтарлықтай қателіктерге алып келуі мүмкін, өйткені орталық нүктенің орны, демек, кескіндердегі координаталар жүйесінің центрі дәл анықталмаған. Сондықтан, бұл мақсатта жеке телескоптарға есептелген хорда ұзындығының нәтижелері қолданылды. Жеке нүктелердегі координаталық қателіктерге байланысты K мәні жеткілікті хорданың мәдерінің қатысуымен орташа мән ретінде анықталды.

Орбиталық параметрлердің келесі мәндері табылды: периоды T_p = 2002.3482 ± 0.0009 (жыл), перицентрдегі қашықтық q = (1.7416±0.0018)×10^{15} см, ЦД массасы M = (4034±13)×10^3 $M_\odot$, эксцентриситет e = 0,88657±0,00011, ρ = (4.76±1.5)×10^6 $M\odot/пс^3$ ~3.5×10^{-16} г/$см^3$, орбита көлбеулігі і = 133°.83±0°.067. Сонымен, алынған орбиталық параметрлер ең мүмкін мәндер ретінде қарастырылады. Біздің еспетеулердегі χ^2 минималды шама 0.6969 тең. Анықталған орбиталық парметрлердің орташа мәнді қателіктері Монте-Карло әдісімен табылды. ЦД гравитациялық өрісінде қозғалатын жұлдыздың ρ параметрлердің ішіндегі ерекше көңіл бөлетін параметр. Ғаламның центріндегі шашыраған массаның орташа тығыздығы. Ғаламның тек центріне қатысты емес, артқы және алдыңғы жағындағы газды бұлттардың сәулеленуі және аясы біртексіз бейнеленген. Массаны дәлдікпен есептеуге үш өлшемді тығыздықтың таралуының функциясын білу қажет, бірақ ол белгізіс.S2 жұлдызының орбитасының параметрлерін есептеу кезінде диффузиялық массаның қосылуы бақылаулармен сәйкес келетіндігі анықталды. Қарапайым жағдайда ρ = const деп алуға болады. Ең жақсы сәйкестік ρ = (5.2±1.5)×10^6 $M_\odot/пс^3$ болады. Дисперсиялық массаның болуы ЦД қатысты орбита апоцентрінің айналуына әкеледі. ЦД әрбір айналуынан кейін барлық орбита 0°.755 бұрылады. Орбитаның толық айналуы 7760 жылда болады.

Түйін сөздер: галактика: центр, әдістер; мәліметтерді талдау, жұлдыздар; кинематика және динамика.

Э.К. Денисюк, А.В. Серебрянский

Астрофизический институт им. Фесенкова, Алматы, Казахстан

ОРБИТА ЗВЕЗДЫ S2=S0-2 И ЦЕНТР ГАЛАКТИКИ

Аннотация. Галактики и квазары являются самыми крупными и массивными объектами во Вселенной. В центре большинства из них расположены ядра большой массы – источники мощного излучения во всех диапазонах длин волн. Изучение происходящих там физических процессов затруднено из-за больших расстояний до этих объектов. Наиболее близким является ядро нашей Галактики. Однако и его изучение связано с большими трудностями. Из-за расстояния в тысячи парсек получить изображение центральной области Галактики можно только при угловом разрешении порядка одной тысячной угловой секунды. Кроме того, центр Галактики закрыт плотными пылевыми облаками. Поэтому наблюдать центр Галактики сквозь облака удается только в инфракрасной (ИК) области спектра. Сверхвысокое угловое разрешение, достигается в астрономии путем создания интерферометров с использованием крупнейших телескопов. В качестве приемников при этом используются высокоэффективные ИК матрицы. С помощью этих технических средств удалось получить как снимки центральной области Галактики, так и спектры различных отдельных объектов в этой области. Оказалось, что в гравитационном поле ядра вращаются десятки звезд. Примерно за 20 лет удалось построить карты движения таких звезд и методом спектрального анализа получить для многих из них зависимости изменения лучевых скоростей от времени. В ряде работ на базе этого наблюдательного материала осуществлялись поиски параметров, характеризующих, как центральное тело (ЦТ), так и орбиты звезд, движущихся в его гравитационном поле. Наиболее исследованной является достаточно яркая звезда S2, ближайшая к ЦТ. Оказалось, что результаты этих исследований, полученных на разных обсерваториях, заметно отличаются друг от друга. Одной из причин такого различия является отсутствие данных о точном положение ЦТ на изображениях центральной области Галактики, полученных с ультравысоким угловым разрешением в ИК диапазоне. В АФИФ разработан метод расчета орбит эмиссионных объектов, движущихся в гравитационном поле ядер сейфертовских галактик, по изменению их лучевых скоростей во времени. Было

решено применить этот метод и для области центра Галактики, используя опубликованные наблюдательные данные для звезды S2. Орбита этой звезды должна быть кеплеровской, возможно, с некоторыми отклонениями.

Помимо данных наблюдений лучевых скоростей для различных эпох наблюдений опубликованы и координаты звезды в окрестностях ЦТ. Координаты даются в миллисекундах дуги (ms). Наблюдения в основном были получены с помощью телескопов: KEK и VLT. Для дальнейшего анализа использовались астрометрические данные, полученные на этих двух телескопах, причем были использованы, только те данные, для которых ошибки определения координат не превышали 1 ms. Метод основан на рекуррентных формулах построения орбиты движения пробного тела в гравитационном поле ЦТ. Для любого момента времени можно определить положение и скорость этого тела в плоскости орбиты. Это позволяет найти все орбитальные параметры звезды S2, которые наилучшим образом согласуются с данными наблюдений, и оценить возможные ошибки этих параметров.

Имеющиеся данные наблюдений позволяют найти такой важный параметр как расстояние от Земли до ЦТ. Для сравнения теоретических координат, которые находятся путем проекции теоретической орбиты на плоскость неба под углом i и выраженных в метрических единицах длины, с угловыми координатами, получаемых из наблюдений, необходимо найти коэффициент перехода K от метрических единиц длины к угловым. Размерность параметра K – ms/м. Расстояние от ЦТ до Солнца определяется по формуле $R=6.6845\times10^{-9}/K$ пс. Проблема решается путем деления длины отрезка между двумя положениями звезды в проекции на небо теоретической орбиты на расстояние между двумя наблюдаемыми положениями звезды для одних и тех же моментов времени. Если использовать для этой цели радиус-векторы, то неопределенность положения ЦТ может привести к значительным ошибкам, поскольку положение ЦТ, а, следовательно, и центра координатной системы на изображениях, определяется неточно . Поэтому для этой цели использовались именно длины хорд, вычисленные отдельно по результатам для каждого телескопа. Из-за ошибок координат в отдельных точках величина K определялась как среднее, полученное с привлечением достаточно большого числа хорд.

Найдены следующие значения орбитальных параметров: период T_p = 2002.3482 ± 0.0009 (в годах), расстояние в перицентре q = $(1.7416\pm0.0018)\times10^{15}$ см, масса ЦТ M = $(4034\pm13)\times10^3$ M⊙, эксцентриситет e = 0,88657±0,00011, ρ = $(4.76\pm1.5)\times10^6$ M⊙/пс^3 ~3.5×10^{-16} г/см^3,наклон орбиты i = 133°.83±0°.067.

Полученные таким образом орбитальные параметры могут рассматриваться как наиболее вероятные. Минимальное значение χ^2 в наших расчетах равно 0.6969.Ошибки средних значений найденных параметров орбиты определялись методом Монте-Карло.

Среди параметров, определяющих движение звезды в гравитационном поле ЦТ специального внимания требует параметр ρ. Это средняя плотность рассеянной массы в центре Галактики. На изображениях центра фон очень неоднороден и представляет собой наложение излучения газовых облаков, которые расположены не только в непосредственном центре Галактики, но и впереди и позади него.

Для точного учета такой массы необходимо знать трехмерную функцию распределения плотности, однако она неизвестна. При расчете параметров орбиты звезды S2 было установлено, что добавление диффузной массы улучшает согласие с наблюдениями. Для простейшего случая можно считать ρ = const. Наилучшее согласие достигается при ρ = $(5.2\pm1.5)\times10^6$ M⊙/пс^3. Присутствие дисперсной массы приводит к вращению апоцентра орбиты относительно ЦТ. После каждого оборота вокруг ЦТ вся орбита поворачивается 0°.755. Полный оборот орбиты происходит за 7760 лет.

Определены параметры орбиты звезды S2≡S0-2, которая движется вблизи центра Галактики. Получены оценки массы центрального тела Галактики $(4034\pm13)\times10^3M_\odot$, а также его расстояние от Солнца, 8333.0±7.0 пс. Предложен метод определения положения сверхмассивного тела в центре Галактики с использованием орбитальных параметров звезды S2.

Ключевые слова: галактика: центр, методы; анализ данных, звезды, кинематика и динамика.

Information about authors:

Denissyuk E.K., doctor of Physical and Mathematical Sciences, Fesenkov Astrophysical Institute. eddenis@mail.ru, https://orcid.org/0000-0001-5020-2557;

Serebryanskiy A.V., doctor of Physical and Mathematical Sciences, Fesenkov Astrophysical Institute. aserebryanskiy@yahoo.com, https://orcid.org/0000-0002-4313-7416

REFERENCES

[1] Ghez, A. M., Duchene, G., Matthews, K., et al. (2003) The First Measurement of Spectral Lines in a Short-Period Star Bound to the Galaxy's Central Black Hole: A Paradox of Youth. ApJ, 586L:127-131, 2003. https://doi.org/10.1086/374804.

[2] Schodel, R., Ott, T., Genzel, R. and 3 more (2003) Stellar Dynamics in the Central Arcsecond of Our Galaxy. ApJ, 596:1015-1034, 2003. https://doi.org/ 10.1086/378122.

[3] Eisenhauer, F., Schodel, R., Genzel, R. and 5 more. (2003) A Geometric Determination of the Distance to the Galactic Center.

[4] ApJ, 597: L.121-134, 2003. DOI 10.1086/380188

[5] Gillessen, S.,Eisenhauer, F., Trippe, S. and 4 more (2009) Monitoring Stellar Orbits Around the Massive Black Hole in the Galactic Center. ApJ, 692: 1075-1109, 2009. https://doi.org/ 10.1088/0004-637X/692/2/1075

[6] Ghez, A. M.; Salim, S.; Weinberg, N. N. and 10 more (2008), Measuring Distance and Properties of the Milky Way's Central Supermassive Black Hole with Stellar Orbits. ApJ, 689:1044-1062,2008.. DOI 10.1086/592738

[7] Gillessen, S.; Plewa, P. M.; Eisenhauer, F. and 9 more (2017). An Update on Monitoring Stellar Orbits in the Galactic Center.ApJ, 837:30-49, 2017. DOI 10.3847/1538-4357/aa5c41

[8] Eisenhauer, F., Genzel, R., Alexander, T. and 18 more.(2005). SINFONI in the Galactic Center: Young Stars and Infrared Flares in the Central Light-Month. ApJ, 628:.246-259,2005. DOI:10.1086/430667.

[9] Gillessen, S.,Eisenhauer, F., Fritz, T. K. and 5 more.(2009). The Orbit of the Star S2 Around SGR A* from Very Large Telescope and Keck Data.ApJ, 707:L.114- L117, 2009. DOI 10.1088/0004-637X/707/2/L114.

[10]Boehle, A.; Ghez, A. M.; Schodel, R. and 11 more.(2016). An Improved Distance and Mass Estimate for Sgr A* from a Multistar Orbit Analysis. ApJ, .830: 17-40, 2016. DOI 10.3847/0004-637X/830/1/17.

[11]Denissyuk, E. K., Valiullin, R. R., Gaisina, V. N. (2015). The mass of the central body of the galaxy Ark 120 and the orbits of objects in its gravitational field. ARep., 59: 123-132, 2015. DOI 10.1134/S106377291412004X..

[12]Denissyuk, E. K., Valiullin, R. R., Gaisina, V. N. (2011). The motion of an emission-line region near the center of the galaxy NGC 4151. ARep., 55: 761-770.

[13]Chu D.S., Do T., Aurelien Hees A. et.al. (2018). Investigating the Binarity of S0-2: Implications for Its Origins and Robustness as a Probe of the Laws of Gravity around a Supermassive Black Hole. Ap.J, 863: 111-114, 2018. DOI 10.3847/1538-4357/aad734.

[14]Sabha, N., Eckart, A., Merritt, D. and 11 more. (2012). The S-star cluster at the center of the Milky Way. On the nature of diffuse NIR emission in the inner tenth of a parsec. A&A, 545:70-82, 2012. DOI 10.1051/0004-6361/201219203.

[15]Eckart A., Mužić, K., Yazici, S., et al. (2013) Near-infrared proper motions and spectroscopy of infrared excess sources at the Galactic center//A&A, 551A: 18-49, 2013. https://doi.org/10.1051/0004-6361/201219994.

NEWS
OF THENATIONAL ACADEMY OF SCIENCES OF THE REPUBLIC OF KAZAKHSTAN
PHYSICO-MATHEMATICAL SERIES
ISSN 1991-346X **https://doi.org/10.32014/2020.2518-1726.31**
Volume 3, Number 331 (2020), 15 – 20

UDC 521.1 524.4

T. Panamarev[1], A. Otebay[1,3], B. Shukirgaliyev[1,2], M. Kalambay[1,3], A. Just[5], R. Spurzem[4,5], P. Berczik[4,5,6], Ch. Omarov[1]

[1]Fesenkov Astrophysical Institute, Almaty, Kazakhstan;
[2]Energetic Cosmos Laboratory, Nazarbayev University, Nur-sultan, Kazakhstan;
[3]Faculty of Physics and Technology, Al-Farabi Kazakh National University, Almaty, Kazakhstan;
[4]National Astronomical Observatories and Key Laboratory for Computational Astrophysics, Chinese Academy of Sciences, Beijing, China;
[5]Astronomisches Rechen-Institut am Zentrum fuer Astronomie der Universitaet Heidelberg, Heidelberg, Germany;
[6]Main Astronomical Observatory, National Academy of Sciences of Ukraine, Kyiv, Ukraine.
E-mail: panamarev@aphi.kz, bekdaulet.shukirgaliyev@nu.edu.kz, otebay@aphi.kz, kalambay.mukhagali@kaznu.kz, omarov@aphi.kz

POPULATION OF DOUBLE WHITE DWARFS IN THE GALACTIC CENTER

Abstract. Upcoming space-born gravitational wave interferometers will monitor gravitational radiation at low frequency range. This will allow to study double white dwarf mergers and improve our understanding of physical processes involved. High stellar densities in galactic cores may imply enhanced binary compact object formation and coalescence compared to the galactic field. In this paper we analyze data from direct one-million-body simulation of the Milky Way Galactic center to describe properties of double white dwarf binaries and discuss their contribution to the gravitational radiation. We show that ~7% of all white dwarf - white dwarf pairs are likely to undergo the gravitational wave driven merger resulting in a merger rate of ~ $10^{-7}\mathrm{yr}^{-1}$. Therefore, we show that double white dwarf merger rate in the Galactic center is larger than that in the Galactic field. The obtained results may be used in future studies of white dwarf merger outcomes and their contribution to the gravitational radiation.

Key words: Galactic center, white dwarf binaries, gravitational waves.

1. Introduction.

The Milky Way Galaxy center is comprised of a central supermassive black hole surrounded by a dense cluster of stars (see e.g. [1], for a review). Due to high stellar densities, the Galactic center is a favorable place for frequent close encounters between stars that eventually may lead to the formation of compact binary pairs. Or, initially closely bound binary may undergo a number of encounters with single stars that eventually reduce its semimajor axis (e.g. [2], [3]). These processes may enhance merger rates of double degenerate binaries. In this paper, we focus on white dwarf - white dwarf (WD-WD) binary systems, which are subject to low-frequency gravitational radiation [4][5]. The gravitational wave emission originating from the compact double white dwarf binaries may be detected by future space-borne interferometers such as LISA [6] and TianQin [7]. The merger may result in a Supernova type Ia explosion or in a new WD of heavier mass ([8]; [9]. Thus, studying the spatial distribution of potential merger candidates and the event rates may serve as a necessary step towards understanding complex physical processes involved during double WD coalescence.

In order to do our study, we analyze the central 10 parsec region of the Galaxy at 5 Gyr after the formation time. The data are provided by a recent direct million-body simulation of the Galactic center [3].

2. Overview of the simulation.

The simulation described in [3] features direct N-body methods to model the Milky Way nuclear star cluster (NSC). The authors achieved the highest to-date resolution in particle number for the Galactic center simulations by modeling the entire NSC with one million stars. Such features as accurate treatment of close encounters [10], formation and evolution of binary stars, single and binary stellar evolution [11][12], provide a large step towards increasing physical realism of the simulation. We refer to the original paper [3] for a more detailed description of the initial conditions and the simulation set up.

3. Results

In figure 1 we show the overall distribution of WD-WD binaries from the simulation in the plane of orbital elements a (semi-major axis, in the units of the astronomical unit, AU) and e (eccentricity). As we can see from the figure, the potential mergers -- binaries with small semi-major axes -- have almost circular orbits. The binaries with eccentric orbits have relatively large separations. According to [13] the merger time of the white dwarfs (each of the components has mass of 1 $M_{\odot}$ separated by 10^{10} cm (i.e $\sim 6.7 \times 10^{-4} AU$) is about 3×10^{-4} years. The separation of the order of 1 AU can result in a merger time, which is larger than a Hubble time. Therefore, in this work, we focus on WD-WD binaries with circular orbits as they have small values of the semi-major axis.

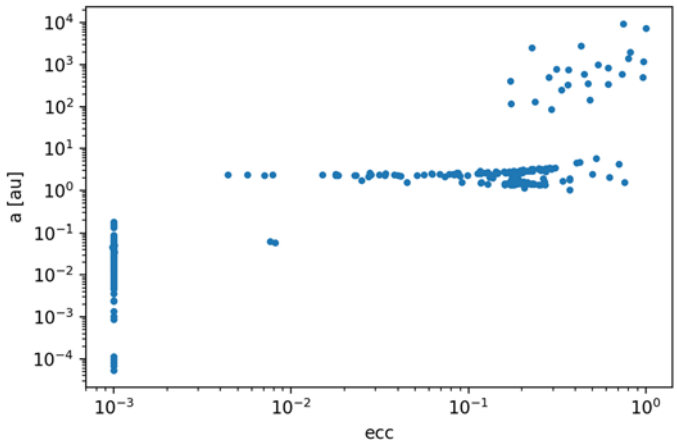

Figure 1 – Distribution of eccentricities and semimajor axis for all double white dwarf (WD-WD) pairs

Figure 2 demonstrates how the WD-WD binaries are distributed spatially within the nuclear cluster in the simulation. Cumulative number distribution of all WD-WD binaries in the cluster and those of them with e = 0 only are shown in blue and orange colors respectively. We can see that about 28% of all double WDs are circular.

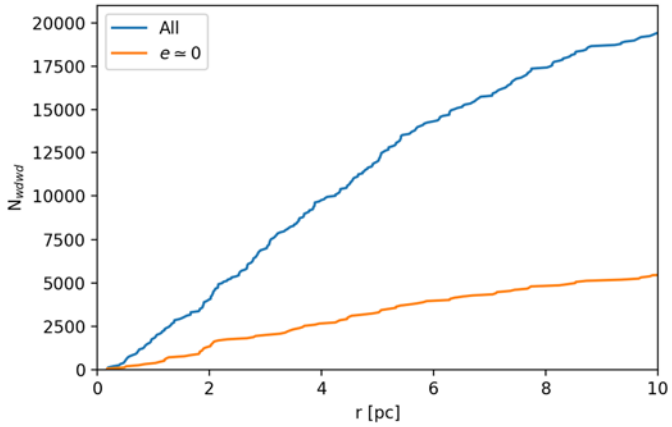

Figure 2 - Cumulative number of WD-WD pairs as function of distance to the supermassive black hole. Blue and orange lines show all pairs and those with small eccentricities

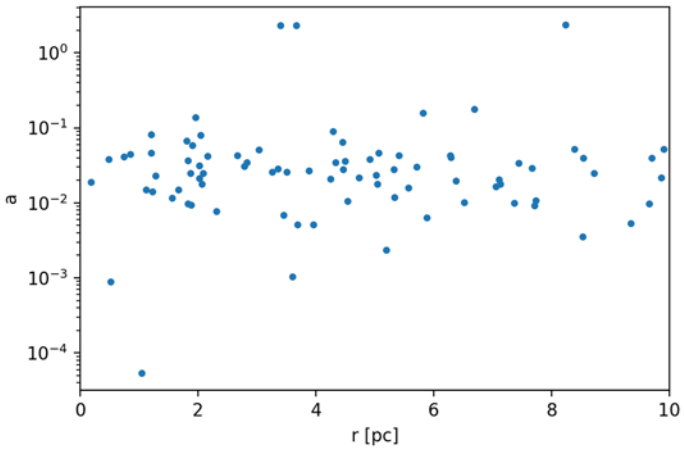

Figure 3 - Distribution of semi-major axes of double WDs (given in AU) as a function of distance from the supermassive black hole (in parsecs)

A more detailed analysis of relative orbital elements of WD-WD pairs shows that there is no clear trend of their semi-major axes with distance from the massive black hole (figure 3).

Now, we follow [13] to compute the time left for these systems to merge due to the gravitational radiation:

$$t_{GW} = \frac{5}{256} \frac{a^4 c^5}{G^3 m_1 m_2 (m_1 + m_2)}, \quad (1)$$

where a is the semi-major axis, c is the speed of light, G is the gravitational constant, m_1 and m_2 are masses of two bodies (in our case white dwarfs). Note that this expression already takes into account that e ~ 0.

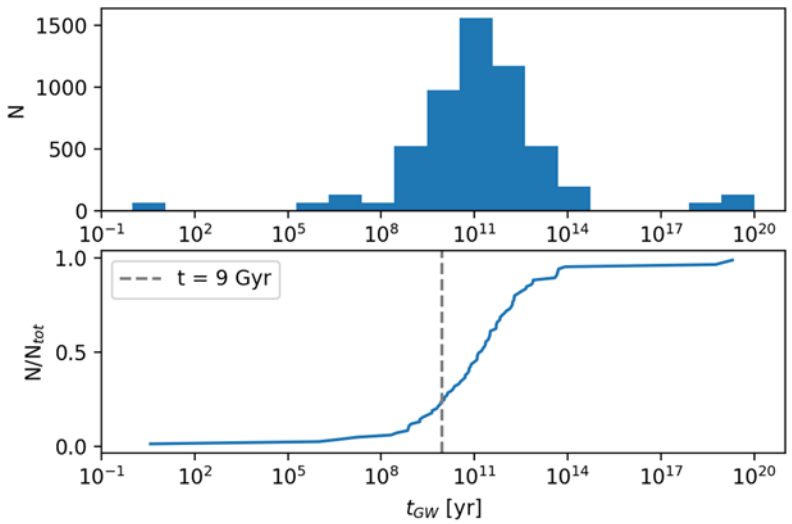

Figure 4 - Top panel. Distribution of time intervals left to merge due to gravitational wave emission for WD-WD pairs with circular orbits. Y-axis shows the total number of pairs in each logarithmic bin. Bottom panel. The same as above, but shows cumulative distribution normalized to the total number of double WD binaries considered in this analysis. Shared X-axis for both panels shows time in years. Vertical dashed line indicates the time of 9 Gyr

The computed time intervals are shown in figure 4. Since we take data at the moment of 5 Gyr after the NSC formation, we check how many binaries merge in ~9 Gyr to select those that merge in a Hubble time after formation. The data yields ~ 24% (~1300 in absolute number) of double WD binaries ending up in coalescence mediated by gravitational emission. Summarizing our findings, we get:

$$N_{merge} = 0.24N_{wd}(e = 0) = 0.24 \times 0.28N_{wd}(all) = 0.067N_{wd}(all), \quad (2)$$

meaning that ~7% of all double white dwarf binaries within 10 pc from the supermassive black hole are likely candidates to undergo gravitational wave driven merger.

We can divide the total number by the time span to get the average rate of these merger events per year:

$$\dot{N} = \frac{N_{merge}}{(t_H - t_0)} = 1.5 \times 10^{-7} yr^{-1}, \quad (3)$$

where t_H is the Hubble time and $t_0 = 5Gyr$.

Thus, our basic calculations predict 1 - 2 events per 10 Myr for the Milky Way Galactic center.

4. Conclusion

We studied the population of double WD binaries in the Galactic center that are likely to undergo gravitational wave driven mergers. We showed that ~7% of all double WDs are good candidates to result in a merger. The obtained number rates imply much higher WD-WD merger rates in the Galaxy center than in the field (see [9], for the latest numbers). Thus, there may be a bigger chance for a simultaneous gravitational wave and electromagnetic observation of a WD merger originating from a galaxy center.

Spatial distribution of double WDs provided by our study may serve as a motivation to conduct more detailed analysis of WD-WD pairs, for example such as computation of gravitational waveforms to account for the background gravitational wave noise detected in LISA range (e.g. [14]).

Acknowledgements

Chingis Omarov, Taras Panamarev and Mukhagali Kalambay gratefully acknowledge the support within MDDIAI-program BR05336383, Bekdaulet Shukirgaliyev gratefully acknowledges the support within grant AP05135753, Aigerim Otebay acknowledges the support within grant AP05134454, all funded by the Ministry of Education and Science of the Republic of Kazakhstan.

Also Bekdaulet Shukirgaliyev, Rainer Spurzem, Andreas Just and Peter Berczik acknowledge the support by the Deutsche Forschungsgemeinschaft (DFG, German Research Foundation) – Project-ID 138713538 – SFB 881 ('The Milky Way System'), by the Volkswagen Foundation under the Trilateral Partnerships grants No. 90411 and 97778. Peter Berczik also acknowledges support by CAS PIFI fellowship and NSFC grant 11673032; NASU special program (CPCEL 6541230).

Т. Панамарев[1], А.Өтебай[1,3], Б. Шукиргалиев[1,2], М. Қаламбай[1,3], А. Юст[5], Р. Шпурцем[4,5], П. Берцик[4,5,6], Ч. Омаров[1]

[1]Фесенков ат. астрофизикалық институты, Алматы, Қазақстан;
[2]Энергетикалық ғарыш зертханасы, Назарбаев Университеті, Нұр-Сұлтан, Қазақстан;
[3]Физика-техникалық факультет, әл-Фараби ат. қазақ ұлттық университеті, Алматы, Қазақстан;
[4]Қытайдың Ұлттық Астрономиялық Обсерваториялары мен Есептеуіш Астрофизика Өзекті Зертханасы, Қытай ғылым академиясы, Бейжің, Қытай;
[5]Астрономиялық есептеу институты, Хайдельберг Университетінің Астрономия орталығы, Хайдельберг, Германия;
[6]Басты Астрономиялық Обсерватория, Украина Ұлттық Ғылым Академиясы, Киев, Украина

ГАЛАКТИКА ОРТАЛЫҒЫНДАҒА ҚОС АҚ ЕРГЕЖЕЙЛІ ЖҰЛДЫЗДАР

Аннотация. Ғарыштық гравитациялық-толқындық интерферометрлер төменгі жиіліктер аймағындағы жұмыс істейді. Ол, жоспар бойынша, гравитациялық сәулеленудің мониторингін жүргізетін болады. Бұл қос ақ ергежейлілердің бірігуін зерттеуге, және бірігу кезінде физикалық үдерістер туралы біздің түсінігімізді жақсартуға мүмкіндік береді. Галактикалық ядролардағы жоғары жұлдызды тығыздықтар ондағы қос шағын объектілердің қалыптасуына және олардың бірігу қарқынын ұлғаюына әкелуі мүмкін. Бұл жұмыста қос ақ ергежейлі жұлдыздардың галактика орталықтарында таралуы, динамикалық қасиеттері және гравитациялық толқын таратуға қосатын үлестері қарастырылған. Құс Жолы галактикасының орталығы жұлдыздардың тығыз шоғырымен қоршалған, орталық аса массивті қара құрдымнан тұрады [1]. Жұлдызды тығыздықтардың

үлкен мәндері жұлдыздардың өзара жақындасуының жиі пайда болуына ықпал етіп, шағын қос объектілердің қалыптасуына алып келуі мүмкін. Егер бастапқыда тығыз байланысқан қос жұлдызды жүйе жалғыз жұлдыздармен бірнеше "соқтығыстар" арқылы өтетін болса, онда энергия алмасу нәтижесінде, олардың өзара қашықтығы айтарлықтай азайуы мүмкін (мысалы [2], [3] қарайық). Жоғарыда сипатталған үдерістер қос жұлдыздардың қосылу ықтималдылығы мен санын арттыруы мүмкін. Осы жұмыста біз ақ ергежейлілерге көп назар аударамыз, себебі олар тығыз жақындасу кезінде гравитациялық сәулелену көзі болып табылады. Және олардың жиіліктік сипаттамалары LISA (6) және TianQin (7) сияқты ғарыштық детекторлардың сезімталдық аймағында жатады. Гравитациялық сәулелену әсерінен қос ақ ергежейлілер энергиясын "жоғалта" бастайды, нәтижесінде қосылу үдерісі орындалады. Қосылудың қалдығы ретінде Ia типтес аса жаңа жұлдыздар немесе массасы жоғары ақ ергежейлілер пайда болуы мүмкін [8][9]. Зерттеу жүргізу үшін, біз аса массалы қара құрдымнан 10 парсек радиустағы галактиканың орталық аймағын таңдап аламыз. Және галактиканың орталық жұлдызды шоғыр қалыптасуына дейін 5 миллиард жыл уақыт кезіннен бастап процесстерді талдаймыз. Бұл зерттеуді іске асыру үшін Құс Жолы Галактикасы орталығының миллион-дене-симуляциясының шығыс мәліметтеріне талдау жасалынды. Барлық қос ақергежейлілердің ~7% гравитациялық толқын тарата бірігуі мүмкін, және бірігу қарқыны шамамен жылына ~ 10^{-7}болатыны бағаланды. Осылайша, біз Галактика ортасында қос ақ ергежейлілердің бірігу қарқыны олардың галактикалық өрістегі қосылу қарқынынан асып тұрғанын көрсеттік. Алынған нәтижелер болашақта қос ақ ергежейлілердің бірігуін және олардың жалпы гравитациялық толқын таратуға қосатын үлесін одан әрі зерттеуге арналған жұмыстарда қолданылуы мүмкін.

Түйін сөздер. Галактика орталығы, қос ақ ергежейлі жұлдыздар, гравитациялық толқындар.

Т. Панамарев[1], А.Отебай[1,3], Б. Шукиргалиев[1,2],
М. Каламбай[1,3], А. Юст[5], Р. Шпурцем[4,5], П. Берцик[4,5,6], Ч. Омаров[1]

[1]Астрофизический Институт им. В.Г. Фесенкова, Алматы, Казахстан;
[2]Энергетическая космическая лаборатория, Назарбаев Университет, Нур-Султан, Казахстан;
[3]Физико-технический факультет, казахский национальный университет
им. аль-Фараби, Алматы, Казахстан;
[4]Национальная астрономическая обсерватория Китая и Ключевая лаборатория,
Вычислительной Астрофизики, Академия наук Китая, Пекин, Китай;
[5]Астрономический вычислительный институт, Центр Астрономии Гейдельбергского Университета,
Гейдельберг, Германия;
[6]Главная Астрономическая Обсерватория, Национальная академия наук Украины, Киев, Украина

ДВОЙНЫЕ БЕЛЫЕ КАРЛИКИ В ЦЕНТРЕ ГАЛАКТИКИ

Аннотация. Запланированные космические гравитационно-волновые интерферометры будут проводить мониторинг гравитационного излучения на низких диапазонах частот. Это позволит изучать слияние двойных белых карликов и улучшить наше понимание протекающих при слиянии физических процессов. Высокие звездные плотности в галактических ядрах могут привести к увеличенному числу формирования двойных компактных объектов и их слияний по сравнению с галактическим полем.

Центр галактики – Млечный Путь – состоит из центральной сверхмассивной черной дыры, окруженной плотным скоплением звезд [1]. Большие значения звездных плотностей способствуют более частому возникновению тесных сближений звезд, которые, в конечном счете, могут привести к формированию компактных двойных объектов. Если же изначально тесно связанная двойная звездная система пройдет через ряд «столкновений» с одиночными звёздами, то в результате энергетического обмена, взаимное расстояние двойной может значительно уменьшиться (см. например [2], [3]). Описанные выше процессы могут увеличить число слияний вырожденных двойных звезд. В настоящей работе мы фокусируем свое внимание на двойных белых карликах, которые, при тесном сближении, являются источником гравитационного излучения, частотные характеристики которого попадают в диапазон чувствительности запланированных космических детекторов, таких как LISA [6] и TianQin [7]. В результате «потери» энергии двойными белыми карликами через гравитационного излучение, происходит слияние, конечным продуктом которого может стать сверхновая тип Ia или более массивный белый карлик [8][9].

Для проведения исследования, мы анализируем центральную область галактики, заключенную в радиусе 10 парсек от сверхмассивной черной дыры в момент времени 5 миллиардов лет от начала формирования центрального звездного скопления галактики. В настоящей работе мы используем данные моделирования центра галактики Млечный Путь, которое было проведено методом прямого интегрирования с использо-

ванием одного миллиона частиц, чтобы исследовать свойства популяции двойных белых карликов и оценить их вклад в гравитационное излучение. Результаты показали, что для ~7% всех пар белый карлик – белый карлик излучение гравитационных волн может привести к слиянию со скоростью ~ 10^{-7} событий в год. Таким образом, скорость слияния двойных белых карликов в центре Галактики превышает их скорость слияния в Галактическом поле. Наши результаты могут быть использованы в дальнейших исследованиях продуктов слияния белых карликов и их вклада в гравитационное излучение.

Ключевые слова: центр Галактики, двойные белые карлики, гравитационные волны.

Information about authors:

Taras Panamarev, Dr.rer.nat, lead researcher at Fesenkov Astrophysical Institute, panamarev@aphi.kz, https://orcid.org/0000-0002-1090-4463;

Otebay Aigerim, M.Sc., junior researcher at Fesenkov Astrophysical Institute, PhD student at Faculty of Physics and Technology, Al-Farabi Kazakh National University, email: otebay@aphi.kz, https://orcid.org/0000-0003-3041-547X;

Shukirgaliyev Bekdaulet, Dr.rer.nat, postdoc, Energetic Cosmos Laboratory, Nazarbayev University and Fesenkov Astrophysical Institute, email: bekdaulet.shukirgaliyev@nu.edu.kz, https://orcid.org/0000-0002-4601-7065;

Kalambay Mukhagali, M.Sc., junior researcher at Fesenkov Astrophysical Institute, PhD student at Faculty of Physics and Technology, Al-Farabi Kazakh National University, email: kalambay.mukhagali@kaznu.kz, https://orcid.org/0000-0002-0570-7270;

Andreas Just, Dr. phil. nat., Prof. Zentrum für Astronomie der Universität Heidelberg, Astronomisches Rechen-Institut. https://orcid.org/0000-0002-5144-9233

Rainer Spurzem, Dr.rer.nat, prof. Zentrum für Astronomie der Universität Heidelberg, Astronomisches Rechen-Institut.

Peter Berczik, Dr.rer.nat, deputy Director of Main Astronomical Observatory, National Academy of Sciences of Ukraine, https://orcid.org/0000-0003-4176-152X

Omarov Chingis, Dr.rer.nat., DirectorFesenkov Astrophysical Institute, omarov@aphi.kz, https://orcid.org/0000-0002-1672-894X

REFERENCES

[1] Genzel R., Eisenhauer F., Gillessen S. (2010) The Galactic Center massive black hole and nuclear star cluster Review of Modern Physisc, Volume 82, Issue 4, pp. 3121-3195.

[2] Hopman C. (2009b) Binary Dynamics Near a Massive Black Hole, The Astrophysical Journal, Volume 700, Issue 2, pp. 1933-1951.

[3] Panamarev T., Just A., Spurzem R., Berczik P., Wang L., Arca Sedda M. (2019) Direct N-body simulation of the Galactic centre, Monthly Notices of the Royal Astronomical Society, Volume 484, Issue 3, p.3279-3290.

[4] Evans C., Iben I. & Smarr L (1987) Degenerate Dwarf Binaries as Promising, Detectable Sources of Gravitational Radiation, Astrophysical Journal Volume 323, P. 129.

[5] Maselli, A.; Marassi, S.; Branchesi, M. (2020) Binary white dwarfs and decihertz gravitational wave observations: From the Hubble constant to supernova astrophysics, Astronomy & Astrophysics, Volume 635, id.A120, 10 pp.

[6] Babak S. et al. (2017), Science with the space-based interferometer LISA. V. Extreme mass-ratio inspirals Physical Review D, Volume 95, Issue 10, id 103012

[7] Luo J. et al. (2016) TianQin: a space-borne gravitational wave detector, Classical and Quantum Gravity, Volume 33, Issue 3, article id. 035010

[8] Wang, B. & Han, Z. (2012) Progenitors of type Ia supernovae, New Astronomy Reviews, Volume 56, Issue 4, p. 122-141.

[9] Cheng S., Cummings J. D., Menard B., Toonen S. (2020) Double White Dwarf Merger Products among High-mass White Dwarfs, The Astrophysical Journal, Volume 891, Issue 2, article id. 160, 7 pp.

[10] Kustaanheimo P., Stiefel E. (1965) Perturbation Theory of Kepler Motion Based on Spinor Regularization, fur Reine Angewandte Mathematik, Volume 218, P. 204.

[11] Hurley J. R., Pols O. R., Tout C. A. (2000) Comprehensive analytic formulae for stellar evolution as a function of mass and metallicity, Monthly Notices of the Royal Astronomical Society, Volume 315, Issue 3, pp. 543-569.

[12] Hurley J. R., Pols O. R., Tout C. A. (2002) Evolution of binary stars and the effect of tides on binary populations Monthly Notices of the Royal Astronomical Society, Volume 329, Issue 4, pp. 897-928.

[13] Peters P. C. (1964) Gravitational Radiation and the Motion of Two Point Masses, Physical Review, vol. 136, Issue 4B, pp. 1224-1232

[14] Robson, T. Cornish,N. J. & Liu C. (2019) The construction and use of LISA sensitivity curves, Classical and Quantum Gravity, Volume 36, Issue 10, article id. 105011

NEWS
OF THENATIONAL ACADEMY OF SCIENCES OF THE REPUBLIC OF KAZAKHSTAN
PHYSICO-MATHEMATICAL SERIES
ISSN 1991-346X **https://doi.org/10.32014/2020.2518-1726.32**
Volume 3, Number 331 (2020), 21 – 25

UDC 524.3-48, 524.3-59, 524.355

Y. K. Aimuratov

Fesenkov Astrophysical Institute, Almaty, Kazakhstan.
E-mail: aimuratov@aphi.kz

GAMMA-RAY BURSTS WITHOUT MEASURED REDSHIFTS I: ENERGY ESTIMATE AND LAT BORESIGHT ANGLE DISTRIBUTION

Abstract. *Context.* With this short note we start a series of communications dedicated to the study of gamma-ray bursts (GRBs) without measured redshifts.

Aims. We make an attempt to estimate energy of GRBs without measured distances based on population of bursts with measured redshift.

Methods. We assume that there is indeed universal bimodal distribution on duration which is followed by all the events. Using data on best-fit spectral parameters from GBM GRB Catalog we calculate energy for each burst given mean redshift values for short/long distribution. Additionally, we cross-correlate GBM GRB Catalog with general GBM Trigger Catalog in order to retrieve information on LAT boresight angle at the moment of event detection.

Results. We obtained estimate energy for each burst and built a distribution plot which follows the idea of bimodal distribution. A scatter plot for LAT boresight angles of short GRBs was obtained.

Conclusions. The energy-based histogram follows a general pattern for short/long distribution having distinct peaks. On the other hand, LAT boresight angles for short events shows quite uniform distribution, and being an instrumental feature, therefore cannot implicitly point to some intrinsic mechanisms responsible for high-energy photons generation.

Keywords: gamma-ray burst; redshift; LAT boresight angle; data analysis.

1. Introduction.

There is essential quantitative information one can calculate knowing the distance to the astrophysical object. Among these values isotropic-equivalent energy is the starting point for inferences in any theoretical model. An estimate of injected energy is crucial information for numerical simulations, especially for modelling the most energetic phenomenon of the universe such as gamma-ray burst (GRB).

The *Fermi Gamma-Ray Space Observatory* (previously GLAST) has detected over two thousand* unique Gamma-Ray Burst (GRB) events during the first decade of operation [1]. Only ~10% of these bursts have measured redshifts therefore making possible a reliable physical interpretation of the processes onsite. Consequently the rest of GRBs do not offer the latter possibility in full though containing spectral information.

The statistics to the date of July 20th 2018 is the following (see **Table 1**): *Fermi*-GBM telescope detected 2367 gamma-ray bursts (100%) among which there are 398 short (16.8%) and 1969 long (83.2%) duration GRBs, both are with and without measured redshift values; out of this total number of bursts the *Fermi*-LAT telescope detected 169 bursts (7.1%) among which there are 14 short and 155 long duration GRBs, both are with and without measured redshift values [2].

* https://heasarc.gsfc.nasa.gov/W3Browse/fermi/fermigbrst.html

Table 1 - GRB detection statistics for all-sky *Fermi*-GBM (8 keV–40 MeV) and *Fermi*-LAT (20 MeV–100 GeV) since the beginning of operational era in July 2008. The first and the last rows correspond to the first [2] and the second [4] LAT catalogs. Percentages in parentheses are related to the total number of bursts by GBM. Numbers were retrieved from online *Fermi*-GBM Burst Catalog and *Fermi*-LAT Burst list.

End time	GBM	$T_{90} < 2$ s	$T_{90} > 2$ s	LAT	$T_{90} < 2$ s	$T_{90} > 2$ s
July 2011	733	122 (16.6%)	611 (83.4%)	35 (4.8%)	5	30
July 2018	2367	398 (16.8%)	1969 (83.2%)	169 (7.1%)	14	155

Within a decade of the *Fermi* operational era there were reported around 30 short GRBs with redshifts measured, among them there is only one GRB 090510 with both measured redshift and GeV photons detected [2]. This means a number of >350 short bursts does not have redshift and roughly same number without GeV photons were observed. As for the long bursts there are more than 200 events with known distances [3].

2. Methods.

In order to estimate energy for GRBs without redshift we take an average value of those short and long bursts with measured redshift. The *secure* median value for the redshift of short GRBs is around unity, while the median redshift value of long bursts is around two [5].

Fixing the redshift at unity (short) and two (long) values we calculate $E_{\rm iso}$ given a spectral model. For every GRB its Flnc_Best_Fitting_Model parameter from GBM catalog indicates the model best fitting the data for a spectrum accumulated over T_{90} duration of the burst [1]. The models used to fit each spectrum are: simple power law (plaw or PL), cutoff power law (comp or CPL), smoothly broken power law (SBPL) and Band function. Depending on model we will have various parameters to consider. The best-fit model is automatically selected by comparison of the values of the likelihood-based Castor C-Statistic (C-STAT). The C-STAT is a modified log-likelihood statistic based on Cash statistic, see [6], and it is used for fitting a model to data set through minimization. The isotropic energy equation has the form:

$$E_{iso} = \frac{4\pi d_L^2}{1+z} S(E_1, E_2, z), \tag{1}$$

where d_L is the luminosity distance and $S(E_1, E_2, z)$ is the fluence accumulated between minimum E_1 and maximum E_2 energy. It is defined by following expression:

$$S(E_1, E_2, z) = T_{90} \int_{E_1/(1+z)}^{E_2/(1+z)} EN(E)dE. \tag{2}$$

Here $N(E)$ defines the best-fit model of the prompt phase spectrum and the integration is done over GBM working energy band. Since GRBs are the cosmological objects then above mentioned luminosity distance will be defined, assuming a flat universe ΛCDM model with Ω_Λ=0.692, Ω_M=0.308, H_0=67.8 km s^{-1} Mpc^{-1} and c=2.998e+10 cm s^{-1}, by following equation [7]:

$$d_L(z, \Omega_\Lambda, \Omega_M) = (1+z)\frac{c}{H_0}\int_0^z \frac{dz\prime}{\sqrt{\Omega_M(1+z')^3+\Omega_\Lambda}}. \tag{3}$$

As can be seen the redshift stays as only unknown parameter. The calculated values of $E_{\rm iso}^{z=1}$ and $E_{\rm iso}^{z=2}$ are shown on **Figure 1** and listed in **Table 2** of the next section.

Another issue to consider for future studies is a boresight angle of the LAT instrument at the moment of GBM trigger. This angle defines the sensitivity of LAT and simply represents itself a viewing angle outside of which no observation is possible. Given orientation coordinates two instruments can calculate mutual directions and when burst location defined by GBM the LAT normal angle is calculated with respect to that pointing and stored in GBM Trigger Catalog. We scan throughout (in order of priority) the *Fermi LAT Second GRB Catalog*,[†] the *Fermi GBM Trigger Catalog*[‡] and GCN archive[§] looking for the LAT boresight angle with regard to the best location of every burst.

[†] https://heasarc.gsfc.nasa.gov/W3Browse/all/fermilgrb.html
[‡] https://heasarc.gsfc.nasa.gov/W3Browse/fermi/fermigtrig.html
[§] https://gcn.gsfc.nasa.gov/

3. Results. We obtained estimate energy for each burst and built a distribution plot which follows the idea of bimodal distribution.

Table 2 lists all short GRBs observed within a decade of GBM operation and columns indicate: burst full name, duration (in seconds), rest-frame spectral peak energy calculated at z=1.0 (in keV), isotropic-equivalent energy calculated at z=1.0 (in erg, rest-frame by definition), and LAT boresight angle at the GBM trigger (in degrees). Although not listed here, a similar table is obtained for long (T_{90} >2 s) duration GRBs, and both tables in full are available upon request.

Table 2 - List of 398 short (T_{90} <2 s) GRBs within August 2008–July 2018 detected by *Fermi*-GBM with estimated isotropic-equivalent energy E_{iso} when given z=1.0 as an average redshift for short bursts. Since the table is large in size we show here only the first and the last three rows. Full table is available upon request

GRB name	T_{90} (s)	$E_{peak}^{z=1}$ (keV)	$E_{iso}^{z=1}$ (erg)	θ (degrees)
080723913	0.192	641.679	6.70615e+50	—
080725541	0.96	2965.18	4.87635e+51	—
080802386	0.576	1244.78	4.81246e+51	—
…	…	…	…	…
180703949	1.536	273.749	4.60329e+52	32
180715741	1.664	1121.59	8.24943e+51	79
180715755	0.704	1804.56	8.58977e+51	75

We built an energy-based histogram for two populations of 1800 long and 363 short GRBs on figure 1. The median values are 2.16e+51 erg (short) and 4.61e+52 erg (long), and two distinct peaks are easily observed.

Regarding the LAT boresight angles there are 363 short GRBs with known θ at the trigger (for 35S-GRB there is no angle information, see table 3), of which 210 bursts were detected at θ <75 degrees, number of 6 short GRBs were triggered at θ =75 degrees and events in amount of 147 were detected at θ >75 degrees.

Table 3 - Distribution of short GRBs with regard to LAT boresight angle.

Total S-GRBs	θ<75 degrees	θ=75 degrees	θ>75 degrees	no θ
398	210	6	147	35

A scatter plot for LAT boresight angles of short GRBs was obtained on figure 2. Labeled red points indicate S-GRBs from the Second LAT Catalog [2]. Note that a large offset of S-GRB 170127067 still had high-energy emission at late repointing. The histogram shows the same distribution stacked in 30 bins.

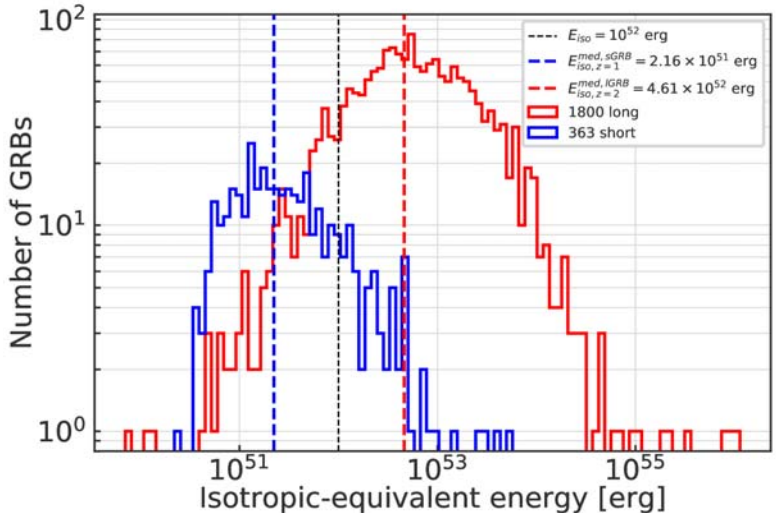

Figure 1 - Histogram of isotropic-equivalent energy for 363 short and 1800 long GRBs for a decade of *Fermi* mission. The values of energy are calculated by assuming average redshifts for short (z=1.0, solid blue) and long (z=2.0, solid red) bursts. Dashed black line indicates E_{iso}=1e52 erg energy. Dashed blue and red lines indicate median energy values

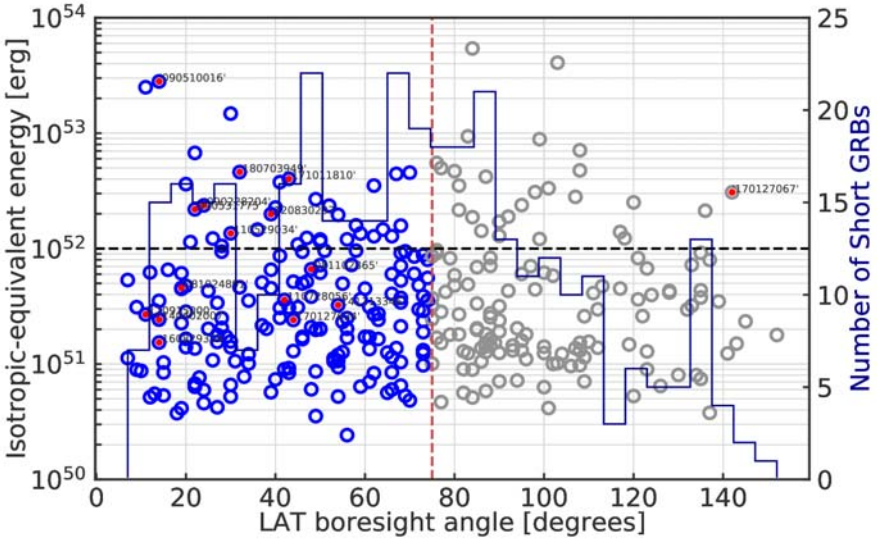

Figure 2 - Distribution of 363 short GRBs by LAT boresight angle and isotropic-equivalent energy calculated under assumption of common z=1. Vertical dashed lines indicates θ =75 degrees threshold angle for LAT instrument, horizontal dashed line indicates E_{iso}=1e52 erg energy

4. Discussion. The energy-based histogram follows a general pattern for short/long distribution having distinct peaks. These two populations when put on E_{peak}-E_{iso} plane stays in accordance with spectral energy correlation for short [9] and long [10] GRBs. The prospect of further detailed study is possible due to the presence of redshift measured bursts [Aimuratov et al. (2020) in *Proceedings of the Fifteenth Marcel Grossmann Meeting*, submitted].

On the other hand, LAT boresight angles for short events shows quite uniform distribution, and being an instrumental feature, therefore, it cannot implicitly point to some intrinsic mechanisms responsible for high-energy photons generation. An outlier GRB 170127C detected ~300 s after GBM trigger [8] is one of the clear examples for prolonged GeV emission of still unknown nature. This implies

5. Acknowledgements. This article is dedicated to Dr. Larissa Andreevna Pavlova and Dr. Boris Ivanovich Demchenko. The work was done with partial support from research grants/programs BR05236322 from MES RK and BR05336383 from AC MDDIAI RK. Author additionally thanks research grant AP05133630 for partial support.

Е. К. Аймуратов

В. Г. Фесенков атындағы астрофизика институты, Алматы, Қазақстан

ҚЫЗЫЛ ЫҒЫСУЫ ӨЛШЕНБЕГЕН ГАММА-СӘУЛЕЛЕНУ ЖАРҚЫЛДАРЫ I: ЭНЕРГИЯНЫ БАҒАЛАУ ЖӘНЕ LAT КӨРУ БҰРЫШТАРЫНЫҢ ҮЛЕСТІРІМІ

Аннотация. *Мәнмәтіні.* Осы қысқаша хабарламамен біз қызыл ығысуы өлшенбеген гамма-сәулелену жарқылдарына (ГСЖ) арналған зерттеулер туралы мақалалар сериясын бастаймыз.

Мақсаты. Біз қызыл ығысуы өлшенген жарқылдар жиынтығына сүйеніп, қашықтығы өлшенбеген ГСЖ популяциясының энергия өлшемін бағалауға әрекет жасаймыз.

Әдісі. Біз барлық оқиғалар расында әмбебап бимодалдық үлестіріміне сай болады деп негіздейміз. GBM GRB каталогындағы әр оқиғаға ең жақсы сәйкес келетін спектрлік параметрлер туралы мәліметтерді және қызыл ығысуы өлшенген қысқа/ұзақ уақытты оқиғалар үшін берілген орташа мәндерді қолдана отырып, біз энергияны есептейміз. Сонымен қатар біз оқиғаларды анықтаған сәтте LAT инструментінің көру бұрышы туралы ақпарат алу үшін GBM GRB каталогын GRB Trigger Catalog жалпы каталогымен өзара салыстырамыз.

Нәтижелері. Біз әр ГСЖ-ның энергиясын есептеп алдық және нәтижесінде бимодалды үлестірім идеясына сәйкес келетін алаңын алдық. Қысқа уақытты оқиғалардың LAT көру бұрыштары үшін шашырау сюжеті алынды.

Қорытындысы. Энергияға негізделген гистограмма нақты шыңдары барын көрсете отырып, қысқа/ұзақ уақытты оқиғалардың үлестіріміне сай жалпы үлгісін ұстанады. Екінші жағынан, қысқа оқиғаларға арналған

LAT көру бұрыштары біркелкі таралуды көрсетеді және инструменталды сипат болып табылады, сондықтан жоғары энергиялы фотондардың пайда болуына жауап беретін кейбір ішкі механизмдерді нақты көрсете алмайды.

Түйін сөздер: гамма-сәулелену жарқылы; қызыл ығысуы; LAT көру бұрышы; деректерді талдау.

Е. К. Аймуратов

Астрофизический институт имени В. Г. Фесенкова, Алматы, Казахстан

ГАММА-ВСПЛЕСКИ БЕЗ ИЗМЕРЕННЫХ КРАСНЫХ СМЕЩЕНИЙ I: ОЦЕНКА ЭНЕРГИЙ И РАСПРЕДЕЛЕНИЕ УГЛОВ ПРИЦЕЛИВАНИЯ LAT

Аннотация. *Контекст.* С этой короткой заметки мы начинаем серию сообщений, посвященных изучению гамма-всплесков (ГВ) без измеренных красных смещений.

Цели. Мы предпринимаем попытку оценить энергию ГВ без измеренных расстояний на основе совокупности всплесков с измеренным красным смещением.

Методы. Мы предполагаем, что, действительно, существует универсальное бимодальное распределение по продолжительности, которому следуют все события. Используя данные о спектральных параметрах из каталога GBM GRB для наиболее подходящих моделей, мы вычисляем изотропную энергию для каждого всплеска, учитывая средние значения красного смещения для распределения коротких/длинных событий. Кроме того, мы производим взаимную корреляцию каталога GBM GRB с общим каталогом GBM Trigger Catalog для получения информации об угле прицеливания LAT в момент обнаружения события.

Результаты. Мы получили оценку энергии для каждого всплеска и построили график распределения, который следует идее бимодального распределения. Получен график распределения углов прицеливания LAT для коротких GRB.

Заключения. Гистограмма по энергиям ГВ следует общей схеме распределения по коротким/длинным событиям, показывая два отчетливых пика. С другой стороны, углы прицеливания LAT для коротких ГВ показывают довольно равномерное распределение, и, являясь инструментальной особенностью, не могут неявно указывать на какие-либо внутренние механизмы, ответственные за образование фотонов высоких энергий.

Ключевые слова: гамма-всплеск; красное смещение; угол прицеливания LAT; анализ данных.

Information about author:

Yerlan Kairatovich Aimuratov, a PhD in Relativistic Astrophysics, Junior Research Associate at the Laboratory of Stars and Nebulae Physics, Department of Observational Astronomy, Fesenkov Astrophysical Institute. Address: Observatory 23, Kamenskoye Plateau, Medeu District, 050020 Almaty, Kazakhstan. aimuratov@aphi.kz, https://orcid.org/0000-0001-5717-6523

REFERENCES

[1] von Kienlin A. et al. (2020) The Fourth Fermi-GBM Gamma-Ray Burst Catalog: A Decade of Data // ASTROPHYS J, 893:46. https://doi.org/10.3847/1538-4357/ab7a18

[2] Ajello M. et al. (2019) A Decade of Gamma-Ray Bursts Observed by Fermi-LAT: The Second GRB Catalog // ASTROPHYS J, 878:52. https://doi.org/10.3847/1538-4357/ab1d4e

[3] Zhang Z. B. et al. (2018) Spectrum-Energy Correlations in GRBs: Update, Reliability, and the Long/Short Dichotomy // PUBLICATIONS OF THE ASTRONOMICAL SOCIETY OF THE PACIFIC, **130**:054202. https://doi.org/10.1088/1538-3873/aaa6af

[4] Ackermann M. et al. (2013) The First Fermi-LAT Gamma-Ray Burst Catalog // ASTROPHYS J SUPPL S, 209:11. https://doi.org/10.1088/0067-0049/209/1/11

[5] Berger E. (2014) Short-Duration Gamma-Ray Bursts // ANNUAL REVIEW OF ASTRONOMY AND ASTROPHYSICS, **52**:43. https://doi.org/10.1146/annurev-astro-081913-035926

[6] Cash W. (1979) Parameter Estimation in Astronomy through Application of the Likelihood Ratio // ASTROPHYS J, 228:939.

[7] Weinberg S. (1972) Gravitation and Cosmology: Principles and Applications of the General Theory of Relativity. Weinheim: Wiley-VCH, 688. ISBN: 978-0-471-92567-5

[8] Moretti E. et al. (2017) GRB 170127C: Fermi-LAT detection // GCN Circular Archive #20544.

[9] Zhang Z. B. et al. (2018) Spectrum-Energy Correlations in GRBs: Update, Reliability, and the Long/Short Dichotomy // PUBLICATIONS OF THE ASTRONOMICAL SOCIETY OF THE PACIFIC, **130**:054202. https://doi.org/10.1088/1538-3873/aaa6af

[10] Amati L. et al. (2019) Addressing the Circularity Problem in the Ep-Eiso Correlation of Gamma-Ray Bursts // MONTHLY NOTICES OF THE ROYAL ASTRONOMICAL SOCIETY LETTERS, **486**:L46. https://doi.org/10.1093/mnrasl/slz056

NEWS
OF THENATIONAL ACADEMY OF SCIENCES OF THE REPUBLIC OF KAZAKHSTAN
PHYSICO-MATHEMATICAL SERIES
ISSN 1991-346X **https://doi.org/10.32014/2020.2518-1726.33**
Volume 3, Number 331 (2020), 26 – 33

UDC 523.45

V.D. Vdovichenko, A.M. Karimov, G.A. Kirienko, P.G. Lysenko
V.G. Teifel, V.A. Filippov, G.A. Kharitonova, A.P. Hogenez

V.G. Fesenkov Astrophysical Institute (FAI) NA of Sci RK, Almaty, Kazakhstan.
E-mail: vdv1942@mail.ru , karalik0@yandex.ru , gak39@mail.ru,lyssenko_petr@mail.ru, teif@mail.ru, filipp.va@mail.ru, gah38@mail.ru, hogenez@gmail.ru

MOLECULAR ABSORPTION BANDS IN JUPITER TROPOSPHERE RESEARCH

Abstract. Based on spectrophotometric observations of Jupiter, made since 2004, some features of the behavior of the methane and ammonia absorption bands on the planet's disk, are discussed. In the meridional course of the observed variations in the equivalent widths of both ammonia and methane in the 6000A - 8000A spectral range, there are both similar elements and differences. Variations in the equivalent widths of ammonia absorption bands at 6450 Å and 7870A show a decrease in absorption in the low and moderate latitudes of the northern hemisphere. In the 7870 Å band, compared to the 6450 Å band, the ammonia absorption depression in the region of the Northern Equatorial Belt is narrower in latitudes and some more deeper. With similar latitudinal variations in methane absorption, systematic differences are observed in the position of extrema for different bands of ammonia and methane. The importance of studying the behavior of absorption bands for optical probing of the troposphere of Jupiter is noted. The alternatives of the model of the troposphere structure and ammonia cloud on Jupiter are discussed. The first model assumes the existence of a geometrically and optically thick ammonia cloud layer. In this layer, the formation of the observed molecular absorption bands in the process of multiple scattering mainly occurs. An alternative model assumes the presence of a geometrically and optically thin layer of ammonia clouds. The bulk of the molecular absorption in this case is created in the troposphere between the cloud layers of ammonia and ammonium hydrosulfide. The need for further research in this direction is noted. One of the important results, so far preliminary, was the differences we found in the latitudinal position of the extremes of the intensities of the molecular absorption bands on Jupiter. This feature is most likely due to the difference in the conditions of formation of different absorption bands in the ammonia cloud layer and the underlying troposphere. The complexity and ambiguity of the mechanism of formation of molecular absorption bands requires further consideration of both various models of the structure of the Jovian atmosphere and further detailed spectral observations of Jupiter, with particular emphasis on the study of weak and moderate absorption bands, which we would like to draw attention to in this publication

Keywords: Jupiter, atmosphere, troposphere, spectrophotometry, ammonia, methane, ammonium hydrosulfide, molecular absorption bands.

Introduction. Along with many unsolved problems associated with the study of Jupiter, one of the main problems is the structure and dynamics of its atmosphere, including the nature and structure of cloud layers located in the troposphere of the planet. Of particular importance in this regard is the study of ammonia, which is one of the small but important components of the atmosphere of Jupiter. Ammonia is one of the cloud-forming substances in the troposphere of Jupiter, and, like methane, plays an important role in the transfer and release of thermal radiation in the infrared and microwave spectral regions. In the process of research of Jupiter atmosphere, study of the behavior of the methane and ammonia molecular absorption bands, observed in the visible and near infrared spectral regions of 5000–9000 Å, becomes necessary. Weak and moderate ones of them can form in the relatively deep layers of the Jovian troposphere, and their observed variations can carry information about local differences in atmospheric structures, including the structure of the planet’s cloud cover. The formation of these bands is rather

complicated, and therefore, the interpretation of observational data requires both model calculations and laboratory studies. Studies of the methane and ammonia absorption bands behavior in different regions of the Jovian disk have been repeatedly considered by some authors, for example, [1-3] for the purpose of using the above bands as a probe of local vertical transparency in the line of sight. It is from these positions that an approach is needed to further study the behavior of molecular absorption, both in the visible spectrum and in the ranges of thermal infrared and radio emission. But it is precisely the visible and nearest infrared region of the spectrum that makes it possible to study the Jovian troposphere based on measurements of the incident and diffusely reflected solar radiation.

Laboratory ammonia and methane spectra

Quantitative estimates of the gas content in the planetary atmosphere require knowledge of the characteristics of the absorbing properties of the molecules of these gases obtained in laboratory studies. Unfortunately, there are not so many laboratory studies of the methane and ammonia absorption bands located in the visible spectrum. Of interest to us are those works that were performed with spectral resolution close to what we used when observing Jupiter. First of all, we mean the works {4-6].

In [1], laboratory profiles of the 5520 Å and 6450 Å ammonia absorption bands, and the growth curves for them, are presented. The growth curve of the 6450 Å NH3 band is important for us. The growth curve is a dependence of the absorption band intensity (equivalent width) on the equivalent thickness or optical path of the absorbing gas, expressed in units of m –amagat. Thus, entering the growth curve with the equivalent absorption band widths observed in the Jupiter spectrum, we can determine the equivalent absorption path in these units. However, we note that this is not equal to the gas abundance in the atmosphere because of the above complex mechanism of absorption bands formation in the gas-aerosol atmosphere of Jupiter.

Similar coefficients for the growth curve of the methane CH4 6190 A absorption band are given in [1]. Weak and moderate absorption bands in the spectrum of Jupiter fall on the linear part of the growth curves, in contrast to strong saturated bands. Due to this, for the NH_3 6450 Å band, we have a ratio of equivalent width and equivalent thickness as 1A per 4 m-amagat, and for 6190 A methane band 1A of equivalent width corresponds to 22 m-amagat of equivalent gaseous thickness. Unfortunately, for other absorption bands, it was not possible to find growth curves in the literature. The study of ammonia absorption in the visible spectral region is described in [7,8] as well as in recent publications [9,10].

Jupiter spectral absorption bands

As noted above, our studies of ammonia absorption on Jupiter were launched in 2004 along with ongoing studies of methane absorption bands. Annual observations are carried out according to a single method and cover more than one period of Jupiter's revolution around the Sun, which is 12 years. The previous results of observations, as well as the methods for their obtaining, are described in a number of our publications, including [11-14]. Most of the observations obtained, were used to study latitudinal variations in ammonia absorption from spectrograms of the central meridian of Jupiter. In addition, we used zonal spectra obtained by scanning the Jovian disk from the south pole to the north one with the spectrograph slit oriented parallel to the equator of the planet. Such measurements give a complete picture of the meridional course of ammonia absorption and the first results were published in 2005 in [15]. Then we drew attention to the presence of a pronounced depression in the intensity of the 7870Å NH3 absorption band in the region of the Northern Equatorial Belt (NEB) on Jupiter.

Figure 1 shows a sample of the Jupiter spectrum with absorption bands of methane and ammonia after dividing by the reference Ganymede spectrum. Particular attention is paid to the study of two weak absorption bands of ammonia on the disk of Jupiter.

Both NH3 6450 Å and NH3 7870 Å bands have relatively low intensity, especially the NH3 6450 Å band. Its equivalent width averages from 5 to 7 Å and the depth at the maximum absorption does not exceed 0.10. The equivalent width of the 7870 Å NH3 band reaches 16–18 Å and its central depth is about 0.2. Note, that earlier, some measurements of the NH3 6450 Å absorption band in some latitudinal belts of Jupiter were described by other authors in [1,16,17].

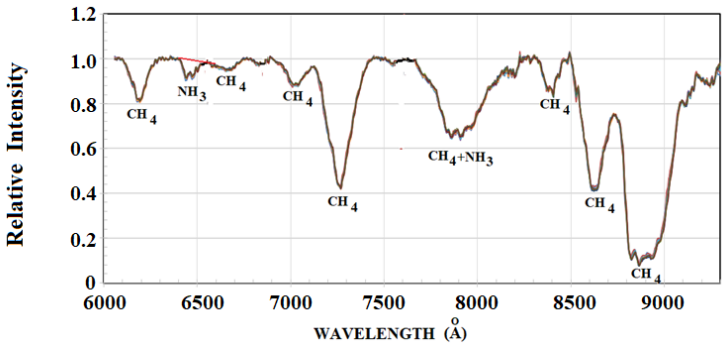

Figure 1 - Jupiter spectrum with absorption bands of methane and ammonia in the wavelength range of 6000 - 9500 Å (SGS spectrograph 4.3 A / pixel).

Table 1 shows these data, as well as our results as the averaged equivalent widths for 2005–2015 years, indicating standard deviations (s_W). In addition, the second column provides the results of observations in 2018 for comparison. The measurements of the same ammonia absorption band in the central part of the Jovian disk and its longitudinal variations are described in [18]. The same authors [19] studied the temporal variations in ammonia absorption for 1979 and 1980.

Table 1 - Equivalent widths of the 6450 Å NH3 absorption band

Region	Year 2018	Tejfel 2018 [12]		Moreno et al. 1988 [14]	Luts, Owen 1980 [2]	
	W(A)	W(A)	sW	W(A)	W(cm-1)	W(A)
SPR	4.2			5.6		
STB	5.1			5.7		
STrZ	5.7	5.92	0.49	7.8	26.4	11.00
SEB	6.0	6.78	0.45	9.8	30.9	12.90
EZ	6.2	6.75	0.32	7.7	23.1-33.0	9.6-13.8
NEB	5.5	6.35	0.35	4.9	20.1	8.30
NTrZ	4.4	5.38	0.36			
NTB	4.7			5.7		
NPR	4.6			7.2		
GRS	4.7				22.2	9.3

The equivalent width in these works was found to be 6 ± 1 Å, which almost coincides with our estimates. Noticeable differences in the estimates of the equivalent width occur in [1 and 16]. And this is true despite the fact that the general nature of the differences in latitudinal belts is similar across all observations. The overall difference in absolute values, as the authors of [1 and 16] correctly point out, is most likely connected with the methodology for conducting the level of the continuous spectrum. The fact is that the 6450 Å NH3 band is superimposed on the short-wavelength wing of the more intense methane absorption band of CH4 6750 Å. Although the residual intensity in this wing is very small, it is still necessary to take it into account when isolating the profile of the ammonia band.

The situation with the separation of the 7870 Å NH3 absorption band is more complicated, since it falls into the center of the more powerful methane band CH4 of 7900 Å. The only way to isolate ammonia absorption is to calculate the ratio of the spectrum of Jupiter to the spectrum of the center of the disk of Saturn, in which ammonia absorption is practically imperceptible. The spectrum of Saturn's disk center was used as a standard for processing all spectrograms. For all other methane and ammonia absorption bands the spectrum of the Saturn ring or the Ganymede spectrum was used as a reference spectrum. An additional control was provided by measurements of the equivalent width of the 7600 Å O_2 (oxygen) telluric absorption band on the spectrograms of the central meridian of Jupiter. The constancy of its value over the entire spectrogram width testified to the reality of the latitudinal variations of the Jupiter absorption bands obtained.

As an example, Fig. 2 shows the results of measurements of the equivalent widths of two ammonia absorption bands and three methane absorption bands in 2017, 2018, and 2019. For ease of comparison and preservation of scale, all values of equivalent widths are normalized to the corresponding values of equivalent widths of each band in the equatorial zone. The graph for 2018 additionally shows the relative course of the equivalent width of the 8870 Å methane absorption band.

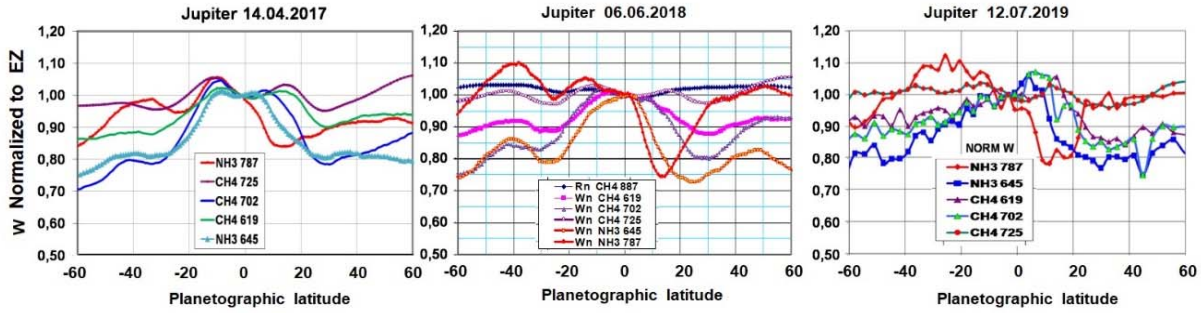

Figure 2 - Relative latitudinal changes in the equivalent widths of the absorption bands of ammonia and methane according to observations in 2017 - 2019

In the meridional course of the observed variations in the equivalent widths of both ammonia and methane in the spectral range of 6000 Å - 8000 Å, there are both similar elements and differences. Variations in the equivalent widths of both methane at 6190 Å and 7020 Å, and ammonia at 6450 Å show a decrease in absorption in the temperate latitudes of the northern hemisphere. Given that methane does not condense and is considered uniformly mixed, this fact most likely indicates local differences in the density and vertical structure of ammonia clouds in the northern and southern hemispheres. In figure 2, one can see that the relative variations in the ammonia band of 7870 Å NH3 compared to the 6450 Å NH3 band are more pronounced and noticeable differences in the latitudinal course at these bands at high latitudes, especially in the northern hemisphere. This feature persists for many years, like the depression in ammonia absorption in the region between EZ and NEB. The maximum ammonia absorption occurs in the temperate latitudes of the southern hemisphere.

The observed difference in the latitudinal position of the extrema of the absorption in different bands deserves special attention and further studies. Similar features of latitudinal shifts of the extrema of the intensities of different methane absorption bands, which are systematic in nature, for all longitudes on Jupiter were discovered and presented earlier in [20], so the reality of such features is not in doubt.

Discussion. As noted above, the observed variations in the molecular absorption bands should be considered as evidence of the presence of zonal and local inhomogeneities in the structure of that part of the Jovian troposphere that is involved in the formation of these bands. As extreme cases, two alternative models can be called. The first assumes the existence of a geometrically and optically thick ammonia cloud layer. Through this layer, deeper into the atmosphere, only part of the scattered radiation can penetrate, while direct sunlight does not pass through this layer. In this case, the theory of radiation transfer can consider this layer as semi-infinite (in the accepted terminology). Almost all of the observed absorption in weak and moderate molecular bands is formed in the process of multiple scattering inside this cloud medium. A small fraction of the absorption of methane bands can be created in the atmospheric layer above clouds, while the concentration of ammonia above the cloud layer decreases sharply, by several orders of magnitude. In this model, the observed absorption variations can be associated with variations in the concentration and volume scattering coefficient of cloud particles and some other factors affecting the effective absorption path. This pathway is estimated from the intensity of the absorption bands and cannot be considered as an estimate of the relative abundance of the absorbing gas in the troposphere.

In an alternative model, it is assumed that the ammonia cloud layer has a relatively small geometric thickness and passes a significant part of direct solar radiation into the atmosphere. In this case, direct sunlight at least reaches a deeper cloud layer. According to most models of the atmosphere of Jupiter, such a layer is a layer of ammonium hydrosulfide NH4SH. This substance has a significant color, but its albedo is not yet known. If it is not too close to zero, then some of the sunlight diffusely reflected by this layer

can go outside. In this case, the intensity of the observed absorption bands will be determined by the double passage through the gas layer located between the two cloud layers. With a very dark substrate of ammonium hydrosulfide, we could not observe absorption in a pure gas. In this case, the presence of scattering particles inside this layer is required.

Even these two idealized models indicate the complexity of the formation of molecular absorption bands observed in the visible and near infrared spectra of Jupiter. In the more distant region of thermal infrared and microwave radio emission, the picture is completely different, since the aerosol component is transparent for these radiations. Zonal and local brightness temperatures of the emitted heat radiation are determined by other factors, as discussed in a number of works carried out for many years under the direction of Glenn Orton (Jet Propulsion Laboratory, California Institute of Technology, Pasadena) and Imke de Pater (University of California, Berkeley). As an example, we note their recent publications [21-24].

The three cloud model of Jupiter's troposphere is considered by many authors, starting with the publication [3,25]. We examined a number of such published models, differing mainly in the accepted initial values of the contents of condensing gases. Estimates of the maximum concentration of particles in the ammonia cloud layer in these models, as a rule, refer to the base of the cloud layer and range from $1 \cdot 10^{-6}$ g / cm^3 [26] to $7 \cdot 10^{-6}$ g / cm^3 [27]. In all models, cloud density decreases with height, but the total thickness of the aerosol layer can be 10 km or more. However, it should be noted that the horizontal and vertical scales of the details of the cloud cover of Jupiter are incommensurable, since even the smallest details which are distinguishable in the best pictures of the planet, have a horizontal length of 1000 or more kilometers. Therefore, significant local variations in the thickness and density of the ammonia cloud layer are quite possible. Regarding presence of a scattering medium in the space between the ammonia and hydrosulfide cloud layers, so far we can only refer to a unique experiment on direct sounding of the atmosphere of Jupiter by a descent vehicle in the Galileo Jupiter Mission [28] project. Although it is believed that the probe fell into a not quite typical region of the planet. Judging by the probe nephelometer, there is a slightly dense aerosol haze rising above the cloud layer of ammonium hydrosulfide.

Based on laboratory growth curves for the absorption bands of ammonia 6450 Å and methane 6190 Å, which were mentioned above, one can show that when these bands are formed inside the inter-cloud gas layer, their equivalent widths may be close or even coincide with those observed. This means that it can be far from simple to separate the two models for the formation of molecular absorption bands discussed above.

Conclusion. Due to limitations on the admissible volume of the article, we examined only briefly and fragmentarily some results and problems of studying the structure of the Jovian atmosphere from the standpoint of its optical sounding. One of the important results, so far preliminary, was the differences we found in the latitudinal positions of the extrema of the intensities of the molecular absorption bands on Jupiter. This feature is most likely due to the difference in the conditions of formation of different absorption bands in the ammonia cloud layer and the underlying troposphere. The complexity and ambiguity of the mechanism of formation of molecular absorption bands requires further consideration of both various models of the structure of the Jovian atmosphere and further detailed spectral observations of Jupiter with special emphasis on the study of weak and moderate absorption bands, which we would like to draw attention to in this publication.

This work was carried out in the framework of grant financing of the Ministry of Education and Science of the Republic of Kazakhstan 0073 / GF4 and AP05131266.

В.Д. Вдовиченко, А.М. Каримов, Г.А. Кириенко, П.Г. Лысенко,
В.Г. Тейфель, В.А. Филиппов, Г.А. Харитонова, А.П. Хоженец

В.Г. Фесенков атындағы Астрофизикалық институт, ҚР ҰҒА (АФИФ), Алматы, Қазақстан

ЗЕРТТЕУДІҢ МОЛЕКУЛАЛЫҚ ЖҰТЫЛУ ЖОЛАҚТАРЫ ЮПИТЕР ТРОПОСФЕРАСЫ

Аннотация. Алып планеталарды, оның ішінде Күн жүйесіндегі ең ірі Юпитер планетасын қашықтан бақылау және өлшеу осы планеталардың физикалық табиғатын зерттеуде жалғыз әдіс болып қала бермек.

1995 жылы іске асырылған ғарыштық міндеті бар GALILEO құрылғысы Юпитердің атмосферасын алдын ала тікелей тексеру бойынша қайталанбас және бірегей болып табылады. Юпитердің тропосферасын қашықтан оптикалық алдын ала тексеру бойынша әдістің бірі планета спектрінің көрінетін және жақын инфрақызыл аймағында бақыланатын метан мен амммиактың молекулалық жолақтарының жұтылу тәртібін зерттеу болып табылады. Аталған екі газ Юпитер атмосферасының терең қатпарларынан шығатын инфрақызыл және микротолқынды сәулелену жылу диапазонында жұтылу жолақтарын пайда болдырып айтарлықтай рөл атқарады. Сонымен қатар, аммиак планетаның көрінетін бұлтты жамылғы құрамының негізі бола отырып Юпитерде бұлт пайда болдыратын фактор болып табылады. Спектралды бақылаулар Юпитер дискіндегі әр түрлі аумақтағы жұтылу жолақтарының интенсивтілігінің вариацияларын зерттеуге мүмкіндік береді және оның тропосферасын оптикалық алдын ала тексерудің әдісі ретінде қызмет атқарады. Біз және басқа да авторлар орындаған жұмыстар, яғни осындай вариацияларды бірнеше жыл бойы зерттеудің нәтижесі бірнеше қызық ерекшеліктерді анықтады, оларды түсіндіру айтарлықтай қиын және бірмәнді емес. Сандық бағалау үшін зертханалық зерттеулерден алынатын молекулалық жолақтардың интенсивтілігі туралы мәліметтер қажет. Алайда мұндай зерттеулер спектрдің көрінетін аймағында әзірше өте аз және олар барлық жұтылу жолақтары үшін емес. Атап айтқанда, интенсивтіліктің (немесе балама ендігі) жұтылған газ қалыңдығына (жұтылудың эквивалентті жолы метрмен - амаго) тәуелділігін көрсететін қисық сызықтар NH3 6450A аммиак пен метан CH4 6190A жолақтары үшін ғана алынған. Осындай қисық сызықтар Юпитер спектрінде осы жолақтарды зерттеу бойынша балама жұтылу жолдарын бағалауға мүмкіндік береді. Біз Юпитердегі аммиакты жұтылуды зерттеуді 2004 жылы бастадық және қазіргі таңда да зерттеу жалғасуда. Аталған зерттеулер толқын ұзындығының миллиметрлік диапазонындағы радио бақылаулар мәліметтерімн сәйкес келетін аммиакты жұтылу вариация енінде бірқатар қызық ерекшеліктерді анықтады. Атап айтқанда, Юпитердің солтүстік экваториалды белдеуіне жақын жерде табылған аммиакты жұтылудың депрессиясы милиметрлік диапазондағы радиотемператураның максимум жарықтылығына сәйкес келді. Осылайша, метан мен аммиактың әр түрлі жолақтарындағы экстремум жұтылулары ендік жағдайда бұрын айтылған айырмашылықтарды растады. Негізінде жұтылу жолақтарының кеңістік-уақыттық вариациясын зерттеу, тропосфера аймағындағы және бұлтты жамылғының құрылымында болып жатқан өзгерістер туралы, қалай болғанда NH4SH аммоний гидросульфидіндегі терең бұлтты қабатына дейін ашуға мүмкіндік береді. Юпитер тропосферасының бірнеше модельдерінде қалың геометриялық және оптикалық аммиакты бұлтты қабаттың бар екені болжануда. Сонымен қатар мұндай бұлтты қабат бұлтты бөлшектердегі көп ретті таралуының арқасында әлсіз молекулалық жұтылу жолақтары үшін де негізгі және басымдылық танытатын рөл атқаруы керек. Ол таза газды атмосферадан жәй ғана қос өтуден артық, тиімді оптикалық жұтылу жолын және бақыланып отырған жолақтың интенсивтілігін шарттауы мүмкін. Осылайша, жұтылу жолағындағы бақыланып отырған вариациялар бұлтты қабаттың көлемді тығыздық вариациясы мен оптикалық сипаттамасымен байланысты болуы керек. Тропосфераның ішіне қарай өтетін тікелей күн сәулесі үшін айтарлықтай мөлдір және оптикалық және геометриялық жіңішке аммиакты бұлтты қабат болып табылатын баламалы модель, яғни гидросульфидті бұлтты қабатқа дейін болуы да мүмкін. Осылайша, бақыланып отырған молекулалық жолақтар газды қабатта осы бұлттардың арасында пайда болады. Қисық сызықтарға сүйене отырып осы тропосфера аймақтағындағы жұтылу, дәл сондай яғни Юпитер спектрінде бақыланатын жұтылу жолағының интенсивтілігіне әкеліп соғуы мүмкін. Осы мақалада біз мына жәйтқа, яғни көрінетін спектр аймағындағы радиобақылаулар мен инфрақызыл мәліметтерімен молекулалық жолақтардың жұтылуын зерттеудің қажеттілігіне, Юпитерде болып жатқан өзгерістерді зерттеу мен оның тропосферасының құрылымының барабар үлгісін таңдауға назар аударғымыз келеді.

Түйін сөздер: Юпитер, атмосфера, тропосфера, спектрофотометрия, аммиак, метан, аммоний гидроульфиді, молекулалық жұтылу жолақтары.

В.Д. Вдовиченко, А.М. Каримов, Г.А. Кириенко, П.Г. Лысенко,
В.Г. Тейфель, В.А. Филиппов, Г.А. Харитонова, А.П. Хоженец

Астрофизический институт им. В.Г.Фесенкова НАН РК (АФИФ), Алматы, Казахстан

МОЛЕКУЛЯРНЫЕ ПОЛОСЫ ПОГЛОЩЕНИЯ В ИССЛЕДОВАНИИ ТРОПОСФЕРЫ ЮПИТЕРА

Аннотация. Дистанционные наблюдения и измерения в исследовании планет-гигантов, в том числе крупнейшей планеты Солнечной системы Юпитера, до сих пор остаются и будут ещё долго оставаться единственным способом изучения физической природы этих планет. Осуществлённое в 1995 году прямое зондирование атмосферы Юпитера спускаемым аппаратом космической миссии GALILEO является уникальным и неповторимым. Одним из способов дистанционного оптического зондирования тропосферы Юпитера может служить изучение поведения молекулярных полос поглощения метана и аммиака, наблюдаемых в видимой и ближней инфракрасной области спектра планеты. Оба этих газа играют также

немаловажную роль, создавая полосы поглощения в диапазонах теплового инфракрасного и микроволнового излучения, выходящих из глубоких слоёв юпитерианской атмосферы. Кроме того, аммиак является облакообразующим фактором на Юпитере, будучи основой состава видимого облачного покрова планеты. Спектральные наблюдения дают возможность исследовать вариации интенсивности полос поглощении в разных участках диска Юпитера и могут служить средством оптического зондирования его тропосферы. Выполнявшиеся нами, наряду с работами других авторов, многолетние исследования таких вариаций выявили ряд интересных особенностей, интерпретация которых представляется достаточно сложной и неоднозначной. Для количественных оценок необходимы данные об интенсивности молекулярных полос, получаемые по лабораторным исследованиям. Однако таких исследований в видимой области спектра пока очень мало и выполнены они не для всех полос поглощения. В частности, кривые роста, представляющие зависимость интенсивности (или эквивалентной ширины) от толщи поглощающего газа (эквивалентный путь поглощения в метрах- амаго) получены только для полосы аммиака NH3 6450A и метанаCH4 6190A. Такие кривые позволяют оценить эквивалентные пути поглощения по измерениям этих полос в спектре Юпитера. Исследования аммиачного поглощения на Юпитере были начаты нами в 2004 году и продолжаются регулярно по настоящее время. Эти наблюдения выявили ряд интересных особенностей в широтных вариациях аммиачного поглощения, коррелирующих с данными радионаблюдений в миллиметровом диапазоне длин волн. В частности, депрессия аммиачного поглощения, обнаруженная вблизи Северного экваториального пояса Юпитера, совпала с максимумом яркостной радиотемпературы в миллиметровом диапазоне. Подтверждаются отмечавшиеся нами ранее различия в широтном положении экстремумов поглощения у разных полос как метана, так и аммиака. Исследования пространственно-временных вариаций полос поглощения, в принципе, дают возможность судить об изменениях, происходящих в структуре облачного покрова и находящейся под ним области тропосферы, по крайней мере, до более глубокого облачного слоя из гидросульфида аммония NH4SH. В большинстве моделей тропосферы Юпитера предполагается существование достаточно толстого геометрически и оптически аммиачного облачного слоя. При этом такой облачный слой должен играть основную и преобладающую роль в формировании даже слабых молекулярных полос поглощения благодаря многократному рассеянию на облачных частицах. Оно может обусловливать эффективный оптический путь поглощения и соответственно интенсивность наблюдаемой полосы, больше чем при простом двойном прохождении через чисто газовую атмосферу. В таком случае наблюдаемые вариации у полос поглощения должны быть связаны с вариациями объёмной плотности и оптических характеристик самого облачного слоя. Однако не исключена и альтернативная модель, в которой аммиачный облачный слой является оптически и геометрически тонким и достаточно прозрачным для прямого солнечного излучения, которое может проходить вглубь тропосферы, по крайней мере, до более глубокого гидросульфидного облачного слоя. В таком случае наблюдаемые молекулярные полосы формируются в газовом слое между этими облаками. Можно показать, основываясь на кривых роста, что поглощение в этой области тропосферы может приводить почти к той же интенсивности полос поглощения, что и наблюдаемая в спектре Юпитера. В данной статье мы хотим обратить внимание на необходимость продолжения исследований молекулярных полос поглощения в видимой области спектра в сочетании с данными инфракрасных и радионаблюдений с целью изучения происходящих на Юпитере изменений и выбора наиболее адекватной модели структуры его тропосферы.

Ключевые слова: Юпитер, атмосфера, тропосфера, спектрофотометрия, аммиак, метан, гидросульфид аммония, молекулярные полосы поглощения.

Information about authors:

Teifel V. G., DTOO V.G. Fesenkov Astrophysical Institute., Doctor of Phys.-Math. Sci., Professor, Head of the Laboratory of Physics of the Moon and Planets, tejf@mail.ru, V.G. Fesenkov Astrophysical Institute (FAI) NA of Sci RK, Almaty, Kazakhstan. https://orcid.org/0000-0003-0093-1975;

Vdovichenko V.D., chief n. S., V.G. Fesenkov Astrophysical Institute (FAI) NA of Sci RK, Almaty, Kazakhstan, vdv1942@mail.ru, https://orcid.org/0000-0002-1957-8203;

Kirienko G.A., Senior Researcher, V.G. Fesenkov Astrophysical Institute (FAI) NA of Sci RK, Almaty, Kazakhstan, gak39@mail.ru, https://orcid.org/0000-0002-1753-4813;

Karimov A.M., Senior Researcher, V.G. Fesenkov Astrophysical Institute (FAI) NA of Sci RK, Almaty, Kazakhstan, karalik0@yandex.ru, https://orcid.org/0000-0003-0797-6252;

Lysenko P.G., NS, V.G. Fesenkov Astrophysical Institute (FAI) NA of Sci RK, Almaty, Kazakhstan, lyssenko_petr@mail.ru, https://orcid.org/0000-0002-4292-782X;

Filippov V.A., Senior Researcher, V.G. Fesenkov Astrophysical Institute (FAI) NA of Sci RK, Almaty, Kazakhstan, filipp.va@mail.ru, https://orcid.org/0000-0001-9013-849X;

Kharitonova G.A., Senior Researcher, V.G. Fesenkov Astrophysical Institute (FAI) NA of Sci RK, Almaty, Kazakhstan, gah38@mail.ru, https://orcid.org/0000-0003-0366-4761;

Hogenez A.P., NS, V.G. Fesenkov Astrophysical Institute (FAI) NA of Sci RK, Almaty, Kazakhstan, hogenez@gmail.com, https://orcid.org/0000-0002-0830-0345

REFERENCES

[1] Lutz, B.L., and Owen T. The visible bands of ammonia: band strengths, curves of growth, and the spatial distribution of ammonia on Jupiter. 1980. Astr. J. **235**: 285-293.

[2] Woodman J. H., Trafton L., and Owen T. 1977. Icarus 32, 314.

[3] Lewis, J.S. 1969. The clouds of Jupiter and the NH3-H2O and NH3-H2S systems. Icarus, 10(3), pp. 365-378.

[4] Giver L.P., Miller J.H., Boese R.W. A laboratory atlas of the 5v1 NH3 Absorption Band at 6475 A with Applications to Jupiter and Saturn // Icarus. 1975. V. 25. P. 34–48.

[5] Giver L.P., 1978. Intensity measurements of the CH4 bands in the region 4350 A to 10600 A. J. Quant. Spectrosc. Radiat. Transfer 19. pp. 311-322.

[6] Fink U., Benner D. Ch., Dick K.A., 1977. Band model analysis of laboratory methane absorption spectra from 4500 to 10500 A. J. Quant. Spectrosc. Radiat. Transfer 18, pp. 447-457.

[7] Bowles N. 2009. Private communication.

[8] Bowles N., Calcutta S., Irwin P., Temple J. 2008. Band parameters for self-broadened ammonia gas in the range 0.74 to 5.24 μm to support measurements of the atmosphere of the planet Jupiter // Icarus. -V.196. -P. 612-624.

[9] Irwin P.G.J., Bowles N., Braude A.S., Garland R., Calcutt S. 2018. Analysis of gaseous ammonia (NH3) absorption in the visible spectrum of Jupiter // Icarus. V. 302.P. 426–436.

[10] Irwin, P. G., Bowles, N., Braude, A. S., Garland, R., Calcutt, S., Coles, P. A., & Tennyson, J. 2019. Analysis of gaseous ammonia (NH3) absorption in the visible spectrum of Jupiter-Update // Icarus. - V. 321. - P. 572-582.

[11] Tejfel V.G., Vdovichenko V.D., Kirienko G.A., Kharitonova G.A. Comparative morphology of molecular absorption on the disks of Jupiter and Saturn . Astron.& Astrophys Transactions, 2003, v.22, N 2, p.135-144

[12] Tejfel V.G., Vdovichenko V.D., Kirienko G.A., Kharitonova G.A., Sinjaeva N.V., Karimov A.A. 2005. Spatially resolved variation in the methane and ammonia absorption in the atmosphere of Jupiter.Astron&Astroph Transactions, V.24, No.4, P. 359-363. NASA-JUNO -https://www.nasa.gov/sites/default/files/thumbnails/image/pia21771.jp

[13] Bondarenko N. N. The study of the ammonia absorption band NH3 787 nm variations in the atmosphere of Jupiter //Astronomical and Astrophysical Transactions. Vol. 28. Issue 2. 2013. - P.81-86.

[14] Tejfel` V.G., Vdovichenko V.D., Lysenko P.G., Karimov A.M., Kirienko G.A., Bondarenko N.N., Filippov V.A., Kharitonova G.A., Khozhenets A.P. (2018) Ammonia in Jupiter` s atmosphere: spatial and temporal variations of the NH_3 absorption ands at 645 and 787 nm, Solar System Research, 52: 480-494

[15] Tejfel V.G., Karimov A.M., Vdovichenko V.D. 2005. Strange latitudinal variations of the ammonia absorption on Jupiter.

Bulletin Amer.Astron.Soc., V.37, № 3, P. 682.1

[16] F. Moreno,R. Rodrigo,A.Sanchez-Lavega and A.Molina, 1988, Spectroscopic observations of the CH_4 6190 A and NH_3 6450 A absorption bands at different regions of the jovian disk. Astron. Astrophys. Suppl. Ser.74, 233-238.

[17] F. Moreno and A. Molina, 1991, Jupiter's atmospheric parameters derived from cpectroscopic observations in the red region during the 1988 opposition. Astron. Astrophys, 241, p.243-250.

[18] Cochran, W.D., Cochran, A.L.: 1980, Longitudinal Variability of Methane and Ammonia Bands on Jupiter, Icarus 42, p. 102-110.

[19] Cochran W.D., Cochran A.L. 1983. Longitudinal variability of methane and ammonia bands on Jupiter. II. Temporal variations // Icarus. V. 56. P. 116–121.

[20] Tejfel V.G., Charitonova G.A., Glushkova E.A., Sinyaeva N.V. 2001. The methane absorption variations Jupiter's disk from zonal CCD – spectrophotometry, Solar System Reseach V.35, N4, P.261-277.

[21] Fletcher, L. N., Greathouse, T. K., Orton, G. S., Sinclair, J. A., Giles, R. S., Irwin, P. G. J., & Encrenaz, T. (2016). Mid-infrared mapping of Jupiter's temperatures, aerosol opacity and chemical distributions with IRTF/TEXES. Icarus, 278, pp. 128-161.

]22] de Pater, I., Sault, R. J., Wong, M. H., Fletcher, L. N., DeBoer, D., & Butler, B. (2019). Jupiter's ammonia distribution derived from VLA maps at 3–37 GHz. Icarus, *322*, pp. 168-191.

[23] Fletcher, L. N., Orton, G. S., Greathouse, T. K., Rogers, J. H., Zhang, Z., Oyafuso, F. A., Bolton, S. 2020. Jupiter's Equatorial Plumes and Hot Spots: Spectral Mapping from Gemini/TEXES and Juno/MWR. arXiv preprint arXiv:2004.00072.

[24] de Pater, I., Sault, R. J., Moeckel, C., Moullet, A., Wong, M. H., Goullaud, C., Cosentino, R. (2019). First ALMA Millimeter-wavelength Maps of Jupiter, with a Multiwavelength Study of Convection. The Astronomical Journal, 158(4), pp. 139-167.

[25] Weidenschilling, S. J., Lewis, J. S. 1973. Atmospheric and cloud structures of the Jovian planets. Icarus 20, 465–476.

[26] Atreya S. K. и др. Jupiter's ammonia clouds – localized or ubiquitous? //Planetary and Space Science. 2005. T. 53. № 5. P. 498-507.

[27] Wong M. H. и др. Fresh clouds: A parameterized updraft method for calculating cloud densities in one-dimensional models // Icarus. 2015. T. 245. P. 273-281.

[28] Ragent, B., Colburn, D. S., Rages, K. A., Knight, T. C. D., Avrin, P., Orton, G. S., Yanamandra-Fisher, P. A., Grams, G. W. 1998. The clouds of Jupiter: Results of the Galileo Jupiter mission probe nephelometer experiment. Journal of Geophysical Research 103, 22891–22910.

NEWS
OF THENATIONAL ACADEMY OF SCIENCES OF THE REPUBLIC OF KAZAKHSTAN
PHYSICO-MATHEMATICAL SERIES
ISSN 1991-346X **https://doi.org/10.32014/2020.2518-1726.34**
Volume 3, Number 331 (2020), 34 – 43

UDC 52-48, 524, 539.14, 539.17

A.V. Dzhazairov-Kakhramanov[1,2], L.T. Karipbayeva[1,2], A.A. Steblyakova[2]

[1]V.G. Fesenkov Astrophysical Institute "NCSRT" NSA RK, Almaty, Kazakhstan;
[2]International Informatization Academy, Almaty, Kazakhstan.
E-mail: albert-j@yandex.ru, larisa_karipbaeva@mail.ru, a_steblyakova@mail.ru

PARTIAL POTENTIALS FOR THE ^{8}Li(p,γ)^{9}Be CAPTURE AT ASTROPHYSICAL ENERGIES

Abstract. The total cross sections of the radiative proton capture on ^{8}Li at astrophysical energies are considered in the framework of the modified potential cluster model with forbidden states, with the classification of the orbital cluster states according to Young diagrams. The recalculation of the total cross sections for ^{9}Be(γ,p_0)^{8}Li photodisintegration is used as experimental data. Parameters for Gaussian partial potentials were obtained for description the ^{8}Li(p,γ)^{9}Be capture at astrophysical energies. Simultaneously, in work of Shoda, & Tanaka (1999), different binary channels of disintegration of ^{9}Be, namely, ^{9}Be(γ,p)^{8}Li, ^{9}Be(γ,d)^{7}Li, ^{9}Be(γ,t)^{6}Li and also ^{9}Be(γ,^{3}He)^{6}He, were experimentally studied. It is evident that the processes of two-body radiative capture connected with them by the detailed balancing principle lead to the synthesis of ^{9}Be and require the corresponding estimation contextually in the astrophysical supplements. Meanwhile, it should be noted that the first three reactions have the Coulomb barrier in channels p^{8}Li, d^{7}Li and t^{6}Li lower than in ^{3}He^{6}He along with ^{4}He^{5}He channels, namely, in the ratio of 3:4. The cross section of ^{8}Li(p,γ)^{9}Be is hard to obtain directly due to low ^{8}Li beam intensity and the small cross section at astrophysical energies. In addition, the difficulty of studying the reaction of ^{8}Li(p,γ)^{9}Be also lies in the fact that the direct experimental measurement of cross sections is practically impossible due to the very short half-life of ^{8}Li – 838 ms. However, as in the case of the neutron capture on ^{8}Li, some indirect methods of extracting direct capture cross sections can be used with the help of the radiative capture model and spectroscopic factor.

Keywords: Nuclear astrophysics; primordial nucleosynthesis; thermal and astrophysical energies; p^{8}Li cluster system; radiative capture; total cross section.

1. Introduction

The study of the formation mechanisms of ^{9}Be directly concerns the problem of the overlap of the $A = 8$ mass gap and the synthesis of heavier elements in the early Universe, as well as the r-process nucleosynthesis in supernovae (see, for example, [1,2]). In the present time, it is considered that ^{9}Be is formed as a result of a two-stage process: the radiative capture of alpha particles $\alpha(\alpha,\gamma)^{8}$Be, leading to the synthesis of the short-half-life isotope ^{8}Be ($t_{1/2} = 6.7\times10^{-17}$s), and radiative neutron capture ^{8}Be(n, γ)^{9}Be [2,3]. In addition, there is the more difficult process of the direct three-particle capture $\alpha\alpha n \rightarrow \gamma\,^{9}$Be, (see, for example, [4–8]).

Simultaneously, in [8], different binary channels of disintegration of ^{9}Be, namely, ^{9}Be(γ,p)^{8}Li, ^{9}Be(γ,d)^{7}Li, ^{9}Be(γ,t)^{6}Li and also ^{9}Be(γ,^{3}He)^{6}He, were experimentally studied. It is evident that the processes of two-body radiative capture connected with them by the detailed balancing principle lead to the synthesis of ^{9}Be and require the corresponding estimation contextually in the astrophysical supplements. Meanwhile, it should be noted that the first three reactions have the Coulomb barrier in channels p^{8}Li, d^{7}Li and t^{6}Li lower than in ^{3}He^{6}He along with ^{4}He^{5}He channels, namely, in the ratio of 3:4.

The cross section of ^{8}Li(p,γ)^{9}Be is hard to obtain directly due to low ^{8}Li beam intensity and the small cross section at astrophysical energies. In addition, the difficulty of studying the reaction of ^{8}Li(p,γ)^{9}Be also lies in the fact that the direct experimental measurement of cross sections is practically impossible due to the very short half-life of ^{8}Li – 838 ms [9]. However, as in the case of the neutron capture on ^{8}Li

[10], some indirect methods of extracting direct capture cross sections can be used with the help of the radiative capture model and spectroscopic factor [9,11].

The $p^8\mathrm{Li}\to{}^9\mathrm{Be}\gamma$ reaction presents significant astrophysical interest because it is included in the list of processes of primordial nucleosynthesis of the Universe [12]. However, its experimental investigation in the astrophysical range has so far been insufficient. Intrinsically, there is only one work [13] where the astrophysical range is considered. In [14], it is also added, where measurements were carried out at higher energies. However, these works were published in the 1960s and we do not currently possess more modern experimental studies of the total cross sections of the considered reaction [15]. This is in spite of the fact that studies of spectra ^{9}Be in the p^{8}Li channel are still continuing [16]. In addition, the available and considered further theoretical results differ so greatly that it is difficult to draw certain conclusions regarding the rate of this reaction. Furthermore, these calculations do not take into account the existence of resonances in the p^{8}Li system at low energies [16].

In the present study, we consider the reaction of the proton capture on ^{8}Li in the frame of the modified potential cluster model (MPCM) [17] and define how the criteria of this model allow us to correctly describe total cross sections and the astrophysical *S*-factor at astrophysical energies. The energy range of 10 keV to 7.0 MeV is considered but only taking into account the structure of resonances up to 2.0 MeV, as discussed previously [16]. The rate of the reaction is calculated at the temperature range of 0.01 to 10 T_9. The analysis of the influence of the location and magnitude of resonances to the value and shape of the reaction rate is presented.

2. Model and calculation methods

Further we use well-known formulas for total cross sections and matrix elements of E*1 transition operators [18] (*$\mathrm{S_i} = \mathrm{S_f} = \mathrm{S}$*)*

$$\sigma_c(NJ,J_\mathrm{f}) = \frac{8\pi K e^2}{\hbar^2 q^3}\frac{\mu\cdot A_\mathrm{J}^2(NJ,K)}{(2S_1+1)(2S_2+1)}\frac{J+1}{J[(2J+1)!!]^2}\sum_{\mathrm{L_i,J_i}} P_\mathrm{J}^2(NJ,J_\mathrm{f},J_\mathrm{i})I_\mathrm{J}^2(J_\mathrm{f},J_\mathrm{i}), \tag{1}$$

where matrix elements of *EJ* – transitions have a form

$$P_\mathrm{J}^2(EJ,J_\mathrm{f},J_\mathrm{i}) = \delta_{\mathrm{S_iS_f}}[(2J+1)(2L_\mathrm{i}+1)(2J_\mathrm{i}+1)(2J_\mathrm{f}+1)](L_\mathrm{i}0J0\mid L_\mathrm{f}0)^2\begin{Bmatrix} L_\mathrm{i} & S & J_\mathrm{i}\\ J_\mathrm{f} & J & L_\mathrm{f}\end{Bmatrix}^2$$

$$A_J(EJ,K) = K^J\mu^J\left(\frac{Z_1}{m_1^J}+(-1)^J\frac{Z_2}{m_2^J}\right),\ I_J(J_f,J_i) = \left\langle\chi_f\middle|r^J\middle|\chi_i\right\rangle \tag{2}$$

Here S_i, S_f, L_f, L_i, J_f, J_i – are total spins and moments of input (*i*) and output (*f*) channel particles, m_1, m_2, Z_1, Z_2 are masses and charges of input channel particles, I_J is the integral over wave functions of the initial χ_i and final χ_f states, as relative motion functions of clusters with intercluster distance *r*, μ – reduced mass.

For the spin part of the magnetic process $M1(S)$ at $J = 1$, the following expression is obtained in the model used ($S_\mathrm{i} = S_\mathrm{f} = S$, $L_\mathrm{i} = L_\mathrm{f} = L$)

$$P_1^2(M1,J_\mathrm{f},J_\mathrm{i}) = \delta_{\mathrm{S_iS_f}}\delta_{\mathrm{L_iL_f}}[S(S+1)(2S+1)(2J_\mathrm{i}+1)(2J_\mathrm{f}+1)]\begin{Bmatrix} S & L & J_\mathrm{i}\\ J_\mathrm{f} & 1 & S\end{Bmatrix}^2,$$

$$A_1(M1,K) = \frac{\hbar K}{m_0 c}\sqrt{3}\left[\mu_1\frac{m_2}{m}-\mu_2\frac{m_1}{m}\right],\ I_J(J_f,J_i) = \left\langle\chi_f\middle|r^{J-1}\middle|\chi_i\right\rangle. \tag{3}$$

Here, *m* is the mass of the nucleus, μ_1, μ_2 are magnetic moments of the clusters, and the remaining notation, are given as in the previous expression.

Constant $\hbar^2/m_0$ is equal to 41.4686 MeV fm^2, where m_0 is the atomic mass unit (amu). The Coulomb potential at zero Coulomb radius $R_\mathrm{coul} = 0$ is written in the form $V_{coul} = 1.439975\cdot Z_1Z_2/r$, where *r* is the relative distance between particles of the initial channel in fm and *Z* are charges of particles in the elementary charge "*e*" units. Furthermore, the magnetic moment of proton $\mu_\mathrm{p} = 2.792847\mu_0$ and ^{8}Li nucleus $\mu(^8\mathrm{Li}) = 1.65356\mu_0$ [18], where μ_0 is the nuclear magneton.

3. Classification of p^8Li states according to Young diagrams

We take Young diagram {431} for ^{8}Li – it was shown in [19] that exactly this diagram corresponds to the ground state (GS) of ^{8}Li, if to consider it in the n^7Li channel. For many other cluster systems, their correspondence to certain Young diagrams were studied by us in [17].

Therefore, for the p^8Li system, we have: {431} + {1} = {531} + {441} + {432} + {4311}. The first diagram {531} is forbidden because it cannot be five nucleons in the *s*-shell – it corresponds to orbital momenta L = 1, 2, 3, determined by the Elliot rule [20]. The second diagram {441} corresponds to L = 1, 2, 3, 4, the third {432} has L = 1, 2, 3 and the fourth {4311} corresponds to L = 0, 2. For the second diagram {441}, we will consider allowed – it corresponds to the ground state (GS) of ^{9}Be in the p^8Li channel [21]. Diagrams {432} and {4311} are not considered because without product tables of Young diagrams [22], it is impossible to understand if they are forbidden or allowed.

Thus, it follows from the given classification that for the p^8Li system (it is known that $J^\pi,T = 2^+,1$ for ^{8}Li [21]) in potentials of *S* waves there is no forbidden state (FS), in *P* waves for diagram {441}, there are FS and allowed state (AS), in *D* and *F* waves there is FS for the same diagram, which can be considered as bound. The state in the $P_{3/2}$ wave corresponds to the GS of ^{9}Be with $J^\pi,T = 3/2^-,3/2$ and lays at the binding energy of p^8Li system of -16.8882 MeV [21]. Some p^8Li scattering states and bound states (BSs) can be mixed by spin with S = 3/2 and 5/2. However, the same as for the n^8Li system [10], here we will consider that the GS of ^{9}Be p^8Li channel is most probably is the $^4P_{3/2}$ level (in spectroscopic notations $^{2S+1}L_J$).

4. Structure of the p^8Li resonance states

Let us consider now the state structure of ^{9}Be, where we consider further the GS and six low-lying resonance states. The GS of ^{9}Be with $J^\pi = 3/2^-$ is at the energy of -16.888 MeV (round off energy down to 1 keV) [16] relatively to the threshold of the p^8Li channel and will considered only as the $^4P_{3/2}$ state.

Table 1 - Comparison of data on the ^{9}Be spectrum from different works. The threshold of the p^8Li channel in ^{9}Be equals 16.888 MeV [21]. The results coinciding for all three works are marked by bold

[16] 2018 year			[23] 2016 year			[21] 2004 year		
E_r, MeV	J^π	$\Gamma_{c.m.}$, keV	E_r, MeV	J^π	$\Gamma_{c.m.}$, keV	E_r, MeV	J^π	$\Gamma_{c.m.}$, keV
–	–	–	0.087(1)	$1/2^-$	0.39(1)	0.0868(8)	$1/2^-$	0.389(1)
0.420(7)	**$5/2^-$**	**210(20)**	**0.410(7)**	**$5/2^-$**	**195**	**0.410(7)**	**$5/2^-$**	**200**
0.610(7)	**$7/2^+$**	**47(7)**	**0.605(7)**	**$7/2^+$**	**47**	**0.605(7)**	**$7/2^+$**	**47**
1.100(30)	$3/2^+$	50(22)	1.132(50)	–	–	1.132(50)	–	–
1.650(40)	$7/2^-$	495(34)	1.688(30)	$5/2^+$	432(50)	1.692(40)	–	–
1.800(40)	$5/2^-$	79(17)	1.758(40)	$7/2^+$	490(81)	1.762(50)	$5/2^-$	300(100)
–	–	–	2.352(50)	$3/2^+$	310(80)	2.312(50)	–	310(80)

Here, the $E1$ capture is possible from $^4S_{3/2}$ scattering wave to the $^4P_{3/2}$ GS of ^{9}Be, that is, the main contribution is given due to the transition $^4S_{3/2}\rightarrow{}^4P_{3/2}$. The spectrum of resonance states of ^{9}Be in the cluster p^8Li channel is listed in Table 1.

We now discuss this spectrum more closely. Given below, the systematization allows *a priori* estimate of the most significant contribution of resonance states in the capture cross section (the resonance states considered in this work are marked by bold italics).

1. The ***first resonance state*** **(1st RS)** is located at 16.975(8) MeV relative to the GS or 0.0868(8) MeV [21] (0.087(1) MeV [23]) in the center of mass (c.m.) relative to the threshold of the p^8Li channel. $J^\pi = 1/2^-$ is given for this level [21,23] that allows us to take L = 1 for it, that is, to consider it quartet $^4P_{1/2}$ resonance. The level width of $\Gamma_{c.m.}$ = 0.39(1) keV is given in [21,23]. It is possible to construct absolutely unambiguous $^4P_{1/2}$ potential of the elastic scattering according these data. Ambiguity of its parameters, with the bound FS at the basic variant of state classification by Young diagrams, will be caused only by the error of width of this resonance [17]. The $M1$ transition $^4P_{1/2}\rightarrow{}^4P_{3/2}$ to the GS is possible for this state.

2. The ***second resonance state*** **(2nd RS)** is located at 17.298(7) MeV relative to the GS or 0.410(7) MeV in the c.m. relative to the threshold of the p^8Li channel [21,23]. $J^\pi = 5/2^-$ is given for this level [21,23] that allows us to take L = 1 for it, that is, to consider it quartet $^4P_{5/2}$ resonance. The level width of

$\Gamma_{c.m.}$ = 200 keV is given in [21] and 195 keV in [23]. The energy 420(7) keV at the width 210(20) keV is given in new work [16]. The $M1$ transition $^4P_{5/2}\rightarrow{}^4P_{3/2}$ to the GS is also possible for this state.

3. The *third resonance state* (3rd RS) is located at 17.493(7) relative to the GS or 0.605(7) MeV in the c.m. relative to the threshold of the p^8Li channel with the width of 47 keV [21,23]. $J^\pi = 7/2^+$ is given for this level [21,23] that us allows to take $L = 2$ for it, that is, to consider it quartet $^4D_{7/2}$ resonance. The energy 610(7) keV at the width 47(7) keV is given in new work [16]. Since, such resonance state corresponds to the $^4D_{7/2}$ wave, and then only $E2$ transition to the GS of ^{9}Be is possible here, which we will not consider due to its small value.

4. The ***fourth resonance state*** **(4th RS)** at energy 1.100 MeV with the width 50(22) keV and momentum $3/2^+$, which is in data [16], can be considered as refinement of data from [21,23]. Neither its width nor its momentum is not given in them, only the energy of 1.132(50) MeV that approximately coincides with new results from [16] is given. If to take the $^4D_{3/2}$ state for it, the $E1$ transition $^4D_{3/2}\rightarrow{}^4P_{3/2}$ to the GS turn out to be possible. We failed to obtain the resonance in the $^4S_{3/2}$ wave with such characteristics; therefore, we consider this wave nonresonance.

5. The *fifth resonance state* (5th RS) according to [21] is located at the energy of 1.692(40) MeV relative to the threshold, but the momentum and the width are not given for them. The similar state at the energy of 1.688(30) MeV with the momentum $5/2^+$ and the width of 432(50) keV is given in [23]. In new work [16], the energy is equal to 1.650(40) MeV and the width of 495(34) keV that coincide with data from [23], but the value $7/2^-$ is given for momentum. If to assume that the last momentum corresponds to 5th RS, so it can refer to the $^4F_{7/2}$ scattering state, and then only $E2$ transition to the GS is possible, which we will not consider.

6. The *sixth resonance state* (6th RS) according to [21] is located at the excitation energy of 18.65(5) MeV or 1.762(50) MeV in the c.m. relatively to the threshold of the p^8Li channel with the width 300(100) keV. $J^\pi = 5/2^-$ is given for this level [21] that allows us to take $L = 1$ for it, that is, to consider it quartet $^4P_{5/2}$ resonance. The $M1$ transition $^4P_{5/2}\rightarrow{}^4P_{3/2}$ to the GS is possible for this resonance. However, the energy of 1.758(40) MeV with the width of 490(81) keV and other momentum $7/2^+$ are given in [23]. At the same time, in new work [16], the energy of 1.800(40) MeV with the width of 79(17) keV and momentum $5/2^-$, coincided with primary data of work [21], are given. If to take for it the last momentum, it can refer to the $^4P_{5/2}$ scattering state and then the $M1$ transition $^4P_{5/2}\rightarrow{}^4P_{3/2}$ to the GS is possible. However, we do not succeed to obtain characteristics of the P wave of continuous spectrum that were noted in Table 1. Therefore, the F scattering wave is compared to it, which gives the $E2$ transition to the GS, but since their contribution is small, we will not consider them.

7. The *seventh resonance state* (7th RS) with the energy of 2.312(50) with the width 310(80) keV and unknown momentum are given in [21]. The energy of 2.352(50) with the width the same width and momentum $3/2^+$ is given in [23]. In new work [16], this and higher states, unfortunately, are not considered. As we have seen above, the results of [23] on two previous levels differ from new data [16]; therefore, the data for this level most probably should be specified, and now we will not consider this resonance.

Slightly higher at excitation energy of 19.420(50) MeV, there is other resonance with the width of 600(100) keV, but it has a presumable momentum $9/2^+$ [23] and cannot lead to $E1$ or $M1$ transitions and we therefore do not consider it. Furthermore, we will base on spectra given in new work [16], including first resonance at 87 keV from [21,23] and limiting by energies not higher the threshold of 2 MeV.

Thus, selected by us, the basic transitions to the GS that are considered here and also P^2 coefficients for total cross sections, given in [17], are presented in Table 2. The obtained values of isotopic spin $2T_i$ for resonance states with J^π_i are given here.

Table 2 - Characteristics of taken into account transitions at the ^{8}Li(p,γ)^{9}Be capture

No.	$[^{2S+1}L_J]_i$	Resonance energy, MeV	J^π_i, $2T_i$	Transition	$[^{2S+1}L_J]_f$, $2T_f = 1$	P^2
1.	$^4S_{3/2}$	–	$3/2^+$ (?)	$E1$	$^4P_{3/2}$	4
2.	$^4D_{3/2}$	1.100 (4th RS)	$3/2^+$, (3?)	$E1$	$^4P_{3/2}$	64/25
3.	$^4P_{1/2}$	0.087 (1st RS)	$1/2^-$, 3	$M1$	$^4P_{3/2}$	10/3
4.	$^4P_{5/2}$	0.410 (2nd RS)	$5/2^-$, 3	$M1$	$^4P_{3/2}$	18/5

As seen in Table 2, for the **1st RS** (0.087) and the **2nd RS** (0.410), the isospin $T = 3/2$. This means that for these states unambiguously there are no channel mixing $p + {}^8\text{Li}$, $d + {}^7\text{Li}$, and also $\alpha + {}^5\text{He}$, which have the isospin $T = 1/2$. Problems of channels coupling are discussed in [24,25]. Thus, the single-channel approach, which we use here, is quite justified, especially allowing for the fact that capture from **1st RS** (0.087) is highest (see further).

5. Criteria of the potential construction

The potentials of resonance waves are constructed in order to correctly describe the location of resonance E_r and its width $\Gamma_{c.m.}$, therefore their parameters are obtained quite unambiguously. GS potentials will be constructed in such a form that allows one to correctly describe the channel binding energy, the charge radius of ${}^9\text{Be}$ and its asymptotic constant in the $p{}^8\text{Li}$ channel. Since, all known values of the asymptotic normalization coefficient (ANC) and the spectroscopic factor S_f, according to which the asymptotic constant (AC) is obtained, have enough large error. The GS potentials also can have few options with different parameters of width. However, at the given values of AC and binding energy, its parameters are constructed absolutely unambiguously.

The radius of ${}^8\text{Li}$ equals 2.327±0.0298 fm, which is given in a database [26], was used in further calculations. The radius of 2.518±0.0119 fm for ${}^9\text{Be}$ also is known from the database [26]. In addition, for example, the value of 2.299(32) fm for ${}^8\text{Li}$ radius was found in [27]. In work [28], for these radiuses, values of 2.30(4) and 2.519(12) fm were obtained, correspondingly. All these data agree well among themselves within the limits of errors. The accurate values of $m({}^8\text{Li}) = 8.022487$ amu [29] and $m_p = 1.0072764669$ amu [30] were used for the masses of nucleus and proton. The charge and mass radius of the proton is equal to 0.8775(51) fm [30]. For 1 amu energy equivalent of 931.4941024 MeV was used [30].

The spectroscopic factor S_f of the GS and A_{NC} ANC are connected by the next way [31]:

$$A_{NC}^2 = S_f \times C^2, \tag{4}$$

where C is the dimensioned asymptotic constant in $\text{fm}^{-1/2}$, which connects with dimensionless AC C_w [32] by $C = \sqrt{2k_0}\,C_w$, and the dimensionless constant C_w defined from the relation [32]:

$$\chi_L(r) = \sqrt{2k_0}\,C_w W_{-\eta L+1/2}(2k_0 r), \tag{5}$$

where $\chi_L(r)$ is the numerical BS radial wavefunction, obtained as the solution of the Schrödinger equation normalized to unit size, $W_{-\eta L+1/2}(2k_0 r)$ is the Whittaker function of the bound state, determining the asymptotic behavior of the wavefunction and obtained as the solution of the same equation without nuclear potential, k_0 is a wavenumber related to the channel binding energy E where $k_0 = \sqrt{2\mu E/\hbar^2}$ in fm^{-1}, η is the Coulomb parameter $\eta = \mu Z_1 Z_2 e^2/(\hbar^2 k_0) = 3.44476\cdot 10^{-2}\,\mu Z_1 Z_2/k_0$, Z_1 and Z_2 are the particle charges, L is the orbital momentum of the bound state.

Note that the spectroscopic factor S_f is used by us only for the standard procedure of the obtaining possible C_w range from the obtained in the experiment A_{NC} value [31,32].

6. Potentials of the $p{}^8\text{Li}$ interaction

As in our previous works [17] for other nuclear systems, we use the potential of the Gaussian form with the point-like Coulomb term with the given orbital momentum L in each partial wave as the $p{}^8\text{Li}$ interaction:

$$V(r,L) = -V_L \exp(-\gamma_L r^2). \tag{6}$$

The ${}^4P_{3/2}$ level we consider as the ground state of ${}^9\text{Be}$ in the $p{}^8\text{Li}$ and such potential should correctly describe the AC for this channel. In order to extract this constant C in form (4) or C_w (5) from the available experimental data, let us consider information regarding the spectroscopic factors S_f and asymptotic normalization coefficients A_{NC}. For example, in [33], except for their own results, the authors add data of previous works. If to separate from these similar results, that is, with closely spaced values of spectroscopic factors that can be presented in the form of table 3.

Table 3 - Data on spectroscopic factors S_f for the GS of ^{9}Be in the p^8Li channel from works [9,11,33,34]. $\overline{S}_f$ is the average value on data interval

Reaction from what S_f was determined	S_f for the $p^8\text{Li}_{GS}$ channel	Ref.
^{8}Li(d,n)^{9}Be	0.64(21)	[33]
^{12}C(^{9}Be,^{8}Li)^{14}N	0.73(15)	[11]
Average value	*0.69, that is,* $\sqrt{S_f}$ = 0.83	
Average value on data interval	$\overline{S}_f$ *= 0.66(22), 0.43–0.88* $\sqrt{\overline{S}_f}$ *= 0.81(14)*	
^{9}Be(^{8}Li,^{9}Be)^{8}Li	1.50(28)	[34]
Potential model	1.50(27)	[9]
Average value on all results	*1.09,* $\sqrt{S_f}$ *= 1.05*	
Data interval on all results	$\overline{S}_f$ *= 1.11(68), 0.43-1.78* $\sqrt{\overline{S}_f}$ *= 1.05(28)*	

Furthermore, the ANC $^4P_{3/2}$ GS in the p^8Li channel was given in [35], where A_{NC} = 10.75(12) fm$^{-1/2}$ was obtained. The constant for the $^6P_{3/2}$ state is much less – 0.25(10) fm$^{-1/2}$ [35]. Therefore, we consider here only one spin channel with S = 3/2. On the basis of expression (4) and average value on interval $\sqrt{S_f}$ = 0.66(22) from Table 2 according works [11,33] for the AC GS, the value C = 13.71(2.52) fm$^{-1/2}$ was obtained, and because $\sqrt{2k_0}$ = 1.307, so dimensionless AC (5) is equal to C_w = 10.49(1.93). However, if to use the average value $\sqrt{S_f}$ on all works from table 3, equals 1.05(28), then for constant C, we obtain a wider data interval 11.06(3.06) fm$^{-1/2}$ and C_w = 8.46(2.34). Consequently, the possible interval of C_w values on two data groups from Table 3 is approximately from 6 (from the latest data) to 12.5 (from the previous results).

Furthermore, two options of the GS potentials with FS, which allow us to obtain the dimensionless asymptotic constant C_w in the given above limits, were obtained. The parameters of these potentials V_L and γ_L, and also main characteristics of the nucleus, obtained with them (binding energy E_b, asymptotic constant C_w, mass radius $\langle R\rangle_m$ and charge radius $\langle R\rangle_{ch}$) are listed in table 4.

Table 4 - GS potential parameters and main characteristics of ^{9}Be

No.	V_L, MeV	γ_L, fm^{-2}	E_b, MeV	C_w	$\langle R\rangle_m$, fm	$\langle R\rangle_{ch}$, fm
1	212.151135	0.17	-16.88820	10.2(1)	2.40	2.46
2	286.178045	0.25	-16.88820	6.6(1)	2.36	2.38

For example, potential No. 1 has the FS and leads to the binding energy -16.88820 MeV. The definition of the calculation expressions used here for the radii is given, for example, in [17]. The above AC errors are defined by their averaging over the distance interval from 6–8 to 10–12 fm, which is the AC stabilization range. The phase shift of the elastic scattering of this potential for the GS $^4P_{3/2}$ smoothly decreases down to zero and at 5.0 MeV has the value of ~330°. Here, we consider that in the presence of two bound FS and AS, the phase shift according to generalized Levinson theorem starting from 360° [20]. Furthermore, another option of the GS potential that leads to a smaller AC given in table 4.

Table 5 - Options of potential parameters with FS for resonance states of nuclear and some characteristics obtained with them. In the two last columns, the experimental values listed above in Table 1 are shown.

No.	$^{2s+1}L_J$	V_J, MeV	γ_J, fm^{-2}	E_r (c.m.), keV	$\Gamma_{c.m.}$, keV	E_r (c.m.), keV	$\Gamma_{c.m.}$, keV
1.	$^4S_{3/2}$	-5	0.1	–	–	–	–
2.	$^4D_{3/2}$	269.242	0.2	1100	56	1100(30)	50(22)
3.	$^4P_{1/2}$	66.69121	0.075	87	~0.4	87(1)	0.39(1)
4.	$^4P_{5/2}$	34.0399	0.04	410	203	420(7)	210(20)

Potential No. 3 from table 5 leads to the $^4P_{1/2}$ scattering phase shift, plotted in figure 1 by the black solid curve, which is shown at energies up to 5.0 MeV and has the resonance at 87 keV. Scattering potential No. 4 has the phase shift $^4P_{5/2}$ presented in figure 1 by the red dashed curve and at the considered energies has the resonance at 410 keV. Potential No. 2 leads to the $^4D_{3/2}$ phase shift shown in figure 1 by the green solid curve. All resonance potentials have the phase shift of 90.0°(1) at the resonance energy and the bound FS.

7. Conclusion

It is possible to construct two-body potentials of the p^8Li interaction, which allow us to correctly describe the available data on characteristics of the bound state of ^{9}Be in the p^8Li channel in the frame of the MPCM. Suggested options of the GS potentials of ^{9}Be in the p^8Li channel allow one to obtain AC within limits of errors available for it and lead to the reasonable description of ^{9}Be radii. Such potentials generally allow the available experimental data for total cross sections of the radiative proton capture on ^{8}Li at low and ultralow energies. Obtained results for total cross sections and static characteristics of ^{9}Be strongly depend of GS potential parameters of this nuclear in the p^8Li channel.

Acknowledgments

This work was supported by the Ministry of Education and Science of the Republic of Kazakhstan (Grant No. AP05130104) entitled “Study of Reactions of the Radiative Capture in Stars and in the Controlled Thermonuclear Fusion” through the Fesenkov Astrophysical Institute of the National Center for Space Research and Technology of the Ministry of Digital Development, Innovation and Aerospace Industry of the Republic of Kazakhstan (RK).

А.В. Джазаиров-Кахраманов[1,2], Л.Т. Карипбаева[1,2], А.А.Стеблякова[2]

[1] В.Г. Фесенков атындағы Астрофизика институты ЕЖШС, Алматы, Казахстан;
[2]Халықаралық Ақпараттандыру Академиясы, Алматы, Қазақстан

АСТРОФИЗИКАЛЫҚ ЭНЕРГИЯЛАРДАҒЫ ^{8}Li(p,γ)^{9}Be ҚАМТУҒА АРНАЛҒАН ҮЛЕСТІК ПОТЕНЦИАЛДАР

Аннотация. Юнга сызбасы бойынша орбиталық кластерлік күйді жіктеумен қатар, тыйым салынған күйдегі модификацияланған потенциалды кластерлі модель аясында, астрофизикалық энергияларда протондарды радиациялық қармауды толық кесу қарастырылған. Эксперименттік мәліметтерді алу үшін ^{9}Be(γ,p_0)^{8}Li фотоқырату реакциясын толық кесуді қайта есептеу қолданылады. Астрофизикалық энергияларда ^{8}Li(p,γ)^{9}Be радиациялық қармау үшін гаусс потенциалдарының көрсеткіштері анықталды. Сонымен қатар, [Shoda, Tanaka (1999)] ^{9}Be: ^{9}Be(γ,p)^{8}Li, ^{9}Be(γ,d)^{7}Li, ^{9}Be(γ,t)^{6}Li, сондай-ақ ^{9}Be($\gamma,^3$He)^{6}He әртүрлі екілік тарату арналары эксперименталды зерттелді. Олардың егжей-тегжейлі тепе-теңдігімен байланысты екі бөлшекті радиациялық басып алу процестері ^{9}Be синтезіне алып келеді және астрофизикалық қосымшалар контекстінде тиісті бағалауды талап етеді. Бұл жағдайда, бірінші үш реакция p^8Li, d^7Li және t^6Li арналарында ^{3}He^{6}He-ге қарағанда төмен құлон кедергісінің болуына, яғни 3:4 қатынасында ^{4}He^{5}He арналарында, атап айтқанда 3:4 қатынасында назар аудару керек. ^{8}Li(p,γ)^{9}Be көлденең қимасы астрофизикалық қызығушылық тудыратын энергия кезіндегі

екінші ^{8}Li шоғырдың және шағын қиманың төмен қарқындылығынан тікелей анықтау қиын. Сонымен қатар, ^{8}Li(p,γ)^{9}Be реакциясын зерттеу мәселесі ^{8}Li-838 мс ядросының жартылай ыдырауының өте аз кезеңінде қималарды тікелей эксперименталды өлшеу мүмкін емес болып табылады. Алайда, n^{8}Li-қармау жағдайында да радиациялық қармау моделін және спектроскопиялық факторды пайдалана отырып, тікелей қармау қимасын алу үшін кейбір жанама әдістер пайдаланылуы мүмкін. ^{9}Be механизмдердің пайда болуын зерттеу $A = 8$ массалы саңылауды еңсеру және ерте Әлемдегі ауыр элементтердің синтезіне, сонымен қатар supernovae *r*-процесс нюклеосинтез мәселесіне тікелей қатынасы бар. Қазіргі таңда ^{9}Be екі сатылы үрдіс нәтижесінде пайда болады деген ой қалыптасты: $\alpha(\alpha,\gamma)^{8}$Be альфа бөлшектердің радиациалық қармауы қысқа ғұмырлы изотоптың ^{8}Be ($t_{1/2}$ =6.7×10^{-17} s) синтезіне, одан кейін ^{8}Be(n,γ)^{9}Be нейтронының радиациалық қармауына әкеліп соғады.Аталған мақалада біз төменгі астрофизикалық энергиядағы $p^{8}\text{Li} \rightarrow {}^{9}\text{Be}\gamma$ реакциясын қарастырамыз, себебі жарияланғанына 20 жыл уақыт болғанына қарамастан «тәжірибелік зеттерулер жоспары» ретінде рөл атқаратын Terasawa et al. фундаменталды жұмысындағы ауыр элементтердің синтезіне алып келетін мәнді үрдістің тізбегіне қосылған. Leistenschneider et al. (2018) жаңа жұмысында келтірілген 2 МэВ-ке дейінгі резонанс құрылымын ескере отырып 10 кэВ-тен 7.0 МэВ-ге дейінгі энергияның аймағы қарастырылған. Бұл реакцияның жылдамдығы 0.01-ден 10 T_9 температура аймағына ғана есептелген. Резонанстар шамалары мен орындарының реакция жылдамдығының формасы мен шамасына әсерінің анализі ұсынылған.

Түйін сөздер: Ядролық астрофизика; бастапқы нюклеосинтез; жылулық және астрофизикалық энергиялар; p^{8}Li кластерлі жүйесі; радиациялық қармау; толық кесу.

А.В. Джазаиров-Кахраманов[1,2], Л.Т. Карипбаева[1,2], А.А.Стеблякова[2]

[1]Астрофизический институт В.Г. Фесенкова "НЦКИТ" АКК МИР РК, Алматы, Казахстан;
[2]Международная Академия Информатизации, пр. Абылай Хана 79, Алматы, Казахстан

ПАРЦИАЛЬНЫЕ ПОТЕНЦИАЛЫ ДЛЯ ^{8}Li(p,γ)^{9}Be ЗАХВАТА ПРИ АСТРОФИЗИЧЕСКИХ ЭНЕРГИЯХ

Аннотация. В рамках модифицированной потенциальной кластерной модели с запрещенными состояниями, с классификацией орбитальных кластерных состояний по схемам Юнга рассмотрены полные сечения радиационного захвата протонов на ^{8}Li при астрофизических энергиях. Перерасчет полных сечений реакции фоторазвала ^{9}Be(γ,p_0)^{8}Li используется для получения экспериментальных данных. Были определены параметры гауссовых потенциалов для радиационного захвата ^{8}Li(p,γ)^{9}Be при астрофизических энергиях. В то же время в [Shoda, Tanaka (1999)] экспериментально исследованы различные бинарные каналы фоторасщепления ^{9}Be: ^{9}Be(γ,p)^{8}Li, ^{9}Be(γ,d)^{7}Li, ^{9}Be(γ,t)^{6}Li, а также ^{9}Be($\gamma,^{3}$He)^{6}He. Очевидно, что связанные с ними детальным равновесием процессы двухчастичного радиационного захвата приводят к синтезу ^{9}Be и требуют соответствующей оценки в контексте астрофизических приложений. При этом, следует обратить внимание на то, что первые три реакции имеют кулоновский барьер в каналах p^{8}Li, d^{7}Li и t^{6}Li ниже, чем в ^{3}He^{6}He равно как и ^{4}He^{5}He каналах, а именно в соотношении 3:4. Поперечное сечение ^{8}Li(p,γ)^{9}Be трудно определить непосредственно из-за низкой интенсивности вторичного ^{8}Li пучка и малого сечения при энергиях, представляющих астрофизический интерес. Кроме того, проблема изучения реакции ^{8}Li(p,γ)^{9}Be заключается еще и в том, что прямое экспериментальное измерение сечений оказывается практически невозможным из-за очень малого период полураспада ядра ^{8}Li - 838 мс. Однако, как и в случае n^{8}Li-захвата, могут быть использованы некоторые косвенные методы для извлечения сечения прямого захвата с использованием модели радиационного захвата и спектроскопического фактора. Исследование механизмов образования ^{9}Be имеет прямое отношение к проблеме преодоления массовой щели с $A = 8$ и синтезу более тяжелых элементов в ранней Вселенной, а также в *r*-процесс нюклеосинтеза в суперновых. В настоящее время сложилось мнение, что ^{9}Be образуется в результате двухступенчатого процесса: радиационный захват альфа-частиц $\alpha(\alpha,\gamma)^{8}$Be приводит к синтезу короткоживущего изотопа ^{8}Be ($t_{1/2}$ =6.7×10^{-17} s), и далее радиационный захват нейтрона ^{8}Be(n,γ)^{9}Be. В данной статье мы рассматриваем реакцию $p^{8}\text{Li}\rightarrow{}^{9}\text{Be}\gamma$ при низких астрофизических энергиях в связи с тем, что она включена в цепочку значимых процессов, которые приводят к синтезу более тяжелых элементов в фундаментальной значимой работе Terasawa et al., которая с момента ее опубликования следующие почти 20 лет играет роль некоторого «плана

практических исследований». Рассмотрена область энергий от 10 кэВ до 7.0 МэВ, но с учетом структуры резонансов только до 2 МэВ, которая была приведена в новой работе Leistenschneider et al. (2018). Скорость этой реакции рассчитана в области температур от 0.01 до 10 T_9. Представлен анализ влияния положения и величины резонансов на величину и форму скорости реакции.

Ключевые слова: Ядерная астрофизика; первичный нюклеосинтез; тепловые и астрофизические энергии; кластерная система p^8Li; радиационный захват; полное сечение.

Information about authors:

Dzhazairov-Kakhramanov A.V., Candidate of Physical and Mathematical Sciences, Fesenkov Astrophysical Institute. Academician of the European Academy of Natural Sciences (EANS), academician of the International Informatization Academy (IIA), awarded of the European Carl Friedrich Gauss medal, Professor of the Russian Academy of Natural Sciences. albert-j@yandex.ru, https://orcid.org/0000-0003-2845-6889;

Karipbayeva L.T., Researcher, Fesenkov Astrophysical Institute, academician of the International Informatization Academy. larisa_karipbaeva@mail.ru, https://orcid.org/0000-0002-6238-2441;

Steblyakova A.A., Researcher, Corresponding member of the International Informatization Academy, awarded of the National Order of Enbek Yzdigi. a_steblyakova@mail.ru, https://orcid.org/0000-0003-2730-922X

REFERENCES

[1] Terasawa M et al. (2001) New nuclear reaction flow during r-process nucleosynthesis in supernovae: critical role of light, neutron-rich nuclei, Astrophys. J., 562:470. DOI: 10.1086/323526.

[2] Casal J, Rodr´ıguez-Gallardo M, Arias JM (2014) Astrophysical reaction rate for ^{9}Be formation within a three-body approach, Phys. Rev. C, 90:044304. DOI: 10.1103/PhysRevC.90.044304.

[3] Robinson AE (2016) Reanalysis of radioisotope measurements of the ^{9}Be(γ,n)^{8}Be cross section, Phys. Rev. C, 94:024613. DOI: 10.1103/PhysRevC.94.024613.

[4] Casal J, Rodr´ıguez-Gallardo M, Arias JM, Gómez-Camacho J (2017) Three-body radiative capture reactions, EPJ Web of Conferences, 165:01010. DOI: 10.1051/epjconf/201716501010.

[5] Arnold CW et al. (2012) Cross-section measurement of ^{9}Be(γ,n)^{8}Be and implications for α+α+n→^{9}Be in the r process, Phys. Rev. C, 85:044605. DOI: 10.1103/PhysRevC.85.044605.

[6] Ishikawal S, Kajino T, Shibagaki Sh, Baha Balantekin A, Michael Famiano A (2017) Proc. 14th Int. Symp. on Nuclei in the Cosmos (NIC2016) JPS Conf. Proc. P.010406.

[7] Sasaqui T, Kajino T et al (2005) Sensitivity of r-process nucleosynthesis to light-element nuclear reactions, Astrophys. J., 634:1173. DOI: 10.1086/497061.

[8] Shoda K, Tanaka T (1999) Clusters in the photodisintegration of ^{9}Be, Phys. Rev. C, 59:239. DOI: 10.1103/PhysRevC.59.239.

[9] Guimaraes V et al (2008) Transfer reactions in the investigation of light–nuclei nucleosynthesis, Rev. Mexicana Fisica, 54:63–68.

[10] Dubovichenko SB, Dzhazairov-Kakhramanov AV (2016) The reaction ^{8}Li(n,γ)^{9}Li at astrophysical energies and its role in primordial nucleosynthesis, Astrophys. J., 819:78(8p.). DOI:10.3847/0004-637X/819/1/78.

[11] Li ZH et al. (2013) New determination of the proton spectroscopic factor in ^{9}Be from the ^{13}C(^{9}Be,^{8}Li)^{14}N angular distribution, Phys. Rev. C, 87:017601. DOI: 10.1103/PhysRevC.87.017601.

[12] Kajino T, Boyd RN (1990) Production of the light elements in primordial nucleosynthesis, Astrophys. J., 359:267–276. DOI: 10.1086/169060.

[13] Clikeman FM, Bureau AJ, Stewart MG (1962) Photoproton Reaction in Be^9, Phys. Rev., 126:1822. DOI: 10.1103/PhysRev.126.1822.

[14] Komar AP, Makhnovsky ED (1965) Photodisintegration of Be^9, Nucl. Phys., 65:662–672. DOI: 10.1016/0029-5582(65)90333-0.

[15] CENTRE FOR PHOTONUCLEAR EXPERIMENTS DATA. 2019; http://cdfe.sinp.msu.ru/exfor/index.php.

[16] Leistenschneider E et al (2018) Spectroscopy of high-lying resonances in ^{9}Be by the measurement of (p,p), (p,d), and (p,α) reactions with a radioactive ^{8}Li beam, Phys. Rev. C, 98:064601. DOI: 10.1103/PhysRevC.98.064601.

[17] Dubovichenko SB (2019) Radiative neutron capture. Primordial nucleosynthesis of the Universe. First English edition. Walter de Gruyter GmbH, Berlin/Munich/Boston. DOI: 10.1515/9783110619607-202.

[18] Neugart R et al. (2008) Precision Measurement of ^{11}Li Moments: Influence of Halo Neutrons on the ^{9}Li Core, Phys. Rev. Lett., 101:132502. DOI: 10.1103/PhysRevLett.101.132502.

[19] Dubovichenko SB, Dzhazairov-Kakhramanov AV (2012) The ^{7}Li(n,γ)^{8}Li radiative capture at astrophysical energies, Ann. der Phys., 524:850. DOI: 10.1002/andp.201200151.

[20] Neudatchin VG, Smirnov YuF (1969) Nucleon associations in light nuclei. Nauka, Moscow. (in Russ.).

[21] Tilley DR et al. (2004) Energy levels of light nuclei A=8, 9, 10, Nucl. Phys. A, 745:155–362. DOI: 10.1016/j.nuclphysa.2004.09.059.

[22] Itzykson C, Nauenberg M (1966) Unitary groups: Representations and decompositions, Rev. Mod. Phys., 38:95. DOI: 10.1103/RevModPhys.38.95.

[23] Sukhoruchkin SI, Sorochenko ZN (2016) Excited Nuclear States, Supplement to I/25 A-F. Edited by H. Schopper. Springer-Verlag, Berlin. DOI:10.1007/978-3-662-48875-1.

[24] Raimondi F et al (2016) Deuteron-induced nucleon transfer reactions within an *ab initio* framework: First application to *p*-shell nuclei, Phys. Rev. C, 93:054606. DOI: 10.1103/PhysRevC.93.054606.

[25] Raimondi F, Hupin G, Navrratil P, Quaglioni S (2018) ^{7}Li(d,p)^{8}Li transfer reaction in the NCSM/RGM approach, Journal of Physics: Conf. Series, 981:012006(11p). DOI: 10.1088/1742-6596/981/1/012006.

[26] Chart of nucleus shape and size parameters (0≤Z≤14) http://cdfe.sinp.msu.ru/cgi-bin/muh/radchartnucl.cgi?zmin=0&zmax=14&tdata=123456.

[27] Sanchez R et al (2006) Nuclear charge radius of ^{11}Li, Hyperfine Interaction, 171:181–188. DOI: 10.1007/s10751-007-9507-6.

[28] Nortershauser W et al (2009) Nuclear Charge Radii of ^{7,9,10}Be and the One-Neutron Halo Nucleus ^{11}Be, Phys. Rev. Lett., 102:062503. DOI: 10.1103/PhysRevLett.102.062503.

[29] Nuclear Wallet Cards, 2015, http://cdfe.sinp.msu.ru/services/ground/NuclChart_release.html.

[30] Constants in the category "Atomic and nuclear constants". 2018; http://physics.nist.gov/cgi-bin/cuu/Value?mud|search_for=atomnuc!.

[31] Mukhamedzhanov AM et al (2003) Asymptotic normalization coefficients from proton transfer reactions and astrophysical S factors for the CNO ^{13}C(p,γ)^{14}N radiative capture process, Nucl. Phys. A, 725:279–294. DOI:10.1016/S0375-9474(03)01618-X.

[32] Plattner GR, Viollier RD (1981) Coupling constants of commonly used nuclear probes, Nucl. Phys. A, 365:8–12. DOI: 10.1016/0375-9474(81)90384-5.

[33] Su Jun et al (2006) Astrophysical Reaction Rates of the ^{8}Li(p,γ)^{9}Be$_{g.s.}$ Direct Capture Reaction, Chin. Phys. Lett., 23:55. DOI: 10.1088/0256-307X/23/1/017.

[34] Camargo O et al (2008) The ^{9}Be(^{8}Li,^{9}Be)^{8}Li elastic-transfer reaction, Phys. Rev. C, 78:034605. DOI: 10.1103/PhysRevC.78.034605.

[35] Nollett KM, Wiringa RB (2011) Asymptotic normalization coefficients from *ab initio* calculations, Phys. Rev. C, 83:041001(R). DOI: 10.1103/PhysRevC.83.041001.

NEWS
OF THENATIONAL ACADEMY OF SCIENCES OF THE REPUBLIC OF KAZAKHSTAN
PHYSICO-MATHEMATICAL SERIES
ISSN 1991-346X **https://doi.org/10.32014/2020.2518-1726.35**
Volume 3, Number 331 (2020), 44 – 51

UDC 52-48, 524, 539.14, 539.17

A.V. Dzhazairov-Kakhramanov[1,2], L.T. Karipbayeva[1,2], A.A. Steblyakova[2]

[1]V.G. Fesenkov Astrophysical Institute "NCSRT" NSA RK, Almaty, Kazakhstan;
[2]International Informatization Academy, Almaty, Kazakhstan.
E-mail: albert-j@yandex.ru, larisa_karipbaeva@mail.ru, a_steblyakova@mail.ru

RADIATIVE TRITIUM CAPTURE ON ^{3}He AT LOW AND ASTROPHYSICAL ENERGIES

Abstract. The radiative tritium capture on ^{3}He at low and astrophysical energies was considered in the framework of the modified potential cluster model. It is shown that on the basis of potentials coincided with scattering phase shifts and the energy of bound state it is possible to correctly represent available experimental data. The two-cluster potential model described in this paper, used intercluster forces with forbidden states, in many cases, allow one correctly to describe some nuclear characteristics for different light and lightest nuclei, and, evidently do not yet exhaust completely their potential. The more especially as reported here methods and results are applicable to certain problems of nuclear astrophysics, concerned to light atomic nuclei and ultralow energies of interacting particles. In other words, these results have direct relationship to thermonuclear processes flowing in the Sun, stars, some other objects of our Universe and Universe in whole, at different stages of its forming and developing. It is possible to use one channel cluster model, which, in more cases, is a good approach to the real existent situation. Such model allows relatively easy to carry out any calculations of nuclear characteristics in scattering processes and bound states, even in that systems, where solving methods of many-body problem either very cumbersome in numerical implementation or do not lead to the concrete quantitative results at all.

Key words: Nuclear astrophysics; primordial nucleosynthesis; light atomic nuclei; radiative capture; thermonuclear processes; potential cluster model.

1. Introduction

The structure of atomic nucleus is very multiform and occasionally discover, as seems, alternative properties. For example, properties of nucleon independent motion, collective demonstration of degree of freedom, association of nucleons into almost independent groups – clusters with characteristics close to properties of correspondent free nuclei can realize in nucleus. Earlier available ideas about permanently existent clusters in nuclei change to the conception that in the process of almost independent motion of nucleons in nucleus such virtual sub-systems as clusters are formed and destroyed. Therefore, it is possible to say only about probability of existence one or another cluster channel in the atomic nucleus [1,2].

However, if this probability is relatively large, it is possible to use one channel cluster model, which, in more cases, is a good approach to the real existent situation. Such model allows relatively easy to carry out any calculations of nuclear characteristics in scattering processes and bound states, even in that systems, where solving methods of many-body problem either very cumbersome in numerical implementation or do not lead to the concrete quantitative results at all.

Certainly, two-body presentation is a certain idealization for really existent situation in nucleus, i.e. suppose that the bound state has the big degree of clusterization for particles of the initial channel. Therefore, the success of this potential model for description of the system of A nucleons in the bound state is determined by the fact how much is the real clusterization of this nucleus in the channel of $A_1 + A_2$

nucleons. At the same time, some nuclear characteristics of individual, even not cluster, nuclei can be predominantly determined by one cluster channel, i.e. to have certain cluster structure at the small contribution of other possible cluster configurations. In this case, the used single-channel cluster model allows one to identify dominating cluster channel, mark and describe that properties of the nuclear system, which is possible to consider as a certain test of single-channel cluster configurations in such nuclei.

Different options of three-body models have intensively developed and purchased big extension in the end of the past century, which were used, for example, for ^{6}Li in the three-cluster np^{4}He channel that allow one correctly to describe many properties of this nucleus [3]. The large success was achieved in the microscopic models like resonating group method (RGM) [4], based on the nucleon-nucleon interactions with the evident extraction of cluster channels.

However, the described above two-cluster potential models described above, used intercluster forces with forbidden states, in many cases, allow one correctly to describe some nuclear characteristics for different light and lightest nuclei, and, evidently do not yet exhaust completely their potential. The more especially as reported here methods and results are applicable to certain problems of nuclear astrophysics, concerned to light atomic nuclei and ultralow energies of interacting particles. In other words, these results have direct relationship to thermonuclear processes flowing in the Sun, stars, some other objects of our Universe and Universe in whole, at different stages of its forming and developing.

2. Interaction potentials and scattering phase shifts

The orbital states in the ^{3}He^{3}H system for ^{6}Li are pure by Young diagrams [5]. Therefore, potentials obtained on the basis of the scattering phase shifts are possible to use directly for considering characteristics of bound states of these nuclei. Results will depend on the clusterization degree of nuclei in the considered cluster channels. Because, the probability of clusterization lithium nuclei is relatively high, then the calculation results should generally reproduce experimental data.

The Gaussian form is used for potentials

$$V(r) = V_0 \exp(-\alpha r^2) + V_c(r) \tag{1}$$

with the point-like Coulomb term. Interaction parameters for pure cluster states in ^{6}Li nucleus, obtained in [6,7], are given in Table 1. In the ^{3}He^{3}H system at $S = 0$ for D and F phase shifts the same potentials are used that for the S and P waves correspondingly.

Table 1 - Potential parameters in the ^{3}He^{3}H system [1,2]. R_c = 0 fm for the ^{3}He^{3}H system

	$S = 1$		$S = 0$	
L_J	V_0, (MeV)	α (fm^{-2})	V_0, (MeV)	α (fm^{-2})
S	–90	0.18	–85.0	0.18
P_0	–52.5	0.2	–	–
P_1	–65.0	0.2	–74.0	0.2
P_2	–80.0	0.2	–	–
D_1	–72.0	0.18	–	–
D_2	–85.0	0.18	–	–
D_3	–90.0	0.18	–	–

Due to the absence of the experimental results, the potentials for the ^{3}He^{3}He system are constructed exclusively on results of the calculation of phase shifts, obtained in the RGM [8,9]. Parameters of such interactions coincide with potentials of the ^{3}He^{3}He system at $S = 0$. There fore, ^{3}He^{3}He it is a system of identical particles, here even L correspond to zero spin, and odd to unit spin.

The quality of the phase shift description is shown in figure 1 with experimental data from woks [10–13] for ^{4}He^{2}H, [14–16] for ^{4}He^{3}H and [17,18] for ^{3}He^{3}H systems. The calculation results of the ^{3}He^{3}He elastic scattering phase shifts obtained in the RGM [19] are shown by crosses in figure 1.

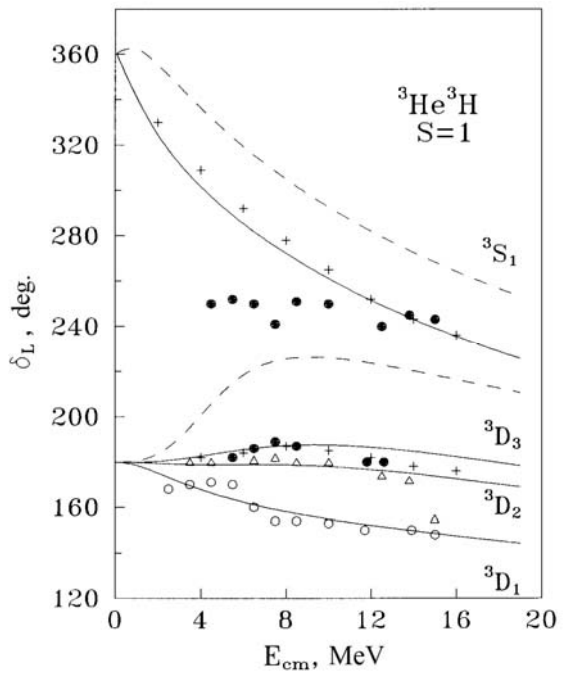

Figure 1a - Phase shifts of the ^{3}He^{3}H scattering. Curves are calculations for potentials with parameters from table 1. Points, triangles and circles are experimental data from [17,18]. Crosses are RGM calculations from [19]

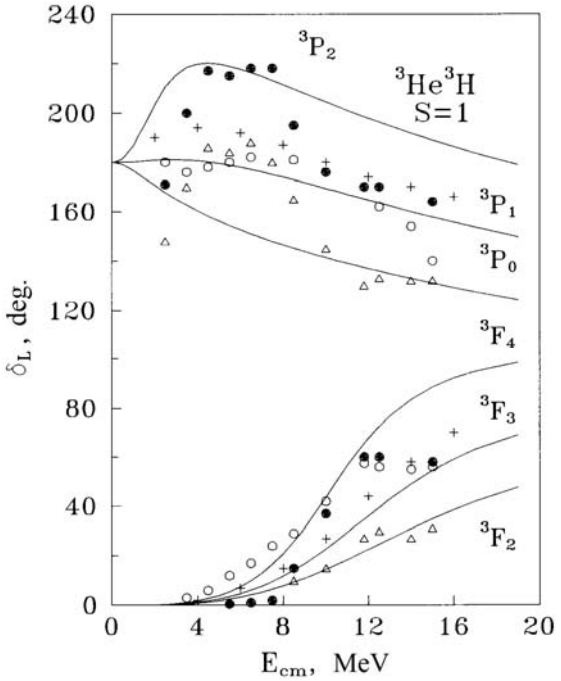

Figure 1b - Phase shifts of the ^{3}He^{3}H scattering. Curves are calculations for potentials with parameters from table 1. Points, triangles and circles are experimental data from [17,18]. Crosses are RGM calculations from [19]

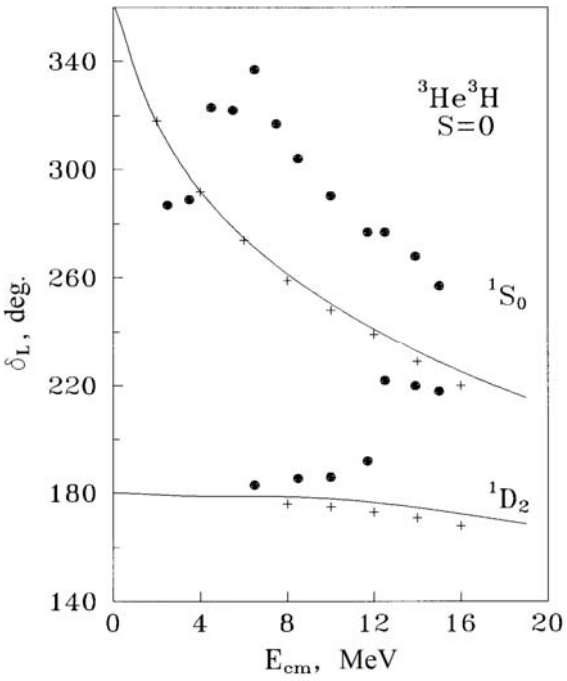

Figure 1c - Phase shifts of the ^{3}He^{3}H scattering. Curves are calculations for potentials with parameters from table 1. Points are experimental data from [17,18]. Crosses are RGM calculations from [19]

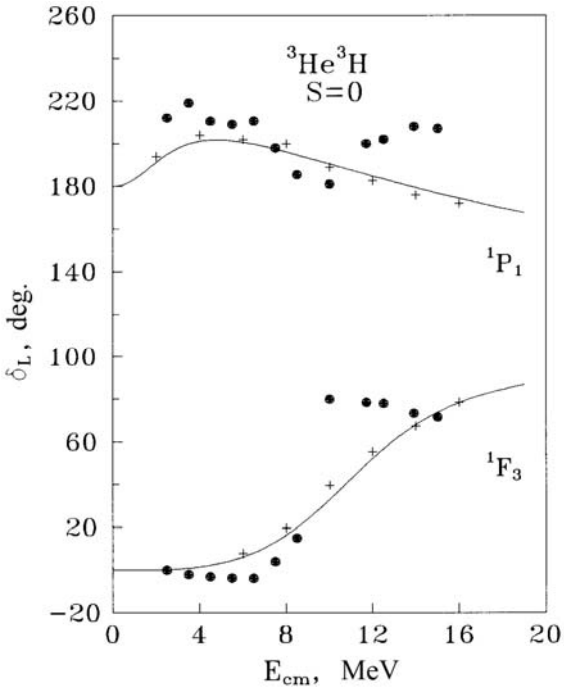

Figure 1d - Phase shifts of the ^{3}He^{3}H scattering. Curves are calculations for potentials with parameters from table 1. Points are experimental data from [17,18]. Crosses are RGM calculations from [19]

3. Total capture cross sections

Using the known equations for matrix elements of different operators, given in [20], one can obtain the final expression [7] for the total capture cross section

$$\sigma_c(NJ,J_{\rm f}) = \frac{8\pi K e^2}{\hbar^2 q^3}\frac{\mu}{(2S_1+1)(2S_2+1)}\frac{J+1}{J[(2J+1)!!]^2}A_{\rm J}^2(NJ,K)\cdot$$

$$\cdot\sum_{\rm L_i,J_i} P_{\rm J}^2(NJ,J_{\rm f},J_{\rm i})I_{\rm J}^2(J_{\rm f},J_{\rm i}), \qquad (2)$$

where matrix elements of *EJ* transitions have the form

$$P_{\rm J}^2(EJ,J_{\rm f},J_{\rm i}) = \delta_{\rm S_iS_f}[(2J+1)(2L_{\rm i}+1)(2J_{\rm i}+1)(2J_{\rm f}+1)](L_{\rm i}0J0\,|\,L_{\rm f}0)^2\begin{Bmatrix} L_{\rm i} & S & J_{\rm i} \\ J_{\rm f} & J & L_{\rm f}\end{Bmatrix}^2 \qquad (3)$$

$$A_J(EJ,K) = K^J\mu^J\left(\frac{Z_1}{m_1^J}+(-1)^J\frac{Z_2}{m_2^J}\right),\ I_J(J_f,J_i) = \left\langle\chi_f\left|r^J\right|\chi_i\right\rangle.$$

In the case of *E*1 capture in the ^{3}He^{3}H cluster channel to the ground state (GS) of ^{6}Li the $P_{\rm J}$ value is presented in the form

$$P_J^2 = 2J_i + 1, \qquad (4)$$

if the capture is to the GS from the scattering states with $L = 2$ and $J_{\rm i} = 1,2,3$ for the initial states with $J_{\rm i} = 0,1,2$ and $L = 1$. In the ^{3}He^{3}H cluster model it is possible also to consider *E*1 transition to the 3^+ resonance state. In this case the $P_{\rm J}$ value is listed in Table 2. Parameters of the ^{3}He^{3}H potentials taken into account spin-orbital splitting are given in Table 1.

Table 2 - Coefficients $P_{\rm J}$ in the ^{3}He^{3}H cluster channel of ^{6}Li nucleus

^{3}He^{3}H (3^+)	
$L_{\rm J}$	P$_{\rm J}$(*E*1)
^{3}P$_2$	42/5
^{3}F$_2$	1/35
^{3}F$_3$	1
^{3}F$_4$	81/7

Calculation results for the total capture cross section with the *S* potential, correctly describing binding energy of the nucleus (see sec. 3), are shown in figure 4a by the solid line [7]. Experimental data are from [21,22]. It is seen that using this potential and *P* interaction, correctly representing energy behavior of scattering phase shifts, allows one to describe experimental results well. Note that there are other measurements of cross sections [23], noticeably differ from reproduced in the figure.

In the case of *M*1 transitions to the GS, the process when the change of the spin state from singlet to triplet takes place was considered. Only the spin term W$_{\rm Jm}$(*S*) with coefficient $-\sqrt{3/2}$ remains in the transition operator. $P_{\rm J}$ is found from (3) for *E*2 transitions to the GS from the *D* wave with $J_{\rm i} = 1, 2, 3$. Results of these calculations are shown in figure 2a by the dotted and dashed curves [7].

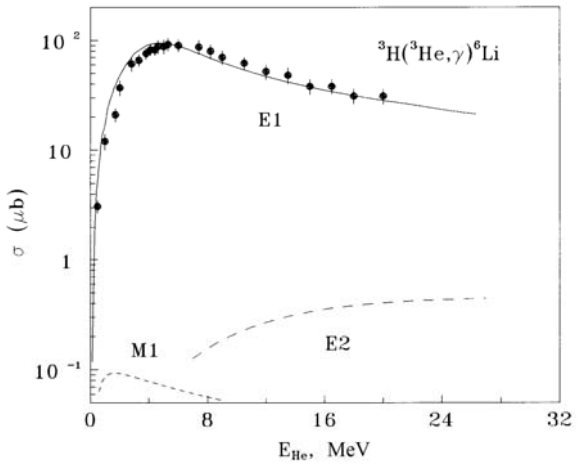

Figure 2a - The total cross section of the radiative tritium capture on ^{3}He with the formation of ^{6}Li in the GS. Solid curve is the calculated $E1$ cross sections for scattering potentials from Table 1. Dotted curve is the cross section of the $M1$ process, dashed curve is the $E2$ cross section. Points are experimental data from [21,22]

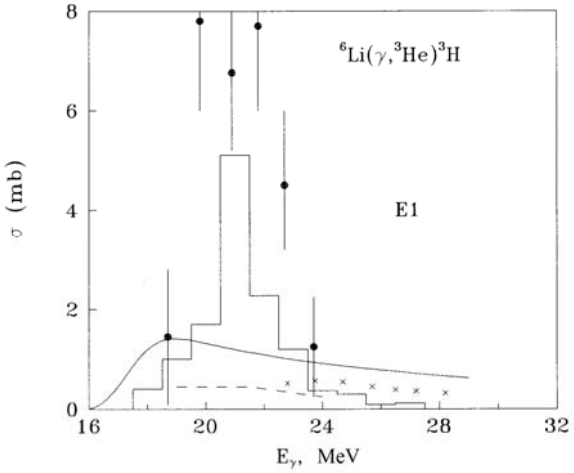

Figure 2b - The total cross section of the photodisintegration process of ^{6}Li. Solid curve is the cross section obtained on the basis of detailed balancing principle from the calculated capture cross sections [7]. Points, histogram, dashed curve and crosses are experimental data from [24–27]

Differences in total experimental cross sections for the ^{6}Li(γ,^{3}He)^{3}H photodisintegration is more than in the case of radiative capture. The measurements results obtained in [24–27] are shown in Fig. 3b. The solid figure shows the results obtained on the basis of detailed balancing principle from the calculating capture cross sections [7].

The astrophysical S-factor for the ^{3}H(^{3}He,γ)^{6}Li capture at low energies is shown in Fig. 3a. The value equals 0.06 keV·b was obtained by the linear extrapolation of the S-factor at zero energy in the $E1$ process.

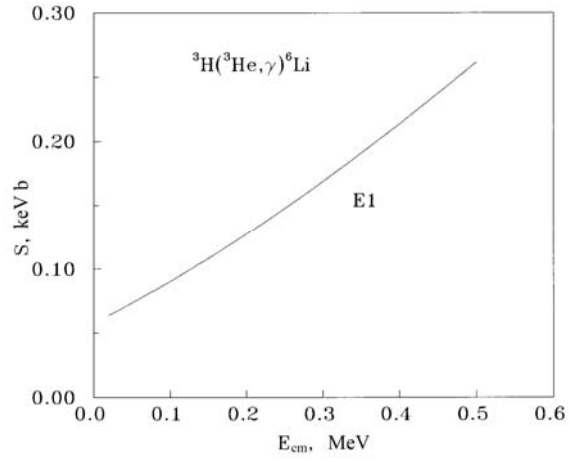

Figure 3a - Astrophysical S-factor for the $E1$ process at the ^{3}H(^{3}He,γ)^{6}Li capture [7].

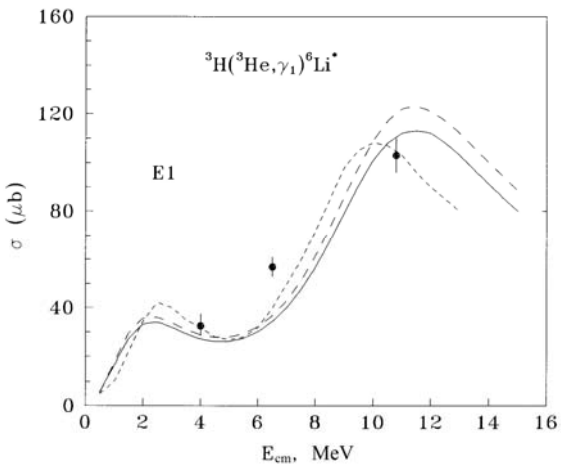

Figure 3b - Total cross sections for the radiative capture process in the ^{3}He^{3}H channel with the formation of the ^{6}Li nucleus in the excited 3^+ state. Points are experimental data from [28]

The calculation results of capture cross sections to the 3^+ level for potentials from Table 1 [7] together with data and computations (dotted curve), obtained in [28], are shown in Fig. 3b. The potentials of the D_3 bound state with the depth 105 MeV (solid curve) and 107.5 MeV (dashed curve) are used here, which were discussed in sec. 3.

4. Conclusion

The radiative tritium capture on ^{3}He at low and astrophysical energies was considered in the framework of the modified potential cluster model. It is shown that on the basis of potentials coincided with scattering phase shifts and the energy of bound state it is possible to correctly represent available experimental data.

Acknowledgments

This work was supported by the Grant of Ministry of Education and Science of the Republic of Kazakhstan through the program No. AP05130104 “Studying of the radiative capture reactions in stars and controlled thermonuclear fusion” through the Fesenkov Astrophysical Institute of the National Center for Space Research and Technology of the Ministry of Defence and Aerospace Industry of the Republic of Kazakhstan (RK).

А.В. Джазаиров-Кахраманов[1,2], Л.Т. Карипбаева[1,2], А.А.Стеблякова[2]

[1] В.Г. Фесенков атындағы Астрофизика институты ЕЖШС, ҚР, Алматы, Қазақстан
[2]Халықаралық Ақпараттандыру Академиясы, Алматы, Қазақстан

ТӨМЕНГІ ЖӘНЕ АСТРОФИЗИКАЛЫҚ ЭНЕРГИЯЛАРДАҒЫ РАДИАЦИЯЛЫҚ ^{3}He^{3}H ҚАРМАУ

Аннотация. Модификацияланған потенциалды кластерлік модель аясында төменгі және астрофизикалық энергиялардағы радиациялық ^{3}He^{3}H қармау қарастырылған. Шашырату кезеңдері және байланысқан энергия күйімен үйлестірілген потенциалдар негізінде алынған эксперименттік мәліметтерді дұрыс жіберуге болатындығы көрсетілген. Мақалада сипатталып отырған, тиым салынған кластерлераралық күшті пайдаланатын, екікластерлі потенциалдық моделдер, көп жағдайда, әр түрлі жеңіл және өте жеңіл ядролардың кейбір ядролық сипаттамаларын дұрыс көрсете білуге мүмкіндік береді және өзінің мүмкіндіктерін әлі толық тауыса қоймаған секілді. Мұнда көрсетіліп отырған әдістер мен нәтижелерді, жеңіл атомдық ядролар мен бөлшектер өзарабайланысының өте төмен энергияларына қатысы бар ядролық астрофизиканың кейбір мәселелерін шешуде қолдануға болады. Басқаша айтқанда, бұл нәтижелердің Күнде, жұлдыздарда, Ғаламның басқа да кейбір нысандарында, бүкіл Ғаламның түрлі қалыптасу кезеңдері мен дамуына қатысты өтетін термоядролық үдерістерге тікелей қатысы бар. Бір арналы кластерлік модельді пайдалануға болады, ол көптеген жағдайларда нақты жағдайға жақсы жақындайды. Мұндай модель шашырау процестері мен байланысты жағдайлардағы, тіпті көптеген денелердің есебін шешу әдістері немесе сандық орындаудағы өте ауқымды немесе нақты сандық нәтижелерге әкелмейтін жүйелерде де Ядролық сипаттамалардың кез келген есебін салыстырмалы түрде оңай орындауға мүмкіндік береді. Атом ядросының құрылымы алуан түрлі және кейде бір бірін жоққа шығаратын құрылымдар табылады. Мысалы, ядрода нуклондардың тәуелсіз қозғалысы, еркіндік дәрежелерінің бірлестігінің көрінісі, ұқсас бос ядролардың құрылымдарының кластерлеріне - ұқсас нуклондардың дербес топтарға бөлінуі мүмкін. Бұған дейінгі ядродағы тұрақты кластерлер ұғымы тәуелсіз нуклондар қозғалысы кезінде ядрода виртуалды жүйе бөлігі – кластерлер пайда болады және бүлінеді деген ұғымға ауысты. Сондықтан, атомдық ядродағы әйтеуір бір кластерлік каналдың бар екендіні туралы ғана айтуға болады. Әрине, екіге бөлінген түсінік ядрода болып жатқан жағдайдың анық мінсіз күйі болып табылады, себебі, бастапқы каналдың бөлшектері үшін кластерлендірудің үлкен дәрежесіне ие деп болжам жасалуда. Сондықтан мұндай потенциалды үлгінің жетістігі байланған күйдегі A нуклондардың жүйесін сипаттауда нуклондардың $A_1 + A_2$ каналындағы осы ядроның шынайы кластерлендірілуі қаншалықты үлген екендігімен анықталады. Сонымен қатар, кейбір кластерлік емес дербес ядролардың сипаттамалары бір анықталған кластерлік каналмен айрықша шарттасуы мүмкін, яғни басқа да мүмкін кластерлік конфигурацияны қосқанда анық кластерлік құрылымға ие болу. Бұл жағдайда пайдаланылып отырған бір каналды кластерлік модель басымдық көрсететін кластерлік каналды теңдестіруге, шарттасқан ядролық жүйенің құрылымын ерекшелеуге және сипаттауға мүмкіндік береді. Сондықтан, бір каналды модельде алынған нәтижелерді осындай ядролардағы кластерлі конфигурацияның бір каналдылығының тесті ретінде қарастыруға болады.

Түйін сөздер: ядролық астрофизика; бастапқы нюклеосинтез; жеңіл атомдық ядролар; радиациялық қармау; жылуядролық үдерістер; потенциалды кластерлік модель.

А.В. Джазаиров-Кахраманов[1,2], Л.Т. Карипбаева[1,2], А.А.Стеблякова[2]

[1]Астрофизический институт В.Г. Фесенкова "НЦКИТ" АКК МИР РК, Алматы, Казахстан;
[2]Международная Академия Информатизации, Алматы, Казахстан

РАДИАЦИОННЫЙ ^{3}He^{3}H ЗАХВАТ ПРИ НИЗКИХ И АСТРОФИЗИЧЕСКИХ ЭНЕРГИЯХ

Аннотация. В рамках модифицированной потенциальной кластерной модели рассмотрен радиационный ^{3}He^{3}H захват при низких и астрофизических энергиях. Показано, что на основе потенциалов, которые согласованы с фазами рассеяния и энергией связанного состояния удается правильно передать имеющиеся экспериментальные данные. Двухкластерные потенциальные модели, описанные в данной статье, использующие межкластерные силы с запрещенными состояниями, во многих случаях, позволяют правильно описывать некоторые ядерные характеристики для самых различных легких и легчайших ядер и, по-видимому, не исчерпали еще полностью свои возможности. Тем более, что изложенные здесь методы и результаты применимы к некоторым задачам ядерной астрофизики, имеющим отношение к легким атомным ядрам и сверхнизким энергиям взаимодействия частиц. Иначе говоря, эти результаты имеют непосредственное отношение к термоядерным процессам, протекающим на Солнце, звездах, некоторых других объектах нашей Вселенной и Вселенной в целом на различных этапах ее формирования и развития. Можно использовать одноканальную кластерную модель, которая во многих случаях оказывается хорошим приближением к реально существующей ситуации. Подобная модель позволяет сравнительно легко выполнять любые расчеты ядерных характеристик в процессах рассеяния и связанных состояниях, даже в тех системах, где методы решения задачи многих тел или очень громоздки в численном исполнении или вообще не приводят к конкретным количественным результатам. Структура атомного ядра очень многообразна и порой обнаруживает, казалось бы, взаимоисключающие свойства. Например, в ядре могут реализоваться свойства независимого движения нуклонов, коллективные проявления степеней свободы, ассоциирование нуклонов в почти независимые группы – кластеры с характеристиками, близкими к свойствам соответствующих свободных ядер. Ранее существовавшие представления о стабильно существующих в ядре кластерах заменились на понимание, что в процессе почти независимого движения нуклонов в ядре формируются и разрушаются виртуальные подсистемы – кластеры. Поэтому можно говорить лишь о вероятности существования в атомном ядре того или иного кластерного канала. Конечно, двухчастичное представление является определенной идеализацией реально существующей в ядре ситуации, т.к. предполагает, что связанное состояние имеет большую степень кластеризации для частиц начального канала. Поэтому успех данной потенциальной модели при описании системы из A нуклонов в связанном состоянии определяется тем, насколько велика реальная кластеризация этого ядра в канале $A_1 + A_2$ нуклонов. В то же время, некоторые ядерные характеристики отдельных, даже не кластерных ядер могут быть преимущественно обусловлены одним определенным кластерным каналом, т.е. иметь определенную кластерную структуру при малом вкладе других возможных кластерных конфигураций. В этом случае используемая одноканальная кластерная модель позволяет идентифицировать доминирующий кластерный канал, выделить и описать те свойства ядерной системы, которые им обусловлены. Поэтому результаты, получаемые в одноканальной модели, можно рассматривать как некоторый тест одноканальности кластерных конфигураций в таких ядрах.

Ключевые слова: ядерная астрофизика; первичный нюклеосинтез; легкие атомные ядра; радиационный захват; термоядерные процессы; потенциальная кластерная модель.

Information about authors:

Dzhazairov-Kakhramanov A.V., Candidate of Physical and Mathematical Sciences, Fesenkov Astrophysical Institute. Academician of the European Academy of Natural Sciences (EANS), academician of the International Informatization Academy (IIA), awarded of the European Carl Friedrich Gauss medal, Professor of the Russian Academy of Natural Sciences. albert-j@yandex.ru, https://orcid.org/0000-0003-2845-6889;

Karipbayeva L.T., Researcher, Fesenkov Astrophysical Institute, academician of the International Informatization Academy. larisa_karipbaeva@mail.ru, https://orcid.org/0000-0002-6238-2441;

Steblyakova A.A., Researcher, Corresponding member of the International Informatization Academy, awarded of the National Order of Enbek Yzdigi. a_steblyakova@mail.ru, https://orcid.org/0000-0003-2730-922X

REFERENCES

[1] Neudatchin V.G., Smirnov Yu.F. (1969) Nucleon associations in light nuclei. Nauka, Moscow. (in Russ.).

[2] Nemets O.F., Neudatchin V.G., Rudchik A.T., Smirnov Yu.F., Chuvil'skii Yu.M. (1988) Nucleon associations in atomic nuclei and nuclear reactions of multinucleon transfers, Naukova Dumka, Kiev, 488 p.

[3] Kukulin V.I. et al. (1984) Detailed study of the cluster structure of light nuclei in a three-body model: (I). Ground state of 6Li, Nucl. Phys. A, 417:128. DOI: 10.1016/0375-9474(84)90327-0.

[4] Mertelmeir T., Hofmann H.M. (1986) Consistent cluster model description of the electromagnetic properties of lithium and beryllium nuclei, Nucl. Phys. A, 459:387. DOI: 10.1016/0375-9474(86)90141-7.

[5] Dzhazairov-Kakhramanov A.V. (2013) Astrophysical S-factors of light atomic nuclei, Lap Lambert Academic Publishing, Saarbrücken, ISBN: 978-3-659-49854-1, 127 p.

[6] Neudatchin V.G. et al. (1992) Generalized potential model description of mutual scattering of the lightest p2H, 2H3He nuclei and the corresponding photonuclear reactions, Phys. Rev. C, 45:1512. DOI: 10.1103/PhysRevC.45.1512

[7] Dubovichenko S.B., Dzhazairov-Kakhramanov AV (1995) Photonuclear processes on 7Li and 7Be in the cluster model for potentials with forbidden states, Yad. Fiz., 58:635. RN: 27012203.

[8] Tompson D., Tang Y.C. (1967) Resonating-Group Calculation of He3-He3 Scattering, Phys. Rev., 159:806. DOI: 10.1103/PhysRev.159.806.

[9] Baye D., Hanck M. (1981) Generator-coordinate study of 3He+3He elastic scattering with a spin-orbit interaction, J. Phys. G, 7:1073. DOI: 10.1088/0305-4616/7/8/013.

[10] Bruno M. et al. (1982) Experimental study on low-energy 2H(α, α)2H elastic scattering, Nuovo Cim. A, 68:35. DOI: 10.1007/BF02902733.

[11] Jenny B et al. (1983) Phase-shift analysis of d-α elastic scattering between 3 and 43 MeV, Nucl. Phys. A, 397:61. DOI: 10.1016/0375-9474(83)90078-7.

[12] Darriulat P. et al. (1967) Phase shift analysis of deuteron-alpha scattering between 10 and 27 MeV, Nucl. Phys. A, 94:653. DOI: 10.1016/0375-9474(67)90438-1.

[13] Barit I.Ya. et al. (1987) Preprint IYaI, Moscow, No. P–0513.

[14] Spiger R., Tombrello T.A. (1967) Scattering of He3 by He4 and of He4 by Tritium, Phys. Rev., 163:964. DOI: 10.1103/PhysRev.163.964.

[15] Barnard A.C., Jones C.M., Phillips G.C. (1964) The scattering of 3He by 4He, Nucl. Phys., 50:629. DOI: 10.1016/0029-5582(64)90235-4.

[16] Ivanovich M., Young P.G., Ohlsen G.G. (1968) Elastic scattering of several hydrogen and helium isotopes from tritium, Nucl. Phys. A, 110:441. DOI: 10.1016/0375-9474(68)90552-6.

[17] Vlastou J. et al. (1977) Scattering of polarised and unpolarised 3He by 3H and high excitation in 6Li, Nucl. Phys. A, 292:29. DOI: 10.1016/0375-9474(77)90354-2.

[18] Batten R. et al. (1970) Elastic scattering of 3He by tritium, Nucl. Phys. A, 151:56. DOI: 10.1016/0375-9474(70)90966-8.

[19] Thompson D.R., Tang Y.C. (1968) Study of 3H+3H, 3H+3He, and 3He+3He systems with the resonating-group method, Nucl. Phys. A., 106:591. DOI: 10.1016/0375-9474(68)90518-6.

[20] Varshalovich D.A., Moskalev A.N., Khersonski V.K. (1975) Quantum theory of angular momentum, Nauka. Leningrad, 436p.

[21] Young A.M., Blatt S.L., Seyler R.G. (1970) Direct Radiative Capture of 3He by Tritons and t+3He Cluster States in 6Li, Phys. Rev. Lett., 25:1764. DOI: 10.1103/PhysRevLett.25.1764.

[22] Blatt S.L. et al. (1968) Reaction T(3He, γ)6Li in the Energy Range 0.5-11 MeV, Phys. Rev., 176:1147. DOI: 10.1103/PhysRev.176.1147.

[23] Nusslin F., Werner H., Zimmerer J. (1966) Der inverse Kernphotoeffekt T(He3,γ)Li6, Z. Naturf. A, 21:1195. DOI: 10.1515/zna-1966-0750.

[24] Murakami A. (1968) 6Li(γ, t)3He and 6Li(γ, pd)3H Reactions, Il Nuovo Cim. B, 55:604. DOI: 10.1007/BF02711673; (1970) J. Phys. Soc. Jap., 28:191. DOI: 10.1143/JPSJ.28.1.

[25] Bazhanov E.B. et al. (1965) Nucl. Phys., 68:191. DOI: 10.1016/0029-5582(65)90379-2.

[26] Sherman N.K., Baglin J.E.E., Owens R.O. (1968) Phototriton Cross Section of Li6, Phys. Rev., 169:771. DOI: 10.1103/PhysRev.169.771.

[27] Sherman N.K., Stewart J.R., Morrison R.C. (1966) Phototritons from Li6, Phys. Rev. Lett., 17:31. DOI: 10.1103/PhysRevLett.17.31.

[28] Mondragon A., Hernandez E. (1990) Negative-parity states in the spectrum of 6Li from elastic scattering and radiative capture of 3He by 3H, Phys. Rev. C, 41:1975. DOI: 10.1103/PhysRevC.41.1975.

NEWS
OF THENATIONAL ACADEMY OF SCIENCES OF THE REPUBLIC OF KAZAKHSTAN
PHYSICO-MATHEMATICAL SERIES
ISSN 1991-346X **https://doi.org/10.32014/2020.2518-1726.36**
Volume 3, Number 331 (2020), 52 – 58

UDK 524.37
МРНТИ 41.25.15

L.N. Kondratyeva, E.K. Denissyuk, I.V. Reva, M.A. Krugov,
G.K. Aimanova, B.K. Omar, B.A. Urmashev, A.T. Mailybayev

V.G. Fesenkov Astrophysical Institute, Almaty, Kazakhstan.
E-mail:lu_kondr@mail.ru, eddenis@mail.ru, alfekka@list.ru, mkrugov@astroclub.kz, agauhar@mail.ru, bauka_beka9296@mail.ru , baydaulet.urmashev@mail.ru, exeor@mail.ru

SPECTRAL AND PHOTOMETRIC STUDY OF TWO OBJECTS IRAS 22023+5249 AND IRAS 06053+1837

Abstract. The objects IRAS 06053+1837 and IRAS 22023+5249, are considered as planetary nebula candidates. They have far infrared colors, which are typical to planetary nebulae. Their rather cool stars are surronded by envelopes, in which some low-excitation emission lines are formed.

BV photometry of the object IRAS 22023+5249, carried out in 2017-2020, resulted the scatter of B and V values within $0^m.25$ and $0^m.10$ respectively. Moreover a tendency of the gradual increasing of brightness is revealed. Absolute fluxes and equivalent widths of the Hβ, Hα, [NII], 6548, 6583A and HeI, 6678A emission lines in the spectrum of IRAS 22023+5249 are determined. The strengthening of the emission lines is confirmed. Most likely increasing of an effective temperrature of the star is responsible for observable variations. As a whole spectral and photometric characteristics of the object IRAS 22023+5249 correspond to its status as a low-excitation planetary nebula.

For the object IRAS 06053+1837observable data are obtained in 2014 -2019. Much larger the scatter of B V R values is observed: $0^m.50$, $0^m.15$ and $0^m.30$ respectively. The only HI emission lines are presented in its spectrum. Asymmetrical profiles of lines have broad wings on the short wavelength side. The evolutionary status of the object is not defined; its characteristics, are more similar to those of the young AeBe Herbig stars.

Key words: emission objects, emission spectrum, B V R magnitudes, individual objects: IRAS 22023+5249, IRAS 06053+1837.

Introduction. The theory of the planetary nebulae formation as a whole has long been developed. But the problem of evolutional progenitors is as important and actual. It is known that some Be stars can develop circumstellar gaseous nebula, which creates an emission spectrum with forbidden lines. In other words, such object looks like as a planetary nebula. Last years some candidates for the planetary nebulae progenitors were found among the objects from IRAS catalog. They have the far infrared color typical for planetary nebulae, and due to such criterion it is possible to distinguish them from the other types of objects. Then the detected radio continuum can confirm the belonging of the object to the planetary nebula candidate [1,2]. Many of the objects from IRAS catalog already have low-excitation emission line spectra. Two of them: IRAS 22023+5249, IRAS 06053+1837 are considered in this paper.

Object IRAS 22023+5249=LS III+52°54=GGR 44=TYC 3969-2206-1 was initially entered in Catalog of early type emission−line stars [3]. Infrared observation of this object showed the presence of C and O rich dust features [4,5]. The high-resolution spectra of IRAS 22023+5249 were studied in Paper of Sarkar et al. [6]. The authors obtained the large heliocentric velocity of the object (-148.3±0.6 kms^{-1}), Teff = 24,000 K and log g = 3.0 ± 0.5. The only data of UBV observations of the object, carried out in 2007–2012, were presented by Arkhipova et al. [7]. The authors registered irregular photometric variability with the maximal amplitude of $0.^m25$ in the V filter. Moreover, an increase in the brightness of the object was accompanied by an increase of the color index (B-V) and by decrease of (U-B) [1].

Object IRAS 06053+1837 = LkHa 209 was included in different observational programs [2,8]. Thus its classification was changing from the star of the spectral class K0 to the possible protoplanetary nebula. Information about this object is also very limited: BVR photometry was carried out in 1986–1995 [2,9]. Our spectral and photometric observations of IRAS 22023+5249 and IRAS 06053+1837 were carried out in 2014–2020.

Observations and data reduction. Photometric observations of the objects were carried out with the Eastern 1-meter Carl Zeiss Jena telescope located at the Tyan-Shan Observatory of Fesenkov Astrophysical Institute. The CCD camera Alta F16M (4096x4096, 9μ) of Apogee and a set of Johnson B V R filters were used. Four standard stars were chosen in the field and were used for calibration. These stars are well-isolated, with a brightness comparable to the object. They are located at small angular distance from the target, thus there is a negligible difference between atmospheric extinction for standards and object. All instrumental BVRc magnitudes of the objects were determined relative to each standard and were transformed to the standard photometric system. The expressions for this procedure were obtained from photometric measurements of the stars from [10]. Obtained images were processed using the Bias, Dark and Flat files. Image measurements are performed using the standard software packages MaximDl 6 and IRAF. Correction for atmospheric extinction and transformation of the obtained brightness to the standard system B V R is carried out using a system of corresponding equations.

Spectral observations were carried out using diffraction spectrograph mounted the telescope AZT-8. CCD camera SBIG ST-8 (1530x1020, 9μ) (AZT-8) was used in 2011, later it was changed by SBIG STT-3200 (2184x1472, 6.8μ). Two spectra of the object werer obtained with the second “WESTERN” 1-meter telescope of TShAO. The telescope is equipped with a new diffraction spectrograph. At the output of the spectrograph, SBIG STT-3200 (2184x1472, 6.8μ) is installed.

During observations, the spectrograms of an objects and standards were obtained with a wide (7"- 10") entrance slit. Standard stars with a known energy distribution were used for calibration of the fluxes. File processing consists of subtracting the dark background and taking into account atmospheric absorption.

Results. Photometric data for the object of the IRAS22023+5249, obtained in 2018–2020 are compiled in table 1. Figure 1 contains our results and those of Arkhipova et al., 2013. During our observations the scattering of the brightness values is less, and the level of brightness is as a whole higher than in previous years.

Table 1 – B and V magnitudes of IRAS22023+5249

Date of observations	JD-2400000	B mag	V mag
08.07.2018	58308.39	12.579±0.050	12.374±0.036
16.09.2018	58378.37	12.848±0.060	12.438±0.037
22.09.2019	58749.14	12.576±0.021	12.331±0.006
13.10.2019	58770.18	12.575±0.037	12.330±0.057
09.11.2019	58797.18	12.613±0.013	12.363±0.008
16.11.2019	58804.23	12.673±0.028	12.426±0.058
29.11.2019	58817.12	12.583±0.035	12.334±0.042
30.11.2019	58818.05	12.575±0.030	12.335±0.060
01.12.2019	58819.12	12.583±0.033	12.355±0.062
16.12.2019	58819.21	12.560±0.010	12.358±0.046
18.01.2020	58867.06	12.63±0.016	12.32±0.011
19.01.2020	58868.05	12.65±0.016	12.32±0.013

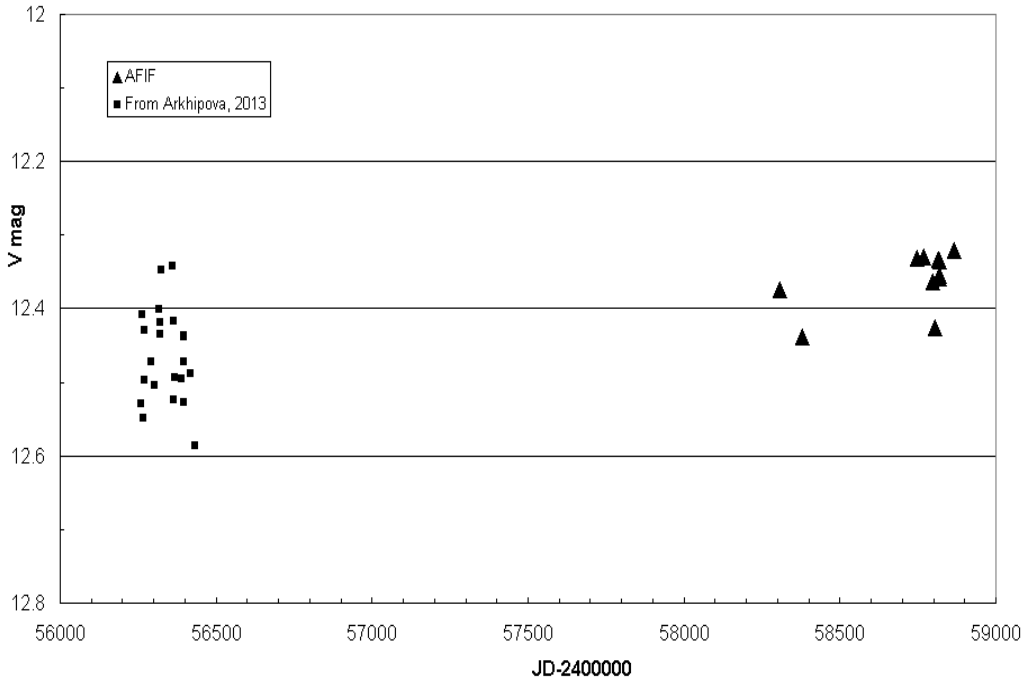

Figure 1 – Light curve of the object IRAS22023+5249 in the V band.

The results of spectral observations are presented in table 3. The absulute fluxes Fabs are expressed in erg $cm^{-2}cek^{-1}$. Accuracy of the EW values is about 10%. Variability of the fluxes is notable in figure 2. There are added data from Arkhipova et al., (2013) in the figure. It is seen, that Fabs(Hα) increased by 40% in comparing with the data, obtained in 2011 – 2013. Besides that the fluxes of the HeI and [NII] emission lines also increased. The ratio F(6717)/F(6731) of the [SII] line intensities corresponds to electron density Ne=3800±800 cm^{-3}.

Table 2- Fluxes and equivalent widths
of the emission lines in the spectrum of IRAS 22023+5249

Ions, λ	Dates of obs.	04.08. 2011	01.09. 2011	15.09. 2017	22.07. 2018	05.08. 2018	13.08. 2018	19.10. 2019	01.12. 2019
Hβ,4861	Fabs* 10^{13}		3.48± 0.22				3.59± 0.32	3.51± 0.32	
	EW(A)		8.7				13	9.4	
Hα,6563	Fabs* 10^{12}	1.69± 0.13		1.93± 0.20	2.17± 0.20	2.35± 0.22			2.15± 0.22
	EW(A)	57		69	48	86			86
[NII],6583	Fabs* 10^{13}	5.44± 0.30		6.04± 0.32	6.23± 0.35	6.27± 0.32			7.09± 0.30
	EW(A)	18		22	14	23			29
HeI,6678	Fabs* 10^{13}			2.61± 0.22		3.62± 0.32			
	EW(A)			0.9		1.4			
[SII],6717	Fabs* 10^{13}			3.92± 0.20		2.68± 0.22			
	EW(A)			1.4		1.0			
[SII],6731	Fabs* 10^{13}			5.92± 0.31		4.41± 0.30			
	EW(A)			2.1		1.7			

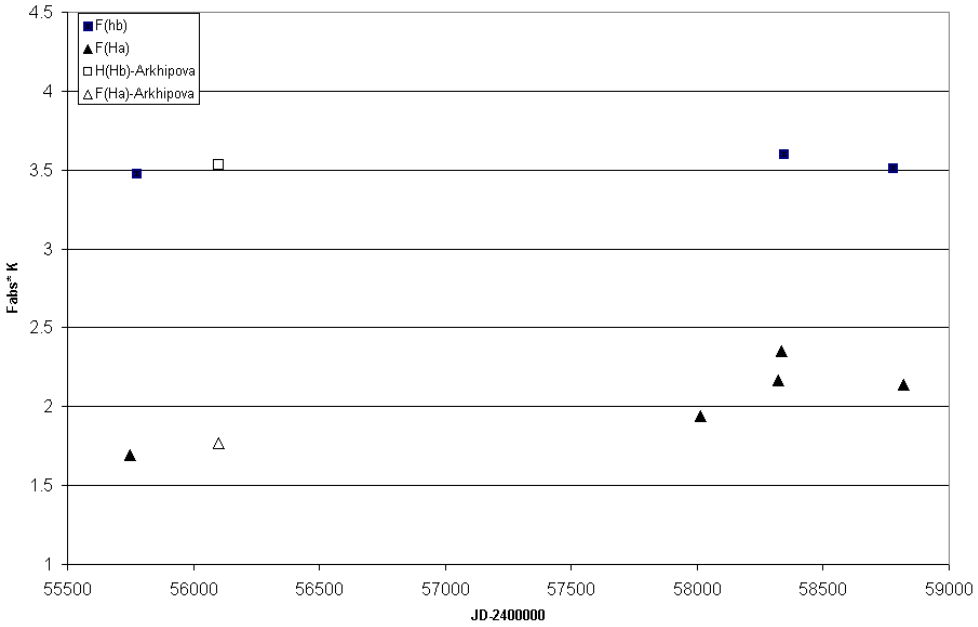

Figure 2 – Variations of the absolute fluxes in the Hα (squares) and Hβ (triangles) emission lines. Empty signs denote data from Arkhipova et al., 2013.

IRAS06053+1837

Our result of B V R observations are compiled in table 3 and in figure 3, where our data are added by the results from [4].

Table 3 – Photometric data for the object IRAS 06053+1837

Date of observations	JD-2400000	Bmag	Vmag	Rmag
14.10.2012	56215.150	12.532±0.020	11.876±0.022	11.779±0.020
24.10.2014	56955.192	12.595±0.024	11.934±0.025	11.937±0.018
24.01.2018	58143.225	13.135±0.028	11.837±0.020	11.644±0.019
05.01.2019	58489.163	12.910±0.022	11.894±0.022	11.731±0.020
25.01.2019	58509.130	13.027±0.032	11.995±0.024	11.921±0.022

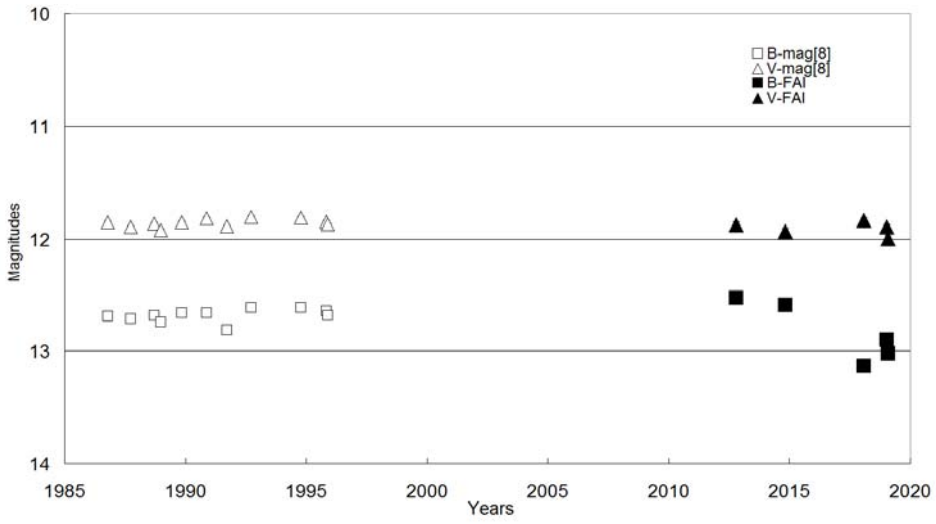

Figure 3 – Light curves of the object IRAS06053+1837 in the B and V bands. Our data data are indicated by squares (B mag) and triangles (V mag). Results from [4] are indicated by the same, but empty signes

Table 4 – Absolute fluxes and equivalent widths of the emissions lines in the spectrum of IRAS 06053+1837

Date of observations	JD-2400000	F(Hβ)*10^{13} ergs/cm^{2}sec	EW(Hβ) (A)	F(Hα)*10^{12} ergs/cm^{2}sec	EW(Hα) (A)
24.10.2014	56955.20	1.82±0.20	2.0±0.20	2.83±0.20	19.7±1.2
27.10.2016	57689.14			2.36±0.25	16.1±1.4
02.12.2018	58455.10			2.39±0.22	19.4±1.2
04.12.2018	58457.08				
05.12.2018	58458.08	1.42±0.16	1.1±0.12		
05.01.2019	58489.36	1.50±0.20	1.4±0.12		
06.01.2019	58490.36			2.07±0.22	19.9±1.2
20.03.2020	58929.06			2.10±0.25	19.6±1.2

It can be noted that over the past six years the absolute fluxes in the emission lines has decreased by 20 -25%. It is clear that an additional experimental information for this object is required.

Conclusion. In terms of evolution, the object IRAS 22023+5249 can represent a transitional stage from the Post-AGB stars to planetary nebulae. A shell consisting of gas and dust has already formed around the star, and the process of its filling is continued. Irregular variability of brightness is most likely connected with the change of circumstellar envelope. The low excitaion of gas in the envelope is due to the quite low temperature of the central source. But observable tendency of gradual increasing of brightness means that the star becomes hotter. Strengthening of the emission line also confirm this transformation of the star.

The object IRAS 06053+1837 Has rather poor emission spectrum, without any forbidden lines. Asymmetrical profile of Hα testifies the presence of stellar wind, due to which the forming of accreation disk and/or circumstellar envelope is continuing. The evolutionary status of the object is not defined; its characteristics, are more similar to those of the young AeBe Herbig stars.

Acknowledgments

The work was supported by the funding program BR05236322 of the Ministry of Education and Science of the Republic of Kazakhstan.

Кондратьева, Э.К. Денисюк, И.В. Рева, М.А. Кругов,
Г.К. Айманова, Б.К. Омар, Б.А. Урмашев, А.Т. Майлыбаев

В.Г. Фесенков атындағы астрофизика институты, Алматы, Қазақстан

ЕКІ НЫСАННЫҢ IRAS 22023+5249 ЖӘНЕ IRAS 06053+1837
СПЕКТРАЛДЫ ЖӘНЕ ФОТОМЕТРИЯЛЫҚ ЗЕРТТЕУІ

Аннотация. Планетарлық тұманның пайда болуы мен эволюциясының жалпы көрінісі осы объектілер туралы жаңа ақпаратпен үнемі және сәтті жаңартылып отырады. Планетарлық тұман бақылау радиотолқыннан рентгенге дейінгі толқындардың кең диапазонында жүзеге асырылады. Планетарлық тұманның тез эволюциялық предшественниктері мәселесі өзекті болып қала бер. Көптеген Ве жұлдыздарының жұлдыз атмосферасынан тез айналуының арқасында пайда болған. Жартылай иондалған газ HI, [OI], FeI, [FeII] эмиссиялық сызықтарын шығарады, басқаша айтқанда, төмен қозу планетарлық тұмандық спектріне ұқсас спектрге

Соңғы жылдары IRAS каталогында планетарлық тұманның эволюциялық прекурсорлары мәртебесіне үміткерлер анықталды. Оларда планетарлық тұманға тән инфрақызыл түс индикаторлары бар және бұл өлшем оларды басқа типтегі объектілерден ажырату үшін қолданылады. IRAS каталогындағы көптеген нысандарда қозу аз. Әдетте мұндай объектілер белсенділіктің жоғарылауымен сипатталады, олар фотометриялық және спектрлік өзгергіштік түрінде көрінеді.

Бұл мақалада екі объектіні зерттеу нәтижелері қарастырылған: IRAS 22023 + 5249, IRAS 06053 + 1837.

Нысан IRAS 22023 + 5249 = LS III + 52◦54 = GGR 44 = TYC 3969-2206-1 бастапқыда эмиссиялық сызықтары бар жұлдыздар каталогына енгізілген. Инфрақызыл бақылаулар шаңның болуын анықтады. Жоғары ажыратымдылықтағы спектрлік бақылаулар объектінің гелиоцентрлік жылдамдығы жоғары екенін көрсетті, ал жұлдыздың тиімді температурасы 24000К құрайды.

IRAS 22023+5249 нысанының 2017–2020 жж. орындалған B V фотометриясы сәйкесінше B және V жолақтарында шамамен $0^m.25$ және $0^m.10$ жұлдыздық шама дисперсиясын көрсетті. Нысанның спектрінде Hβ, Hα, [NII], 6548, 6583A, [SII], 6717, 6731A және HeI, 6678A эмиссиондық сызықтардың абсолютті ағындары мен эквиваленттік ені анықталды, сонымен қатар олардың біртіндеп күшеюі тіркелді. Сонымен, соңғы 10 жыл ішінде Hα және [NII] сәулелену сызықтарындағы сәулелену 1,5 есе өсті. [SII], 6717, 6731A сызықтарының қатынасынан анықталған газдың электронды тығыздығы Ne = 3800 ± 800 см-3 құрайды. Орталық жұлдыз температурасының артуы нысанның бақыланып отырылған құбылыстарына жауапты секілді.

Жалпы айтқанда IRAS 22023+5249 нысанының спектралды және фотомериялық сипаттамалары өзінің жағдайына, яғни төменгі қозудағы планетарлық тұмандыққа сай.

Нысан IRAS 06053 + 1837 = LkHa 209 көптеген бақылау бағдарламаларының қатысушысы болды. Оның жіктелуі әрдайым өзгеріп отырды: K класындағы жұлдыздан протопланетарлық тұманға дейін. Жалпы, бұл объект туралы ақпарат айтарлықтай шектеулі. Әдебиетте 1986 - 1995 жылдары алынған фотометриялық мәліметтер бар.

IRAS 06053+1837 атты нысанға бақылау мәліметтері 2012 -2019жж. алынды. Сәйкесінше, бұл нысанда B V R шамалары мәндерінің айтарлықтай үлкен шашылымы байқалады: $0^m.50$, $0^m.15$, $0^m.30$ спектрде сутектің эмиссиялық сызықтары ғана бар. Сызықтардың ассиметриялық профильдері қысқа толқындық шекарада кең қанатқа ие. Нысанның эволюциялық мәртебесі белгісіз, өзінің жеке сипаттамарына орай Хербигтің AeBe типті жас жұлдыздарға ұқсас.

Түйін сөздер: эмиссиялық нысандар, эмиссиялық сызықтар, B V шамалар, жеке нысандар: IRAS 22023+5249, IRAS 06053+1837.

Л.Н. Кондратьева, Э.К. Денисюк, И.В. Рева, М.А. Кругов,
Г.К. Айманова, Б.К. Омар, Б. А. Урмашев, А.Т. Майлыбаев

Астрофизический институт В.Г. Фесенкова, Алматы, Казахстан

СПЕКТРАЛЬНЫЕ И ФОТОМЕТРИЧЕСКИЕ ИССЛЕДОВАНИЯ ДВУХ ОБЪЕКТОВ IRAS 22023+5249 И IRAS 06053+1837

Аннотация. Общая картина происхождения и эволюции планетарных туманностей постоянно и успешно пополняется новой информацией об этих объектах. Наблюдения планетарных туманностей проводятся в широком диапазоне длин волн от радиодиапазона до рентгеновского. Проблема непосредственных эволюционных предшественников планетарных туманностей сохраняет свою актуальность. Известно, что многие звезды класса Be обладают околозвездной оболочкой, которая сформировалась из атмосферы звезды, благодаря ее быстрому вращению. Околозвездные оболочки, частично ионизованные, излучают эмиссионные линии HI, [OI], FeI, [FeII], иными словами, имеют спектр, подобный спектру планетарных туманностей низкого возбуждения. В последние годы кандидаты на статус эволюционных предшественников планетарных туманностей выявлены в каталоге IRAS. Они имеют инфракрасные показатели цвета, типичные для планетарных туманностей, и именно этот критерий используется для того, чтобы отличить их от объектов других типов. Многие объекты из Каталога IRAS уже имеют спектры низкого возбуждения. Как правило, подобные объекты отличаются повышенной активностью, которая проявляется в виде фотометрической и спектральной переменности.

В данной статье обсуждаются результаты исследования двух объектов: IRAS 22023+5249, IRAS 06053+1837

Объект IRAS 22023+5249=LS III+52°54=GGR 44=TYC 3969-2206-1 первоначально входил в каталог звезд с эмиссионными линиями. Инфракрасные наблюдения выявили присутствие пыли. Спектральные наблюдения с высоким разрешением показали, что объект имеет высокую гелиоцентрическую скорость, и эффективная температура звезды составляет 24000K.

Наши фотометрические наблюдения, проведенные в 2017 – 2020 гг., показали высокую дисперсию звездных величин порядка $0^m.25$ и $0^m.10$, в B и V полосах, соответственно. Более того, наблюдается тенденция постепенного усиления блеска. В спектре объекта определены абсолютные потоки и эквивалентные ширины эмиссионных линий Hβ, Hα, [NII], 6548, 6583A, [SII],6717, 6731A and HeI, 6678A. Отмечается постепенное усиление абсолютных потоков, особенно заметное в «красном» диапазоне спектра. Так, за последние 10 лет излучение в эмиссионных линиях Hα и [NII] увеличилось в 1.5 раза. Электронная плотность газа, определенная по отношению линий [SII],6717, 6731A, составляет $Ne=3800\pm800 cm^{-3}$.

Наблюдаемые изменения объекта IRAS 22023+5249 можно объяснить повышением эффективной температуры центральной звезды. В целом спектральные и фотометрические характеристики данного объекта соответствуют его статусу – планетарной туманности низкого возбуждения.

Объект IRAS 06053+1837 = LkHa 209 был участником многих наблюдательных программ. Его классификация все время менялась: от звезды класса К до протопланетарной туманности. В целом информация об этом объекте довольно ограниченная. В литературе есть фотометрические данные, полученные в 1986–1995 гг.

Наши наблюдения объекта IRAS 06053+1837 выполнялись в 2012–2020 гг. Фотометрические данные показали, что блеск объекта долгое время находится на одном уровне, но дисперсия значений достаточно велика: $0^m.50$, $0^m.15$ и $0^m.30$, в B V R полосах, соответственно. В 2019г наметилось небольшое ослабление блеска, особенно заметное в полосе В. В спектре IRAS 06053+1837 присутствуют только эмиссионные линии водорода. Ассиметричные профили линий имеют широкие крылья на коротковолновой границе, что свидетельствует о наличии звездного ветра. Эволюционный статус объекта не определен, по своим характеристикам он похож на молодые звезды типа AeBe Хербига.

Ключевые слова: эмиссионные объекты, эмиссионные линии, B V величины, индивидуальные объекты: IRAS 22023+5249, IRAS 06053+1837.

Information about authors:

Kondratyeva L.N., Doctor of Physical and Mathematical Sciences, V.G. Fesenkov Astrophysical Institute. lu_kondr@mail.ru, https://orcid.org/0000-0002-6302-2851;

Denissyuk E.K., Doctor of Physical and Mathematical Sciences, V.G. Fesenkov Astrophysical Institute. eddenis@mail.ru, https://orcid.org/0000-0001-5020-2557;

Reva I.V., Junior researcher, V.G. Fesenkov Astrophysical Institute. alfekka@list.ru, https://orcid.org/0000-0001-9944-8398;

Krugov M.A., Engineer V.G. Fesenkov Astrophysical Institute. mkrugov@astroclub.kz, https://orcid.org/0000-0002-2788-2176;

Aimanova G. K., Doctor of Physical and Mathematical Sciences, V.G. Fesenkov Astrophysical Institute. agauhar@mail.ru, https://orcid.org/0000-0002-3869-8913;

Omar B.K- Engineer, V.G. Fesenkov Astrophysical Institute. bauka_beka9296@mail.ru, https://orcid.org/0000-0003-2423-6424;

Urmashev B.A., Doctor of Physical and Mathematical Sciences, V.G. Fesenkov Astrophysical Institute. baydaulet.urmashev@mail.ru, https://orcid.org/0000-0001-7641-198X;

Mailybayev A.T., Doctor of Physical and Mathematical Sciences, V.G. Fesenkov Astrophysical Institute. exeor@mail.ru, https://orcid.org/0000-0002-0967-0727

REFERENCES

[1] Ratag M.A., Pottasch S.R., Zijlstra A.A., et al. **(1990)** Planetary nebulae near the galactic center. Astronomy and Astrophysics. Vol. 233. P.181. (in Eng.).

[2] Van de Steene G.C., Pottasch S. R. **(1995)** Radio continuum observations of planetary nebula candidates from the northern hemisphere. Astronomy and Astrophysics. Vol 299. P.238. (in Eng.).

[3] Wackerling L. R. **(1970)** A catalogue of early-type stars whose spectra have shown emission lines. MNRAS. Vol. 73. P. 153. (in Eng.).

[4] Cerrigone, L., Hora, J. L., Umana, G., & Trigilio, C. **(2009)**. Spitzer Detection of Polycyclic Aromatic Hydrocarbons and Silicate Features in Post-AGB Stars and Young Planetary Nebulae. The Astrophysical Journal. Vol. 703. P.585. DOI:10.1088/0004-637X/703/1/585 (in Eng.).

[5] Gauba G., Parthasarathy M. **(2004)**. Circumstellar dust shells of hot post-AGB stars. Astronomy and Astrophysics.Vol. 417. P. 201. DOI: 10.1051/0004-6361:20031769 (in Eng.).

[6] Sarkar G., Garcia-Hernandez D.A., Parthasarathy M., et al. (2012). High resolution spectroscopy of the high velocity hot post-AGB star LS III+52◦24 (IRAS 22023+5249). MNRAS. Vol. 421. P. 679. DOI: 10.1111/j.1365-2966.2011.20345.x (in Eng.).

[7] Arkhipova V.P., Burlak M.A., Esipov V.F. et al. **(2013)**. Nonstationarity of Hot Post-AGB Objects: Variations of the Brightness and Spectrum of IRAS 01005+7910, IRAS 22023+5249, IRAS 22495+5134. Astronomy Letters. Vol. 39. P. 619. DOI: 10.1134/S1063773713090016 (in Eng.).

[8] Grankin K.N., Melnikov S.Yu., Bouvier J., et al. **(2007)**. Results of the ROTOR-program. I. The long-term photometric variability of classical T Tauri stars. Astronomy and Astrophysics. Vol. 461. P.183. DOI: 10.1051/0004-6361:20065489 (in Eng.).

[9] Herbst W., Shevchenko V.S. **(1999)** A photometric catalog of Herbig Ae/Be stars and discussion of the nature and cause of the variations of UX Orionis stars. The Astronomical Journal. Vol. 118. P.1043. DOI: 10.1086/300966 (in. Eng.).

[10] Landolt A. **(2013)**. UBVRI photometric standard stars around the sky at +50 deg declination. The Astronomical Journal, Vol. 146. P. 131. DOI: 10.1088/0004-6256/146/5/131 (in Eng.).

NEWS
OF THENATIONAL ACADEMY OF SCIENCES OF THE REPUBLIC OF KAZAKHSTAN
PHYSICO-MATHEMATICAL SERIES
ISSN 1991-346X **https://doi.org/10.32014/2020.2518-1726.37**
Volume 3, Number 331 (2020), 59 – 65

UDC 523.62

G.S. Minasyants[1], T.M. Minasyants[1], V.M. Tomozov[2]

[1]Fesenkov Astrophysical Institute, Almaty, Kazakhstan;
[2]Institute of Solar-Terrestrial Physics, Irkutsk, Russia.
E-mail: gennadii_minasya@mail.ru, tamara@aphi.kz, tom@iszf.irk.ru

COMPARISON OF CHARACTERISTICS OF PHOTONS FLUXES VARIOUS ENERGIES IN THE DEVELOPMENT OF SOLAR GAMMA FLARES

Abstract. The characteristics of photons fluxes of various energies during the development of flares with high-energy gamma rays are considered. Observations on FERMI, SDO, GOES spacecraft were used. Photons fluxes with energies E_k = (12-25) keV, E_k = (50-100) keV and E_k > 100 MeV for 19 flares events were compared. Comparison of quantitative and temporal characteristics of photons profiles of X-ray energy range with properties of bright flares plasma showed that for almost all events the moments of onset of peaks (12-25) keV and maximum values (50-100) keV of photons in counts/s refer to the time interval from the beginning of flares development within 22 minutes. The same result is noted for events with the most intense maximum fluxes in ($\gamma \cdot cm^{-2} \cdot s^{-1}$) for high energy photons > 100 MeV. This supports the assumption of the most effective acceleration of particles during the simultaneous development of the direct flare process and the accompanying coronal mass injection, resulting in the creation of maximum fluxes values of highly energetic gamma photons. Flares events with the most intense maximum fluxes in ($\gamma \cdot cm^{-2} \cdot s^{-1}$) for high energy photons > 100 MeV do not show the highest values of the number of photons in the X-ray energy ranges, indicating differences in the efficiency of photons formation mechanisms of different energies. According to observations, the most likely source of quantitative amplification of flares photons with energies (12-25) keV is the results of bremsstrahlung radiation of bright flares emission in corona, and for photons with energies (50-100) keV - in the area of upper photosphere and temperature minimum.

Keywords: Solar flares, flare plasma emission, coronal mass ejection, X-ray and gamma ray.

Introduction. With use of the observation data obtained by means of the modern solar spacecrafts (SC) there was an opportunity to study properties of flare fluxes photons of different energy. During the impulse phase of flares, the main mechanism of particle acceleration is the release of free magnetic energy in the active region due to its dissipation in current sheets caused by magnetic reconnection followed by stochastic acceleration during the development of various plasma instabilities [1-3]. The process of magnetic reconnection occurs in both the corona and the chromosphere of the Sun [4]. As a result of the effect of magnetic reconnection, flows of fast-moving plasma, heat waves and highly energetic charged particles are observed from the area of primary energy release, some of which propagate along magnetic flux tubes into the underlying layers of the solar atmosphere. When interacting with denser plasma in loop bases, X-rays, gamma rays are generated and plasma is heated. Rapid heating of the plasma in the photosphere and chromosphere results in its "evaporation" and rising upward and filling the entire volume of magnetic arches. During this period, the greatest increase in soft X-rays is observed.

It is generally assumed that the occurrence of flares and associated coronal mass ejections (CME) is closely related to the imbalance of magnetic structures of the active regions during their evolution. As the magnetic structures of the active regions with the magnetic field polarities on the line of separation develop, the filaments are continuously complicated. Above the filaments there are closed loops of magnetic field, which create a generally closed magnetic configuration of the entire active area up to coronal heights. At continuous action of shear movements on the bases of magnetic loops along the line of

polarity separation, the filament (prominence) loses stability and begins to climb up rapidly, opening the magnetic structure and forming the "core" of CME. It is possible that it is with the process of "breaking" the vertices of coronal magnetic loops that the moving filament is associated with the impulse phase of the flare, because energy release is recorded in these areas and hard X-ray sources are observed.

An important source of particle acceleration in flares is their acceleration on shock wave fronts arising from the propagation of CME from the active regions to the upper layers of the corona and in the interplanetary environment. When protons of flares accelerate to Ek > 500 MeV energies, due to their nuclear interaction with the substance of the solar atmosphere, neutral pion are generated [5], at the decay of which gamma rays of high energy photons > 100 MeV produces.

The given physical, structural and dynamic properties of the active regions during the development of flares processes indicate the possible action of several mechanisms in the formation of photons of different energies.

Results of observation data processing. Properties fluxes of flares photons with energies E_k = (12-25) keV, E_k = (50-100) keV and E_k > 100 MeV were compared. From the list of 32 events presented in the works G.H. Share et al. [6,7] and with time resolution of 1 min for gamma ray fluxes E_k > 100 MeV, the only 19 of events that occurred in the period 2011-2017 were selected. This limitation is due to the mandatory presence in the observation data of profiles of quantitative changes of photons with energies E_k = (12-25) keV, E_k = (50-100) keV. Observations from FERMI spacecraft using GBM and LAT instruments were used.

Table 1 shows some characteristics of photon fluxes in X-ray energy intervals (12-25) keV and (50-100) keV, as well as of sustained gamma ray with energies > 100 MeV.

Table 1 - Characteristics of flares and fluxes of photons different energies

	Date GOES X-ray Class, Start	GBM peak (12-25) keV counts/s UT	GBM max (50-100) keV counts/s UT	LAT $F^{max}_{\gamma>100MeV}$ $\gamma \cdot cm^{-2} \cdot s^{-1}$ UT
1	07/03/2011 M3.7 19:43	$1.2 \cdot 10^5$ 20:03	$1.0 \cdot 10^4$ 20:02	$2.3 \cdot 10^{-5}$ 20:26
2	07/06/2011 M2.5 06:16	$6.9 \cdot 10^4$ 06:26	$1.3 \cdot 10^4$ 06:25	$5.5 \cdot 10^{-5}$ 08:00
3	04/08/2011 M9.3 03:41	$5.9 \cdot 10^5$ 03:54	$1.5 \cdot 10^4$ 03:52	$4.3 \cdot 10^{-5}$ 05:06
4	09/08/2011 X6.9 07:48	$1.2 \cdot 10^6$ 08:08	$7.0 \cdot 10^5$ 08:06	$7.7 \cdot 10^{-4}$ 08:03
5	06/09/2011 X2.1 22:12	$8.7 \cdot 10^5$ 22:20	$4.2 \cdot 10^5$ 22:19	$5.7 \cdot 10^{-4}$ 22:27
6	07/09/2011 X1.8 22:32	$1.0 \cdot 10^6$ 22:38	$1.7 \cdot 10^5$ 22:37	$1.6 \cdot 10^{-5}$ 23:37
7	24/09/2011 X1.9 09:21	$8.0 \cdot 10^5$ 09:42	$4.0 \cdot 10^5$ 09:35	$1.6 \cdot 10^{-4}$ 09:43
8	09/03/2012 M6.3 03:22	$1.3 \cdot 10^6$ 03:39	$8.0 \cdot 10^3$ 03:41	$1.3 \cdot 10^{-5}$ 03:50
9	03/06/2012 M3.3 17:48	$1.7 \cdot 10^5$ 17:55	$2.5 \cdot 10^4$ 17:53	$3.8 \cdot 10^{-4}$ 17:54
10	23/10/2012 X1.8 03:13	$8.3 \cdot 10^5$ 03:16	$2.5 \cdot 10^5$ 03:15	$2.3 \cdot 10^{-5}$ 04:17
11	27/11/2012 M1.6 15:52	$1.1 \cdot 10^5$ 15:57	$9.0 \cdot 10^3$ 15:55	$2.5 \cdot 10^{-5}$ 15:59
12	11/04/2013 M6.5 06:55	$2.1 \cdot 10^5$ 07:10	$3.0 \cdot 10^3$ 07:10	$1.7 \cdot 10^{-4}$ 07:13
13	13/05/2013 X2.8 15:48	$7.8 \cdot 10^5$ 16:07	$2.3 \cdot 10^5$ 16:04	$3.8 \cdot 10^{-5}$ 17:42
14	14/05/2013 X3.2 01:00	$9.4 \cdot 10^5$ 01:13	$2.4 \cdot 10^5$ 01:08	$1.7 \cdot 10^{-5}$ 01:42
15	11/10/2013 M4.9 07:01	$4.1 \cdot 10^4$ 07:17	$2.2 \cdot 10^2$ 07:10	$4.7 \cdot 10^{-4}$ 07:19
16	25/10/2013 X1.7 07:53	$2.7 \cdot 10^5$ 08:07	$2.6 \cdot 10^3$ 08:07	$2.5 \cdot 10^{-5}$ 08:17
17	28/10/2013 M4.4 14:57	$1.6 \cdot 10^5$ 14:59	$6.0 \cdot 10^2$ 14:59	$2.6 \cdot 10^{-5}$ 15:45
18	25/02/2014 X4.9 00:39	$8.1 \cdot 10^5$ 00:53	$5.0 \cdot 10^5$ 00:46	$1.5 \cdot 10^{-3}$ 01:22
19	10/09/2017 X8.2 15:44	$1.0 \cdot 10^6$ 16:22	$8.0 \cdot 10^5$ 16:12	$1.3 \cdot 10^{-2}$ 16:00

The second column of the table shows the peak values of the number of photons (12-25) keV counts/s determined for each event during the maximum period of their fluxes and presented on the site of FERMI GBM. Using FERMI GBM QUICKLOOK graphs, the maximum photons (50-100) keV counts/s (third column) were determined. And accordingly, to obtain maximum photons fluxes F^{max} $\gamma \cdot cm^{-2} \cdot s^{-1}$ with energies > 100 MeV and time resolution 1 minute (fourth column), were used observation graphs on the

FERMI LAT and published in [6,7]. In table additionally indicates the start time of each flares event, as well as the moments of onset of peaks and maximum quantitative values for photons of different energies.

Using the data presented in the table, separate graphs were constructed taking into account the photon energy intervals showing the peak and maximum photons fluxes values for the respective moment after the flare began. All considered events are conditionally divided into two groups: the first (red dots) - flares, which had the highest values of gamma-ray fluxes $F^{max}_{\gamma>100MeV}>1.0\cdot10^{-4}$ ($\gamma\cdot cm^{-2}\cdot s^{-1}$) and the second group (black dots) - the rest, with smaller values.

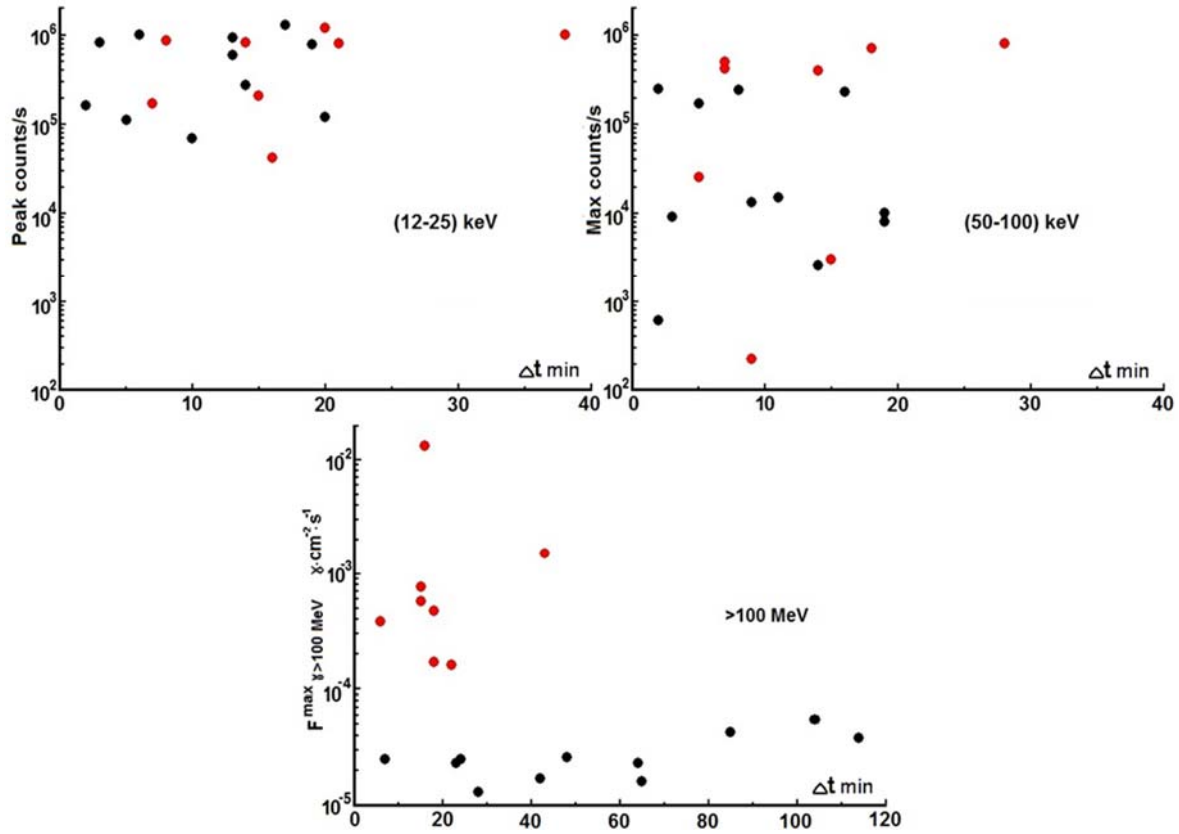

Figure 1 - Comparison of peak values (peak counts·s^{-1}) of photons (12-25) keV, maximum values (max counts · s-1) of photons (50-100) keV and maximum values of gamma-fluxes ($F^{max}_{\gamma>100MeV}$ $\gamma\cdot cm^{-2}\cdot s^{-1}$) with time interval value in minutes after flares start

Both upper graphs in figure 1 with quantitative values of X-ray energy photons show approximately the same contribution of both groups of events to the range of observed values. This indicates that there is no clear link between the effectiveness of photons amplification mechanisms with X-ray and gamma energies. A clear example: of all the events taken for consideration, the lowest values of the number of photons with X-ray energies were found for the flare of October 11, 2013, included in the 1-st group of events with the highest values fluxes of photons with gamma energy >100 MeV.

Except for one event, for all others, the moments of emergence of peaks (12-25) keV and the maximum values (50-100) keV of photons in counts/s lie in the range of time from the beginning of development of flares within 22 min. The same conditions correspond also to the most intensive maximum fluxes in ($\gamma.cm^{-2}.\ s^{-1}$) for photons of gamma energy >100 MeV. This supports the conclusion in the article [8] about the most efficient formation of high-energy gamma rays due to the very intense acceleration of particles (with the energy of protons E_k > 500 MeV), when flare development simultaneously with shock waves of CME.

In most events, the peak values for (12-25) keV were observed slightly later than maxima in the profiles of (50-100) keV.

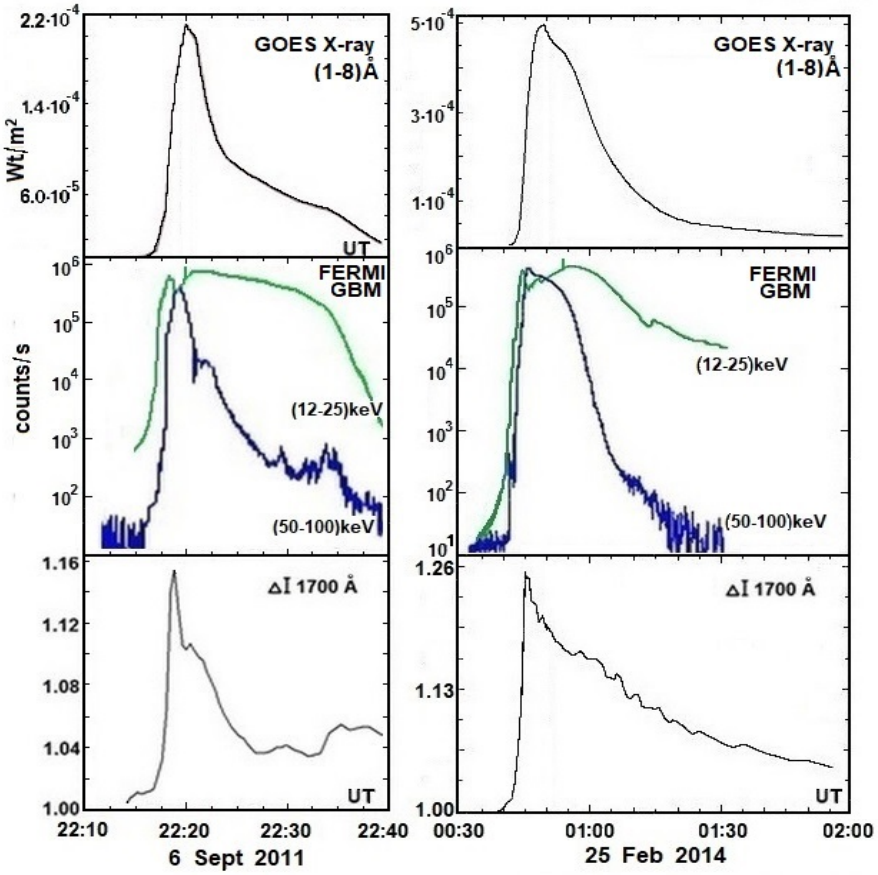

Figure 2 - Comparison of the temporary development profiles of GOES X-ray (1-8) Å flares, quantitative changes of photons (12-25) keV, (50-100) keV and relative ultraviolet intensity of flares emission for the events of September 6, 2011 and February 25, 2014. Peaks photons (12-25) keV marked on the corresponding profiles with small vertical ledges

Comparison of profiles of temporary changes of quantity of photons to energy (50-100) keV shows their good coincidence to relative of photosphere of flare emission ΔI λ1700 Å. This is expressed not only in the similarity of profiles view, but also, most importantly, in the simultaneous onset of maximum values. The corresponding photons profiles with energies (12-25) keV show a longer time interval with maximum values, which is most characteristic of changes in the intensity of flares emission in the corona.

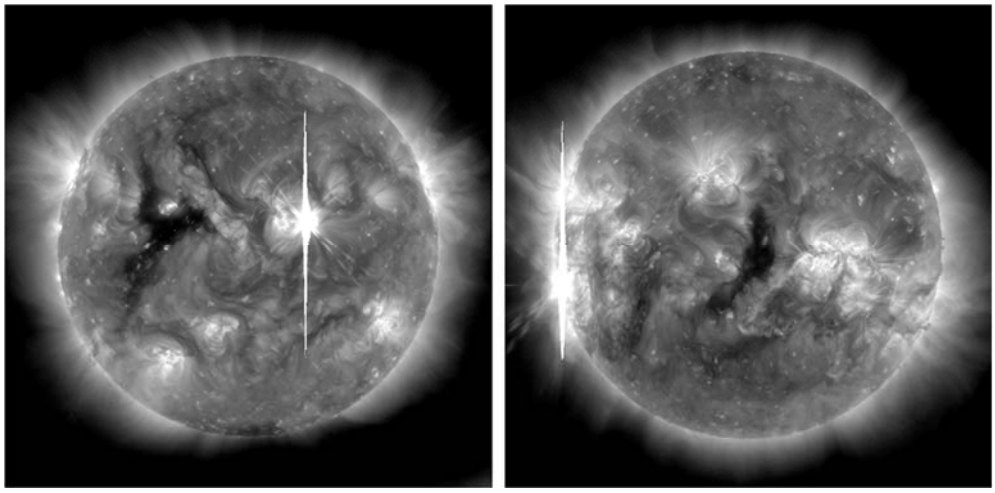

Figure 3 - Fe λ193Å corona photogeliograms (data spacecraft SDO) 6 September 2011 22:20:19 and 25 February 2014 00:53:30

By way of example, Figure 3 shows images of the λ193Å corona (Fe XII, XXIV) obtained on the SDO for the events of September 6, 2011 and February 25, 2014 during peaks quantity of photons (12-25) keV. Bright rays from region of flares plasma directed in opposite directions indicate the presence of solar excess intensity at these moments for the spacecraft photo matrix pixels in imaging.

This results in an observed overflowing of charges to adjacent pixels having no excess of them - the instrumental effect of blooming. Coronal photogeliograms most accurately reflect changes in both luminance and time characteristics of photons having energy (12-25) keV.

Thus, it is possible to assume the source of excess number of photons with energies (12-25) keV - bremsstrahlung radiation due to of flare emission coronal plasma (λ193Å), and for photons (50-100) keV due to bright emission of photospheric plasma (λ1700Å).

Main results and conclusion. The processing of observation material obtained on modern spacecrafts allows to detect new properties in the development of traditionally studied phenomena of solar activity.

It has been found that the maximum values of the quantitative characteristics of photon flares fluxes having X-ray energy at intervals (12-25) keV and (50-100) keV are observed during the initial development period of the flares, within 22 minutes. But the most surprising thing is that such a picture is present for the most powerful $F^{max}_{\gamma>100MeV}>1.0\cdot10^{-4}$ ($\gamma\cdot cm^{-2}\cdot s^{-1}$) fluxes of photons gamma rays. This indicates the most effective particle acceleration with the simultaneous development of the flare process and high-speed coronal ejection. This results in the formation of the most powerful fluxes of energetic gamma photons.

The photons fluxes characteristics in the X-ray energy intervals (12-25) keV and (50-100) keV are determined by the behavior of the bright flare emission in the corona (for the first interval) and in the photosphere, respectively, for the second energy interval.

Acknowledgements

The authors thank the teams of scientists responsible for carrying out experiments on the spacecrafts FERMI, SDO, GOES and for providing observation data published on the Internet.

The work is supported by the Targeted Financing Program BR05336383 Aerospace Committee of the Ministry of digital development, innovations and aerospace industry of the Republic of Kazakhstan and Institute of Solar and Terrestrial Physics of the Siberian Branch of the Russian Academy of Sciences (II.16.3.1 project).

Г.С. Минасянц[1], Т.М. Минасянц[1], В.М. Томозов[2]

[1]В.Г. Фесенков атындағы астрофизикалық институты, ҚР ҰҒА (АФИФ), Алматы, Қазақстан;
[2]Күн-жер физика институты РҒА СБ, (ИСЗФ). Иркутск, Ресей

КҮННІҢ ГАММА-СӘУЛЕЛЕНУІНІҢ ДАМУЫ КЕЗІНДЕ ӘРТҮРЛІ ЭНЕРГИЯЛЫ ФОТОНДАРДЫҢ СӘУЛЕЛЕНУ АҒЫНЫНЫҢ СИПАТТАМАЛАРЫН САЛЫСТЫРУ

Аннотация. Жоғары энергиялы гамма-сәулеленуінің жарқылы кезіндегі әртүрлі энергиялы фотон ағындарының сипаттамалары қарастырылды. Біз FERMI, SDO, GOES ғарыштық аппараттарының бақылау мәліметтерін пайдаландық. 19 жарқыл үшін Ek = (12-25) keV, E_k = (50-100) keV және E_k>100 MeV энергиялы фотон ағындарына салыстырулар жүргізілді. Рентген сәулелерінің энергиялық аймағының фотон профильдерінің сандық және уақытша сипаттамаларын жарқын алау плазмасының қасиеттерімен салыстыру барлық оқиғалар үшін шыңның басталуы (12–25) keV және максималды мәндері (50–100) keV, фотондардың counts/s даму уақыт аралығының 22 минутке созылады. Дәл осындай нәтиже жоғары энергиялы фотондар үшін >100 MeV максималды ағындары бар оқиғаларда байқалады (γ $см^{-2}$ $с^{-1}$). Бұл тікелей алау процесінің бір мезгілде дамуы кезінде бөлшектердің үдеуін және жарылыс кезінде жүретін тәждік массаның шығуын растайды, нәтижесінде жоғары энергиялы гамма-сәулелерінің максималды ағындары пайда болады. Жоғары энергиялы фотондар үшін >100 MeV максималды ағындары (γ $см^{-2}$ $с^{-1}$) бар жарқылдар оқиғалары рентгендік энергия диапазонындағы фотон санының ең жоғары мәндерін көрсетпейді, бұл әртүрлі энергиялы фотондарының түзілу механизмдерінің тиімділігіндегі айырмашылықтарды көрсетеді. Рентген аймағында жарқ етулердің дамуы аяқталған уақыттан кейін гамма сәулелену ағынының макисмалды күшейуі, жоғары

энергиялы фотондар үшін >100 MeV барлық төменгі шамадағы оқиғалар үшін бақыланады. Сондықтан да, гамма сәулелер ағынының қарқынды дамуының күшейуінің максималды мәнге жетуі күн тәжінің шығатын ағындары қоздыратын соққы толқындар болуы мүмкін.

Уақыт өте келе фотондар санының кескінінің өзгерулерін (50-100) keV энергиямен салыстыру кезінде, оның ΔI λ1700Å салыстырмалы фотосферадағы жарқылды плазманың интенсивтілігімен жақсы сәйкес келетіндігін көрсетеді. Бұл тек кескіннің түрінің ұқсастығын ғана емес, сонымен бірге максималды мәндердің бір уақытта басталуын көрсетеді. (12–25) кэВ энергиялы фотондарға сәйкес кескіндер максималды мәндермен ұзақ уақыт аралығын көрсетеді, бұл күн тәждегі жарқылды сәулеленуінің интесивтілігінің өзгеруіне тән. Көптеген жағдайларда, (12–25) кэВ шыңы кескіндердегі максимумнан (50-100) кэВ-ге қарағанда біршама кешірек болады. Бақылауларға сәйкес, (12-25) keV энергиялы фотондар жарқылының сандық күшейу көзі, күн тәжінің аймағында жарықырау кезіндегі тежегіш сәулеленуі себеп, ал (50-100) keV энергиялы фотондар үшін фотосфера аймағы және температура минимумы болып табылады.

Түйін сөздер: күн жарқылы, жарық эмиссиялы плазмалар, күн тәжінен шығарылатын массалар, рентген және гамма сәулеленулері.

Г.С. Минасянц[1], Т.М. Минасянц[1], В.М. Томозов[2]

[1]Астрофизический институт им. В.Г.Фесенкова НАН РК (АФИФ), Алматы, Казахстан;
[2] Институт солнечно-земной физики СО РАН (ИСЗФ), Иркутск, Россия

СОПОСТАВЛЕНИЕ ХАРАКТЕРИСТИК ПОТОКОВ ИЗЛУЧЕНИЯ ФОТОНОВ РАЗНЫХ ЭНЕРГИЙ ПРИ РАЗВИТИИ СОЛНЕЧНЫХ ГАММА-ВСПЫШЕК

Аннотация. Рассмотрены характеристики потоков фотонов различных энергий при развитии вспышек с высокоэнергичным гамма-излучением. Использовались данные наблюдений на космических аппаратах FERMI, SDO, GOES. Проведено сопоставление потоков фотонов с энергиями E_k = (12-25) keV, E_k = (50-100) keV и E_k>100 MeV для 19 вспышечных событий. Сравнение количественных и временных характеристик профилей фотонов рентгеновского диапазона энергий со свойствами яркой вспышечной плазмы показало, что почти для всех событий моменты наступления пиковых (12-25) keV и максимальных значений (50-100) keV фотонов в counts/s относятся к интервалу времени от начала развития вспышек в пределах 22 минут. Такой же результат отмечается и для событий с наиболее интенсивными максимальными потоками в ($\gamma \cdot cm^{-2} \cdot s^{-1}$) для фотонов высоких энергий >100 MeV. Это подтверждает предположение о наиболее эффективном ускорении частиц в период одновременного развития прямого вспышечного процесса и сопровождающего вспышку коронального выброса массы, приводящим в итоге к возникновению максимальных значений потоков высокоэнергичных гамма-квантов. Вспышечные события с наиболее интенсивными максимальными потоками в ($\gamma \cdot cm^{-2} \cdot s^{-1}$) для фотонов высоких энергий >100 MeV не показывают наиболее высоких значений количества фотонов в диапазонах рентгеновских энергий, что указывает на отличия в эффективности механизмов образования фотонов разных энергий. Практически для всех событий с пониженными значениями количества фотонов высоких энергий >100 MeV наблюдается максимальное усиление потоков гамма излучения в период после окончания развития вспышек в рентгеновском диапазоне. Поэтому в этих случаях определяющую роль в усилении потоков гамма излучения до максимальных значений играют, вероятнее всего, ударные волны, возбуждаемые корональными выбросами.

Сопоставление профилей изменения со временем количества фотонов с энергиями (50-100) keV показывает их хорошее совпадение с относительной интенсивностью фотосферной вспышечной плазмы ΔI λ1700Å. Это выражается не только в подобии вида профилей, но и, что особенно важно, в одновременном наступлении максимальных значений. Соответствующие профили фотонов с энергиями (12-25) keV показывают более продолжительный по времени интервал с максимальными значениями, что наиболее характерно для изменений интенсивности вспышечной эмиссии в короне. В большинстве событий пиковые значения для (12-25) keV наступают несколько позже максимумов в профилях (50-100) keV. Согласно наблюдениям, наиболее вероятным источником количественного усиления вспышечных фотонов с энергиями (12-25) keV являются результаты тормозного излучения яркой вспышечной эмиссии в области короны, а для фотонов с энергиями (50-100) keV – в области фотосферы и температурного минимума.

Ключевые слова: солнечные вспышки, яркая эмиссия плазмы, корональные выбросы массы, рентгеновское и гамма-излучение.

Information about authors:

Minasyants Gennady Sergeevich, Candidate of Physical-Mathematical Sciences, Leading Researcher, Fesenkov Astrophysical Institute. Almaty, Kazakhstan, e-mail: gennadii_minasya@mail.ru, https://orcid.org/0000-0002-6962-2831;

Minasyants Tamara Mihailovna, Candidate of Physical-Mathematical Sciences, Senior Researcher, Fesenkov Astrophysical Institute, Almaty, Kazakhstan, e-mail: tamara@aphi.kz, https://orcid.org/0000-0001-7349-3967

Tomozov Vladimir Mihailovich, Candidate of Physical-Mathematical Sciences, Senior Researcher, Institute of Solar-Terrestrial Physics, Irkutsk, Russia, e-mail: tom@iszf.irk.ru, https://orcid.org/0000-0002-0784-9782

REFERENCES

[1] Altyntsev A.T., Banin V.G., Kuklin G.V., Tomozov V.M. Solar Flares. Moscow, Science, 1982. 246 p.

[2] Priest E.R., Forbs T. Magnetic Reconnection. Magnetohydrodynamic Theory and Applications]. Moscow, Fizmatlit Publ., 2005. 591 p.

[3] Somov B.V. Plasma Astrophysics: Reconnection and Flares. New York, Springer, 2013, 504 p. DOI: 10.1016/S02731177(97)00968-X.

[4] Li Y., Sun X., Ding M.D., Qiu J., Priest E.R. Imaging observations of magnetic reconnection in a solar eruptive flare. Astrophys. J. 2017, vol. 835, 190, 8 p. DOI: 10.3847/1538-4357/835/2/190.1.

[5] Murphy R.J., Dermer C.D., Ramaty R. High-energy processes in solar flares. Astrophys. J. Suppl. 1987, vol. 63, pp. 721–748.

[6] Share G.H., Murphy R.J., Tolbert A.K., Dennis B.R., White S.M., Schwartz R.A., Tylka A.J. Characteristics of sustained >100 MeV ray-emission associated with solar flares. arXiv:1711.01511v1 [astro-ph.SR]. 2017a, 83 p.

[7] Share G.H., Murphy R.J., Tolbert A.K., Dennis B.R., White S.M., Schwartz R.A., Tylka A.J. Characteristics of thirty second-stage >100 MeV γ-ray events accompanying solar flares. ApJS in review, arXiv 1711.01511v1. 2017b, 34 p.

[8] Minasyants G.S., Minasyants T.M., Tomozov V.M. Features of development of sustained fluxes of high-energy gamma-ray emission at different stages of solar flares. Solar-Terrestrial Physics. 2019. Vol. 5. No. 3. P. 10–17. DOI: 10.12737/stp-53201902.

NEWS
OF THENATIONAL ACADEMY OF SCIENCES OF THE REPUBLIC OF KAZAKHSTAN
PHYSICO-MATHEMATICAL SERIES
ISSN 1991-346X **https://doi.org/10.32014/2020.2518-1726.38**
Volume 3, Number 331 (2020), 66 – 72

UDC 523.62

G.S. Minasyants[1], T.M. Minasyants[1], V.M. Tomozov[2]

[1]Fesenkov Astrophysical Institute, Almaty, Kazakhstan;
[2]Institute of Solar-Terrestrial Physics, Irkutsk, Russia.
E-mail: gennadii_minasya@mail.ru, tamara@aphi.kz, tom@iszf.irk.ru

FEATURES OF MAGNETIC STRUCTURE OF SUNSPOTS GROUPS AT DEVELOPMENT OF SUSTAINED FLUXES HIGH ENERGY GAMMA RAY

Abstract. The research of magnetic structure of sunspots groups which were sources of three highest values of fluxes gamma ray with energy of photons >100 MeV for all the time of observations on Large Area Telescope (LAT), on board the Spacecraft (SC) Fermi Gamma-ray is conducted. At the same time observed fluxes of gamma ray had also the greatest duration of existence. For comparison, group of spots of similar magnetic class was attracted, but in the absence in it of events that are sources of gamma ray. As a result of the analysis, a characteristic feature of the structure of magnetic fields was revealed: it is that in these sunspots groups inside the region of one polarity there is a very close location of the magnetic field of the opposite polarity. This occurs in the consequence of the interpenetration of cores and umbrae, as concentrated magnetic field carriers, of one polarity inside the field of another polarity. Observations show the existence of a rather long neutral line with very high magnetic field gradients, which affect the growth of active processes in the sunspots regions and, most importantly, the growth of proton acceleration efficiency on high-speed shock fronts and shock waves of CME.

Therefore, groups of magnetic class sunspots BD and BGD, having a structure of close interweaving of magnetic fields of opposite polarities, exhibit extreme activity and are proposed to allocate them into special subclasses - BDe and BGDe (extreme). In the absence of such a property in the magnetic field structure, there is no significant enhancement of activity in the sunspots groups of BD and BGD classes.

Keywords: Structure of magnetic field of sunspots groups, high energetic gamma rays from flares, magnetic subclasses with extreme activity.

Introduction. The most powerful active phenomena in the Sun are solar flares which usually are accompanied by the coronal mass ejection (CME). On modern representations, the flare and CME are considered as the uniform process connected with violations of balance of magnetic structure in active region. Development of flare is connected with allocation of free magnetic energy in active region owing to her dissipation in current sheets because of magnetic reconnection with the subsequent action of stochastic acceleration at development of various plasma instability [1-3]. At development of active region its magnetic structure with the filaments which are located on the line of the section of polarities of magnetic field continuously becomes complicated. Over filaments the closed loops of magnetic field which create in general the closed magnetic configuration of all active region up to coronal heights are located. At continuous impact of shift movements on bases of magnetic loops along neutral line of magnetic field filament (prominence) loses stability and begins to rise up in an expedited manner, opening magnetic structure and forming "core" of ejection of CME [4].

Shock waves of CME are considered as the main source of the accelerated solar protons to energy> 500 MeV at their distribution, both in corona of the Sun, and in the interplanetary environment [5]. According to results [6], protons with the energy exceeding 300 MeV in interaction with substance of the solar atmosphere are capable to generate the neutral and charged pi mesons (peonies) at which disintegration is formed a gamma ray. In cases of acceleration of flare protons to energy Ek> 500 MeV,

neutral peonies become sources of ray of gamma photons of high energy >100 MeV which is registered devices FERMI LAT.

Thus, summarizing results of the researches conducted earlier, we come to a conclusion that very important factor in development of the flare process leading to education high-energy gamma ray is the structure of magnetic field of active region, as represents the purpose of further researches.

Properties of magnetic structure of sunspots groups for events with the most intensive and long fluxes high-energy gamma ray

The national Center NOAA publishes the observation data of solar active regions received on various observatories with the indication of magnetic classification of sunspots groups of: A – unipolar, B – bipolar, BG – bipolar with irregularly located polarities, BD – the delta the structure in which at least one spot includes umbrae of opposite polarity and the most complex – BGD includes in addition to previous irregularly located cores of opposite polarities. (stp_space-weather_solar-data_solar-features_sunspot-regions_usaf_mwl.html).

The numerous, earlier conducted researches showed that the active regions possessing the most complex magnetic structure (classes BD and BGD) are sources of overwhelming number of the highest powerful proton events with *pfu*>10^3 (the maximum value of flux of protons >10 MeV) [7].

In our research four events are used, three of which had the highest maximum values of flux gamma ray $9.0 \cdot 10^{-4}$ $\gamma \cdot cm^{-2} \cdot s^{-1} \leq F^{max}_{\gamma>100\,MeV} \leq 2.4 \cdot 10^{-3}$ $\gamma \cdot cm^{-2} \cdot s^{-1}$, (Fermi LAT Maximum Likelihood). At the same time, duration of fluxes of gamma photons with energy E_k >100 MeV was the largest - from 7 to 20 hours (figure 1). [https://hesperia.gsfc.nasa.gov/fermi/lat/qlook/LAT_qlook_plots.htm].

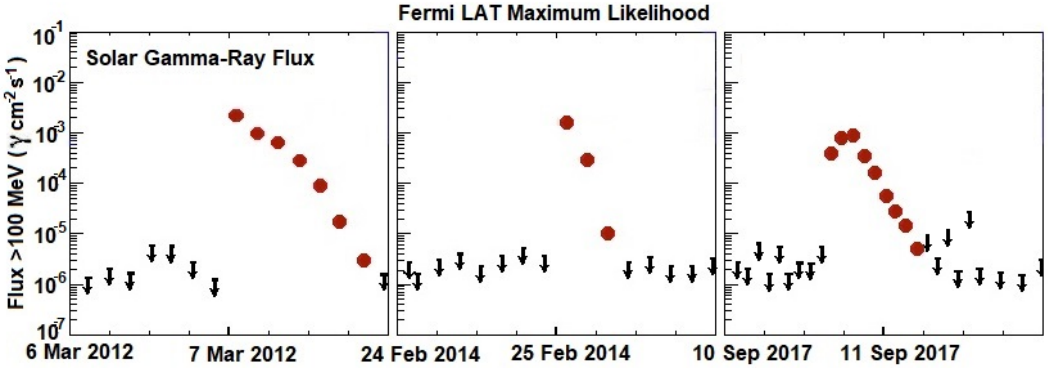

Figure 1 - Events of the highest intensity and the biggest duration
of fluxes gamma photons >100 MeV during observations of the Sun on telescope Fermi

Especially for comparison the fourth event which occurred in the group of spots of a BGD class is attracted, but in it there were no flux of gamma ray. The main characteristics of the considered flare events are presented in table 1.

Table 1

Data, Location yyyy/mm/dd, deg	GOES X-Ray Class, Start	SEP Flux (pfu)	CME Speed, km s^{-1}	Duration $F_{\gamma>100MeV}$ hours	$F^{max}_{\gamma>100\,MeV}$ $\gamma\ cm^{-2}\ s^{-1}$
2012/03/07, N17E15	X5.4, 00:02	6310	2684	20	$2.4 \cdot 10^{-3}$
2014/02/25, S12E82	X4.9, 00:39	103	2147	7	$1.8 \cdot 10^{-3}$
2017/09/10, S08W83	X8.2, 15:35	1490	3163	12	$9.0 \cdot 10^{-4}$
2014/10/24, S12W22	X3.1, 21:07	-	184	-	-

Necessary to make a remark concerning rather low observed *pfu* value for powerful SEP - event on February 25, 2014. It is connected about arrangement of flare on longitude - actually east edge of disk the Sun. Therefore, in near-earth space of SC GOES were registered only an insignificant part of a flare flux of protons (table 1, the 3rd column).

Pictures with of SC Solar Dynamics Observatory are given below: a photosphere, color and black-and-white magnetograms for four considered groups of spots (figure 2,3).

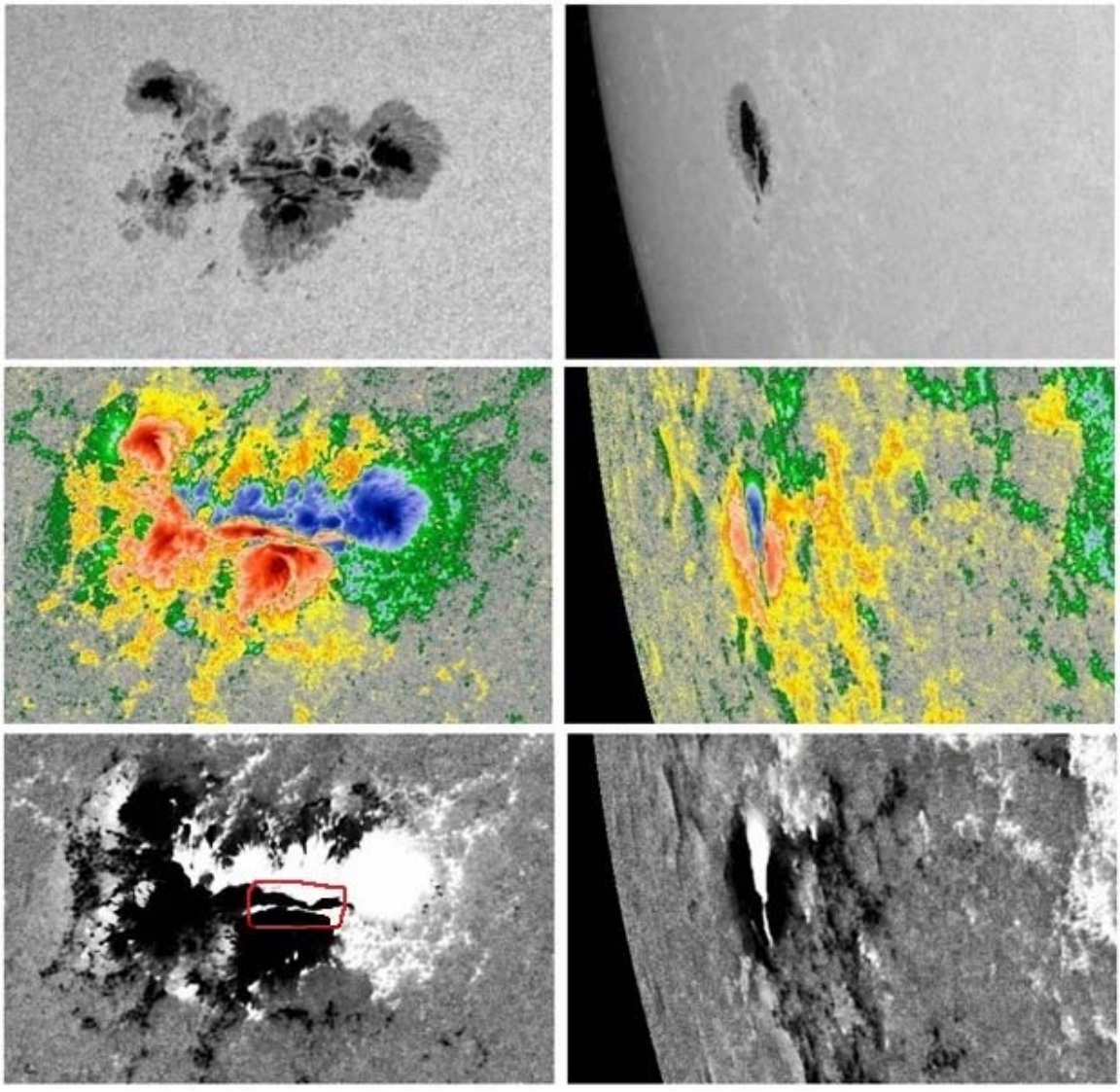

a) b)

Figure 2 - a) On March 7, 2012 00h AR 1429; S=1310 millionths of the solar hemisphere (msh); N17 E15; group of spots of the class BGD; The area border with close located four layers of the alternating umbrae of opposite polarities is marked in red color on a black-and-white magnetogram. b) On February 25, 2014 00h AR 1990; S=250 msh; S12 E82; group of spots of the class BD

Comparison of structure of a magnetic field of four active regions which groups of solar spots have the complex magnetic configuration (classes BD and BGD) indicates presence in three cases of her additional very important property (figure 2a, and figure 3a). It is that in these groups of spots in region of one polarity the magnetic field of opposite polarity is observed. It results from interpenetration of umbrae of spots and pores as concentrated carriers of a magnetic field of one polarity in the field of other polarity. Only the close arrangement of two separate cores and large-scale magnetic fields of different polarities is characteristic of the fourth event (figure 3b) that didn't lead to very noticeable strengthening of the activity processes in AR2192. Quite compact AR2192 (class BGD) considerably exceeded other considered groups on the area. During passing on a disk of the Sun in it there were 95 flares of X-ray Class C, 33 flares of Class M and 6 flares of Class X. But at the same time, not a single proton event and not a single geomagnetic storm have been registered. Flares were accompanied by several Coronal Mass Ejections with very small speed.

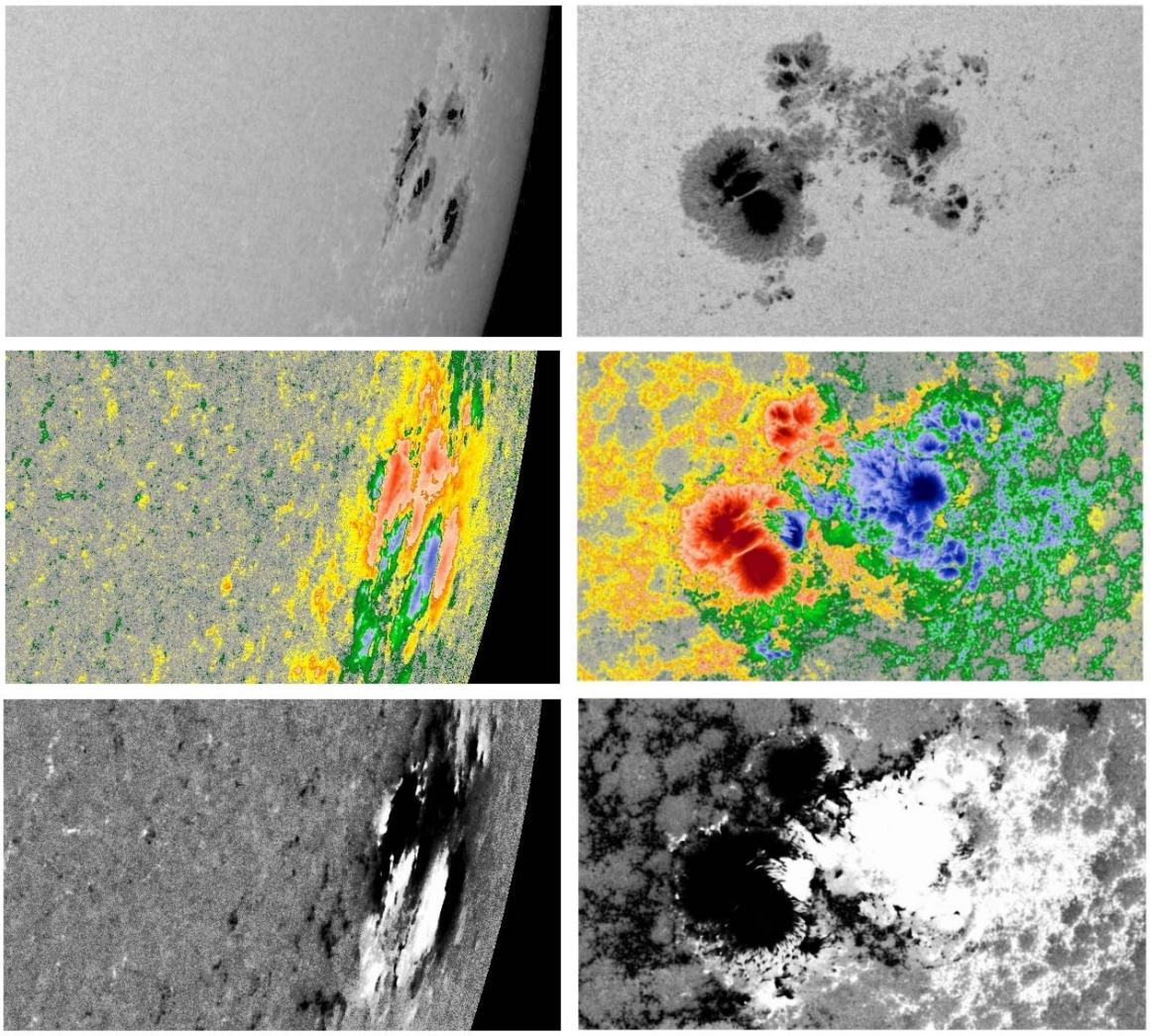

a) b)

Figure 3 - a) On September 9, 2017 00h UT; AR 2673; S=1000 msh; S08 W74; group of spots of the class BGD; b) On October 25, 2014 00h UT; AR 2192; S=2500 msh; S12 W22; group of spots of the class BGD. The delta structure of group is defined by presence of umbrae of opposite polarities at the western part of a penumbra of the main multicores spot

It should be noted one more characteristic property of sunspots groups with the mixed polarities – very high gradients of a magnetic field on quite long part of the neutral line in the active regions.

Possibly, very high speeds of coronal mass ejections which accompanied development of flares were affected by the complex structure of magnetic field in first three (table 1) the considered active regions. The additional research showed that in the period of 2010-2017 on SC SOHO at development of 9 flare events coronal mass ejections which linear speeds exceeded 2000 km/s were observed. And only for 6 CME them sources (the active regions) were on a visible disk of the Sun. Thus, three more were added to three already considered events with high-speed CME. For them the following data are revealed: On January 23, 2012, V_{CME} =2175 km/s, M8.7, $F^{max}_{\gamma>100\,MeV}$=2.3·10^{-5} γ·см$^{-2}$·с$^{-1}$; On January 27, 2012, V_{CME} =2508 km/s, X1.7, $F^{max}_{\gamma>100\,MeV}$=3.0·10^{-5} γ·см$^{-2}$·с$^{-1}$; On May 13, 2013, V_{CME} =2625 km/s, X3.2, $F^{max}_{\gamma>100\,MeV}$=3.5·10^{-5} γ·см$^{-2}$·с$^{-1}$. Duration of fluxes gamma ray with energy of photons > 100 MeV according to observations on Fermi LAT (Maximum Likelihood) is from 2 to 5 hours. And the most important – sunspot groups had the complex magnetic structure with the mixed opposite polarities. That is, the assumption of relations of the linear speed of coronal mass ejections at development of flares with structure of a magnetic field of the active region is confirmed. To quantify the complexity of the magnetic structure of the active region the parameter can be used - the length of the neutral line of the magnetic

field, only those pieces where they pass between the cores and the umbrae of opposite polarities. So for the considered four events, length of pieces of the neutral line with the specified properties is respectively: On March 7, 2012 – 6.9 degrees., on February 25, 2014 – 3.2 degrees., on September 10, 2017 – 5.8 degrees, on October 25 2014 – 1.0 degree.

In areas of the active region with closely spaced umbrae of opposite polarities, the neutral line has many bends and the magnetic field has very high gradients. The length of the neutral line in such a complex magnetic field structure clearly characterizes its effect on the size of the eruptive filament, its mass, and the speed of coronal mass ejection in the further development of the active processes.

As a result of the unique location of the umbrae of different polarities in the active region of March 7, 2012, an area was formed, where a number of four layers were located, representing a sequential alternation of magnetic fields of opposite polarities (see Fig.2a). It is remarkable that the similar structure remained during all development of fluxes high energy gamma ray (20 hours). At the same time, in the gamma ray of solar flare March 7, 2012 on Fermi LAT the maximum values of energy of quanta of 4-4.5 GeV were registered [8].

Conclusion. Thus, the sunspots groups possessing most the complex structure of a magnetic field (classes BD and BGD) show extreme activity in cases of mixed of umbrae of opposite polarities. In such magnetic structures, there are extended neutral lines with very high magnetic field gradients. Therefore, the active regions having such unique magnetic structure feature should be allocated in special subclasses - BDe and BGDe (extremal). In the absence of such property in structure of a magnetic field, significant strengthening of activity in sunspots groups of the classes BD and BGD isn't observed.

Acknowledgements. Authors express gratitude to groups of the scientists supervising carrying out experiments on SC FERMI, SDO, GOES, SOHO for providing the experimental data published on the Internet and also the staff of the National Center NOAA for the publication of results of observations of solar active regions.

The work is supported by the Targeted Financing Program BR05336383 Aerospace Committee of the Ministry of digital development, innovations and aerospace industry of the Republic of Kazakhstan and Institute of Solar and Terrestrial Physics of the Siberian Branch of the Russian Academy of Sciences (II.16.3.1 project).

Г.С. Минасянц[1], Т.М. Минасянц[1], В.М. Томозов[2]

[1]В.Г. Фесенков атындағы астрофизикалық институты, ҚР ҰҒА (АФИФ), Алматы, Қазақстан;
[2]Күн-жер физика институты РҒА СБ, (ИСЗФ). Иркутск, Ресей

ЖОҒАРЫ ЭНЕРГИЯЛЫҚ ГАММА-СӘУЛЕЛЕНУІНІҢ ҰЗАҚ МЕРЗІМДІ АҒЫМДАРЫН ДАМЫТУДАҒЫ ДАҚ ТОПТАРЫНЫҢ МАГНИТТІК ҚҰРЫЛЫМЫНЫҢ ЕРЕКШЕЛІКТЕРІ

Аннотация. Күндегі көптеген белсенді құбылыстардың ішінде ең қуатты энергиялы жарқылдар және күн тәжімен байланысты шығарулар болып саналады. Олар жоғары жылдамдықты бөлшектер ағындарының және әртүрлі спектрлік аймақтардағы, соның ішінде гамма аймағындағы энергетикалық сәулеленудің көзі болып табылады.

Жарқыл процесінің негізі тікелей бөлшектердің үдеуі болып табылады. Себебі, көптеген зерттеулер магниттік құрылымы ең күрделі аймақтар (BD және BGD кластары) жоғары рентген сәулелері мен жоғары энергиялы протондардың максималды ағындары бар ең қуатты жарқылдың басым көзі болып табылатындығын көрсетті. LAT FERMI гамма телескопы арқылы бүкіл уақыт бойы бақыланған >100 МэВ кванттық энергиялы ең жоғары үш гамма-сәулелену ағынының көзі болған күннің белсенді аймақтарының магниттік құрылымдары зерттелді. Сонымен қатар, бақыланған гамма-сәулелік ағындары өмір сүру уақыты ұзақ болды. Салыстыру үшін ұқсас магниттік кластың белсенді аймағы таңдалып, бірақ онда гамма-сәулеленудің пайда болуына әкелетін ерекшеліктер болмады.Орындалған талдау нәтижесінен белсенді энергетикалық оқиғалары бар белсенді аймақтарға тән магнит өрісі құрылымының қасиеті - қарама-қарсы полярлы жақын орналасқан ядролар және дақтар көлеңкесін бөлетін жеткілікті ұзын бейтарап сызықтың болуы анықталды. Бұл басқа полярлық өрістің ішіндегі бір полярлы магнит өрісінің шоғырлануының тасымалдаушылары ретінде ядролар мен көлеңкелердің өзара әсерлесуі нәтижесінде пайда болады. Бұл

жағдайларда жүргізілген бақылаулар бейтарап сызықтардың көлденең магнит өрісінің градиентінің өте жоғары мәндері бар, дақтар көлеңкесіндегі тік өріс градиентінің мәндерінен 5 есе жоғары бөліктерінің бар екендігін көрсетеді. Мүмкін, бұл магнит өрісінің осындай күрделі құрылымы энергияның таралуы кезінде бос магниттік энергияны тиімді шығаруға мүмкіндік береді (қайта қосу процесі) және бұл өте маңызды, жоғары жылдамдықты соққы фронттары мен күн тәжі шығарылымдардың соққы толқындарында протонды үдетудің тиімділігінің едәуір артуына әкелуі мүмкін.

Белсенді аймақта әртүрлі полярлықтардың көлеңкелерінің бірегей орналасуы нәтижесінде 2012 жылғы 7 наурызда қарама-қарсы полярлықтары бар магнит өрістерінің тізбектей ауысуын білдіретін төрт қабат бір-бірінің қасында орналасқан аймақ пайда болды. Бір ерекшелігі, ұқсас құрылым жарқылдағы гамма-сәулелік ағындардың бүкіл дамуы кезінде сақталды (20 сағат). Сонымен бірге, жарқыл процесінің жоғары энергиялы гамма-сәулесінде, Fermi LAT-да максималды кванттық энергия 4 ~ 4,5 ГэВ тіркелді.

Сондықтан, қарама-қарсы полярларлы магнит өрістерінің тығыз орналасуы құрылымы бар BD және BGD магниттік кластар дақтары өте белсенді және оларды арнайы ішкі кластарға бөлуі ұсынылады - BD және BGD (extreme). Магнит өрісінің құрылымында мұндай қасиет болмаған жағдайда, BD және BGD кластар топтарында белсенділіктің айтарлықтай өсуі байқалмайды.

Түйін сөздер: Дақтар топтарының магниттік өрісінің құрылымы, жарқылдардан жоғары энергиялы гамма-сәуле шығару, экстремалды белсенділігі бар магниттік класс тармақтары.

Г.С. Минасянц[1], Т.М. Минасянц[1], В.М. Томозов[2]

[1]Астрофизический институт им. В.Г.Фесенкова НАН РК (АФИФ), Алматы, Казахстан;
[2] Институт солнечно-земной физики СО РАН, (ИСЗФ), Иркутск, Россия

ОСОБЕННОСТИ МАГНИТНОЙ СТРУКТУРЫ ГРУПП ПЯТЕН ПРИ РАЗВИТИИ ДЛИТЕЛЬНЫХ ПОТОКОВ ВЫСОКОЭНЕРГИЧНОГО ГАММА-ИЗЛУЧЕНИЯ

Аннотация. Среди многочисленных активных явлений на Солнце событиями с наиболее мощной энергетикой считаются вспышки и связанные с ними корональные выбросы. Они являются источниками как высокоскоростных потоков частиц, так и энергичного излучения в различных областях спектра, в том числе и в гамма – диапазоне.

Основой вспышечного процесса является прямое ускорение частиц. Многочисленные, ранее проведенные исследования показали, что активные области, обладающие наиболее сложной магнитной структурой (классы BD и BGD), являются источниками подавляющего числа самых мощных вспышек с высокими рентгеновскими баллами и максимальными значениями потоков высокоэнергичных протонов. В представленной работе изучены события, магнитные структуры активных областей которых были источниками трех самых высоких максимальных потоков гамма-излучения с энергиями квантов >100 MeV за все время наблюдений на гамма-телескопе LAT FERMI. При этом наблюдаемые потоки гамма-излучения имели также наибольшую продолжительность времени существования. Для сопоставления была привлечена активная область подобного магнитного класса, но с отсутствием в ней особенностей, приводящих к появлению гамма-излучения. В результате выполненного анализа выявлена характерная особенность структуры магнитных полей: она заключается в том, что в этих группах пятен внутри области одной полярности наблюдается очень близкое расположение магнитного поля противоположной полярности. Это происходит в результате взаимопроникновения ядер и теней как концентрированных носителей магнитного поля одной полярности внутрь поля другой полярности. Наблюдения в этих случаях показывают существование довольно протяженных участков нейтральной линии с очень высокими значениями градиента горизонтального магнитного поля, более чем в 5 раз превышающими значения вертикального градиента поля в тени пятен. Вероятнее всего, такая сложная структура магнитного поля позволяет эффективно освобождать свободную магнитную энергию в ходе диссипации энергии в токовых слоях (процесс пересоединения) и, что особенно важно, может приводить к существенному росту эффективности ускорения протонов на высокоскоростных ударных фронтах и ударных волнах корональных выбросов.

В результате уникального расположения теней разных полярностей в активной области 7 марта 2012 г. образовалась область, где рядом располагаются четыре слоя, представляющие последовательное чередование магнитных полей с противоположными полярностями. Примечательно, что подобная структура сохранялась в течение всего развития потоков гамма излучения во вспышке (20 часов). При этом, в высокоэнергичном гамма-излучении вспышечного процесса на Fermi LAT были зарегистрированы максимальные значения энергий квантов ~ 4-4.5 GeV.

Поэтому группы пятен магнитного класса BD и BGD, обладающие структурой тесной переплетенности магнитных полей противоположных полярностей, проявляют экстремальную активность и их предлагается

выделить в особые подклассы – BDe и BGDe (extreme). При отсутствии такого свойства в структуре магнитного поля не наблюдается существенного усиления активности в группах пятен классов BD и BGD.

Ключевые слова: структура магнитного поля групп пятен, высокоэнергичное гамма излучение вспышек, магнитные подклассы с экстремальной активностью.

Information about authors:

Minasyants Gennady Sergeevich, Candidate of Physical-Mathematical Sciences, Leading Researcher, Fesenkov Astrophysical Institute. Almaty, Kazakhstan, e-mail: gennadii_minasya@mail.ru, https://orcid.org/0000-0002-6962-2831;

Minasyants Tamara Mihailovna, Candidate of Physical-Mathematical Sciences, Senior Researcher, Fesenkov Astrophysical Institute, Almaty, Kazakhstan, tamara@aphi.kz, https://orcid.org/0000-0001-7349-3967;

Tomozov Vladimir Mihailovich, Candidate of Physical-Mathematical Sciences, Senior Researcher, Institute of Solar-Terrestrial Physics, Irkutsk, Russia, tom@iszf.irk.ru, https://orcid.org/0000-0002-0784-9782

REFERENCES

[1] Altyntsev A.T., Banin V.G., Kuklin G.V., Tomozov V.M. “Solar Flares”, Moscow: Science, P.246, 1982.

[2] Prist E.R., Forbes T. ”Magnetic reconnection. Magneto-hydrodynamic theory and applications”, Moscow: Fizmatlit, P.591, 2005.

[3] Somov B.V. “Plasma Astrophys.: Reconnection and Flares”, Springer: New York. P.504, 2013.

[4] Golovko A.A., Kuklin G.V., Mordvinov A.V., Tomozov V.M. “The role of shear motions in the production of a preflare situation”, Contributions of the Astronomical Observatory Skalnate Pleso, v. 15, pp. 243-250, 1986.

[5] Tylka A.J., Share G.H., William F., Dietrich W.F. “Solar Protons above 500 MeV in the Sun’s Atmosphere and in Interplanetary Space”, Report EGU General Assembly, Vienna, Austria 27 April – 02 May 2014. Geophysical Research Abstracts Vol. 16, EGU2014-16847, 2014.

[6] Murphy R.J., Dermer C.D., Ramaty R. “High-energy processes in solar flares”, Astrophys. J. Suppl., V. 63, pp. 721-748, 1987.

[7] Minasyants G.S., Minasyants T.M. “Solar Active Regions and Cosmic Weather”, LAMBERT, P.144, 2013.

[8] Ajello M., Albert A., Allafort A. et al. Impulsive and long duration high-energy gamma-ray emission from the very bright 2012 March 7 solar flares // Astrophys. J. V.789:20 (15pp), 2014 July 1. doi:10.1088/0004-637X/789/1/20.

NEWS
OF THENATIONAL ACADEMY OF SCIENCES OF THE REPUBLIC OF KAZAKHSTAN
PHYSICO-MATHEMATICAL SERIES
ISSN 1991-346X **https://doi.org/10.32014/2020.2518-1726.39**
Volume 3, Number 331 (2020), 73 – 80

УДК 520.823, 524.3-13
МРНТИ 41.51.27, 41.51.41

A. Serebryanskiy[1], **A. Kusakin**[1], **I. Reva**[1,2], **Ch. Omarov**[1]

[1] Fesenkov Astrophysical Institute, Almaty, Kazakhstan;
[2] Al-Farabi Kazakh National University, Al-Farabi Avenue 71, Almaty, Kazakhstan.
E-mail: serebryanskiy@yahoo.com, un7gbd@gmail.com, alfekka@gmail.com, chingis.omarov@gmail.com

RESULTS FROM TIEN-SHAN SURVEY TO SEARCH FOR VARIABLE STARS: OBSERVATIONS, TARGET SELECTION AND DATA PROCESS

Abstract. We present the first results of the photometric survey at Tien-Shan Observatory (TSO) of the fields around Galactic equator using Zeiss-1000 telescope. Here we report on criteria selection of target fields, observation strategy and statistics of photometric observations. We also provide description of data process and differential photometric reduction to extract differential light curves. In total, 23 fields in the range of 40°-210° Galactic longitude and ±5° Galactic latitudes were observed during 2014-2018. Each filed was observed for at least 3 hours long with cadence range 30-180 sec in Johnson-Cousine filters V and R, or in integrated light. As a result, long duration light curves for about 10 000 stars were obtained. A visual inspection of the light curve from each run was carried out for each star in the field that successfully passed the photometry process in at least 70%-75% of the total duration of observations, which made it possible to identify stars with unambiguous signs of variability. Analysis of the light curves of these stars leads to the identification of 33 variable stars. Among them, 31 stars are previously unknown variables not presented in catalogs of variable stars.

Key words: CCD observations: data analysis; methods: light curve analysis, photometry.

Introduction. The TSO survey was initiated in 2018 as campaign in frame of program BR05236322 aims to search for compact and ultra-compact binary systems (UCB), including interacting binary systems (AM Cvn), uncatalogued variable stars of know type, unclassified variables and object with other type of variability phenomena. The survey initially was motivated by the fact that the observed number of AM CVn is 12 times less than was predicted [1]. Thus, the refinement of the amount of AM CVn can provide an opportunity to clarify the models of the formation of such systems and their evolution. Also, it was realized that survey observations can detect variable stars of other types of variability including those usable for asteroseismic studies, systems with exoplanets, etc.

Conducting survey observations to search for UCB and AM CVn by one observatory is justified by the fact that the periods of brightness variation in these objects are about several tens of minutes (the most interesting are systems with periods of 20-35 minutes or less), and the amplitudes from 1.0 to 0.01 in magnitudes [2], that is, are within the accuracy of photometry obtained on meter-class telescopes on TSO.

Selection of star fields for TSO survey. The main criteria for selecting star fields of interest for the survey is optimal star density on CCD frame. On one hand, it should not be too high for successful PSF photometry, and on the other hand, it should be sufficient for the high efficiency of the survey. Another criterion is availability of the selected field for long-time observations. For the current survey this criterion is ~3 hours, which is dictated by two the most important factors: 1) ability to observe up to 2-3 fields per night, 2) to detect periods of brightness variation from 1.5 hours and less, which is one of the main objectives of the survey. At last but not least, the selected fields should not overlap with targets from other survey campaigns, such as, for instance, VPHAS+ and OWS. All the above criteria are met by the fields located at ±5 degrees of galactic latitude and from 40 to 210 degrees of galactic longitude. Also, it is desirable to have relatively bright White Dwarf (WD) candidates as well as the absence of bright stars in

the selected field to avoid contamination in case of long exposure. The presence of at least one WD candidate with a magnitude of 17.5 mag or brighter in the field was determined from the catalog analysis [3]. This choice is due to the combination of a requirement for the accuracy of photometry, exposure time and duration of observations.

The criterion of WD presence is due to the high scientific interest in the study of these objects. Most of the WD (25% to 50%) shows the presence of metals in their atmospheres, which is most likely the result of destruction of the remains of earth-type planets or asteroids in their vicinity. The study of planetary systems around WD makes it possible to conclude the formation of such systems in Main Sequence stars (MS), for which direct observations of planets are difficult. Thanks to "Kepler" space mission, many exoplanets have been discovered, but mostly near relatively cold and dwarf stars. The question arises-is this fact a reflection of reality, that is, some feature of the formation and evolution of planetary systems, or it is the result of "bad" statistics due to limitation of observations. Indeed, the most reliable parameters of exoplanets are determined by radial velocities, and this is difficult for large mass stars because for such stars the influence of exoplanet is quite weak. The same is true for very hot stars, which do not have sufficient absorption lines by which radial velocities can be confidently measured.

The study of planetary systems around WD allows us to extend the time scale of studies of the evolution of planetary systems to several billion years and, therefore, to impose additional restrictions on the theory of their formation and evolution. Statistics of observations of such systems will shed light on the problem of survival of planets at evolution period when the parent star passes the stage of the "red giant" and multiple events of expelling outer layers. The conclusions of the modern theories describing the process of survival of the planets are quite controversial. Besides, there are suggestions that the expelled envelope of a "red giant" can be a source of formation of new planets.

Moreover, observations of oscillating WD are of great interest for fundamental science, because the period changes in DAV-type WD can be caused by their cooling rates which provide an upper limit on the masses of axions that are considered as one of the candidates in components of "dark matter". Variation of oscillation periods of the DV-type WD allows us to test the nature of the interaction of leptons in the framework of some unified theories of electroweak interaction in the low energy regime.

Analysis of GAIA and OWS catalogs. As a result of the analysis of GAIA and SVO catalogs [3] the list of high-priority star fields satisfied the above-mentioned criteria is compiled and present in table 1. The fields location on the celestial sphere relative to the plane of the Galaxy is shown in figure 1, where the dotted line is depict Galactic equator, empty squares are the fields planned for observation, orange shows the fields with a single epoch of observations, blue squares are the fields observed in two epochs and green squares are the fields with several epochs of observations.

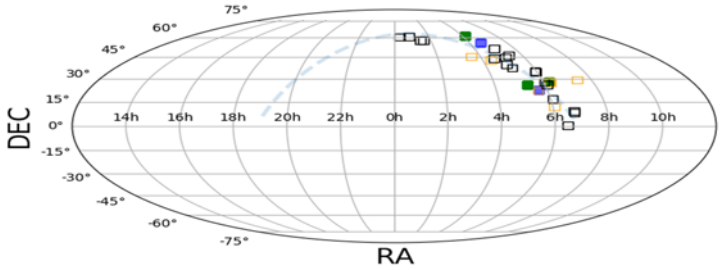

Figure 1 - The star fields locations, selected for TSO survey relative to galactic plane

Table 1 - The list of the high-priority fields selected for TSO survey

Field No.	RA [h:m:s]	DEC [d:m:s]	Field No.	RA [h:m:s]	DEC [d:m:s]	Field No.	RA [h:m:s]	DEC [d:m:s]
1	2	3	4	5	6	7	8	9
19-2	19:59:33	+24:54:46	19-5	20:00:39	+20:32:39	21-9	05:56:39	+35:09:33
18-6	04:22:18	+42:53:42	19-3	20:50:37	+36:14:14	21-6	06:02:28	+27:56:24
19-1	19:38:23	+26:39:56	19-4	01:26:48	+57:42:23	21-8	06:45:55	+08:36:52

Continuation of the table 1

1	2	3	4	5	6	7	8	9
19-6	19:57:57	+33:55:05	19-7	19:39:02	+26:55:38	21-7	06:44:16	+09:24:55
19-9	01:35:36	+57:31:29	19-8	00:17:14	+60:13:43	18-8	06:03:50	+12:22:19
20-1	22:16:59	+59:51:09	20-2	19:23:22	+20:21:00	18-7	04:33:40	+55:26:33
20-4	04:54:49	+39:52:35	20-3	04:34:49	+44:11:20	18-4	05:38:06	+22:32:49
20-7	19:44:12	+13:50:32	20-5	05:04:18	+37:31:18	18-9	06:14:59	+28:05:49
20-8	05:08:09	+44:50:38	20-6	20:37:16	+32:42:00	18-10	06:15:38	+27:50:00
21-1	05:20:41	+46:03:34	20-9	04:58:14	+51:06:56	16-1	05:16:36	+26:07:25
21-3	00:50:58	+60:31:17	21-2	21:47:42	+50:26:20	16-2	07:25:41	+29:27:18
21-5	06:28:32	+00:38:54	21-4	06:04:06	+17:07:31	16-3	04:07:06	+60:55:28
18-1	22:29:20	+52:10:38	18-2	05:38:35	+22:39:10	18-11	06:15:19	+28:13:03
18-3	23:01:15	+54:37:04	18-5	03:33:07	+45:25:44			

Observations and archive data. Observations were carried out at the TSO (76°58'18".5E, 43°03'26".3N, altitude is 2723 meters, international Observatory code is N42) on the meter class telescope Zeiss-1000 “Vostochny”, equipped with Apogee Alta U16M CCD having Kodak KAF-16803 chip with physical pixel size of 9 μm and dimension of 4096×4096 pixels. A field corrector/focus reducer which reduces equivalent focal length to 6665 mm, is installed, which gives the telescope FOV of 19'×19' and a spatial resolution of 0".56/pixel. For observations in 2016, the Zeiss-1000 “Vostochny” telescope equipped with Apogee Alta U9000 CCD camera having a Kodak KAF-09000 chip with the dimension of 3056×3056 pixels and physical pixel size of 12 μm was used. The telescope's FOV was the same as for observations in 2018-2019, but with scale of 0".37/pixel. To improve the signal-to-noise ratio, observations were made in the second binning. In total, 12 fields were observed in 2019. Information on observations is given in Table 2, it can be seen that some fields were observed for several epochs.

Table 2 - Statistics of observations conducted in 2019

Field No.	Date [d/m/y]	Duration [h.]	V [frames]	Rc [frames]	Exposure [sec]	Field No.	Date [d/m/y]	Duration [h.]	V [frames]	Rc [frames]	Exposure [sec]
18-2	22/02/2019	3.5	161	---	60	18-9	27/02/2019	3.0	141	---	60
18-4	29/01/2019	3.8	155	---	60	18-9	12/03/2019	3.1	106	---	90
18-5	27/01/2019	3.3	---	100	60/120	18-9	08/02/2019	3.6	120	---	60
18-6	01/02/2019	3.5	153	---	60	18-10	13/03/2019	3.0	102	---	90
18-7	02/02/2019	4.1	178	---	60	18-11	20/03/2019	3.5	116	---	90
18-7	23/02/2019	4.7	220	---	60	18-8	05/03/2019	2.9	224	---	60

To search for variable stars using the technique of pipeline analysis [4], we also analyzed archival data of observations with the desired duration carried out in the period of 2016-2018. The statistics of these observations are given in table 3.

Table 3 - Statistics of archival data used for purpose of the survey

Field No.	Date [d/m/y]	Duration [h.]	No filter [frames]	V [frames]	Rc [frames]	Exposure [sec]	Field No.	Date [d/m/y]	Duration [h.]	V [frames]	Exposure [sec]
1	2	3	4	5	6	7	8	9	10	11	12
16-1	15/01/2016	7.2	732	---	---	20	16-3	01/11/2016	8.2	280	90
16-1	24/01/2016	7.7	762	---	---	20	16-3	04/11/2016	5.6	191	90

Continuation of the table 3

1	2	3	4	5	6	7	8	9	10	11	12
16-1	25/01/2016	8.6	857	---	---	20	16-3	07/11/2016	5.1	174	90
16-2	20/01/2016	6.9	---	---	800	20	16-3	09/11/2016	6.6	219	90
16-3	26/10/2016	8.1	---	254	---	90	18-1	05/12/2018	2.9	221	30
16-3	27/10/2016	8.5	---	277	---	90	18-2	05/12/2018	2.8	131	60
							18-3	15/12/2018	1.1	55	60

Data analysis. As the main tool for preliminary analysis of the data we use IRAF (http://ast.noao.edu/data/software) package. Averaged CCD frame of bias (Master Bias) is obtained by "*zerocombine*" task (*iraf.iraf.ccdred*) and dark current (Master Dark) is obtained by "*darkcombine*" task (*iraf.imred.ccdred*). Master Bias and Master Dark are additive sources of noise and must be subtracted from CCD image of the target (with Master Bias first subtracted from Master Dark). The heterogeneity of the sensitivity of the CCD (flat-field frame) is a multiplicative component, so the CCD image of the target should be divided by the flat-field. An averaged CCD flat-field frame (Master Flat) was obtained for each filter in which the object was observed and corrected for the dark current of corresponding exposure. To obtain Master Flat we use the "*flatcombine*" task (*iraf.imrad.ccdred*). The object frames were processed with "*ccdproc*" (*iraf.iraf.ccdred*) task using appropriate Master Dark and Master Flat frames.

To carry out PSF photometry of sources on pre-processed CCD frames, a software package implemented on *Python* utilizing such libraries as "*pyraf*", "*astropy*" [5], "*scamp*" [6], "*astroquery*" is used. More details can be found in [4]. Photometric parameters were determined as follows. Assuming that the PSF profile of the star is close to the Gauss function we have $\sigma_{PSF} = FWHM_{PSF}/2\times(2\ln 2)^{-1/2}$. Preliminary estimation of FWHM of the PSF was determined from observation conditions, i.e. from seeing parameter, which for TSO is ~2".5. The radius of the aperture to determine the total flux is set by the criterion of "five sigmas" $A_{ph} = 5\times\sigma_{PSF}$. The sky background level was determined within aperture $A_{sky} = 6\times\sigma_{PSF}$, in 5 pixels wide ring. The size of the PSF profile used for approximation is $R^{fit}_{PSF} = 5\times\sigma_{PSF} - 1$. The saturation level was assumed to be 60000 ADU.

The "*scamp*" package [6] is used for the astrometric plate solution and "*SExtractor*" [7] is used to search for objects on the CCD frame. An example of the accuracy of the obtained photometric estimates is shown in figure 2. Analysis of photometric results was carried out only for those stars whose photometric errors did not exceed 0.05 mag. This choice is due to the aim of finding variable stars with an amplitude of brightness variation of the order of hundredths of a magnitude.

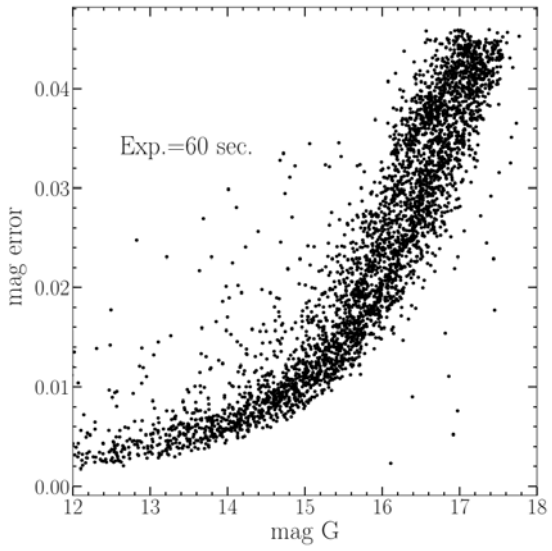

Figure 2 - Dependence of photometric precision (mag error) on stellar magnitude (mag G)

To obtain the light curves of the differential magnitudes of each of the stars in the CCD frame, we use the method of constructing a synthesized reference light curve utilizing all the stars in the field. This choice is mainly dictated by the following factors: 1) the construction of a synthesized reference curve for all stars in the field can significantly reduce the impact of inaccurate photometry for each star, 2) one may not knows the spectral class of the target star, and therefore cannot adequately choose the comparison star for each target with suspected variability. Since the total number of stars in a CCD image ranges from several hundred to several thousand, we can assume that the photometric accuracy of the reference light curve is much higher than that of the analyzed star and does not take into account errors of referent light curve in further analysis.

A total of 23 fields were analyzed using the pipeline procedure. Photometric measurements were obtained for ~10 000 stars with duration of observations of at least 3 hours for each run. A visual inspection of the light curve from each run was carried out for each star in the field that successfully passed the photometry process in at least 70%-75% of the total duration of observations, which made it possible to identify stars with unambiguous signs of variability. The full list of suspected variable stars is presented in table 4.

Table 4 - The list of suspected variable stars

Field No.	GAIA ID	RAJ2000 [h:m:s]	DECJ2000 [d:m:s]	Field No.	GAIA ID	RAJ2000 [h:m:s]	DECJ2000 [d:m:s]
16-1	3420722996343786496	05:16:09.7	+26:02:45.3	18-1	2000667342122793472	22:30:15.9	+52:00:02.7
	3420728150304526976 (KUV 05134+2605, ZZB)	05:16:27.8	+26:08:37.2		2000668544713613952	22:30:12.2	+52:03:22.5
	3420726084425443200	05:15:59.1	+26:03:25.9		2000677993641422208	22:29:14.5	+52:03:02.4
16-3	473900064311871488	04:06:19.7	+60:56:30.6		2000680742420926976	22:30:27.8	+52:06:18.4
	473906008546567168	04:06:18.6	+61:03:08.5		2000681876292067968	22:30:10.9	+52:08:57.1
	473706893862387328	04:07:13.0	+60:47:18.3		2000684586402884864	22:29:54.1	+52:08:48.6
	473712872456844544 (NGC 1501, RPHS)	04:06:59.4	+60:55:14.4		2000685758942457728	22:29:44.1	+52:12:16.6
	473900304830038144	04:06:13.4	+60:57:13.4		2000686239978998400	22:30:08.0	+52:14:34.3
18-2	3404213726175547776	05:38:27.3	+22:38:11.4		2001434835597456768	22:28:45.8	+52:17:00.5
	3404200257158109824	05:38:54.1	+22:32:08.4	18-7	277089853758788352	04:34:22.1	+55:31:36.5
	3404217746264940032	05:38:10.8	+22:41:01.7		277091262508123264	04:33:06.3	+55:28:02.3
18-4	3404189944938309120	05:37:26.4	+22:30:51.7		277091739248814208	04:33:13.7	+55:31:56.6
18-5	241766668329744896	03:33:41.1	+45:23:50.6		277092155861283712 (TYC 3736-373-1)	04:33:24.6	+55:33:07.3
	241771856649828992	03:32:58.5	+45:21:07.0		277093014852191616	04:34:25.9	+55:34:13.0
18-6	229267969902029696	04:23:13.9	+42:49:37.7		277091911047501568	04:33:36.4	+55:31:42.7
18-10	3433368376498172160	06:15:21.9	+27:50:33.0	18-8	3342732093967192576	06:03:46.4	+12:28:08.8
18-11	3433415586778288768	06:15:55.7	+28:12:34.7				

Conclusion. Survey observations of 15 selected fields were carried out on TSO using Zeiss-1000 telescope in 2019. Photometric pipeline data analysis conducted for 23 fields, including observations for 2016 and 2018. As a result, light curves for about 10 000 stars with the duration of observations at least 3 hours were obtained. Analysis of the light curves of these stars leads to the identification of 33 variable stars. Among them, 31 stars are previously unknown variables. To determine the type of detected variable stars, it is necessary to investigate the amplitude-period parameters of these candidates, their location on color-magnitude diagram and to carry out spectral analysis. These results will be presented in the separate paper.

Acknowledgments. This work has been partially supported by the program BR05236322 of the Ministry of Education and Science of the RK and the scientific and technical program BR05336383 Aerospace Committee of the Ministry of Defense and Aerospace Industry of the Republic of Kazakhstan. Authors used Matplotlib [8] for producing figures.

А. Серебрянский[1], **А. Кусакин**[1], **И. Рева**[1,2], **Ч. Омаров**[1]

[1] ЕЖШС «В.Г. Фесенков атындағы Астрофизика институты», Алматы Қазақстан;
[2] әл-Фараби атындағы ҚазҰУ, Алматы, Қазақстан

АЙНЫМАЛЫ ЖҰЛДЫЗДАРДЫ ІЗДЕУ БОЙЫНША ТЯНЬ-ШАНЬДЫҚ ФОТОМЕТРИЯЛЫҚ ШОЛУДЫҢ НӘТИЖЕЛЕРІ: БАҚЫЛАУЛАР, НЫСАНДАРДЫ ТАҢДАУ ЖӘНЕ МӘЛІМЕТТЕРДІ ТАЛДАУ

Аннотация. 2018 жылы Тянь-Шань обсерваториясында BR05236322 бағдарламасын іске асыру аясында, ықшам және ультра ықшам екілік жүйелерге (UCB) үміткерлерді іздеуді, соның ішінде өзара әрекеттесетін екілік жүйелерді (AM Cvn) іздеуге арналған байқау науқаны, бұрын белгісіз ауыспалы жұлдыздар, өзгермелілігі белгісіз типті жұлдыздар. Бұл шолу AM CVn мөлшері болжанғаннан 12 есе аз болғандығымен негізделген [1]. Осылайша, AM CVn нөмірін қайта қарау мұндай жүйелер мен олардың эволюциясының модельдерін жарықтандыруға көмектеседі. Сонымен қатар, зерттеу жұмыстарын бақылау барысында басқа ауыспалы жұлдыздарды, оның ішінде астросеизмге қызығушылық танытатын объектілерді, экзопланеталары бар жүйелерді және т.б. зерттеуге болатындығы анықталды.

Zeiss-1000 телескоптары көмегімен Тянь-Шань обсерваториясында (TSAO) Галактика жазықтығында таңдалған аймақтарды зерттеудің алғашқы нәтижелері келтірілген. Мақалада күтілетін өрістерді таңдау әдістемесі, бақылаулар мен мұрағатталған деректер статистикасы, дифференциалды жарқырау қисықтарын алу мақсатында қолданылған деректерді талдау мен дифференциалды фотометрия процестері сипатталған. 2014-2019 ж аралығындағы бақылау маусымдары кезінде 40° -дан 210° -қа дейінгі галактикалық бойлық пен ± 5° галактикалық ендік бойынша 23 облыс анықталды.

Байқау Zeiss-1000 «Восточный» метрлік класты телескопында, Apogee Alta U16M CCD CCD камерасымен жабдықталған, Kodak KAF-16803 чипті процессоры бар, пиксель өлшемі 9 мкм және жалпы чиптің өлшемі 4096 × 4096 пиксель. Өрісті түзеткіш (фокусты төмендеткіш) эквивалентті фокусты 6665 мм-ге дейін төмендетуге мүмкіндік берді, ол өрістің өлшемін 19'×19' және кеңістіктік 0" 56 пиксел/пиксель берді. 2016 жылы бақылаулар Zeiss-1000 «Восточный» телескопында да жүргізілді, бірақ Apogee Alta U9000 CCD CCD камерасымен Kodak KAF-09000 чипі бар, өлшемі 3056 × 3056 пиксель және физикалық өлшемі 12 мкм. Сонымен бірге, телескоптың өрісі 2018-2019 жылдардағы бақылаулармен бірдей болды, бірақ масштабы 0". 37/пиксель. Сигналдар/шу деңгейінің жоғарылауына қол жеткізу үшін үшінші биннингте бақылау жүргізілді.

Таңдалған облыстардың әрқайсысы Johnson-Cousin V және R кең жолақты сүзгілерінде, сондай-ақ толық жарықта 30 секундтан 180 секундқа дейін, кем дегенде 3 сағат үздіксіз бақыланды.

Фотометриялық талдау үшін біз Python ортасында және "*pyraf*", "*astropy*" [5], "*scamp*" [6], "*astroquery*" кітапханаларында жасалған бағдарламалық жасақтаманы қолдана отырып, PSF фотометрия әдісін қолдандық. Тікелей дифференциалды жарық қисығын алу үшін өрістегі барлық жұлдыздардың фотометриялық ақпаратын қолдана отырып, синтезделген анықтамалық жарық қисығын құру әдісін қолдандық. Бұл стратегияны таңдау келесі факторларға байланысты болды: 1) синтезделген салыстыру жарық қисығы бір салыстыру жұлдызының шу деңгейін айтарлықтай төмендетеді 2) біз зерттелген жұлдыздың спектрлік класын жиі білмейтіндіктен, сәйкес келетін жұлдызды дұрыс таңдай алмаймыз. CCD кадры шеңберіндегі жұлдыздардың жалпы саны жүздеген немесе тіпті мыңға жетуі мүмкін болғандықтан, фотометрияның дәлдігі зерттеліп жатқан жұлдыздың жарық қисығындағы шу деңгейі ғана болады деп болжауға болады.

Нәтижесінде, бақылаудың әр жиынтығы үшін шамамен 10 000 жұлдыз үшін ұзақ мерзімді жарық қисықтары алынды және әр учаске үшін бақылаудың жалпы ұзақтығының 75% -дан кем емес фотометриядан өткен әр жеке өріс жұлдыздарының жарық қисықтарынан визуалды тексеру жүргізілді, бұл жұлдыздарды біркелкі анықтауға өзгергіштік белгілері мүмкіндік берді. Осы жарық қисықтарының талдауы бойынша өзгеретін 33 жұлдыз анықталды. Олардың ішінде 31 жұлдыз өзгермелі жұлдыздар каталогында көрінбейтін жаңа болып табылады.

Түйін сөздер: CCD бақылаулары: деректерді талдау; әдістер: жарқырау қисығын талдау, фотометрия.

А. Серебрянский[1], **А. Кусакин**[1], **И. Рева**[1,2], **Ч. Омаров**[1]

[1] ДТОО «Астрофизический институт им. В.Г. Фесенкова», Алматы, Казахстан;
[2] КазНУ им. аль-Фараби, Алматы, Казахстан

РЕЗУЛЬТАТЫ ТЯНЬ-ШАНСКОГО ФОТОМЕТРИЧЕСКОГО ОБЗОРА ПО ПОИСКУ ПЕРЕМЕННЫХ ЗВЕЗД: НАБЛЮДЕНИЯ, ВЫБОР ОБЪЕКТОВ И АНАЛИЗ ДАННЫХ

Аннотация. В 2018 году, в рамках выполнения программы BR05236322 на Тянь-Шанской обсерватории, была инициирована кампания по проведению поисковых наблюдений для поиска кандидатов в компактные и ультра-компактные двойные системы (UCB), включая взаимодействующие двойные системы (AM Cvn), ранее неизвестные переменные звезды, звезды с неизвестным типом переменности. Данный обзор был мотивирован тем фактом, что количество AM CVn в 12 раз оказалось меньше, чем предсказано [1]. Таким образом, пересмотр числа AM CVn помог бы пролить свет на модели формирования таких систем и их эволюцию. Кроме того, было выяснено, что в процессе обзорных наблюдений представляется возможность исследовать другие переменные звезды, включая объекты интересные для астросейсмологии, системы с экзопланетами и др.

В данной статье представлены первые результаты обзора избранных площадок в плоскости Галактики, выполненные на обсерватории Тянь-Шань (ТШАО) с использованием телескопов Цейсс-1000, описана методика выбора перспективных полей для обзора, статистика полученных наблюдений и архивных данных, процесс анализа данных и дифференциальной фотометрии с целью получения дифференциальных кривых блеска. В общей сложности были проведены наблюдения 23 площадок в диапазоне от 40° до 210° галактической долготы и ±5° галактической широты в течении наблюдательных сезонов 2014-2019 годов.

Наблюдения были выполнены на телескопе метрового класса Цейсс-1000 “Восточный”, оснащенный ПЗС-камерой Apogee Alta U16M CCD с чипос Kodak KAF-16803, с размером каждого пикселя 9 мкм, а полный размер чипа 4096×4096 пикселей. Корректор поля (он же редьюсер фокуса) позволил сократить эквивалентный фокус до 6665 мм, что дало поле размером 19'×19' и пространственным разрешением 0".56/пиксель. Наблюдения в 2016 были выполнены также на телескопе Цейсс-1000 “Восточный”, но уже с ПЗС камерой Apogee Alta U9000 CCD с чипом Kodak KAF-09000 размером 3056×3056 пикселей и физическим размером каждого пикселя 12 мкм. При этом поле телескопа было таким же, как и для наблюдений в 2018-2019, но с масштабом 0".37/пиксель. Для достижения более высокого отношения Сигнал/Шум наблюдения выполнялись в третьем биннинге.

Каждая из выбранных площадок наблюдалась непрерывно на протяжении, как минимум, 3 часов с экспозицией от 30 сек до 180 сек с использованием широкополосных фильтров V и R системы Джонсона-Кузина, а также в интегрированном свете.

Для фотометрического анализа использовалась методика PSF-фотометрии с использованием разработанного в среде *Python* программного обеспечения и библиотек “*pyraf*”, “*astropy*” [5], “*scamp*” [6], “*astroquery*”. Для получения непосредственно дифференциальных кривых блеска был использован метод построения синтезированной референтной кривой блеска с использованием фотометрической информации всех звезд в поле. Такой выбор стратегии был продиктован следующими факторами: 1) синтезированная кривая блеска сравнения значительно уменьшает вклад шума от отдельно взятой звезды сравнения; 2) поскольку мы зачастую не знаем спектральный класс исследуемой звезды, мы не можем правильно выбрать соответствующую звезду сравнения. Поскольку общее число звезд в поле ПЗС-кадра может достигать сотен и даже тысяч, мы можем сделать предполагаем, что точность фотометрии только уровнем шума в кривой блеска исследуемой звезды.

В результате были получены продолжительные кривые блеска для порядка 10000 звезд. для каждого сета наблюдений и для каждой площадки была выполнена визуальная проверка кривых блеска каждой отдельной звезды поля, прошедшей процедуру фотометрии, как минимум, на протяжении 75% от общей продолжительности наблюдений, что позволило выявить звезды с однозначными признаками переменности. В результате анализа этих кривых блеска было выявлено 33 переменные звезды. Среди них 31 звезда – это новые, не представленные в каталогах переменных звезд.

Ключевые слова: ПЗС наблюдения: анализ данных; методы: анализ кривых блеска, фотометрия.

Information about authors:

Serebryanskiy A., Ph.D., Fesenkov Astrophysical Institute, aserebryanskiy@yahoo.com, https://orcid.org/0000-0002-4313-7416;

Reva I.V., Fesenkov Astrophysical Institute. alfekka@list.ru, https://orcid.org/0000-0001-9944-8398;

Kusakin A., Doctor of Physical and Mathematical Sciences, Fesenkov Astrophysical Institute, un7gbd@gmail.com, https://orcid.org/0000-0002-7756-546X;

Omarov Ch., Doctor of Physical and Mathematical Sciences, Fesenkov Astrophysical Institute, chingis.omarov@gmail.com, https://orcid.org/0000-0002-1672-894X

REFERENCES

[1] Carter P. J., Marsh T. R., Steeghs D., Groot P. J., Nelemans G., Levitan D., Rau A., Copperwheat C. M., Kupfer T., Roelofs G. H. A. A search for the hidden population of AM CVn binaries in the Sloan Digital Sky Survey // Monthly Notices of the Royal Astronomical Society. 2013. Mar. T. 429, № 3. C. 2143-2160.

[2] Toma R., Ramsay G., Macfarlane S., Groot P. J., Woudt P. A., Dhillon V., Jeffery C. S., Marsh T., Nelemans G., Steeghs D. The OmegaWhite Survey for short period variable stars - II. An overview of results from the first four years // Monthly Notices of the Royal Astronomical Society. 2016. Nov. T. 463, № 1. C. 1099-1116.

[3] Jimenez-Esteban F. M., Torres S., Rebassa-Mansergas A., Skorobogatov G., Solano E., Cantero C., Rodrigo C. A white dwarf catalogue from Gaia-DR2 and the Virtual Observatory // Monthly Notices of the Royal Astronomical Society. 2018. Nov. T. 480, № 4. C. 4505-4518.

[4] Serebryanskiy, A., Serebryakov, S., Ergeshev, A. methodology of pipeline data reduction for astrometry and photometry of a large array of CCD observations // NEWS of the National Academy of sciences of the Republic of Kazakhstan. 2018. Physico-Mathematical Series. T. 3, № 319. C. 122-133.

[5] Robitaille T. P., Tollerud E. J., Greenfield P., Droettboom M., Bray E., Aldcroft T., Davis M., Ginsburg A., Price-Whelan A. M., Kerzendorf W. E., Conley A., Crighton N., Barbary K., Muna D., Ferguson H., Grollier F., Parikh M. M., Nair P. H., Guenther H. M., Deil C., Woillez J., Conseil S., Kramer R., Turner J. E. H., Singer L., Fox R., Weaver B. A., Zabalza V., Edwards Z. I., Bostroem K. A., Burke D. J., Casey A. R., Crawford S. M., Dencheva N., Ely J., Jenness T., Labrie K., Lim P. L., Pierfederici F., Pontzen A., Ptak A., Refsdal B., Servillat M., Streicher O., Astropy C. Astropy: A community Python package for astronomy // Astronomy & Astrophysics. 2013. Oct. T. 558.

[6] Bertin, E. Automatic Astrometric and Photometric Calibration with SCAMP, Software for Calibrating AstroMetry and Photometry // Astronomical Data Analysis Software and Systems XV ASP Conference Series. 2006. V.351, Proceedings of the Conference Held 2-5 October 2005 in San Lorenzo de El Escorial, Spain. Edited by Carlos Gabriel, Christophe Arviset, Daniel Ponz, and Enrique Solano. San Francisco: Astronomical Society of the Pacific. P.112

[7] Bertin, E. SExtractor: Software for source extraction // Astronomy and Astrophysics Supplement. 1996. V.117. P.393-404.

[8] Hunter J. D. Matplotlib: A 2D graphics environment // Computing in Science & Engineering. 2007. May-Jun. T. 9, № 3. C. 90-95.

NEWS
OF THENATIONAL ACADEMY OF SCIENCES OF THE REPUBLIC OF KAZAKHSTAN
PHYSICO-MATHEMATICAL SERIES
ISSN 1991-346X **https://doi.org/10.32014/2020.2518-1726.40**
Volume 3, Number 331 (2020), 81 – 91

УДК 520.88, 520.82.054
МРНТИ 41.23.29, 41.51.41

A. Serebryanskiy, **G. Aimanova**, **L.Kondat'eva**, **Ch. Omarov**

Fesenkov Astrophysical Institute, Almaty, Kazakhstan.
E-mail: aserebryanskiy@yahoo.com, agauhar@mail.ru, lu_kondr@mail.ru, chingis.omarov@gmail.com

FIRST RESULTS FROM TIEN-SHAN SURVEY TO SEARCH FOR VARIABLE STARS: LIGHTCURVE ANALYSIS AND VARIABLE STAR CLASSIFICATION

Abstract. We present the first results of the light curve analysis of variable stars identified in Tien-Shan survey conducted on Tien-Shan Observatory (TSO) using Zeiss-1000 telescope. Here we report on 33 high amplitude variable stars among which 31 is previously uncatalogued variables. Using data from the StarHorse catalog, as well as results from the MIST project, Color-Magnitude Diagram and appropriate evolutionary tracks were constructed for each field and individual variable star, corresponding to the star's mass and metallicity. For two objects, we performed spectral observations on the Zeiss-1000 "Zapadny" telescope using a slit spectrograph. The obtained spectra were compared with synthesized spectra. The preliminary identification of variability type of each star is based on parameters of variability (amplitudes and periods) determined from periodograms analysis, evolution stage based on evolutionary track on Color-Magnitude Diagram and, for some targets, on spectral information.

Key words: methods: light curve analysis, photometry; stars: variable stars.

Introduction. Stellar variability plays crucial role in understanding many aspects of stellar structure, galaxy evolution, cosmology, formation and evolution of binary systems and in many other astrophysical problems [1, 2]. Light curve analysis of variable stars is main instrument in discovery of extra-solar planets [3,4,5].

Despite many different campaigns and surveys aimed on variable star discovery and analysis there are many new phenomenon and variability type discoveries still going on. Also, there are several examples of variable stars which is the only object of their kind. For example WD1145+017 is the only known white dwarf with evidence of disintegration phenomenon. To search for variable stars with short period variability the survey was initiated at TSO. One of the goals for TSO survey is search for ultra-compact binary systems (UCB), including interacting ultra-compact binary systems (AM CVn). Searching for UCB and AM CVn conducted by means of single observatory is justified by the fact that the periods of brightness variation in these objects are about several tens of minutes and the amplitudes from 1.0 to 0.01 in magnitudes [6], that is, are within the accuracy of photometry obtained by the telescopes in the TSO.

Additionally, TSO survey can detect variable stars of other types of variability including those intentionally valuable for asteroseismic studies, systems with exoplanets, etc. Project description, strategy for field selection and data reduction process is presented in separate paper in this volume (Paper I). There we reported on discovery of new variables stars from visual inspection of individual light curves. In this part we present detailed analysis of light curve of suspected variable stars using periodorgam analysis, inspecting their evolution stage and spectra.

Stellar parameters, CMD and evolutionary tracks. A visual inspection of the light curves was carried out for each star in each field that successfully passed the photometry process in at least 70%-75% of the total duration of observations, which made it possible to identify stars with unambiguous evidence of change in brightness. The full list of stars with detected variability is presented in table 5 of paper I.

To determine the type of detected variable stars, it is necessary to investigate the amplitude-period characteristics of the light curves, as well as the evolutionary status of the stars and, if possible, spectral characteristics (Sp). To clarify the evolutionary status of the stars, we found their physical characteristics from the GAIA catalog and constructed color-magnitude diagram (CMD) with superimposed theoretical evolutionary tracks obtained from the MIST project [7,8]. The physical parameters of the detected variables, according to the GAIA catalog, are given in table 1, where π is the parallax, Gmag is the magnitude in GAIA G filter.

Table 1 - Parameters of identified variable stars

GAIA ID	π [mas]	Gmag [mag]	T_{eff} [K]	R [R_{Sun}]	L [L_{Sun}]	GAIA ID	π [mas]	Gmag [mag]	T_{eff} [K]	R [R_{Sun}]	L [L_{Sun}]
3420722996343786496	1.8659	13.04	4649.38	1.93	1.575	3404213726175547776	0.7416	15.65	4855.00	1.30	0.847
3420728150304526976	6.7595	16.77	8868.67	---	---	3404200257158109824	0.7620	12.54	5926.25	3.33	12.294
3420726084425443200	0.7500	15.72	3854.00	2.51	1.252	3404217746264940032	0.3361	15.06	4837.26	---	---
4739000643118714 88	1.1686	14.95	4228.92	1.70	0.832	3404189944938309120	0.7505	12.80	7058.25	2.10	9.884
473906085465671 68	---	15.93	4039.89	---	---	241766668329744896	0.3486	16.98	4904.71	---	---
473706893862387328	0.1217	15.33	4687.15	---	---	241771856649828992	---	17.75	---	---	---
473712872456844544	0.5673	14.24	7031.00	1.45	4.597	229267969900 29696	1.9891	13.52	4866.05	1.29	0.841
473900304830038144	0.4015	15.49	4855.50	2.59	3.368	277089853758788352	0.2152	16.94	4832.62	---	---
2000667342122793472	0.4200	13.91	7111.67	2.22	11.311	277091262508123264	0.9893	13.03	4374.00	4.39	6.352
2000668544713613952	0.4973	13.65	6519.50	2.51	10.268	277091739248814208	0.4404	16.71	4374.25	---	---
2000677993641422208	0.1093	16.14	6582.00	---	---	277092155861283712	0.9312	16.49	4315.86	0.98	0.303
2000680742420926976	0.3075	13.13	5983.00	---	---	277093014852191616	0.1927	15.71	5008.72	---	---
2000681876292067968	0.2046	15.32	6940.00	---	---	277091911047501568	0.1641	16.34	4740.56	---	---
2000684586402884864	0.2592	14.03	6413.50	4.18	26.626	3342732093967192576	0.5688	15.09	5324.00	1.75	2.204
2000685758942457728	0.2795	13.98	7179.25	3.17	24.013	3433368376498172160	0.7081	16.00	4593.60	1.35	0.733
2000686239978998400	0.3612	14.46	7812.50	1.69	9.560	3433415586778288768	0.2012	15.24	4895.75	---	---
2001434835597456768	1.0201	16.65	4896.07	0.59	0.178						

There is no data in GAIA catalog for the star 241771856649828992, but we identified this object in the SDSS catalog as J033258.00+452113.5 and find the following parameters: T_{eff} = 5440.0 K, $[Fe/H]_1$ = 0.042 [9]. It should be noted here that GAIA data for extinction in the G band and "reddening" E(BP-RP) should be used with caution since their accuracy is such that the values for individual star are unreliable and therefore it makes sense to work only with an ensemble of values. Much work to refine GAIA data for individual stars were done in the StarHorse project [10]. From the StarHorse catalog, we selected only those stars for which reliable estimates were obtained. An example of a database query on the project website (https://gaia.aip.de/query/) in our case might look as follows:

```
SELECT g.source_id, s.MG0, s.BPRP0, s.TEFF50, s.MET50, s.MASS50
FROM gdr2.gaia_source AS g, gdr2_contrib.starhorse AS s
WHERE g.source_id = s.source_id AND s.SH_OUTFLAG LIKE '00000'
AND s.SH_GAIAFLAG LIKE '000' AND 1=CONTAINS(POINT('GALACTIC',g.l,g.b),
CIRCLE('GALACTIC',196.37,-4.64,1.))
```

Table 2 shows the parameters of some of the variable stars for which data is available in the StarHorse catalog. A comparative analysis of the data from table 1 and table 2 shows a significant discrepancy of values for some stellar parameters. In further analysis, especially for determining the type of variability of a star, in the case where the parameters of the star cannot be determined from the StarHorse catalog we use the parameters from the GAIA catalog, except for the T_{eff} value.

Table 2 - Parameters of the detected variable stars from the StarHorse catalog

GAIA ID	T_{eff} [K]	[Fe/H]	M [M_{Sun}]	GAIA ID	T_{eff} [K]	[Fe/H]	M [M_{Sun}]
420722996343786496	8088	-0.24	1.57	3404217746264940032	6476	-0.12	1.64
473900064311871488	7519	-0.59	1.27	3404189944938309120	7338	-0.33	1.58
473706893862387328	12996	-0.14	3.66	241766668329744896	5903	0.47	1.21
473712872456844544	5263	-0.39	0.90	229267969902029696	5800	0.15	1.03
473900304830038144	7831	-0.19	1.72	277091262508123264	9658	-0.14	2.45
2000667342122793472	7660	-0.21	1.75	277091739248814208	6562	-0.19	1.21
2000680742420926976	6058	-0.29	1.84	277092155861283712	5575	0.46	1.05
2000684586402884864	6669	-0.09	1.80	3342732093967192576	6265	-0.59	1.02

Using data from the StarHorse catalog, as well as results from the MIST project, CMD and appropriate evolutionary tracks were constructed for each field and individual variable star, corresponding to the star's mass and metallicity. These diagrams are shown in figures 1-3. GAIA ID of the stars is given in legends to the figures.

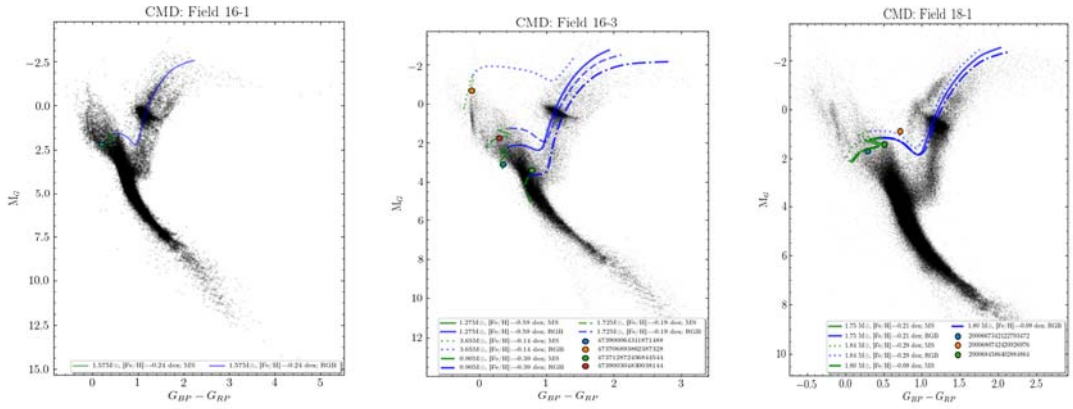

Figure 1 – CMD and evolution tracks for selected variable stars
on the field 16-1 (on the left), 16-3 (in the middle) and 18-1 on the right

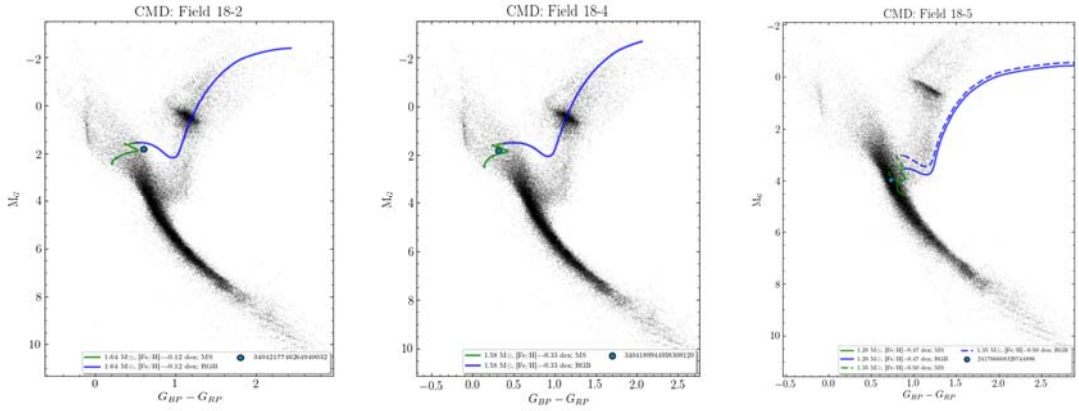

Figure 2 – CMD and evolution tracks for selected variable stars
on the field 18-2 (on the left), 18-4 (in the middle) and 18-5 on the right

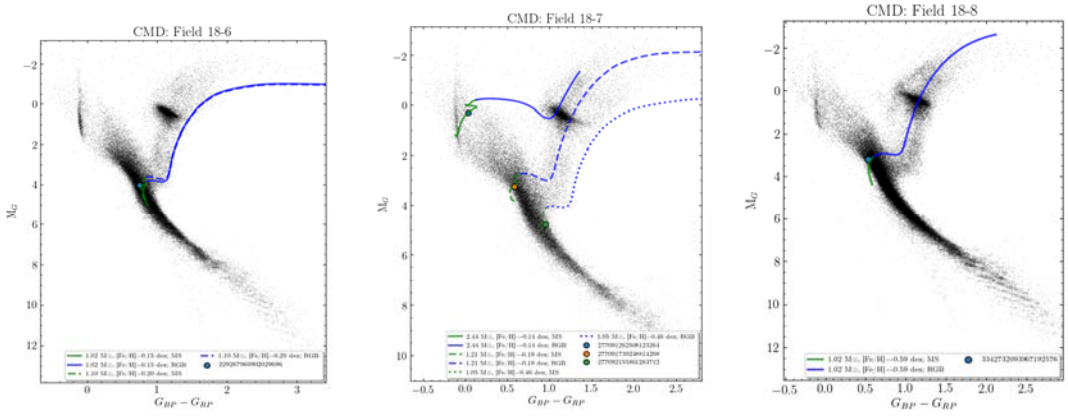

Figure 3 – CMD and evolution tracks for selected variable stars
on the field 18-6 (on the left), 18-7 (in the middle) and 18-8 on the right

Light curve analysis, amplitude-period parameters

The main tool of the light curves analysis utilized in this work is periodogram using two algorithms implemented in the project GATSPY [11] and PyAstronomy (https://github.com/sczesla/PyAstronomy) with successive steps of the ”pre-whitening”, that is, subtracting the detected period of the light curve followed by computing “cleaned” periodogram. The search for oscillation periods was carried out in the range of periods (П) from 0.003 d to 0.15 d. As an example, and due to pages limit here we show the results for selected stars.

473900304830038144 (field 16-1): the physical parameters (T_{eff} and M_{Sun}), its position on the CMD diagram, and the period of variability (~1.8 - 2.3 hours) indicate that this star belongs to the DSCT type. The light curve is shown in figure 4. Periodograms with an indication of reliable peaks are shown in figure 5. Analysis of the light curve gives the following parameters of pulsation: $П_1$ = 0.08410±0.00004 (d), A_1 = 0.0096±0.0009 mag, $П_2$ = 0.08934±0.00004, A_2 = 0.0081±0.0008.

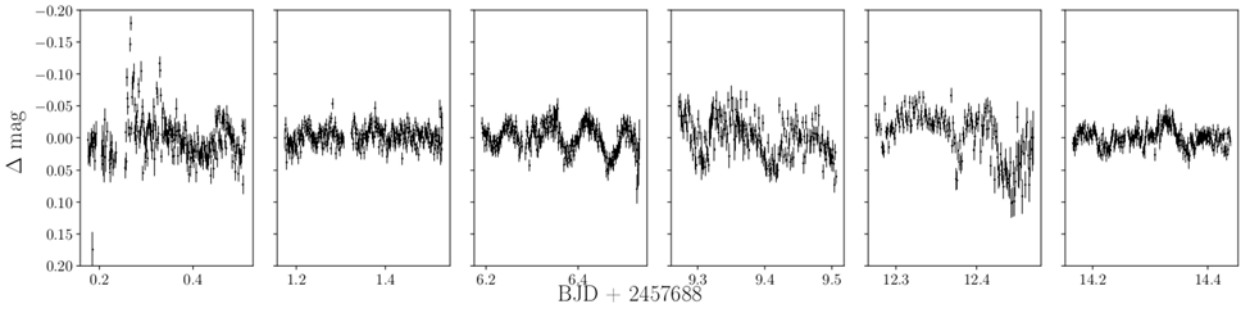

Figure 4 - Light curve of the star 473900304830038144

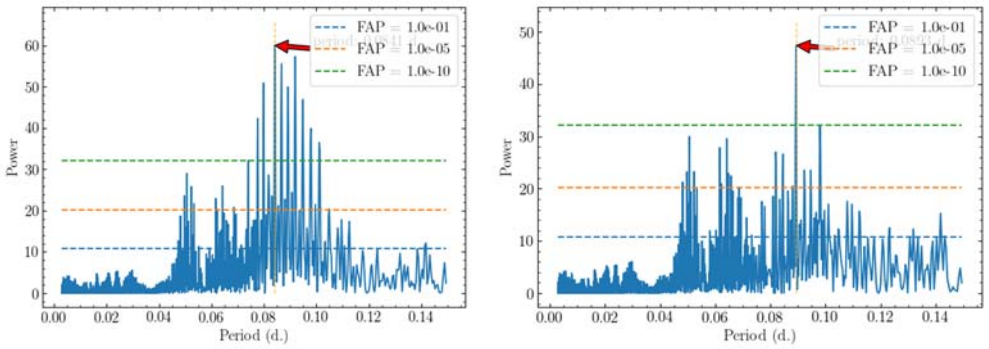

Figure 5 - Periodograms for the star 473900304830038144 with indication of found periods

473906008546567168 (field 16-3): the light curve (figure 6) shows the changes in brightness from minimum to maximum with an amplitude of about 0.3 magnitude and a period of ~0.1 days. The analysis reveals three modes of oscillations: Π_1=0.13885±0.00002 (d), A_1=0.112±0.003 mag, Π_2=0.06488±0.00003 (d), A_2=0.021±0.002 mag, Π_3 = 0.1213±0.0001 (d), A_3 = 0.020±0.002 mag. The corresponding periodograms are shown in figure 7. The nature of the pulsations suggests that this star belongs to the HADS (high amplitude DSCT).

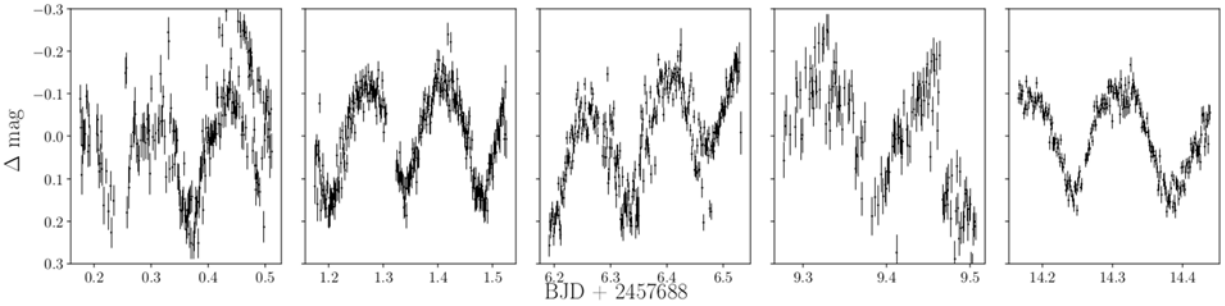

Figure 6 - Light curve of the star 473906008546567168

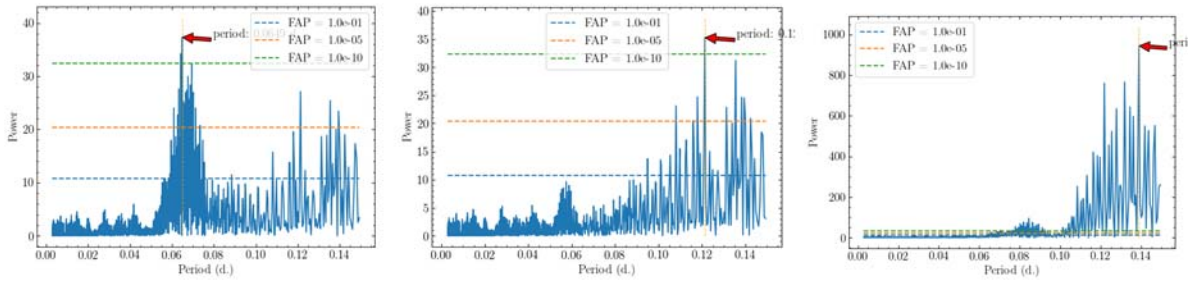

Figure 7 - Periodograms for the star 473906008546567168 with indication of found periods

277091262508123264 (field 18-7): the analysis of the CMD diagram (figure 3) shows that it is the Main Sequence star of spectral type A (T_{eff} was used). The light curve is shown in figure 8. Despite the short duration of the light curve, the star shows the presence of a rich spectrum of pulsations, which may be due to the irregular variability. If we exclude the possible periods 0.2 d and to limit the periods search within the duration of one epoch (~3 hours), we reliably detect three modes: Π_1=0.0811±0.0004 d, A_1=0.0103±0.0007 mag, Π_2=0.0599±0.0003 d, A_2=0.0057±0.0006 mag, Π_3 = 0.0445±0.0002 d, A_3 = 0.0041±0.0005 mag (figure 9). The nature of the oscillations shows that this variable may belong to the DSCT, but it may be of roAp type. The object is of particular interest for subsequent observations and possibly asteroseismic analysis.

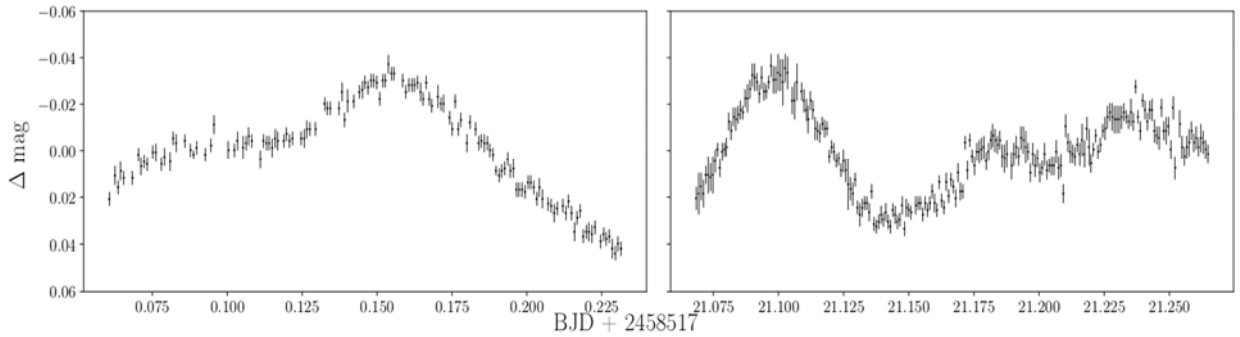

Figure 8 - Light curve of the star 277091262508123264

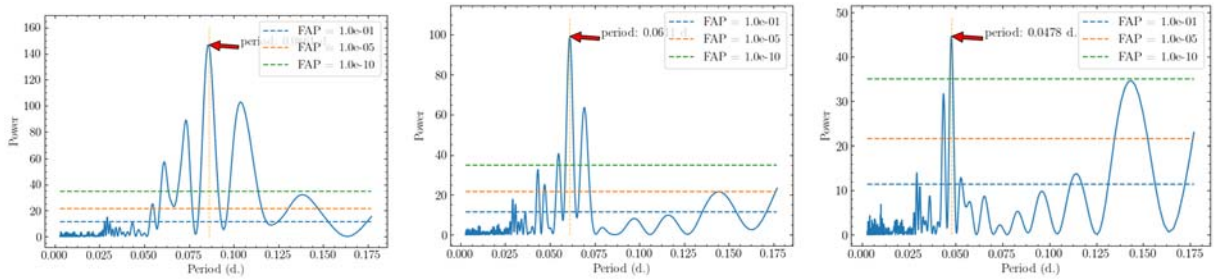

Figure 9 - Periodograms for the star 277091262508123264 with indication of found periods

Catalog of variable stars and types of variability

The classification of the type of variability was made based on the obtained oscillation parameters (period and amplitude), the position of the star on the CMD evolutionary track, as well as using an available spectral data. For two objects, we performed spectral observations on the Zeiss-1000 "Zapadny" telescope using a slit spectrograph. The obtained spectra were compared with synthesized spectra computed utilizing the SPECTRUM package [12] and based on grids of atmospheric models from [13].

For the star designated in the GAIA catalog as 3404189944938309120 we found the following parameters according to the StarHorse project: T_{eff} = 7338K, [Fe/H] = -0.33, M_* = 1.58 M_{Sun}. Based on these parameters, synthesized spectra were constructed with the spectral resolution corresponding to our observations for two values of T_{eff} – 7250K and 8000K, with the parameter *log*g = 4.0 and [Fe/H] = -0.5. A comparison of the synthesized spectra with the spectrum obtained at TSO is shown in Figure 10. From comparison with model spectra, it can be concluded that the data of the StarHorse project correspond to reality and this variable star can be attributed to the DSCT type with a high probability.

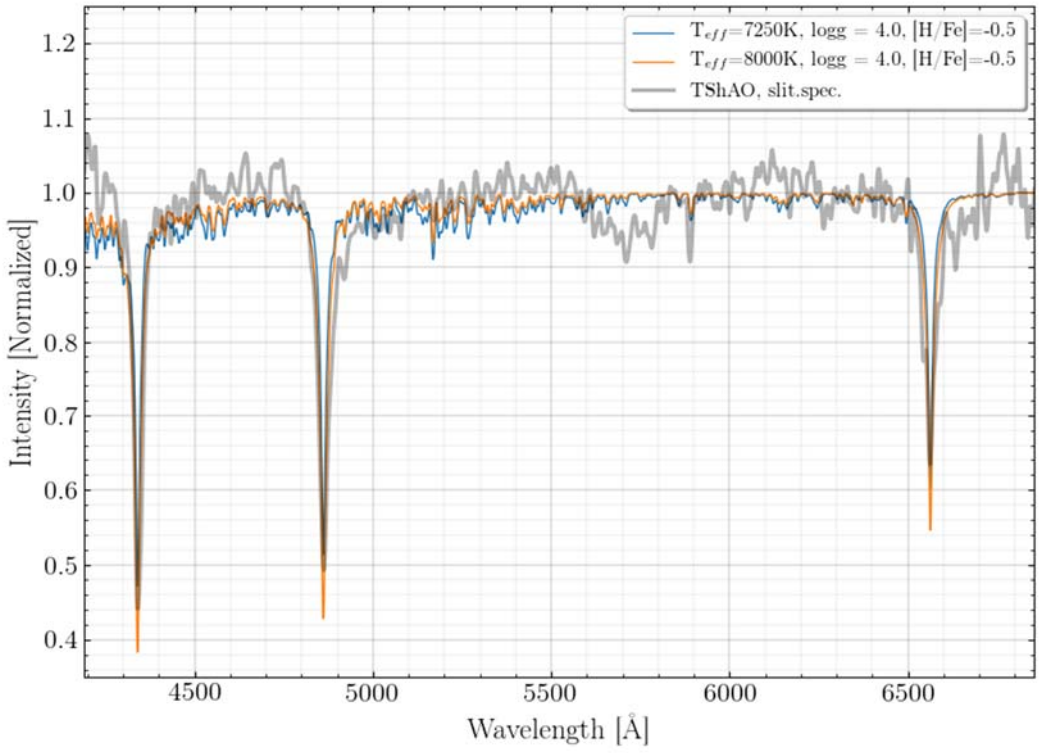

Figure 10-Comparison of spectra obtained at the TSO using a slit spectrograph mounted on the Zeiss-1000 "Zapadny" telescope with synthesized spectra for two T_{eff} values

Table 3 - Detected variable stars from TSO survey

GAIA ID	Π	σ_{Π}	A	σ_A	Type
3420722996343786496	0.0485 0.0925 0.0708	0.00001 0.0001 0.0001	0.0033 0.0026 0.0023	0.0003 0.0003 0.0023	DSCT
3420726084425443200	---	---	0.7	0.0001	EB
3420728150304526976	a rich spectrum of pulsations				ZZB
473706893862387328	0.0867 0.0347 0.0344	≈0.0001	0.05-0.1	≈0.0003	SX Phoenix, βCep(?)
473712872456844544	a rich spectrum of pulsations				PNCS
473900064311871488	0.3765	≈0.0001	≈0.6	≈0.0003	EV
473900304830038144	0.08410 0.08934	0.00004 0.00004	0.0096 0.0081	0.0009 0.0008	DSCT
473906008546567168	0.13885 0.06488 0.12130	0.00002 0.00003 0.00010	0.112 0.021 0.020	0.003 0.002 0.002	DSCT
2000667342122793472	≈0.05	≈0.01	≈0.025	≈0.001	DSCT
2000668544713613952	>0.15	---	≈0.020	---	DSCT
2000677993641422208	≈0.1	---	≈0.10	---	DSCT
2000680742420926976	>0.15	---	≈0.20	---	DSCT
2000681876292067968	0.060 0.042	0.001 0.001	0.037 0.015	0.002 0.001	DSCT
2000684586402884864	>0.15	---	≈0.03	---	DSCT(?)
2000685758942457728	≈0.12	---	0.03	---	DSCT(?)
2000686239978998400	0.0363	0.0005	0.0151	0.0008	DSCT
2001434835597456768	>0.2	---	>0.6	---	EV(?)
3404200257158109824	Nonregular, with amplitude ≈ 0.01				IV(?)
3404213726175547776	>0.2	---	0.4	0.001	EV
3404217746264940032	Nonregular, with amplitude ≈ 0.01				IV(?)
3404189944938309120	Nonregular, with amplitude ≈ 0.01				DSCT(?)
241766668329744896	>0.12	---	>0.5	---	EV(?)
241771856649828992	>0.15	---	≈0.1	---	DSCT(?)
229267969902029696	---	---	≈0.5	<0.001	EB
2770898537587883 52	0.0820	0.0003	0.025	0.003	DSCT(?)
2770908158315015 68	Nonregular, with amplitude ≈0.2				(?)
2770912625081232 64	0.0811 0.0599 0.0445	0.0004 0.0003 0.0002	0.0103 0.0057 0.0041	0.0007 0.0006 0.0005	DSCT, roAP(?)
2770917392488142 08	≈0.125	≈0.001	≈0.1	≈0.001	DSCT(?)
2770921558612837 12	≈0.30	≈0.01	≈0.6	≈0.001	EV
2770930148521916 16	Nonregular, with amplitude ≈ 0.01				(?)
3342732093967192576	>0.12	≈0.01	≈0.3	≈0.01	EV(?)
3433368376498172160	>0.12	≈0.01	≈0.3	≈0.01	EV(?)
3433415586778288768	≈0.1	---	≈0.03	---	DSCT(?)

For a star with the number 277091262508123264 according to the GAIA catalog classification, we found the following parameters of this star according to the StarHorse project: T_{eff} = 9658K, [Fe/H] = -0.14, $M_* = 2.45\ M_{Sun}$. It should be noted that for this object, there is a large discrepancy in the T_{eff} values between the GAIA and StarHorse data. Therefore, we also consider the parameters of this star obtained from the LAMOST project: T_{eff} = 7088 K, [Fe/H] = 0.043. Based on these parameters, synthesized spectra were constructed with a spectral resolution corresponding to our observations and those of the LAMOST project for two values of T_{eff} - 7000K and 9500K, with the *log*g = 4.0 and [Fe/H] = 0.0. A comparison of synthesized spectra with the spectra obtained at TSO and in the LAMOST project is shown in figure 11. From figure 11, we can conclude that the data from the StarHorse project does not seem to be correct and LAMOST gives more accurate value. From the obtained comparison, we can conclude that this star also likely belongs to the DSCT variable type.

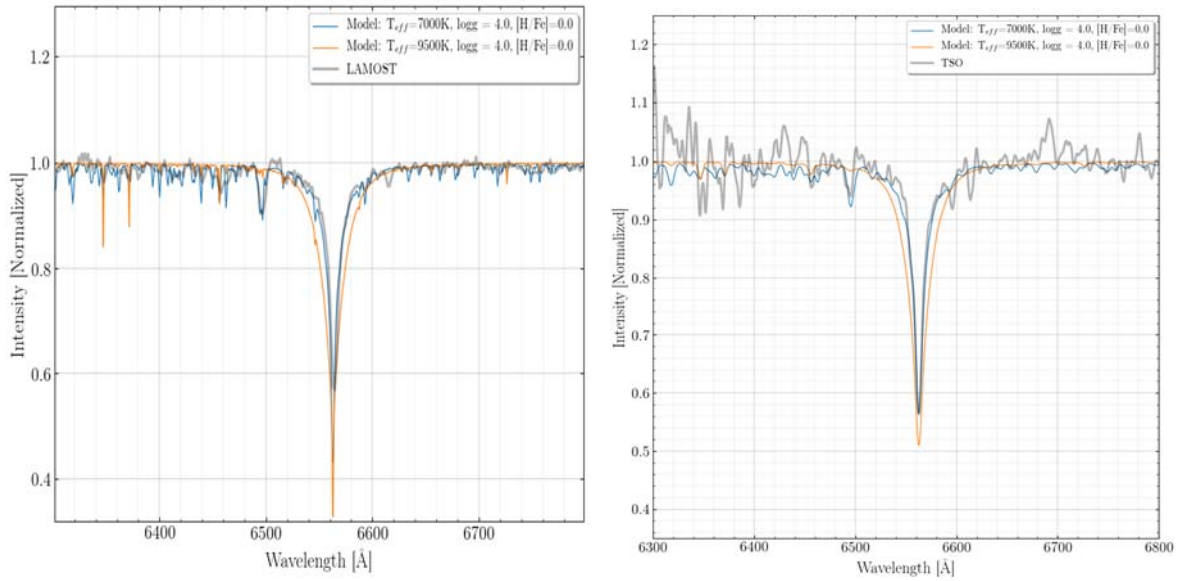

Figure 11-Comparison of the spectra obtained in the LAMOST project (left) and at the TSO (right) on a slit spectrograph mounted on the Zeiss-1000 "Zapadny" telescope with synthesized spectra for two T_{eff} values

More accurate spectral characteristics can be obtained from iterative approximation (or MCMC method) of model spectra to the observed ones, using a grid of models with a certain step in the values of [Fe/H], *log*g and T_{eff}.

Conclusion

Survey observations of 15 selected fields were carried out. Photometric pipeline data analysis conducted for 23 fields, including observations for 2016 and 2018. As a result, light curves for 9836 stars with the duration of observations at least 3 hours were obtained. Analysis of the light curves of these stars leads to the identification of 33 variable stars. Among them, 31 stars are previously unknown variables. The amplitude-period analysis of the light curves of the identified variables was carried out, which allowed us to give a preliminary classification of their type of variability. Where possible, we analyzed the color-magnitude diagrams and constructed the corresponding evolutionary tracks. Table 8 presents the main information obtained on the detected variable stars.

Acknowledgments

This work has been partially supported by the program BR05236322 of the Ministry of Education and Science of the RK and the scientific and technical program BR05336383 Aerospace Committee of the Ministry of Defense and Aerospace Industry of the Republic of Kazakhstan. Authors used Matplotlib [14] for producing figures.

А. Серебрянский, Г**. Айманова**, **Л. Кондратьева**, **Ч. Омаров**

ЕЖШС «В.Г. Фесенков атындағы Астрофизика институты»

ТЯНЬ-ШАНЬДА ӨЗГЕРМЕЛІ ЖҰЛДЫЗДАРДЫ ІЗДЕУДЕГІ ФОТОМЕТРИЯЛЫҚ ЗЕРТТЕУДІҢ АЛҒАШҚЫ НӘТИЖЕЛЕРІ: ЖАРЫҚ ҚИСЫҚТАРЫН ТАЛДАУ ЖӘНЕ ӨЗГЕРМЕЛІ ЖҰЛДЫЗДАРДЫҢ ЖІКТЕЛУІ

Аннотация. Айнымалы жұлдыздарды іздеуге арналған көптеген науқандарға қарамастан, барлық жаңа айнымалылардың, соның ішінде бұрын белгісіз болған кластардың ашылуы жалғасуда. Сонымен қатар, ерекше нысандар бар. Мысалы, WD1145 + 017 – қазіргі кездегі экзопланеталық жүйелердің бұзу феноменінің бар болуының дәлелдеуі бар белгілі жалғыз ақ ергежейлі. Қысқа мерзімді айнымалы жұлдыздарды іздеу үшін ТШОА-да фотометриялық науқан басталған болатын. Оның мақсаттарының бірі – өзара әрекеттесетін ультра-ықшам екілік жүйелерді (AM CVn) қоса алғанда, екілік ықшам жүйелерді (UCB) іздеу. Мұндай жүйелерді бір обсерваторияның күшімен іздеу олардың жарықтық вариациясының бірнеше ондаған минутқа созылатындығымен, ал жарық вариациясының амплитудасы жұлдыздық шамамен 0,01-ден 1,0-ге дейінгі аралықта өзгеретіндігімен ақталған. Сонымен қатар, мұндай зерттеу басқа ауыспалы жұлдыздардың түрлерін, соның ішінде астросейсмологияға қызығушылық тудыратын объектілерді, экзопланеталары бар жүйелерді және т.б. іздеу үшін пайдаланылуы мүмкін.

Тянь-Шань обсерваториясында (ТАО) Zeiss-1000 телескопының көмегімен жүргізілген фотометриялық зерттеу барысында анықталған өзгермелі жұлдыздардың жарық қисықтарын талдаудың алғашқы нәтижелері ұсынылды. Мұнда біз 33 жоғары амплитудалы ауыспалы жұлдыздар туралы баяндаймыз, олардың ішінде 31 бұрын айнымалы жұлдыздар каталогына енбеген.

Жұлдыздардың айнымалылық түрін анықтау үшін олардың жарық қисықтарын талдап, амплитудасы мен периодтарын анықтау керек, сонымен қатар жұлдыздың эволюциялық күйін және егер мүмкіндік болса, оның спектрлік сипаттамаларын да анықтау керек (Sp). Бұл жұмыста жарық қисықтарын талдаудың негізгі құралы – тербеліс спектрін «ағарту» тізбекті қадамдары бар PyAstronomy пакеті (https://github.com/sczesla/PyAstronomy) және GATSPY пакет алгоритмі көмегімен орындалған периодограммаларды құру. Біз тербелістердің периодтарын 0.003-тен 0.15 күнге дейінгі аралықта іздедік. Мақалада мысал ретінде бірнеше жұлдыздарға арналған жарық қисықтары келтірілген.

StarHorse каталогындағы деректерді, сондай-ақ MIST жобасының нәтижелерін қолдана отырып, сәйкес металлылыққа және анықталған өзгермелі жұлдыздардың массасына эволюциялық жолдар түсті-жарықтығы диаграммаларында алынды.

Цейсс-1000 «Батыс» ТШАО телескопында екі нысанда спектрлік бақылау жүргізілді. Алынған спектрлер модельді спектрлермен салыстырылды. Әрбір жұлдыздың өзгергіштік түрін алдын-ала анықтау периодограммалармен анықталатын тербеліс режимдерінің параметрлеріне (амплитудасы мен периодтары), түсті жарықтылық диаграммаларына (CMD) негізделген эволюция сатысына және кейбір жұлдыздарға спектрлік ақпарат негізінде жасалады.

Нәтижесінде айнымалылық кластары және өзгергіштік параметрлері бар 33 жұлдыздың тізімі пайда болды: 17 DSCT жұлдызы, 2 EB (тұтылған екілік), 7 EV (эллипстік айнымалы), 2 IV (дұрыс емес айнымалы), 1 PNCS (планетарлық тұмандылықтың орталық жұлдызы), 1 ZZB (ақ ергежейлі) және 2 белгісіз айнымалылық типі бар жұлдыз.

Түйін сөздер: әдістер, жарық қисықтарын талдау, фотометрия, жұлдыздар, ауыспалы жұлдыздар.

А. Серебрянский, Г**. Айманова**, **Л. Кондратьева**, **Ч. Омаров**

ДТОО «Астрофизический институт им. В.Г. Фесенкова»

ПЕРВЫЕ РЕЗУЛЬТАТЫ ТЯНЬ-ШАНСКОГО ФОТОМЕТРИЧЕСКОГО ОБЗОРА ПО ПОИСКУ ПЕРЕМЕННЫХ ЗВЕЗД: АНАЛИЗ КРИВЫХ БЛЕСКА И КЛАССИФИКАЦИЯ ПЕРЕМЕННЫХ ЗВЕЗД

Аннотация. Несмотря на большое количество разных кампаний по поиску переменных звезд, открытие все новых переменных, включая неизвестных ранее классов, продолжается. Кроме того, встречаются уникальные объекты. Например, WD1145+017 – единственный известный в настоящий момент белый карлик с доказательством существования феномена разрушения экзопланетных систем. Для поиска переменных

звезд с короткими периодами была предпринята фотометрическая кампания на ТШОА. Одной из ее целью является поиск двойных компактных систем (UCB), включая взаимодействующие ультра-компактные двойные системы (AM CVn). Поиск таких систем силами одной обсерватории оправдан тем, что вариации блеска у них имеют периоды несколько десятков минут, а амплитуды вариации блеска – от 0.01 до 1.0 звездной величины. Кроме того, такой обзор может быть использован для поиска других типов переменных звезд, включая объекты, имеющие интерес для астросейсмологии, системы с экзопланетами и др.

В этой статье представлены первые результаты анализа кривых блеска переменных звезд, выявленных в ходе фотометрического обзора, проведенного на Тянь-Шаньской обсерватории (ТШАО) с помощью телескопа Цейсс-1000. Здесь мы сообщаем о 33 высокоамплитудных переменных звездах, среди которых 31 – ранее не вошедшие в каталоги переменных звезд.

Для определения типа переменности у звезд необходимо проанализировать их кривые блеска и определить амплитуды и периоды, а также определить эволюционный статус звезды и, если есть такая возможность, ее спектральные характеристики (Sp). Основным инструментом анализа кривых блеска в данной работе является построение периодограмм, реализованное с применением алгоритма пакета GATSPY и пакета PyAstronomy (https://github.com/sczesla/PyAstronomy) с последовательными шагами “отбеливания” спектра колебаний. Поиск периодов колебаний проводился нами в диапазоне периодов от 0.003 до 0.15 суток. В статье в качестве примера приведены кривые блеска лишь для нескольких звезд.

Используя данные каталога StarHorse, а также результаты проекта MIST, были получены и нанесены на диаграммы Цвет-Светимость эволюционные треки для соответствующей степени металличности и массы обнаруженных переменных звезд.

Для двух объектов были проведены спектральные наблюдения на телескопе Цейсс-1000 “Западный” ТШАО с использованием щелевого спектрографа. Полученные спектры сравнивались с модельными спектрами. Предварительная идентификация типа изменчивости каждой звезды осуществляется на основе параметров мод колебаний (амплитуд и периодов), определяемых по периодограммам, стадии эволюции – на основе диаграмм цвет-светимость (CMD) и для некоторых звезд – на основе спектральной информации.

В результате был получен список из 33 звезд с параметрами осцилляций и классом переменности: 17 звезд DSCT, 2 EB (затменные двойные), 7 EV (элиптические переменные), 2 IV (неправильные переменные), 1 PNCS (центральная звезда планетарной туманности), 1 ZZB (белый карлик) и 2 звезды с неизвестным типом переменности.

Ключевые слова: методы, анализ кривых блеска, фотометрия, звезды, переменные звезды.

Information about authors:

Serebryanskiy A., Ph.D., Fesenkov Astrophysical Institute, aserebryanskiy@yahoo.com, https://orcid.org/0000-0002-4313-7416;

Kondratyeva L.N., Doctor of Physical and Mathematical Sciences, Fesenkov Astrophysical Institute. lu_kondr@mail.ru, https://orcid.org/0000-0002-6302-2851;

Aimanova G. K., Doctor of Physical and Mathematical Sciences, Fesenkov Astrophysical Institute. agauhar@mail.ru, https://orcid.org/0000-0002-3869-8913;

Omarov Ch., Doctor of Physical and Mathematical Sciences, Director, Fesenkov Astrophysical Institute, chingis.omarov@gmail.com, https://orcid.org/0000-0002-1672-894X

REFERENCES

[1] Szabados L. Selected new results on pulsating variable stars // Contributions of the Astronomical Observatory Skalnate Pleso. 2019. T. 49, № 2. C. 171-182.

[2] Paparo M. An Observer's View on the Future of Asteroseismology // Frontiers in Astronomy and Space Sciences. 2019. May. T. 6.

[3] Auvergne M., Bodin P., Boisnard L., Buey J. T., Chaintreuil S., Epstein G., Jouret M., Lam-Trong T., Levacher P., Magnan A., Perez R., Plasson P., Plesseria J., Peter G., Steller M., Tiphene D., Baglin A., Agogue P., Appourchaux T., Barbet D., Beaufort T., Bellenger R., Berlin R., Bernardi P., Blouin D., Boumier P., Bonneau F., Briet R., Butler B., Cautain R., Chiavassa F., Costes V., Cuvilho J., Cunha-Parro V., Fialho F. D., Decaudin M., Defise J. M., Djalal S., Docclo A., Drummond R., Dupuis O., Exil G., Faure C., Gaboriaud A., Gamet P., Gavalda P., Grolleau E., Gueguen L., Guivarc'h V., Guterman P., Hasiba J., Huntzinger G., Hustaix H., Imbert C., Jeanville G., Johlander B., Jorda L., Journoud P., Karioty F., Kerjean L., Lafond L., Lapeyrere V., Landiech P., Larque T., Laudet P., Le Merrer J., Leporati L., Leruyet B., Levieuge B., Llebaria A., Martin L., Mazy E., Mesnager J. M., Michel J. P., Moalic J. P., Monjoin W., Naudet D., Neukirchner S., Nguyen-Kim K., Ollivier M., Orcesi J. L., Ottacher H., Oulali A., Parisot J., Perruchot S., Piacentino A., da Silva L. P., Platzer J., Pontet B., Pradines A., Quentin C., Rohbeck U., Rolland G., Rollenhagen F., Romagnan R., Russ N., Samadi R., Schmidt R., Schwartz N., Sebbag I., Smit H., Sunter W., Tello M., Toulouse P., Ulmer B., Vandermarcq O., Vergnault E., Wallner R., Waultier G., Zanatta P. The CoRoT satellite in flight: description and performance // Astronomy & Astrophysics. 2009. Oct. T. 506, № 1. C. 411-424.

[4] Borucki W. J., Koch D., Basri G., Batalha N., Brown T., Caldwell D., Caldwell J., Christensen-Dalsgaard J., Cochran W. D., DeVore E., Dunham E. W., Dupree A. K., Gautier T. N., III, Geary J. C., Gilliland R., Gould A., Howell S. B., Jenkins J. M., Kondo Y., Latham D. W., Marcy G. W., Meibom S., Kjeldsen H., Lissauer J. J., Monet D. G., Morrison D., Sasselov D., Tarter J., Boss A., Brownlee D., Owen T., Buzasi D., Charbonneau D., Doyle L., Fortney J., Ford E. B., Holman M. J., Seager S., Steffen J. H., Welsh W. F., Rowe J., Anderson H., Buchhave L., Ciardi D., Walkowicz L., Sherry W., Horch E., Isaacson H., Everett M. E., Fischer D., Torres G., Johnson J. A., Endl M., MacQueen P., Bryson S. T., Dotson J., Haas M., Kolodziejczak J., Van Cleve J., Chandrasekaran H., Twicken J. D., Quintana E. V., Clarke B. D., Allen C., Li J., Wu H., Tenenbaum P., Verner E., Bruhweiler F., Barnes J., Prsa A. Kepler Planet-Detection Mission: Introduction and First Results // Science. 2010. Feb 19. T. 327, № 5968. C. 977-980.

[5] Ricker G. R., Winn J. N., Vanderspek R., Latham D. W., Bakos G. A., Bean J. L., Berta-Thompson Z. K., Brown T. M., Buchhave L., Butler N. R., Butler R. P., Chaplin W. J., Charbonneau D., Christensen-Dalsgaard J., Clampin M., Deming D., Doty J., De Lee N., Dressing C., Dunham E. W., Endl M., Fressin F., Ge J., Henning T., Holman M. J., Howard A. W., Ida S., Jenkins J. M., Jernigan G., Johnson J. A., Kaltenegger L., Kawai N., Kjeldsen H., Laughlin G., Levine A. M., Lin D., Lissauer J. J., MacQueen P., Marcy G., McCullough P. R., Morton T. D., Narita N., Paegert M., Palle E., Pepe F., Pepper J., Quirrenbach A., Rinehart S. A., Sasselov D., Sato B. e., Seager S., Sozzetti A., Stassun K. G., Sullivan P., Szentgyorgyi A., Torres G., Udry S., Villasenor J. Transiting Exoplanet Survey Satellite // Journal of Astronomical Telescopes Instruments and Systems. 2015. Jan-Mar. T. 1, № 1.

[6] Toma R., Ramsay G., Macfarlane S., Groot P. J., Woudt P. A., Dhillon V., Jeffery C. S., Marsh T., Nelemans G., Steeghs D. The OmegaWhite Survey for short period variable stars - II. An overview of results from the first four years // Monthly Notices of the Royal Astronomical Society. 2016. Nov. T. 463, № 1. C. 1099-1116.

[7] Choi J., Dotter A., Conroy C., Cantiello M., Paxton B., Johnson B. D. MESA ISOCHRONES AND STELLAR TRACKS (MIST). I. SOLAR-SCALED MODELS // Astrophysical Journal. 2016. Jun. T. 823, № 2.

[8] Dotter A. MESA ISOCHRONES AND STELLAR TRACKS (MIST) 0: METHODS FOR THE CONSTRUCTION OF STELLAR ISOCHRONES // Astrophysical Journal Supplement Series. 2016. Jan. T. 222, № 1.

[9] Miller A. A. THE SYNTHETIC-OVERSAMPLING METHOD: USING PHOTOMETRIC COLORS TO DISCOVER EXTREMELY METAL-POOR STARS // Astrophysical Journal. 2015. Sep. T. 811, № 1.

[10] Anders F., Khalatyan A., Chiappini C., Queiroz A. B., Santiago B. X., Jordi C., Girardi L., Brown A. G. A., Matijevic G., Monari G., Cantat-Gaudin T., Weiler M., Khan S., Miglio A., Carrillo I., Romero-Gomez M., Minchev I., de Jong R. S., Antoja T., Ramos P., Steinmetz M., Enke H. Photo-astrometric distances, extinctions, and astrophysical parameters for Gaia DR2 stars brighter than G=18 // Astronomy & Astrophysics. 2019. Aug 12. T. 628.

[11] VanderPlas J. T., Ivezic Z. PERIODOGRAMS FOR MULTIBAND ASTRONOMICAL TIME SERIES // Astrophysical Journal. 2015. Oct. T. 812, № 1.

[12] Gray R. O., Corbally C. J. THE CALIBRATION OF MK SPECTRAL CLASSES USING SPECTRAL-SYNTHESIS. 1. THE EFFECTIVE TEMPERATURE CALIBRATION OF DWARF STARS // Astronomical Journal. 1994. Feb. T. 107, № 2. C. 742-746.

[13] Castelli F., Kurucz R. L. Is missing FeI opacity in stellar atmospheres a significant problem? // Astronomy & Astrophysics. 2004. May. T. 419, № 2. C. 725-733.

[14] Hunter J. D. Matplotlib: A 2D graphics environment // Computing in Science & Engineering. 2007. May-Jun. T. 9, № 3. C. 90-95.

NEWS
OF THENATIONAL ACADEMY OF SCIENCES OF THE REPUBLIC OF KAZAKHSTAN
PHYSICO-MATHEMATICAL SERIES
ISSN 1991-346X **https://doi.org/10.32014/2020.2518-1726.41**
Volume 3, Number 331 (2020), 92 – 99

UDC 524.31

V. M. Tereschenko

Fesenkov Astrophysical Institute, Almaty, Kazakhstan.
E-mail: volter2307@mail.ru

SPECTROPHOTOMETRIC STANDARDS 8^m-10^m. II.THE EQUATORIAL ZONA FROM 0^h TO 12^h.

Abstract. This article is the second paper from cycle of notices, which devoted of the creation of spectrophotometric standards of intermediate brightness. In paper the absolute energy distribution in visual region of spectra for 12 B-A-stars 8^m-10^m were present. The standards such brightness is necessary first of all for calibration of the spectral observations on the big telescopes. The investigated stars-standards are located along the celestial equator ($\delta = \pm 3^\circ$) in the range of right ascensions from 0^h to 12^h. Observations were made on the telescopes of AZT-8 and Zeiss-600 with the help of a diffraction spectrograph with toroidal grating. The receiver of radiation was served CCD-camera ATIC 490EX. Equipment, observation methods, reductions and computations detailed described in our first paper. The distribution of energy was studied in the range of 345нм - 665nm, the spectral resolution of the data is 5nm, the relative standard error of the received data - from 2 to 6%. The reliability of the results is assessed by comparing the calculated and directly observed star magnitudes of the investigated stars in the UBV-system.

Key words: stars, energy distribution, spectrophotometrical standards.

Introduction. In spectrophotometric observations of celestial bodies, stars with good known energy distribution in their spectrums serve as standards. As a rule, these are non- variable stars of early spectral classes. Their spectrums have long areas, some free of strong spectral lines. These areas suitable are used to standardize of the spectra of investigated objects and calibrate equipment. In present time the out-atmospheric distribution of energy in the visible region of the spectrum has been studied for about one and a half thousand stars. Almost all of them are brighter than 6 magnitude and only a third of them belong to the early spectral classes. In the publications there are about a hundred 7^m- 8^m-standards stars [1-3] and only a few dozen of the weaker stars with known energy distribution [4]. But standards should be as large as possible, as the productiveness of observations and accuracy of the measuring data depends on them quantity.

Naturally the observations on large telescopes require weaker standards. A brief overview of the works on the investigation of energy distribution in the spectra of stars is given in our article [5]. In the same paper also a substantiated relevance research of energy distribution in the spectrums of stars of intermediate brightness (8^m-10^m). It is well known that the creation of spectrophotometric standards belongs to the class of "eternal" tasks, as over time more weak standards are required, more accurate, with higher spectral resolution and covering an ever wider interval Spectrum. In addition, the more standards, the higher the performance and accuracy of observations. This work is the second in a series of works devoted to the creation of spectrophotometric standards of intermediate brilliance. In this article for 12 stars-standards 8^m -10^m the distribution of energy in the visual spectrum given. The stars-standards are located near the equator (±3 degrees) and evenly on direct ascent in the zone from 0h to 12h.

Observations was carry out with the CCD-spectrograph, which specifically for absolute measurements was manufactured. The spectrum have registering by the CCD-camera ATIC 490EX. The spectrograph had installing either on the 70-centimetre AZT-8 (D:F-1:16) or on the 60-cm "Zeiss-600" (1:12) located on the Kamenskoe Plateau (height = 1350m). Five stars from the catalogue [5] served as primary standards. A full list of primary standards and their main characteristics are available in our article [5]. The observations were carried out by differential method of equal heights. This allowed used the

average value of the coefficient of the transparency of atmosphere for the place of observations in the reductions. Each star was observed 6 to 12 times.

Table 1 - List of explored stars and their main characteristics

No.	HD (BD)	α_{2000}	δ_{2000}	V	B-V	Sp
1	1112	$00^h\ 15^m\ 27.3^s$	-03° 39' 15"	9.11^m	-0.06^m	B9V
2	12021	01 57 56.1	-02 05 58	8.85	-0.06	B8V
3	18571	02 5916.8	01 14 40	8.63	+0.03	A0V
4	24520	03 54 07.0	02 11 02	8.62	+0.09	A0V
5	28190	04 27 03.5	04 16 51	9.04	+0.08	B9V
6	289997	05 10 07.8	-00 16 58	9.96	+0.06	B9V
7	42334	06 10 08.7	00 42 36	9.31	+0.03	B8III
8	50087	06 51 40.6	00 19 36	9.08	+0.04	B8III
9	63367	07 48 44.4	01 56 21	9.05	+0.01	B9V
10	BD+01 2119	08 32 43.6	00 53 49	10.13	-0.07	A0
11	86027	09 55 59.6	02 47 55	8.37	-0.02	A0V
12	97917	11 15 48.3	-02 17 58	8.90	-0.11	B8IV
13*	23009	03 41 38.1	-00 09 49	8.64	0.21	A2III

*- primary standard

Unfortunately, more than a third of the observational data were throw away, mainly due to the low and unstable transparency of the earth's atmosphere. Due to the rapid growth of Almaty and global climate change, the number of photometric nights on the Kamenskoe Plateau has decreased significantly in recent years. The transparency of the atmosphere as a whole has decreased, and the brightness of the sky has greatly increased. The resulting spectra were processed in the MaxImDL-6 package. The process of processing frames is detailed in the work [5].

Numerical reductions was made according to the formula:

$$E_*(\lambda) = E_{st}(\lambda) \cdot [I_*(\lambda) / Ist(\lambda)] \cdot [\Delta t_{st} / \Delta t_*] \times p_{av}(\lambda)^{-\Delta M}, \quad (1)$$

where the E_* and Est are the outside atmospheric values of the spectral density of the energy illuminance created by the star and the standard; I_* and Ist - amount of counts in CCD-camera from star and standard in the 5nm intervals; Δt_{st} and Δt_* - the duration of exposures to the standard and the star; P_{av}- the average coefficient transparency of earth atmosphere; Mst = Mst - M_* - the difference of air masses between the standard and the star.

Due to the relative proximity of the software stars and the standards, the difference of air masses for the absolute majority of observations did not exceed 0.05. The difference of time between star observations and standards was usually less than half an hour, but sometimes reached an hour.

The processing of frames of the stellar spectra was carried out by standard means. At first frame was cleaned from hot pixels, then was calibrated and, finally, subtracted background.

At numerical reductions for primary standards was used values of monochromatic illuminations and counts for the quasi-continuous spectrum. The values of illuminations in the spectral lines region were obtained in advance through graphic interpolation. The counts in regions of the hydrogen lines on obtained registrogrammes were also interpolated. This procedure could be performed by numerical method using a computer, presenting the interpolation curve as a polynomial. However, we used the "manual" method. The treated registrogrammes we printed out and then the printouts interpolated in region of hydrogen lines. The interpolated values of counts were entered into the computer. This "hybrid" method is longer and somewhat is archaic. However, compared to purely computer, it is more reliable. The pixels of CCD-camera in advance was broken down into 50-angstrom intervals. The hydrogen line Hβ served as reference point of wavelength on registrogrammes. Spectrograph operate in the range of 340nm to 670nm The region of registration of radiation in our case is determined by the spectral sensitivity and size of the CCD-matrix.

The results of observations of twelve stars - spectrophotometric standards of intermediate brilliance are presented in Table 2. Unfortunately, the CCD camera used does not allow to register the radiation shorter than 345m. For some stars, we decided to extrapolate the energy distribution curves by one or two

points in the red region of spectrum - up to 6700A. As the extrapolation interval is small, she was quite confident. Extrapolated values in the table are marked with an asterisk.

Table 2 - Extra-atmospheric energy distribution in the spectrums of the stars studied.
Units - "watt/m^{2}m" - 10^{-7}, wavelength - in angstroms.

No.	1	2	3	4	5	6	7	8	9
HD (BD)	001112	012021	018571	024520	028190	289997	042334	050087	063367
3475	87	170	102	71	53	39	76	73	100
3525	87	166	94	78	54	39	76	73	97
3575	85	159	98	81	60	39	78	70	93
3625	85	162	96	82	59	38	79	78	92
3675	85	158	105	84	59	39	77	81	98
3725	96	164	110	90	68	43	76	88	101
3775	109	183	153	117	94	50	88	110	118
3825	133	216	194	159	123	59	104	131	151
3875	165	256	237	196	152	69	121	153	172
3925	168	262	269	237	172	71	123	157	180
3975	188	288	292	263	182	76	137	175	206
4025	197	300	309	293	200	82	142	178	215
4075	178	273	285	266	180	77	131	164	197
4125	170	255	272	249	169	74	126	152	191
4175	175	258	275	263	183	76	130	158	196
4225	173	256	269	263	177	72	126	151	189
4275	162	238	251	245	165	69	117	146	176
4325	143	214	227	206	140	61	107	132	158
4375	143	210	225	201	141	62	106	129	161
4425	147	213	228	217	151	64	109	134	169
4475	144	207	220	221	149	62	105	129	164
4525	141	200	215	216	145	61	102	126	158
4575	136	195	208	208	141	59	99	121	152
4625	135	191	204	205	137	58	95	118	147
4675	131	184	200	200	134	56	94	118	144
4725	125	176	190	193	130	54	91	114	137
4775	118	167	183	182	126	52	86	108	127
4825	107	151	170	160	110	46	77	98	114
4875	102	143	163	144	100	44	74	93	112
4925	108	149	169	156	111	46	77	98	119
4975	109	150	168	165	114	46	79	98	120
5025	106	145	163	165	110	45	76	97	115
5075	104	143	158	163	109	44	74	93	114
5125	102	138	157	158	108	43	72	91	110
5175	98	135	152	155	106	42	71	90	108
5225	96	130	148	151	102	41	70	89	106
5275	92	125	143	147	100	40	68	87	100
5325	90	122	139	141	96	39	65	83	98
5375	88	119	138	139	97	38	64	82	96
5425	86	115	134	137	94	38	63	81	94
5475	85	113	131	135	91	37	61	78	92
5525	83	109	126	131	90	37	59	76	89
5575	80	107	126	131	89	35	60	77	88
5625	79	106	123	128	84	34	58	75	85
5675	77	103	119	123	82	33	55	72	82
5725	75	99	117	120	84	33	54	71	81
5775	73	96	114	117	79	31	52	69	79
5825	71	93	111	114	76	30	50	67	76
5875	70	92	109	114	76	29	49	64	75
5925	68	89	106	110	74	29	49	64	74
5975	67	87	102	106	72	29	47	63	73
6025	65	86	101	104	71	28	47	62	72
6075	63	81	98	101	69	27	47	62	70
6125	62	80	98	100	68	27	46	60	69

No.	1	2	3	4	5	6	7	8	9
6175	60	79	95	98	68	27	43	58	67
6225	58	75	93	96	64	25	42	56	65
6275	56	73	89	94	62	24	41	54	62
6325	55	72	88	90	61	24	41	54	62
6375	55	69	86	89	60	24	40	53	61
6425	53	67	84	88	60	23	39	52	58
6475	52	65	81	84	58	22	38	52	57
6525	47	61	76	76	51	21	36	50	52
6575	45	59	75	71	49	21	34	48	51
6625	48	62	82	*80	*55	*22	*37	*50	*54
6675	*47	*60	80	*79	*54	*21	*36	*50	*53

Table 2, continued

No.	10	11	12	13	No.	10	11	12	13
HD (BD)	+01 2119	086027	097917	023009	HD (BD)	+01 2119	086027	097917	023009
3475	28	187	159	75	5125	45	191	122	146
3525	31	166	165	76	5175	45	189	119	142
3575	30	165	157	77	5225	44	186	119	139
3625	33	169	159	78	5275	42	175	112	137
3675	34	174	152	79	5325	41	171	107	133
3725	33	191	152	84	5375	40	166	106	132
3775	38	217	168	112	5425	40	165	104	130
3825	58	275	202	142	5475	39	159	101	128
3875	70	320	236	159	5525	39	155	98	125
3925	68	329	237	174	5575	37	154	94	123
3975	79	369	249	133	5625	36	150	91	121
4025	84	396	263	239	5675	35	143	87	119
4075	77	363	239	196	5725	34	139	86	116
4125	74	340	230	171	5775	33	133	83	115
4175	77	355	232	220	5825	32	132	81	112
4225	76	340	227	217	5875	33	129	78	110
4275	70	323	217	209	5925	32	127	76	108
4325	63	287	195	144	5975	32	123	74	105
4375	63	284	190	182	6025	31	121	72	103
4425	67	299	193	194	6075	30	118	69	101
4475	66	288	187	192	6125	29	115	68	100
4525	64	281	182	188	6175	29	113	67	98
4575	62	271	176	183	6225	28	110	64	97
4625	60	264	168	180	6275	26	107	63	95
4675	59	257	164	177	6325	27	103	60	93
4725	56	244	154	172	6375	26	103	58	92
4775	52	230	147	168	6425	25	96	56	90
4825	46	205	134	146	6475	25	95	55	88
4875	43	195	129	112	6525	22	87	51	82
4925	47	207	133	154	6575	22	84	49	68
4975	49	209	132	154	6625	*23	88	53	85
5025	47	201	127	152	6675	*22	*86	51	83
5075	47	199	124	149					

*- interpolated and extrapolated values.
Wavelengths belong to the centers of averaging intervals.

Comparison with photometry. Since the spectral distribution of energy for the studied stars was obtained for the first time, it is not possible to estimate the external convergence of the data obtained by comparison. We can only assess the internal convergence of data by calculating, for example, a relative average error. The average value of these errors for ultraviolet (345nm - 400nm) and visible (405nm - 665nm) areas of the spectrum is between 6% and 2%. Here the sensitivity of the matrix is smaller and the transparency is lower.

A rough estimate of our results can obtained by oblique means - comparing the observed stellar values for the studied stars with calculated values out of energy distributions. The calculated discrepancies give, albeit roughly, a picture about of the reliability of our data and allow us to discard the obviously erroneous values of energy distributions. Wherein we are assume that a observed magnitudes and color-indexes is true.

For comparison, we decided to use the UBV system. As mentioned above, for our stars not only the spectral energy distribution, but also the photometric data in the band "U" absent. Therefore we were able to assess resemblance only in B and V bands by calculating the stellar magnitude V and the color-index B-V. The calculations of stellar magnitude V was made by a well-known formula:

$$Vcal = -2.5\times \log\Sigma E(\lambda)\times S(\lambda)\times\Delta\lambda + const \quad (2),$$

where Vcal is a calculated magnitude; E (λ) - the monochromatic outside atmosphere illuminance; S (λ) - the response curve of the band of photometric system; Δλ - the spectral interval of the averaging;

The color-index (B-V)cal was calculated on the formula:

$$(B\text{-}V)cal = -2.5\log [\Sigma E(\lambda)\times S_B(\lambda) / \Sigma E(\lambda)\times S_V(\lambda)] + const \quad (3)$$

The reaction curves of bands taken from the monograph V. Straizhys [10].

The numerical value of the constants depend from the zero-point of scale of stellar magnitudes, the unit system used and the interval of averaging. Since the averaging interval for all wavelengths is the same, it can be included in the value of constant. Then for all stars was calculated the differences:

$$\delta V = Vcal - Vobs, \quad (4)$$

$$\delta(B\text{-}V) = (B\text{-}V)cal - (B\text{-}V)obs \quad (5)$$

Their values are represented in table 3.

Table 3 - Calculated residuals for V and (B-V)

№	HD (BD)	Vobs	Vcal	δV	(B-V)obs	(B-V)cal	δ(B-V)
1	1112	9.11^m	9.11^m	0.00^m	-0.06^m	-0.02^m	0.04^m
2	12021	8.85	8.95	0.10	-0.06	-0.03	0.03
3	18571	8.63	8.63	0.00	0.03	-0.02	-0.05
4	24520	8.62	8.61	-0.01	0.09	0.06	-0.03
5	28190	9.04	9.03	-0.01	0.08	0.04	-0.04
6	289997	9.96	10.02	0.06	0.06	-0.01	-0.07
7	42334	9.31	9.47	0.16	0.03	-0.03	-0.06
8	50087	9.08	9.19	0.11	0.04	0.00	-0.04
9	63367	9.05	9.02	-0.03	0.01	-0.03	-0.04
10	+01 2119	10.13	9.95	-0.18	-0.07	0.02	0.09
11	86027	8.37	8.42	0.05	-0.02	-0.07	-0.05
12	97917	8.90	8.92	0.02	-0.11	-0.13	-0.02
13	Sec_2	8.64	8.67	0.03	0.21	0.21	0.00

Table 3 shows that residuals for some stars can reach more than 0.1^m. Stars with such residuals should not be used as standards. The dimmest star has maximum residuals which, apparently, indicates on the instrumental of their origin. In general, the calculated values of the V are not show of systematic differences with the observed ones, but our color-indexes B-V look a little blue. The residuals are generally the same as for catalogs obtained by photovoltaic method, in which also have significant differences. Each such case requires additional observations and analysis. The dependence of the obtained residuals on the stellar magnitude and color-index are represented on figures 1 and 2.

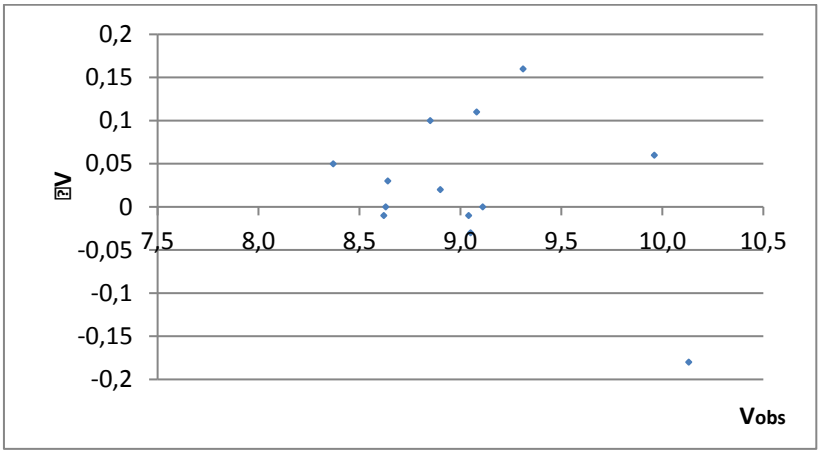

Figure 1 - The dependence of the residuals δV on the stellar magnitude V

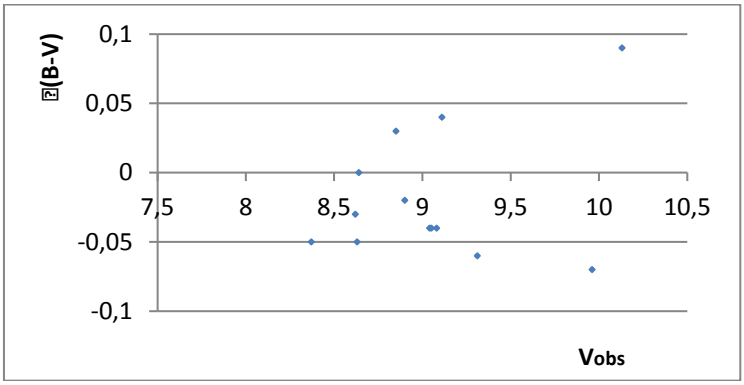

Figure 2 - The dependence of the residuals δ(B-V) on the stellar magnitude V

In conclusion, I express my sincere gratitude to Bobryashova T.A. for her great help in conducting observations and processing them.

The work was executed within program 05336383 "Development of space monitoring technologies and forecasting of natural resources, man-made changes in the environment, creation of space technology and ground space infrastructure, exploration of objects of near and near space".

В. М. Терещенко

«В.Г. Фесенков атындағы астрофизика институты» ЕЖШС, Алматы, Қазақстан

8^m-10^m СПЕКТРОФОТОМЕТРЛІК СТАНДАРТТАР II. 0^h ден 12^h ЭКВАТОРЛЫҚ АЙМАҚ

Аннотация. Бұл жоспарланған кезекті жұмыстың екінші мақаласы, спектрофотометрлік аралық жарқырау стандарттарын құруға арналған. 8^m-10^m жұлдыздық шамадағы 12 B-A жұлдыздар үшін көорінерлік аймақтағы спектрлеріндегі абсолютті энергияның таралуы көрсетілген. Зертелген жұлдыздар 0^h ден 12^h аралықтағы тура шарықтауда аспан экваторына көлбеу (δ = ± 3˚) орналасқан. Үлкен телескоптарда жүргізілетін жұлдыздардың спектрлеріндегі энергияның таралуы туралы мәліметтер спектрлік бақылауларды стандарттауға қажет. Абсолюттік өлшеулерді жүргізу үшін, арнайы дифракциалық спектрограф жасалған, соның көмегімен АЗТ-8 және Цейсс-600 телескоптарымен бақылаулар орындалды. Спектрограф "ATIC 490" ЗБА (зарядталған байланыс аспабы) – камерасымен жабдықталған. Біздің бірінші жұмысымызда аспап, бақылау әдісі және редукциялау туралы мәліметтер толық сипатталған. Энергияның таралуы 340–660 нм аймағында зерттелді, алынған мәліметтердің спектрлік ажыратылымдылығы 5 нм, ал алынған мәліметтердің салыстырмалы орташа квадраттық қателігі 2-ден 6%-ке дейін. Бақылаулар тең биіктіктегі дифференциалды

әдісіпен жүргізілді, бұл Жер атмосферасының мөлдірлік коэффициентінің орташа мәнін редукция кезінде байқылауды орындау үшін пайдалануға мүмкіндік берді. Бақылау нәтижелері кесте түрінде берілді. ЗБА-камерасы арқылы жұлдыздар спектірінің кең аймақтағы атмосферадан тыс энергияның таралуы туралы мәліметтердің алғашқы рет алынғанын атап айтуымыз қажет.

Жұлдыздардың спектріндегі энергияның таралуы туралы басқа авторлар зерттеген мәліметтер жоқ. Осы себепті алынған нәтижелердің сенімділігі жанама әдіспен – UBV жүйесінде зерттелген жұлдыздардың есептелген және тікелей бақыланған жұлдыздық шамаларын салыстыру арқылы бағаланды. Қажетті тұрақтылықтар негізгі фотометриялық және спектрофотометрлік стандарттардың бірі - Вега бойынша есептелді. Тұрақтылардың сандық шамалары бірліктер жүйесіне, нөлдік нүктенің қабылданған шамасына, жұлдыздардың спектрлеріндегі энергияның таралуына орташалау аралығы мен Вега үшін қабылданған калибровкаға байланысты. Айтып кетерлік жағдай, Каменко үстіртіндегі атмосфераның мөлдірлігі жыл сайын нашарлап және айнымалы болып бара жатыр, бақылаулар жүргізілді. Осы себепті бақылаулардың үштен бір бөлігі іске жарамсыз болды. Бақылау мәліметтеріне сыни тұрғыдан қараудың арқасында зерттелген жұлдыздар үшін энергияның таралуы фотоэлектрлік әдіспен алынған спектрофотометриялық каталогтардың дәлдігімен салыстырылды. Келесі жұмыста 12-ден 24 сағат аймақтағы жұлдыздарға энергияның таралуы ұсынылады.

Түйін сөздер: жұлдыздар, энергияның таралуы, спектрофотометрлік стандарттар.

В. М. Терещенко

ДТОО «Астрофизический Институт им Фесенкова», Алматы, Казахстан

СПЕКТРОФОТОМЕТРИЧЕСКИЕ СТАНДАРТЫ 8^m-10^m . II. ЭКВАТОРИАЛЬНАЯ ЗОНА ОТ 0^h до 12^h.

Аннотация. Это вторая статья из намеченного цикла работ, посвященных созданию спектрофотометрических стандартов промежуточного блеска. В ней представлено абсолютное распределение энергии в видимой области спектра для 12 B-A-звезд 8^m-10^m. Исследованные звезды расположены вдоль небесного экватора ($\delta = \pm 3^\circ$) в интервале прямых восхождений от 0^h до 12^h. Данные о распределении энергии в спектрах звезд промежуточного блеска необходимы, прежде всего, для стандартизации спектральных наблюдений, проводимых на крупных телескопах. Наблюдения выполнены на телескопах АЗТ-8 и Цейсс-600 с помощью дифракционного спектрографа, специально изготовленного для абсолютных измерений. Спектрограф оснащен ПЗС-камерой “ATIC 490”. Подробно аппаратура, методы наблюдений и редукций описаны в первой нашей работе. Распределение энергии исследовано в интервале 340нм - 660нм, спектральное разрешение полученных данных составляет 5нм, относительная среднеквадратичная ошибка полученных данных - от 2 до 6%. Наблюдения выполнены дифференциальным методом равных высот, что позволило использовать в редукциях среднее значение коэффициента прозрачности земной атмосферы для места наблюдений. Результаты наблюдений представлены в табличном виде. Стоит отметить, что данные о внеатмосферном распределении энергии в столь широкой области спектра звезд с помощью ПЗС-камеры получены впервые.

Данных других авторов о распределении энергии в спектрах исследованных звезд нет. По этой причине достоверность полученных результатов оценена косвенным методом - путем сравнения вычисленных и непосредственно наблюдаемых звездных величин исследованных звезд в системе UBV. Необходимые константы были вычислены по Веге - одному из основных фотометрических и спектрофотометрических стандартов. Численные значения констант зависят от системы единиц, принятого нуль-пункта звездных величин, интервала усреднения для распределения энергии в спектрах звезд и принятой для Веги калибровки. Подчеркнем, что прозрачность атмосферы на Каменском плато, где проводились наблюдения, с каждым годом ухудшается и становится более изменчивой. По этой причине более трети наблюдений было выброшено. Благодаря критическому подходу к данным наблюдений распределение энергии для исследованных звезд получено с точностью, сравнимой с точностью спектрофотометрических каталогов, полученных фотоэлектрическим методом. В следующей работе будут представлены распределения энергии для звезд в зоне от 12 до 24 часов.

Ключевые слова: звезды, распределение энергии, спектрофотометрические стандарты.

Information about author:
Tereschenko V. M., Candidate of Physical and Mathematical Sciences, Fesenkov Astrophysical Institute; volter2307@mail.ru; https://orcid.org/0000-0001-8021-0347

REFERENCES

[1] Hamuy Mario, Suntzeff N. B., Heathcote S.R.., Walker A.R., Gigoux P., Philips M. M. (1994) Southern spectrophotometric standards. II. *Publications of the Astronomical Society of the Pacific Vol. 106*. P. 566–589.

[2] Borisov I. N., Glushneva I. N., Shenavrin V. I. (1998) Spectrophotometric standards of 7^m - 8^m: *Astronomical and Astrophysical Transactions. Vol. 17*. P. 309–320.

[3] Tereschenko V. M. (2002) Intermediate-Brightness Equatorial Spectrophotometric Standards. *Astronomy Reports. Vol. 46 (3)*. P. 224–232.

[4] Bohlin R.C., Dickinson M.E., and Callzetti. (2001). Spectrophotometric standards from the far-ultraviolet to the near-infrared: STIS and NICMOS fluxes. *Astron. J. Vol. 122*. P. 1218–1228.

[5] Tereschenko V.M. (2018) Spectrophotometric standards 8^m - 10^m. I. Equipment, methods and first results. *News of the NAS RK, phys.-math. ser. Vol .4 (320)*. P. 42–47.

[6] Kharitonov A.V., Tereschenko V. M., Knyazeva L.N. (2011) Spectrophotometricheskiy catalog zvezd. (in Russ.) [Spectrophotometric Catalogue of Stars] Almaty. Kazak Universitety. 304 P.

[7] Tereschenko V. M., Shamro A.V. (2017) Spektrograf dlay absoluytnych izmereniy. Skhema i konsrtuktsiay optiko-mekhanicheskogo bloka (in Russ.) [Spectrograph for Absolute Measurements. Plan and Construction of Optic-mechanic Block*]. News of the NAS RK - phys.-math. ser. Vol.5 (315*) . P. 152–159.

[8] Mironov A.V. (2008) Osnovy fotometriiy. [Principles of Photometry]. *M. Fizmatlit*. 260 p.

[9] Burnashev V.I., Burnasheva B.A. (2016) Fotometriya i spektrofotometriya zvezd i galaktik. [Photometry and spectrophotometry of Stars and Galaxies]. Simferopol, Antikva, 382 p.

[10] Straizhys V. (1977). Mnogotsvetnaya fotometriya zvezd. [Multicolor Stellar Photometry].Vilnius, Mokslas, 312 p.

NEWS
OF THENATIONAL ACADEMY OF SCIENCES OF THE REPUBLIC OF KAZAKHSTAN
PHYSICO-MATHEMATICAL SERIES
ISSN 1991-346X **https://doi.org/10.32014/2020.2518-1726.42**
Volume 3, Number 331 (2020), 100 – 107

UDC 524.31

V. M. Tereschenko

Fesenkov Astrophysical Institute, Almaty, Kazakhstan.
E-mail: volter2307@mail.ru

SPECTROPHOTOMETRIC STANDARDS 8^m-10^m. III. THE EQUATORIAL ZONA FROM 12^h TO 24^h

Abstract. This article is the third paper from cycle of notices, which devoted of the creation of spectrophotometric standards of in-termediate brightness. In paper the absolute energy distribution in visual region of spectra for 12 B-A-stars 8^m-10^m were present. The investigated stars-standards are located along the celestial equator ($\delta = \pm 3^\circ$) in the range of right ascensions from 0^h to 12^h. Together with the stars from the second work of this cycle, they form a system of equatorial standards of intermediate brilliance. As a product of these two works, the total number of spectrophotometric standards of 8m-10m in the visible spectrum area has more than doubled.

Equipment, observation methods, reductions and computations detailed described in our first and second papers. The distribution of energy was studied in the range of 340nm - 665nm, the spectral resolution of the data is 5nm, the relative standard error of the received data - from 2 to 6%. The reliability of the results is assessed by comparing the calculated and directly observed star magnitudes of the investigated stars in the UBV-system. For several stars, the distribution of energy in their spectrums, in addition to the observations, was calculated by photometric data. Differences between them in the ultraviolet region can reach 20-30% due to differences in the course of energy distribution curves in their spectrums, errors in spectral classification and determination of interstellar absorption.

Keywords: stars, energy distribution, spectrophotometric standards, comparison with photometry.

Introduction. This work is a continuation of the work on the creation of spectrophotometric standards of intermediate brightness [1,2]. Once again, the creation of spectrophotometric standards remains an urgent task. There should be as many standards as possible, as the number of observations and the accuracy of the data obtained depend on them. This paper presents the distribution of energy in the visible spectrum area for 12 stars of the early spectral classes of 8^m - 10^m. As in the work [2], the stars studied are located along the equator (±3 degrees), but cover the zone from 12^h to 24^h. Together with the stars from the second work of this cycle, they form a system of equatorial standards of intermediate brightness. Thanks to these two works, the total number of stars - spectrophotometric standards of 8^m-10^m in the visible area of the spectrum has more than doubled.

Observations, reductions and results. The list and main characteristics of the stars studied are given in table 1. The second column contains numbers on HD catalogs, if they are not in it - on the BD catalog. In general, the stars studied are slightly dimmer than the stars from the previous work [2]. The five stars recommended in the standards are weaker than 10^m. The stars observed have not been specifically investigated for the change, but they do not appear as variables in the SIMBAD database. It should be noted that, unfortunately, even in modern photometric catalogs, the differences between magnitudes V and color-indexes B-V are relatively often 0.05^m or more. The accuracy of spectral classification in most cases is one or two subclasses.

The observations are made on the 70-centimetre reflector AZT-8 (D : F = 1 : 16) and on the 60-cm "Zeiss-600" (D : F = 1 : 12) with the help of spectrograph, which is specifically designed for absolute measurements (SAM) [3] . The dispersing element of the spectrograph is the toroidal diffraction grate and the detector is the CCD camera ATIC-490EX.

Table1 - List of investigated stars and their main characteristics

№	HD or BD	α_{2000}	δ_{2000}	V	B - V	Sp
1	BD+01 2668	$12^h\ 13^m\ 25.3^s$	01° 09' 22"	10.29^m	-0.09^m	B5*
2	BD+02 2711	13 42 19.0	01 30 18	10.26	-0.11	B5
3	BD+02 2790	14 14 25.9	01 47 58	10.11	0.03	A0
4	HD136161	15 19 14.7	-02 10 02	8.86	0.28	A3V(A2V)
5	HD151355	16 46 47.0	02 12 34	8.85	-0.09	B4/5V
6	HD162628	17 51 52.6	02 53 59	8.28	0.16	B9.5V
7	HD174648	18 51 41.0	-01 45 35	8.81	0.09	B9.5V
8	HD185296	19 38 21.0	01 30 14	9.68	0.23	B9II
9	BD -03 4950	20 34 43.6	-02 41 44	10.00	0.09	A0 (B8)
10	BD+01 4436	21 10 11.5	02 14 20	9.99	0.03	A0
11	HD215112	22 42 58.0	-02 40 57	8.25	-0.03	B9IV-V
12	BD+02 4661	23 23 38.20	02 55 57	10.05	0.38	F2

*- the spectral class was "assigned" according to the color-index B-V.

The five stars from the catalogue [3] were used as primary standards, and information about them is given in our work [1]. The observations were carried out by a method of equal heights, which allowed the average value of the atmosphere's transparency factor for observation seating to be used in reductions. Each star was observed 3 to 8 times. Due to the unstable transparency of the atmosphere, more than a third of the data obtained from the observations were released. Note that the astronomical climate on the observatory “Kamenskoye Plateau” is deteriorate every year. The deterioration of transparency and the increase in the brightness of the sky are due to the rapid growth of the metropolis (Almaty), and the decrease in the number of clear time - global climate change. Apparently, it is no longer rational to observe the fundamental photometry and absolute spectrophotometry here.

The resulting CCS spectrograms are processed in the MaxIm DL-6 package. The process of processing personnel and necessary reductions is detailed in our works. Let's focus only on measurements of star spectrums - primary standards.

For secondary standards we took the values of luminosities and counts for the quasi-continuous spectrum. The lighting values for them in the hydrogen lines area were obtained earlier by graphic interpolation of energy distribution curves. Line counts for each register were also interpolated. This procedure can be done by numerical method using a computer, however, we used a "manual" method. Calibrated and with a subtracted register background, we printed out and made the transcripts interpolate in the hydrogen lines. The countdowns were re-entered into the computer. The hydrogen line H_β was a rapper at the breakdown of the spectrum by 50-angstrom intervals. The resulting non-atmospheric values of monochromatic light for twelve stars, recommended as spectrophotometric standards of intermediate brightness are presented in table 2.

Table 2 - The energy distribution for investigated stars in the absolute units [10^{-7} watt $m^{-2}m^{-1}$]

HD or BD	BD+01 2668	BD+02 2711	BD+02 2790	HD 136161	HD 151355	HD 162628	HD 174648	HD 185296
λ, A	1	2	3	4	5	6	7	8
3425	42.0	59.2	30.8	57	251	183	87	34.4
3475	41.2	64.1	30.9	54	241	162	95	30.7
3525	39.2	63.3	27.9	69	232	164	91	29.7
3575	42.1	61.5	31.9	61	231	166	89	31.2
3625	40.0	60.8	29.3	60	230	165	90	33.1
3675	41.8	55.1	36.9	60	220	166	91	35.6
3725	43.0	56.8	41.1	63	219	184	103	42.0
3775	51.1	55.0	47.4	75	224	215	121	49.1
3825	58.4	64.3	56.0	96	245	265	153	61.4
3875	67.7	73.5	64.2	110	270	314	177	70.7
3925	68.2	74.3	70.0	122	280	348	194	76.3
3975	73.3	79.4	71.7	143	299	396	212	84.0

Continuation of the table 2

1	2	3	4	5	6	7	8	9
4025	72.3	79.2	70.9	160	291	417	225	85.1
4075	67.4	72.0	64.0	144	268	372	205	80.5
4125	64.0	69.7	64.2	147	258	364	200	77.2
4175	65.7	68.3	66.9	158	257	389	209	79.7
4225	64.4	66.3	63.4	153	245	375	201	77.3
4275	60.0	60.8	57.6	145	231	354	188	74.4
4325	55.2	56.0	51.8	126	205	296	165	67.9
4375	55.5	55.3	55.0	135	204	309	167	68.1
4425	55.4	53.9	56.4	143	203	328	175	70.0
4475	54.1	52.8	55.8	142	195	322	173	68.6
4525	51.5	51.9	54.7	140	193	320	170	68.3
4575	49.6	50.5	53.3	138	186	315	167	66.7
4625	47.9	48.0	51.7	137	181	309	164	66.0
4675	46.4	47.1	50.1	136	175	305	160	64.0
4725	43.6	45.2	47.6	131	166	291	154	61.8
4775	41.0	41.9	43.8	126	156	273	144	60.3
4825	37.9	38.7	39.3	113	143	241	129	55.8
4875	36.6	37.7	38.2	106	138	225	122	53.7
4925	39.0	38.0	41.8	117	140	250	133	57.2
4975	37.6	37.3	42.0	120	141	257	137	58.5
5025	36.4	35.5	41.6	119	138	257	135	57.7
5075	36.2	35.4	40.8	120	135	254	133	57.8
5125	35.8	34.2	39.4	117	131	248	129	56.4
5175	34.9	33.7	38.3	113	127	241	126	54.7
5225	33.7	32.3	37.1	114	123	236	123	54.1
5275	31.7	31.8	36.2	112	118	230	118	53.2
5325	30.9	30.3	35.2	108	114	224	115	52.6
5375	30.4	29.5	35.0	108	109	220	113	52.5
5425	30.8	28.8	34.6	108	107	217	110	52.5
5475	28.8	27.6	33.1	107	105	213	109	51.6
5525	27.9	26.4	32.7	105	102	210	107	51.3
5575	27.6	26.2	31.8	101	101	210	106	51.0
5625	27.3	25.5	30.7	100	97	205	103	50.0
5675	25.5	25.1	30.4	100	94	200	100	49.4
5725	25.6	23.6	29.8	99	92	198	99	48.7
5775	24.4	23.2	29.1	97	89	191	96	47.3
5825	23.6	22.4	28.2	96	86	188	94	47.3
5875	22.7	22.2	27.4	94	82	183	92	46.0
5925	21.9	21.5	27.2	93	82	183	90	45.3
5975	21.5	20.8	27.5	92	81	180	88	44.7
6025	21.3	20.7	25.9	90	79	178	88	43.8
6075	20.6	20.1	25.3	89	76	173	86	42.9
6125	19.0	19.6	25.4	88	74	169	82	42.5
6175	19.2	19.1	24.5	86	72	164	80	40.7
6225	17.8	18.6	24.2	85	70	162	80	39.5
6275	18.3	18.1	22.8	81	68	156	78	39.4
6325	17.6	*17.6	*22.4	*79	*67	*152	*77	38.2
6375	16.6	*17.2	*21.9	*78	*65	*148	*77	37.5
6425	16.0	*16.8	*21.5	*76	*63	*144	*71	36.4
6475	15.8	*16.5	*21.0	*74	*62	*141	*69	35.2
6525	14.7	*15.6	*19.6	*70	*59	*131	*63	33.4
6575	14.0	*14.7	*17.3	*62	*55	*115	*61	33.0
6625	16.0	*15.3	*19.6	*69	*58	*131	*67	35.1
6675	16.5	*15.0	*19.4	*69	*56	*129	*65	33.5

Table 2, continued

λ, A	BD-03 4950	BD+01 4436	HD 215112	BD+02 4661	λ, A	BD-03 4950	BD+01 4436	HD 215112	BD+02 4661
	9	10	11	12		9	10	11	12
3425	28.3	23.1	236	30.0	5075	44.5	45.5	239	47.9
3475	25.7	28.7	214	27.0	5125	42.4	44.1	231	46.5
3525	28.1	22.8	238	36.0	5175	41.4	42.8	224	45.3
3575	28.5	25.0	209	30.8	5225	40.4	41.5	220	44.9
3625	28.5	24.7	206	29.4	5275	39.2	39.9	213	45.1
3675	28.6	27.8	210	31.5	5325	38.5	39.2	204	44.5
3725	30.8	31.3	221	31.4	5375	38.2	38.2	202	43.9
3775	33.2	36.1	245	32.2	5425	38.1	37.5	199	43.7
3825	45.5	50.0	298	37.4	5475	37.3	36.8	192	44.1
3875	51.7	63.0	366	44.3	5525	36.7	35.6	188	43.6
3925	58.3	68.6	387	44.2	5575	35.7	34.3	182	42.4
3975	64.4	78.4	419	51.4	5625	34.4	33.6	182	42.9
4025	67.5	79.4	448	58.3	5675	34.8	33.3	178	42.7
4075	64.9	73.3	420	57.2	5725	33.8	31.8	172	42.1
4125	66.4	75.9	399	55.2	5775	33.0	31.4	166	41.9
4175	68.3	76.8	411	56.6	5825	32.5	30.9	164	40.7
4225	64.5	76.3	399	55.5	5875	30.5	30.3	161	40.7
4275	58.8	70.3	375	54.2	5925	28.1	29.3	157	39.9
4325	56.1	60.8	332	51.6	5975	27.6	28.3	153	39.6
4375	58.3	61.7	331	52.1	6025	28.1	27.8	146	39.1
4425	59.8	65.7	345	53.6	6075	28.5	27.6	142	37.1
4475	58.4	64.8	335	53.8	6125	28.9	26.4	146	37.2
4525	57.8	62.4	326	53.8	6175	27.8	25.3	138	36.7
4575	56.6	60.5	313	53.8	6225	27.2	24.3	134	35.7
4625	54.5	59.5	308	53.4	6275	26.8	24.3	131	35.5
4675	53.0	58.0	298	52.7	6325	25.9	22.9	126	35.1
4725	50.6	54.6	287	51.0	6375	24.7	22.5	125	34.8
4775	47.2	52.0	271	49.8	6425	23.2	21.1	121	33.0
4825	42.7	45.7	247	46.8	6475	22.5	21.2	118	32.4
4875	43.4	42.1	229	45.2	6525	21.0	19.0	109	30.8
4925	45.7	45.8	248	47.9	6575	20.1	17.6	103	30.3
4975	46.0	47.0	249	47.5	6625	21.4	19.2	103	31.7
5025	45.0	46.1	244	47.9	6675	22.8	18.8	104	31.4

For six stars spectral observations was execute in region from 3400A to 6300A. For them, the energy distribution curves in the area of 6300A-6650A were extrapolated. In Table 2, these values are marked with an asterisk. Extrapolation is done for several reasons. First, extrapolated data can be used for standardization. Second, they allow comparisons of V and B-V energy calculated from energy distribution with directly observed photometric data. Extrapolation in this area is quite confident, as the course of curves of normal energy distribution here for stars of close spectral classes and interstellar absorption varies slightly. At extrapolation was use normal energy distributions obtained in the works [5, 6]. And, finally, in order to represent data of table 2 in identical form for all stars.

Comparison with photometrical data. Spectral energy distribution for the studied stars was obtained for the first time. Roughly assess the reliability of the received data can be indirectly - by comparing the observed stellar magnitudes with the magnitudes calculated from energy distributions. The resulting discrepancies will to some extent characterize the reliability of our results. This method has been used by us quite often and are detail described, in particular, in the work [2]. Therefore here we let us remind only that the calculations used the reaction curves of the photometric bands received by V.Straizys [7] and the necessary constants were defined on the star Vega. Differences between the calculated from the spectral energy distribution and the directly observed V magnitudes V and color- indexes B-V are represented in Table 3 and on figures 1,2. Only two stars have big discrepancies in the band V : HD162628 и BD+02 4661. The reason of these discrepancies we not know.

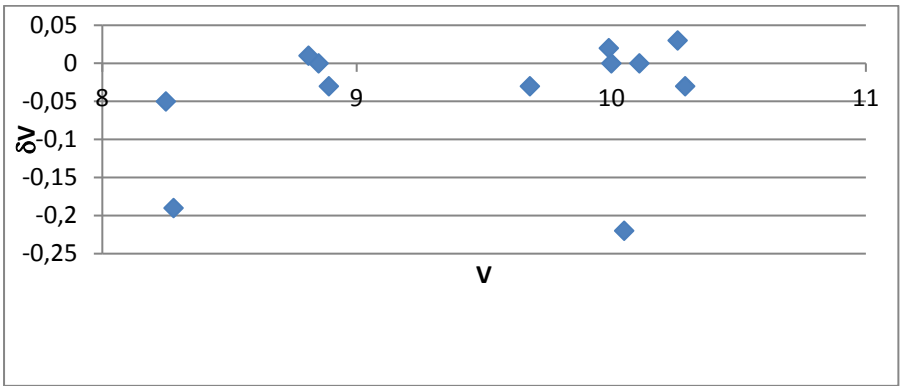

Figure 1 - Dependence of discrepancies δV from stellar magnitude V

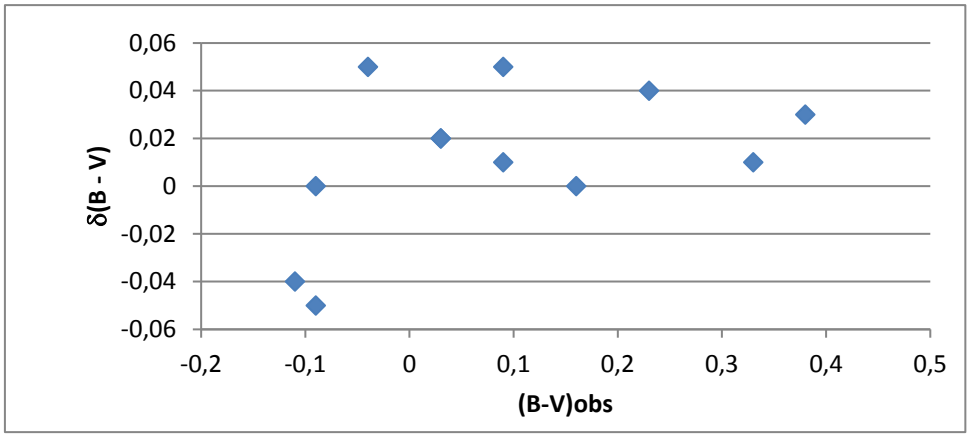

Figure 2 - Dependence of discrepancies δ(B - V) from color-index (B - V)

Table 3 - Comparison with the observed photometric data

No.	HD or BD	n	Vobs	Vcal	δV	(B-V)obs	(B-V)cal	δ(B-V)
1	BD+01 2668	8	10.29	10.26	-0.03	-0.09	-0.09	0.00
2	BD+02 2711	5	10.26	10.29	0.03	-0.11	-0.15	-0.04
3	BD+02 2790	3	10.11	10.11	0.00	0.03	0.05	0.02
4	HD136161	4	8.89	8.86	-0.03	0.33	0.34	0.01
5	HD151355	7	8.85	8.85	0.00	-0.09	-0.14	-0.05
6	HD162628	3	8.28	8.09	-0.19*	0.16	0.16	0.00
7	HD174648	5	8.81	8.82	0.01	0.09	0.10	0.01
8	HD185296	5	9.68	9.65	-0.03	0.23	0.27	0.04
9	BD -03 4950	5	10.00	10.00	0.00	0.09	0.14	0.05
10	BD+01 4436	4	9.99	10.01	0.02	0.03	0.06	0.02
11	HD215112	4	8.25	8.20	-0.05	-0.04	0.01	0.05
12	BD+02 4661	6	10.05	9.83	-0.22*	0.38	0.41	0.03

n - number of observations
*- stars with the big discrepancies δV

For three stars, we compared the observed energy distributions in their spectrums with the distributions that are calculated from photometric data. The method of calculating the distribution of energy in spectra of stars (absolutization) is set out in works [8, 9]. It can be used in the absence of data on energy distribution in spectra of stars selected as standards. According to figures 3-5, there are significant

differences between observed and calculated energy distributions for the same stars, especially in the ultraviolet region. Discrepancies there are not only in the values themselves, but also in the course of distribution curves. These are primarily due to the significant difference in the course of normal energy distribution curves in the ultraviolet region for the stars of the early spectral classes. In addition, in this region it is more difficult into account interstellar absorption.

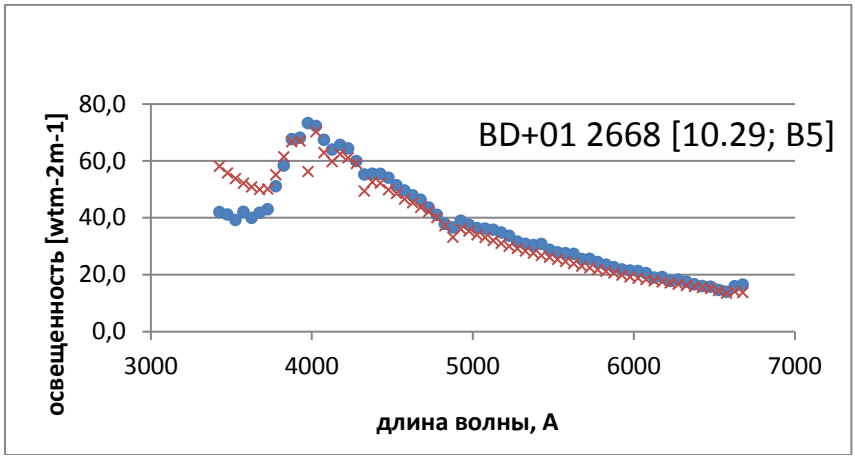

Figure 3 - Energy distribution in spectra BD +01 2668. • - observed, × - computed

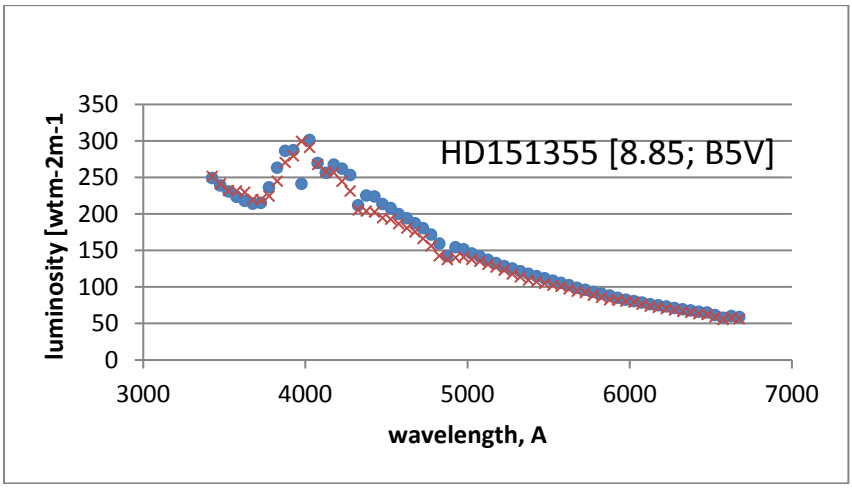

Figure 4 - Energy distribution in spectra HD151355. • - observed, × - computed

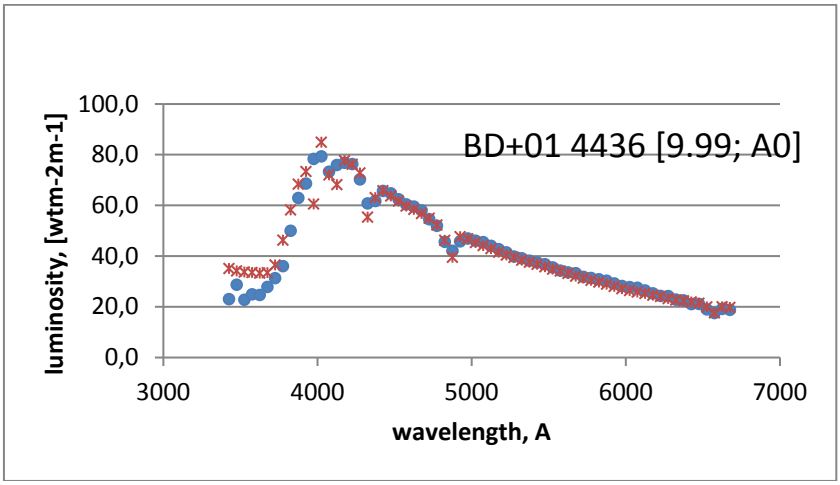

Figure 5 - Energy distribution in spectra BD +01 4436. • - observed, × - computed

In conclusion we let's make a critical remark concerning of task of the creation spectrophotometrical standards. It would seem that due to the mass introduction into astronomy of CCD cameras, allowing to

automate both the process of observations and their processing, the task of creating spectrophotometric standards should be solved much faster. However currently a works on their creation are very small. There are several reasons. One of them is the unpopularity of this kind of investigations which certainly does not promises any discoveries. At the same time, they require a lot of time, good photometric nights, strict adherence to the methodology, stable operation of the equipment. Therefore, despite their importance, they are unattractive even among astronomers, especially the young. Of course, in the end, such a network of spectrophotometric standards will be created with the help of space telescopes. However, no such mission has been planned so far. And, apparently, it will have to wait a long time.

I express my sincere gratitude to T. Bobryashova for her great help in carry out observations and processing them.

The work was supported by the funding program BR05236322 of the Ministry of Education and Science of the Republic of Kazakhstan and program "Development of space monitoring technologies and forecasting of natural resources, man-made changes in the environment, creation of space technology and ground space infrastructure, exploration of objects of near and near space" (No. 05336383).

В. М. Терещенко

«В. Г. Фесенков атындағы Астрофизика институты» ЕЖШС, Алматы, Қазақстан

8^m- 10^m СПЕКТРОФОТОМЕТРЛІК СТАНДАРТТАР III. 12^h ден 24^h ЭКВАТОРЛЫҚ АЙМАҚ

Аннотация. Бұл жоспарланған кезекті жұмыстың үшінші мақаласы, спектрофотометрлік аралық жарқырау стандарттарын құруға арналған. 8^m-10^m жұлдыздық шамадағы 12 B-A жұлдыздар үшін көзге көрінерлік аймақтағы спектрлеріндегі абсолютті энергияның таралуы көрсетілген. Зерттелген жұлдыздар 12^h ден 24^h аралықтағы тура шарықтауда аспан экваторына көлбеу ($\delta = \pm 3^\circ$) орналасқан. Екінші жұмыстағы жұлдыздармен бірге олар аралық жарқыраудың экваторлық стандарттар жүйесін құрайды. Спектрдің көрінерлік аймақтағы 8^m-10^m жұлдыздық шамадағы спектрофотометрлік стандарттардың жалпы саны екі жұмыстың арқасында екі есеге өсті. Энергияның таралуы 340нм–660 нм аймағында зерттелді, алынған мәліметтердің спектрлік ажыратылымдылығы 5нм, ал алынған мәліметтердің салыстырмалы орташа квадраттық қателігі 2-ден 5% -ға дейін. ЗБА-камерасымен жабдықталған дифракциялық спектрографтың көмегімен АЗТ-8 және Цейсс-600 телескоптарында бақылаулар орындалды. Аппаратура, бақылау әдісі, редукциялау және есептеулер алғашқы кезеңді екі жұмыста толық келтірілген. Зерттелген жұлдыздардың нәтижелері тікелей бақылаулардың және есептелген жұлдыздық шамаларды салыстыру арқылы дұрыстығы алдыңғы жұмыстардағыдай дәлелденді. Сонымен қатар, бірнеше жұлдыздар үшін спектрлеріндегі энергияның таралуы фотометрлік мәліметтер бойынша есептелді. Спектрлік класындағы жұлдыздар үшін ультракүлгін аймақтағы бақылау және есептеу шамаларының айырмашылығы 20-30% дейін жетуі мүмкін. Олар жақын спектрлік кіші кластардың ыстық жұлдыздардағы энергияның қалыпты таралуы қисықтарының үлкен айырмашылықтары мен спектрлік жіктеудегі қателіктерге байланысты. Мақаланың қорытынды бөлімінде стандарттар құру бойынша жұмыстың маңыздылығы мен өзекті еместігі туралы мәселе көтерілген.

Түйін сөздер: спектрофотометрлік стандарттар, экваториалық аймақ, спектрограф, жұлдыздар.

В. М. Терещенко

ДТОО «Астрофизический Институт им Фесенкова», Алматы, Казахстан

СПЕКТРОФОТОМЕТРИЧЕСКИЕ СТАНДАРТЫ 8^m-10^m . III. ЭКВАТОРИАЛЬНАЯ ЗОНА ОТ 12^h до 24^h.

Аннотация. Данная статья является третьей из серии работ, посвященных созданию спектрофотометрических стандартов промежуточного блеска. В ней представлено абсолютное распределение энергии в видимой области спектра для 12 B-A-звезд 8^m-10^m. Исследованные звезды расположены равномерно вдоль небесного экватора ($\delta = \pm 3^\circ$) в интервале прямых восхождений от 12^h до 24^h. Совместно со звездами из

второй работы данной серии они образуют систему экваториальных стандартов промежуточного блеска. Благодаря этим двум работам, общее число спектрофотометрических стандартов 8^m-10^m в видимой области спектра увеличилось более чем вдвое. Распределение энергии исследовано в интервале 340нм - 660нм, спектральное разрешение составляет 5нм, относительная с.к.о. полученных данных в среднем составляет от 2 до 5%, возрастая на краях исследуемого интервала до 7-8%. Наблюдения выполнены на телескопах АЗТ-8 и Цейсс-600 с помощью спектрографа с тороидальной дифракционной решеткой. Приемником излучения служила ПЗС-камера ATIC-490EX. Подробно аппаратура, методы наблюдений, редукций и вычислений описаны в первых двух работах этого цикла. Как и в более ранних работах, достоверность полученных результатов оценена путем сравнения вычисленных и непосредственно наблюдаемых звездных величин исследованных звезд. Кроме того, для нескольких звезд распределение энергии в их спектрах было также вычислено по фотометрическим данным. Различия в ультрафиолетовой области для звезд спектрального класса В между наблюдаемыми и вычисленными значениями могут достигать 20-30%. Они обусловлены большими различиями в ходе кривых нормального распределения энергии в звездах близких спектральных подклассов и ошибками в спектральной классификации. В заключительной части статьи затронут вопрос о важности и, одновременно, непрестижности работ по созданию стандартов.

Ключевые слова: спектрофотометрические стандарты, экваториальные зоны, спектрограф, звезды.

Information about author:
Tereschenko V. M., Candidate of Physical and Mathematical Sciences, Fesenkov Astrophysical Institute; volter2307@mail.ru, https://orcid.org/0000-0001-8021-0347

REFERENCES

[1] Tereschenko V. M. (2018) Spectrophotometric standards 8^m - 10^m. I. Equipment, methods and first results. *News of the NAS RK, phys.-math. ser. Vol .4 (320).* P. 42 - 47.

[2]. Tereschenko V. M. (2020) Spectrophotometric standards 8^m - 10^m. II.The equatorial zone from 0^h to 12^h. *News of the NAS RK, phys.-math. ser. Vol .3 (331).* Present Volum.

[3] Tereschenko V. M., Shamro A.V. (2017) Spektrograf dlay absoluytnych izmereniy. Skhema i konsrtuktsiay optiko-mekhanicheskogo bloka (in Russ.) [Spectrograph for Absolute Measurements. Plan and Construction of Optic-Mechanic Block*]. News of the NAS RK - phys.-math. ser. Vol.5 (315*) . P. 152 - 159.

[4] Kharitonov A.V., Tereschenko V. M., Knyazeva L. N. (2011) Spektrofotometrichesky katalog zvezd [Spectrophotometric catalogue of stars]. Алматы. «Казак Университеті». 304 P. ISBN 9965-29-626-X

[5] Knyazeva L.N., Kharitonov A. V. (1995) On the Normal Energy Distribution in Stellar Spectra: Main-Sequence B Stars. Astronomy Reports, vol. 40, No. 6. Pp. 823-828.

[6] Knyazeva L.N., Kharitonov A. V. (1993) K voprosu o normalnom raspredelenii energii v spectrakh zvezd. Zvezdy A0-A2 glavnoy posledovatelnosti [On the Normal Energy Distribution in Stellar Spectra: Main-Sequence A0-A2 Stars. Astron. Zhurn., vol. 40, No. 6. Pp. 823-828.

[7] Straizys V. (1977), Mnogotsvetnaya fotometriya zvezd [Multicolor stellar photometry], Vilnius, Mokslas, 312p.

[8] Zasov A/V, Postnov K.A. (2006) Obschaya astrofizika [General Astrophysics]. Fryazino, Vek2. 496 P. ISBN-5-85099-169-7

[9] Tereschenko V. M. (2017) Абсолютизация спектрального распределения энергии по фотометрическим данным. [The Absolutization of spectral energy distribution of stars on spectral and photometric data]. *News of the NAS RK, phys.-math. ser. Vol. 4 (314).* P. 136-142.

NEWS
OF THENATIONAL ACADEMY OF SCIENCES OF THE REPUBLIC OF KAZAKHSTAN
PHYSICO-MATHEMATICAL SERIES
ISSN 1991-346X **https://doi.org/10.32014/2020.2518-1726.43**
Volume 3, Number 331 (2020), 108 – 117

iD D-3717-2019
UDK 550.388.2; 550.380:523.985.3; 523.9-739
IRSTI 37.15.23; 37.15.21; 37.15.29

N.M. Salikhov, G.D. Pak

Institute Ionosphere, Almaty, Kazakhstan.
E-mail: N1_NazyF@mail.ru; gpak1@yandex.ru

IONOSPHERIC EFFECTS OF SOLAR FLARES AND EARTHQUAKE ACCORDING TO DOPPLER FREQUENCY SHIFT ON AN INCLINED RADIO PATH

Abstract. The effects in the ionosphere and the fine structure of ionospheric response to the action of X-ray and ultraviolet radiation of C1.7 - M5.2 classes flares occurred during solar cycle 24 (2014–2016) have been studied. The study was carry out using method of Doppler sounding of the ionosphere on an inclined radio path with a high time resolution (sampling frequency 25 Hz), which is based on the principle of the phase locked loop (PLL). It was shown that the intensity of C3.0-class solar flares is a minimum threshold when the appearance of disturbances in the ionosphere could be detected by the Doppler frequency shift (DFS) method. Solar flares less than C3.0-class were not reflected in Doppler frequency variations. The most expressed ionospheric response, recorded in the Doppler frequencies, occurred to X-ray flares with a sharp onset, flares with a smooth increase intensity gave a much less response. An unusual effect of the appearance of high-frequency component in Doppler frequency records in the interference beat form has been detected, indicating the occurrence of ionized heterogeneities in the ionosphere during solar flares. The appearance of high frequency component on the Doppler frequency shift records was also registered during the M5.1 earthquake. The application of Doppler frequency shift method that use the PLL loop has greatly expanded the ability to record and analyze the mechanisms of appearance the ionospheric disturbances during solar flares and earthquakes.

Key words: Doppler frequency shift, ionosphere, solar flares, earthquake**.**

1. Introduction. Solar flares are manifested themselves by bursts of radiation flux in all ranges of the electromagnetic spectrum from radio waves to X-rays and is the pulse energy source causing short-term disturbances in the ionosphere. The main disturbance effect on the ionosphere in solar flares is X-ray and extreme ultraviolet radiation (EUV). The X-ray flux emitted during the flare can increase by several orders. The X-ray and EUV bursts lead to a marked increase in the electron concentration in the ionosphere, depending on the spectral distribution of energy, which eventually, is shown in variations of Doppler frequency at the respective frequencies in the region of radio wave reflection. Various methods and instruments are used to investigate ionospheric disturbances, including vertical sounding ionosondes, incoherent scatter radars, transionospheric sounding by GPS navigation satellite signals, etc. The most effective of the well-known ionosphere methods is Doppler shift sounding. This study uses the method of Doppler measurements developed at the Ionosphere Institute [1], which is based on the principle of the phase-locked loop (PLL). This method was used for remotely detect disturbances in the ionosphere during industrial and underground nuclear explosions [1-4], for registration of ionospheric signatures to launch vehicles [5] and study of lithospheric-atmospheric-ionospheric coupling in earthquakes [4]. The advantage of this method is high time resolution, high accuracy of Doppler frequency measurements under multipath

signal conditions, possibility to organize round-the-clock continuous observations, which allows to detect short-term processes in the ionosphere with high time and frequency resolution [6-8]. The purpose of the study was to investigate the characteristics of ionospheric response to solar flares of different classes according to the data on Doppler sounding of ionosphere.

2. Methology. Continuous Doppler sounding of the ionosphere was performed during 38 solar flares that occurred during the period 2014-2016 of 24-th solar cycle. Doppler measurements of signals reflected from the ionosphere were carried out on a different inclined radio path (sampling frequency 25 Hz), using signals from radio transmitters located in China, Kyrgyzstan and Kuwait. Information about solar flares was obtained from the site (www.tesis.lebedev.ru). The intensity of X-ray flux in the energy range 0.5-10 keV (wavelength 0.5-8 Å) was analyzed according to the data of satellite GOES-13 (ftp:/ft/ftp.swpc.noaa.gov/pub); radio flux density at 27.8 cm (F27.8) and 10.7 cm (F10.7) - according to the Callisto solar radio spectrograph data (www.ionos.kz), which located on Radiopoligon Orbita; extreme solar ultraviolet (0.1-7 nm) - according to the data of extreme ultraviolet spectrophotometer ESP_QUAD of the NASA Solar Dynamics Observatory (SDO) satellite (http:/p.color.edu/eve/data). Extreme ultraviolet has the greatest effect on the F2 region of the ionosphere [9] and the lower layer of the ionosphere (D-region) is most affected by X-ray radiation. Ionospheric regions from altitudes of 110 km to 200 km respond to ionizing X-ray as well as ultraviolet radiation. The paper highlights the most characteristic Doppler frequency shift (DFH) records of X-ray solar flares. The work presents the most characteristic Doppler Frequency Shift (DSH) records during X-ray solar flares.

3. Results. Doppler measurements during the C3.0-class flare of May 12, 2015 were carried out on an inclined radio path between points Urumqi, China (44.133N 86.883E) - Radiopoligon Orbita, Kazakhstan (43.058N 76. 973E). A radio transmitter with a capacity of 100 kW (f=5960 kHz) of a radio broadcasting station located in Urumcius was used. The radio receiver of the Doppler measurements was located in Radiopoligon Orbita. A transmitter with a power of 100 kW (f = 5960 kHz) of a radio broadcasting station located in Urumqi (China) and a radio receiver located on the Radiopoligon Orbita (Kazakhstan), were used. The distance (D) between the radio transmitter and the radio receiver is 808.55 km. To determine the radio wave reflection height between Urumqi - Radiopoligon Orbita, an ionospheric electron concentration profile was used, which was calculated using a model IRI-2012 (figure 1). The reflection height of the radio wave for the common component, calculated taking into account the electron concentration profile and the data of model IGRF12, was 179.712 km. (Figure 1a).

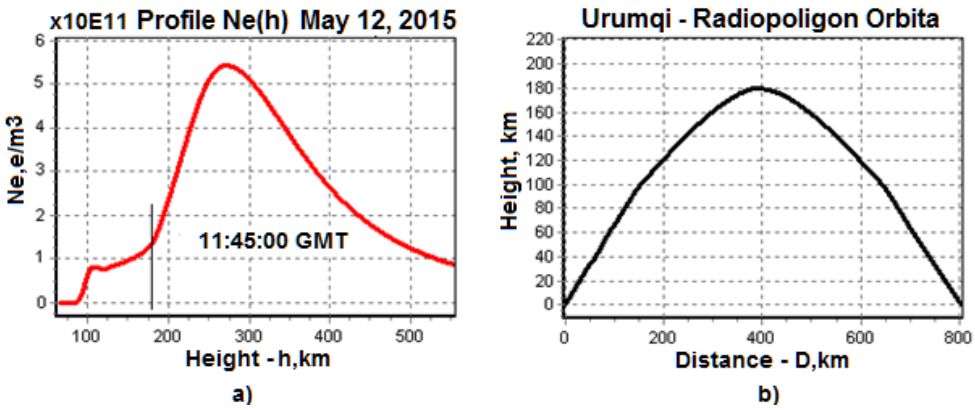

Figure 1 – Profile of electron concentration for time 11:45:00 (GMT) calculated according to model IRI-2012 (a) and trajectory of radio path of signal transmission (f = 5960 kHz) from Urumchi to Radiopoligon Orbita (b). The vertical line indicates a point on the curve where the ionosphere electron concentration corresponds to the reflection point of radio wave at height of 179.712 km, F1-region of ionosphere

Increase the intensity of X-ray and ultraviolet radiation lead to an increase the electron concentration in the ionosphere during the flare. It's the rate of change in electron concentration that is being leaded the response Doppler shift during the flare. Figure 2 show graphs of X-ray, extreme ultraviolet and radio (right Y-axis), and Doppler frequency shift of ionospheric signal (left Y-axis) during the solar flare. The obtained data demonstrate the obvious relationship of Doppler frequency shift with dynamic of basic

indicators of solar activity during C3.0-class flare. The graph shows that the maximum amplitude of Doppler shift (reflection height 179.7 km) corresponds to the initial step of increasing the rate of the ionizing EUV and X-ray flow. And as ultraviolet and X-ray intensity maximizes, Doppler frequency shift variations return to the background level. In contrast to X-ray and EUV, changes of radio flux (F10,7 and F27,8) during flare were more short-lived with the expressed exit to a maximum, just as in the Doppler shift.

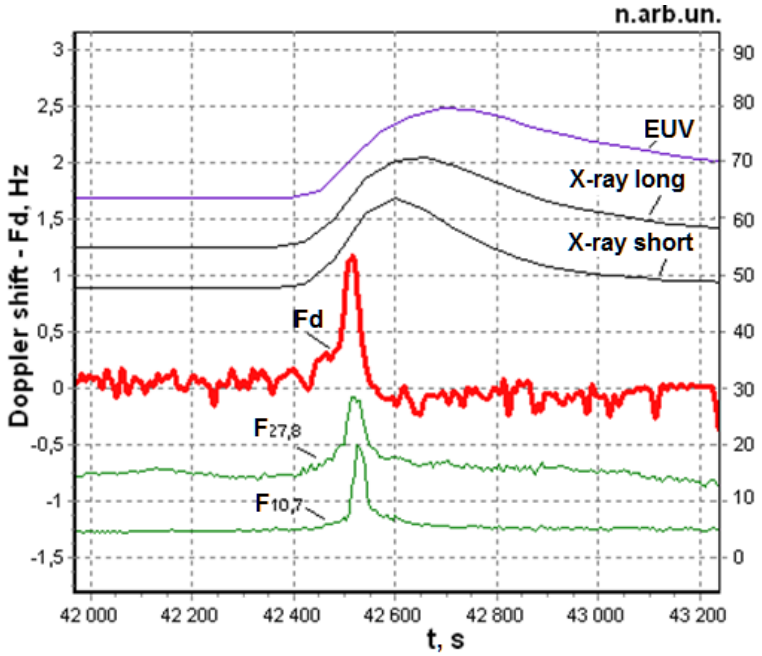

Figure 2 – Ionosphere response to C3.0-class flare in variations of Doppler frequency shift (Fd) on an inclined radio path Urumqi - Radiopoligon Orbita (left Y-axis) and EUV (right Y-axis); X-ray long (0.1 - 0.8 nm) and X-ray short (0.05 - 0.4 nm) and solar radiation flux density $F_{10,7}$ and $F_{27,8}$ (right Y-axis). X-axis – time in seconds from the beginning of the day May 12, 2015

The pulse effect of flare electromagnetic energy on the ionosphere allows determining inertia-time constant of the ionosphere at specific heights. The concept of inertia-time constant of ionosphere was first implemented by E.V. Appleton in 1953 [10]. A comparison the time of exit on a maximum of X-ray and EUV relative to the onset ionospheric response to the solar flare by Doppler data is presented in table 2.

Table 2 – Time of an exit to a maximum of Doppler frequency shift, intensity X-ray and EUV radiation from the beginning of ionospheric reaction to the solar flares

Doppler frequency shift Fd	X-ray short 0,05 - 0,4 nm	X-ray long 0,1 - 0,8 nm	EUV 0,1 - 7 nm
84s	166s	224s	277s

During the C3.0-class solar flare, which occurred on May 12, 2015, the ionosphere time constant for the height of 179 km, determined by the Doppler method, was 84 seconds, which is much in line with D. M. Baker, K. Davies calculations [11]. Analysis of the data (table 2) and the graphs (figure 2) showed that X-ray reached the maximum intensity more rapidly, than the output to the maximum of ultraviolet radiation. While the time of peak response in the Doppler shift was significantly less. Given that the Doppler shift changes proportional to the rate change of total electron content [9], it can be assumed that mainly X-ray short determines the ionospheric response in F1-region to a flare compared to the EUV, which has a predominant effect on the F2-region [12]. It is noted that the most expressed response of Doppler frequency shift occurs to X-ray flares with sharp start. In contrast, X-ray with a smooth escalating is accompanied by a significantly smaller response in the Doppler frequency shift.

In order to determine threshold sensitivity of Doppler method for detection of disturbances in ionosphere, Doppler frequency shift records were analyzed in case of weak solar flares of different intensity of C1.7-C3.0 class, which occurred sequentially within one day. Table 3 shows the main characteristics of the 4 solar flares on May 12, 2015 (tesis.lebedev.ru).

Table 3 – Characteristics of C1.7-C3.0-classes solar flares that occurred on May 12, 2015

Solar flare class	Active area	Beginning	Maximum	End
		GMT		
C2.6	2339	02:15:00	03:02:00	03:42:00
C2.2	2339	04:27:00	04:32:00	04:37:00
C1.7	2339	10:40:00	10:46:00	10:50:00
C3.0	2339	11:45:00	11:51:00	11:56:00

It has been established that flares of less than C3.0-class did not impinge on the Doppler frequency shift recordings. The ionospheric response was recorded only for C3.0-class flares, the intensity of which may be considered to be a threshold for such ionosphere condition, which is accompanied by Doppler frequency shift.

In order to determine the effects of the solar flares on the upper and lower layers of ionosphere, simultaneous of the Doppler measurements were made on the inclined radio path of Kuwait – Radiopoligon Orbita (f=15090 kHz, D=3007.211 km) and Urumchi – Radiopoligon Orbita (f=7260 kHz, D=808,546 km). The frequencies of the radio transmitters were specifically selected so that the radio wave reflected from the F2-region and the F1-region of ionosphere. The height of reflection of the radio wave was determined by the method described above. The radio frequency f=7260 kHz was reflected from the height 185.650 km. A radio signal from Kuwait came to the reception area in two hops, reflecting from 292 km of F2 region of the ionosphere. According to the GOES-13 and SDO satellite (NASA) data, during the C5.1-class flare on July 07, 2016, there were bursts in the X-ray and ultraviolet fluxes (Figure 3). The response of ionosphere to the flare was recorded on the DFS records at f=15090 kHz (duration of disturbance - 324s, Doppler shift amplitude - 1.302 Hz) and on the DFS records at f=7260 kHz (duration of disturbance - 750s, maximum Doppler shift amplitude reached 2.698 Hz).

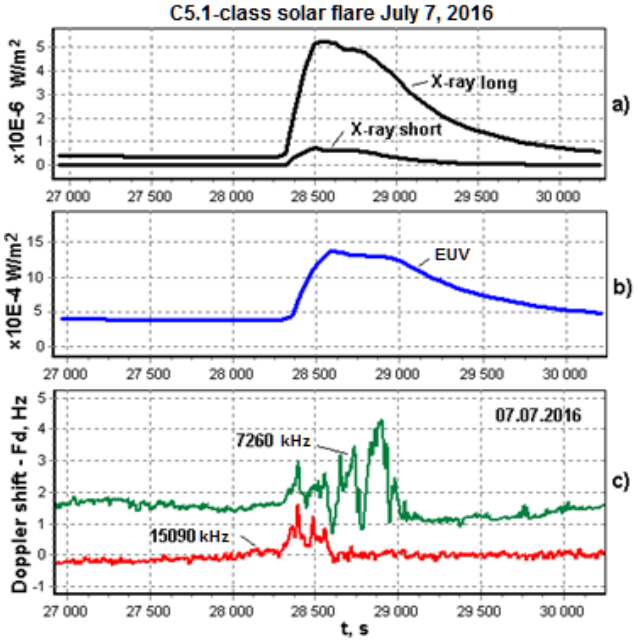

Figure 3 – Ionosphere response to C5.1-class solar flare in variations of Doppler frequency shift:
a) – X-ray long (0.1 - 0.8 nm) and X-ray short (0.05 - 0.4 nm); b) – EUV (0,1 - 7 nm); c) – variations of Doppler frequency shift on an inclined radio path Urumqi - Radiopoligon Orbita (7260 kHz) and Kuwait - Radiopoligon Orbita (15090 kHz).
X-axis – time in seconds from the beginning of day July 7, 2016

Figure 3c shows a significant difference in the duration of DFS perturbations on different radio paths, as well as appearance of a distinct zug with oscillations with periods from 179s to 240s (f=7260 kHz). Comparison of DFS variation records at two different frequencies suggests that the F1-region of the ionosphere is more sensitive to X-ray and ultraviolet radiation than the F2-region. Noted, that there are no periods in X-ray and EUV fluxes that could correlate with periods that had arisen in the zugs of Doppler frequency variations (figure 3). This suggests that the appearance of a clear zug of oscillations in DFS may be due to the passage of acoustic gravity waves (AGW) at the heights of radio wave reflection at a moment of X-ray and ultraviolet effects on the ionosphere.

Analysis of monitoring results of DFS at radio path Urumqi - Radiopoligon Orbita (860 km) and Red River - Radiopoligon Orbita (164 km) revealed the appearance of high-frequency component in the interference beat form on the Doppler records during two solar flares. The characteristics of solar flares are shown in table 3.

Table 3 - Characteristics of solar flares March 9, 2015 and May 8, 2014

Date dd, mm, yy	Solar flare class	Active area	Beginning	Maximum	End
			по времени GMT		
09.03. 2015	C4.0	2297	10:02:00	10:08:00	10:16:00
05,08. 2014	M5.2	2056	10:59:00	10:07:00	10:18:00

Data processing allowed us to identify the appearance a high-frequency component on the DFS records about 2.5 minutes before the main ionospheric response to C4.0-class flare and after it (figure 4a).The calculation of amplitude dynamic spectrum of the high-frequency component revealed Doppler frequencies in the range of 0.66 Hz to 12.5 Hz. (figure 4b).

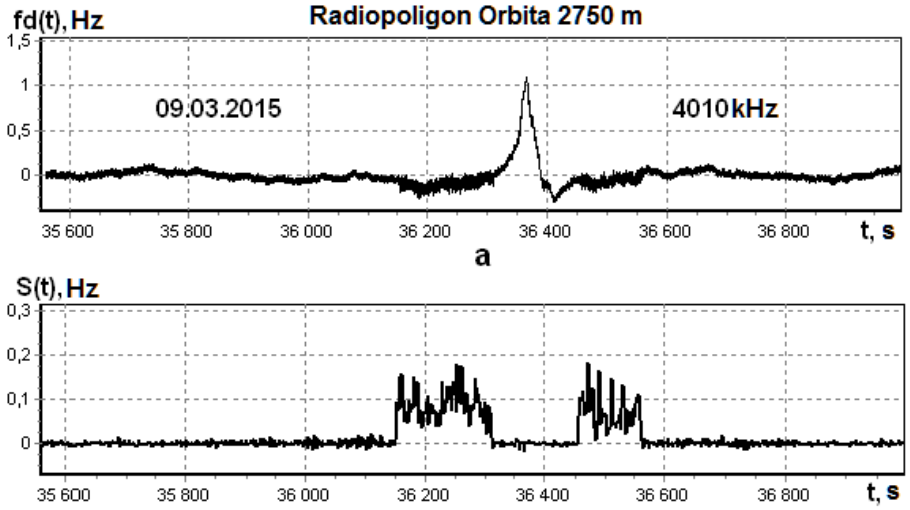

Figure 4 – Ionosphere response to C4.0-class solar flare March 9, 2015: Doppler frequency shift (a) on an inclined radio path Red River – Radiopoligon Orbita and (b) dynamic spectrum of DFS amplitude in the range of 0,66 -12,5 Hz. X-axis – time in seconds past 00 hour (GMT)

The appearance of high frequency component in DFS variations was also recorded during M5.2-class flare August 5, 2014 (figure 5). Comparison of figures 4 and 5 shows the dependence of the expression and duration of these effects on the intensity of the solar flares. In a case of C4.0-class flare the duration of a high frequency disturbance in ionosphere was approximately 400 seconds, DFS amplitude reached 1Hz, and for the M5.2-class flare with perturbation duration of more than 1,000 seconds, the DFS reached magnitude of 3Hz. The appearance of high-frequency variations in DFS during solar flares of the C4.0 and M5.2 classes is quite a rare effect, significantly different from our previous observations, as well as those described in the literature.

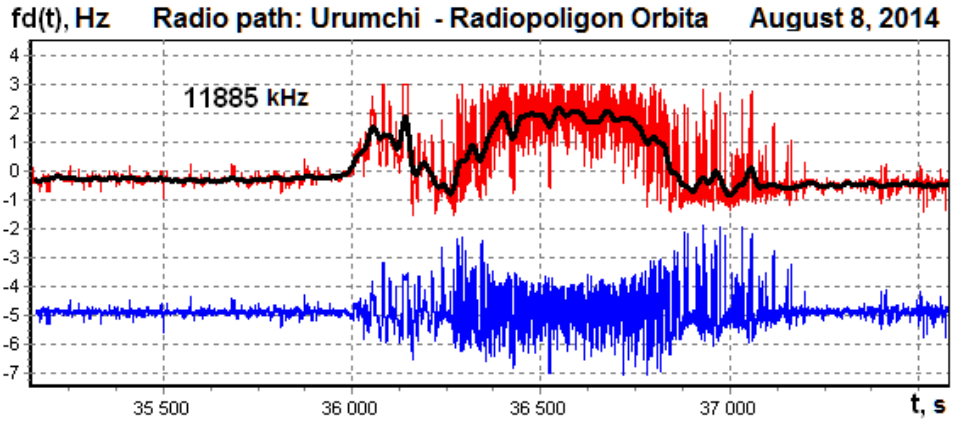

Figure 5 – Ionosphere response to M5.2-class solar flare May 8, 2014 in variations of Doppler frequency shift on Urumchi - Radiopoligon Orbita radio path. The upper graph (red) is variations of DFS and its low frequency component (black line). The lower graph (blue) is a high frequency component in variations of DFS. For ease of analysis, the lower chart is shifted along the Y axis. X-axis – time in seconds past 00 hour (GMT)

The appearance of high frequency variations in Doppler frequencies of ionospheric signal was also recorded during the earthquake. For an example we will consider the results of Doppler frequency shift registration during the earthquake occurred on March 15, 2015 at 14:01:01 by GMT, m_b=5.1 Epicenter coordinates: 42.92N and 76.89E. The earthquake occurred 30 km south from Almaty town and felt in Almaty town with intensity 4 by MSK-64 scale (www.kndc.kz). Figure 6 shows the epicenter location relative to the radio path Red River - Radiopoligon Orbita. Design azimuth in direction from transmitter to receiver was 72,144 °, distance from transmitter to receiver - 204 km. Calculation of the trajectory of radio waves for frequency f=4010 kHz was carried out by the computer program according to the IGRF12 model for the common component taking into account the magnetic field (calculation of radio path was performed by V.M.Krasnov).

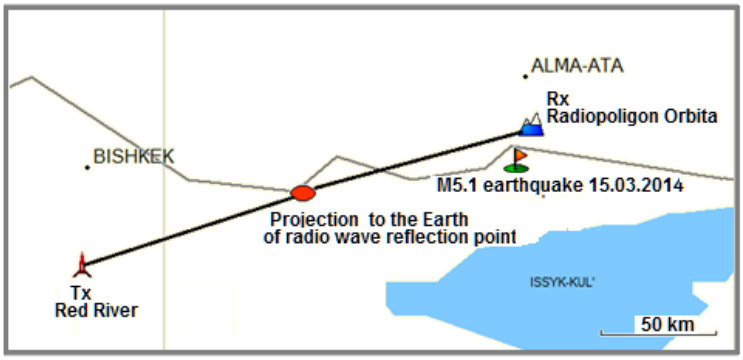

Figure 6 - Layout of radio path Red River (Tx) – Radiopoligon Orbita (Rx) relative to the earthquake epicenter March 15, 2015

The following parameters of the radio track were determined by calculation: height of reflection of radio waves (182.26 km), distance from the reflection point of the transmitter (110.43 km), distance from the epicenter of the earthquake to the projection of the reflection point of radio waves to the Earth (93.7 km), azimuth (262°), distance from the epicenter to Radiopoligon Orbita (16.8 km), azimuth (23.7°), distance from the epicenter to the point of radio waves reflection (84.22 km), azimuth (264 748°). This location of the epicenter relative to the radio path makes it possible to detect disturbances from the different ionospheric layers: from F2-region (estimated height 182.26 km) and the lower ionosphere layers. Analysis of the Doppler measurements showed that 5 minutes after earthquake, high frequency variations appeared on the records of the Doppler frequency shift as the outcome of additional beams arrival, which formed interference beat with a large amplitude beam at the input of Doppler radio receiver

(figure 7a). Calculations demonstrated a marked increase in the Doppler dynamic power spectrum in the range of 5-12 Hz in 4 min 51s after mainshock (figure 7b). Note that this time is quite sufficient to propagate the perturbation from the lithosphere to the heights of the ionosphere.

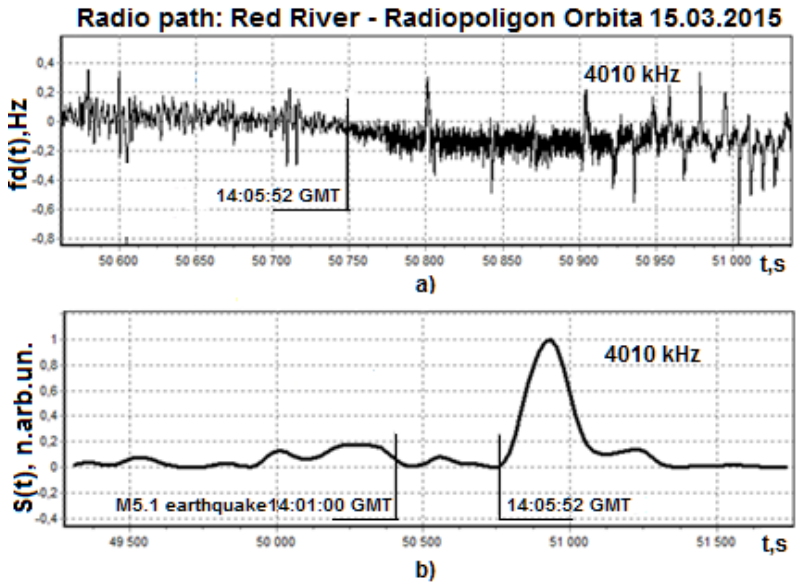

Figure 7 – Ionospheric response to M5.1 earthquake in variations of Doppler frequency shift
a) - high frequency variations of Doppler frequency shift (dark plot section);
b) - dynamic power spectrum of Doppler frequency shift variations (f=5-12 Hz).
X-axis – time from the beginning of the day March 15, 2015

The reflection of smaller-amplitude radio wave appears to have occurred when the radio signal passing above the earthquake epicenter. According to [13], additional ionized layers may be formed in the lower ionosphere at heights of 40-80 km above the earthquake preparation zone, which is in the opinion of by pulling the metal ions from the troposphere into the upper atmosphere by means of an anomalous electric field. There were no disturbances in the Doppler frequency shift associated with the earthquake preparation on March 15, 2015. In particular, this can be explained by the fact that the projection on Earth of the radio wave reflection point was not under the earthquake epicenter, but at a distance of 93.7 km in the north-east direction along the radio path Red River - Radiopoligon Orbita.

4. Resume. The effects in the ionosphere and the fine structure of ionospheric response to the action of X-ray and ultraviolet radiation of C1.7 - M5.2 classes flares occurred during solar cycle 24 (2014–2016) have been studied. The study was carry out using method of Doppler sounding of the ionosphere on an inclined radio path with a high time resolution (sampling frequency 25 Hz), which is based on the principle of the phase locked loop (PLL). It was shown that the intensity of C3.0-class solar flares is a minimum threshold when the appearance of disturbances in the ionosphere could be detected by the Doppler frequency shift (DFS) method. Solar flares less then C3.0-class were not reflected in Doppler frequency variations. The most expressed ionospheric response, recorded in the Doppler frequencies, occurred to X-ray flares with a sharp onset, flares with a smooth increase intensity gave a much less response. Against the background of disturbances in the ionosphere in solar flares, the appearance of zugs was recorded, which are detected during the passage of acoustic-gravitational waves (AGV) in the ionosphere. An unusual effect of the appearance of high-frequency component in Doppler frequency records in the interference beat form has been detected, indicating the occurrence of ionized heterogeneities in the ionosphere during solar flares. The appearance of high frequency component on the DFS records was also registered during the M5.1 earthquake, though the mechanisms of the occurrence of additional ionized regions in the lower ionosphere in earthquake and solar flares are different. The application of Doppler frequency shift method that use the PLL loop has greatly expanded the ability to record and analyze the mechanisms of appearance the ionospheric disturbances during solar flares and earthquakes.

Н.М.Салихов, Г.Д.Пак

ДТОО «Ионосфера институты» АҚ НЦКИТ, Алматы, Қазақстан

КӨЛБЕУ РАДИОТРАССАДА ЖИІЛІКТІҢ ДОПЛЕРЛІК ЖЫЛЖУ ДЕРЕКТЕРІ БОЙЫНША КҮН ЖАРҚЫЛДАРЫ МЕН ЖЕР СІЛКІНІСТЕРІНІҢ ИОНОСФЕРАЛЫҚ ӘСЕРЛЕРІ

Аннотация. Ионосферадағы әсерлесілер және Күн белсенділігінің 24 циклі (2014-2016 жж.) ішінде болған С1.7 - М5.2 класты күн тұтану кезінде рентген және ультракүлгін сәулеленудің әсерінен жұқа құрылымыды тербелістер зерттелді. Жұмыста Ионосфера институтында әзірленген доплерлік өлшеу әдісі қолданылды, оның негізінде жиілікті фазалық автоподстройкасының ілгегіні (ЖФАР) ң жұмыс принципі жатыр. Бұл әдіс өнеркәсіптік және жер асты ядролық жарылыстарды жүргізу кезінде ионосферадағы наразылықтарды қашықтықтан анықтау үшін, зымыран тасығыштарды ұшыру кезінде ионосфераның үнін тіркеу үшін және жер сілкінісі кезінде литосфералық-атмосфералық-ионосфералық байланыстарды зерттеу кезінде қолданылды. Әдістің артықшылығы жоғары уақытша рұқсат (25 Гц дискреттеу жиілігі), көп сәулелік сигнал жағдайында доплерлік жиіліктерді өлшеудің жоғары дәлдігі, тәулік бойы үздіксіз бақылауды ұйымдастыру мүмкіндігі болып табылады. Доплерлік өлшеулер Қытай, Қырғызстан және Кувейт орналасқан радиохабар таратқыштарының сигналдарын пайдалана отырып, түрлі көлбеу радиотрассаларда жүргізілді.

Ионосферадағы ауытқуларды анықтау үшін доплерлік әдістің шекті сезімталдығын анықтау мақсатында С1.7-С3.0 класының әр түрлі қарқындылығы әлсіз Күн жарқылы кезінде жиіліктің доплерлік ығысуы жазбаларына талдау жасалды, бір күн ішінде ретімен орын алды. С3.0 класындағы күн жарқылының қарқындылығы ионосферада ауытқулардың пайда болуы жиіліктің доплерлік жылжу әдісімен тіркеуге болатын ең аз шекті болып табылады. Тұтану класына аз-3.0 емес тигізді жазбаларында доплеровского ығысуы жиілікті ионосферного сигнал.

Доплерлік жиіліктің жылжуында тіркелген ионосфераның ең айқын көрінісі күрт басталуы бар күн рентгендік жарқылға айналды, қарқынды баяу өршу айтарлықтай аз үн берді.

Ионосфераның жоғарғы және төменгі қабаттарына күн тұтану әсерінің ерекшеліктерін анықтау үшін Кувейт - орбитаның радиополигоны (f=15090 кГц, D=3007,211 км) және Урумчи - орбитаның радиополигоны (f=7260 кГц, D=808,546 км). Көлбеу радиотрассаларында жиіліктің доплерлік жылжуын бір мезгілде өлшеу жүргізілді. Радиотаратқыштардың жиіліктері радиотолқындар ионосфераның F2 және F1-аймағынан көрінетіндей арнайы таңдалған. Кувейттен (f=15090 кГц) Радиосигнал қабылдау пунктіне ионосфераның 292 км F2 биіктігінен көріне отырып, екі секіру арқылы келді. Әр түрлі радиотрассаларда ЖДЖ қозу ұзақтығындағы елеулі айырмашылық, сондай-ақ f=7260 кГц жиілігінде 179с-тан 240с-қа дейінгі өзгермелі кезеңмен тербелістердің айқын цуг пайда болуы белгіленді.

Рентген және ультракүлгін сәулеленуде доплерлік жиіліктің цугында пайда болған кезеңдер жоқ. Бұл ЖДЖ нұсқаларында тербелістердің нақты цугасының пайда болуы Күн жарқылы рентген және ультракүлгін сәулеленудің ионосферасына әсер ету сәтінде радиотолқынның шағылысу биіктігінде акустико-гравитациялық толқындардың (АГТ) өтуіне байланысты болуы мүмкін. Екі түрлі жиіліктегі доплерлік ауысудың вариация жазбаларын салыстыру F1-ионосфера аймағы F2 аймағына қарағанда рентгендік және ультракүлгін сәулеленудің әсеріне аса сезімтал деп пайымдауға негіз береді.

Интерференциялы соқтығыстар түріндегі доплерлік жиіліктердің уақытша вариацияларының жазбаларында жоғары жиілікті құраушының пайда болуының ерекше әсері анықталды, ол ионосферада күн жарқылдары кезінде иондалған біртектіліктің пайда болуын куәландырады.

С4.0 және М5.2 класстағы күн тұтану кезінде ионосфералық сигналдың жиілігінің доплерлік ығысу вариацияларында жоғары жиілікті құрамдауыштың пайда болуы бұл біздің алдыңғы бақылаулардан, сондай-ақ әдебиетте сипатталған айтарлықтай ерекшеленетін өте сирек әсер. Ионосфералық сигналдың ЖДЖ жазбаларында жоғары жиілікті құраушының пайда болуы, сондай-ақ жер сілкінісі кезінде mb=5.1 магнитудасы тіркелген, бірақ төменгі ионосферада күн жарқылдары және жер сілкінісі кезінде қосымша иондалған облыстардың пайда болу механизмдері әртүрлі екенің көрсетеді

ЖФАР ілмегін пайдалана отырып, жиіліктің допплерлік жылжуын тіркеу әдісін қолдану, күн жарқылдары және жер сілкінісі кезінде ионосферада ұйытқулардың пайда болу механизмдерін талдау мүмкіндігін едәуір кеңейтеді.

Түйін сөздер: доплерлік жиілік ығысуы, ионосфера, күн жарқылдары, жер сілкінісі.

Н.М.Салихов, Г.Д.Пак

ДТОО «Институт ионосферы» АО НЦКИТ, Алматы, Казахстан

ИОНОСФЕРНЫЕ ЭФФЕКТЫ СОЛНЕЧНЫХ ВСПЫШЕК И ЗЕМЛЕТРЯСЕНИЙ ПО ДАННЫМ ДОПЛЕРОВСКОГО СДВИГА ЧАСТОТЫ НА НАКЛОННОЙ РАДИОТРАССЕ

Аннотация. Исследованы эффекты в ионосфере и тонкая структура отклика ионосферы на воздействие рентгеновского и ультрафиолетового излучений во время солнечных вспышек класса C1.7 - M5.2, произошедших за период 2014–2016 гг. в течение 24 цикла солнечной активности. В работе использовали метод доплеровских измерений, разработанный в Институте ионосферы, в основе которого лежит принцип работы петли фазовой автоподстройки частоты (ФАПЧ). Этот метод применялся для дистанционного обнаружения возмущений в ионосфере при проведении промышленных и подземных ядерных взрывов, для регистрации отклика ионосферы при запусках ракетоносителей и при исследовании литосферно-атмосферно-ионосферных связей при землетрясениях. Преимуществом метода является высокое временное разрешение (частота дискретизации 25 Гц), высокая точность измерения доплеровских частот в условиях многолучевого сигнала, возможность организации круглосуточных непрерывных наблюдений. Доплеровские измерения проводили на разных наклонных радиотрассах, используя сигналы радиовещательных передатчиков, находящихся в Китае, Кыргызстане и Кувейте.

С целью определения пороговой чувствительности доплеровского метода для выявления возмущений в ионосфере был выполнен анализ записей доплеровского сдвига частоты при слабых солнечных вспышках разной интенсивности класса C1.7-C3.0, последовательно произошедших в течение одного дня. Показано, что интенсивность солнечных вспышек класса C3.0 является минимальным порогом, когда появление возмущений в ионосфере можно зарегистрировать методом доплеровского сдвига частоты. Вспышки классом меньше C3.0 никак не отразились на записях доплеровского сдвига частоты ионосферного сигнала.

Наиболее выраженный отклик ионосферы, зарегистрированный в доплеровском сдвиге частоты, происходил на солнечные рентгеновские вспышки с резким началом, вспышки с плавным нарастанием интенсивности давали значительно меньший отклик.

Для выяснения особенностей воздействия солнечной вспышки на верхние и нижние слои ионосферы были проведены одновременные измерения доплеровского сдвига частоты на наклонных радиотрассах Кувейт - Радиополигон Орбита (f=15090 кГц, D=3007,211 км) и Урумчи - Радиополигон Орбита (f=7260 кГц, D=808,546 км). Частоты радиопередатчиков были специально выбраны так, чтобы радиоволны отражались от F2 и F1-области ионосферы. Радиочастота f=7260 кГц отражалась от высоты 185,650 км. Радиосигнал из Кувейта (f=15090 кГц) приходил в пункт приема двумя скачками, отражаясь от высоты 292 км F2-области ионосферы. Установлена существенная разница в длительности возмущений ДСЧ на разных радиотрассах, а также появление отчетливого цуга колебаний с изменяющимся периодом от 179с до 240с на частоте f=7260 кГц. Отмечено, что в рентгеновском и ультрафиолетовом излучении отсутствуют периоды, которые возникли в цугах вариаций доплеровской частоты. Это позволяет предположить, что появление четкого цуга колебаний в вариациях ДСЧ может быть связано с прохождением акустико-гравитационных волн (АГВ) на высотах отражения радиоволны в момент воздействия на ионосферу энергии рентгеновского и ультрафиолетового излучений солнечной вспышки. Сравнение записей вариаций доплеровского сдвига частоты на двух разных частотах дает основание полагать, что F1-область ионосферы более чувствительна к воздействию рентгеновского и ультрафиолетового излучения, чем область F2.

Обнаружен необычный эффект появления высокочастотной составляющей на записях временных вариаций доплеровских частот в виде интерференционных биений, который свидетельствует о возникновении ионизированных неоднородностей в ионосфере при солнечных вспышках. Появление высокочастотной составляющей в вариациях доплеровского сдвига частоты ионосферного сигнала во время солнечных вспышек C4.0 и M5.2 класса – это довольно редкий эффект, существенно отличающийся от предыдущих наших наблюдений, а также описанных в литературе. Появление высокочастотной составляющей на записях доплеровского сдвига частоты ионосферного сигнала было зарегистрировано также во время землетрясения магнитудой m_b=5.1, хотя механизмы возникновения дополнительных ионизированных областей в нижней ионосфере при землетрясении и солнечных вспышках различны.

Применение метода доплеровского сдвига частоты на наклонной радиотрассе, в основе которого лежит принцип работы петли ФАПЧ, существенно расширило возможности регистрации и анализа механизмов появления возмущений в ионосфере при солнечных вспышках и землетрясениях.

Ключевые слова: доплеровский сдвиг частоты, ионосфера, солнечные вспышки, землетрясение.

Information about authors:

Salikhov Nazif – Candidate of Physical and Mathematical Sciences, Principal research scientist of the Laboratory of diagnostics and forecasting of geophysical situation, the author of elaborating system of Doppler sounding of the ionosphere. The author made a significant contribution to the investigation of solar-terrestrial and lithospheric-ionospheric coupling. The author approved the final version of the article before submitting it for publication. N1_NazyF@mail.kz, http://orcid.org/0000-0002-6150-0207;

Pak Galina, Candidate of Biological Science, leading researcher of the Laboratory of diagnostics and forecasting of geophysical situation. The author made a significant contribution to the experiment, data acquisition and processing. gpak1@yandex.ru

REFERENCES

[1] Krasnov VM, Zheleznyakov EV, Salikhov NM (1995) Method of remote detection of underground nuclear explosion. Preliminary Patent Number 1743 [Preliminary patent of the Republic of Kazakhstan] [Sposob distancionnogo obnaruzhenija podzemnogo jadernogo vzryva. Nomer predvaritel'nogo patenta 1743 [Predvaritel'nyj patent Respubliki Kazahstan] (in Russian).

[2] Alperovich LS, Afraimovich EL, Vugmeister BO, Gokhberg MB, Drobzhev MI, Erushchenkov AI, . . . Fedorovich GV (1985) Acoustic explosion wave [Akusticheskaja volna vzryva] Izvestia Physics of the Solid Earth 11, 32-42 (in Russ.).

[3] Drobzhev VI, Zheleznyakov EV, Idrisov IK, Kaliev MZ, Kazakov VV, Krasnov VM, … Shingarkin AD (1987) Ionospheric effects of the acoustic wave above the epicenter of an industrial explosion [Ionosfernye projavlenija akusticheskoj volny nad jepicentrom promyshlennogo vzryva] Radiophysics and Quantum Electronics 30:12, 1047-1051 (in Russ.). DOI: 10.1007/BF01035385

[4] Salikhov NM & Pak GD (2018) Experimental study of distribution of perturbations from the lithosphere to ionosphere at the example of underground nuclear explosions and earthquakes [Jeksperimental'noe issledovanie rasprostranenija vozmushhenij ot litosfery do ionosfery na primere podzemnyh jadernyh vzryvov i] NNC RK Bulletin, 2(74), 69-77 (In Russ.). ISSN 1729-7516.

[5] Salikhov NM, Pak GD, Kryakunova ON, Milyutin VI, Mayevskaya VI, Nikolayevskiy NF & Tsepakina IL (2016) Effects of carrier rockets launches from “Baikonur” and “Vostochniy” cosmodromes on the surface atmosphere and ionosphere and its ecological significance [Jeffekty v prizemnoj atmosfere i ionosfere na zapuski raket-nositelej s kosmodroma "Bajkonur" i "Vostochnyj" i ih jekologicheskaja znachimost'] NNC RK Bulletin, 2(66), 135-145 (in Russ.). ISSN 1729-7516.

[6] Krasnov VM, Salikhov NM, Zhumabaev BT (2013) History and prospects of Doppler method of ionosphere research in Kazakhstan. Geodynamics and Solar-Earth Relations [Istorija i perspektivy doplerovskogo metoda issledovanija ionosfery v Kazahstane. Geodinamika i solnechno-zemnye svjazi] Almaty. 214-225 (in Russ.).

[7] Salikhov NM (2016) New method for detecting of ionization flares in ionosphere by a hard- and software complex of Doppler measurements on inclined radio path [Novyj metod registracii dinamiki vspyshek ionizacii v ionosfere apparatno-programmnym kompleksom doplerovskih izmerenij na naklonnoj radiotrasse] News of NAS RK. Series of physico-mathematical 4:308, 27-33 (in Russ.). ISSN 1991-346X.

[8] Salikhov NM & Somsikov VM (2014) The hardware -software complex for registration of Doppler frequency shift of ionosrheric radiosignals above the earthquake epicenter [Apparatno-programmnyj kompleks dlja registracii doplerovskogo sdviga chastoty ionosfernyh radiosignalov nad epicentrami zemletrjasenij] News of NAS RK. Series of physico-mathematical, 4:296, 116-121 (in Russ.).

[9] Davies K (1973) Radio waves in the ionosphere [Radiovolny v ionosfere] Moscow. Mir (in Russian).

[10] Appleton EV (1953) A Note on the "Sluggishness" of the Ionoshere. Journal of Atmospheric and Terrestrial Physics, 3, 282-284 (in Eng.).

[11] Baker DM & Davies K (1966) Solar Flare Effects and Relaxation Time of the Ionosphere. Journal of Geophysical Research, 71, 840 (in Eng.).

[12] Kunicyn VE, Nazarenko MO, Nesterov IA, Padohin AM (2015) Solar flare forcing on ionization of upper atmosphere. Comparative study of several major X-class events of 23rd and 24th solar cycles. Moskow University Physics Bulletin Physics.Astronomy, 70(4), 95-101 (in Eng.). DOI: 10.3103/S0027134915040128

[13] Pulinets SA, Boyarchuk KA, Hega VV and Karelin AV (2002) Conception and model of seismo-ionosphere-magnetosphere coupling. Seismo-Electromagnetics: Lithosphere-Atmosphere-Ionosphere Couplin. Eds. M.Hayakawa and O.A.Molchanov, TERRAPUB, Tokyo, 353-361 (in Eng.).

NEWS
OF THENATIONAL ACADEMY OF SCIENCES OF THE REPUBLIC OF KAZAKHSTAN
PHYSICO-MATHEMATICAL SERIES
ISSN 1991-346X **https://doi.org/10.32014/2020.2518-1726.44**
Volume 3, Number 331 (2020), 118 – 126

УДК: 528.85; 517.958; 551.510.513:629.78
МРНТИ: 89.27-57.29-41

V.F. Grichshenko[1], A.A. Mukushev[2]

[1]SLLP "Ionosphere Institute", Almaty, Kazakhstan;
[2]al-Farabi Kazakh National University, Almaty, Kazakhstan.
E-mail: labreab@mail.ru

CIRCUIT SIMULATION OF SINGLE FAILURES OF MEMORY MODULES OF ON–BOARD ELECTRONICS

Abstract. The main objective of the work is the circuit simulation of single failures of a cell of memory modules under given conditions and parameters of transistors of a memory element during the passage of a single particle.

The ionization current and critical charges are determined, which lead to a single failure and to the inversion of the logical state of the memory module cell.

Application area. The results can be used in the design of microprocessor systems of on-board elecronics of spacecraft.

Keywords: circuit simulation, critical charge, ionization current, on-board equipment.

Relevance of the problem. It is known that during the operation of various spacecraft (SC) as a result of the action of cosmic rays (CR) on-board electronics failures **are ,** which leads to emergency situations, and in some cases to the loss of satellites, for example, «KazSat -1» and «Phobos-Soil».

In various countries (France, Russia, USA, China) in cases where it is necessary to predict the behavior of complex structures in space during long-term space flights, or to identify processes that lead to emergency situations in orbit, when decision-making requires preliminary “playback” Several options for the development of events and their consequences are used to simulate the behavior of systems in real conditions.

Therefore, in this work, we use the method of circuit simulation, which is a highly efficient and relatively low-cost method that allows us to evaluate the complex influences of space factors (SF) on the functional state and failures of on-board electronics.

Status of the issue. Distinguish satellite failures for reasons of occurrence, as well as for their impact on the loss of performance of individual on-board systems.

The reasons for the occurrence include the complex influence of SF, including: radiation exposure to solar (SCR) and galactic (GCR) cosmic rays, particles of the Earth’s radiation belts (RP), solar electromagnetic radiation, magnetospheric plasma, SC intrinsic atmosphere, microgravity, micrometeorites and others SF. In more detail, the radiation effects of outer space on the failures of on-board electronic equipment under microgravity conditions were considered by the authors in [1].

It should be noted that the use of electronic components of increased reliability in the on-board electronic equipment does not eliminate the likelihood of failures due to external factors of space.

Falures in the performance of individual on-board systems can result from design errors, poor preflight testing, deterioration of the mechanical and electrical components of systems, incorrect commands or operations due to errors by operators or ground systems, and other causes that are identified by hardware developers in the analysis of failures.

Classification of failures of electronic on-board equipment. In this work, single failures caused by the influence of CR nuclei will be considered as the most dangerous from the point of view of emergency situations in the control systems of on-board equipment.

The types of failures that are most often observed in ground-based modeling experiments and real conditions:

SEU (single event upset) - single reversible failures in **integrated circuits (ICs)** with regular logic, manifested in the form of loss of information in individual cells;

SEL (single event latchup) - single events ("latch" effect) caused by the inclusion of parasitic thyristor structures when protons or heavy CR nuclei enter the sensitive volume of CMOS ICs;

SEHE (single event hard error) - a single microdose effect associated with local release of energy in the sensitive volume of active IC elements upon the entry of protons or CR nuclei with subsequent "dose" failure of this element (after thermal annealing, a return to the working state is usually observed);

SEFI (single event functional interrupt) - a single effect of functional interruption (most characteristic of functionally complex Large Integrated Circuits (LSIs), such as microprocessors, controllers, etc.);

SEB (single event burnout) - a single burnout effect in powerful MOS transistors associated with the opening of a parasitic bipolar transistor when protons or CR nuclei hit;

SEGR (single event gate rupture) - a single breakdown effect of **a gate dielectric** in MOS structures upon the entry of protons or CR nuclei;

SES (single event snapback) - a single effect **of secondary breakdown** in n-MOS transistors;

SET (single event transient) is a transitional ionization reaction caused by the entry of a proton or CR nuclei into the sensitive region of the IP. The effect can manifest itself in the form of current pulses in the output circuits in analog ICs and in mixed type ICs, and can also lead to distortion of information in high-frequency optical information transmission lines [2].

Earlier, the authors of this work presented the mechanism of occurrence of failures (SEU) in memory modules during the passage of a single CR particle under microgravity conditions [1] and circuit simulation of failures (SEL) as a result of the occurrence of electrostatic discharges [3].

In this work, the circuit simulation of failures (SEU and SEL) was carried out on the storage devices (memory) of the CMOS structure, by the action of the ionization current caused by the passage of the CR ionizing particle. This is facilitated by the characteristics of CMOS structures: ultra-low power consumption in a static state and high noise immunity.

The mechanism of formation of the ionization current. In the general case, the single-fault effect is associated with the ingress of single particles into the active region of the transistor, followed by the formation of an **ionization track** inside the transistors and the generation of electron-hole pairs.

Free carriers of electric charge are created along the track of the ionizing particle. The average energy required to create one electron – hole pair in silicon is 3.6 eV [4].

An example of the formation of an ionization current caused by the radiation effect in an n-channel transistor (nMOS) is shown in Figure 1.

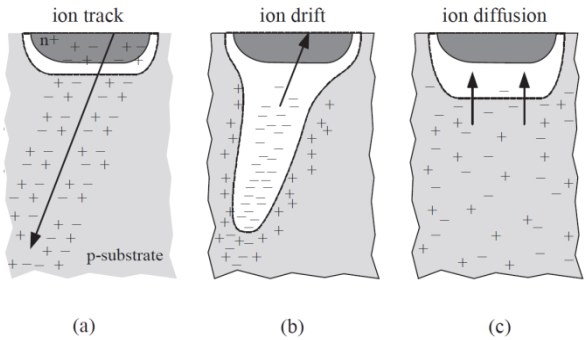

Figure 1 – The mechanism of formation of failure caused by a single CR particle

Figure 1 shows the stages of formation of the ionization current and the time diagram of this current, including:

1a - a charged particle passes near a p-n junction with reverse bias and creates free electron-hole pairs; 1b - electrons pulled up by a positively charged drain field drift toward it, expanding the depletion region and creating an ionization current pulse; 1c - the charge remaining after the end of the pulse continues to deviate into the depletion region until it is collected or recombined.

A single reversible faulures (SEU) in a memory cell occurs when a charged particle collides with a sensitive region of the transistor and causes a change in the state of this cell. In a memory cell, especially in a node storing a high logical level, reverse biases between the drain and the substrate are very sensitive to SEU-type failure caused by ionizing particles. This is due to the fact that the storage node is supported by a relatively weak pull-up transistor (pMOS transistor) compared to a strong step-down transistor (nMOS transistor) on another node [5].

The collection of the charge generated by the influence of the CR particle is shown in figure 1. The collected charge Q_{coll} depends on the type of ionizing particle, trajectory, energy value and location of the impact. The range Q_{coll} is from 1 to hundreds of pC. Usually, the critical charge Q_{coll} for a static memory cell is understood as the minimum charge that can be collected by the affected node to change the logical state of the memory cell Reverse biased nMOS transistors are most sensitive to the effects of CR particles due to the presence of a field and a large space charge region. Thus, Q_{coll} is smaller than the Q_{crit} storage node, then the current generated by the pull-up transistor will prevent the bit from turning over. The value Q_{crit} can be defined as:

$$Q_{crit} = \int_0^{\tau_F} I_D dt = \left(C_{\min} \times V_{dd}\right) + \left(I_{dp} \times T_F\right), \quad (1)$$

where $C_{\min}$ is the minimum capacity of the transistor body, V_{dd} is the voltage of the memory cell, I_{dd} is the maximum drainage conductivity pMOS of the transistor, and T_F is the switching time of the memory cell.

Currently, various models based on the concept of threshold voltage are known. These include Level1-Level3, MOS Model 9, BSIM3, BSIM4. The BSIM4 model is the most reliable and describes all the necessary parameters for mathematical expression 1. A significant difference between compact models is the choice of basic variables, in terms of which physical processes in a transistor are described.

From expression 1 it is seen that the value of the critical charge depends on the circuitry parameters of MOS transistors. Therefore, we used SPICE parameters of a compact circuitry model of a transistor (SPICE - Simulation Program with Integrated Circuit Emphasis) [6].

We have developed geometric models of transistors, presented in figure 2, corresponding to the technological process of 0.5 microns.

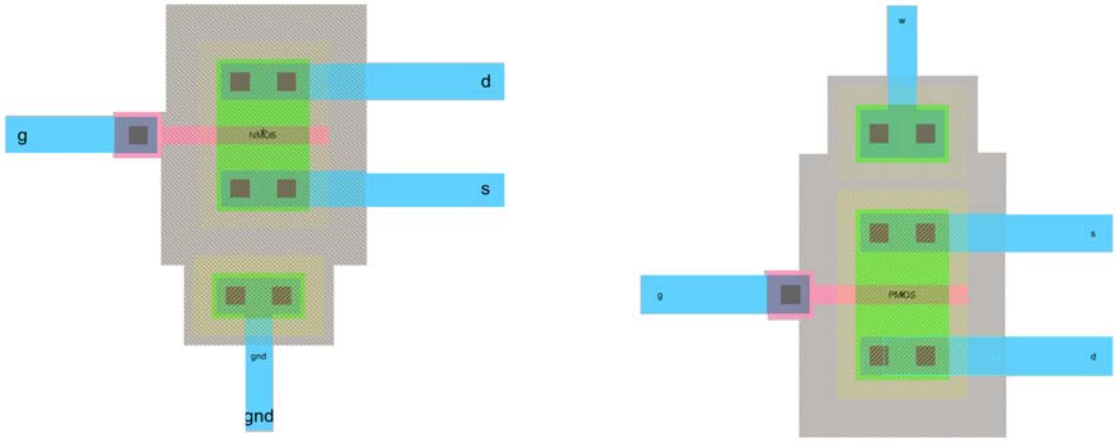

а) б)

Рисунок 2 – Геометрические модели МОП транзисторов

Physico-topological models of nMOS and pMOS transistors have also been developed using the BSIM4 model.

The physico-topological models of nMOS and pMOS transistors shown in Figure 1 were created with the aim of extracting the circuit parameters of MOS transistors. Physico-topological models of MOS

transistors were created using Electric VLSI computer-aided design. This application is used to design ultra-large integrated circuits.

: As a result of the design, a netlist (list of parameters and specifications) of MOS transistors was obtained, a fragment of which is presented below:

*** SPICE deck for cell PMOS_IV{lay} from library tut_2
*** Created on Ср апр 22, 2020 20:00:47
*** Last revised on Ср апр 22, 2020 20:27:49
*** Written on Ср апр 22, 2020 20:29:26 by Electric VLSI Design System, version 9.07
*** Layout tech: mocmos, foundry MOSIS
*** UC SPICE *** , MIN_RESIST 4.0, MIN_CAPAC 0.1FF, MIN_TF 1.2NS
*CMOS/BULK-NWELL (PRELIMINARY PARAMETERS)……

Note that the analytical model for the induced current waveform for collecting charges on ion tracks is usually approximated by a double exponential curve with fast rise and fall times:

$$I_{ioniz}(t) = \frac{Q_0}{\tau_F - \tau_R}\left[e^{(-t/\tau_R)} - e^{(-t/\tau_F)}\right], \quad (2)$$

where Q_0 is the total charge collected from one particle, τ_F is the current decay time associated with the diffusion charge collection time (~ 0.1 ... 0.4 ns), τ_R is the current rise time associated with the carrier drift time through the SCR of the pn junction (~ 10 ... 50 ps). The simulated ionization current pulse is considered in figure 1 with an explanation.

The value of the conduction current I_{dp} at which a single failure will occur can only be estimated by circuitry modeling the effects of single CR cores using a general-purpose electronic circuit simulator SPICE.

The effect of CR nuclei on the sensitive region of a transistor in an SPICE simulator is simulated by the ionization current of a passing particle. To simulate the ionization current, an equivalent circuit was created consisting of a circuit model of a field-effect transistor and a model of a current generator connected in parallel with the p-n junction of the drain. Figure 3 shows the macromodel of the replacement of the ionization current caused by the action of CR nuclei.

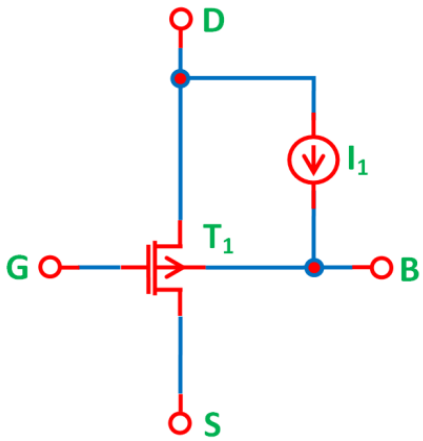

Figure 3 – Macromodel of ionization current substitution caused by exposure to CR nuclei

In the simulation scheme of a single failure in a 6 static memory cell, the stock p-n junctions of closed transistors are vulnerable at the ingress of a single particle.

Figure 4 shows a static memory element (cell).

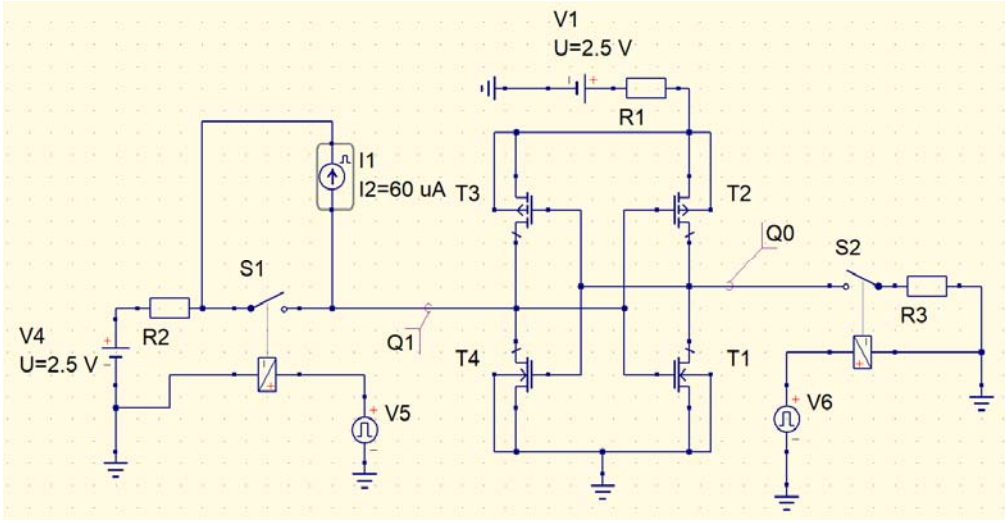

Figure 4 – The memory element of the storage device based on CMOS structures

The main elements of a memory cell are pairs of CMOS transistors (transistors T_1, T_2 and T_3, T_4, respectively), which is a logical inverter, shown in Figure 3. In such an inverter, when transmitting logical signals, one of the transistors is always open and the other is closed. Switches S1 and S2 are used to set the initial conditions for simulation.

Circuit simulation of a single element failure was performed as follows. Suppose, initially, transistors T_4 and T_1 are open in a memory cell, and transistors T_3 and T_2 are closed. The conduction current I_{dp} caused by the passage of the ion is modeled by a current source connected in parallel with the affected transistor in accordance with Figure 2. Then, a surge in the current induced by the ingress of a particle causes two competing processes in the memory cell: absorption of the excess charge and positive feedback operation.

It is also easy to notice that the ionization currents of the drains of open transistors confirm the logical state of the memory cell. Only the ionization currents of the drains of the closed transistors T_3 and T_2 contribute to the switching of the memory cell. In this case, the drain current of a closed-n channel transistor T_2 reduces the voltage at the inputs of transistors T_4 and T_3 , the ionization current of a closed-p channel transistor T_3 reduces the voltage at the inputs of transistors T_1 and T_2 .

In virtual modeling, a memory element was exposed to a current amplitude of up to 36 mA. The simulation results show that the cell is in a stable state, although there are minor bursts, are presented in figure 5a. Since these bursts do not exceed the threshold value, it can be assumed that the memory element provides storage of a bit of information. With an increase in the amplitude of the ionization current over 36 mA, the memory element changes its state, thereby ensuring a single failure to store one bit of information. The obtained time dependence is presented in figure 5b.

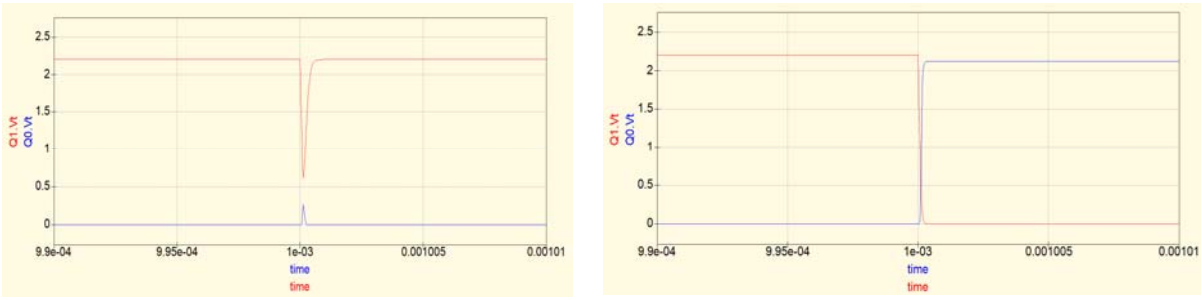

а) б)

Figure 5 - Time dependence on the outputs (Q_0, Q_1) of the memory cell and the effect of the ionization current
a) up to 36 mcA per memory element, b) over 36 mcA per memory element

From the simulation results presented in Figures 5a and 4b, it can be seen that a single CR particle does not always cause a single failure. To do this, it must fall on the sensitive part of the memory cell and also add a charge in excess of the critical value.

The results of evaluating the critical charge at various supply voltages of the memory element obtained by circuit simulation are presented in table 1.

Table 1 – Values of critical charge and conduction current at various supply voltages

	Supply voltage V_{dd} = 2.5 V	Supply voltage V_{dd} = 3.3 V	Supply voltage V_{dd} = 5 V
Conductivity current value I_{dp}, μA calculated in the circuit simulation program	30	80	160
The value of the critical charge Q_{crit}, pC at the corresponding conductivity current I_{dp} μA	36	96	193

From the presented results it is seen that an increase in the supply voltage of the memory element contributes to an increase margin in the critical charge, leading to inversion of the memory cell.

The dependence of the critical charge Q_{crit} on the supply voltage V_{dd} and conduction current I_{dp}, leading to the inversion of the logical state of the memory module cell, is presented in table 1.

Thus, in the work, circuit simulation of a memory module cell failure was performed under given conditions and parameters of the memory element transistors when passing a single particle.

The conductivity current and the voltage value of the memory element at which the cell state switched, that is, a single failure, were determined.

The critical charge value which leads to the inversion of the logical state of the memory module cell is determined.

The work was carried out according to the republican budget program 008 “Applied scientific research in the field of space activity within the framework of the scientific and technical program“ Development of space technologies for monitoring and forecasting of natural resources, technological changes in the environment, creation of space technology and ground space infrastructure, research of near and deep space objects (program code 0.0799 for 2018-2020); under the project “Creation of an integrated system for predicting radiation hazard and methods for protecting onboard electronic equipment for spacecraft of various purposes under the complex influence of space factors” (reg. No. 0118PK00801).

В. Ф. Грищенко[1], А. А. Мукушев[2]

[1]"Ионосфера институты" ЕЖШСД, Алматы, Қазақстан;
[2]Әл-Фараби Қазақ ұлттық университеті, Алматы, Қазақстан

ЭЛЕКТРОНДЫҚ БОРТТЫҚ АППАРАТУРАНЫҢ ЖАДЫ МОДУЛЬДЕРІНІҢ ЖАЛҒЫЗІЛІКТІ ІСТЕН ШЫҒУЛАРЫН СЫЗБА НҰСҚАМЕН МОДЕЛЬДЕУ

Аннотация. Жұмыстың негізгі мақсаты берілген шарттар кезінде әртүрлі мақсаттағы ғарыш аппараттарының (ҒА) борттық электронды аппаратурасының істен шығуларын сызбанұсқалық модельдеу және ғарыш сәулелерінің (ҒС) жалғыз бөлшектерінің өтуі кезінде жады элементінің транзисторларының параметрлері болып табылады.

Мәселе өзектілігі. Ғарыштық сәулелердің (ҒС) әсері нәтижесінде әртүрлі мақсаттағы ҒА пайдалану кезінде борттық электрондық жүйелердің істен шығуы орын алатыны белгілі, бұл штаттан тыс жағдайларға, ал кейбір жағдайларда спутниктердің, мысалы, KazSat-1 және «Фобос-грунт» жоғалуына алып келеді. Сондықтан бұл жұмыста жоғары тиімді және салыстырмалы төмен шығынды әдіс болып табылатын, біреңсараң ғарыш сәулелерінің (ҒС) өту кезінде жады элементінің транзисторларының схемотехникалық параметрлерін бағалауға мүмкіндік беретін схемотехникалық модельдеу әдісі қолданылады.

Мәселенің жағдайы. Істен шығудың пайда болу себептері бойынша, сондай-ақ олардың жекелеген борттық жүйелердің жұмыс істеу қабілеттілігінің жоғалуына әсері бойынша ажыратылады. Пайда болу себептеріне ҒКФ-ның кешенді әсері жатады, оның ішінде: күн (КҒС) және галактикалық (ГҒС) ғарыш сәулелерінің радиациялық әсері, жердің радиациялық белдеулерінің бөлшектері (ЖРБ); микрогравитация, микрометеориттер және басқа да ҒК факторлары. Жекелеген борттық жүйелердің жұмыс істеу

қабілеттілігінің жоғалуына жобалау кезінде қателер, ұшар алдындағы сапасыз тексеру, жүйелердің механикалық және электр компоненттерінің тозуы, операторлардың немесе жер үсті жүйелерінің қателері салдарынан қате командалар немесе операциялар және нақты жағдайларда істен шығуларды талдау кезінде аппаратураны әзірлеушілер сәйкестендіретін басқа да себептер әкелуі мүмкін.

Жұмыста ҒС ядроларының әсерінен туындаған, борттық аппаратураны басқару жүйелерінде штаттан тыс жағдайлардың пайда болуы тұрғысынан неғұрлым қауіпті, оның ішінде: SEU (single event upset) – жеке ұяшықтарда ақпаратты жоғалту түрінде көрінетін тұрақты логикасы бар ИС – да жалғыз қайтымды ақаулар; SEL – (single event latchup) – ҒС өтуі кезінде КМОП ИС сезімтал беттерінде паразиттік тиристорлық құрылымдардің қосуы ("ысырма" әсері) және басқа да істен шығудан туындауы бірең-сараң оқиғаларға алып келеді.

Бұл жұмыста ИС дайындау кезінде басым болып табылатын КМОП-құрылымда жүргізілген есте сақтау құрылғыларына (СҚ) радиациялық әсер ету кезінде істен шығулардының схемотехникалық моделдеудің (SEU және SEL) нәтижелері келтіріледі.

Транзисторлардың ішіндегі ионизациялық трекің және электронды тесіктер жұптарының пайда болуымен транзисторындағы n-каналда (nMOS) сәулелену әсерінен туындаған иондану тогының пайда болу кезеңдері мен механизмі қарастырылады.

Жады элементінің *бірең сараң істен шығуын схемотехникалық модельдеу орындалды*. Сұлбалық параметрлерді бағалау үшін BSIM4 моделін және Electric VLSI автоматтандырылған жобалау жүйесін пайдалана отырып n-МОП және p-МОП транзисторларының физика-топологиялық модельдерін қолдану арқылы транзисторлардың геометриялық үлгісі әзірленді. Бірең сараң істен шығу кезіндегі өткізгіштер тогының мәні, SPICE жалпы мақсаттағы электрондық схемалардың симуляторын пайдалана отырып бағаланды.

Spice-симулятордағы ҒС ядроларының транзисторының сезімтал аймағына әсер етуі ток көзімен байаланыстырады, ол далалық транзистордың схемотехникалық моделінен және p-n ағын өткеліне параллель қосылған ток генераторы моделінен тұратын макромодельдің баламалы схемасында моделденеді. ҒС ядроларының әсерінен туындаған иондау тоғын алмастыру макромоделі құрылды.

Виртуалды моделдеуде берілген параметрлердің жады элементі 36 мкА дейінгі амплитудамен ток әсеріне ұшырайды. Модельдеудің нәтижелері ұяшық тұрақты күйде және шекті мәннен аспайтын елеусіз өзгерістер бар екенін көрсетті, сондықтан жады элементі ақпарат битінің сақталуын қамтамасыз ете алады. Иондау тогының амплитудасы 36 мкА жоғары болғанда жады элементі өзінің жай-күйін өзгертеді, осылайша бір ақпарат битін сақтауда бірең сараң істен шығуды көрсетті.

Әртүрлі қоректену кернеуінде критикалық зарядтың және өткізгіштік тогының мәндері берілген. Жад элементінің қуат кернеуін арттыру жад ұяшығының инверсиясына әкелетін сыни заряд бойынша қордың артуына ықпал ететіні көрсетілген.

Өткізгіштік тогы және ұяшықтың күйін ауыстырып қосу, яғни жалғыз істен шығу болған жады элементінің қуат кернеуінің шамасы анықталды.

Жад модульдері ұяшығының логикалық күйінің инверсиясына әкелетін критикалық зарядтың шамасы анықталды.

Осылайша, жұмыста жеке-дара бөлшектердің өтуі кезінде жады элементінің транзисторларының параметрлері мен берілген шарттар кезінде жад модульдерінің ұяшықтарының істен шығуының схемотехникалық моделдеуі орындалды. Алынған нәтижелер әртүрлі мақсаттағы ҒА борттық электрондық аппаратурасында пайдалану үшін микропроцессорлық жүйелерді жобалау кезінде пайдаланылуы мүмкін.

Түйін сөздер: тізбекті модельдеу, критикалық заряд, иондану тогы, борттық жабдық.

В. Ф. Грищенко[1], А. А. Мукушев[2]

[1]ДТОО "Институт ионосферы", Алматы, Казахстан;
[2]Аль-Фараби Казахский национальный университет, Алматы, Казахстан

СХЕМОТЕХНИЧЕСКОЕ МОДЕЛИРОВАНИЕ ОДИНОЧНЫХ ОТКАЗОВ МОДУЛЕЙ ПАМЯТИ ЭЛЕКТРОННОЙ БОРТОВОЙ АППАРАТУРЫ

Аннотация. Основной целью работы является схемотехническое моделирование отказов бортовой электронной аппаратуры космических аппаратов (КА) различного назначения при заданных условиях и параметров транзисторов элемента памяти при прохождении одиночной частицы космических лучей (КЛ).

Акутальность проблемы. Известно, что во время эксплуатации КА различного назначения в результате воздействия космических лучей (КЛ) происходят отказы бортовых электронных систем, что приводит к

нештатным ситуациям, а в некоторых случаях и к потере спутников, например, KazSat -1 и «Фобос-грунт». Поэтому в данной работе используется метод схемотехнического моделирования, являющийся высокоэффективным и относительно низкозатратным методом, позволяющий оценить схемотехнические параметры транзисторов элемента памяти при прохождении одиночной частицы космических лучей (КЛ).

Состояние вопроса. Различают отказы КА по причинам возникновения, а также по их влиянию на потерю работоспособности отдельных бортовых систем. К причинам возникновения относится комплексное влияние ФКП, в том числе: радиационное воздействие солнечных (СКЛ) и галактических (ГКЛ) космических лучей, частиц радиационных поясов Земли (РПЗ); микрогравитация, микрометеориты и другие факторы КП. К потере работоспособности отдельных бортовых систем могут привести ошибки при проектировании, некачественная предполетная проверка, износ механических и электрических компонентов систем, некорректные команды или операции вследствие ошибок операторов или наземных систем и другие причины, которые идентифицируются разработчиками аппаратуре при анализе отказов в реальных условиях.

В работе рассматриваются одиночные отказы, вызванные воздействием ядер КЛ, как наиболее опасные с точки зрения возникновения нештатных ситуаций в системах управления бортовой аппаратуры, в том числе: SEU (single event upset) – одиночные обратимые сбои в ИС с регулярной логикой, проявляющиеся в виде потери информации в отдельных ячейках; SEL (single event latchup) – одиночные события радиационного защелкивания (эффект «защелки»), вызванные включением паразитных тиристорных структур при КЛ в чувствительный объем КМОП ИС и другие отказы.

В данной работе приводятся результаты схемотехнического моделирования отказов (SEU и SEL) при радиационном воздействии на запоминающие устройства (ЗУ), которое проводилось на КМОП-структуре, являющейся доминирующей при изготовлении ИС.

Рассматриваются этапы и механизм образования тока ионизации, вызванного радиационным эффектом в n-канальном транзисторе (nMOS) с последующим образованием внутри транзисторов ионизационного трека и генерации электронно-дырочных пар.

Выполнено с*хемотехническое моделирование одиночного сбоя* элемента памяти. Для оценки схемотехнических параметров были разработаны: геометрическая модель транзисторов, с использованием модели BSIM4 и физико-топологические модели n-МОП и p-МОП транзисторов с использованием системы автоматизированного проектирования Electric VLSI. Значение тока проводимости, при котором происходит одиночный отказ, оценивался с использованием симулятора электронных схем общего назначения SPICE.

Воздействие на чувствительную область транзистора ядер КЛ в SPICE-симуляторе имитируется источником тока, который моделируется в эквивалентной схеме макромодели, состоящей из схемотехнической модели полевого транзистора и модели генератора тока, включенного параллельно p-n переходу стока. Создана макромодель замещения тока ионизации, вызванного воздействием ядер КЛ.

Представлена схемотехническая SPICE модель элемента памяти на основе КМОП – структур. Показано, что в схеме моделирования одиночного сбоя в статическом элементе памяти, уязвимого к попаданию одиночной частицы, являются стоковые p-n переходы закрытых транзисторов. Рассмотрен механизм образования тока проводимости, вызванного прохождением одиночной частицы КЛ, который моделируется источником тока, подключенного параллельно пораженному транзистору.

В виртуальном моделировании элемент памяти заданных параметров подвергался воздействию тока амплитудой до 36 мкА. Результаты моделирования показали, что ячейка находится в устойчивом состоянии и имеются незначительные всплески, которые не превышают порогового значения, поэтому элемент памяти обеспечивает хранение бита информации. При увеличении амплитуды тока ионизации свыше 36 мкА элемент памяти изменяет своё состояние, тем самым обеспечивает одиночный отказ в хранении одного бита информации.

Представлены значения критического заряда и тока проводимости при различных напряжениях питания. Показано, что увеличение напряжения питания элемента памяти способствует увеличению запаса по критическому заряду, приводящему к инверсии ячейки памяти.

Определен ток проводимости и величина напряжения питания элемента памяти, при котором произошло переключение состояние ячейки, то есть одиночный отказ.

Определена величина критического заряда, которая приводит к инверсии логического состояния ячейки модулей памяти.

Таким образом, в работе выполнено схемотехническое моделирование отказа ячейки модулей памяти при заданных условиях и параметров транзисторов элемента памяти при прохождении одиночной частицы. Полученные результаты могут быть использованы при проектировании микропроцессорных систем для использования в бортовой электронной аппаратуре КА различного назначения.

Ключевые слова: схемотехническое моделирование, критический заряд, ток ионизации, бортовая аппаратура.

Information about authors:

Grichshenko V.F., candidate of phys. math sciences, associate professor. Head Laboratory of Reliability and Security of Orbital and Terrestrial Space Systems; http://orcid.org/0000-0003-2244-5599;

Mukushev A.A., al-Farabi Kazakh National University. PhD doctoral student of the Faculty of Mechanics and Mathematics, Department of Mechanics

REFERENCES

[1] Musabayev T., Zhantayev Zh., Grichshenko **V.** Complex influence of Space environment on materials and electronics devices in the conditions of microgravity // Advances in Space Researches. Elsevier, 2016, 58, P.1138-1145. IF–1,406**.** https://doi.org/10.1016/j.asr.2016.05.030

[2] https://www.sciencedirect.com/journal/advances-in-space-research/vol/58/issue/6 (in Eng.).

[3] Kuznetsov N.V. Radiation conditions in the orbits of spacecraft // In: Space Model. under the editorship of M.I. Panasyuk, L.S. Novikov. M.: Science, 2007. T.1. C. 25-30. ISBN: 978-5-98227-418- http://kdu.ru/node/659. (in Rus.)

[4] Zhantaev Zh.Sh., Grishchenko V.F., Mukushev A. Circuit modeling of protection of electronic equipment from electrostatic discharge. News of NAS RK. Series of physico-mathematical- №4, 2016, p. 15-19. ISSN 1991-346X , http://physics-mathematics.kz/index.php/en/chive (in Rus.)

[5] Wang F.,Agrawal V. (2008) Single event upset: An embedded tutorial, 21st International Conference on VLSI Design (VLSID 2008), pp. 429-434. DOI:10.1109/VLSI.2008.28 (in Eng.).

[6] https://www.eng.auburn.edu/~agrawvd/TALKS/tutorial_6pg.pdf

[7] Baumann R. (2005) Soft errors in advanced computer systems, Design Test of Computers, IEEE, vol. 22, no. 3, pp. 258 -266. DOI: 10.1109/MDT.2005.69 (in Eng.).

[8] https://ieeexplore.ieee.org/document/1438282

[9] [1] Liu W. (2010) MOSFET Models for SPICE Simulation: Including BSIM3v3 and BSIM4, Wiley-IEEE Press, USA. ISBN: 978-0-470-54718-2

[10]https://www.wiley.com/en-kz/MOSFET+Models+for+SPICE+Simulation:+Including+BSIM3v3+and+BSIM4-p-9780471396970 (in Eng.).

NEWS
OF THENATIONAL ACADEMY OF SCIENCES OF THE REPUBLIC OF KAZAKHSTAN
PHYSICO-MATHEMATICAL SERIES
ISSN 1991-346X **https://doi.org/10.32014/2020.2518-1726.45**
Volume 3, Number 331 (2020), 127 – 134

УДК 528; 519.876.5, 004.891
МРНТИ: 20.23.27; 28.23.29

A.B. Kairanbayeva[1], D.V. Panyukova[2], G.B. Nurpeissova[3], K.A. Turekulova[4]

[1]Institute of the Ionosphere, National Center for Space Research and Technology, Almaty, Kazakhstan
[2]The Satbaev University, Almaty, Kazakhstan;
[3]The Caspian University, Almaty, Kazakhstan;
[4] The Institute of Seismology, Almaty, Kazakhstan.
E-mail: kairanbaeva_a@mail.ru; haleth@mail.ru; kerey97@mail.ru; turekulova.is@mail.ru

INTELLECTUAL FORECASTING OF LANDSLIDES

Abstract. All over the world remote monitoring and satellite imaginary is taking part in urban and construction planning. Therefore, while biggest city of Republic of Kazakhstan is placed on a land with a risk of landslides, it is reasonable to use satellite technologies to assess the land surface deformation before construction started. The remote monitoring is providing results as an array of numeric data that can be converted into a surface map. However, besides real time monitoring of possible landslides, it is possible to forecast such deformation in dynamic. Such dynamical model is presented as an array of time series of parameters, which then can be converted into dynamically changed map. Analytical modeling can provide such forecasting with high accuracy but demand decent amount of data for every forecasting case. Intellectual methods of forecasting operate with lack of information and provide results with acceptable margin of error. Authors suggest designing intellectual models on periodic data from satellite images for landslides' forecasting. Moreover, best-designed model can become a base for software package to provide such dynamic modeling of land's deformation online for public and private use.

Key words: GPS, remote sensing, landslide processes, intellectual models, forecasting, dynamic model.

Introduction. Research relevance is defined by decay of built structures near and in one of the most populated city in Kazakhstan – Almaty – because of landslides, mudflows and dramatic changes of climatic conditions. That confirms importance of modern GIS usage developed on the basis of ground and space monitoring data for forecasting dangerous situations (mudflows, landslides) and diagnostics of land's condition.

Nowadays technologies of satellite imagery and remote monitoring are widely used all over the world at land use [1, 2] and urban areas planning [3-5]. This significantly reduces the working time of specialists and optimizes the work at a planning stage of various works at the state and local levels.

Mapping landslides near built structures is necessary condition for making optimal technical decisions in their construction and operation due to possible destruction of the slope. Number of researches on the forecasting of landslide's risk was carried out over the past two decades around the world [6-21]. For mapping the landslide's risks, the researchers used various approaches, which can be grouped into three main types: statistical, computer modeling and analytical techniques. If there is a necessity to process a large data set, then use of analytical methods are almost impossible. So, the statistical techniques and computer modeling is widely implemented. In computer modeling with GIS technology following methods are mainly used: decision making trees, support vector points and neural modeling [7-21].

Scientific novelty of research is related to the use of modern satellite technologies with use of intellectual model to forecast the risk of landslides of the areas for future or present construction. The study of the mechanisms of slope processes occurrence using modern satellite technology and mathematical modeling leads to new knowledge in the theory of forecasting the risk of landslides and their influence on the land's building characteristics.

To build intellectual model and improve the accuracy of forecasting the risk of landslides by computer modeling detailed digital elevation model and field data in an area can be used. Evaluation of slope processes using GIS to forecast condition of building lands in Kazakhstan has not been done and proposes a great scientific interest.

Satellite images as a time series data. Remote monitoring and satellite imaginary can be used to observe the land surface and its deformation. For example, such monitoring can be provided by use of principle of radar interference. The difference in time delay between sent and received by satellite signal (red signal on the picture 1) represents the difference in surface level. Consequently, such difference in received parameters can show any deformation or landslide. Furthermore by all received from satellite data about monitored surface a map can be formed. If satellites provide a remote monitoring in a periodic manner, resulting maps can form a dynamic model of the surface deformation.

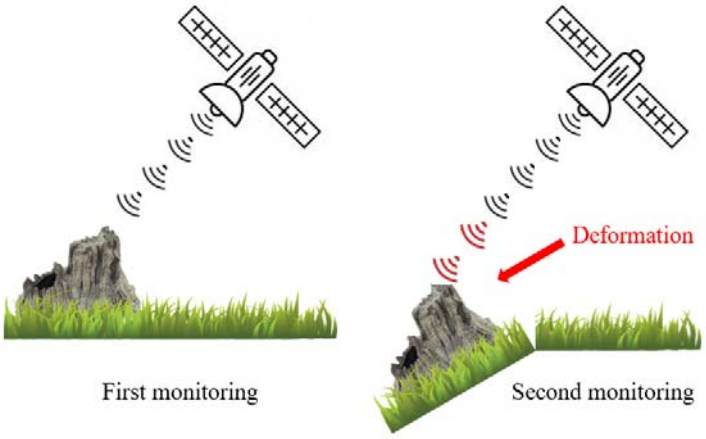

Picture 1 - Method of radar interference in remote monitoring

Satellite images of land for landslides' detection is delivered in form of data sheets about monitored surface as shown in picture 2. Thereat every line describes specific characteristic of the exact coordinates [6].

Then such data is processed to form a surface map as on picture 3 [6] where every parameter is presented on a z-axis for every coordinate specified on x- and y-axis of the graph. The same parameters can be represented in color or in combination of color and height. Author recommend combined method for representing surface deformation for unqualified users.

The implication is that any monitored surface can be presented as an array of numeric data, where its coordinates are shown as an element indexing:

$$Z = \begin{bmatrix} Z_{11} & Z_{12} & \cdots & Z_{1m} \\ Z_{21} & Z_{22} & & Z_{2m} \\ \vdots & & \ddots & \vdots \\ Z_{n1} & Z_{n2} & \cdots & Z_{nm} \end{bmatrix} \quad (1)$$

where Z is one of parameters received from monitoring, n and m are indexes representing coordinates of monitored surface.

Furthermore, the deformation of surface or landslide processes in exact coordinates in dynamic can be presented as a time series of an element in the array:

$$Z_{11} = \{Z_{11}^1(t), Z_{11}^2(t+T), Z_{11}^3(t+2\cdot T), \ldots\}, \quad (2)$$

where Z is one of parameters received from monitoring, t is time, and T is period of time between satellite images.

The resulting form of data can be used to form a mathematical model or design and train an intellectual model for the landslide processes' forecasting.

Lon	Lat	Z	Vel_mm_y_	Coherence	D_20150115	D_20180210
76,823888	43,280471	711,875116	-11,193887	0,694304	0	-40,588146
76,823889	43,280416	724,121679	-8,731388	0,670136	0	-25,104536
76,823889	43,280471	709,486996	-5,370865	0,681943	0	-11,350699
76,823892	43,280434	724,202657	-8,889476	0,69234	0	-24,358576
76,823893	43,280452	709,406511	-4,871862	0,666525	0	-11,289376
76,823895	43,279994	705,810231	-1,896947	0,747738	0	-4,014318
76,823897	43,28047	714,881492	-4,060597	0,66099	0	-10,300287
76,823898	43,28047	713,399774	-3,720258	0,67345	0	-8,853598
76,823899	43,280012	707,656516	-2,496723	0,718306	0	-5,717471
76,823899	43,280452	713,049197	-4,432741	0,761461	0	-9,929994
76,823899	43,280012	705,78585	-1,912691	0,795292	0	-2,329161
76,823903	43,280433	724,359914	-8,949328	0,66616	0	-24,439787
76,823903	43,280231	716,457603	-2,90916	0,675994	0	-10,883619
76,823904	43,28003	705,738837	-2,059825	0,788465	0	-1,850743
76,823906	43,280029	707,430014	-2,05429	0,770657	0	-8,137006
76,823908	43,280029	707,76529	-2,442406	0,723007	0	-9,137286
76,823908	43,280249	716,362962	-2,712636	0,781478	0	-2,636459
76,82391	43,280267	716,531821	-3,066086	0,674425	0	-17,121803
76,823911	43,280468	715,659589	-9,377769	0,667267	0	-36,229301
76,823913	43,283454	714,019161	0,819217	0,710332	0	4,901161
76,823921	43,280449	713,246561	-4,366353	0,73583	0	-10,232582
76,823921	43,280431	711,110533	-4,652173	0,714882	0	-7,789934
76,823923	43,280449	709,461361	-4,05126	0,674233	0	-9,950661
76,823924	43,280247	716,595356	-2,484826	0,701137	0	-3,312304
76,823929	43,283581	712,699376	-0,175425	0,742918	0	2,631488
76,823931	43,280448	713,459047	-3,560992	0,679144	0	-8,998888

Picture 2 - Data received from satellite imagery [6]

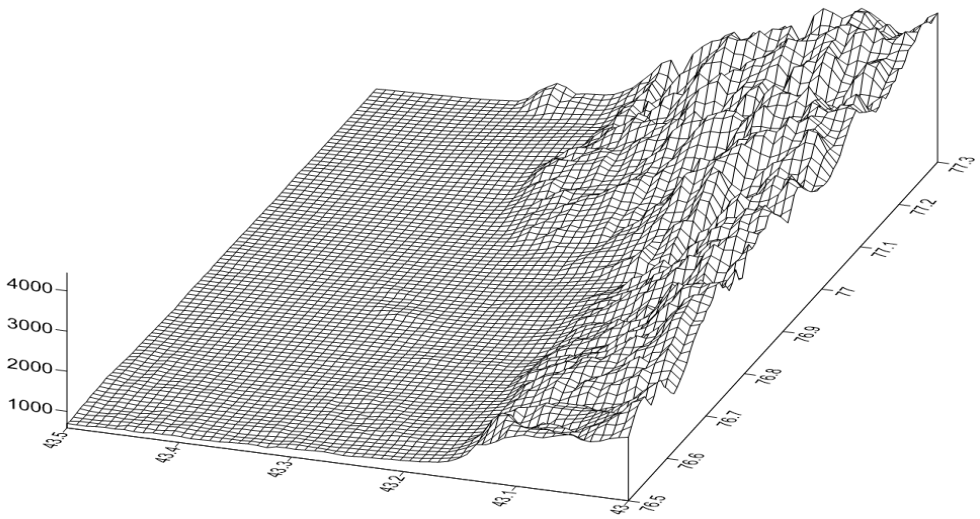

Picture 3 - Resulting map of monitored surface [6]

Intellectual method of forecasting of time series. Any data that is presented as a time series can be extrapolated with some level of accuracy [22]. This is one of the main principles used in all forecasting methods. These methods can be divided in three main groups: statistical, computer modeling and analytical techniques. While analytical methods give high accuracy in forecasting, they cannot be implemented in case of large amount of processed parameters or small amount of prior incoming data. Whereas intellectual methods provide a forecasting within reasonable accuracy even in case of information lack.

Intellectual methods include developed regression models, neural networks and expert systems or some combination of them. Choice of exact model for every particular forecasting task is executed by comparing the performance of each researched method [23].

Hereinbefore has been described that satellite imaginary can be presented as array of time series data. Authors suggest that such data can be used in designing and training intellectual methods for forecasting of landslides and other surface deformation on a moderate area of Taldikorgan state and Almaty city.

To achieve this goal, periodic remote monitoring of several areas should be provided. Afterward received satellite images should be converted into arrays of time series data. Then this arrays should be divided in two groups: bigger arrays for training (nearly 90 % of all data) and smaller (nearly 10%) – for testing. After that, several models based on different intellectual approaches should be trained on the training data arrays.

The assessment of received model should be provided on previously formed testing arrays. If required accuracy will not be satisfied, models should be modified by combining methods that shown best results. Beside accuracy, the operating time and implementation simplicity should be considered as a choice criterion. In a result, best model can be used for practical implementation.

Possible practical implementation of a forecasting method for landslides' processes

The best forecasting model can be used as a base processor for software package aimed to provide dynamic model of surface deformation to public and private users. The proposed algorithm of interaction between the software package and a user is shown on picture 4.

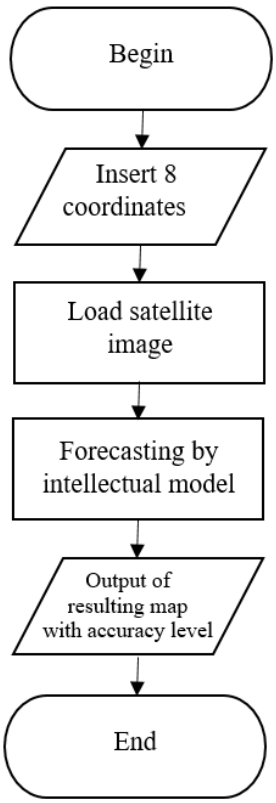

Picture 4 - Operational algorithm of proposed software package

A user has to provide only eight coordinates (longitude and latitude for four corners of required sector). Then the software download a satellite image of the area in a form of numeric data. This numeric array is processed by the forecasting model, which extrapolates it into another forecasted array. As a result, the forecasted array is converted into the surface map with prediction accuracy limits that is presented to a user.

Proposed software package eliminate requirements for user's proficiency in programming or modeling, as long as in satellite geodesy. At the same time, it provide possibility to remote assessment of exact land for future deformation or landslides. Such preliminary diagnostic in dynamic can decrease economical expenses on pre-construction research of the area on the spot to rule out a possibility of building on a future landslide. Intended users include either governmental committees for urban planning or private constructor who is narrowing down the exact spot for future building.

А.Б. Қайранбаева[1], Д.В. Панюкова[2], Г.Б. Нүрейсова[3], К.А. Турекулова[4]

[1]Ионосфера институты, Ұлттық ғарыштық зерттеулер мен технологиялар орталығы, Алматы, Қазақстан;
[2] Сәтбаев университеті, Алматы, Қазақстан;
[3]Каспий қоғамдық университеті, Алматы, Қазақстан;
[4]Сейсмология институты, Алматы, Қазақстан

ЖЕР КӨШКІНДЕРІН ИНТЕЛЕККТУАЛДЫ БОЛЖАУ ЖҮЙЕСІ

Аннотация. Қазақстанның ірі қалаларында, Алматыда және оған жақын жерлерде орналасқан ғимараттар мен қалалық инфрақұрылымдар ауа райының күрт өзгеруіне байланысты сырғыма (көшкін), сел ағындарының әсерінен жиі бұзылады. Сондықтан да зерттеу өзекті болып табылады. Жер үсті-ғарыштық мониторинг деректері негізінде әзірленген қазіргі заманғы геоақпараттық технологияларды қауіпті жағдайларды болжау (селдер, көшкіндер) және құрылысқа пайдаланылатын жерлердің жай-күйін диагностикалау үшін пайдалану маңызды болып табылады.

Қазіргі уақытта бүкіл әлемде жерді пайдалануды жоспарлау кезінде ғарыштық түсірілім және қашықтықтан мониторинг жасау технологиялары жалпы міндеттер үшін де, қала аумақтарын жоспарлау үшін де белсенді пайдаланылады. Бұл мамандардың жұмыс уақытын айтарлықтай үнемдеуге және мемлекеттік, жергілікті деңгейдегі түрлі жұмыстарды жоспарлау кезеңінде жұмысты барынша оңтайландыруға мүмкіндік береді.

Сырғыманы картаға түсіру - көлбеу құлаудың ықтимал аудандарын ескере отырып, әртүрлі құрылыстармен мен инфрақұрылым объектілерін жобалау және қызмет көрсету кезінде оңтайлы техникалық шешімдер қабылдау үшін қажетті шарт. Соңғы екі онжылдықта бүкіл әлемде көшкін қаупін болжау бойынша зерттеулер жүргізілді. Сырғыманың қауіп-қатер карталарын жасау үшін зерттеушілер үш тәсілге топтастыруға болатын түрлі тәсілдерді қолданды: статистикалық, компьютерлік модельдеу және аналитикалық әдістер. Үлкен көлемді деректерді өңдеу қажет болған жағдайда аналитикалық әдістерді қолдану мүмкін емес, сондықтан статистикалық әдістер мен компьютерлік моделдеу кеңінен қолданылады.

Мұндай зерттеулердің ғылыми жаңалығы - қазіргі заманғы спутниктік технологиялар мен математикалық модельдеуді пайдалануға байланысты, құрылыс жоспарланған жер аймағында көшкін пайда болу қаупін болжаудың интеллектуалдық модельдерін пайдалану. Қазіргі заманғы спутниктік технологияларды және моделдеудің математикалық әдістерін қолдана отырып, беткейлік үдерістердің пайда болу механизмдерін зерттеу көшкіндердің пайда болу қаупін болжау теориясында жаңа білім алуға мүмкіндік береді.

Осы мақалада компьютерлік модельдеу арқылы интеллектуалды модельдер құру және болжаудың дәлдігін арттыру үшін мыналар пайдаланылады: рельефтің сандық моделі; құрылысқа жоспарланған жер аумағындағы спутниктік кескіндер мен зерттеу деректері. Қазақстанда құрылысқа жоспарланған жерлердің жай-күйін болжау үшін ГАЖ технологияларын қолдану арқылы көлбеу үрдістер мен шамадан тыс сулану аймақтарын бағалау бұрын жүргізілген жоқ және ғылыми қызығушылық тудырады.

Ұсынылған зерттеу әдістемесі спутниктік суреттерден радарлық интерференцияны пайдалану арқылы алынған сандық мәліметтер мен зерттелетін аймақтағы беттің деформациясы картасының байланысына негізделген. Сонымен, жер бетіндегі сырғыманың ықтималдығы зерттелетін аймақ үшін белгілі бір уақытта бетінің күйін сипаттайтын мәліметтер жиынтығын алу қажет. Осындай ғарыштық зерттеулер сериясын белгілі бір уақыт аралығында белгілі бір жиілікпен жүргізген кезде осы жер учаскесін сипаттайтын әр параметр үшін уақыттық сандық мәндер алынады. Бұл шамаларды уақыт өзгерісіне байланысты беткі

деформацияны сипаттайтын карталар сериясына айналдырылған кезде, зерттелетін аймақта беткейлік өзгерістер мен ықтимал сырғыма процестерінің динамикалық моделі алынады.

Егер нақты деректер жеткілікті болса, уақыт қатарларын процесті аналитикалық модельсіз интеллектуалды болжау әдістерін қолдана отырып сәтті жалғастыруға болады. Жоғарыда айтылғандай, ғарыштық зондылауды қолдана отырып, жер бетіндегі уақыт бойынша деформацияны шектеулі параметрлердің уақыттық қатарлары ретінде көрсетуге болады. Демек, мұндай қатарларды аздаған ғана қателігі бар интеллектуалды әдістердің көмегімен "болашаққа экстраполяциялау" мүмкін. Шындығында, бұл шектеулі бастапқы қателіктермен салыстырмалы түрде аз қателіктерді көшкін процестерін болжауға арналған бірқатар модельдерді алуға мүмкіндік береді. Бұл болжау әдістерінің ішінде қазіргі заманғы регрессиялық болжау модельдері, нейрондық желілердің әртүрлі түрлері, анық емес логика және осы әдістердің әртүрлі комбинациясы қолданылады. Интеллектуалды модельді бағалау және таңдау екі негізгі критерийлерге жүгінеді: а) енгізудің қарапайымдылығы және кіріс ақпаратын өңдеу жылдамдығы; б) болжау дәлдігі.

Таңдалған болжау моделінің негізінде авторлар қолданушыға жер бетінің белгілі бір бөлігінің деформациясы туралы болжам алуға мүмкіндік беретін толыққанды бағдарламалық өнімді құруды ұсынады. Қосымшаның келесі жұмыс реті ұсынылады: а) пайдаланушы зерттелетін аймақтың шектік координаттарын белгілейді; б) бағдарламалық пакет ғарыштық зондылау жүйелерінен мәліметтер массиві түрінде қажетті кескінді сұрайды; в) деректер таңдалған модельден алынған болжамды нәтижелерге сәйкес белгілі уақыт аралығында экстраполяция жасалады; г) болжамды деректер массиві ықтимал қатені азайта отырып, сұралған аймақтың динамикалық деформация картасы түрінде пайдаланушыға көрсетіледі. Мұндай бағдарламалық жасақтама мемлекеттік және жеке құрылыстар кезінде жоспарланған жер учаскелерін нақты зерттеудің экономикалық шығындарын едәуір азайтуға мүмкіндік береді.

Түйін сөздер: GPS, қашықтықтан зондылау, көлбеу процестер, интеллектуалды модельдер, болжау, динамикалық модель.

А.Б. Кайранбаева[1], Д.В. Панюкова[2], Г.Б. Нурейсова[3], К.А. Турекулова[4]

[1]Институт ионосферы, Национальный центр космических исследований и технологий, Алматы, Казахстан;
[2]Университет им.К.И. Сатпаева, Алматы, Казахстан;
[3]Каспийский университет, Алматы, Казахстан;
[4]Институт сейсмологии, Алматы, Казахстан

ИНТЕЛЛЕКТУАЛЬНОЕ ПРОГНОЗИРОВАНИЕ ОПОЛЗНЕЙ

Аннотация. Актуальность исследования определяется тем, что в крупнейшем городе Казахстана – Алматы и близ него здания и городская инфраструктура часто разрушаются под воздействием оползней, селевых потоков, обусловленных резкими изменениями погодных условий, что говорит о важности использования современных геоинформационных технологий, разработанных на основе данных наземно-космического мониторинга, для прогноза опасных ситуаций (сели, оползни) и диагностики состояния земель, используемых под строительство.

В настоящее время во всем мире при планировании землепользования активно используются технологии космической съемки и дистанционного мониторинга как для общих задач, так и для планирования городских территорий. Это позволяет значительно сократить время работы специалистов и максимально оптимизировать работу еще на этапе планирования различных работ государственного и местного уровня.

Картирование оползней – необходимое условие для принятия оптимальных технических решений при проектировании и обслуживании различных строений и инфраструктурных объектов с учетом вероятных областей разрушения склона. В течение последних двух десятилетий исследования по прогнозированию риска возникновения оползней проводились во всем мире. Для создания карт риска возникновения оползней исследователи использовали различные подходы, которые можно сгруппировать по трем главным типам: статистические, компьютерное моделирование и аналитические методы. При необходимости обработки большого массива данных применение аналитических методов почти невозможно, поэтому более широко применяются статистические методы и компьютерное моделирование.

Научная новизна подобных исследований связана с использованием современных спутниковых технологий и математического моделирования с использованием интеллектуальных моделей прогнозирования, риска возникновения оползней в районе земель, планируемых под строительство.

Изучение механизмов возникновения склоновых процессов с привлечением современных спутниковых технологий и математических методов моделирования позволяет получить новые знания в теории прогноза риска возникновения оползней.

Для построения интеллектуальных моделей и повышения точности прогнозирования компьютерным моделированием в данной статье предполагается использовать: детальную цифровую модель рельефа; данные космических съемок и исследований в районе земель, планируемых под строительство. Оценка склоновых процессов и зон избыточного увлажнения с использованием ГИС-технологий для прогнозирования состояния земель, планируемых под строительство, на территории Казахстана ранее не проводилась и представляет значительный научный интерес.

Предлагаемая методика исследования основана на взаимосвязи числовых данных, полученных с помощью радарной интерференции со спутниковых снимков и карты деформации поверхности в снимаемом районе. Так для исследуемого на вероятность оползней участка земной поверхности необходимо получить массив данных, описывающий состояние этой поверхности на определенный момент времени. При проведении ряда таких космических съемок с определенной периодичностью за определенный отрезок времени будут получены временные ряды числовых значений для каждого параметра, описывающего этот участок земли. При преобразовании этих значений в ряд карт, описывающих деформацию поверхности во времени, будет получена динамическая модель изменения поверхности и вероятных оползневых процессов на исследуемом участке.

При наличии достаточного количества фактических данных временной ряд может быть успешно продолжен с помощью интеллектуальных методов прогнозирования даже без аналитического моделирования процесса. Как было сказано выше, деформацию поверхности земли во времени, снятую с помощью космического зондирования, можно успешно представить, как массив временных рядов ограниченного числа параметров. А, следовательно, такие ряды возможно «экстраполировать в будущее» с помощью таких интеллектуальных методов с приемлемой погрешностью. Фактически это дает возможность получить ряд моделей прогнозирования оползневых процессов с относительно небольшой погрешностью при ограниченных изначальных данных. Среди таких методов прогнозирования используются современные регрессионные модели прогнозирования, нейронные сети разного рода, нечеткая логика и различные комбинации этих методов. Оценка и выбор интеллектуальной модели основываются на двух базовых критериях: а) простоте реализации и скорости обработки входящей информации; б) точности прогнозирования.

На основе выбранной модели прогнозирования авторы предлагают создать полноценный программный продукт, позволяющий пользователю получать прогноз по деформации заданного им участка земной поверхности. Предполагается следующая последовательность работы приложения: а) пользователь задает, ограничивающие координаты исследуемого участка; б) программный пакет запрашивает необходимый снимок с систем космического зондирования в виде массива данных; в) данные экстраполируются на определенный период времени вперед, согласно результатам прогноза, полученным из выбранной модели; г) спрогнозированный массив данных выводится пользователю в виде динамической карты деформации запрашиваемого участка с приведением вероятной погрешности. Применение такого программного продукта может существенно сократить экономические затраты на фактическое исследование участков земель, планируемых под строительство как в государственном, так и в частном строительстве.

Ключевые слова: GPS, дистанционное зондирование, склоновые процессы, интеллектуальные модели, прогнозирование, динамическая модель.

Information about authors:

Kairanbayeva Ainur Berikkalievna – Institute of the Ionosphere, National Center for Space Research and Technology, Scientific secretary, PhD kairanbaeva_a@mail.ru, https://orcid.org/0000-0001-9827-4082;

Panyukova Dina Vasilyevna – The Satbayev University, The department of Automation and control, PhD candidate, haleth@mail.ru, https://orcid.org/0000-0002-2567-5106 ;

Nurpeissova Gulnara Baibolovna – The Caspian University, Professor, kerey97@mail.ru, https://orcid.org/0000-0003-4642-3829;

Turekulova Kulyanda Abilovna - Institute of Seismology, engineer of the highest category in laboratory of “Seismic resilience of buildings and constructions“ turekulova.is@mail.ru, https://orcid.org/0000-0001-9709-6413

REFERENCES

[1] Seyed A.B., Ming Zh., Sajad Sh., Yun Zh. A hierarchical rule-based land use extraction system using geographic and remotely sensed data: A case study for residential uses. Transportation Research Part C: Emerging Technologies. 2014. Vol.47. P. 155–167.

[2] Seyed A.B., Ming Zh., Yun Zh. Development of a land use extraction expert system through morphological and spatial arrangement analysis. Engineering Applications of Artificial Intelligence. 2015. Vol. 37. P. 221–235.

[3] Saeed B., Ali A. Introducing a novel model of belief–desire–intention agent for urban land use planning. Engineering Applications of Artificial Intelligence. 2013. Vol. 26. P. 2028–2044.

[4] Michael M. Remote sensing for urban planning and management: The use of window-independent context segmentation to extract urban features in Stockholm. Computers, Environment and Urban Systems. 2015. Vol. 52. P.1–9.

[5] Matthew M., Abduwasit G., Tashpolat T., Filiberto P., Pedro L-C., Ümüt H., Mamat S, Mario C. Effects of green space spatial pattern on land surface temperature: Implications for sustainable urban planning and climate change adaptation. ISPRS Journal of Photogrammetry and Remote Sensing. 2014.Vol. 89. P.59–66.

[6] Ground-space monitoring of technogenic processes in urban areas and assessment of the status of large technical facilities: research report (interim, part 1) / Subsidiary LLP "Institute of ionosphere". Almaty, 2019. 62p. Inv. №0219RK00124

[7] Biswajeet P. Remote sensing and GIS-based landslide hazard analysis and cross-validation using multivariate logistic regression model on three test areas in Malaysia. Advances in Space Research 45 (2010) 1244–1256.

[8] Iswar D., Alfred S., Norman K., Vinay K. Dadhwal. Landslide susceptibility mapping along road corridors in the Indian Himalayas using Bayesian logistic regression models. Geomorphology 179 (2012) 116–125.

[9] Ye Fei, He Chuan, Wang Shi-min, Zhang Jin-long. Landscape design of mountain highway tunnel portals in China. Tunnelling and Underground Space Technology 29 (2012) 52–68.

[10] Biswajeet P. A comparative study on the predictive ability of the decision tree, support vector machine and neuro-models in landslide susceptibility mapping using GIS. Computers & Geosciences 51 (2013) 350–365.

[11] Bovenga F., Wasowski J., Nitti D.O., Nutricato R., Chiaradia M.T.. Using COSMO/SkyMed X-band and ENVISAT C-band SAR interferometry for landslides analysis. Remote Sensing of Environment 119 (2012) 272–285.

[12] Seo Jin Ki, Chittaranjan Ray. Using fuzzy logic analysis for siting decisions of infiltration trenches for highway runoff control. Science of the Total Environment 493 (2014) 44–53.

[13] Guzzetti F., Carrarra A., Cardinali M., Reichenbach, P., 1999. Landslide hazard evaluation: a review of current techniques and their application in a multi- scale study, Central Italy. Geomorphology 31, 181–216.

[14] Bai S.B., Wang J., Zhang F.Y., Pozdnoukhov A., Kanevski, M.F., 2008. Prediction of landslide susceptibility using logistic regression: a case study in Bailongjiang River Basin, China. The 4th International Conference on Natural Computation, The 5th International Conference on Fuzzy Systems and Knowledge Discovery. 25–27 August 2008, Jinan, China. FSKD, 4, 647–651. 10.1109/FSKD.2008.524.

[15] Bai S.B., Wang J., Pozdnoukhov A., Kanevski M.F., 2009. Validation of Logistic Regression Models for Landslide Susceptibility Maps. CSIE, 2, 355–358. WRI World Congress on Computer Science and Information Engineering, 2009.

[16] Lee S., Ryu J.H., Won J.S., Park H.J. Determination and application of the weights for landslide susceptibility mapping using an artificial neural network .Engineering Geology, 71 (2004), pp. 289–302.

[17] Pradhan B., Lee S., Buchroithner M.F. A GIS-based back-propagation neural network model and its cross-application and validation for landslide susceptibility analyses. Computers, Environment and Urban Systems, 34 (3) (2010), pp. 216–235.

[18] Pradhan B., Chaudhari A., Adinarayana J., Buchroithner M.F.. Soil erosion assessment and its correlation with landslide events using remote sensing data and GIS: a case study at Penang Island, Malaysia. Environmental Monitoring & Assessment, 184 (2) (2012), pp. 715–727.

[19] Akgun A., Turk N. Landslide susceptibility mapping for Ayvalik (Western Turkey) and its vicinity by multicriteria decision analysis. Environmental Earth Sciences, 61 (3) (2010), pp. 595–611.

[20] Bui D.T., Pradhan B., Lofman O., Revhaug I., Dick O.B.. Spatial prediction of landslide hazards in Hoa Binh province (Vietnam): a comparative assessment of the efficacy of evidential belief functions and fuzzy logic models. Catena, 96 (2012), pp. 28–40.

[21] Akgun A., Sezer E.A., Nefeslioglu H.A., Gokceoglu C., Pradhan B. An easy-to-use MATLAB program (MamLand) for the assessment of landslide susceptibility using a Mamdani fuzzy algorithm. Computers & Geosciences, 38 (1) (2012), pp. 23–34.

[22] Panyukova D., Nurpeissova G. Review of modern approaches for power load forecasting // The 15th International Scientific Conference "Information Technologies and Management". Riga, 2017. pp.69-71.

[23] Panyukova D.V., Shiryayeva O.I. Review of modern approaches for electric power consumption forecasting. Vestnik KazNRTU, 6 (136) (2019), pp. 509-513.

NEWS
OF THENATIONAL ACADEMY OF SCIENCES OF THE REPUBLIC OF KAZAKHSTAN
PHYSICO-MATHEMATICAL SERIES
ISSN 1991-346X **https://doi.org/10.32014/2020.2518-1726.46**
Volume 3, Number 331 (2020), 135 – 141

УДК 528, 681.5.01, 621.316
МРНТИ: 20.23.27; 27.37.17; 44.29.29

D.V. Panyukova[1], A.B. Kairanbayeva[2], G.B. Nurpeissova[3], K.V. Panyukov[4]

[1]The Satbaev University, Almaty, Kazakhstan;
[2]Institute of the Ionosphere, National Center for Space Research and Technology, Almaty, Kazakhstan;
[3]The Caspian University, Almaty, Kazakhstan;
[4]The ITMO University, Saint Petersburg, Russia.
E-mail: kairanbaeva_a@mail.ru; haleth@mail.ru; kerey97@mail.ru; dartm1994@gmail.com

SMART GRIDS WITH GIS TECHNOLOGY

Abstract. Nowadays republican grid in Kazakhstan is regulated to have automated electric power accounting system for every energy supplying entity. However, with wide implementation of units on renewable energy sources (RES), especially in private sector, such measures will not be enough. World scientific community propose a number of methods to modernize grids on national or regional level. One of them is to transit from AC power transmission system to DC power transmission system. It leads to easier connection of plant on RES to the grid and cost-effectiveness in power transmission per each kilometer. Other modern approach is real-time digital simulation. Such simulation gives information on grid's functioning after emergency switching to plan all necessary balancing measures. Next modernization step is in use of phasor measurement units in real-time monitoring for each element of the grid. All of previously specified methods can be developed into GIS on electric power supplement, consumption and transmission. A decentralization on the GIS basis can be implemented to the grid to minimize control delay for the whole system. Authors propose an optimization task for decentralized smart grid on the GIS basis. Such approach allows minimizing reaction time on emergency and power balancing. In addition, it gives opportunity for proper planning of future power construction.

Key words: smart grid, GIS, decentralization, optimization task, real-time digital simulation, HVDC.

Introduction. The Kegoc as a main regulatory authority in the Kazakhstan stated that every power suppling organizations have to implement automated electric power accounting system before connecting to the grid [1]. It became obligatory as a main instrument to support real-time capacity balancing in the electricity market. To the date, such balancing is a difficult but feasible task, as most power generating facilities operate at the republican or regional level and are stations on traditional fuel or HPP (plants with high production predictivity). Kazakhstan government wants to support the worldwide ecological trend to switch at least partly power production in the republic to renewable energy sources (RES). While with the active implementation of generating stations on RES, the issue of balancing the energy market is becoming more and more complicated by the stochastic nature of their production. Even greater difficulties will arise if plants on RES will be mostly low-powered and privately owned [2]. So, new modernization approaches should be considered.

Smart grid approaches. In the world, a number of approaches for modernization of state-scale energy systems are proposed. One of them is the transition from AC transmission systems to DC transmission systems [3-5]. Such transition allows connecting sources on RES with minimal complex of converting equipment. While now a small private power system with RES plants and accumulators has to include inverters to convert power into AC form before supplying it into a central grid. Furthermore, high-voltage DC power transmission systems (HVDC) transmit electric power over long distances with less cost and loss than AC transmission lines. The difference in transmission cost makes possible even extra continental connection of the grids. Transmission so long could provide a possibility to balance stations on

RES by themselves with a change of weather worldwide. Another advantage is in absents of phases. It gives the ability to connect national grids with different nominal frequencies. Also opens a possibility for power producers and consumers work in one grid without first balancing them by phase. The main difficulty in implementing such transmission systems is the high cost of DC-to-AC conversion equipment. This requires significant capital costs. Especially with the widespread use of AC networks in our republic and in many other countries of the world. However with development of the technology equipment price is dropping.

For both DC and AC networks, real-time simulation systems (RTDS) become the primary control tool [6-8] as time of reaction is becoming crucial in proper dispatching of a grid. Such systems are actively implemented in emergency automation, frequency and voltage control of generation units, power electronic's management, power dispatching and grid's real-time and systematic management systems. RTDS allow real-time assessment of the consequences after connection or emergency shutdown of one of the phases. Real-time simulation lies at the heart of the optimal decision on balancing a power system at different levels. Large-scale real-time digital simulators or LSRTDS provide an opportunity to investigate even the launch of district-scale networks from a fully de-energized state. At the same time by LSRTDS technique one tool by 0-3 kHz frequency is sufficient for observation of a gird's operation in the whole spectrum of frequencies.

One of monitoring tools for emergency automation is Phasor Measurement Unit (PMU) [8-10]. These units send real-time information about the state of power objects to data hubs for use in grid's control centers. The information from PMUs can be obtained in two ways. By one way, the PMU is physically connected through current and voltage amplifiers to controlled points of a power grid. In second case, the values are obtained from the special interface boards. Anyhow the information consist not only electric parameters, but also their synchronization to exact time code. The obtained data can be used to monitor and visualize the state of the power network in real time and simulate the behavior of the network by RTDS in case of possible outages or connections. Besides RTDS, PMUs are increasingly implemented to the emergency automation equipment. The difficulties of implementing PMU are in the novelty of technology, which means that the principle of work is proprietary and the level of standardization is still low.

Decentralized smart grids. The previously described technologies can also be used in the classic centralized power grid, which remains relevant in the case of large government and corporate power generating stations. While the widespread implementation of RES plants leads to a large number of potential suppliers of electricity from the private sector. Moreover, the probabilistic nature of such plants' generation increases the probability of critical delays in decision-making even for real-time monitoring systems in centralized dispatching. Therefore, in parallel with the modernization of monitoring and modelling systems, the scientific community propose to use the principles of grid's decentralization [11, 12]. Beside shorter period of the reaction, decentralization increases the robustness of the system as the controlling functions are not tied only to the dispatching center but are parceled out to the spot. Such control distribution ensures proper functionality in a grid even with communication failure between dispatching center and end units of the grids.

While in centralized system all controlling and balancing is provided in republican or regional centers in decentralized grids such problems are solved on the spot. Only if there is some power undersupply or surplus the local grid requests balancing from the dispatching center above. However, it become actual only with wide implementation of small power plants near private costumers to minimize transmission loss of the energy.

Biggest challenge for decentralization is in proper dispatching while it is irrational to have human dispatcher at the smallest units of the grid. Hence dispatching should be provided automatically. At the same time, automation of any entity demands proper mathematical description of it's functioning that is economically impractical.

The authors propose to use Holon method for decentralization of a grid. This concept assumes that some part of the system or subsystem named as Holon has the same character and mathematical

description as a whole system named Holarchy [13]. Furthermore, even lower subdivision of the Holon has the same description too. This approach allows implementing the same mathematical calculation and optimization process for a grid's unit at any level resulting in same controlling basis for whole system. First step then is in formulization of the optimization task for the decentralized grid on any level.

Main economical goal for a grid's element – Holon – is to import less and export more power to the external parts of the grid. It leads to optimization task of minimization of upload from outside (negative value means Holon is supplying the system):

$$\int_0^t P_C(t)dt \to min, \tag{1}$$

or for discrete representation

$$\sum_{n=0}^{T} P_C(n) \to min, \tag{2}$$

where P_C is the power uploaded from outside of a Holon, *t* and *T* is a considered period in continuous and discrete form.

Required power can be calculated as

$$P_c(t) = P_l(t) + P_b(t) + P_t(t,d) - P_s(t) - C_a U_a \frac{dSoC}{dt} \tag{3}$$

where $P_l(t)$ is the sum of power loads in a Holon, $P_b(t)$ is the sum of power required for balancing, $P_t(t,d)$ is the sum of power required for transmission from supplying units to consumers within a Holon, $P_s(t)$ is the sum of power generation, C_a, U_a and SoC are capacity, voltage and state of charge of accumulators in a Holon, *t* is time, *d* is transmission distance between exact consumer and supplier.

Optimization of (1) and (3) will lead to proper control for a grid or its part. Some parts of optimization task can be reduced to zero. For a high-level Holons accumulators are absent and will be considered zero as power balancing could be provided by slowing down stations with controllable production. Whereas for lower level Holons loads or supply could be missing and become zero.

Smart grid with GIS. In any case, power transmission, monitoring and modelling systems require data visualization and recording for humans use. Usually it is done by superimpose grid's parameters on geographical maps according to plants and consumers' placing. Nevertheless, such visualization is not a fully valid geographic information system (GIS), as it does not use any of geographical parameters accept for visual understanding of grid's zoning. While zoning also is provided by administrative principles but not by geographical placing.

Proper GIS for power grids can provide several undeniable advantages. Firstly, such GIS can stimulate the reasonable zoning of the Republican power system into subsystems, taking into account the power generated and consumed in specific geographical locations. Moreover, GIS information also can become key factor for optimizing the loss of electricity transmission between the supplier and the consumer. Especially with implementation of decentralization concept. In addition, connection of meteorological GIS to the GIS for power grids will help with stochastic character of power production from RES plants. Finally, such GIS for power grids can help in planning the location for the construction and launch of new power plants and infrastructure for power transmission systems.

Historically grid's zoning in Kazakhstan was based on administrative principles, as main power supplying stations are state or public owned. With implementation of small power plant's in private sector zoning enforced to be done on geographical principle. Even more, zoning have to be periodically reconsidered because of new plugging of consumers or supplier.

Decentralization of a grid will not decrease an importance of GIS for power grids rather the opposite as the division into Holons should be provided on basis of placing and connection. Furthermore,

optimization task (1) and (3) takes into account, among other things, the distance for power transmission between the network's facilities obtained from the GIS of the power grid. Such a distance is the length of all power transmission lines through which electricity must pass to the consumer, other than the shortest distance between objects.

The main problems with balancing of a grid with RES plants is in their almost unpredictable power production. The integration of real time meteorological information gives possibility to predict with high accuracy power production from RES or power consumption in short-term [14]. Therefrom GIS for power grids needs to include process and visualization of meteorological information to control and dispatching system with RES plants as can be seen on picture. It includes temperature, pressure, wind speed at several heights, solar radiation.

Beside real-time controlling, GIS information should be used for planning of grids further modernization. Geographical parameters and landscape, closeness to the costumers should be considered as main factors for choice of placing for every planned new power plant or station. Above that for RES plants wind or solar potential at the exact spot should be considered. All of these parameters can be presented on real-time GIS for power grid.

GIS for power grid with real-time wind data

Conclusion. All over the world power plants on RES are represented more and more not only on governmental and regional level, but also in private sector. It challenges power grid's control and dispatching with high level of uncertainty.

RTDS with PMU can be used for simulation and real-time decision-making within a grid. Transition from AC power transmission to HVDC eases RES plants' connection and decrease power transmission loss. Decentralization of a grid leads to faster dispatching, robustness of a system and reduces power transmission distances. In addition, it gives possibility to scale automation solutions with less research.

Described approaches can answer to the problems of modern power grids both in classical form with centralized dispatching and public power plants and as an advanced grid with decentralization and wide private RES implementation. While GIS for power grid will make it possible to understand what is happening in the grid, to respond quickly to emergencies and phase imbalances, as well as to plan further expansion of the grid and construction of new plants and infrastructure.

Д.В. Панюкова[1], А.Б. Қайранбаева[2], Г.Б. Нүрейсова[3], К.В. Панюков[4]

[1]Ионосфера институты, Ұлттық ғарыштық зерттеулер мен технологиялар орталығы, Алматы, Қазақстан;
[2] Сәтбаев университеті, Алматы, Қазақстан;
[3]Каспий қоғамдық университеті, Алматы, Қазақстан;
[4] ИТМО университеті, Санкт-Петербург, Ресей

ГАЖ ТЕХНОЛОГИЯЛАРЫН ҚОЛДАНАТЫН ИНТЕЛЕКТУЛДЫ ЭНЕРГОЖҮЙЕЛЕР

Аннотация. Қазақстанның заманауи энергетикалық жүйесінде барлық энергиямен жабдықтаушы ұйымдар үшін электр энергиясын коммерциялық есепке алудың автоматтандырылған жүйелері болу міндет. Бұл электр энергиясының нарығында нақты уақыт режимінде тепе-теңдікті қолдау үшін жасалады. Бүгінгі күні мұндай теңдестіру қиын міндет, бірақ қолдан келеді, электр энергиясын өндіретін қондырғылардың көпшілігі республикалық немесе аудандық деңгейде жұмыс істейді және дәстүрлі отынды немесе гидроэлектростанцияны пайдаланатын станциялар болып табылады (өндірудің болжамдылығы жоғары). Жаңартылатын энергия көздерін (ЖЭК) пайдаланатын генераторлық станцияларды белсенді түрде енгізу нәтижесінде, олардың өндірісінің стохастикалық сипатына байланысты энергия нарығын теңдестіру мәселесі күрделене түсуде. Егер ЖЭК генераторларының көбі қуаты төмен және жеке меншік болса, одан да үлкен қиындықтар туындайды.

Әлемде мемлекеттік энергетикалық жүйелерін жетілдірудің бірқатар тәсілдері ұсынылған. Солардың бірі айнымалы токтың беріліс жүйесінен тұрақты ток беру жүйесіне ауысу. Бұндайы өзгеріс жаңартылатын энергия көздеріне ең аз түрлендіргіш құралдар жиынтығымен қосуға мүмкіндік береді. Бірақ, ең бастысы, үлкен қашықтыққа электр энергиясын жоғары вольтты тұрақты ток жүйелерінмен (HVDC) берудің құны мен шығыны айнымалы ток желілеріне қарағанда төмен. Тағы бір артықшылығы - электр энергиясын өндірушілер мен тұтынушыларды оларды фазалық түрде теңгерімсіз қосу мүмкіндігі. Бұндай тарату жүйелерін іске асырудағы негізгі қиындық – тұрақты токты ауыспалы токқа түрлендіруге арналған жабдықтың қымбаттығы. Біздің республикада және әлемнің көптеген елдерінде айнымалы ток желілері кең қолданылады, сондықтан бұл айтарлықтай көп шығынды қажет етеді.

Тұрақты және ауыспалы ток желілері үшін негізгі басқару құралы нақты уақыт режимінде имиталяциялау жүйелері (RTDS) болып табылады. Мұндай жүйелер төтенше жағдайларды және жалпы энергия жүйелерін басқаруда белсенді енгізілуде. RTDS бір фазаны қосу немесе апаттық түрде өшіру салдарын нақты уақыт режимінде бағалауға және әртүрлі деңгейдегі энергия жүйесін теңгеру туралы ең жақсы шешім қабылдауға мүмкіндік береді. Сонымен қатар, 0-3 кГц жиілікті қолдануға байланысты, бүкіл жиілік спектрінде қуат жүйесінің жұмысын бақылау үшін бір құрал жеткілікті. Нақты уақыттағы ауқымды цифрлық симмуляторлар немесе LSRTDS тіпті аймақтық масштабтағы желілерді толығымен энергиясыз күйден іске қосуды зерттеуге мүмкіндік береді.

Төтенше жағдайларды автоматтандыруды бақылау құралдарының бірі - синхрофазорлар (PMU). Бұл құрылғылар нақты уақыт режимінде энергетикалық қондырғылардың жай-күйі туралы ақпаратты энергетикалық диспетчерлік орталықтарда пайдалану үшін деректерді жинақтағыштарға жібереді. Алынған мәліметтер электр желісінің күйін нақты уақыт режимінде бақылау мен визуализациялау үшін және тоқтап қалу немесе қосылу жағдайында желінің әрекетін модельдеу үшін қолданыла алады. PMU енгізудегі қиындықтар технологияның жаңалығында, олардың жұмыс принципі «жабық», ал стандарттауы әлі де төмен деңгейде.

Қалай болғанда да, электр энергиясын беру жүйелері де, мониторинг және модельдеу жүйелері географиялық ақпараттық жүйелер (ГАЖ) арқылы визуализацияны және есепке алуды қажет етеді. Бұл белгілі бір географиялық жерлерде өндірілген және тұтынылатын қуаттарды ескере отырып, республиканың энергетикалық жүйесін кіші жүйелерге саналы түрде аудандастыру үшін қажет. Сондай-ақ, ГАЖ-дан жеткізуші мен тұтынушы арасындағы электр энергиясын берудегі шығынды оңтайландыру міндеттері туралы ақпаратты ескеру керек. Дегенмен, одан басқа, электр желілеріне арналған мұндай ГАЖ жаңа электр станциялары мен электр беру жүйелері үшін инфрақұрылымның құрылысын және іске қосылуын жоспарлауға көмектеседі.

Бұрын сипатталған технологияларды ірі мемлекеттік және корпоративті электр станциялары жағдайында өзекті болып қала беретін классикалық орталықтандырылған электр желілерінде қолдануға болады. Ал жаңартылатын энергия қондырғыларын кеңінен енгізу жеке сектордан электр энергиясын жеткізушілердің көбеюіне әкеледі. Осындай қондырғылардың дамуын ескере отырып, орталықтандырылған жоспарлау нақты уақыт режимінде бақылау жүйелері үшін де шешім қабылдау кезіндегі маңызды кешігулердің ықтималдығын арттырады. Сондықтан ғылыми қауымдастық мониторинг және модельдеу жүйелерін жетілдірумен қатар энергети желілерің орталықсыздандыру қағидаттарын қолдануды ұсынады.

Авторлар әртүрлі деңгейдегі орталықтандырылмаған энергия жүйесін Холон әдісі негізінде оңтайландыру мәселесін тұжырымдады. Сонымен қатар, энергия жүйесінің ГАЖ-ден алынған желілік нысандар арасындағы электр энергиясын беру қашықтықты ескереді. Бұл қашықтық нүкте-объектілер арасындағы ең қысқа қашықтық емес, электр қуаты тұтынушыға өтуі керек барлық электр желілерінің ұзындығы.

Сипатталған тәсілдерді ГАЖ қолданатын эенргия жүйесімен қолдану энергия желісінде не болып жатқанын толық түсіну үшін, төтенше жағдайлар мен фазалық теңгерімсіздіктерге жылдам амал жасау үшін, сондай-ақ желіні одан әрі кеңейту және жаңа нысандар мен инфрақұрылым салуды дұрыс жоспарлау үшін қажет.

Түйін сөздер: интеллектуалды энергия жүйелері, ГАЖ, орталықсыздандыру, оңтайландыру мәселесі, электр жүйелерін модельдеу, тұрақты ток беру жүйелері.

Д.В. Панюкова[1], А.Б. Кайранбаева[2], Г.Б. Нуреисова[3], К.В. Панюков[4]

[1]Университет им.К.И. Сатпаев, Алматы, Казахстан;
[2]Институт ионосферы, Национальный центр космических исследований и технологий, Алматы, Казахстан;
[3]Каспийский университет, Алматы, Казахстан;
[4]Университет ИТМО, Санкт-Петербург, Россия

ИНТЕЛЛЕКТУАЛЬНЫЕ ЭНЕРГОСИСТЕМЫ С ГИС-ТЕХНОЛОГИЯМИ

Аннотация. В современной энергосистеме Казахстана регламентировано наличие автоматизированных систем коммерческого учета электроэнергии для всех энергоснабжающих организаций. Это сделано для поддержки балансирования мощностей на рынке электроэнергии в режиме реального времени. На сегодняшний день такое балансирование – задача сложная, но выполнимая, т.к. большинство энергогенерирующих объектов работают на республиканском или районом уровне и представляют собой станции на традиционном топливе или ГЭС (с высокой предикативностью выработки). При активном внедрении генераторных станций на возобновляемых источниках энергии (ВИЭ) вопрос балансирования энергорынка резко усложняется в связи со стохастическим характером их выработки. Еще большие затруднения возникнут если генераторы на ВИЭ будут по большей части маломощные и в частном владении.

В мире для энергосистем государственного масштаба предлагается ряд подходов для модернизации. Один из них – переход с систем передачи электроэнергии переменного тока на системы передачи постоянного тока. Такой переход позволяет подключать источники на ВИЭ с минимальным комплексом преобразующего оборудования. Но, что более важно, себестоимость и потери передачи электроэнергии на большие расстояния по высоковольтным системам постоянного тока (HVDC) ниже, чем по линиям передач переменного тока. Еще одно их достоинство в возможности подключать производителей и потребителей электроэнергии без предварительного выравнивания их по фазе. Основной сложностью для внедрения подобных систем передачи является дороговизна оборудования для преобразования постоянного тока в переменный. А, учитывая, повсеместное использование сетей переменного тока в нашей республике и во многих других странах мира, это требует существенных капитальных затрат.

Для сетей как постоянного, так и переменного тока основным инструментом управления становятся системы моделирования в реальном времени (RTDS). Такие системы активно внедряются в противоаварийную автоматику и системы управления энергосетями. RTDS позволяют в реальном времени оценить последствия подключения или аварийного отключения одной из фаз и принять оптимальное решение по балансированию энергосистемы разного уровня. При этом за счет частотной характеристики 0-3 кГц достаточно одного инструмента для наблюдения за работой энергосистемы во всем спектре частот. Крупномасштабные цифровые симуляторы реального времени или LSRTDS дают возможность для исследования пуска даже сетей районного масштаба из полностью обесточенного состояния.

Одним из инструментов мониторинга для противоаварийной автоматики являются синхрофазоры (PMU). Эти устройства отправляют информацию в реальном режиме времени о состоянии энергообъектов в концентраторы данных для использования в диспетчерских центрах энергосетей. Полученные данные могут быть использованы для мониторинга и визуализации состояния энергосети в режиме реального времени и моделирования поведения сети при возможных отключениях или подключениях. Сложности внедрения PMU – в новизне технологии, а значит – «закрытости» принципа работы и пока еще низком уровне стандартизации.

В любом случае как системы передачи электроэнергии, так и системы мониторинга и моделирования систем требуют визуализации и учета данных через геоинформационные системы (ГИС). Это необходимо для обоснованного зонирования республиканской энергосистемы на подсистемы, учитывая вырабатываемые и потребляемые мощности в конкретных географических локациях. Так же необходимо принимать в расчет информацию с ГИС для задач оптимизации потерь на передачу электроэнергии между поставщиком и потребителем. Но, кроме этого, такая ГИС для энергосетей может помочь в планировании местоположения постройки и запуска новых энергостанций и инфраструктуры для систем электропередач.

Ранее описанные технологии могут быть использованы и в классической централизованной энергосети, которая остается актуальной в случае больших государственных и корпоративных энергогенерирующих станций.

Тогда как повсеместное внедрение установок на ВИЭ приводит к появлению большого числа потенциальных поставщиков электроэнергии из частного сектора. А, с учетом вероятностного характера выработки таких установок, централизованная диспетчеризация повышает вероятность критических задержек в принятии решений даже для систем мониторинга реального времени. Поэтому параллельно с модернизацией систем мониторинга и моделирования научным сообществом предлагается использовать принципы децентрализации энергосетей.

Авторами сформулирована задача оптимизации для децентрализованной энергосистемы разного уровня на основе метода Холонов. В ней учитывается в том числе и расстояние для передачи электроэнергии между объектами сети, получаемая из ГИС энергосистемы. Такое расстояние представляет собой не кратчайшее расстояние между точками-объектами, а длину всех линий электропередач, по которым электроэнергия должна пройти до потребителя.

Реализация описанных подходов с ГИС энергосистемы даст возможность полного понимания происходящего в сети, оперативного реагирования на аварийные ситуации и фазовые дисбалансы, а также обоснованного планирования дальнейшего расширения энергосети и постройки новых объектов и инфраструктуры.

Ключевые слова: интеллектуальные энергосистемы, ГИС, децентрализация, задача оптимизации, моделирование энергосистем, системы передачи постоянного тока.

Information about authors:

Panyukova Dina Vasilyevna – The Satbayev University, The department of Automation and control, PhD candidate, haleth@mail.ru, https://orcid.org/0000-0002-2567-5106;

Kairanbayeva Ainur Berikkalievna, Institute of the Ionosphere, National Center for Space Research and Technology, Scientific secretary, PhD, kairanbaeva_a@mail.ru, https://orcid.org/0000-0001-9827-4082;

Nurpeissova Gulnara Baibolovna, The Caspian University, Professor, kerey97@mail.ru, https://orcid.org/0000-0003-4642-3829;

Panyukov Kerey Vasilyevich, The ITMO University, master's student, dartm1994@gmail.com, https://orcid.org/0000-0001-5461-7872

REFERENCES

[1] Electric energy of Kazakhstan: key facts. https://www.kegoc.kz/ru/elektroenergetika/elektroenergetika-kazahstana-klyuchevye-fakty. By the date 25.12.2019

[2] Crijns-Graus W., Renewable Energy: Past Trends and Future Growth in 2 Degrees Scenarios, Energy Procedia, 2016, I. 100, pp 14-21.

[3] Abdulrahman A., Santiago B., Omar E., Grain A., Callum M. HVDC Transmission: Technology Review, Market Trends and Future Outlook. Renewable and Sustainable Energy Reviews. Volume 112, September 2019, Pages 530-554.

[4] Andreas V., Lejla H., Adélie B., Line R., Spyros Ch.. Chance-constrained AC optimal power flow integrating HVDC lines and controllability. International Journal of Electrical Power & Energy Systems. Volume 116, March 2020.

[5] Ruslan U., Alexandr G., Ahmed A. Zaki D., Aleksey S., Nikolay R., Mikhail A., Alisher A., Vladimir R., Omer A., Ziad M. Ali, Ahmed I., Raef A., Analysis of application of back-to-back HVDC system in Tomsk electric power system. Energy Reports. Volume 6, November 2020, Pages 438-444

[6] Bing L., Haoran Zh., Shuning G., Shuju H., Digital real-time co-simulation platform of refined wind energy conversion system. International Journal of Electrical Power & Energy Systems. Volume 117, May 2020.

[7] Dalmo C. Silva J., Janaína G. O., Pedro M. de Almeida, Cecilia B. Control of a multi-functional inverter in an AC microgrid – Real-time simulation with control hardware in the loop. Electric Power Systems Research Volume 172, July 2019, Pages 201-212

[8] Chen H, et all. Integration of RTDS with RPG Synchrophasor Applications and Analysis of Simulation Scenarios at Southern California Edison, North America Power Symposium (NAPS) 2012, 9 – 11 September 2012.

[9] Pietro T., David M., Mario L., Davide B., Daniele G., A Tuned Lightweight Estimation Algorithm for Low-Cost Phasor Measurement Units. IEEE Transactions on Instrumentation and Measurement, 2018Volume: 67 , Issue: 5 , P. 1047 - 1057.

[10] Rafiullah K., Kieran M., David L., Sakir S. Design and Implementation of Security Gateway for Synchrophasor Based Real-Time Control and Monitoring in Smart Grid. IEEE Access, 2017, Volume: 5, P. 11626–11644.

[11] Coelho V.N., Cohen M.W., Coelho I.M., Liu N., Guimarães F.G., Multi-agent systems applied for energy systems integration: State-of-the-art applications and trends in microgrids, Applied Energy, 2017, I. 187, pp 820-832.

[12] Abidi M.G., Smida M.B., Khalgui M., Li Zh., Wu N., Multi-agent oriented solution for forecasting-based control strategy with load priority of microgrids in an island mode – Case study: Tunisian petroleum platform. Electric Power Systems Research, 2017, I. 152, pp 411-423.

[13] Panyukova D., Holarchy theory for small-sized power grids // GEOLINKS International Conference on Geoscience. – Athens, Greece, 26-29 March 2019. T.2. pp.123-131.

[14] Son H., Kim Ch., Short-term forecasting of electricity demand for the residential sector using weather and social variables, Resources, Conservation and Recycling, 2017, I. 123, pp 200-207.

NEWS
OF THENATIONAL ACADEMY OF SCIENCES OF THE REPUBLIC OF KAZAKHSTAN
PHYSICO-MATHEMATICAL SERIES
ISSN 1991-346X **https://doi.org/10.32014/2020.2518-1726.47**
Volume 3, Number 331 (2020), 142 – 150

UDK 550.385
IRSTI 37.15.33

O. I. Sokolova, S. N. Mukasheva

Institute of the Ionosphere, National Center for Space Research and Technology, Almaty, Kazakhstan.
E-mail: olgsokolova@yandex.ru; snmukasheva@gmail.com

THE METHODS FOR CALCULATION OF DECLINATION (D) FOR SPACED OF MAGNETIC OBSERVATORIES

Abstract. Calculations of the base values of the geomagnetic declination from the experimental data and from the data computed from various modern geomagnetic field models for spaced of geomagnetic observatories are presented: «Almatinskaya» (AAA) [43.25° N; 76.92° E] Institute of the Ionosphere, Almaty, Kazakhstan; «Kluchi» (NVS) of the Russian Academy of Sciences, Novosibirsk, Russia [54.85° N; 83.23° E]; «Irkutsk» (IRT) of the Institute of Solar-Terrestrial Physics of, Irkutsk, Russia [52.17° N, 104.45° E]. The characteristics of the results of the study of the time course and the spatial distribution of the values of the geomagnetic declination are given. The estimation of accuracy of calculation of geomagnetic declination by modern models of a geomagnetic field is presented. It is shown that the values of geomagnetic declination for spaced of geomagnetic observatories AAA, NVS, IRT from observed observational data change their values by years, so for AAA and NVS there is an increase, and for IRT the decrease in the values of geomagnetic declination. For NVS and AAA, geomagnetic declination moves eastward, and for IRT in the west. It is shown that the performed calculations of geomagnetic declination for two models International Geomagnetic Reference Field and World Magnetic Model for the coordinates AAA, NVS and IRT agree well with each other over the years, with small differences in seconds; the geomagnetic declination values for AAA increase in years with a gradient of about 0.6 min/year, for NVS decrease with a gradient of about 1.6 min/year, for IRT decrease with a gradient of about -4.5 min/year; model-calculated geomagnetic declination for AAA and NVS have an eastern direction, and for IRT, the western direction.

Key words: declination, the experimental data, magnetic observatory, world magnetic models.

1. Introduction. The geomagnetic declination is of fundamental economic technical and practical importance which defines great interest to this element of the geomagnetic field in many sectors of the national economy and in science. The geomagnetic declination D is designed to orientate the movement of objects in space and used to solve various scientific and production problems, e.g. during construction of nuclear and hydraulic power plants, power lines, undergrounds, for preparation of air navigation charts. The magnetic declination changes with time and in space, of which account must be taken during accurate determination of magnetic azimuths of headings. To obtain reliable information about the declination D for any area it is necessary to have the data on declination at several ground points (stations) [1,2]. The best option is to resume an observation program at the secular variation points (SVP) within the Republic of Kazakhstan. But because the resumption of the SVP involves some difficulties, calculations of D using the geomagnetic field models can be used, e.g., IGRF (International Geomagnetic Reference Field), and/or other more detailed models. To solve the problems of high-precision navigation of a moving object it is necessary to know two types of initial data at each trajectory point: 1) position of an object (current coordinates); 2) direction of movement. The first type of data, current coordinates of an object, is provided using the satellite navigation system. The second type of data, direction of movement, is usually determined based on measurement of azimuth with respect to position of the north geomagnetic pole. The coordinates of geomagnetic pole do not remain constant – they drift over time, hence, an error is introduced into the azimuth value. Position of the north magnetic pole (NMP) according to Olsen model CHAOS (A Model of Earth's Magnetic Field derived from CHAMP), confirmed by ground surveys is

shown in figure 1 [3]. Forecast of the NMP position for the next few years is made based on the assumption that the average speed and direction of the NMP movement did *not change after 2007*. Direction of geomagnetic pole relative to geographic one at each point of the Earth is determined by the value of the geomagnetic field declination, and this value is measured in geomagnetic observatories with high precision by state-of-the-art magnetometers. Multi-year measurements of declination D, which are conducted by magnetic observatories, show that the magnetic declination varies over time. For example, in the observatory of Pleschenitsy (Belarus) the declination increased from D = 5˚ 02.7' to D = 7˚ 07.7' (1960÷2006); in the observatory of Belsk (Poland) the declination increased from D = 2˚ 04.2' to D = 4˚ 37.7' (1996÷2005); in Irkutsk (Russia) the declination from the east in 1887 D = +2˚ 24' crossed a zero value in 1934 moved westward in 2001 D = -2˚ 24' [1].

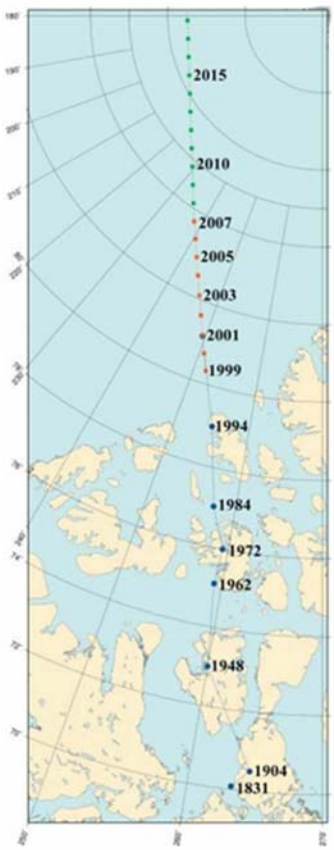

Figure 1 – The NMP position according to direct measurements (blue circles), data computed from the geomagnetic field model CHAOS (red cubes), forecasted position (green cubes) for the next few years [3]

Accordingly, account is taken of the changes in the magnetic declinations during precision navigation to reduce errors during determination of azimuth. All modern navigation charts contain information on the amount of declination of the geomagnetic field. Due to the geomagnetic pole drift these charts should be updated. In addition, for precision navigation of aircrafts, the leading international airports regularly take measurements of the geomagnetic field declination. When it is impossible to obtain reliable information on declination D for any area under field conditions, computation of the geomagnetic declination from geomagnetic field models can be used. The geomagnetic field models make it possible to calculate magnetic field of the Earth and its components in certain coordinates in view of various sources of the field [4-14]. There are several such models, let us provide the most well-known ones of these: International Geomagnetic Reference Field (IGRF) http://www.ngdc.noaa.gov/IAGA/. IGRF model represents the main field without external sources. Coefficients used in IGRF models are based on various data, such as: geomagnetic measurements taken by observatories; aerial photography data [9-12]; World Magnetic Model (WMM) http://www.geomag.bgs.ac.uk. The WMM is the standard model used by the U.S. Department of Defense, the U.K. Ministry of Defence, the North Atlantic Treaty Organization

(NATO) and the International Hydrographic Organization (IHO) when solving scientific-production problems [13,14]. The goal of this work is to describe the methods for calculation of geomagnetic declination (D) for spaced of magnetic observatories.

2. Calculations of declination D base values based on experimental data obtained at spaced geomagnetic observatories

Magnetic observatories provide information about the geomagnetic field using the data of variation stations, the sensors of which are relative instruments with rather narrow measuring range. Absolute values of variations are occasionally determined by carrying out the fundamental observations through which reveal the base values in nT of zero stresses in the measuring channels of digital stations [15-21]. For example, the adopted values in the observatory of Irkutsk are the intervals of constant base values with jerks between these intervals. In the observatory of Novosibirsk, the observable data are approximated by smoothing spline (between jerks). In the geomagnetic observatory "Almatinskaya", obtaining of "adopted" base values is the approximation of initial data by some function that most optimally reflects the behavior of the base lines. The parametric approximation is used, the function type is determined in advance, the objective is to select the optimum coefficients. Base values are computed using the following equations: X=FcosIcosD, Y=FcosIsinD, Z=FsinI,

where X – northern component, Y – eastern component, Z – vertical component, F – total field intensit (vector field amplitude), I – inclination (the angle between the field vector and the horizontal plane measured downwards from horizontal axis). Calculations based on the results of observations in observatories also consist of calculation of the average angles and determination of the declination in angular minutes using the equation:

$$D_i = \text{atan}\left(\frac{Yi}{Xi}\right),$$

where D – declination of the geomagnetic field (the angle of the horizontal component the field from true north, measured clockwise).

To obtain actual values of declination D three spaced geomagnetic observatories, IMOs members – "Almatinskaya" geomagnetic observatory [43.25°N; 76.92°E] of the Institute of Ionosphere, Almaty, RK; "Kluchi" geophysical observatory of the Russian Academy of Sciences (RAS), Novosibirsk, RF [54.85°N; 83.23°E]; "Irkutsk" geomagnetic observatory of the Institute of Solar-Terrestrial Physics of the RAS, Irkutsk, RF [52.17°N, 104.45°E].

In "Almatinskaya" geomagnetic observatory (IAGA code AAA), observations of declination D are made by Lemi-203 ferrobprobe declinometer based on 3T2KP theodolite. To obtain absolute values of the geomagnetic field from variation data it is required to add the values of basic levels of variometers to variations. At Novosibirsk complex magnetic ionospheric station ("Kluchi" geophysical observatory) (IAGA code NVS), declination D observations are conducted by ferroprobe (declinometers-inclinometers) magnetometers based on non-magnetic Theo020B and 3T2KP theodolites. The observational technique for declination D is standard. Elements used in computation of the average annual values of declination D for geophysical observatory NVS are components X, Y, Z of the geomagnetic field. In "Irkutsk" geomagnetic observatory (IAGA code IRT), observations of declination D are made by THEO-010A and Lemi-203 ferroprobe declinometers/inclinometers. Elements used in computation of the average annual values of declination D for IRT are H, D, Z (H-horizontal component; D-declination; Z-vertical component of the geomagnetic field). Actual values of D obtained using the data of geomagnetic observatories AAA, NVS, IRT for the period of 2005-2017 are shown in table 1.

Thus, the actual values of geomagnetic declination D for spaced geomagnetic observatories "Almatinskaya", "Kluchi", "Irkutsk" for the period 2005-2017 were found as a result of calculations. Let us note that the obtained values of declination D for NVS and AA are positive, and values of declination D for IRT are negative. This suggests that declinations D for Novosibirsk and Almaty move eastward and declinations D for Irkutsk move westward. The declination calculation results based on observatories' observed data show changes in values D by years, thus, there was an increase in values D for AAA and NVS and decrease for IRT.

Table 1 – Average annual values of geomagnetic declination D obtained from experimental data at geomagnetic observatories AAA, NVS, IRT

Year	AAA The Republic of Kazakhstan (43.25°N;76.92°E)		NVS Russia (54.85°N;83.23°E)		IRT Russia (52.17°N;104.45°E)	
	D deg min	Elements	D deg min	Elements	D deg min	Elements
2005	4 46.6	XYZ	8 26.5	XYZ	-2 48.7	DHZ
2006	4 47.5	XYZ	8 23.9	XYZ	-2 53.4	DHZ
2007	4 47.8	XYZ	8 22.2	XYZ	-2 57.5	DHZ
2008	4 49.2	XYZ	8 20.6	XYZ	-3 02.0	DHZ
2009	4 51.2	XYZ	8 18.9	XYZ	-3 06.6	DHZ
2010	4 52.6	XYZ	8 17.7	XYZ	-3 11.4	DHZ
2011	4 52.9	XYZ	8 16.2	XYZ	-3 15.6	DHZ
2012	4 57.0	XYZ	8 16.2	XYZ	-3 16.8	DHZ
2013	5 0.0	XYZ	8 16.2	XYZ	-3 25.2	DHZ
2014	5 3.6	XYZ	8 16.2	XYZ	-3 28.8	DHZ
2015	5 5.4	XYZ	8 16.2	XYZ	-3 32.4	DHZ
2016	5 7.2	XYZ	8 15.0	XYZ	-3 39.0	DHZ
2017	5 9.0	XYZ	8 13.8	XYZ	-3 47.4	DHZ

3. Calculations of declination D from the modern models of the geomagnetic field for spaced geomagnetic observatories

It is known that the general geomagnetic field is composed of several magnetic fields generated by various sources. These are the main field which is formed by the sources in the Earth's liquid outer core, it changes very slowly; the field of magnetic anomalies of the Earth's crust, the changes are very slow; the external fields caused by currents in the ionosphere and magnetic sphere of the Earth, the changes are very rapid; the field of electric currents in the Earth's crust and Earth's external mantle, currents are formed during changes in the external fields, the changes are rapid; ocean currents also have their effect. The modern models of the magnetic field make it possible to calculate slow (secular) variations without regard for very rapid changes caused by solar activity. The modern models also do not take into account the magnetic anomalies. But because the magnetic anomalies are few, and the majority of the main components of the geomagnetic field are subject to slow (secular) variations, the accuracy of geomagnetic parameters computed from models is quite high. Thus, accuracy in computations of the geomagnetic declination obtained by IGRF and WMM models is about 0.5° (30') [17, 19]. In view of the foregoing, two models of the geomagnetic field were picked to calculate the declination D for spaced geomagnetic observatories. The average annual values of declination D for geomagnetic observatory AAA [43.25°N; 76.92°E], geophysical observatory NVS [54.85°N; 83.23°E] and geomagnetic observatory IRT [52.17°N; 104.45°E] were computed with IGRF and WMM models for the period of 2005-2017.

Table 2 shows the values of declination D for geomagnetic observatories AAA, NVS, IRT received from computations using two models IGRF and WMM for the period of 2005-2017. Both models showed that D for AAA increase with a gradient of about 0.6 min/year, positive values of D point to eastward declination for calculation site coordinates. The values of magnetic declinations for NVS observatory decrease with a gradient of about 1.6 min/year, positive values of declination D point to eastward declinations for calculation site coordinates. The values of geomagnetic declinations for IRT reduce with a gradient of about -4.5 min/year, the negative values of D point to westward declination for calculation site coordinates.

Thus, the average annual values of geomagnetic declinations D (2005-2017) for coordinates of AAA, NVS and IRT observatories computed with two models (IGRF and WMM) correlate well with each other by years, with minor variances in seconds. Model calculations also showed that the average annual values of geomagnetic declinations D for geomagnetic observatory AAA increase by years with a gradient of about 0.6 min/year, for geomagnetic observatory NVS decrease with a gradient of about 1.6 min/year, for geomagnetic observatory IRT decrease with a gradient of about -4.5 min/year. The geomagnetic declinations for AAA and geomagnetic observatory NVS are eastern (positive) and geomagnetic declinations for IRT are western (negative).

Table 2 – Model calculated average annual values of D for geomagnetic observatories AAA, NVS, IRT for the period of 2005-2017

Year	AAA The Republic of Kazakhstan (43.25°N;76.92°E)		NVS Russia (54.85°N;83.23°E)		IRT Russia (52.17°N;104.45°E)	
	IGRF D deg min	WMM D deg min	IGRF D deg min	WMM D deg min	IGRF D deg min	WMM D deg min
2005	4 45.7	4 46.2	8 40.0	8 40.0	-2 54.3	-2 52.7
2006	4 46.3	4 46.9	8 38.3	8 38.3	-2 58.7	-2 57.0
2007	4 46.9	4 47.6	8 36.5	8 36.5	-3 03.2	-3 01.7
2008	4 47.6	4 48.2	8 34.7	8 34.8	-3 07.6	-3 06.2
2009	4 48.2	4 48.9	8 32.9	8 33.0	-3 12.1	-3 10.7
2010	4 48.9	4 49.7	8 31.2	8 31.3	-3 16.6	-3 15.2
2011	4 49.7	4 50.3	8 29.9	8 29.6	-3 20.6	-3 19.6
2012	4 53.5	4 54.9	8 30.9	8 30.5	-3 24.5	-3 23.6
2013	4 55.7	4 57.1	8 30.7	8 30.4	-3 28.3	-3 27.5
2014	4 57.8	5 0.2	8 30.5	8 30.2	-3 32.2	-3 35.9
2015	4 59.9	5 0.9	8 30.2	8 30.3	-3 36.1	-3 39.5
2016	5 2.4	5 3.5	8 30.7	8 30.6	-3 38.9	-3 42.9
2017	5 4.9	5 6.2	8 31.2	8 31.0	-3 41.6	-3 46.5

4. Comparative analysis of the results of D declination calculation based on experimental geomagnetic data and various modern models of the geomagnetic field

Experimentally calculated values of declination D show that the geomagnetic declination varies in space most strongly. Thus, values of declination D for various coordinates may differ relative to each other by 1.5-2 times. For example, for coordinates of "Almatinskaya" observatory D= 4˚46.6', and for coordinates of "Kluchi" observatory D =8˚26.5' (table 1). The values of geomagnetic declinations D found as a result of calculations using IGRF and WMM models (table 2) also show that D may vary significantly at spaced ground points.

The geomagnetic declination D also varies over time. Analysis of data received from observatories' observations showed that for the period of 2005-2017 the values of geomagnetic declinations D for geomagnetic observatory AAA increased from 4˚46.6' in 2005 to 5˚09.0' in 2017; for the same period the values D for NVS reduced from 8˚26.5' to 8˚13.8'; D for geomagnetic observatory IRT went down from -2˚48.7' in 2005 to -3˚47.4' in 2017 (table 1). According to the data obtained based on model calculations, the values of geomagnetic declinations D for geomagnetic observatory AAA increased by 4.0 min (IGRF) and 4.1 min (WMM) (table 2); for the same period D for geomagnetic observatory NVS reduced by 10.1 min (IGRF) and by 10.4 min (WMM) (table 2); D for IRT reduced by 26.3 min (IGRF) and by 26.9 min (WMM) (table 2). Let us note that the values of geomagnetic declinations D obtained as a result of computation from IGRF and WMM models correlate well with the data obtained by observatory's observations (table 1).

It is known that per each 1 km of the line length (topographic map) deviation of 1˚ gives 17.5m. Consequently, deviation of 0.2÷4.0 min gives 0.06÷1.16 m; 4.0÷6.0 min − 1.16÷1.75 m; 13.0÷15.0 min − 3.8÷4.4 m [1,2]. Thus, calculations of declinations D for spaced points using IGRF and WMM models result in insignificant variances of about 0.06÷4.4 m from actual observatory data. The geomagnetic declinations D obtained based on WMM model more accurately reflect the real picture of changes D, since model calculated declinations D are more close to the values calculated based on observatory's observations. The above given calculations of D confirm high accuracy of D calculation based on IGRF and WMM models. For example, accuracy of magnetic declinations received based on this model for coordinates of observatory AAA is up to 4 min (0.07˚), for observatory NVS is up to 15 minutes (0.25˚), for observatory IRT is up to 6 min (0.1˚).

5. Conclusion. Thus, the average annual values of the geomagnetic declinations D were obtained for spaced geomagnetic observatories "Almatinskaya", "Kluchi", "Irkutsk" for the period of 2005-2017. The results of declination calculations based on observatories' observed data show changes in values D by years, and so, there was an increase for AAA and NVS and decrease of the values of the geomagnetic

declination D for IRT. The geomagnetic declinations move eastward for NVS and AAA and westward for IRT. Performed calculations of the geomagnetic declinations D using two models IGRF and WMM for the period of 2005-2017 for coordinates AAA, NVS and IRT showed that the values D correlate well with each other by years, with minor variances in seconds; the values of the geomagnetic declinations for AAA increase by years with a gradient of about 0.6 min/year, for NVS decrease with a gradient of about 1.6 min/year, for IRT decrease with a gradient of about -4.5 min /year; model calculated geomagnetic declinations for AAA and NVS are directed eastward and for IRT are directed westward. Comparison analysis of experimental and model calculated values D showed that the values D for spaced objects obtained based on IGRF and WMM models correlate well with the values D calculated based on observatory's observations. Spatial and temporal heterogeneity of the geomagnetic declinations was confirmed. The values of the geomagnetic declinations D obtained based on experimental observatory data and computations from IGRF and WMM models show that D may vary considerably at spaced ground points by 1.5–2 times relative to each other. For example, for coordinates of "Almatinskaya" observatory D=4˚46.6', and for coordinates of "Kluchi" observatory D = 8˚26.5'. The geomagnetic declination D also varies with time. The values of magnetic declinations obtained from observatory observations show that for the period of 2005-2017 the values of the geomagnetic declinations D for AAA increased; for the same period for NVS and IRT reduced. According to the data received based on model calculations, the values of the geomagnetic declinations D for AAA increased by 4.0 min (IGRF) and by 4.1 (WMM); for the same period for NVS D went down by 10.1 (IGRF) and by 10.4 (WMM); for IRT D went down by 26.3 min (IGRF) and by 26.9 min (WMM). The WMM model of the magnetic field more accurately reflects the real picture of the changes in the geomagnetic declinations, since the values of the geomagnetic declinations D obtained from computations based on it are more close to actual observatory data. The values D obtained from computations based on IGRF also have minor discrepancies with the actual observatory values D. Data analysis showed that the accuracy of calculation based on IGRF and WMM models is very high, thus, the accuracy of the magnetic declination in these models for coordinates of observatory AAA is up to 4 min (0.07˚), for observatory NVS is up to 15 min (0.25˚), for observatory IRT is up to 6 min (0.1˚). Hence, it might be advisable to use both models IGRF and WMM for calculations of D in any areas (except for abnormal ones), when it is impossible to measure declinations D with a site visit. However, it is worth noting that the models of the magnetic field reduce the accuracy of calculated geomagnetic parameters over the years (by the end of a time interval given in the models).

The work was performed under project PH 0118PK00799 as part of special purpose scientific and technical program O.0799.

О. И. Соколова, С. Н. Мукашева

Ионосфера институты, Ұлттық ғарыштық зерттеулер мен технологиялар орталығы, Алматы, Қазақстан

КЕҢІСТІКТІК ТАРАТЫЛҒАН МАГНИТТІК ОБСЕРВАТОРИЯЛАР ҮШІН ГЕОМАГНИТТІ КЕМУДІ (D) ЕСЕПТЕУ ӘДІСТЕРІ

Аннотация. Геомагнитті ауытқудың экономикалық-техникалық және практикалық маңызы зор, бұл халық шаруашылығының көптеген салаларында және ғылымда геомагнитті өрістің осы элементіне үлкен қызығушылықты анықтайды. D геомагниттік төмендеу кеңістікте объектілердің қозғалысын бағдарлау үшін қызмет етеді және әртүрлі ғылыми және өндірістік міндеттерді шешу кезінде, мысалы, атом және гидроэлектростанцияларын, электр беру желілерін, метрополитендерді салу кезінде, аэронавигациялық карталарды жасау үшін пайдаланылады. Магниттік төмендеу уақыт ағымымен және кеңістікте өзгереді, бұл бағыттардың магниттік азимуттарын нақты анықтау кезінде ескеру қажет. D төмендеу туралы сенімді ақпарат алу үшін кез келген аумақ үшін бірнеше жер пункттерінде (нүктелерінде) төмен түсу жөніндегі деректер болуы қажет. Ең жақсы нұсқа-Қазақстан Республикасының аумағында ғасырлық жүріс пункттеріндегі бақылау бағдарламасын жаңарту. Бірақ ғасыр жүрісі пункттерін жаңарту белгілі бір қиындықтармен байланысты болғандықтан, геомагнитті өріс үлгілері бойынша D есептерін, мысалы Igrf (International Geomagnetic Reference Field) геомагнитті өріс халықаралық анықтамалық моделі және/немесе басқа да егжей-тегжейлі модельдер бойынша пайдалануға болады.

Қозғалыстағы объектінің жоғары дәлдіктегі навигация міндеттерін шешу үшін қозғалыс траекториясының әрбір нүктесінде бастапқы деректердің екі түрін білу қажет: 1) объектінің орналасқан жері

(ағымдағы координаттар); 2) қозғалыс бағыты. Деректердің бірінші Түрі, объектінің ағымдағы координаттары спутниктік навигациялық жүйелердің көмегімен қамтамасыз етіледі. Екінші деректер типі, қозғалыс бағыты, әдетте, солтүстік геомагниттік полюстің жағдайына қатысты азимутты өлшеу негізінде анықталады. Геомагнитті полюстің координаттары тұрақты болып қала бермейді-уақыт өте келе дрейфуют, тиісінше азимут көлеміне қате енгізіледі. Олсен CHAOS (CHAOS (A Model of Earth's Magnetic Field derived from CHAMP) моделіне сәйкес солтүстік магниттік полюстің орны.

Геомагнитті полюс бағыты жердің әрбір нүктесіндегі географиялық жағынан геомагнитті өрістің төмендеу шамасымен анықталады және бұл шама жоғары дәлдікпен геомагнитті обсерваторияларда қазіргі магнитометрлермен өлшенеді.

Осы жұмыстың мақсаты кеңістіктік-таратылған магниттік обсерваториялар үшін геомагнитті кемуді (D) есептеу әдісін сипаттау болып табылады.

Эксперименталды деректер бойынша және кеңістіктік-таратылған геомагнитті обсерваториялар үшін әртүрлі қазіргі заманғы модельдер бойынша есептелген геомагнитті өріс деректері бойынша геомагнитті ауытқудың базалық мәндерінің есептері ұсынылған: «Алматинская» (AAA) [43.25°N; 76.92°E] Ионосфера институты, Алматы қ., ҚР; Ресей Ғылым академиясының (РҒА) «Ключи» (NVS) геофизикалық обсерваториясы, Новосибирск қ., РФ [54.85°N; 83.23°E]; Күн-Жер физикасы институтының «Иркутск» (IRT), Иркутск қ., РФ [52.17°N, 104.45°E].

"Алматинская" геомагнитті обсерваториясында (IAGA коды AAA) 3Т2КП теодолит базасында Lemi-203 феррозонды деклинометрмен D қисаюын бақылауды жүргізеді. Новосибирск кешенді магнитті-ионосфералық станциясында ("Ключи" геофизикалық обсерваториясы) (IAGA коды NVS) D қисаюын бақылауды феррозонды (деклинометрлер-инклинометрлер) магнитті Theo020B және 3Т2КП теодолиттер базасында магнитометрлермен жүргізеді. Геомагнитті обсерваториясы "Иркутск" (IAGA коды IRT) жүргізеді және бақылау өзін D феррозондовыми деклинометрами/инклинометрами THEO-010A және Lemi-203. 2005-2017 жылдар аралығында AAA, NVS, IRT геомагнитті обсерваторияларының деректері бойынша алынған D нақты мәндері.

Геомагниттік ауытқу мәндерінің уақытша жүрісін және кеңістіктік таралуын зерттеу нәтижелеріне сипаттама берілді. Геомагнитті өрістің қазіргі заманғы модельдерімен геомагнитті ауытқуын есептеу дәлдігін бағалау ұсынылған. Бақыланған обсерваторлық деректер бойынша AAA, NVS, IRT кеңістіктік - таратылған геомагниттік обсерваториялар үшін геомагнитті ауытқулардың мәндері жылдар бойынша өз мәнін өзгертетіні көрсетілген, сондықтан AAA және NVS үшін ұлғаю, ал IRT үшін геомагнитті ауытқу мәндерінің азаюы орын алады. NFS және AAA үшін геомагниттік ауытқулар шығыс бағытта, ал IRT үшін батыс бағытта жылжиды. AAA, NVS және IRT координаттары үшін igrf және WMM екі үлгісі бойынша геомагнитті ауытқулардың орындалған есептері секундта аз айырмашылықтары бар жылдар бойынша өзара жақсы келісіледі; AAA үшін геомагнитті ауытқулардың мәндері шамамен 0.6 мин/жыл градиентімен жылдар бойынша ұлғаяды, NVS үшін шамамен 1.6 мин/жыл градиентімен азаяды, IRT үшін ретті градиентпен азаяды-4.5 мин/жыл; AAA және IRT үшін модельді есептелген геомагнитті NVS шығыс бағыты бар, ал IRT батыс үшін.

Түйін сөздер: геомагнитті төмендеу, эксперименттік деректер, әлемдік магниттік модельдер.

О. И. Соколова, С. Н. Мукашева

Институт ионосферы, Национальный центр космических исследований
и технологий, г. Алматы, Казахстан

МЕТОДЫ РАСЧЕТА ГЕОМАГНИТНОГО СКЛОНЕНИЯ (D) ДЛЯ ПРОСТРАНСТВЕННО- РАЗНЕСЕННЫХ МАГНИТНЫХ ОБСЕРВАТОРИЙ

Аннотация. Геомагнитное склонение имеет важное экономико-техническое и практическое значение, что определяет большой интерес к этому элементу геомагнитного поля во многих отраслях народного хозяйства и в науке. Геомагнитное склонение D служит для ориентировки движения объектов в пространстве и используется при решении различных научных и производственных задач, например, при строительстве атомных и гидроэлектростанций, линий электропередач, метрополитенов, для составления аэронавигационных карт. Магнитное склонение изменяется с течением времени и в пространстве, что необходимо учитывать при точном определении магнитных азимутов направлений. Для получения достоверной информации о склонении D для любой территории необходимо иметь данные по склонению в нескольких пунктах (точках) местности. Лучший вариант – это возобновление на территории Республики Казахстан программы наблюдений на пунктах векового хода. Но так как возобновление пунктов векового хода связано с определенными трудностями, то можно использовать расчеты D по моделям геомагнитного

поля, например, Международная Справочная Модель Геомагнитного Поля IGRF (International Geomagnetic Reference Field) и/или другие более детальным моделям.

Для решения задач высокоточной навигации движущегося объекта необходимо знать в каждой точке траектории движения два типа исходных данных: 1) местоположение объекта (текущие координаты); 2) направление движения. Первый тип данных, текущие координаты объекта, обеспечивается с помощью спутниковых навигационных систем. Второй тип данных, направление движения, как правило, определяется на основе измерения азимута относительно положения северного геомагнитного полюса. Координаты геомагнитного полюса не остаются постоянными – дрейфуют со временем, соответственно вносится ошибка в величину азимута. Положение северного магнитного полюса, согласно модели Олсена CHAOS (A Model of Earth's Magnetic Field derived from CHAMP, подтвержденной наземными исследованиями.

Направление на геомагнитный полюс относительно географического в каждой точке Земли определяется величиной склонения геомагнитного поля, и эта величина с высокой точностью измеряется в геомагнитных обсерваториях современными магнитометрами.

Целью настоящей работы является описание метода расчета геомагнитного склонения (D) для пространственно-разнесенных магнитных обсерваторий.

Представлены расчеты базовых значений геомагнитного склонения по экспериментальным данным и по данным рассчитанным по различным современным моделям геомагнитного поля для пространственно-разнесенных геомагнитных обсерваторий: «Алматинская» (AAA) [43.25°N; 76.92°E] Институт ионосферы, г. Алматы, Республика Казахстан; геофизическая обсерватория «Ключи» (NVS) Российской академии наук, г. Новосибирск, Россия [54.85°N; 83.23°E]; геомагнитная обсерватория «Иркутск» (IRT) Института Солнечно-земной физики Российской академии наук, г. Иркутск, Россия [52.17°N, 104.45°E].

В геомагнитной обсерватории «Алматинская» (IAGA код AAA) проводят наблюдения склонения D феррозондовым деклинометром Lemi-203 на базе теодолита 3Т2КП. В Новосибирской комплексной магнитно-ионосферной станции (геофизическая обсерватория «Ключи») (IAGA код NVS) наблюдения склонения D проводят феррозондовыми (деклинометрами-инклинометрами) магнитометрами на базе немагнитных теодолитов Theo020B и 3Т2КП. В геомагнитной обсерватории «Иркутск» (IAGA код IRT) проводят наблюдения склонения D феррозондовыми деклинометрами/инклинометрами THEO-010A и Lemi-203. Реальные значения D, полученные по данным геомагнитных обсерваторий AAA, NVS, IRT за период 2005-2017 гг.

Дана характеристика результатам исследования временного хода и пространственного распределения значений геомагнитного склонения. Представлена оценка точности расчета геомагнитного склонения современными моделями геомагнитного поля. Показано, что значения геомагнитных склонений для пространственно- разнесенных геомагнитных обсерваторий AAA, NVS, IRT по наблюдаемым обсерваторским данным меняют свои значения по годам, так для AAA и NVS происходит увеличение, а для IRT уменьшение значений геомагнитного склонения. Для NVS и AAA геомагнитные склонения смещаются в восточном направлении, а для IRT в западном. Показано, что выполненные расчеты геомагнитных склонений по двум моделям (Международная Справочная Модель Геомагнитного Поля (IGRF) и Всемирная Модель Магнитного Поля (WMM)) для координат AAA, NVS и IRT, хорошо согласуются между собой по годам, имея небольшие различия в секундах; значения геомагнитных склонений для AAA увеличиваются по годам с градиентом порядка 0.6 мин/год, для NVS уменьшаются с градиентом порядка 1.6 мин/год, для IRT уменьшаются с градиентом порядка -4.5 мин/год; модельно рассчитанные геомагнитные склонения для AAA и NVS имеют восточное направление, а для IRT западное.

Ключевые слова: геомагнитное склонение, экспериментальные данные, мировые магнитные модели.

Information about authors:

Sokolova Olga Ivanovna, Institute of the Ionosphere, National Center for Space Research and Technology, Head of the sector of lithospheric-ionospheric relations, olgsokolova@yandex.ru, https://orcid.org/0000-0003-1426-9302;

Mukasheva Saule Nurmukhambetova, Institute of the Ionosphere, National Center for Space Research and Technology, leading researcher, Candidate of Physical and Mathematical Sciences, snmukasheva@gmail.com, https://orcid.org/0000-0002-1609-4430

REFERENCES

[1] Karataev G.I., Karagodina O.I. (2008) Spatio-temporal characteristics of magnetic declination on the territory of Belarus and practical aspects of its monitoring, Litasphere, 2: 127-135 (in Russ.).

[2] Cherepin V.I., Soloviev A.N. (2005) Applied issues of engineering geodesy. Part I. Engineering and graphic work on a topographic and geodetic map (plan). SPbGLTA 25-81(in Russ.).

[3] *Olsen N., Lühr H., Sabaka T. J., Mandea M., Rother M., Tøffner-Clausen L., Choi S.* (2006) CHAOS-A model of Earth's magnetic field derived from CHAMP, Ørsted, and SAC-C magnetic satellite data, Geophys. J. Int., 166: 67-75. DOI:10.1111/j.1365246X.2006.02959.x.

[4] Maus S., Yin F., Lühr H., Manoj C., Rother M., Rauberg J., Michaelis I., Stolle C., Müller R. D. (2008) Resolution of direction of oceanic magnetic lineations by the sixthgeneration lithospheric magnetic field model from CHAMP satellite magnetic measurements, Geochem. Geophys. Geosyst., 9, Q07021. DOI:10.1029/2008GC001949

[5] Merrill R.T., McElhinny M.W., McFadden P.L. (1996) The magnetic field of the earth: paleomagnetism, the core and the deep mantle. San Diego: Academic Press. NATO Standardization Agency, 2011. STANAG 7172 Use of Geomagnetic Models (2nd ed).

[6] Friis-Christensen E., Lühr H., Hulot G. (2006) Swarm: A constellation to study the Earth's magnetic field, Earth Planets Space, 58: 351-358. DOI:10.1186/BF03351933

[7] Lühr H., Maus S. (2010) Solar cycle dependence of quiet-time magnetospheric currents and a model of their near-Earth magnetic fields, Earth Planets Space, 62: 843-848. DOI:10.5047/eps.2010.07.012

[8] Thomson A. W. P., Lesur V. (2007) An Improved Geomagnetic Data Selection Algorithm for Global Geomagnetic Field Modelling, Geophysical Journal International, 169(3): 951-963. DOI: 10.1111/j.1365-246X.2007.03354.x.

[9] Finlay C. C., Maus S., Beggan C. D., Bondar T. N., Chambodut A., Chernova T. A., Chulliat A., Golovkov V. P., Hamilton B., Hamoudi M., Holme R., Hulot G., Kuang W., Langlais, V. Lesur, F. J. Lowes, H. Luhr, S. Macmillan, M. Mandea, S. McLean, C. Manoj, M. Menvielle B., Michaelis I., Olsen N., Rauberg J., Rother M., Sabaka T. J., Tangborn A., Toffner-Clausen L., Thebault E., Thomson A. W. P., Wardinski I., Wei Z., Zvereva T. I. (2010) International Geomagnetic Reference Field: the eleventh generation, Geophys. J. Int., 183(3): 1216-1230.

[10] Alken P., Maus S., Chulliat A., Manoj C. (2005) NOAA/NGDC Candidate Models for the 12th generation, International Geomagnetic Reference Field, Earth Planets Space, 67:68. DOI: 10.1186/s40623-015-0215-1.

[11] Lesur V., Macmillan S., Thomson A. (2005) The BGS magnetic field candidate models for the 10th generation IGRF. Earth, Planets and Space, 57(12): 1157-1163. DOI: 10.1186/BF03351899.

[12] Hamilton B.,. Ridley V. A, Beggan C. D., Macmillan S. (2015) The BGS magnetic field candidate models for the 12th generation IGRF, Earth, Planets and Space, 67(1). DOI: 10.1186/s40623-015-0227-x.

[13] Maus S., Macmillan S., McLean S., Hamilton B., Thomson A., Nair M., and Rollins C. (2010) The US/UK World Magnetic Model for 2010-2015. //NOAA Tech. Report NESDIS/NGDC.

[14] Chulliat A., Macmillan S., Alken P., Beggan C., Nair M., Hamilton B., Woods A., Ridley V., Maus S., Thomson A. (2015) The US/UK World Magnetic Model for 2015-2020: Technical Report, National Geophysical Data Center, NOAA. DOI: 10.7289/V5TB14V7.

[15] Sokolova O.I., Andreev A.A., Burlakov G.V., Kachusova O.L., Kryakunova O.N, Levin Yu. N., Nikolaevskiy N.F. (2016) System for Recording Variations of Earth's Magnetic Field at the "Alma-Ata" Geomagnetic Observatory. J. Ind. Geophys. Union, Special Volume, 2: 76-79.

[16] Kryakunova O., Yakovets A., Monstein C., Nikolayevskiy N., Zhumabayev B., Gordienko G., Andreyev A., Malimbayev A., Levin Yu., Salikhov N., Sokolova O., Tsepakina I. (2015) Space Weather Studies Using Ground-based Experimental Complex in Kazakhstan, Sun and Geosphere, 10/2: 177 -181 ISSN 1819-0839 Special Edition "2015 UN/Japan Workshop on Space Weather"

[17] Gordin V.M. (2004) Essays on the history of the geomagnetic measurements. M.: IPE RAS, 9-51(in Russ.).

[18] INTERMAGNET Technical Reference Manual (2011) Ver. 4.5 Edinburg, UK.

[19] Nechaev S. (2006) Guide to stationary geomagnetic observations. Irkutsk: Publishing House of the Institute of Geography SB RAS, 35-71(in Russ.).

[20] Jankowski J., Sucksdoff C. (1996) Guide for magnetic measurements and observatory practice, Published by IAGA. Warszawa. Poland, 86-118.

[21] Minasyants G.S., Minasyants T.M., Vdovichenko V.D., Bibossinov A. G. (2019) Properties of ultraviolet emission at development of solar flares, News of the National Academy of sciences of the Republic of Kazakhstan, 3 (325):56-64. https://doi.org/10.32014/2019.2518-1726.24

NEWS
OF THENATIONAL ACADEMY OF SCIENCES OF THE REPUBLIC OF KAZAKHSTAN
PHYSICO-MATHEMATICAL SERIES
ISSN 1991-346X **https://doi.org/10.32014/2020.2518-1726.48**
Volume 3, Number 331 (2020), 151 – 159

UDC 51-74, 519.876.5

N.S. Sydyk, A. Zh. Bibossinov, S.M. Nurakynov

Institute of Ionosphere JSC "NCSRT", Almaty, Kazakhstan.
E-mail: nurmahambet.s@gmail.com; bibossinov@gmail.com; nurakynov@gmail.com

MATHEMATICAL MODEL OF THE GEOMECHANICAL STATE OF THE UPPER PART OF THE EARTH'S CRUST BASED ON SALOME-MECA

Abstract. This article provides a brief description of the Saloma-meca software platform. An approach to the analysis of the geodynamic state of the upper crust of urban areas based on Saloma-meca is described. A generalized block diagram of the work of software and mathematics is built. Geometric models of the earth's crust have been developed for the city of Almaty. Test calculations of the distribution of SSS for the untouched mountain range were carried out according to the averaged data of soil densities based on Saloma-meca for the initial approximation in calculating the stress-strain state of the earth's crust in Almaty.

Keywords: Geodynamics, geomechanics, SSS, Saloma-meca, mathematical model, deformation.

Introduction. The stress-strain state (SSS) of the earth's crust is studied mainly in connection with the solution of the problem of assessing the stability of the earth's crust during an earthquake. The parameters of the Earth's crust SSS are one of the main indicators in the construction of a seismic hazard forecast map. To construct maps of the parameters of the SSS, a digital representation of such data as the relief of the day surface and the relief of the sole of the earth's crust, tectonic faults, the field of gravity anomalies, velocities of individual lithosphere blocks, etc. is necessary. The possibility of obtaining this information is related to the achievements of modern space technologies, primarily ground-space monitoring, radar imaging, the development of primary and thematic processing of remote sensing data (RS) and the accumulated experience of theoretical and practical work. Based on these digital data, it is possible to build a reliable geomechanical model of the earth's crust of individual sections.

Software package. The object of research is the geomechanical condition of soils near urban structures, as well as the territories of Almaty. Figure 1 shows a generalized block diagram of the operation of software and mathematics. The physical process is the ongoing movement of soil near urban structures. Research, in general terms, is carried out in two interrelated areas - modeling and observation.

By modeling we mean the consideration of the physical model of the process and the construction of its mathematical representation using the equations of mathematical physics. The mathematical model is based on the well-known equations of mechanics of deformable solids to describe the geodynamic state of the earth's crust. The physical and mathematical models used in the software are models of elastic and elastic-plastic environment.

Under the supervision, it is assumed the collection, processing and analysis of GPS data from global and local networks, processing of radar satellite images, data on soil structures, data on building structures, geomechanical parameters, strength and density data.

GAMIT and GLOBK are the software packages for the primary processing of high-precision GPS observations for monitoring the geodynamic state of the lithosphere.

At the initial stage, these experimental data are used to adjust the mathematical model of the physical process and formulate the problem - to determine the initial approximation and boundary conditions.

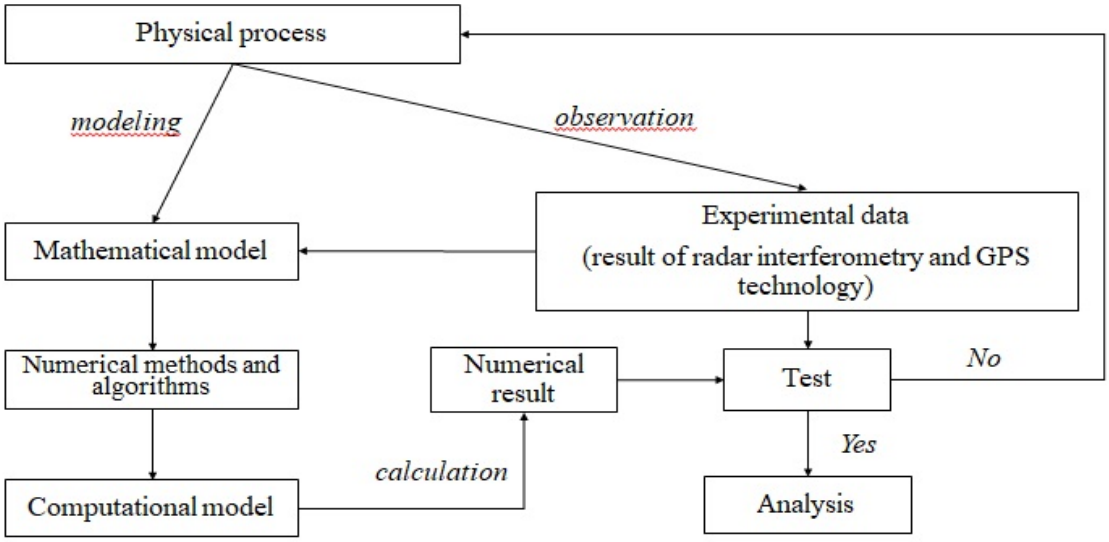

Figure 1 - A generalized block diagram of the operation of software and mathematics

After constructing and adjusting the mathematical model for the basic equations of mathematical physics, a numerical model is built, the initial-boundary-value problem is solved, where the calculation area is the corresponding grid representation of the earth's crust of the studied regions.

At this stage, additional grid modeling programs are used - SALOME - MECA, OpenFOAM, OpenCFD, FLAC3D.

After obtaining the numerical results - the two-dimensional and three-dimensional distribution of the main parameters of the stress-strain state of the upper part of the earth's crust, the data are checked with the original experimental data and analyzed.

SALOME-MECA software platform. SALOME is a general structure for pre and post processing. Code_aster - for solving (solver) of thermomechanical problems [1]. Salome-Meca is the integration of the code_aster solver in the Salome platform, including the AsterStudy module for computer-aided design.

Salome-Meca is an open platform that can integrate scientific solutions for modeling various physical fields and implement a wide range of computer simulations. The tasks are to analyze the behavior of the model with sufficient accuracy and performance to help in making decisions on the issues raised. Salome-Meca initially comes with CAD modeling, mesh algorithms, 3D visualization and advanced features for processing simulation data.

Key features. Numerical analysis [2] of complex industrial systems requires scientists and engineers to integrate most fields of physics, such as materials science, solid mechanics and structural dynamics, fluid physics and thermohydraulics, nuclear physics and radiation, and electromagnetism. These domains can be combined into a single modeling environment, the Salome-Meca platform. The main features of the Salome-Meca platform are:

- Designing the geometric representation of physical systems (CAD modeling) and the associated discrete model (mesh functions for solvers of finite elements or finite volumes);
- Ability to integrate domain-specific solvers into normalized software components with standard interfaces to facilitate the integration of various physical domains;
- Monitoring of computational workflows defined as graphs of distributed software components, including CAD modeling, solutions for specific areas and data processing components;
- Analysis of modeling data, in particular using visualization of physical fields resulting from computational work processes.

In this context, the key point of the platform is the use of standard data models to describe physical concepts for numerical analysis and to ensure interaction between software components. For example, the MED data model defines a normalized representation for describing geometry cells and fields of physical modeling values. This data model is a key feature of the platform. It comes with a software implementation (MED file library) for saving files and exchanging simulation data between components.

SALOME Mesh and visualization components offer MED format interfaces for importing or exporting data. Domain-specific solvers that interact with SALOME, it is recommended that you use the MED format for input and output files. This configuration leads to a high level of associativity between software components for building modeling workflows.

In addition to processing and visualizing grid and field data, the SALOME platform contains additional modules designed for advanced data analysis:

Data assimilation and optimization environment, for example, for recalibrating model parameters by comparing simulation data with experimental measurements (ADAO module).

Distribution of uncertainties [3] in the modeling workflow, for example, to estimate the uncertainty of the resulting simulation data, taking into account the given uncertainty of the input parameters (OPENTURNS module).

Development of numerical experimental plans, for example, parametric modeling, by examining the indicated area of the space of modeling parameters (PARAMETRIC module).

The theoretical basis. A continuous and homogeneous medium is capable of experiencing deformations of only two types - a change in volume and a change in shape. Volumetric deformations are caused by normal stresses and ultimately lead to separation. Changes in shape caused by shear stresses lead to shear.

The relationship between stresses and strains is most often assumed to be linear, i.e. corresponding to Hooke's law. A power relationship between stress and strain is used in the nonlinear theory of elasticity. These are the main essence and quality of the model of a continuous medium, on the basis of which the mathematical theory of the mechanics of a deformable body is built without taking into account time and temperature factors.

Here are some relationships and dependencies that will be used later to describe the stress-strain state of the rock mass using the continuum mechanics. These relations are studied in detail in courses in the theory of elasticity and plasticity, and are used in rock mechanics, which allows us to confine ourselves to a brief presentation of the basic formulas of the theory of stresses and strains.

A necessary condition for the applicability of these relations in their practical use is the fulfillment of the hypothesis of continuity of the medium, which consists in the continuity of stresses and displacements, as functions of the coordinates of a point [4, 5].

At each point of a continuous medium, a stress-strain state is characterized by a symmetric stress tensor (1.1), a symmetric strain tensor (1.2), and a displacement vector (1.3):

$$\boldsymbol{\sigma} = \begin{bmatrix} \boldsymbol{\sigma_{xx}} & \boldsymbol{\sigma_{xy}} & \boldsymbol{\sigma_{xz}} \\ \boldsymbol{\sigma_{yx}} & \boldsymbol{\sigma_{yy}} & \boldsymbol{\sigma_{yz}} \\ \boldsymbol{\sigma_{zx}} & \boldsymbol{\sigma_{zy}} & \boldsymbol{\sigma_{zz}} \end{bmatrix}; \tag{1.1}$$

$$\boldsymbol{\varepsilon} = \begin{bmatrix} \boldsymbol{\varepsilon_{xx}} & \boldsymbol{\varepsilon_{xy}} & \boldsymbol{\varepsilon_{xz}} \\ \boldsymbol{\varepsilon_{yx}} & \boldsymbol{\varepsilon_{yy}} & \boldsymbol{\varepsilon_{yz}} \\ \boldsymbol{\varepsilon_{zx}} & \boldsymbol{\varepsilon_{zy}} & \boldsymbol{\varepsilon_{zz}} \end{bmatrix}; \tag{1.2}$$

$$\vec{\boldsymbol{u}} = \begin{bmatrix} \boldsymbol{u} \\ \boldsymbol{v} \\ \boldsymbol{w} \end{bmatrix}; \tag{1.3}$$

For relatively small strains, the strain tensor is expressed in terms of the displacement vector as follows:

$$\boldsymbol{\varepsilon_{ij}} = \frac{\boldsymbol{1}}{\boldsymbol{2}}\left(\frac{\boldsymbol{\partial u_i}}{\boldsymbol{\partial x_j}} + \frac{\boldsymbol{\partial u_j}}{\boldsymbol{\partial x_i}}\right);\ \boldsymbol{i = x, y, z;} \tag{1.4}$$

called the Cauchy equations.

The movement of an element of a rock mass is determined by the forces applied to it, calculating it we obtain differential equations of motion:

$$\begin{cases} \rho \dfrac{\partial^2 u}{\partial t^2} = \dfrac{\partial \sigma_{xx}}{\partial x} + \dfrac{\partial \sigma_{xy}}{\partial y} + \dfrac{\partial \sigma_{xz}}{\partial z} + \rho F_x; \\ \rho \dfrac{\partial^2 v}{\partial t^2} = \dfrac{\partial \sigma_{yx}}{\partial x} + \dfrac{\partial \sigma_{yy}}{\partial y} + \dfrac{\partial \sigma_{yz}}{\partial z} + \rho F_y; \\ \rho \dfrac{\partial^2 w}{\partial t^2} = \dfrac{\partial \sigma_{zx}}{\partial x} + \dfrac{\partial \sigma_{zy}}{\partial y} + \dfrac{\partial \sigma_{zz}}{\partial z} + \rho F_z; \end{cases} \quad (1.5)$$

where ρ is the density of the medium; F - volume forces, t - time.

The above equations are general relations of the continuum mechanics, regardless of its physical and mechanical properties. These equations are not enough to describe the process of deformation of the medium. Additional relationships are required between stresses, strains, their velocities and a number of other factors, which are called equations of state of the medium. The mechanical equations of state of bodies, including all of the above parameters, are quite complex. Therefore, they are usually limited to the simplest models of the medium, which describe the basic properties and main features of the mechanical processes. Based on them, a further refinement of the deformation process is made.

We give some of the equations of the mechanical states of inelastic media that are most common in the theory of plasticity and rock mechanics. The simplest are the equations of the deformation theory of plasticity, connecting the components of stress and strain,

$$\begin{cases} \varepsilon_x - \dfrac{1}{3}\theta^e = \psi(\sigma_{xx} - \sigma);\ \varepsilon_{yz} = \psi\sigma_{yz}; \\ \varepsilon_y - \dfrac{1}{3}\theta^e = \psi(\sigma_{yy} - \sigma);\ \varepsilon_{xz} = \psi\sigma_{xz}; \\ \varepsilon_z - \dfrac{1}{3}\theta^e = \psi(\sigma_{zz} - \sigma);\ \varepsilon_{xy} = \psi\sigma_{xy}; \end{cases} \quad (1.6)$$

where Θe = 3 (1-2ν) σ / E; ν, E — Poisson's ratio and elastic modulus of the medium, respectively; ψ is a certain function of the invariants of tensors and deviators of stresses and strains, σ is the average (or hydrostatic) pressure at a point.

Note that the volumetric strain in this theory is elastic and is related to the mean pressure σ by Hooke's law.

Due to its simplicity, these equations are widely used to solve engineering problems in the study of rock deformation. For ψ = (1- ν) / E they turn into Hooke's law and are essentially its generalization to nonlinear media.

Let us present in general form the basic equations of the theory of elasticity in an invariant form [6], which are used to determine the stress-strain state of rocks.

The equation of motion in invariant form:

$$\rho \frac{\partial^2 \vec{u}}{\partial t^2} = \mathbf{div}(\sigma) + \rho \vec{F}; \quad (1.7)$$

Cauchy equations:

$$\varepsilon = \mathbf{sym}(\nabla \vec{u}) \equiv \frac{1}{2}\left(\nabla \vec{u} + (\nabla \vec{u})^{\mathrm{T}}\right); \quad (1.8)$$

The equation of state of elastic media (Hooke's Law), expressed in terms of the Lame coefficients:

$$\sigma = \lambda\, \mathbf{trace}(\varepsilon)\mathbf{I} + 2\mu\varepsilon; \quad (1.9)$$

Where

$$\lambda = \frac{E\nu}{(1+\nu)(1-2\nu)}, \mu = \frac{E}{2(1+\nu)}, K = \frac{E}{3(1-2\nu)}; \quad (1.10)$$

E is the elastic modulus (Young); ν is the Poisson's ratio; K is the volume expansion module.

The system of equations (1.1) - (1.3) includes 15 equations and 15 unknowns (6 components of the stress tensor, 6 components of the strain tensor, 3 components of the displacement vector), and is a closed system.

The general statement of the problem of determining the stress-strain state of rocks is as follows [7]. Given the boundary conditions (the displacement field or the velocity vector field) and the given initial approximation (SSS from the untouched mountain massif), determine the components of the stress and strain tensors at each point of the study area.

The initial approximation is the SSS of the untouched mountain range, calculated according to the following formulas.

$$\boldsymbol{\sigma_{zz} = \gamma H, \sigma_{xx} = \sigma_{yy} = k\gamma H;} \quad (1.11)$$

where γ is the weight per unit volume of the rock mass, k is the lateral pressure coefficient. Under the assumption of a hydrostatic stress distribution, k = 1; with non-hydrostatic distribution - 0 <k <1; under the assumption of A.N. Dinnik –k = ν / (1 - ν).

Methodology for calculating the SSS of the upper horizons of the earth's crust. The general methodology for determining the SSS of the upper horizons of the earth's crust is as follows.

The calculation area is determined (in this case, Almaty with an area of 36x36 km^2, to a depth of 5 km.). A geometric model of the studied region is constructed, as shown in figure 2.

As the boundary conditions, GPS data is used, the initial approximation is the SSS of the untouched mountain range.

Further, the system of equations (1.1) - (1.3) is solved by the iterative method. At each iteration step, equation (1.1) is first solved - from this distribution of the components of the strain tensor, the displacements at each point in the volume are calculated. Next, from the Cauchy equations (1.2), we find the values of the strain tensor [8, 9]. From the equation of state (1.3), the new distribution of the stress tensor values is found back. This iteration process is repeated until the difference between the results of the iteration is not small enough.

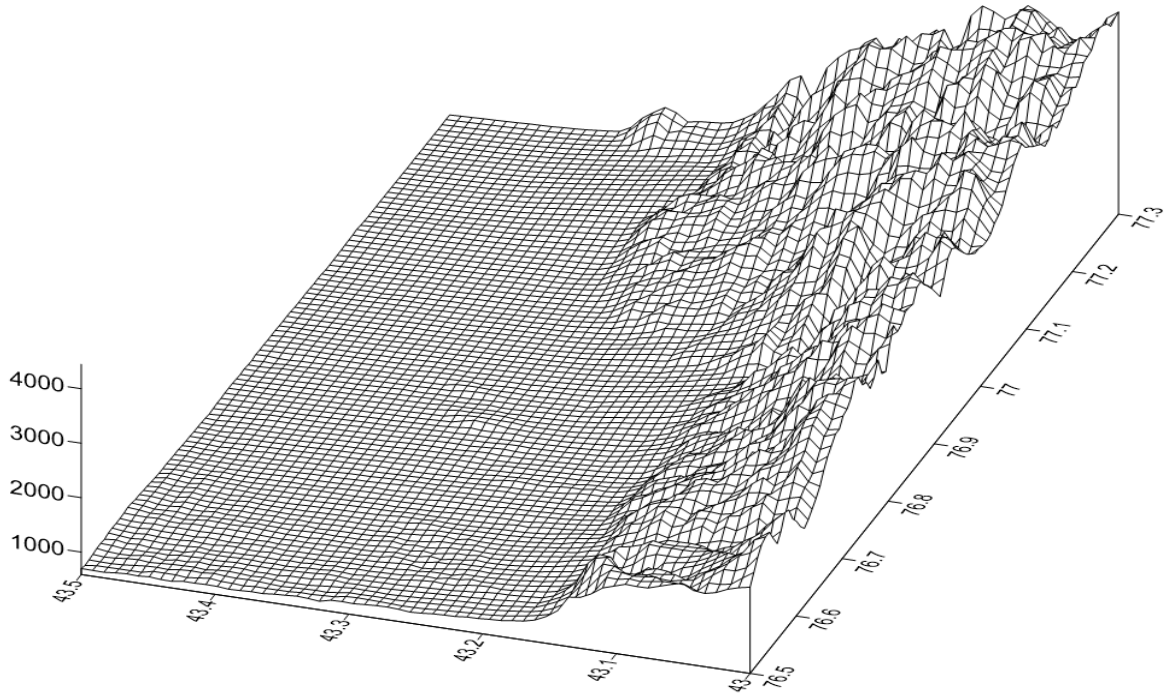

Figure 2 - Curved grid of the calculation area.
Territory of Almaty 36x36 km^2

Results and its discussion. Geometric models of the earth's crust have been developed for the city of Almaty.

The basic methods for studying the deformation and strength of rocks are analyzed. Expressions are determined for the components of the deformation tensor of the upper horizons of the earth's crust using an inhomogeneous field of displacements of the earth's surface according to GPS observations.

Test calculations of the SSS distribution for the untouched mountain massif, that is, of its own weight (Figure 3), were carried out according to the averaged data of soil densities for the initial approximation when calculating the stress-strain state of the earth's crust in Almaty.

It was also calculated the distribution of stress from its own weight in a slice of land at around 0 meters above sea level (figure 4).

Modeling of the stress-strain state of the earth's crust can be used to develop a monitoring system in the region in order to predict the geodynamic state of the earth's crust and major seismic events. The main difference from traditional approaches is the identification of anomalous zones by the distribution of geodynamic parameters, as a result of geomechanical modeling using a database of geological and geophysical data.

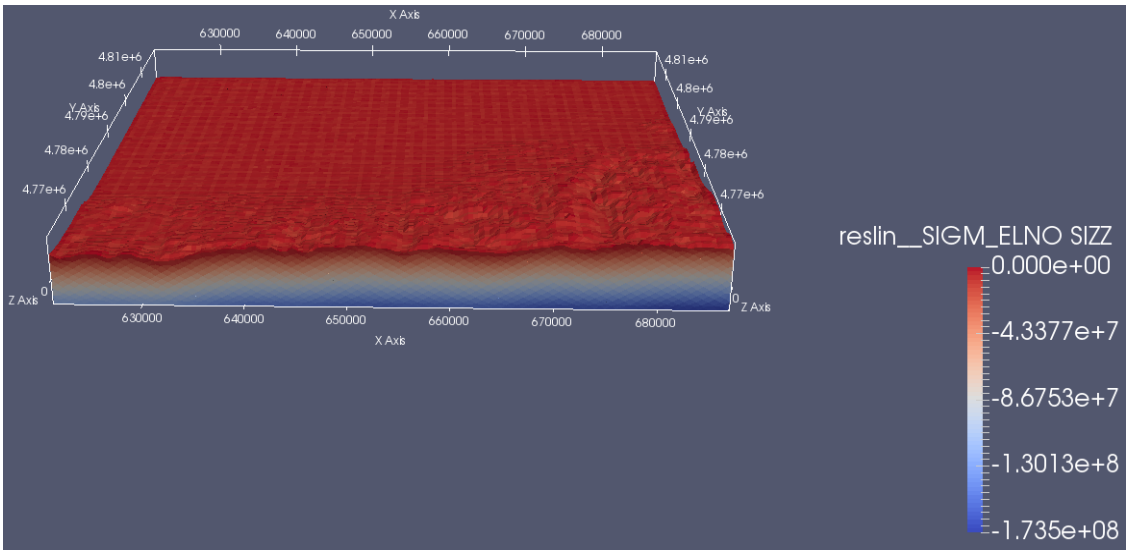

Figure 3 - Setting the first approximation of stress from its own weight

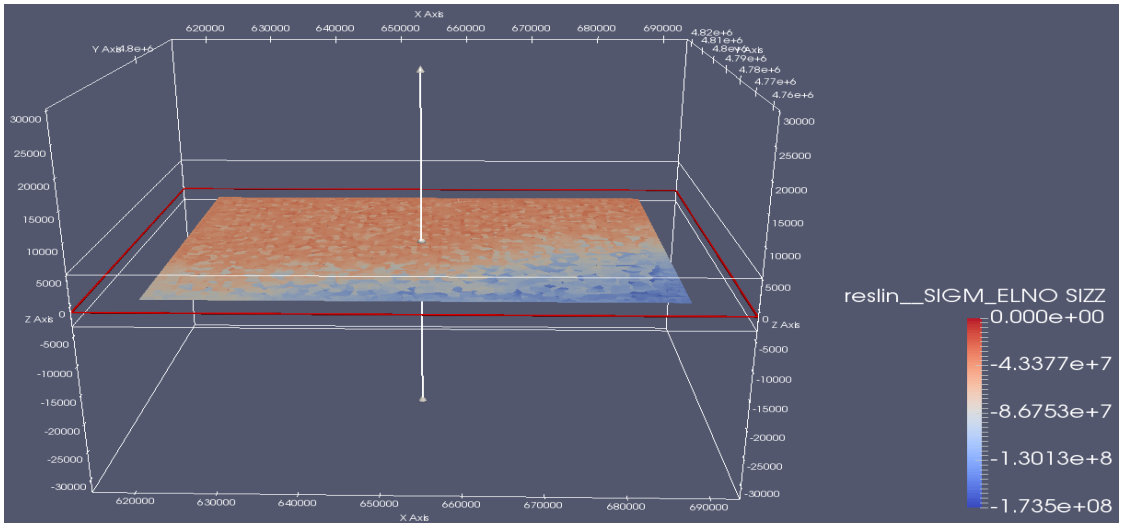

Figure 4 - Stress distribution at a depth of 0 m

Conclusion. Mathematical models of the stress-strain state that describe the geodynamic state of the earth's crust over time and the development of science become more accurate and correct, and the Salome-Meca software platform has already contributed. The program is not familiar to a large number of specialists and is only gaining popularity, but even so it is one of the best multifunctional complexes with free access. In general, the development of the system of geodynamic and geophysical monitoring of the earth's crust is necessary both for a deeper study and understanding of the processes occurring in it, and for predicting the further development of these processes in time, and for assessing seismic hazard in the studied region. Estimates of the stress-strain state of the earth's crust based on mathematical models of the geomechanical state using modern seismicity data, complex experimental data of representative GPS monitoring, will advance the problem of practical earthquake prediction.

These works are carried out with financial state support in the framework of the scientific and technical project “Ground-based space monitoring of technogenic processes in urban areas and assessment of the status of large technical facilities”.

Н.Қ. Сыдық, А.Ж. Бибосынов, С. М. Нұрақынов

Ионосфера институты, «ҰҒЗТО» АҚ, Алматы, Қазақстан

SALOME-MECA НЕГІЗІНДЕГІ ЖЕР ҚЫРТЫСЫНЫҢ ЖОҒАРҒЫ БӨЛІГІНІҢ ГЕОМЕХАНИКАЛЫҚ ЖАҒДАЙЫНЫҢ МАТЕМАТИКАЛЫҚ МОДЕЛІ

Аннотация. Жер қыртысының геодинамикалық жай-күйін сипаттайтын кернеулі-деформацияланған күйдің математикалық модельдері уақыт ағымымен және ғылымның дамуымен дәлірек және дұрыс болып келеді және Salome-Meca бағдарламалық платформасыда бұл салаға өз үлесін қосты. Бағдарлама көп мамандарға таныс емес және енді қарқын алып келе жаса да, ең үздік тегін, қолжетімді көпфункционалды кешендердің бірі болып табылады. Salome-Meca түрлі физикалық салаларды модельдеу үшін ғылыми шешімдерді біріктіріп, компьютерлік симуляцияның кең спектрін іске асыра алады. Salome-Meca платформасының негізгі ерекшеліктері мыналар болып табылады: физикалық жүйелердің геометриялық көрінісін жобалау (CAD-модельдеу) және онымен байланысты дискретті модель (соңғы элементтердің немесе соңғы көлемдердің торларының функциялары); түрлі физикалық домендерді біріктіруді жеңілдету үшін стандартты интерфейстермен нормаланған бағдарламалық компоненттерге доменге тән торларды біріктіру мүмкіндігі.; CAD-модельдеуді, нақты облыстар үшін шешімдерді және деректерді өңдеу компоненттерін қоса алғанда, бөлінген бағдарламалық компоненттердің графиктері ретінде анықталған есептеулердің жұмыс процестерін қадағалау; есептеу жұмыс процестерінің нәтижесінде туындайтын физикалық өрістерді визуализациялау арқылы модельдеу деректерін талдау.

Бұл мақалада Saloma-meca негізінде қала құрылыстарына жақын жерлердің, сондай-ақ Алматы қаласы аумағының жер қыртысының жоғарғы бөлігінің геодинамикалық жай-күйін талдау әдісі сипатталған. Жалпы алғанда, талдау өзара байланысты екі бағытта жүзеге асырылады – модельдеу және бақылау.

Тұтас және біртекті орта тек екі түрдің деформациясын сынауға қабілетті – көлемнің өзгеруі және пішіннің өзгеруі. Көлемді деформациялар қалыпты кернеудің әсерінен туындайды және ақырында үзуге әкеледі. Жанама кернеулерден туындайтын пішіннің өзгеруі кесікке әкеледі.

Кернеулер мен деформациялар арасындағы байланыс көбінесе сызықты, яғни Гука Заңына сәйкес қабылданады. Кернеу мен деформация арасындағы дәрежелік тәуелділік серпімділіктің сызықсыз теориясында қолданылады. Уақыт пен температура факторларын ескермей Деформацияланатын дене механикасының математикалық теориясы құрылатын тұтас орта моделінің негізгі мәні мен сапасы осындай.

Тұтас ортаның әрбір нүктесіндегі кернеулі-деформацияланған жай-күй кернеудің симметриялы тензорымен, деформацияның симметриялы тензорымен және орын ауыстыру векторымен сипатталады.

Салыстырмалы түрде кіші деформациялар кезінде деформация тензоры Коши теңдеулері деп аталатын орын ауыстыру векторы арқылы көрінеді. Тау жыныстары массивінің қозғалысы дифференциалды қозғалыс теңдеулерін есептей отырып, оған қоса берілген күштермен анықталады. Жоғарыда келтірілген теңдеулер оның физика-механикалық қасиеттеріне қарамастан тұтас орта механикасының жалпы арақатынасы болып табылады. Бұл теңдеулер ортаны деформациялау процесін сипаттау үшін жеткіліксіз. Кернеулер, деформациялар, олардың жылдамдықтары және орта жағдайының теңдеулері деп аталатын басқа да бірқатар факторлар арасындағы қосымша қатынастар қажет.

Кернеу теңдеулері, деформация және орнын ауыстыру жүйелері 15 теңдеуді және 15 белгісізді (6 кернеу тензоры компоненті, 6 деформация тензоры компоненті, 3 орын ауыстыру векторының компоненті) қамтиды және тұйық жүйе болып табылады. Тау жыныстарының кернеулі-деформацияланған күйін анықтау

мақсатының жалпы қойылымы былайша көрінеді. Берілген шекаралық жағдайлар кезінде (жылжу өрісі немесе жылдамдық векторының өрісі) және осы бастапқы жақындау кезінде зерттелетін аумақтың әрбір нүктесіндегі кернеу мен деформация тензорларының компоненттерін анықтау. Бастапқы жақындағанда, нөлдік емес тау-кен массивінің КДК алынады.

Жер қыртысының жоғарғы көкжиектері учаскелерінің КДК анықтаудың жалпы әдістемесі келесідей: есептеу аймағы анықталады (бұл жағдайда Алматы қаласы ауданы 36х36 км^2, 5 км тереңдікке дейін). Зерттелетін аймақтың геометриялық моделі құрылады. Шекаралық шарттар ретінде GPS деректері пайдаланылады, бастапқы жақындау арқылы қозғалмайтын тау массивінің КДК алынады.

Бұдан әрі итерациялық әдіспен кернеу, деформация және орнын ауыстыру теңдеулерінің жүйесі шешіледі. Итерацияның әрбір қадамында бірінші болып кернеу теңдеуі шешіледі-бұл бөлуден деформация тензорының компоненті көлемнің әрбір нүктесінде орын ауыстырулар есептеледі. Бұдан әрі – Коши теңдеулерінен деформация тензорының мәні болады. Күй теңдеуінен - кері кернеу тензоры мәндерінің жаңа бөлінуі анықталады. Бұл итерация процесі итерация нәтижелері арасындағы айырмашылық аз болғанша қайталанады.

Алматы қ.жер қабатының кернеулі-деформацияланған жағдайын есептеу кезінде бастапқы жақындау үшін Saloma-meca негізінде топырақ тығыздығының орташаланған деректері бойынша күш түсірілмеген тау-кен алқабы үшін кернеулі-деформацияланған жағдайды бөлудің тестілік есептері жүргізілді. Сондай-ақ, теңіз деңгейінен 0 метр белгідегі жер кесіндісінде өз салмағынан кернеуді бөлу есептелді.

Жер қыртысының кернеулі-деформацияланған жай-күйін модельдеу жер қыртысының геодинамикалық жай-күйін және ірі сейсмикалық оқиғаларды болжау мақсатында өңірдегі мониторинг жүйесін дамыту үшін пайдаланылуы мүмкін. Дәстүрлі тәсілдерден негізгі ерекшелігі геологиялық-геофизикалық деректер базасын пайдалана отырып геомеханикалық үлгілеу нәтижесі ретінде геодинамикалық параметрлерді бөлу бойынша аномальды аймақтарды анықтау болып табылады.

Түйін сөздер: Геодинамика, геомеханика, КДК, Saloma-meca, математикалық модель, деформация.

Н.К. Сыдык, А.Ж. Бибосынов, С. М. Нуракынов

Институт ионосферы АО «НЦКИТ», Алматы, Казахстан

МАТЕМАТИЧЕСКАЯ МОДЕЛЬ ГЕОМЕХАНИЧЕСКОГО СОСТОЯНИЯ ВЕРХНЕЙ ЧАСТИ ЗЕМНОЙ КОРЫ НА ОСНОВЕ SALOME-MECA

Аннотация. Математические модели напряжённо-деформированного состояния, описывающие геодинамическое состояние земной коры, с течением времени и развитием науки становятся более точными и корректными и программная платформа Salome-Meca уже внесла свой вклад. Программа не знакома большому количеству специалистов и только набирает популярность, но даже при этом является одним из лучших многофункциональных комплексов с бесплатным доступом. Salome-Meca может интегрировать научные решения для моделирования различных физических областей и реализовывать широкий спектр компьютерных симуляций. Основными особенностями платформы Salome-Meca являются: проектирование геометрического представления физических систем (CAD-моделирование) и связанной с ним дискретной модели (функции сетки для решателей конечных элементов или конечных объемов); возможность интегрировать специфичные для домена решатели в нормализованные программные компоненты со стандартными интерфейсами, чтобы облегчить объединение различных физических доменов; наблюдение за рабочими процессами вычислений, определенными как графики распределенных программных компонентов, включая CAD-моделирование, решения для конкретных областей и компоненты обработки данных; анализ данных моделирования, в частности с использованием визуализации физических полей, возникающих в результате вычислительных рабочих процессов.

В данной статье описан подход к анализу геодинамического состояния верхней части земной коры вблизи городских сооружений, а также территорий г.Алматы на основе Saloma-meca. Анализ, в общих чертах, осуществляется в двух взаимосвязанных направлениях – моделирование и наблюдение.

Сплошная и однородная среда способна испытывать деформации только двух видов – изменение объема и изменение формы. Объемные деформации вызываются действием нормальных напряжений и приводят, в конечном счете, к отрыву. Изменения формы, вызываемые касательными напряжениями, приводят к срезу.

Связь между напряжениями и деформациями чаще всего принимается линейной, т.е. соответствующей закону Гука. Степенная зависимость между напряжениями и деформацией используется в нелинейной теории упругости. Таковы основная суть и качество модели сплошной среды, на базе которой строится математическая теория механики деформируемого тела без учета факторов времени и температуры.

Напряженно-деформированное состояние в каждой точке сплошной среды характеризуется симметричным тензором напряжений, симметричным тензором деформации и вектором перемещении.

При относительно малых деформациях тензор деформации выражается через вектор перемещений называемые уравнениями Коши. Движение элемента массива горных пород определяется приложенными к нему силами, подсчитав которые получим дифференциальные уравнения движения. Приведенные выше уравнения являются общими соотношениями механики сплошной среды независимо от ее физико-механических свойств. Этих уравнений недостаточно для описания процесса деформирования среды. Необходимы дополнительные соотношения между напряжениями, деформациями, их скоростями и рядом других факторов, которые называют уравнениями состояния среды.

Системы уравнений напряжений, деформации и перемещении включают в себя 15 уравнений и 15 неизвестных (6 компонент тензора напряжении, 6 компонент тензора деформации, 3 компоненты вектора перемещений), и являются замкнутой системой. Общая постановка задачи определения напряженно-деформированного состояния горных пород выглядит следующим образом. При заданных граничных условий (поле перемещении или поле вектора скорости) и данном начальном приближений определить компоненты тензоров напряжений и деформации в каждой точке исследуемой территорий. Начальным приближением принимается НДС нетронутого горного массива.

Общая методика определения НДС участков верхних горизонтов земной коры выглядит следующим образом: определяется область вычисления (в данном случае г.Алматы с площадью 36х36 км^2, до глубин 5 км). Строится геометрическая модель исследуемого региона. В качестве граничных условий используются данные GPS, начальным приближением берется НДС нетронутого горного массива.

Далее итерационным методом решается система уравнений напряжений, деформации и перемещении. В каждом шаге итерации первым решается уравнение напряжений – от данного распределения компонент тензора деформации просчитываются перемещения в каждой точке объема. Далее – из уравнений Коши находятся значения тензора деформации. От уравнения состояния – обратно находится новое распределение значений тензора напряжений. Этот процесс итерации повторяется до состояния, когда разница между результатами итерации не будет достаточно малой.

Были проведены тестовые расчеты распределения НДС для не тронутого горного массива, по осредненным данным плотностей грунтов на основе Saloma-меса для начального приближения при расчете напряженно-деформированного состояния земной коры г. Алматы. Также было просчитано распределение напряжения от собственного веса в срезе земли на отметке 0 метров над уровнем моря.

Моделирование напряженно-деформированного состояния земной коры могут быть использованы для развития системы мониторинга в регионе в целях прогноза геодинамического состояния земной коры и крупных сейсмических событий. Основным отличием от традиционных подходов является выявление аномальных зон по распределению геодинамических параметров как результат геомеханического моделирования с использованием базы геолого-геофизических данных.

Ключевые слова: Геодинамика, геомеханика, НДС, Saloma-меса, математическая модель, деформация.

Information about authors:

Sydyk N.K. Institute of Ionosphere, JSC NCSRT, Almaty, Kazakhstan, head of the Cartography and GIS sector, PhD doctor student; nurmahambet.s@gmail.com; https://orcid.org/0000-0003-1429-2393;

Bibossinov A.Zh., Institute of Ionosphere, JSC NCSR, Almaty, Kazakhstan, **Deputy chairman of the board, PhD;** bibossinov@gmail.com**;** http://orcid.org/0000-0002-5219-4279;

Nurakynov S.M., Institute of Ionosphere, JSC NCSRT, Almaty, Kazakhstan, head of the Cartography and GIS Laboratory; nurakynov@gmail.com; https://orcid.org/0000-0001-9735-7820

REFERENCES

[1] [Electronic resource]. URL: https://code-aster.org/spip.php?rubrique2

[2] [Electronic resource]. URL: https://code-aster.org/UPLOAD/DOC/Formations/01-overview-2.pdf

[3] [Electronic resource]. URL: https://code-aster.org/UPLOAD/DOC/Formations/02-salome.pdf

[4] Nikolaevsky V.N. The defining equations of plastic deformation of granular media / Applied Mathematics and Mechanics, 1971. N.35. №6. P. 1070-1082 (in Russian).

[5] Biot M.A. Mechanics of incremental deformations. N.Y., 1965. 497 p.

[6] J.N. Reddy. An Introduction to continuum mechanics. Cambridge University Press, 2003. 354p.

[7] Research Conference on shear strength of Cohesive soils. U.S.A., University of Colorado, Boulder:American society of Civil Engineers,1960. – 1164p.

[8] Bishop A.U. Shear strength parameters of undisturbed and crushed soil samples // In: Mechanics. New in foreign science, vol. 2. "Determining the laws of soil mechanics" / edited by V.N.Nikolaevsky. M.: Publishing House "Mir", 1975. P. 7-75 (in Russian).

[9] FLAC and Numerical Modeling in Geomechanics. Proceedings of the international symposium / Edited by Christine Detournay & Roger Hart. Balkema, 1999. 512 p.

NEWS
OF THENATIONAL ACADEMY OF SCIENCES OF THE REPUBLIC OF KAZAKHSTAN
PHYSICO-MATHEMATICAL SERIES
ISSN 1991-346X **https://doi.org/10.32014/2020.2518-1726.49**
Volume 3, Number 331 (2020), 160 – 168

UDC 528.41

A.S. Urazaliyev[1,2], G. M. Kyrgizbayeva[2], S. N. Nurakynov[1]

[1]Institute of Ionosphere JSC "National Centre Research and Technology", Almaty, Kazakhstan;
[2]Satbayev University, Almaty, Kazakhstan.
E-mail: aset_urazaliev@mail.ru, guldana_km@mail.ru, nurakynov@gmail.com

TRANSFORMATION OF COORDINATES OF GEODETIC NETWORK WITH USE OF SATELLITE TECHNOLOGIES ON THE EXAMPLE THE TERRITORY ATTACHED TO THE CITY OF ALMATY

Abstract. This article discusses the method of satellite measurements at the points of the planned and high-rise justification in the attached territories to the city of Almaty. In accordance with the decree of the President of the Republic of Kazakhstan dated April 16, 2014 No. 798, land plots from the Almaty region with a total area of 23,200 hectares with 27 settlements located on them and a population of more than 92 thousand people were annexed to the city of Almaty.

The increase in the territory of the city of Almaty is carried out in order to develop it, ensure security and law and order, improve the functioning of industrial infrastructure, expand access roads, build social facilities, and bus stations. The object of research is the Eastern border of the city of Almaty, the land of Kolsay and Sulusay villages, with an area of 4412.0 hectares. The existing local system of coordinates (further - LCS) the city of Almaty developed in the 60th years of the XX century was calculated on 20 – 30 years' development plan for the city. Now in connection with numerous expansion of borders of the city, LCS doesn't meet requirements imposed to their accuracy when using modern methods of measurements.

Key words: the local coordinate system, state geodetic points, satellite technology, transformation of coordinates.

Introduction. Today, for the successful use of LCS in modern conditions of widespread use of satellite technologies, a number of problems are hindering:

- LCS is a flat rectangular geodetic network, therefore, when expanding the territory to use the local coordinate system, for example, in the annexed territories, in the territories of nearby cities, airports, the difference between the values of the parameters measured on the ground and on a large-scale plan increases.
- When using modern satellite methods to achieve high accuracy, the contractor needs to know either the parameters of the transition to the spatial geocentric coordinate system, or to the state coordinate system of 1942 (SK-42), which are closed. Therefore, these works can only be performed in post-processing mode, subject to the relevant regime requirements. These conditions greatly complicate the processes of geodetic work and make them economically less efficient.
- In some cases, the city network in the process of their development and expansion of the territories of economic development was thickened and supplemented by poor quality support networks that do not meet modern requirements for coordinate accuracy and methods for fixing geodetic points on the ground.
- The accuracy of the local coordinate system created on the basis of the SK – 42 coordinate system does not meet modern requirements and amounts to 1/50 000–1/150 000 or up to several decimeters at a distance of 15–20 km [4,5]. In addition, in the process of development of thickening networks in LCS, the state of things was aggravated by new additional errors. Some points in local coordinate systems have not been preserved, and in many cases it is not clear on the basis of which support points the technical

documentation of the engineering infrastructure was created. In many cases, on the borders of the annexed territories that previously had different local coordinate systems, residuals occur, reaching a meter or more. These shortcomings are inherent in the local coordinate system due to its significant size, because there is a problem of distortion during reduction to the plane.

The choice of satellite geodetic measurement method. To date, the geodetic coordinate system must meet two seemingly difficult compatible basic requirements:

- the coordinate system should ensure the effective use of modern technologies of global navigation satellite systems (GNSS);
- the coordinate system should provide the maximum possible realization of the potential of geodetic and cartographic data created to date by using traditional tools and methods.

An effective tool for topographic and geodetic production has proved itself to be the methodology for determining spatial coordinates by means of satellite geodetic measurements. The homogeneous high accuracy of urban geodetic networks is achieved by applying reasonable optimal methods for satellite observations and appropriate methods for processing them, as well as by using the optimal geometry of the points, their uniform density and the maximum possible combination of old and new geodetic networks [2].

Static survey is a classic survey method, well suited for all sizes of bases (short, medium and long). At least two receiver antennas, centered above the points, simultaneously collect measurement data at the ends of the basis for a period of time.

These two receivers must simultaneously track four (or more) satellites, record data with the same period and have the same elevation angle. The duration of the measurement session can vary from several minutes to several hours. The optimal duration of the observation session is determined empirically and depends on the following factors

- Lengths of the measured baseline.
- The number of satellites in view.
- Geometric factor (Dilution of Precision, DOP).
- The location of the antenna.
- The level of activity of the ionosphere.
- The type of receivers used.
- Requirements for accuracy.
- The need to resolve carrier phase ambiguity.

For base lines, dual-frequency receivers are used. Dual frequency receivers have two big advantages. First, measurements at two frequencies provide greater accuracy than single-frequency receivers when determining long bases even during increased activity of the ionosphere (ionospheric storms). Secondly, dual-frequency receivers require significantly shorter measurement sessions to obtain determinations of a given accuracy [6].

The coordinates and heights of state geodetic points (hereinafter SGP) located in the north-eastern border of the city of Almaty: the lands of the village of Almerek should have been used as starting geodetic points:

- SGP "Pokrovka" class 2 with a height mark from the leveling of class 4,
- SGP "Pervomayskaya" 3 classes with a height mark from leveling 3 classes,
- SGP "Alatau" class 2,
- SGP "Kyzylgayrat" 1st category with a height mark from leveling 4 classes,
- SGP "Pumping" 1 category with a height mark from leveling 4 classes.

As a result of processing the obtained materials of preliminary observations and the calibration of the initial SGP, the SGP Alatau, the center of which was destroyed at the time of the measurements, was excluded from the source [7].

Also, when processing the results of GPS measurements in various areas (on the plain and in the mountains) and the analysis of calibration and network equalization of altitude values, it was concluded that it is impossible to obtain the heights of the determined polygonometry points with a given accuracy specification. Therefore, all conducted static GPS measurements were used to obtain only the planned

position of the polygonometry points of the developed air defense. The altitude values of points of the developed network are obtained by the combined method. For some points, leveling courses of grade 4 were laid, and the heights of the remaining points were determined by RTK observations with control for benchmarks and polygonometry points whose heights were obtained from leveling of grade 4 and above.

Using the GNSS Credo software package, processing of satellite geodetic measurements was performed, according to the measured:

- the distance from the satellite to the receiver by code (pseudorange);
- the distance from the satellite to the receiver in the phase of the carrier frequency (Phase);
- the era (date and time) in which the measurement was made.

It should also be noted that the importance for calculations are ephemeris (satellite orbit parameters).

The initial data were satellite geodetic measurements and ephemeris in the format of Trimble satellite geodetic receivers. The calculation of satellite geodetic measurements in differential mode is performed. In this mode, the simultaneous operation of two or more receivers is assumed, with each pair of receivers working simultaneously forms a baseline — a vector in space that can be calculated from observational data. The main simulated value in the calculation of the baseline is the double difference of the phase observations. Simplified positioning equation for phase measurements can be expressed as follows:

$$\Phi rs = f/c * (\rho rs + with * (\delta tr + \delta ts) + \delta tr - \delta ion) + Nrs + \varepsilon \quad (1)$$

where, Φrs – the measured value of the phase for receiver r to satellite s; ρrs – geometrical distance between the receiver and the satellite; δtr, δts – corrections of hours of the receiver and the satellite; Nrs – phase ambiguity (unknown number of the whole cycles of the phase bearing); δtr, δion - tropospheric and ionospheric delays; ε – other factors of influence; f – frequency of electromagnetic wave of the signal; c – light speed.

Double differences (2) are formed by forming the difference of the equations, first between two satellites from one receiver (thus compensating for the correction of the receiver's clock and partly the influence of the atmosphere), then between two satellites along two receivers (the satellite clocks and, to a greater extent, the influence of the atmosphere) are compensated . In this case, when forming the differences, the integer nature of the ambiguity is preserved (3).

$$\Phi dd = f/c * (\rho dd + \delta trdd - \delta iondd) + Ndd + \varepsilon dd \quad (2)$$

where,

$$Ndd = Nr1s1\ Nr1s2 - (Nr2s1\ Nr2s2) \quad (3)$$

The preservation of the integer nature of the ambiguity in modeling is one of the factors ensuring high accuracy in calculating the baseline. In the calculation, equations of double differences are formed, the unknown of which are the corrections to the coordinates of the determined receiver and the values of the ambiguities. Solving the system of equations using the least squares method, we obtain the values of the ambiguities at which the sum of the squared corrections (VTPV) is minimal. However, these values are not integer, which does not correspond to the initial definition of ambiguity. Each rounding of the parameter obtained by solving the system of equations leads to a departure from the minimum VTPV. The problem is to find a set of ambiguities that leads the solution in the least way away from the minimum VTPV obtained by the least squares method and to prove that this set is indeed optimal. The criterion for the acceptability of an integer solution is the ratio. Each of the integer sets of ambiguities - candidates takes the solution away from the minimum VTPV by dVTPV. The ratio is obtained as the quotient of dVTPV (best candidate) / dVTPV (second best candidate). Thus, the larger the ratio, the more reliable the obtained integer solution can be considered true. If the ratio is greater than the threshold, the final calculation of the baseline is performed provided that the ambiguities are fixed (fixed solution), if less than the threshold, the solution obtained by modeling the ambiguities remains - a floating solution [8].

After importing the statistical satellite measurement data, the baselines between the SGP points are calculated: *Nasosnyi-Kyzylgairat, Nasosnyi-Pokrovka, Pokrovka-Kyzylgairat, Nasosnyi-Pervomaika, Pervomaika-kyzylqairat, Pervomaika-Pokrovka* which is shown in figure 1.

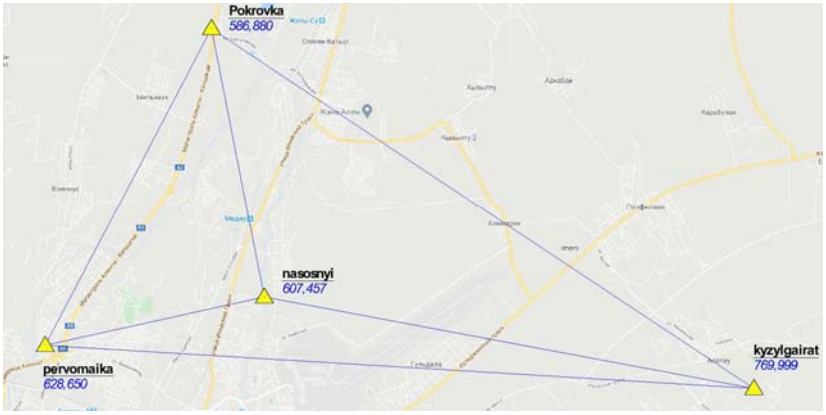

Figure 1 - Scheme of the SGP network of the studied area

Based on the processing of baselines, the following statements are compiled:

- processing of baselines, which contains the results reflecting the quality of the performed GNSS measurements (UPC and covariance of the elements of the baseline)

- coordinates of points along baselines, containing coordinates in the WGS system of 84 stations

the position of the receivers for points along each baseline, as well as the length of the baseline in space and the ellipsoidal distance between two stations, obtained by solving the inverse geodesic problem on an ellipsoid.

The main simulated measurements in calculating the baseline are the double differences of the phase observations.

With the development of geodetic networks by satellite methods, closed figures can be formed from vectors, the so-called polygons. Checking the closure of polygons before adjusting the network is a way to check the quality of the calculation of baselines and reject bad decisions.

Closing polygons consists in summing vectors within a closed shape. In the absence of measurement errors, the sum of the vectors forming a closed polygon will be zero. In reality, even under good observation conditions, obtaining zero values. In addition to the quality of the decision of the baselines, the closure of the polygons also reveals errors in measuring the heights of the receivers.

After processing the base lines, in the presence of redundant measurements or several starting points, it is necessary to carry out the adjustment of the satellite geodetic network. In the GNSS system, adjustment is performed in the spatial geocentric coordinate system WGS84, the adjustment results are reduced to the projection plane of the user coordinate system.

The initial data for adjustment are processed baselines (vectors) reduced to the centers of points and their covariance matrices, as well as the coordinates of the starting points. The adjustment module simulates the coordinates on an ellipsoid, which allows you to assign points as initial points in plan and height separately.

According to the adjustment results, a statement of corrections of equalized vectors and a catalog of coordinates of the equalized points are shown which are shown in table 1 and 2.

Table 1 - Statement of corrections of equalized vectors

Vector	Correction X	Correction Y	Correction Z	Norms. correction X	Norms. correction Y	Norms. correction Z
nasosnyi-kyzylqairat	- 0.011	0.003	- 0.005	- 3.168	0.520	- 0.739
nasosnyi-Pokrovka	0.007	0.008	0.006	0.007	0.008	0.006
Pokrovka-kyzylqairat	0.002	- 0.005	- 0.008	0.657	- 0.861	- 1.179
nasosnyi-pervomai	0.000	0.007	0.009	- 0.026	1.054	1.284
pervomai-kyzylgairat	0.000	0.010	0.031	0.044	1.199	3.554
pervomai-Pokrovka	0.001	0.003	- 0.004	0.320	0.421	- 0.596

Table 2 - Catalog of coordinates of equalized points

Name	Coordinates, m			H (ell)
	N	E	H	
Pokrovka	4810726.660	660950.703	586.880	586.880
kyzylgairat	4801558.739	674802.845	769.999	769.999
nasosnyi	4803889.719	662299.424	607.457	607.457
Pervomaiskaya	4802656.158	656706.149	628.650	628.650
kyzylqairat	4801558.736	674802.842	769.991	769.991

The list of corrections of equalized vectors contains corrections to the components of the baselines (VΔX, VΔY, VΔZ) obtained from the least-squares solution of the system of parametric correction equations. Also, the normalized correction calculated by the formula is displayed in the statement:

$$Vnormi = Vi/\sigma i \quad (4)$$

where σi – vector component of base line (ΔX, ΔY or ΔZ), by results of three-dimensional equalizing.

After receiving the catalog of coordinates of the equalized points, the point of the State Enterprise "Kyzylgayrat" was excluded in which the error in the conversion exceeded 5 cm. Coordinate transformation parameters were determined in the CREDO TRANSKOR software package, where 3 points participated. A graphical representation will help to display project points and show comparisons of the relative positions of the combined points. Figure 2 shows a visual representation of the calculated coordinate offsets in the UTM43N coordinate system relative to the local coordinate system.

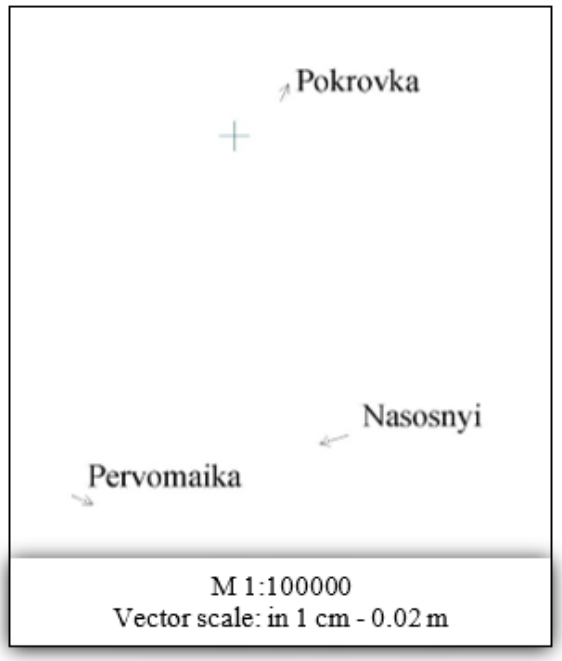

Figure 2 - The difference between the coordinates of the points of the coordinate systems UTM 43N and LCS

According to the results of the search for parameters by the coordinate systems UTM - LCS, we obtain the accuracy that meets the requirements of regulatory documents:

- the largest planned error is 28 mm;
- the smallest planned error is 7 mm;
- the transition parameter from UTM to the local coordinate system is determined by applying the Helmert transform method, which is shown in figure 3.

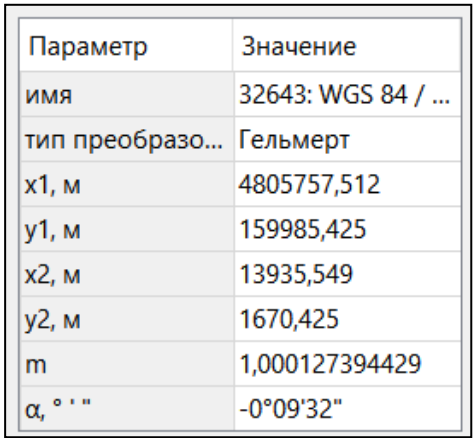

Параметр	Значение
имя	32643: WGS 84 / ...
тип преобразо...	Гельмерт
x1, м	4805757,512
y1, м	159985,425
x2, м	13935,549
y2, м	1670,425
m	1,000127394429
α, ° ' "	-0°09'32"

Figure 3 - Transition parameters from WGS 84 to LCS

Where the fields “x1”, “y1” are designated as the coordinates of the starting point in the UTM 43N coordinate system, “x2”, “y2” are the coordinates of the starting point in the local coordinate system, the calculated scale factor is displayed in the “m” field, in the “ α "is the value of the angle of rotation [9].

Using the transition key shown in Figure 3, we perform the coordinate transformation, the results of which are shown in Table 3.

Table 3 - Transformed coordinates of SGP points

Payment order N	Initial coordinate system of UTM			Final coordinate system LCS			Standart error		
	Point name	N	E	Point name	N	E	Vn	Ve	Vs
1	2	3	4	5	6	7	8	9	10
Points participating in determination of parameters									
1	Pokrovka	4810726.660	660950.703	Pokrovka	18907.970	2622.040	0.017	0.007	0.018
2	Nasosnyi	4803889.719	662299.424	Nasosnyi	12073.948	3989.915	- 0.008	- 0.028	0.029
3	Pervomaiskaya	4802656.158	656706.149	Pervomaiskaya	10824.730	- 1600.680	- 0.008	0.021	0.022

The proposed algorithm for calculating the parameters of the transition to the local coordinate system is applicable only for this study area.

The results of the work revealed a number of problems in the state of the existing SGN in Almaty. Based on the work done, a conclusion is made about the unsatisfactory condition of the existing geodetic base of Almaty. This is also confirmed by the study of information from various works, the actual state of network points, used coordinate and high-altitude systems, static GPS observations at points of the state geodetic network (hereinafter - SGN) of classes 1 and 2, it was decided to make a large number of GPS observations on points of the SGN in order to identify their suitability for use in the development of air defense.

According to the measurement results, it was found that determining the relative position of the GHS and the observed air defense points in terms of and especially in height within the tolerance is possible only in small local areas.

The initial coordinates of the points used have marginal errors in terms of and in height of the relative position and orientation. The use of reference stations of different companies located in the city of Almaty was not used due to the fact that single reference stations in Almaty were determined by various methods and their spatial position is heterogeneous, which does not contribute to high-quality high-precision measurements. They are not suitable not only for the development of air defense, but also for the production of topographic surveys at a distance of more than 10 km from the reference station, and centering works for capital construction more than 3-5 km.

Conclusion. Based on the foregoing, there is currently an urgent need to modernize the existing GHS and create on its basis a new unified frame geodetic network in Almaty using satellite measurements.

Thus, the local coordinate system, to one degree or another, is characterized by the main disadvantages:

- low and heterogeneous accuracy of the reference geodetic networks;
- the impossibility (due to operational restrictions) to effectively apply modern satellite technology in the existing local coordinate system.

As a consequence of these factors, a complex of problems arises, without the solution of which the operation of the local coordinate system is difficult, and sometimes impossible. The problems are related to the need to determine with high accuracy the parameters of the transition from the local coordinate system to the state system of geodetic coordinates SK-42. Coordinate errors of the reference geodetic networks in the LCS, and often the unknown coordinates of the points of these networks in the SK-42 coordinate system, make this requirement quite difficult.

The solution to this problem is very complicated, because the errors of the old local geodetic networks and the local coordinate system affect. Consequently, there is a need to modernize geodetic structures (urban geodetic networks) and, on their basis, modernize the LCS of the city, provided that the discrepancies in the catalogs of local coordinate systems and, accordingly, in the large-scale maps and plans available, in engineering and legal documentation are minimized.

А. С. Уразалиев[1], Г. М. Қырғызбаева[1], С. М. Нуракынов[2]

[1]Сәтбаев Университеті, Алматы, Қазақстан;
[2]Ионосфера институты, «ҰҒЗТО» АҚ, Алматы, Қазақстан

АЛМАТЫ ҚАЛАСЫНА ҚОСЫЛҒАН АУМАҚ МЫСАЛЫНДА СПУТНИКТІК ТЕХНОЛОГИЯЛАРДЫ ПАЙДАЛАНА ОТЫРЫП, ГЕОДЕЗИЯЛЫҚ ЖҮЙЕНІҢ КООРДИНАТАСЫН ТРАНСФОРМАЦИЯЛАУ

Аннотация. Бұл мақалада Алматы қаласына қосылған аумақтардағы жобалық-биіктік негіз пункттеріндегі спутниктік өлшеу әдісі қарастырылады. Қазақстан Республикасы Президентінің 2014 жылғы 16 сәуірдегі № 798 Жарлығына сәйкес Алматы қаласына жалпы ауданы 23 200 га, онда орналасқан 27 елді мекен және халық саны 92 мың адамнан асатын жер учаскелері қосылды.

Алматы қаласының аумағын ұлғайту оны дамыту, қауіпсіздік пен құқықтық тәртіпті қамтамасыз ету, өнеркәсіптік инфрақұрылымның жұмыс істеуін жақсарту, кіру магистральдарын кеңейту, әлеуметтік объектілерді, автовокзалдарды салу мақсатында жүргізіледі. Зерттеу объектісі Алматы қаласының шығыс шекарасындағы аумағы 4412,0 га болатын Көлсай және Сұлусай ауылдары. XX - ғасырдың 60 жылдары әзірленген Алматы қаласының жергілікті координата жүйесі (бұдан әрі - ЖКЖ) қаланы дамытудың 20-30 жылдық жоспарына ғана есептелген. Қазіргі уақытта қала шекарасының бірнеше рет кеңейтілуіне байланысты, ЖКЖ қазіргі заманауи әдістерді пайдалану кезіндегі олардың дәлдігіне қойылатын талаптарға жауап бермейді [1].

Кредо ГНСС бағдарламалық пакетін қолдану арқылы спутниктік геодезиялық өлшеулер өңделді, мұнда спутниктік геодезиялық өлшеулер мен эфемерлер бастапқы деректер болды. Статистикалық спутниктік өлшеулер деректерін импорттағаннан кейін келесі пунктер арасындағы негізгі сызықтар есептелді: Насосный-Кызылгайрат, Насосный - Покровка, Покровка - Кызылгайрат, Насосный - Первомайская, Первомайская - Кызылгайрат, Первомайская - Покровка. Базалық өңдеудің негізінде жасалды: орындалған GNSS өлшеулерінің сапасын көрсететін нәтижелерді қамтитын бастапқы сызбаны өңдеу парағы (ОКҚ және базалық элементтердің ковариациясы); эллипсоид бойынша кері геодезиялық есепті шешу жолымен алынған ғарыштағы базалық сызықтың ұзындығы және екі станция арасындағы эллипсоидтық қашықтық, сонымен қатар әр базалық сызық бойындағы нүктелер үшін қабылдау станцияларының WGS84 жүйесіндегі координаталардан тұратын негізгі координаттар парағы.

Базалық есептеу сапасын тексеру және дұрыс емес шешімдерді қабылдамау үшін полигондар желіні теңестіру алдында тұйықталды. Базалық сызықтарды өңдегеннен кейін жерсеріктік геодезиялық желі теңестірілді. GNSS жүйесінде түзету WGS84 кеңістіктік геоцентрлік координат жүйесінде жүргізілді, түзету нәтижелері таңдалған координаталар жүйесінің проекцияланған жазықтыққа өтеді. Түзету нәтижелері бойынша теңестірілген векторларды түзету туралы есеп және теңестірілген нүктелер координаттарының

каталогы жасалады. Түзетілген нүктелердің координаттарының каталогы жасалды, қателік 5 см-ден асқан Қызылғайрат геодезиялық пунктін алып тастау туралы шешім қабылданды.

UTM 43N және ЖКЖ арасындағы координаталарды трасформациялау параметрлерін анықтауда 3 пункт қатысқан Кредо ТРАНСКОР бағдарламалық пакетінде жүргізілді. Іздеу нәтижелері бойынша өтпелі параметрлер анықталды: ең үлкен қате - 28 мм; ең аз қате - 7 мм; Сонымен қатар, UTM-ден жергілікті координат жүйесіне ауысу параметрі Хельмерт түрлендіру әдісі арқылы анықталады. Алайда, жергілікті координаттар жүйесіне көшу параметрлерін есептеу алгоритмі тек осы зерттеу аймағында қолданылады.

Өлшеу нәтижелері бойынша жоспардағы геодезиялық пунктер мен бақыланатын нүктелердің салыстырмалы позициясын және биіктігін анықтау тек шағын аудандарда мүмкін екендігі анықталды. Жоғарыда айтылғандарға сүйене отырып, қазіргі кезде қолданыстағы геодезиялық желіні жаңарту және оның негізінде спутниктік өлшеулерді қолдана отырып, Алматы қаласының жаңа бірыңғай геодезиялық желісін құру қажеттілігі туындайды.

Түйін сөздер: жергілікті координата жүйесі, мемлекеттік геодезиялық пункттер, спутниктік технологиялар, координата трансформациясы

А. С. Уразалиев[1], Г. М. Қырғызбаева[1], С. М. Нурақынов[2]

[1] КазНИТУ им. К. И. Сатпаева, Алматы,
[2] Институт ионосферы АО «НЦКИТ», Алматы, Казахстан

ПРЕОБРАЗОВАНИЕ КООРДИНАТ ГЕОДЕЗИЧЕСКОЙ СЕТИ С ИСПОЛЬЗОВАНИЕМ СПУТНИКОВЫХ ТЕХНОЛОГИЙ НА ПРИМЕРЕ ТЕРРИТОРИЙ, ПРИСОЕДИНЕННЫХ К Г. АЛМАТЫ

Аннотация. В данной статье рассматривается метод спутниковых измерений на пунктах планово-высотной основы в присоединенных к городу Алматы территориях. В соответствии с Указом Президента Республики Казахстан от 16 апреля 2014 года № 798 к городу Алматы присоединены земельные участки с Алматинской области общей площадью 23 200 га с расположенными на них 27 поселениями и численностью населения более 92 тысяч человек [1].

Увеличение территории города Алматы проводится в целях его развития, обеспечения безопасности и правопорядка, улучшения функционирования промышленной инфраструктуры, расширения въездных магистралей, строительства социальных объектов, автовокзалов. Объектом исследования является восточная граница города Алматы, земли с. Кольсай и с. Сулусай, площадью 4412,0га. Существующая местная система координат (далее – МСК) города Алматы, разработанная в 60 годы XX-века, была рассчитана на 20–30 летний план развития города. В настоящее время в связи с неоднократным расширением границ города, МСК не отвечает требованиям, предъявляемым к их точности при использовании современных методов измерений.

С применением программного комплекса Кредо ГНСС была выполнена обработка спутниковых геодезических измерений, где исходными данными послужили спутниковые геодезические измерения и эфемериды в формате спутниковых геодезических приемников Trimble.

После импорта данных статистических спутниковых измерений рассчитаны базовые линии между пунктами ГГП: Насосный - Кызылгайрат, Насосный - Покровка, Покровка - Кызылгайрат, Насосный - Первомайская, Первомайская - Кызылгайрат, Первомайская - Покровка. На основе обработки базовых линий составлены: ведомость обработки базовых линий, которая содержит результаты отражающее качество выполненных GNSS-измерений (СКП и ковариации элементов базовой линии); ведомость координат точек по базовым линиям, содержащая координаты в системе WGS 84 станций стояния приёмников для точек по каждой базовой линии, а также длину базовой линии в пространстве и эллипсоидальное расстояние между двумя станциями, полученное путём решения обратной геодезической задачи на эллипсоиде.

Выполнено замыкание полигонов перед уравниванием сети для проверки качества расчета базовых линий и отбраковки плохих решений.

После обработки базовых линий выполнено уравнивание спутниковой геодезической сети. В системе ГНСС уравнивание производилось в пространственной геоцентрической системе координат WGS84, результаты уравнивания редуцируются на плоскость проекции выбранной системы координат. По результатам уравнивания составлен ведомость поправок уравненных векторов и каталог координат уравненных пунктов. Составлен каталог координат уравненных пунктов, было решено исключить пункт ГГП "Кызылгайрат" в которой погрешность превышал 5см.

Определение параметров преобразования координат между UTM 43N и МСК осуществлялась в программном комплексе Кредо ТРАНСКОР, где участвовало 3 пункта. По результатам пойска параметров перехода выявлены: наибольшая плановая ошибка составляет 28 мм; наименьшая плановая ошибка составляет – 7 мм; помимо этого, определен параметр перехода из UTM в местную систему координат, применив метод преобразования Гельмерта. Однако, предложенный алгоритм расчета параметров перехода в местную систему координат, применим только для данного исследуемого участка.

По результатам измерений выявлено, что определение взаимного положения ГГС и наблюдаемых пунктов ПВО в плане и особенно по высоте в пределах допуска возможно только на небольших локальных площадях. Исходя из вышесказанного в настоящее время стоит острая необходимость модернизации существующей ГГС и создания на ее базе новой единой каркасной геодезической сети г. Алматы с использованием спутниковых измерений.

Ключевые слова: местная система координат, государственные геодезические пункты, спутниковые технологии, преобразование координат.

Information about authors:

Urazaliyev A.S., Institute of Ionosphere, JSC NCSRT, Almaty, Kazakhstan, Head of Urban area modeling sector, PhD doctor student; aset.urazaliyev@gmail.com; https://orcid.org/0000-0001-7444-2897;

Kyrgyzbayeva G.M., Kazakh National Research Technical University named after K.I.Satbayev, Almaty, candidate of Engineering Sciences, assistant professor; guldana_km@mail.ru; https://orcid.org/0000-0002-4869-0587;

Nurakynov S.M., Institute of Ionosphere, JSC NCSRT, Almaty, Kazakhstan, head of the Cartography and GIS Laboratory, PhD doctor student; nurakynov@gmail.com; https://orcid.org/0000-0001-9735-7820

REFERENCES

[1] Official Decree of the President of the Republic of Kazakhstan Internet resource 798 17.04.2014 of. About change of borders of the city of Almaty of Https://kodeksy-kz.com/norm_akt/source-Prezident/type-Ukaz/798-17.04.2014.htm (in russian).

[2] Genike A.A., Pobeninsky G. G. Global satellite positioning systems and their application in geodesy. M.: Kazgeocentre, 2004. page 280. 355 pages (in russian).

[3] Poklad G. G., Gridnev S.P. Geodeziya: manual for higher education institutions. M.: Academic project, 2007. page 403-412. 592 pages (in russian).

[4] The instruction for development of film-making justification and shooting of the situation and relief using GKINP (GNTA)-12-004-07 GPS and GLONASS global navigation satellite systems, Astana, 2008. 79 pages (in russian).

[5] Basic provisions about the state geodetic and leveling networks of the Republic of Kazakhstan of GKINP (GNTA)-01−020−09, Astana, 2009. 20 pages (in russian).

[6] Small beard, A. V. Creation and reconstruction of city geodetic networks on satellite technologies: geodesy / A.V. Borodko, S.V. Erukov, G.G. Pobedinsky, H.K. Yambayev//Geodesy and cartography. 2004. No. 2. Page 10-12(in russian).

[7] Urazaliyev A. S., Kyrgizbayeva G.M. Development of the technique of determination of planned coordinates in the local coordinate system of the city of Almaty//the Collection of works of the international scientific and practical conference "The Innovation Technologies – the Key to the Successful Solution of Fundamental and Applied Tasks in Ore and Oil and Gas Sectors of Economy of RK". Almaty, 2019. Page 1001–1005 (in russian).

[8] User's guide of the software of Credo of GNSS (in russian).

[9] User's guide of the software of Credo of TRANSKOR (in russian).

NEWS
OF THENATIONAL ACADEMY OF SCIENCES OF THE REPUBLIC OF KAZAKHSTAN
PHYSICO-MATHEMATICAL SERIES
ISSN 1991-346X **https://doi.org/10.32014/2020.2518-1726.50**
Volume 3, Number 331 (2020), 169 – 176

UDC 550.348; 550.385.4

Zhu. Sha. Zhantayev[1], G. Ya. Khachikyan[1],
S. A. Pulinets[2], B.T. Zhumabayev[1], N.S. Toyshiev[1]

[1]Institute of Ionosphere JSC "National Centre Research and Technology", Almaty, Kazakhstan;
[2]Space Research Institute of the Russian Academy of Sciences, Moscow, Russia.
E-mail: admion1@mail.ru

RESEARCH OF VARIATIONS OF SEISMIC ACTIVITY IN CONNECTION WITH VARIATIONS OF STRUCTURE AND DYNAMICS OF THE EARTH'S RADIATION BELT

Abstract. For earthquakes with a magnitude of M≥4.5 that occurred on the planet in 1973-2017 (more than 220 thousand events in accordance with the NEIC USGS seismological catalog), the values of the McIlvine parameter (L) indicating the distance of geomagnetic lines to the center of the Earth at the equator, expressed in the radii of the earth are calculated, The histogram of the distribution of the number of earthquakes depending on the parameter L showed a decrease in their number with an increase in L, but two intervals stand out against the trend: 3.3≤ L ≥3.7 and 2.1≤ L ≥2.25, in which the number of earthquakes is statistically significantly decreased / increased relatively to the trend. Deviations are positively correlated with an decreased / increased population of these lines by high-energy particles in the radiation belt. After the magnetic storms devastate the external electron belt with the concomitant formation of rings of relativistic electrons in the inner magnetosphere around certain L, an increase in seismic activity occurs at the base of these lines on the earth's surface, but with a delay of ~ 2 months. So, after a magnetic storm on March 24, 1991, an additional radiation belt was formed around L = ~ 2.6, and on May 30, 1991, an M7.0 earthquake in Alaska occurred at the base of L = 2.69. After a magnetic storm on September 3, 2012, an additional belt formed around 3.0≤ L≤ 3.5, and on October 28, 2012, an M7.8 earthquake occurred off the coast of Canada at the base of L = 3.32. After a magnetic storm on June 23, 2015, a belt of relativistic electrons formed around L = 1.5-1.8, and in September 2015 seismic activity significantly increased at the base of these geomagnetic lines and it is interesting that at the same time on September 16, 2015, an M8.3 earthquake occurred in Chile, though at the base of the lower geomagnetic line L = 1.12.

Key words: radiation belt, geomagnetic storm, earthquake.

Introduction. One of the areas of scientific research at the Institute of Ionosphere of the National Center for Space Research and Technology is the study of solar-terrestrial communications, including solar-lithospheric communications [1-5]. Statistically significant correlations between variations of solar and seismic parameters were established, but the physical mechanism of the correlations found has not yet been developed. It is assumed that the Earth's radiation belt can be one of the communication intermediaries, since it is found the precipitation of charged particles along the geomagnetic line (L), immersed in the earth's crust inside the region of the future epicenter [6-8]. Methods were developed for a short-term forecast of strong earthquakes from the data on the precipitation of charged particles from the radiation belt (Former USSR patent No. 1583906, IPC5 G01V5 / 00, 08/07/1990; patent of the Russian Federation No. 1762644 MPK5 G01V3 / 00 /, 06/30/1994). However, in practice, these techniques are not yet used. One of the reasons is that there is no statistically reliable information on the relationship between processes in the lithosphere and the Earth's radiation belt obtained on rather long series of experimental data. This work aims to fill this gap to some extent.

Earthquake distribution depending on the value of the McIlvine parameter. The Earth's radiation belt is mainly filled with electrons in the upper part and protons in the lower part. These particles

undergo rotational and translational movements around and along geomagnetic lines in accordance with the energy of charged particles [9]. Geomagnetic lines can be characterized by the McIlvine parameter (L), indicating (in terrestrial radii) the distance from the top of the line above the geomagnetic equator to the center of the Earth [10].

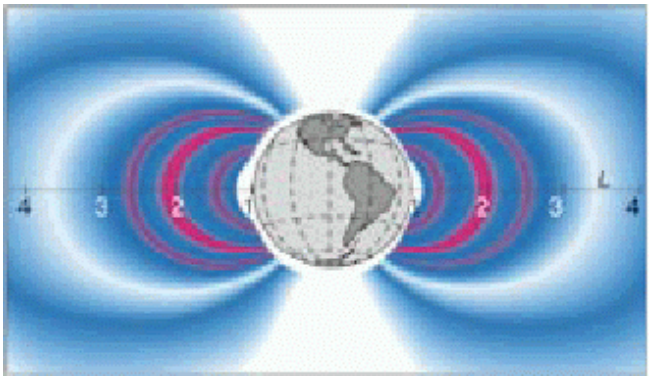

Figure 1 - Meridional section of the Earth's radiation belt with the Mc Ilvine parameter (L) from [9]

The studies were conducted according to the NEIC global seismological catalog (USGS) (https://earthquake.usgs.gov/earthquakes/search). We used data on earthquakes with a magnitude of M≥4.5, recorded on the planet in 1973-2017 (more than 220 thousand events). For the epicenter of each earthquake, the value of the parameter L was calculated by the technique presented earlier in [11], which uses the computer codes of the GEOPACK program [12]. Figure 2 shows on a logarithmic scale a histogram of the distribution of the number of earthquakes depending on the values of the parameter L at the epicenters.

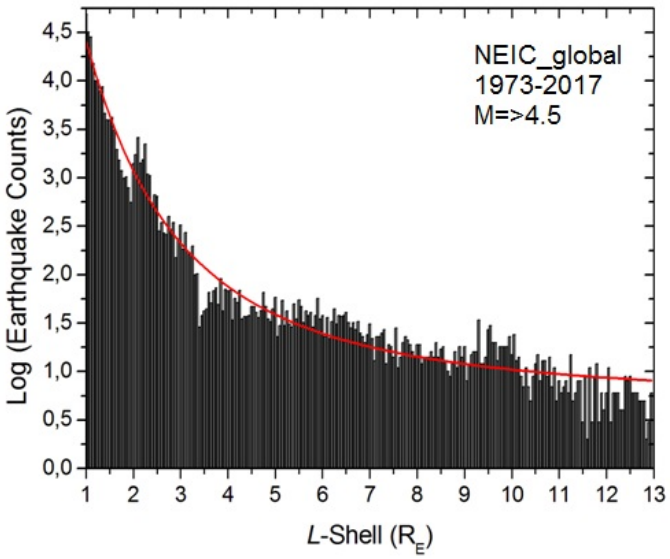

Figure 2 - Distribution of the number of earthquakes with M≥4.5 recorded on the planet in 1973-2017 (more than 220 thousand events) depending on the McIlvine parameter L

Figure 2 shows that the number of earthquakes decreases with increasing L, the observed trend (red curve) can be approximated by the Lorentz equation:

$$\text{Log } N = Y_0 + (2A/\pi) [W / (4 (L - Xc)^2 + W^2)],$$

where N is the number of earthquakes, L is the McIlvine parameter, $Y_0 = 0.91 \pm 0.06$; $Xc = -1.36 \pm 1.01$; $W = 3.25 \pm 1.38$; $A = 57.4 \pm 43.7$, with a correlation coefficient of R = 0.98, and a probability of P = 95%.

Figure 3 shows the deviations of the number of earthquakes from the trend, where two horizontal dash-dotted lines indicate the double standard deviation SD = 0.17.

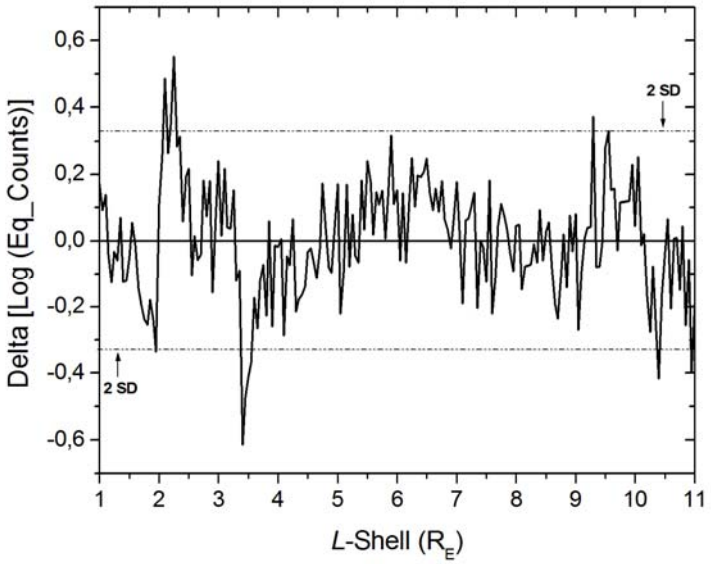

Figure 3 - Distribution according to the McIlvine parameter of the deviation of the number of earthquakes from the trend in Figure 1

In figure 3, two L-gaps ($2.1 \leq L \leq 2.25$) and ($3.3 \leq L \leq 3.7$) are distinguished, where positive / negative deviations from the trend are statistically significant - exceed the 2SD level. Comparing figures 3 and figure 1, it is not difficult to understand that negative deviations in the number of earthquakes around ($3.3 \leq L \leq 3.7$) coincides with the region of the radiation belt around L = ~ 3.5 (white color in figure 1), which separates its internal and external parts and in which the population of magnetic lines by charged particles is weakened. As for the positive deviations in figure 3 around of ($2.1 \leq L \leq 2.25$), they fall in the region in radiation belt around L = ~ 2 (red in figure 1), where the population of geomagnetic lines by charged particles is the highest.

The dynamics of the radiation belt and seismic activity. The main source of disturbances in the radiation belt are magnetic storms, and especially strong ones. Immediately after the onset of the storm, the outer electronic part of the belt "inflates" as it were, and begins to occupy not only the upper part of the magnetosphere, but also its middle and inner parts. After a few days or weeks, the volume of the electron belt is compressed, and after a few more days - weeks, it is restored to the state that was before the magnetic storm. But, in the inner magnetosphere an additional belt of high-energy electrons is formed around geomagnetic lines with smaller L, which can exist for several days up to a year or more [13-17]. Such an effect was first discovered after a strong magnetic storm that occurred on March 24, 1991. At this time, the CRRES satellite was located on the geomagnetic shell L = ~ 2.6 and its instruments detected powerful fluxes of electrons with E ~ 15 MeV and protons with E ~ 20-110 MeV [18]. These flows formed a new (additional) radiation belt around L = ~ 2.6, which lasted about two years and was observed also by the MIR orbital station [9]. Figure 4 shows a histogram of the number of earthquakes with M≥4.5 at the base of L = 2.5 - 2.7 in different months of 1991. We see that the largest number of earthquakes occurred in May, that is, approximately two months after the start of the magnetic storm. The strongest in this situation was the M7.0 earthquake in Alaska, which occurred on 05.30.1991 at 13.29 UT with the coordinates of the epicenter 54.57^0 N, 161.61^0 E at the base of the magnetic line L = 2.69, which belongs to the new radiation belt.

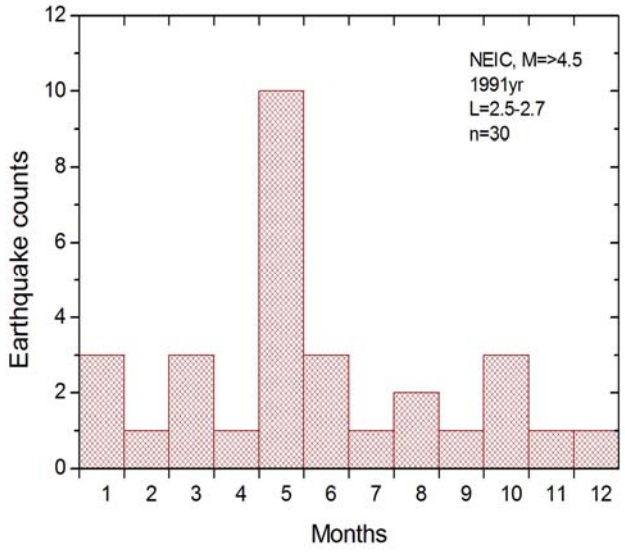

Figure 4 - A histogram of the number of earthquakes with a magnitude
of M≥4.5 that occurred on the planet at the base of geomagnetic lines L = 2.5 - 2.7 in different months of 1991

During the operation of the Van Allen Probes satellites (2012–2019), two very bright cases of the formation of new radiation belts after geomagnetic storms were recorded [14, 16]. In both cases, there was an increase in seismic activity at the base of the geomagnetic lines of the new radiation belts, also with a delay of about two months [19]. So, after a magnetic storm on September 3, 2012, an additional belt of relativistic electrons formed around $3.0 \leq L \leq 3.5$ [14], and on October 28, 2012, a strong M7.8 earthquake occurred off the coast of Canada with coordinates 52.79^0N, 132.1^0W at the base L = 3.32, which falls precisely on the center of the newly formed radiation belt. Also, it was shown in [16] that after a magnetic storm on June 23, 2015, a new belt of relativistic electrons formed around L = 1.5–1.8 (figure 5). Analysis of seismic data in regions penetrated by geomagnetic lines L = 1.5-1.8 showed (figure 6) that their number increased significantly in September 2015, which again shifted by a couple of months relative to the beginning of a magnetic storm.

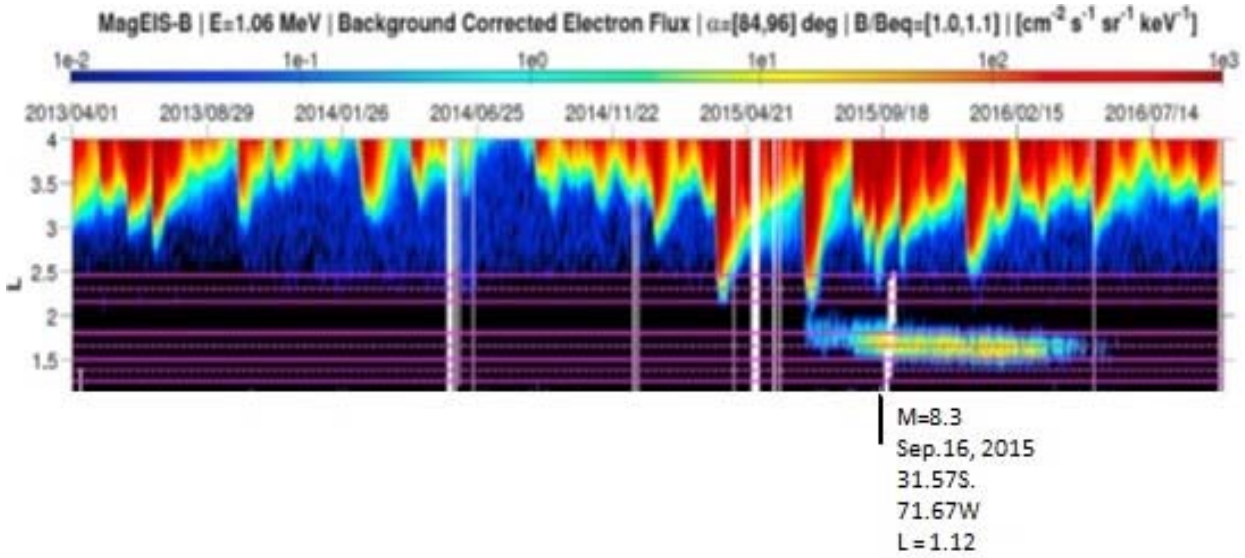

Figure 5 - Distribution over time and geomagnetic lines of the average daily values
of the electron flux with E = 1.06 MeV from April 2013 to September 2016 from [16]

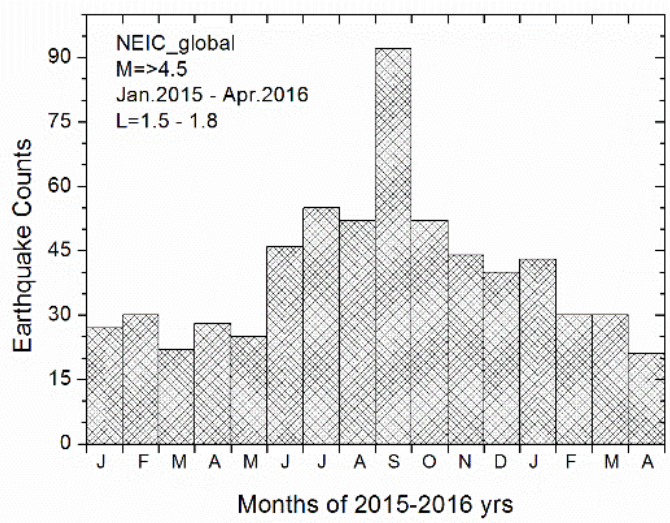

Figure 6 - The number of earthquakes with M≥4.5 that occurred at the base of the geomagnetic lines L = 1.5–1.8 in each month from January 2015 to April 2016

In figure 5, the arrow below marks the date of the very strong M8.3 earthquake that occurred in Chile on September 16, 2015 with the coordinates of the epicenter 31.57°S, 71.67°W. On average, only one earthquake with a magnitude of 8.0 or more occurs annually on the planet. Interestingly, in 2015, the time of the occurrence of such an event was timed to coincide with the period of development of the additional radiation belt after the geomagnetic storm, although on the lower geomagnetic line L = 1.12. We can add that this case is not an isolated one, a similar situation occurred after the strongest geomagnetic storms in late October – November 2003 (Halloween Storm), which resulted in the formation of a new belt of relativistic electrons at L<1.5 [13], which lasted more than a year. During this period, three major earthquakes occurred on the planet in a very short period of time (December 2004 - March 2005). They are: M8.1, December 23, 2004; M9.1, December 26, 2004; and M8.6, March 28, 2005.

Conclusion Data on earthquakes with M≥4.5 that occurred on the planet in 1973-2017 (more than 220 thousand events) demonstrate a statistically significant increase / decrease in their number at the base of geomagnetic lines with enhanced / weakened population of charged particles in the radiation belt. The process of emptying the external electronic radiation belt by a geomagnetic storm, followed by the formation of a new (additional) radiation belt in the inner magnetosphere is accompanied, after about two months, by an increase in seismic activity at the base of the geomagnetic lines of the new radiation belt. The results may be considered as a factual material for the development of the physical mechanism of solar-terrestrial, including solar-lithospheric relationships.

Ж. Ш. Жантаев[1], Г. Я. Хачикян[1], С.А. Пулинец[2], Б.Т. Жумабаев[1], Н.С. Тойшиев[1]

[1]Ионосфера институты, «ҰҒЗТО» АҚ, Алматы, Қазақстан;
[2]РҒА Ғарыштық зерттеулер институты, Мәскеу, Ресей

ЖЕРДІҢ РАДИАЦИЯЛЫҚ БЕЛДЕУЛЕРІНІҢ ДИНАМИКАСЫ МЕН ВАРИАЦИЯЛАРЫНЫҢ ҚҰРЫЛЫМЫНА БАЙЛАНЫСТЫ СЕЙСМИКАЛЫҚ БЕЛСЕНДІЛІК ВАРИАЦИЯЛАРЫН ЗЕРТТЕУ

Аннотация. Жұмыстың мақсаты-негізгі сейсмотектоникалық белдеулер мен жердің радиациялық белдеуінің құрылымы және динамикасы арасындағы сәйкестік дәрежесін анықтау. Орбиталық станцияларындағы Салют-6, жасанды жерсерік Метеордағы МИР, OREOL-3, Intercos-Bulgaria-1300, GAMMA, SAMPEX, Demeter аспаптарымен алынған нәтижелерді негізге ала отырып, күшті жер сілкінісінен бірнеше сағат алдында болашақ эпицентр ауданы ішінде жер қыртысына тиелген геомагниттік күш сызығы (L) бойындағы радиациялық белдіктен зарядталған бөлшектер төгілуі мүмкін екенін көрсетті [6-8]. Бұл нәтижелер бұрынғы КСРО-да патенттер берілген радиациялық белдіктен оқталған бөлшектердің төгілуі туралы деректер бойынша күшті жер сілкіністерінің орны мен уақытын қысқа мерзімді болжаудың

әзірленген әдістемелерінің негізіне алынды: № 1583906, МПК5 G01V5/00, 07.08.1990 ж, ал кейіннен Ресей Федерациясында: №1762644 МПК 5 G01V3/00/, 30.06.1994 ж. Алайда, іс жүзінде бұл әдістемелер әлі де пайдаланылмайды, себебі сейсмикалық белсенділіктің ағымдағы вариациялары мен жердің радиациялық белдеуі арасындағы сәйкестік дәрежесі туралы нақты түсінік жоқ. Жою үшін, кейбір дәрежеде, осы бос орын L параметрінің мәндері бойынша жер сілкіністерінің санын бөлу гистограммасы алынды. Ол үшін 1973-2017 жж. планетада орын алған M≥4.5 магнитудасы бар жер сілкіністері үшін NEIC (USGS) жаһандық сейсмологиялық каталогының деректері пайдаланылды (220 мың оқиға). Әрбір эпицентр үшін халықаралық геомагнитті өрістің анықтамалық моделін (IGRF) және GEOPACK бағдарламасының компьютерлік кодтарын қолдану арқылы L параметрінің мәні есептелген [12]. Магнитудасы 4.5 және одан да көп жер сілкіністерінің таралу гистограммасы L параметріне байланысты олардың саны L ұлғаюымен азайғанын көрсетті (L мәндері төменгі географиялық ендерден жоғары, ал жер сілкіністерінің саны ендіктің ұлғаюымен азайатыны белгілі). Байқалатын тренд R=0.98 корреляция коэффициенті бар Лоренц теңдеуімен аппроксимациялануы мүмкін. Сонымен қатар, гистограмма тренд аясында екі L-аралықтың бөлінетінін көрсетті: 3.3≤ l ≥3.7 және 2.1≤ l ≥2.25, онда жер сілкіністерінің саны статистикалық жағынан трендке қатысты едәуір төмендеген/жоғарылаған, бұл жердің радиациялық белдеуінде осы геомагниттік сызықтардың төмен/жоғары қоныстануымен оң байланысты. Радиациялық белдеуде зарядталған бөлшектермен қоныстану тығыздығы жоғары геомагнит желілерімен нөмірленген сейсмикалық белсенді өңірлерде сейсмикалық белсенділік артты, ал қоныстану тығыздығы аз геомагнит желілерімен нөмірленген өңірлерде сейсмикалық белсенділік төмендеді деген қорытынды жасалды. Радиация белдеулеріндегі динамикалық процестердің сейсмикалық процестермен байланысын зерттеу үшін CRESS, SAMPEX және Van Allen Probes спутниктерімен алынған және жұмыстардағы геомагнитті дауылдан кейінгі радиациялық белдеу құрылымының драмалық өзгерістері туралы деректер қолданылды [13-18]. Драматизм-геомагнитті дауыл басталғаннан кейін релятивистік электрондармен қоныстанған радиациялық белдеудің сыртқы бөлігі "үрленеді" және жоғарғы магнитосфераны ғана емес, өтпелі қабатты (slot region) алады. Бірнеше сағаттан кейін (күн) электрондық белдеу қысылады, содан кейін бірнеше күннен кейін – геомагнитті дауылға дейін қалпына келтіріледі. Бірақ сонымен қатар, ішкі магнитосферада L параметрінің аз мәні бар геомагниттік сызықтардың айналасында релятивистік электрондардан қосымша белдеу қалыптасады, ол бірнеше күннен бір жылға дейін және одан да көп өмір сүре алады. Алғаш рет мұндай әсер 1991 жылдың 24 наурызында геомагнитті дауылдан кейін CRRES [18] және орбиталық станциясы "МИР" [9], жерсеріктерінде тіркелді, жаңа (қосымша) радиациялық белдеу L=~2.6 геомагнитті сызық айналасында қалыптасқан кезде. Сейсмологиялық деректерді талдау геомагниттік сызықтармен нөмірленген өңірлерде L=2.5-2.7, жер сілкіністерінің саны ~2 айдан кейін ал 1991 жылғы 30 мамырда айтарлықтай өсті, жаңа радиациялық белдікке жататын L=2.69 геомагнитті желі негізінде Аляскада M=7. 0 жер сілкінісі орын алды. 2012 жылдың 3 қыркүйегінде геомагнитті дауылдан кейін "Van Allen Probes" жерсеріктері 3.0 ≤ L ≤ 3.5 [14] геомагнитті желілердің айналасында қосымша радиациялық белдеуді тіркеді, ал 2012 жылдың 28 қазанында ~2 ай өткен соң жаңа радиациялық белдеуге жататын L=3.32 негізінде Канада жағалауындағы күшті M=7.8 жер сілкінісі болды. Геомагнитті Дауылдан кейін 2015 жылғы 23 маусымда L=1.5-1.8 геомагнитті сызықтардың айналасында релятивистік электрондардың жаңа белдеуі қалыптасты, ал осы сызықтардың негізінде сейсмикалық белсенділік тек 2015 жылдың қыркүйегіне дейін ғана ең жоғары деңгейге жетті. Алынған нәтижелерді күн-жер, оның ішінде күн-литосфералық байланыстардың физикалық механизмін әзірлеу үшін нақты материал ретінде қарастыруға болады.

Түйін сөздер: радиациялық белдеу, геомагнитті дауыл, жер сілкінісі

Ж. Ш. Жантаев[1], Г. Я. Хачикян[1], С.А. Пулинец[2], Б.Т. Жумабаев[1] , Н.С. Тойшиев[1]

[1]Институт ионосферы АО «НЦКИТ», Алматы, Казахстан;
[2]Институт космических исследований РАН, Москва, Россия

ИССЛЕДОВАНИЕ ВАРИАЦИЙ СЕЙСМИЧЕСКОЙ АКТИВНОСТИ В СВЯЗИ С ВАРИАЦИЯМИ СТРУКТУРЫ И ДИНАМИКИ РАДИАЦИОННОГО ПОЯСА ЗЕМЛИ

Аннотация. Цель работы – определить степень соответствия между структурой и динамикой основных сейсмотектонических поясов и радиационного пояса Земли. Постановку задачи обусловили результаты, полученные приборами на орбитальных станциях Салют-6, МИР на ИСЗ Метеор, OREOL-3, INTERCOSMOS-BULGARIA-1300, GAMMA, SAMPEX, DEMETER, которые показали, что за несколько часов перед сильным землетрясением может происходить высыпание заряженных частиц из радиационного пояса вдоль геомагнитной силовой линии (*L*), погруженной в земную кору внутри района будущего

эпицентра [6-8]. Эти результаты легли в основу разработанных методик краткосрочного прогноза места и времени сильных землетрясений по данным о высыпании заряженных частиц из радиационного пояса, на что были выданы патенты в бывшем СССР: № 1583906, МПК5 G01V5/00, 07.08.1990г, а потом в Российской Федерации: №1762644 МПК5 G01V3/00/, 30.06.1994 г. Однако, на практике эти методики пока не используются и отчасти по той причине, что нет четкого понимания о степени соответствия между текущими вариациями сейсмической активности и радиационного пояса Земли. Для устранения, в некоторой степени, данного пробела получена гистограмма распределения количества землетрясений по значениям параметра *L*. Для этого были использованы данные глобального сейсмологического каталога NEIC (USGS) для землетрясений с магнитудой M≥4.5, произошедших на планете в 1973-2017 гг. (более 220 тысяч событий). Для каждого эпицентра было рассчитано значение параметра *L* с использованием международной справочной модели геомагнитного поля (IGRF) и компьютерные коды программы GEOPACK [12]. Гистограмма распределения количества землетрясений с магнитудой 4.5 и более в зависимости от параметра *L* показала, что их количество уменьшается с увеличением *L* (значения *L* увеличиваются от низких географических широт к высоким, а количество землетрясений, как известно, уменьшается с увеличением широты). Наблюдаемый тренд может быть аппроксимирован уравнением Лоренца с коэффициентом корреляции R=0.98. Одновременно, гистограмма показала, что на фоне тренда выделяются два *L*-промежутка: 3.3≤ *L* ≥3.7 и 2.1≤ *L* ≥2.25, на которых количество землетрясений статистически значимо понижено/повышено относительно тренда, что положительно коррелирует с пониженной/повышенной заселенностью этих геомагнитных линий заряженными частицами в радиационном поясе Земли. Сделан вывод, что в сейсмоактивных регионах, пронизанных геомагнитными линиями с высокой плотностью заселения заряженными частицами в радиационном поясе, сейсмическая активность повышена, а в регионах, пронизанных геомагнитными линиями с малой плотностью заселения, сейсмическая активность понижена. Для исследования связи динамических процессов в радиационном поясе с сейсмическими процессами были использованы данные о драматических изменениях структуры радиационного пояса после геомагнитных бурь, полученные спутниками CRESS, SAMPEX, и Van Allen Probes и детально проанализированные в работах [13-18]. Драматизм заключается в том, что после начала геомагнитной бури внешняя часть радиационного пояса, заселенная релятивистскими электронами, «раздувается» и начинает занимать не только верхнюю магнитосферу, но и переходный слой (slot region). Спустя несколько часов (дней) электронный пояс сжимается, а затем спустя еще несколько дней – восстанавливается до состояния, которое было до геомагнитной бури. Но при этом, во внутренней магнитосфере вокруг геомагнитных линий с малыми значениями параметра *L* формируется дополнительный пояс из релятивистских электронов, который может существовать от нескольких дней до года и более. Впервые такой эффект был зарегистрирован после геомагнитной бури 24 марта 1991 г. спутником CRRES [18] и орбитальной станцией «МИР» [9], когда новый (дополнительный) радиационный пояс сформировался вокруг геомагнитной линии *L* = ~2.6. Анализ сейсмологических данных показал, что в регионах, пронизанных геомагнитными линиями *L*=2.5-2.7 количество землетрясений заметно повысилось спустя ~2 месяца, а 30 мая 1991 г. произошло сильное M7.0 землетрясение на Аляске в основании геомагнитной линии *L*=2.69, принадлежащей новому радиационному поясу. После геомагнитной бури 3 сентября 2012 г. спутники «Van Allen Probes» зарегистрировали дополнительный радиационный пояс вокруг геомагнитных линий 3.0 ≤ L ≤ 3.5 [14], а спустя ~2 месяца 28 октября 2012 г. произошло сильное M7.8 землетрясение у побережья Канады в основании *L*=3.32, принадлежащей новому радиационному поясу. После геомагнитной бури 23 июня 2015г сформировался новый пояс релятивистских электронов вокруг геомагнитных линий *L*=1.5-1.8 [16], а сейсмическая активность в основании этих линий достигла максимального уровня только к сентябрю 2015 г. Полученные результаты можно рассматривать как фактический материал для разработки физического механизма солнечно-земных, в том числе, солнечно-литосферных связей.

Ключевые слова: радиационный пояс, геомагнитная буря, землетрясение.

Information about authors:

Zhantayev Zhu.Sha., Institute of Ionosphere, JSC NCSRT, Almaty, Kazakhstan, Director, Doctor of Physical and Mathematical Sciences, Corresponding member of NAS RK; admion1@mail.ru; https://orcid.org/0000-0002-9189-9546;

Khachikyan G.Ya., Institute of Ionosphere, JSC NCSRT, Almaty, Kazakhstan, Main scientific worker, Doctor of Physical and Mathematical Sciences; galina.khachikyan@gmail.com; https://orcid.org/0000-0003-3043-1728;

Pulinets S. A., Институт космических исследований РАН, г. Москва, Россия, Main scientific worker, Doctor of Physical and Mathematical Sciences; pulse1549@gmail.com; https://orcid.org/0000-0003-3944-6686;

Zhumabayev B., N., Institute of Ionosphere, JSC NCSRT, Almaty, Kazakhstan, Chief of geomagnetic department, Candidate of Physical and Mathematical Sciences; beibit.zhu@mail.ru; https://orcid.org/0000-0001-7882-0277;

Toyshiev N. S., Institute of Ionosphere, JSC NCSRT, Almaty, Kazakhstan, Chief of geomagnetic sector, toyshiev@yandex.ru; https://orcid.org/0000-0002-4255-9641

This work was performed according to RBP-008 “Development of space technologies for monitoring and forecasting natural resources, technological changes in the environment, creation of space technology and ground space infrastructure, research of space objects” in the frame of a project “Development of statistical models of spatio-temporal variations of seismic characteristics in connection with variations in the structure and dynamics of the Earth’s radiation belt (2018-2020), Registration number: 0118PK00797.

ЛИТЕРАТУРА

[1] Zhantayev Zhu. Sha., Kurmanov B.K., Khachikyan G.Ya., Kim A.S., Zhumabaev B.T. (2013). Lithospace weather: the current state of the problem. Geodynamics and solar-terrestrial communications. Almaty. 2013. P. 20-39.

[2] Zhantayev Zhu. Sha., Zhumabaev B.T., Khachikyan G.Ya., Toyshiev N., Kairatkyzy D. (2015). Variations of solar and global seismic activity in 21-24 solar cycles. N e w s of the National Academy of Sciences of the Republic of Kazakhstan series of physical. N 4 (2015). P. 63-70. ISSN 1991-346X.

[3] Zhantayev, Zhu. Sha., Khachikyan, G. Ya., & Sadykova, A. B. (2019). The influence of solar activity on the seismic regime of the earth's crust on the example of the Northern Tien Shan. Trigger effects in geosystems: materials of the V International Conference / Ed. V.V. Adushkin, G.G. Kocharyan. M .: TORUS PRESS. 2019. ISBN 978-5-94588-268-3. P.365-373.

[4] Zhantayev Zhu. Sha., K. E. Abdrakhmatov , G. Ya. Khachikyan. (2020). Research of solar-lithospheric relationships in North Tian Shan attracting paloseismic data. N e w s of the National Academy of Sciences of the Republic of Kazakhstan series of geology and technical sciences. Vol. 1, N 439 (202). P. 138–145. ISSN 2224-5278. UDC 550.348. https://doi.org/10.32014/2020.2518-170X.17

[5] Khachikyan G.Ya., Zhumabaev B.T., Toyshiev N.S., Kaldybaev A., Nurakynov S. (2016). Variations in solar activity and the spatio-temporal distribution of strong earthquakes (M≥7.0) on the territory of Eurasia in 1973-2014. N e w s of the National Academy of Sciences of the Republic of Kazakhstan. Series of physical. N 4 (2016) P. 40-45. ISSN 1991-346X.

[6] Aleksandrin, S.Yu., Galper A.M., Grishantzeva L.A., Koldashov S.V., Maslennikov L.V., Murashov A.M., Picozza P., Sgrigna V., Voronov S.A. (2003). High-energy charged particle bursts in near-Earth space as earthquake precursors. Annales Geophysics. Vol. 21. N 2 (2003). P. 597-602.

[7] Anagnostopoulos, G. C., Vassiliadis, and Pulinets, S. (2011). Characteristics of flux-time profiles, temporal evolution, and spatial distribution of radiation-belt electron precipitation bursts in the upper ionosphere before great and giant earthquakes, Annales of Geophysics. Vol. 55. Doi:10.4401/ag-5365- 2011.

[8] Zhang, X., Fidani, C., Huang, J., Shen, X., Zeren, Z., and Qian, J. (2013). Burst increases of precipitating electrons recorded by the DEMETER satellite before strong earthquakes. Natural Hazards Earth System Science. N 13 (2013). P. 197-209. Doi:10.5194/nhess-13-197-2013.

[9] Galper M.A. (1999). Earth radiation belt. Soros Educational Journal. N 6 (1999). www.eduhmao.ru/var/db/files/3456.9906_075.pdf.

[10] McIlwain C.E. (1961). Coordinates for mapping the distribution of geomagnetically trapped particles. Journal Geophysical Research. Vol. 66. N 11 (1961) P. 3681–3691.

[11] Khachikyan G.Ya., Inchin A.S. (2010). Using a geocentric solar-magnetosphe coordinate system to study the earth's seismicity. Applied space research in Kazakhstan. N 6 (2010). P. 143-149.

[12] Tsyganenko N.A (2008). Geopack: A Set of Fortran Subroutines for Computations of the Geomagnetic Field in the Earth’s Magnetosphere. http://geo.phys.spbu.ru/~tsyganenko/Geopack2008.

[13] Baker D.N., Kanekal S.G., Horne R.B., Meredith N. P., Glauert S.A., (2007). Low-altitude measurements of 2–6 MeV electron trapping lifetimes at 1.5 ≤ L ≤ 2.5. Geophysical Research Letters. Vol. 34. N 20 (2007). https://doi.org/10.1029/2007GL031007.

[14] Thorne R. M., W. Li, B. Ni, Q. Ma, J. Bortnik, D. N. Baker, H. E. Spence, G. D. Reeves, M. G. Henderson, C. A. Kletzing, W. S. Kurth, G. B. Hospodarsky, D. Turner, and V. Angelopoulos (2013). Evolution and slow decay of an unusual narrow ring of relativistic electrons near L~3.2 following the September 2012 magnetic storm. Geophysical Research Letters. Vol. 40. P. 3507–3511. Doi:10.1002/grl.50627.

[15] Li X., D. N. Baker, H. Zhao, K. Zhang, A. N. Jaynes, Q. Schiller, S. G. Kanekal, J. B. Blake, M. Temerin (2017). Radiation belt electron dynamics at low L (<4): Van Allen Probes era versus previous two solar cycles. Journal Geophysical Research. Vol.122. Doi:10.1002/2017JA023924.

[16] Claudepierre S. G., Reeves G.D., O'Brien T. P., Fennell J. F., Blake J. B., Clemmons J. H., Looper M. D., Mazur J. E., Roeder J. L., Turner D. L. (2017). The hidden dynamics of relativistic electrons (0.7-1.5 MeV) in the inner zone and slot region. Journal Geophysical Research. Space Physics. Vol. 122. Doi:10.1002/2016JA023719.

[17] Baker D. N., Erickson P. J., Fennell J. F., Foster J . C., Jaynes A. N., Verronen P. T. (2018). Space Weather Effects in the Earth’s Radiation Belts. Space Science Reviews. 2018. 60 p. Doi 10.1007/s11214-017-0452-7.

[18] Blake, J. B., Kolasinski, W. A., Fillius, R. W., Mullen, E. G. (1992). Injection of electrons and protons with energies of tens of MeV into $L<3$ on 24 March 1991. Geophysical Research Letters. Vol. 19. N 8 (1992). P. 821–824. https://doi.org/10.1029/92gl00624

[19] Khachikyan G.Ya. (2019). Observed response of Earth’s lithosphere to solar wind and radiation belt variations. The Tenth Moscow Solar System Symposium (10M-S^3). IKI RAS. Moscow. Russia. October 7-11, 2019. Book of Abstracts. 10MS3-PS-92. P. 474-475. https://ms2019.cosmos.ru/docs/10m-s3-abstract-book.pdf

NEWS
OF THENATIONAL ACADEMY OF SCIENCES OF THE REPUBLIC OF KAZAKHSTAN
PHYSICO-MATHEMATICAL SERIES
ISSN 1991-346X **https://doi.org/10.32014/2020.2518-1726.51**
Volume 3, Number 331 (2020), 177 – 182

UDC 528.481

Zh. Sh. Zhantayev, A. A. Kaldybayev, S. M. Nurakynov, A.S. Urazaliyev, A. B. Kairanbayeva

Institute of Ionosphere JSC "National Centre Research and Technology", Almaty, Kazakhstan.
E-mail: admion1@mail.ru; azamat.kaldybayev@gmail.com; nurakynov@gmail.com;
aset_urazaliev@mail.ru; kairanbaeva_a@mail.ru

SCIENTIFIC AND METHODOLOGICAL BASES OF GPS MONITORING OF INTENSIVE MOVEMENTS OF THE EARTH'S CRUST IN THE EARTHQUAKE-PRONE REGIONS OF KAZAKHSTAN

Abstract. Over the past 40 years, the damage caused by natural disasters in the world has increased 9 times, and their frequency 5 times, while the growth rate of economic damage from natural disasters exceeds the growth rate of industrial production. Disasters that have occurred in recent years are characterized by a large number of people who died at the same time. In this regard, the decisions of the United Nations, other international organizations and the law of the Republic of Kazakhstan emphasize that governments, international organizations and scientific institutions should be included in the fight against disasters, where Kazakhstan is no exception to the global patterns of emergencies and their negative impact on the social sphere and the environment. Over the past hundred years, destructive and catastrophic earthquakes have occurred in the seismically active territories of Kazakhstan, such as Vernensky (1887), Chilik (1889), Keminsky (1911), the latter, two of which are the strongest in the continental part of Eurasia for the whole history of observations. The occurrence of such seismic catastrophes in the future is very likely and is a consequence of the previous stages of the geological development of the region and its current geodynamic position. All this indicates the need to study the manifestations of geodynamic processes, identify precursors of seismic activity.

Key words: earth's crust, earthquake-prone areas, GPS monitoring, velocity rates.

Introduction. Over the past twenty years, GPS technology has become one of the main in the study of modern slow movements of the Earth's surface, as having the highest sensitivity for large areas and providing acceptable accuracy in determining speed parameters. Among the scientific and technical problems solved by the world community in the direction of geodynamic GPS monitoring are the following main tasks of the study: - determine the quantitative parameters of modern territory movements and the sources of modern geodynamic activity; - study the basic geodynamic factors that determine dangerous natural processes; - study the destructive zones of the lithosphere: fault structure, stress state; - study the seismic processes in the zones of modern geodynamic activity of the lithosphere; - highlight the patterns of temporal variations of natural processes as a basis for their prediction; - develop preventive measures to reduce the risk of natural disasters.

When studying modern geodynamic processes throughout the country on the basis of a system of high-precision satellite GNSS measurements, it is necessary to adapt the incoming data to the solution of geodynamic problems and thereby ensure seismic safety in the study area, which justifies the choice of research direction. The presence of experimental GNSS data, coupled with a sufficient density of the GPS-observation network, allows us to study in detail the deformation processes of the earth's surface at various spatial-scale levels in Kazakhstan.

Detailed networks for monitoring the seismic activity of the region. The territory of the Northern Tien Shan can serve as a test site for the development of a methodology for monitoring and studying modern geodynamic processes in Kazakhstan based on high-precision GPS observations. The North Tien Shan seismically active zone is clearly traced in the latitudinal direction along the ridge. Kyrgyz, Zailiysky

and Kungei Alatau epicenters of strong earthquakes. They reach the highest density in the longitude range from the 73rd to the 79th meridian, where the focal zones of the strongest earthquakes Keminsky in 1911 (M = 8.2) and Chiliksky in 1883 (M = 8.3) fall [6].

Since 1993, many years of research on the study of modern movements in the Northern Tien Shan were carried out as part of the International Project with the participation of specialists from the Massachusetts Institute of Technology, specialists from Kyrgyzstan and Kazakhstan [7]. In addition, starting in 2009. The Ionosphere Institute and the Institute of Seismology implemented the work on the deployment of a regional network consisting of 11 GPS stations (figure 1). These stations are used for continuous observations in the foothills of the Ile Alatau in the zone of a possible earthquake with a magnitude of 9 points, which makes it possible to evaluate seismic activity in the on-line mode.

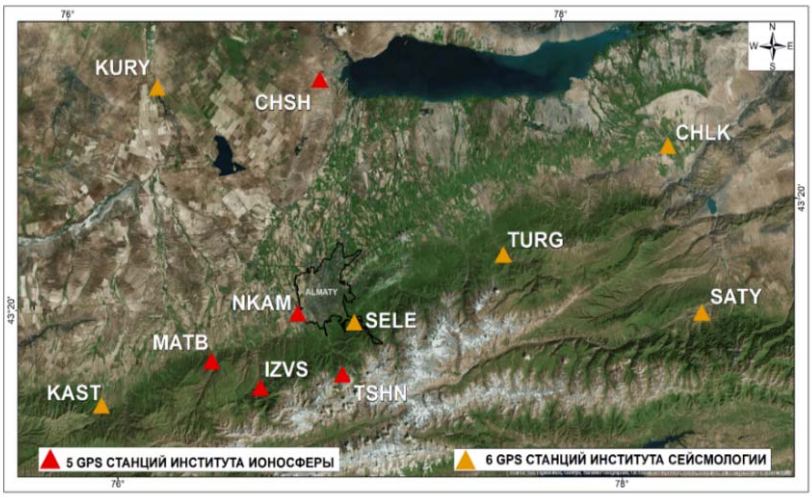

Figure 1 - Location of local GPS stations in the Northern Tien Shan

In 2013, Leica Geosystems [8] deployed a network of 30 differential GPS stations throughout Kazakhstan, designed to solve geodetic tasks in construction and other areas of the national economy. In addition, in 2015, a network of 19 GPS stations with the same purpose was deployed in Kazakhstan by the efforts of the Trimble company [9]. These stations are located in the largest centers and cover 80% of the territory (figure 2).

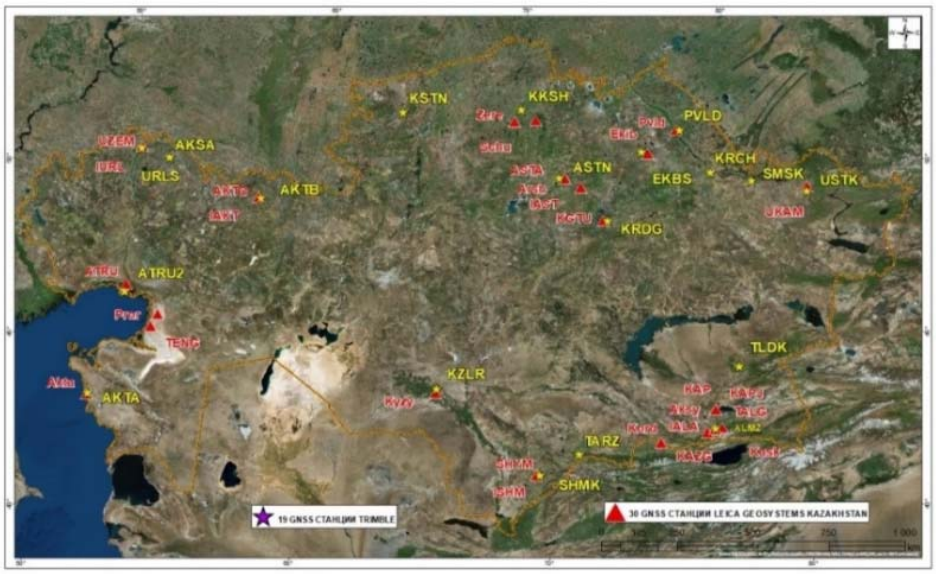

Figure 2 - Network of GPS stations “Leica Geosystems Kazakhstan” and “Trimble”

Technique for processing GPS measurements with the GAMIT / GLOBK software package. Currently, there are several software designed for the primary processing of GPS data. According to the results of a comparative analysis of software such as GIPSY / OASIS II [10], The BERNESE GPS software [11] and GAMIT / GLOBK [12], the research team came to the conclusion that all of the above software systems have good technical characteristics. However, with a detailed comparison of software products for processing GPS data, one can see several advantageous differences between GAMIT / GLOBK and other software [13]. The GAMIT / GLOBK software package is a non-commercial software product that is implemented free of charge for the scientific community. For this project, GAMIT / GLOBK was obtained from the site [14] of the Massachusetts Institute of Technology (MIT) in the USA. The GLOBK program [15] combines the daily coordinates of stations into long-term time series, checks the time series to identify and remove outliers, stabilizes the optimal coordinate solution with the construction of a time series of component values, and calculates displacement rates. The final GLOBK result is an "org" file that contains all the information for time series and speeds with the construction of a confidence ellipse. Based on the data obtained, using the graphic package GMT [16], time series of coordinate changes are constructed with daily discreteness for three components (North, East, Up) for each GPS station. The diagram below demonstrates the full cycle of complex processing of GPS measurements (figure 3).

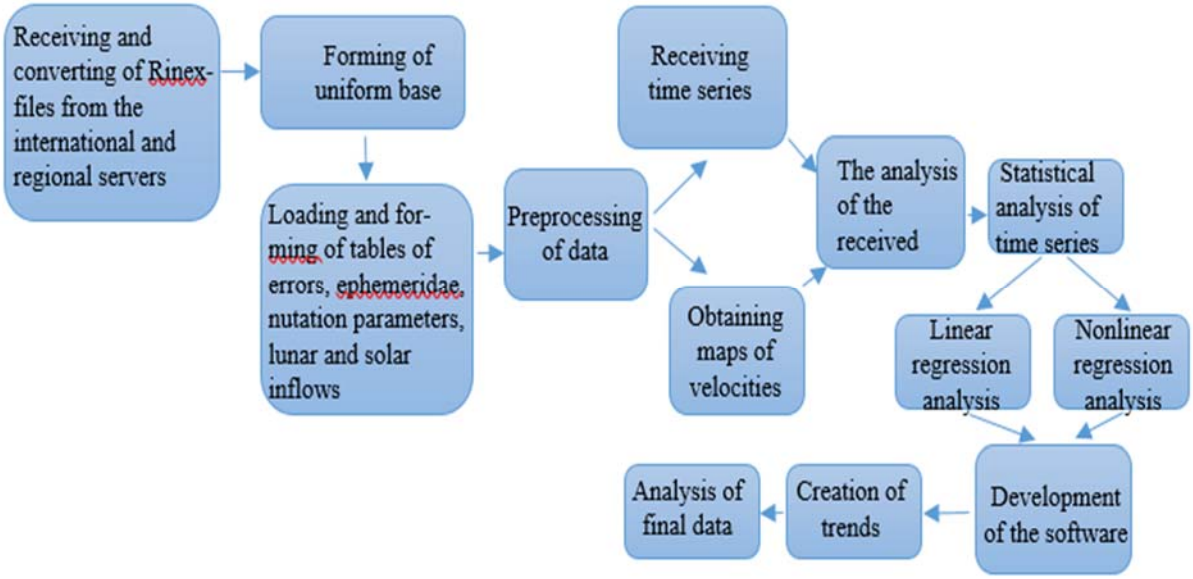

Figure 3 - Technological scheme of the GPS data processing

At each stage, intermediate results are output that can serve to assess the accuracy of the processing quality. The format of the output data is described in the manuals for the use of programs [12]. The final results of the primary processing are the following data: - the coordinates of the observation points and their errors for each processed day; - graphs of changes in the coordinates of observation points for 3 components with different discreteness (starting from the day); - the speeds of individual points and their errors in the form of tables; - maps of the field of velocity vectors of the earth's surface at various spatial scales.

According to the developed GPS data processing technique, primary data processing was carried out according to the results of observations for 2010-2017 at 11 regional stations of the Northern Tien Shan. GNSS stations are additionally included in the processing for the purpose of referencing and equalizing the coordinates of local stations in the global network. A catalog of the coordinates of GPS stations included in the processing for 2010-2017 was compiled in the EURA08 reference system (table).

The final table of speeds relative to the Eurasian continent for 2010-2017

SUMMARY VELOCITY ESTIMATES FROM GLOBK Ver 5.20I								
E & N Rate E & N Adj. E & N +- RHO H Rate H adj. +- SITE								
(deg) (deg) (mm/yr) (mm/yr) (mm/yr) (mm/yr)								
4.52	3.05	4.52	3.05	1.35	1.45 -0.008	7.81	7.81	2.72CHLK
2.17	4.59	2.17	4.59	1.43	1.47 -0.035	1.54	1.54	3.47 TURG
-0.81	2.42	-0.19	-0.10	0.10	0.10 0.007	0.71	-0.01	0.02 SELE
1.64	-0.32	1.64	-0.32	1.21	1.26 -0.011	5.37	5.37	1.53 CHSH
0.26	5.86	0.26	5.86	1.23	1.29 -0.007	0.24	0.24	1.68 TSHN
4.06	1.80	4.06	1.80	1.33	1.39 0.006	1.88	1.88	2.54 IZVS
2.27	1.87	2.27	1.87	1.25	1.31 0.002	4.25	4.25	2.02 MATB
0.15	-1.99	0.15	-1.99	1.25	1.30 0.004	5.57	5.57	1.93 KURY
0.70	1.52	0.70	1.52	1.32	1.43 -0.013	-0.65	-0.65	2.86 KAST
-1.75	2.55	-0.14	1.83	0.83	0.83 -0.003	1.05	-0.34	0.17CHUM
-0.45	1.42	0.40	-1.53	0.71	0.72 -0.005	2.03	0.32	0.17 POL2
5.96	-14.7	5.96	-14.7	1.24	1.29 -0.003	12.42	12.42	1.78SUMK
2.83	9.56	2.83	9.56	1.35	1.40 -0.007	-5.50	-5.50	2.00 KAZA_

Conclusion. The obtained results of processing primary data for the territories of the Northern Tien Shan are grouped in time series from 2010 to 2017 inclusive. The speed of the GPS stations was calculated as the increment of the linear trend of the series for the entire observation period. The trend corresponds to regional geodynamic surface movements due to the interaction of the Eurasian platform and the Indian plate. In addition, in a long-term series of measurements, there are such interference as significant intervals of missing values, random single emissions and due to malfunctions of recording equipment (lack of electricity, preventive maintenance, etc.) or adjustment of a priori models included in the processing.

Ж. Ш. Жантаев, А. А. Қалдыбаев, С. М. Нұрақынов, А.С. Уразалиев, А.Б. Қайранбаева

Ионосфера институты, «ҰҒЗТО» АҚ, Алматы, Қазақстан

ҚАЗАҚСТАННЫҢ СЕЙСМИКАЛЫҚ ҚАУІПТІ АЙМАҚТАРЫНДАҒЫ ЖЕР ҚЫРТЫСЫНЫҢ ҚАРҚЫНДЫ ҚОЗҒАЛЫСЫН GPS МОНИТОРИНГІЛЕУДІҢ ҒЫЛЫМИ-ӘДІСТЕМЕЛІК НЕГІЗДЕРІ

Аннотация. Әлемде соңғы 40 жылда табиғи апаттардан келген залал 9 есе өсті, ал олардың жиілігі 5 есе өсті, бұл ретте табиғи апаттардан болған экономикалық залалдың өсу қарқыны өнеркәсіптік өндіріс көлемінің өсу қарқынынан озады . Соңғы жылдары болған апаттарға бір уақытта қаза тапқан адамдардың көп саны тән (2018 жылғы Индонезиядағы жер сілкінісінен). Осыған байланысты, Біріккен Ұлттар Ұйымының, басқа да халықаралық ұйымдардың шешімдерінде және ҚР Заңында апатқа қарсы күреске үкіметтер, халықаралық ұйымдар мен ғылыми институттар енгізілуі тиіс. Төтенше жағдайлардың пайда болуының және олардың әлеуметтік сала мен қоршаған ортаға теріс әсерінің жалпы әлемдік заңдылықтарынан Қазақстан алшақ емес. Соңғы жүз жылдан бері Қазақстанның сейсмобелсенді аумақтарында Верненское (1887ж.), Шелек (1889ж.), Кеминск (1911ж.) сияқты жойқын және апатты жер сілкінісі болды, олардың соңғы екеуі бүкіл бақылау тарихындағы Еуразияның континентальды бөлігінде ең күшті болып табылады. Болашақта осындай сейсмикалық апаттардың пайда болуы өңірдің геологиялық дамуының алдыңғы кезеңдерінің және оның қазіргі геодинамикалық позициясының салдары болып табылады. Осының барлығы геодинамикалық процестердің көріністерін зерттеу, сейсмикалық белсенділіктің хабаршыларын анықтау қажеттілігін көрсетеді.

Мониторинг жүйесі-бұл уақыт аралығында бақылау, деректерді талдау және өзара байланысты шешімдер қабылдау және нақты объектінің жағдайы туралы ақпарат беретін құрылғылар мен тәсілдердің кешені. Кез келген мониторингтің мақсаты табиғи және техногендік сипаттағы төтенше жағдайларға дайындалу керектігін ескертуге мүмкіндік беретін мәліметтерді жинау, оның ішінде қауіпті процестерді пайда болу кезеңінде анықтау болып табылады.

Бұл мақалада бүкіл ел көлемінде қазіргі геодинамикалық процестерді зерттеу үшін спутниктік мониторинг қарастырылады. Ол үшін келіп түскен деректерді геодинамикалық міндеттерді шешуге бейімдеу қажет, сол арқылы сейсмикалық қауіпті аумақтарды дұрыс жабуды қамтамасыз ету қажет, бұл сейсмикалық

аудандауда және күшті жер сілкіністерін болжамдауда маңызды практикалық мәнге ие. Жер беті қозғалысын нақты уақытта мониторингілеу субмиллиметрлік дәлдікпен жылжуды қадағалауға және сейсмобелсенді аймақтарда орналасқан материктер, литосфералық плиталар сияқты жекелеген геологиялық блоктардың динамикалық жаңартылып отыратын қозғалыс карталарын құруға мүмкіндік береді. Осы деректер бойынша жер қыртысының кернеулерінің өсу жылдамдығын және деформациясын кернеудің критикалық деңгейге жетіп және жинақталған энергия жер сілкінісі түрінде босатылған сәтке дейін анықтайды. Мұндай ақпарат сейсмобелсенді аумақтардың тектоникалық процестерін зерттеуде, жер бетіндегі референстік тіректің шынайы орнын белгілеуде де ғылыми-практикалық қызығушылық танытады.

Түйін сөздер: жер қыртысы, жер сілкінісі қаупі бар аумақтар, спутниктік мониторинг, қозғалу деңгейі

Ж. Ш. Жантаев, А. А. Калдыбаев, С. М. Нуракынов, А.С. Уразалиев, А.Б. Кайранбаева

Институт ионосферы АО «НЦКИТ», Алматы, Казахстан

НАУЧНО-МЕТОДИЧЕСКИЕ ОСНОВЫ GPS МОНИТОРИНГА ИНТЕНСИВНЫХ ПОДВИЖЕК ЗЕМНОЙ КОРЫ В СЕЙСМОАКТИВНЫХ РЕГИОНАХ КАЗАХСТАНА

Аннотация. В мире за последние 40 лет ущерб от природных катастроф возрос в 9 раз, а их частота в 5 раз, при этом темпы роста экономического ущерба от стихийных бедствий опережают темпы роста объемов промышленного производства [1]. Для катастроф, произошедших в последние годы, характерно большое количество единовременно погибших людей (от землетрясения 2018 года в Индонезии) [2]. В связи с этим, в решениях Организации Объединенных Наций, других международных организаций и в законе РК [3] подчёркивается, что в борьбу с бедствиями должны включиться правительства, международные организации и научные институты.

Казахстан не является исключением из общемировых закономерностей возникновения ЧС и их негативного воздействия на социальную сферу и окружающую среду. За последние сто с небольших лет в сейсмоактивных территориях Казахстана произошли разрушительные и катастрофические землетрясения, такие как Верненское (1887г.), Чиликское (1889г.), Кеминское (1911г.), последние, два из которых относятся к самым сильным на континентальной части Евразии за всю историю наблюдений. Возникновение подобных сейсмических катастроф в будущем весьма вероятно и является следствием предыдущих этапов геологического развития региона и его современной геодинамической позиции. Все это свидетельствует о необходимости изучения проявлений геодинамических процессов, выявления предвестников сейсмической активности.

Система мониторинга – это комплекс устройств и способов наблюдения на интервале времени, анализа данных и принятия решений, связанных между собой и предоставляющих информацию о состоянии конкретного объекта. Целью любого мониторинга является сбор сведений, позволяющих предупредить о подготовке чрезвычайной ситуации природного и техногенного характера, в том числе выявление опасных процессов на стадии их зарождения.

В данной статье рассматривается GPS мониторинг для изучения современных геодинамических процессов в масштабах всей страны. Для этого необходимо адаптировать поступающие данные к решению геодинамических задач и, тем самым, обеспечить достоверное покрытие сейсмоопасных территорий, что имеет важное практическое значение в сейсморайонировании и прогнозе сильных землетрясений [4]. Мониторинг движений земной поверхности в реальном времени позволяет отслеживать смещения с субмиллиметровой точностью и составлять динамически обновляемые карты движения, как материков, литосферных плит, так и отдельных геологических блоков, находящихся в сейсмоактивных областях. По этим данным определяют скорость нарастания напряжений и деформаций земной коры до момента, когда напряжение станет критическим и накопленная энергия высвободится в виде землетрясения [5]. Такая информация представляет научно-практический интерес, как при изучении тектонических процессов сейсмоактивных территорий, так и при установлении истинного положения наземного референсного каркаса.

Ключевые слова: земная кора, сейсмоопасные территорий, GPS мониторинг, скорости смещений.

Information about authors:

Zhantayev Zhu.Sha., Institute of Ionosphere, JSC NCSRT, Almaty, Kazakhstan, Director, Doctor of Geological and Mineralogical Sciences, Corresponding member of NAS RK; admion1@mail.ru, https://orcid.org/0000-0002-9189-9546;

Kaldybayev A.A., Institute of Ionosphere, JSC NCSRT, Almaty, Kazakhstan, Deputy Director for Scientific Research, doctor PhD; azamat.kaldybayev@gmail.com; https://orcid.org/0000-0002-0563-282X;

Nurakynov S.M., Institute of Ionosphere, JSC NCSRT, Almaty, Kazakhstan, head of the Cartography and GIS Laboratory, PhD doctor student; nurakynov@gmail.com; https://orcid.org/0000-0001-9735-7820;

Urazaliyev A.S., Institute of Ionosphere, JSC NCSRT, Almaty, Kazakhstan, Head of Urban area modeling sector, PhD doctor student; aset.urazaliyev@gmail.com; https://orcid.org/0000-0001-7444-2897;

Kairanbayeva A. B., Institute of Ionosphere, JSC NCSRT, Almaty, Kazakhstan, scientific secretary, doctor PhD s; kairanbaeva_a@mail.ru; https://orcid.org/0000-0001-9827-4082

REFERENCES

[1] Decree of the Government of the Republic of Kazakhstan. About the Concept of the prevention and liquidation of natural and man-made emergencies and the improvement of the state management system in this area: approved. November 09, 2010, No. 1154.

[2] Indonesiaearthquake: Hugesurgeindeathtoll [Electronic resource] / BBCNews. 2018; https://www.bbc.com/news/world-asia-45697553.

[3] Law of the Republic of Kazakhstan. On natural and man-made emergencies: approved. July 5, 1996 No. 19-I // as amended. and add. - 2014, January - 13.

[4] Steblov G.M., Kogan M.G., Freymueller J.T., Titkov N.N., Ekstrom G., Gabsatarov Y.V., Vasilenko N.F., Nettles M., Prytkov A.S. and Frolov D.I. The size and rupture of the great 2013 deep-focus earthquake beneath the Sea of Okhotsk: constraints from GPS. // AGU Fall Meeting: California, 2013. C. 55-57.

[5] Steblov G. M., Kogan M.G., Levin B. V., Vasilenko N. F., Prytkov A. S., Frolov D. I. The size and rupture of the great 2013 deep-focus earthquake beneath the Sea of Okhotsk: constraints from GPS. // AGU Fall Meeting:. California, 2007. C. 68-70.

[6] Zubovich A.V., Wang X., Scherba Y.G., Schelochkov G.G., Reilinger R., Reigber C., Mosienko O.I., Molnar P., Michajljow W., Makarov V.I., Li J., Kuzikov S.I., Herring T.A., Hamburger M.W., Hager B.H., Dang Y., Bragin V.D., Beisenbaev R.T. GPS velocity field for the Tien Shan and surrounding regions // Tectonics. – 2010. – Vol. 29. – TC6014.

[7] Abdrakhmatov K.Ye., Aldazhanov S.A, Hager B.H., Hamburger M.W., Herring T.A., Kalabaev K.B., Makarov V.I., Molnar P., Panasyuk S.V., Prilepin M.T., Reilinger R.E., Sadybakasov I.S., Souter B.J., Trapeznikov Yu. A., Tsurkov V.Ye., Zubovich A.V. Relatively recent construction of the Tien Shan inferred from GPS measurements of present-day crustal deformation rates // Nature. Vol. 384, Issue 6608. 450 p.

[8] Leica Geosystems Kazakhstan [Electronic resource] / Spider Business Center; http://gnss.geosystems.kz/

[9] Trimble network of stations [Electronic resource] / Trimble® PivotWeb; http://gnss.geotronix.kz/TrimblePivotWeb/Map/SensorMap.aspx

[10] Kaniuth K., Völksen C. Comparison of the BERNESE and GIPSY/OASIS II Software Systems Using EUREF Data // Mitt. des Bundesamtes fur Kartographie und Geodasie. 2003. Vol. 29. P.314-319

[11] Dach R., Hugentobler U., Fridez P., Meindl M. Bernese GPS Software Version 5.0. Astronomical Institute, University of Bern, Switzerland, 2007. 640 p.

[12] Herring T.A., King R. W., Mc Clusky S. C. Gamit: GPS Analysis at MIT. Version 10.4. Cambridge: Massachusetts Institute of Technology, 2010. – 162 p.

[13] Araszkiewicz A., Figurski M., Kroszczyński K. Combining of Gnss solutions from bernese and gamit // EGU General Assembly. Vienna, 2010. p.4588.

[14] GAMIT-GLOBK Downloads [Electronic resource] / GAMIT-GLOBK; http://geoweb.mit.edu/~simon/gtgk/down.htm

[15] Herring T.A., King B.W., McClusky S.C. Global Kalman filter VLBI and GPS analysis program. Release 10.6 EAPS. MIT, 2015. p. 95.

[16] GMT-The Generic Mapping Tools [Electronic resource].: http://gmt.soest.hawaii.edu

NEWS
OF THENATIONAL ACADEMY OF SCIENCES OF THE REPUBLIC OF KAZAKHSTAN
PHYSICO-MATHEMATICAL SERIES
ISSN 1991-346X **https://doi.org/10.32014/2020.2518-1726.52**
Volume 3, Number 331 (2020), 183 – 190

UDC 528.85/.87(15)

Zh. Sh. Zhantayev, D. V. Chepashev,
A. A. Kaldybaev, S. M. Nurakynov, K. M. Ungarov

Institute of Ionosphere JSC "NCSRT", Almaty, Kazakhstan.
E-mail: admion1@mail.ru, chepashev_daniker@mail.ru, azamat.kaldybayev@gmail.com,
nurakynov@gmail.com, kelis9696@mail.ru

MAPPING FREQUENCY OF OIL SPILLS IN THE CASPIAN SEA USING SENTINEL-2 OPTICAL IMAGES

Abstract. The main goal of this work is to evaluate the capabilities of optical images in the problem of detecting oil spills, testing them in the task of mapping zones with a high frequency of oil spills during one year. Using SAR imagery, sometimes it is difficult to separate anthropogenic oil spills and false targets, usually called "look-alikes". Using optical images for oil spill detection, we rely on the spectral characteristics of objects, and although the reflectivity varies depending on the thickness and composition of the slick, in most cases, oil spills can be distinguished from "look-alikes". The region near Absheron peninsula was selected as a study area. Optical images of the Sentinel-2 (A, B) satellites were used to detect oil spills and calculate the zones of their most frequent occurrence. Object based approach was chosen for segmentation and classification images. The map of hot spots with high frequencies of oil spills during 2019 year was presented in this article. Conclusions about the advisability of using optical images along with radar data for monitoring oil spills were made.

Key words: oil spills detection, Caspian Sea, Sentinel-2, optical imagery.

Introduction. The environmental situation in the Caspian Sea, which is literally saturated with products of the oil industry, is one of the acute issues for the littoral states. The Caspian Sea is subject to increasing anthropogenic impact, there is an increase in water pollution by oil products, heavy metals, and chemical products. At a rapid pace, there is a decrease in marine bioresources. The main sources of sea pollution are: river runoff; industrial and municipal effluents; oil production at sea and onshore; transportation of oil products by sea or through pipelines; flooding/drainage of the coastal zone as a result of the rise/fall of the Caspian level [1].

Oil spills at sea can be of natural origin (natural oil emissions due to fractures of geological structures, griffins, mud volcanoes), but in most cases they are of anthropogenic nature: they arise as a result of ships and tankers discharging ballast and bilge water, due to the removal of oil stains or pollution with river flows, industrial effluents, in the event of accidents of ships and tankers, in the breakdown of offshore oil pipelines, in the discharge of drill cuttings and in accidents due to exploratory drilling and industrial production [2,3]. This is especially felt in offshore zones where oil and gas fields are being developed, oil is extracted and transported. Oil pollution in coastal zones has a detrimental effect on flora and fauna, leads to pollution of coastlines, which entails large material losses associated with the cleaning of these territories. The marine ecosystem of the Caspian Sea, a closed reservoir, which self-cleaning ability is very small, is especially sensitive. Almost every year, there are reports of the death of sturgeon, seals, birds, in the carcasses of which oil products are found [4].

International experience shows that space monitoring methods are the most effective way to detect and evaluate the development dynamics of most natural and a number of man-made emergencies, in particular oil spills. Modern systems of remote sensing make it possible to obtain overview and detailed information about emergencies of various sizes in large areas. At the same time, space monitoring

methods are much more economical than traditional ground-based data collection methods. It is practically impossible to control oil spills in the Caspian Sea scattered over a gigantic area (over 377,155 thousand square kilometers) by traditional land-based methods, and the use of aerial observations is expensive and can only be carried out in limited local areas. Therefore, remote sensing is the most effective method for timely detection of oil spills in the Caspian Sea with its large territory.

There are two types of sensors used in remote sensing - active (radar) and passive (optical).

Both types of sensors have their advantages and disadvantages. Optical sensors can detect oil spills only in the daytime when there is no cloud, fog or smoke above the area of interest, that is, when nothing obscures the object from the sensor. Radar images can detect oil spills despite the cloudiness and time of day. Also, a large coverage area of radar images is an advantage. Nevertheless, there are weather conditions under which radar images are "powerless" for this task, namely, rain, and wind force above the sea surface beyond the interval of 2.5-12.5 m/s [5-8]. Due to many of the advantages listed above, radar is now the most common means of oil spill remote sensing.

However, using SAR imagery, sometimes it is difficult to separate anthropogenic oil spills and false targets, usually called “look-alikes”, which include low wind areas, areas, sheltered by land, rain cells, organic films, grease ice, wind fronts, up-welling zones, oceanic fronts, algae blooms, current shear zones, etc. One group of researchers showed that even with extensive processing of SAR (synthetic aperture radar) imagery, 20% of the images reported as “oil spills” were still “look-alikes” [9]. This means that using only radar images to monitor oil spills, about a fifth of all detected objects will be false targets, and when calculating their total area or analyzing maps built on such data, the error will be large.

Using optical images for oil spill detection, we rely on the spectral characteristics of objects, and although the reflectivity varies depending on the thickness and composition of the slick, in most cases, oil spills can be distinguished from “look-alikes”. Of course, limitations of optical imagery are a serious obstacle to monitoring efficiency. But in cases when mapping accuracy is more important, optical images are needed.

So, purpose of this work was to test opportunities of optical imagery in oil spill detection task by trying mapping hot spots with high frequency of oil spills during year.

Study area. The region near Absheron peninsula was chosen for a reason. Oil spills detected more often in this region than in other regions of the Caspian Sea. Accurate oil spill frequency map of this region, built by using optical sensors, will be useful for future oil spill monitoring. There are 3 oil fields in this region: Oil Rocks Settlement, Chilov and Pirallahi Islands. Oil Rocks Settlement is located 35 km from the coast of the Caspian Sea. Its development began in 1949. Oil Rocks is an industrial settlement in Baku, Azerbaijan. A full town on the sea, it was the first oil platform in Azerbaijan, and the first operating offshore oil platform in the world, incorporating numerous drilling platforms [10]. Pirallahi Island is located 1.6 km from the coast of the Caspian Sea. Chilov Island is located 16 km from the coast of the Caspian Sea [11]. The map of the Oil Rocks Settlement, Chilov and Pirallahi Islands is presented in figure 1(b).

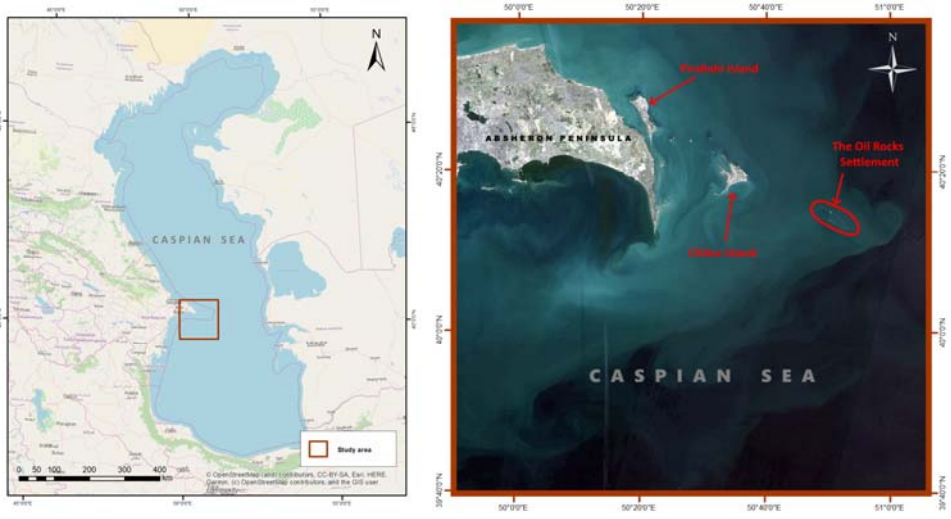

a) b)

Figure 1 – a) Study area; b) Map of the Oil Rocks Settlement, Pirallahi and Chilov Islands

Methods and data processing. Optical images of the Sentinel-2 (A, B) satellites were used to detect oil spills and calculate the zones of their most frequent occurrence during 2019. Sentinel-2 is an Earth observation mission from the Copernicus Programme that systematically acquires optical imagery at high spatial resolution (10 m to 60 m) over land and coastal waters. The mission is a constellation with two twin satellites, Sentinel-2A and Sentinel-2B [11].

Eighteen L1C images with less than 20% cloud cover were downloaded from the USGS Earthexplorer website. Downloaded images were pre-processed to obtain L2A imagery from L1C. Sen2Cor Processor was used for that purpose. Sen2Cor is a processor for Sentinel-2 Level 2A product generation and formatting that performs the atmospheric, terrain and cirrus correction of Top-Of-Atmosphere Level 1C input data. Sen2Cor creates Bottom-Of-Atmosphere, optionally terrain and cirrus corrected reflectance images. In addition, Sen2Cor generates Aerosol Optical Thickness, Water Vapor, Scene Classification Maps and Quality Indicators for cloud and snow probabilities. Its output product format is equivalent to the Level 1C User Product: JPEG 2000 images, three different resolutions, 60, 20 and 10 m [12, 13].

Object based segmentation and classification was used for oil spill detection. In contrast to pixel-based classification that classify pixels one-by-one, object-based approach first groups image pixels into spectrally homogenous image objects using an image segmentation and then classifies the individual objects [14, 15]. Then detected oil spills objects were checked through visual interpretation. After all, GIS overlay analysis was performed for computation of oil spill frequency, and determination of spatiotemporal distribution. The workflow for the detection of oil spill frequency presented in figure 2.

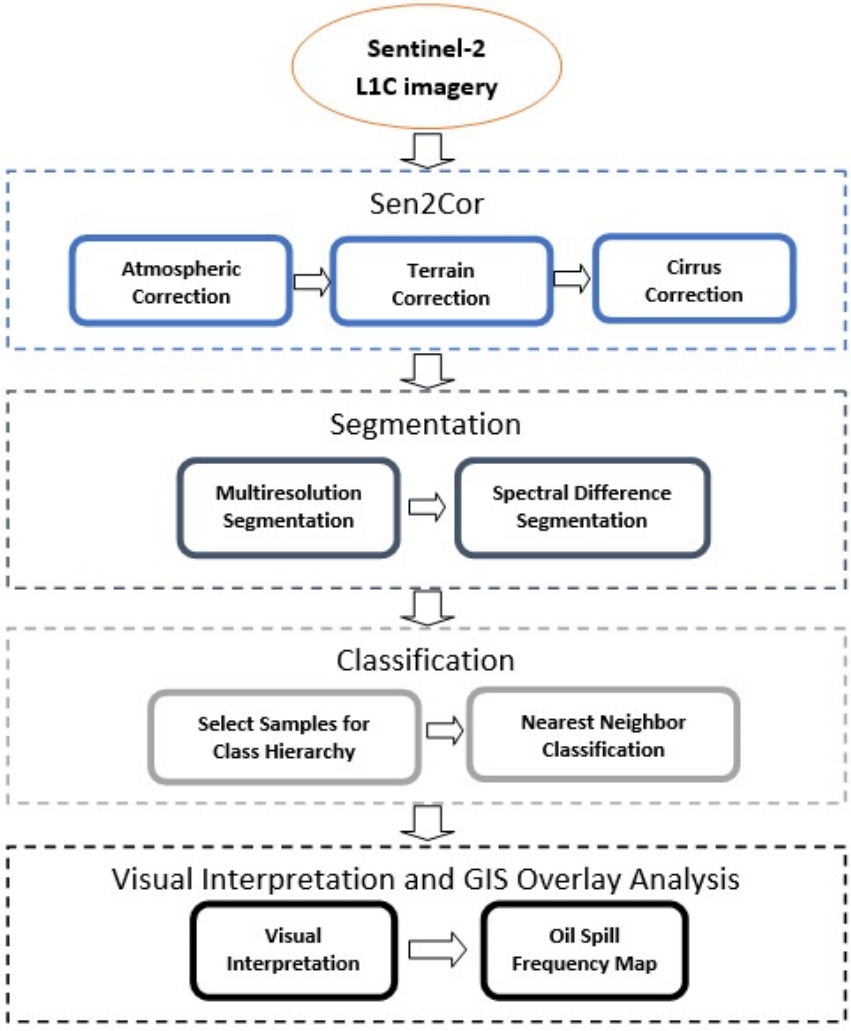

Figure 2 – Workflow for the detection of oil spill frequency

Results and discussion. Oil spills in the study area for the most cases are easily detected visually in the visible range of the electromagnetic spectrum, they usually have a silver-blueish color (figure 3 a, b), which indicates the thinness of the slicks [16].

a) b)

Figure 3 – Well visible oil spills (a-The Oil Rocks Settlement, b – Pirallahi Island)

But it should be noted that in some cases in the zones of accumulation of biogenic material such as surface seaweeds or sunken kelp beds oil detection was difficult. One of that cases presented in figure 4. Under many conditions, oil is not visible on the surface of the water [17]. Oil spills on shorelines is difficult to identify positively because seaweeds look similar to oil and oil cannot be detected on darker shorelines [18].

Figure 4 – One of difficult cases

In addition, there remain limitations such as cloudiness in the images. Indeed, many pictures for 2019 were cloudy over 20%. This is completely unsuitable for operational monitoring.

Therefore, it is better to take an integrated approach, namely the use of both radar and optical images. This approach also partially solves the issue of validation in those days when the sensing days coincides of both radar and optical sensors. This allows us to compare the obtained oil spill detection results. Example of that comparing presented in figure 5 (a, b), where we see the correspondence.

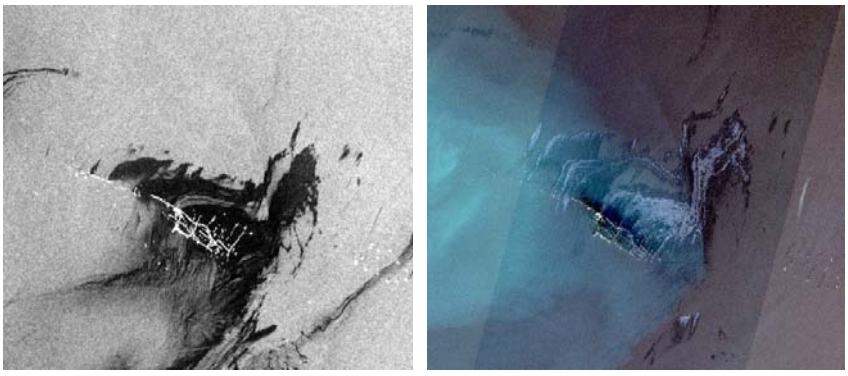

a) b)

Figure 5 – a) Radar image on 26th of April; b) Optical image on same date

The detection of oil spill from Sentinel-2 images and multi-temporal GIS overlay analysis resulted in the map of hot spots with high frequencies of oil spills during 2019 year, presented in figure 6. On the map we see that the main hotspot of oil spills is the Oil Rocks Settlement, what was to be expected. The medium class of oil leak sources were observed around the Oil Rocks Settlements and Chilov Islands and the small and occasional leak sources were observed around Pirallahi Island.

This map will allow to increase the accuracy and reliability of detected oil spills in future monitoring. For example, the oil spill areas with no overlaps and far away from the oil spill hot spots will not be mapped because of the lower reliability of occurrence.

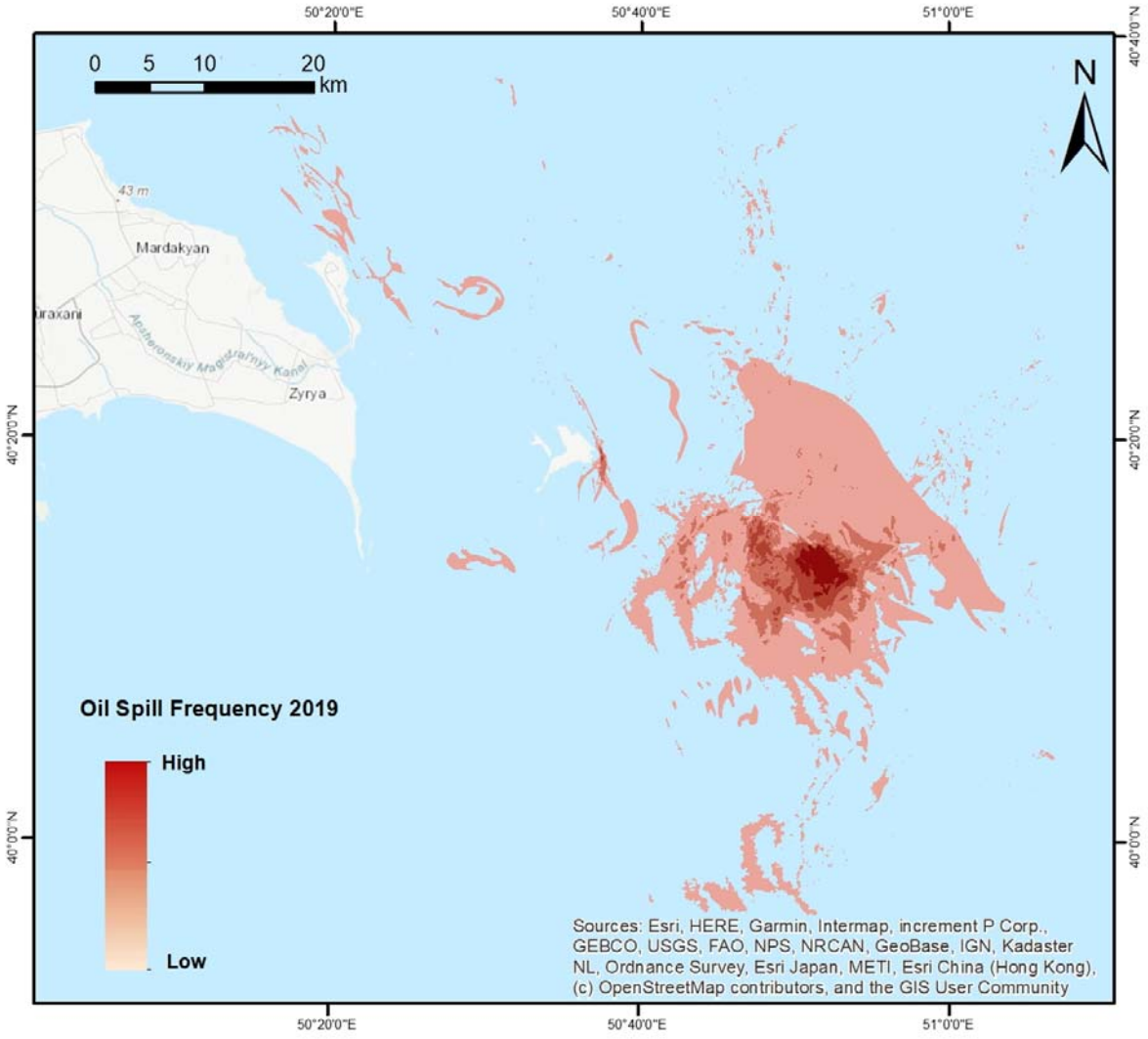

Figure 6 – Map of oil spill frequency in 2019

Conclusion. Research in this direction will be continued with the use of more remote sensing data, their statistical analysis, with the aim of increasing the likelihood of detecting oil pollution and its practical application. Preliminary results are considered successful and consistent, with a high degree of applicability to other Sentinel-2 satellite imagery. Further testing and proper tuning of the proposed object-oriented methodology should be carried out using SAR images.

These works are carried out with financial support by the CS MES RK, in the framework of the scientific and technical program O.0782 “Development of a multi-purpose aerospace forecast monitoring system (MAKSM), as well as the creation on its basis of services for the comprehensive presentation of emergency and natural-generated emergency information in conjunction with semantic and geospatial data”.

Ж. Ш. Жантаев, Д. В. Чепашев, А. А. Қалдыбаев, С. М. Нұрақынов, К. М. Унгаров

ЕЖШС «Ионосфера институты» АҚ «Ұлттық ғарыштық зерттеулер мен технологиялар орталығы», Алматы, Қазақстан

SENTINEL-2 ОПТИКАЛЫҚ СУРЕТТЕРІН ПАЙДАЛАНА ОТЫРЫП, КАСПИЙ ТЕҢІЗІНДЕГІ МҰНАЙДЫҢ ТӨГІЛУ ЖИІЛІГІН КАРТАҒА ТҮСІРУ

Аннотация. Мұнай өнеркәсібінің өнімдерімен ластанған Каспий теңізіндегі экологиялық жағдай – жағалау маңындағы мемлекеттер үшін маңызды проблемалардың бірі. Каспий теңізі күннен күнге антропогендік әрекетке ұшырауда. Жыл сайын судың мұнай өнімдерімен ластануы артып келеді. Теңіз биоресурстарының қысқаруы тез қарқын алуда. Халықаралық тәжірибе көрсеткендей, ғарыштық мониторинг әдістері көптеген табиғи және техногендік төтенше жағдайлардың, атап айтқанда, мұнайдың төгілуінің даму динамикасын анықтау мен бағалаудың неғұрлым тиімді тәсілі болып табылады. Қазіргі заманғы қашықтықтан зондылау жүйелері үлкен аумақтардағы әртүрлі көлемдегі төтенше жағдайлар туралы шолу және толық ақпарат алуға мүмкіндік береді. Сонымен қатар, ғарыштық мониторинг әдістері деректерді жинаудың дәстүрлі жерүсті әдістерінен әлдеқайда үнемді. Қашықтықтан зондылауда сенсорлардың екі түрі қолданылады - активті (радарлық) және пассивті (оптикалық). Сенсорлардың екі түрінің де өз артықшылықтары мен кемшіліктері бар. Көптеген артықшылықтардың арқасында радарлық суреттер қазіргі уақытта мұнайдың төгілуін қашықтықтан зондылаудың ең көп таралған құралы болып табылады. Алайда, радарлық суреттерді пайдалана отырып, кейде антропогендік мұнай төгілуін және оларға ұқсас жалған объектілерді бөліп алу қиын болады және әдетте оларға "look-alikes" деп аталатын, желсіз аймақтарды, табиғи текті органикалық пленкаларды, балдырлардың гүлденуін және т. б. қамтиды. Бұл жұмыстың негізгі мақсаты – бір жыл ішінде мұнай төгілуінің жоғары жиіліктері пайда болатын аймақтарды картаға түсіру және мұнай төгілуін анықтау мақсатында оптикалық суреттердің мүмкіндіктерін бағалау. Апшерон түбегінің маңындағы Каспий теңізі ауданы зерттеу ауданы ретінде таңдалды. Мұнайдың төгілулері Каспий теңізінің басқа аймақтарына қарағанда осы өңірде жиі анықталады, сондықтан оптикалық сенсорларды пайдалана отырып салынған осы өңірдегі «Мұнайдың жиі төгілу аймақтары картасы» болашақта мұнай төгілуінің мониторингі үшін пайдалы болады. Sentinel-2 (A, B) жерсеріктерінің оптикалық бейнелері мұнайдың төгілуін анықтау және олардың жиі пайда болу аймақтарын есептеу үшін пайдаланылды. Жүктелген суреттер L1C-ден L2A суретін жасайтын Sen2Cor утилитасы арқылы алдын ала өңделді. Пикселдерді бір-бірден жіктейтін пикселдер негізіндегі жіктемеге қарағанда, объектілі-бағытталған тәсіл алдымен бейненің пикселдерін бейненің сегменттеуін пайдалана отырып, спектрлік біртекті объектілерге топтастырады, содан кейін жекелеген объектілерді жіктейді. Мұнай төгілуі ретінде жіктелген объектілер көзбен шолу арқылы тексерілді. 2019 жыл ішінде мұнай төгілуінің жоғары жиіліктері бар аймақтардың картасы ұсынылды. Салынған карта бойынша 2019 жылы мұнай төгілуінің ең жиі көздері анықталды, атап айтқанда "Мұнай тастары", "Чилов" және "Пираллахи" кен орындары. Сондай-ақ, мақалада кейбір төгілулерді көрнекі түсіндіру кезінде туындаған қиындықтардың мысалдары келтірілген. Нәтижесінде, «мұнайдың төгілуін мониторингілеу үшін радиолокациялық деректермен қатар оптикалық бейнелерді пайдалану да орынды», - деген қорытынды жасалды.

Түйін сөздер: мұнай төгілуін анықтау, Каспий теңізі, Sentinel-2, оптикалық суреттер.

Ж. Ш. Жантаев, Д. В. Чепашев, А. А. Калдыбаев, С. М. Нуракынов, К. М. Унгаров

ДТОО «Институт ионосферы» АО «Национальный центр космических исследований и технологий», Алматы, Казахстан

КАРТИРОВАНИЕ ЧАСТОТЫ РАЗЛИВОВ НЕФТИ В КАСПИЙСКОМ МОРЕ С ИСПОЛЬЗОВАНИЕМ ОПТИЧЕСКИХ ИЗОБРАЖЕНИЙ SENTINEL-2

Аннотация. Экологическая ситуация на Каспийском море, которое буквально насыщено продуктами нефтяной промышленности, является одной из острых проблем для прибрежных государств. Каспийское море подвержено возрастающему антропогенному воздействию. С каждым годом увеличивается загрязнение воды нефтепродуктами. В быстром темпе происходит сокращение морских биоресурсов. Международный опыт показывает, что методы космического мониторинга являются наиболее эффективным способом выявления и оценки динамики развития большинства природных и техногенных чрезвычайных ситуаций, в частности разливов нефти. Современные системы дистанционного зондирования позволяют получать

обзорную и подробную информацию о чрезвычайных ситуациях различных размеров на больших территориях. В то же время методы космического мониторинга намного экономичнее традиционных наземных методов сбора данных. В дистанционном зондировании используются два типа сенсоров - активный (радарный) и пассивный (оптический). Оба типа сенсоров имеют свои преимущества и недостатки. Благодаря многим преимуществам, радарные снимки в настоящее время являются наиболее распространенным средством дистанционного зондирования разливов нефти. Однако, используя радарные снимки, иногда бывает трудно отделить антропогенные разливы нефти и ложные объекты, похожие на них, и обычно называемые «look-alikes», которые включают безветренные области, органические пленки естественного происхождения, цветение водорослей и т. д. Используя же оптические изображения для обнаружения разливов нефти, мы полагаемся на спектральные характеристики объектов, и хотя отражательная способность варьируется в зависимости от толщины и состава пятна, в большинстве случаев разливы нефти можно отличить от похожих ложных объектов. Основная цель данной работы - оценить возможности оптических снимков в задаче обнаружения разливов нефти, опробовав их в задаче картирования зон с высокой частотой появления разливов нефти в течение одного года. Район Каспийского моря возле Апшеронского полуострова был выбран в качестве района исследований. Разливы нефти обнаруживаются в этом регионе чаще, чем в других регионах Каспийского моря, поэтому карта зон с частыми разливами нефти в этом регионе, построенная с использованием оптических сенсоров, будет полезна для будущего мониторинга разливов нефти. Оптические изображения спутников Sentinel-2 (A, B) использовались для обнаружения разливов нефти и расчета зон их наиболее частого появления. Скачанные снимки были предварительно обработаны с помощью утилиты Sen2Cor, генерирующей изображения L2A из L1C. Объектно-ориентированный подход был выбран для сегментации и классификации изображений. В отличие от классификации на основе пикселей, которая классифицирует пиксели по одному, объектно-ориентированный подход сначала группирует пиксели изображения в спектрально однородные объекты изображения с использованием сегментации изображения, а затем классифицирует отдельные объекты. Объекты, классифицированные как разливы нефти, проверялись путем визуальной интерпретации. Был проведен анализ наложения и представлена карта зон с высокими частотами появления разливов нефти в течение 2019 года. По построенной карте, были определены наиболее частые источники разливов нефти за 2019 год, а именно месторождения «Нефтяные камни», «Чилов» и «Пираллахи». Также в статье приведены примеры сложностей, возникших при визуальной интерпретации некоторых разливов, и сделаны выводы о целесообразности использования оптических изображений наряду с радиолокационными данными для мониторинга разливов нефти.

Ключевые слова: обнаружение разливов нефти, Каспийское море, Sentinel-2, оптические снимки.

Information about authors:

Zhantayev Zhu. Sha., Institute of Ionosphere, JSC NCSRT, Almaty, Kazakhstan, Director, Doctor of Geological and Mineralogical Sciences, Corresponding member of NAS RK; admion1@mail.ru; https://orcid.org/0000-0002-9189-9546;

Chepashev D. V., Institute of Ionosphere, JSC NCSRT, Almaty, Kazakhstan, Researcer, PhD student; chepashev_daniker@mail.ru; https://orcid.org/0000-0002-8417-3990;

Kaldybaev A. A., Institute of Ionosphere, JSC NCSRT, Almaty, Kazakhstan, Deputy Director, PhD; azamat.kaldybayev@gmail.com, https://orcid.org/0000-0002-0563-282X;

Nurakynov S. M., Institute of Ionosphere, JSC NCSRT, Almaty, Kazakhstan, head of the Cartography and GIS Laboratory, PhD student; nurakynov@gmail.com; https://orcid.org/0000-0001-9735-7820;

Ungarov K. M., "Institute of Ionosphere", JSC "National Center of Space Research and Technology", Almaty, Kazakhstan; kelis9696@mail.ru; https://orcid.org/0000-0001-9692-1346

REFERENCES

[1] Lavrova O.U., Mityagyn M.I. Satellite monitoring of coastal anthropogenic pollution [Sputnikovyi monitoring antropogennyh zagryaznenyi pribrezhnoi zony] // Zemlya i Vselennaya, (2008) №1. pp. 26-34. ISSN: 0044-3948 (in Russian).

[2] Nesterova M.P. Methods and means of combating oil pollution of the World Ocean waters. Problems of chemical pollution of the World Ocean waters [Metody i sredstva borby s neftyanym zagryazneniem vod Mirovogo okeana. Problema himicheskogo zagryazneniya vod Mirovogo okeana], T. 8., L.: Gidrometeoizdat, (1989), p. 208 (in Russian).

[3] Izrael U.A., Ciban' A.V. Anthropogenic Ocean Ecology [Antropogennaya ekologiya okeana], Moscow: Flinta Nauka, (2009). p. 529 ISBN: 978-5-9765-0879-8 (in Russian).

[4] [Mass death of fish occurs in the Caspian Sea. Available at: https://neftegaz.ru/news/incidental/323916-v-kaspiyskom-more-proiskhodit-massovaya-gibel-ryby/ (accessed on 28 March 2020)]

[5] Stark J.S., Riddle M.J., Snape I, Scouller R.C. Human impacts in Antarctic marine soft sediment assemblages: correlations between multivariate biological patterns and environmental variables at Casey Station. Estuarine, Coastal and Shelf Science (2003);56:717. DOI: 10.1016/S0272-7714(02)00291-3

[6] Stark J.S, Riddle M.J, Smith S.D.A. Influence of an Antarctic waste dump on recruitment to nearshore marine soft-sediment assemblages. Marine Ecology Progress Series (2004); 276:53. DOI: 10.3354/meps276053

[7] Raymond T.C, Snape I. Using triage for environmental remediation in Antarctica: Triage for environmental remediation in Antarctica. Restoration Ecology (2016); 25(1). DOI: 10.1111/rec.12383

[8] Northcott K.A, Snape I, Connor M.A, Stevens G.W. Water treatment design for site remediation at Casey Station, Antarctica: site characterization and particle separation. Cold Regions Science and Technology (2003); 37:169. DOI: 10.1016/S0165-232X(03)00039-9

[9] Nedwed T, Coolbaugh T, Tidwell A. Subsea dispersant use during the Deepwater Horizon incident. AMOP (2012);506.

[10] [Oil Rocks field in Azerbaijan provides up to 70% of SOCAR's oil gas extraction volume. Available at: https://www.oilandgas360.com/oil-rocks-field-in-azerbaijan-provides-up-to-70-of-socars-oil-gas-extraction-volume/ (accessed on 03 April 2020)]

[11] Bayramov E., Buchroithner M., Bayramov R. Detection of oil pollution hotspots and leak sources through the quantitative assessment of the persistence and temporal repetition of regular oil spills in the Caspian Sea using remote sensing and GIS. ISPRS Annals of Photogrammetry, Remote Sensing and Spatial Information Sciences (2015). II-3/W5. 451-457. DOI: 10.5194/isprsannals-II-3-W5-451-2015

[12] [Copernicus Open Access Hub. Available at: https://scihub.copernicus.eu/ (accessed on 25 March 2020)]

[13] [Sentinel-2 Toolbox. Available at: https://sentinel.esa.int/web/sentinel/missions/sentinel-2/ (accessed on 27 March 2020)]

[14] Main-Knorn M., Pflug B., Louis J., Debaecker V., Muller-Wilm U., Gascon F. Sen2Cor for Sentinel-2. In: Conference on Image and Signal Processing for Remote Sensing, 23., (2017), Warsaw, Poland. Proceedings. Bellingham: SPIE. DOI: 10.1117/12.2278218

[15] Darwish A., Leukert K., Reinhardt W. Image segmentation for the purpose of object-based classification. In: Geoscience and Remote Sensing Symposium, (2003). IGARSS'03. Proceedings. 2003 IEEE International. IEEE, pp. 2039–2041 DOI: 10.1109/IGARSS.2003.1294332

[16] Karathanassi, V., Topouzelis K., Pavlakis P., Rokos D. An object-oriented methodology to detect oil spills. International Journal of Remote Sensing 27, no. 23 (2006): 5235-5251. DOI: 10.1080/01431160600693575

[17] Smith T.G, Geraci J.R, St Aubin D.J. Reaction of bottlenose dolphins, Tursiops truncatus, to a controlled oil spill. Canadian Journal of Fisheries and Aquatic Sciences (1983);40(9):1522e5. DOI: 10.1139/f83-175

[18] Fingas M., Brown C.E. A Review of Oil Spill Remote Sensing. Sensors, (2017); 18(1):91. DOI: 10.3390/s18010091

NEWS
OF THENATIONAL ACADEMY OF SCIENCES OF THE REPUBLIC OF KAZAKHSTAN
PHYSICO-MATHEMATICAL SERIES
ISSN 1991-346X **https://doi.org/10.32014/2020.2518-1726.53**
Volume 3, Number 331 (2020), 191 – 201

UDC 910.1, 911.9

Zh. Sh. Zhantayev, S.M. Nurakynov,
S.V. Gavruk, B.A. Iskakov, N.K. Sydyk, A.A. Merekeyev

Institute of Ionosphere JSC "NCSRT", Almaty, Kazakhstan.
E-mail: admion1@mail.ru; nurakynov@gmail.com; mjdagot@gmail.com;
berikiskakov@gmail.com; nurmahambet.s@gmail.com , aiba99@mail.ru

CREATION OF A GEOPORTAL AND ITS ROLE IN OPERATIONAL MONITORING OF THE NATURAL AND MANMADE EMERGENCY CHARACTER IN THE TERRITORY OF THE REPUBLIC OF KAZAKHSTAN

Abstract. This article discusses the space monitoring system, its composition and functional diagram of the basic elements of the system and remote access services to the resources and results of the space monitoring system. The composition of the information support of the system, its formats and sources, and the frequency of updates are described. The basic structure of the geoportal, namely, the subsystem for collecting satellite and ground data, a database, processing and expert interpretation, integration and dissemination of monitoring data, is briefly described. The whole cycle of space monitoring work is described for each priority area, from obtaining raw data to uploading emergency monitoring data to the geoportal in Kazakhstan, including operational data from space monitoring of forest and steppe fires, GPS monitoring of intense movements of the earth's crust, space monitoring of floods, space monitoring oil pollution of the Caspian Sea with the corresponding "screenshots". The geoportal interface is described.

Key words: Geoportal, space monitoring of emergency situations, remote sensing, GIS, geodynamics, fires, floods, oil spills.

Introduction. With the development of space and information technology, emergency monitoring using satellite data is gaining tremendous relevance. World experience shows that the main, and often the only source of information on the basis of which decisions are made on measures to eliminate emergency situations are space monitoring systems [1, 2]. And among them, the most popular is operational monitoring of emergencies, such as fires, snow cover, floods, oil pollution and GPS monitoring of movements of the earth's crust. Since the main emphasis is on efficiency, it is necessary to take into account timely notification of not only the relevant authorities, but also ordinary citizens of our country. In this regard, the urgent need to create a single geoportal that contains relevant information on all of the above emergencies arises on its own. There are no analogues of a complete and comprehensive space emergency monitoring system using the latest achievements of remote sensing and GIS, not only in Kazakhstan, but throughout Central Asia.

Creation of a geoportal. At the moment, the geoportal has become the main source for transmitting the results of space monitoring of emergency situations to all interested parties. To achieve this goal, first of all, it is necessary for the geoportal to physically be able to work with large amounts of spatial data and with a large number of users, as well as to develop a technology for updating spatial databases of the geoportal that ensures optimal and timely, including operational, downloading of new data. Thus, having studied the world experience [3, 4] in the technology of creating geoportals, it was decided to develop our own product from scratch. This approach has several advantages: creating a product on the basis of separate off-the-shelf software solutions, the licenses of which allow their use to create your own software. The source code of such programs is available for viewing, studying and changing and allows

you to fully control the system development process and get a product that fully meets the requirements; a simpler opportunity to expand the system's functionality on its own and significantly save time and financial resources necessary for the development of the system by reducing the amount of work; users get a system that fully meets their expectations.

Software components. The main component of the geoportal is a server application whose tasks include receiving and processing all incoming user requests, as well as sending responses to these requests. The server part also includes the industrial Database Management System (DBMS), the task of which is to store user data and spatial information. In addition, to formulate a response to a spatial query, a component complying with OGC specifications [5] is required.

Thus, the developed geoportal is based on the following software components:

- operating system - Linux Debian. Distinctive features of Debian are: Advanced Packaging Tool (APT) package management system, strict package policy, repositories with a huge number of packages, as well as high quality of released versions. [6];

- DBMS - PostgreSQL with PostGIS extension for working with geometric data types. PostgreSQL was chosen for the following reasons: free; wide functionality for working with geometric objects [7, 8]; support by various geographic information systems (ArcGIS, QGIS, GeoServer); availability of open access to extensive documentation;

- web server - Apache. The main advantages of Apache are reliability, configuration flexibility and cross-platform (the ability to work on different operating systems) [9]. It allows you to connect external modules to provide data, use a DBMS to authenticate users, modify error messages, etc. Apache HTTP Server supports modularity;

- Python programming language. This actively developing programming language over time has become virtually the standard language in the field of science and data processing [10].

- display of cartographic information on the client side - OpenLayers. An open source library written in JavaScript designed to create maps based on a software interface (API) [11]. OpenLayers allows you to very quickly and easily create a web-based interface for displaying cartographic materials presented in various formats and located on different servers;

- processing of geospatial data - GDAL library GDAL - an open source library [12] for reading and writing raster and vector geospatial data formats. The library provides calling applications with a single abstract data model for all supported formats.

Figure 1 presents a diagram demonstrating the composition and structure of the software of the developed system, its functional purpose and distribution across the servers.

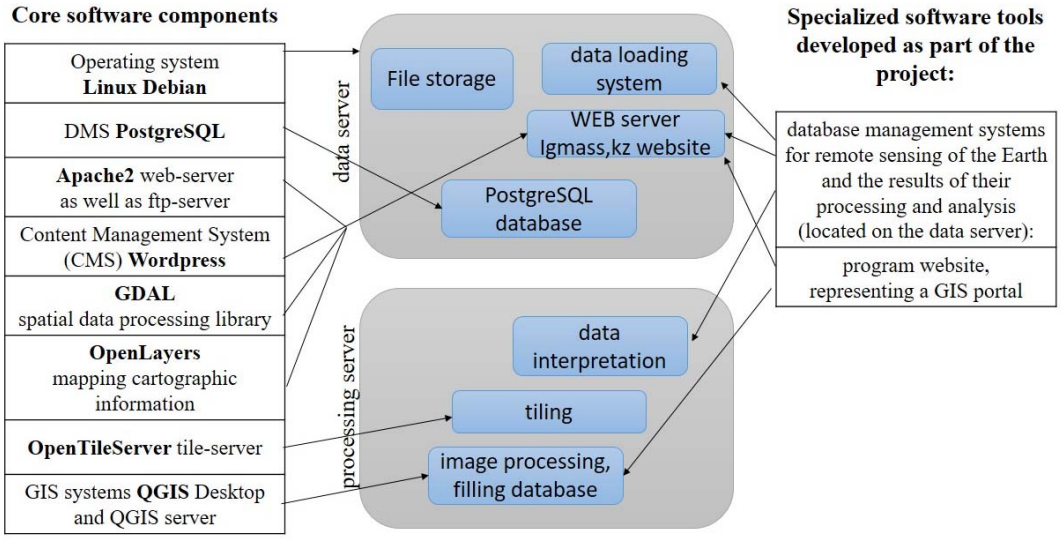

Figure 1 - Composition and structure of software system under development

Input data, processing and interpretation. Processing and interpretation of data is carried out both manually in the data interpretation unit, and automatically in the image processing unit. The input data is

tabular data and raster images in the file storage, the output is vectorized data in the database. The function of the processing and interpretation level is to obtain emergency information from the source data, for example:

- separation of vectorized information from raster satellite imagery – hotspots (thermal anomalies), burned areas, flooded areas, oil spills;
- calculations according to GPS stations of displacement velocity vectors and their interpolation;
- processing and vectorization of hydrometeorological data necessary for modeling and forecasting forest and steppe fires, floods, oil spills.

Database for monitoring fires and burned areas. In modern conditions, the most effective and efficient solution to this problem is achieved using space monitoring systems. Satellites allow you to detect fires ranging from fractions of a hectare to several tens of hectares, depending on the intensity of combustion and the state of the atmosphere, which allows you to provide the most complete information about the entire forest and steppe territory and significantly reduce the cost of the work compared with aviation monitoring of fires.

During the day over ten (figure 2) remote sensing satellites fly over the territory of Kazakhstan. The main satellites for the rapid detection of fires and building maps of burned areas are the TERRA and AQUA satellites with MODIS (Moderate Resolution Imaging Spectroradiometer) spectrometers and NOAA satellites with the AVHRR (Advanced Very High Resolution Radiometer) spectrometer. Based on the data of these satellites, foci of fires and burned areas with a frequency of twice a day for 0.5-1 hours from the receipt of satellite images are detected. When identifying hot spots, the vector of the fire sources is cleaned from constant sources of high temperatures, associated mainly with industrial activities.

This meets the main monitoring requirement - efficiency. The whole process: downloading images, processing and obtaining the necessary layers and uploading to the geoportal are fully automated.

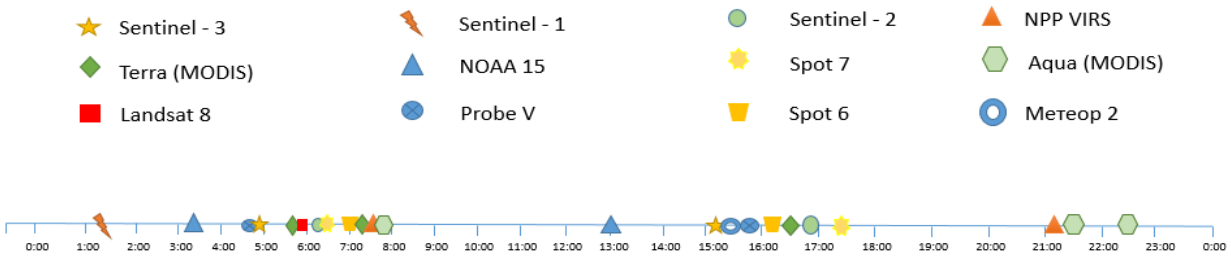

Figure 2 - The pattern of the passage of remote sensing satellites during the day over the territory of Temirtau, Karaganda region

For a more detailed analysis of burned-out territories, images from satellites of the Landsat family and Sentinel-2 are used every seven days. In case of high cloud cover, radar images from the Sentinel-1 satellite are used. Also, during the fire hazard season, the following tasks are performed:

- maps of the dynamics of the hot spots and the dynamics of the areas affected by the fires are built;
- zoning of the territory according to the risk of fire;
- if necessary, modeling and assessment of the risk of fire hazard is carried out taking into account the characteristics of the terrain (vegetation, soil moisture, incline, wind, slope aspect, distance to the route, settlement and fire hydrant) and weather data. These processes are done manually. Figure 3 and 4 show the hot spots and burned areas, respectively, in the form of screenshots by displaying the igmass.kz site (geoportal).

Received daily maps with fire sources form a time series, the analysis of which allows you to get a variety of characteristics of the dynamics of the situation with fires, including cartographic, tabular and chart forms.

Flood monitoring database. Space monitoring of the passage of flood waters (figure 5) and the disappearance of snow cover, as necessary, can be carried out at three levels [13]. At the first level, daily analysis is carried out using MODIS low-resolution satellite data (spatial resolution 250 m). As an auxiliary, night shots of NOAA AVHRR and MODIS in the infrared range are used. Their use is due to the fact that for some regions there is less cloud cover at night compared with the daytime period. Despite the low resolution, the value of MODIS data is that the survey is conducted daily.

Figure 3 - Screenshot of the igmass.kz site display and the open hotspot page

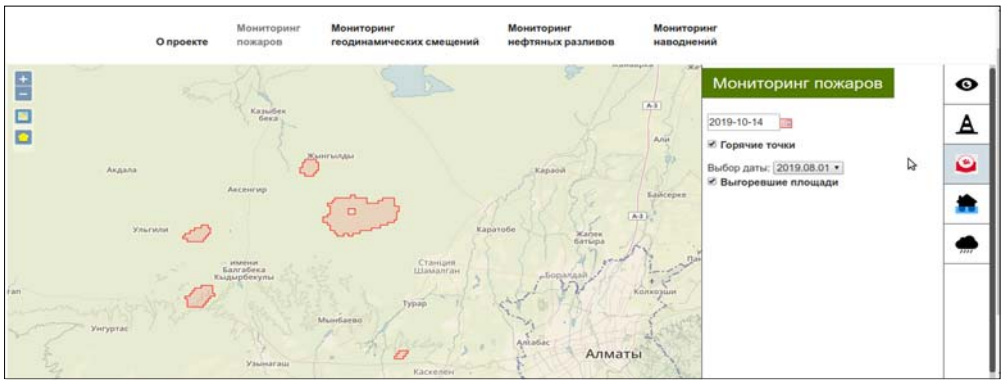

Figure 4 - Screenshot of the igmass.kz site display and the open burned area monitoring page

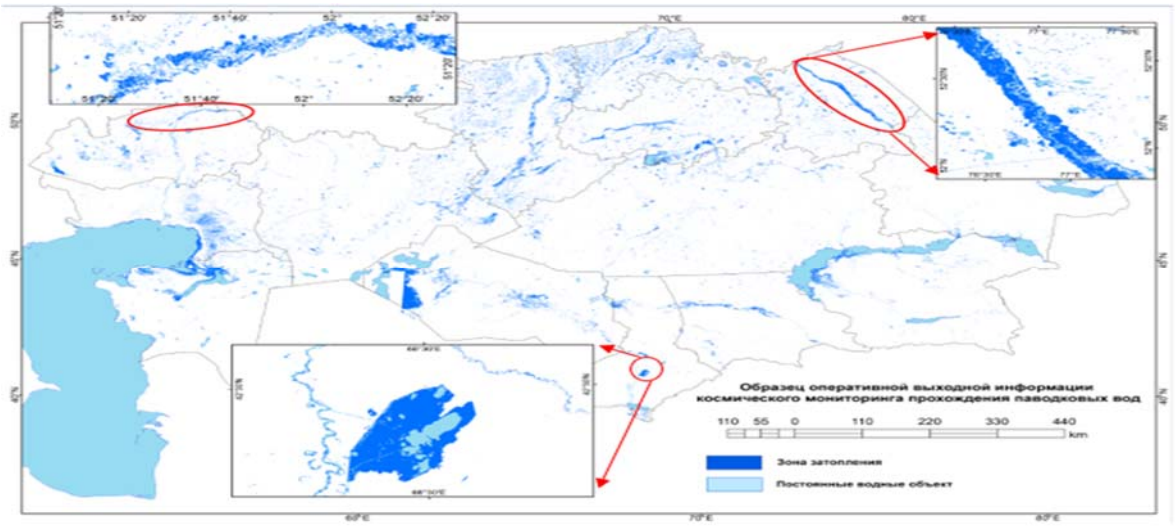

Figure 5 - A sample of the operational output of space monitoring of the passage of flood waters

At the second level, as they are received (the survey is performed every 7-10 days), medium-resolution data (spatial resolution 15-70 m), for example, Landsat data, as well as radar data, in particular images of the European Sentinel 1 satellite, are involved. A feature of radar data is that it is not affected by cloudiness or the time of day. They allow you to see the area covered by clouds, which is important for spring conditions, when often the entire territory of the region is covered with dense clouds.

At the third level, if it is necessary to analyze the situation in especially critical cases, optical and radar remote sensing arrays of high and ultrahigh resolutions are used.

Using the data from the MODIS sensor, space-time monitoring of snow and ice cover melting is performed twice a day (snow cover with highlighting snow melting zones), once a day mapping of flood

zones (with additional use of data from Landsat, Sentinel-1-2 satellites) 0.5-1 hours after receiving the space image.

Mapping of total flood zones is carried out once a decade. And zoning of territories according to the degree of risk of flooding using hydrometeorological information for the last 5 years and archival data from Landsat, Sentinel-2 satellites - once a season.

Also, modeling and forecasting the development of large floods would be done as necessary during the period of flooding. For this, relevant hydrometeorological and cartographic information, DEM with a resolution of 10 m, and maps of the dynamics of the water surface of reservoirs are used.

Oil spill monitoring database. Currently, the issue of pollution of the Caspian Sea, which is saturated with oil industry facilities, is highly relevant. Of great importance for Kazakhstan is the control of such objects and phenomena that pose a potential and real threat of natural and man-made emergencies, such as accidental oil spills that entail significant damage to the environment [14].

Oil spills are monitored using data from the Sentinel-1A, B satellites, European Earth remote sensing satellites, which are part of the space group of satellites for the Copernicus Global Environmental and Safety Monitoring. Sentinel-1 products are available in real time, free of charge for all data users, including the general public, scientific and commercial users. Shooting is performed in the C-band (wavelength 6 cm) in one polarization (HH or VV) and double polarization (HH + HV or VH + VV). To verify the results obtained, optical images of the satellites of the Landsat and Sentinel-2 family are used.

In the period from March 1 to December 31, after processing the data of the aforementioned satellites, we get a map of oil pollution of the Caspian Sea, taking into account the temperature data of the water surface, speed and direction of the driving wind, maps – schemes of the main sources of oil pollution in the sea, in particular: ship routes , as well as the epicenter of earthquakes 1 time in 3 days for 0.5-1 hours from the moment the data are received. The attributive information contains data on time, satellite, area, perimeter, and most importantly, on the coordinates of pollution (figure 6); maps of the dynamics of changes in the total area of oil pollution over the week and month; maps of the intensity of oil pollution of the Caspian Sea per month, per decade, per year.

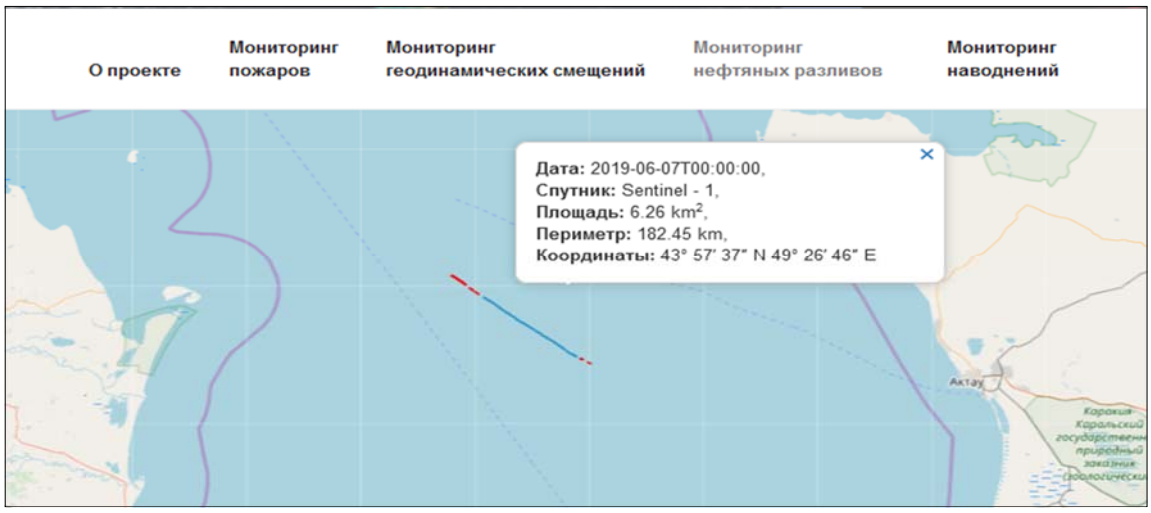

Figure 6 - An example of obtaining attribute information

Using data processing from the MODIS sensor and the Landsat satellite, we obtain maps of the ice conditions of the Caspian Sea for a decade.

As necessary and / or in case of major accidents associated with an oil spill, modeling of the movement of oil pollution using temperature data of the water surface, speed and direction of the driving wind is carried out.

Database of monitoring of geodynamic displacements. To calculate the geodynamic displacements of the surface, data from a high-precision satellite navigation network (SVSK RK) from 112 GPS stations, commissioned in 2016 by JSC "NC" Kazakhstan Karysh Sapary "JSC, Leica Geosystem Kazakhstan JSC,

and TRIMBLE GEOTRONICS LLP, are used. Data collection, transmission and archiving is carried out via GSM communication channels on the servers of service organizations.

The input information is presented in the form of text files and includes the following data: GPS station hardware characteristics, digital elevation model (in meters), Moho sole digital model (km), tectonic faults (vectors), digital heat flow model, surface velocity components (mm / year) in the directions SN, WE, Up and the module of horizontal speed. Schematic maps of the distribution of the velocities of the earth's surface and the parameters of the stress-strain state of the earth's crust of the seismically active region (Almaty test site) have been compiled.

After processing data from 49 permanent GPS stations in Kazakhstan, including 19 TRIMBLE stations (Geotronics LLP), 20 LEICA stations (LEICA Kazakhstan JSC), 10 stations in the Almaty seismic test site (DTOO Ionosphere Institute and Institute Seismology of the Ministry of Education and Science of the Republic of Kazakhstan) once a quarter, a map of the displacement velocity of GPS stations of the territory of Kazakhstan is calculated (figure 7) (vector, velocity field).

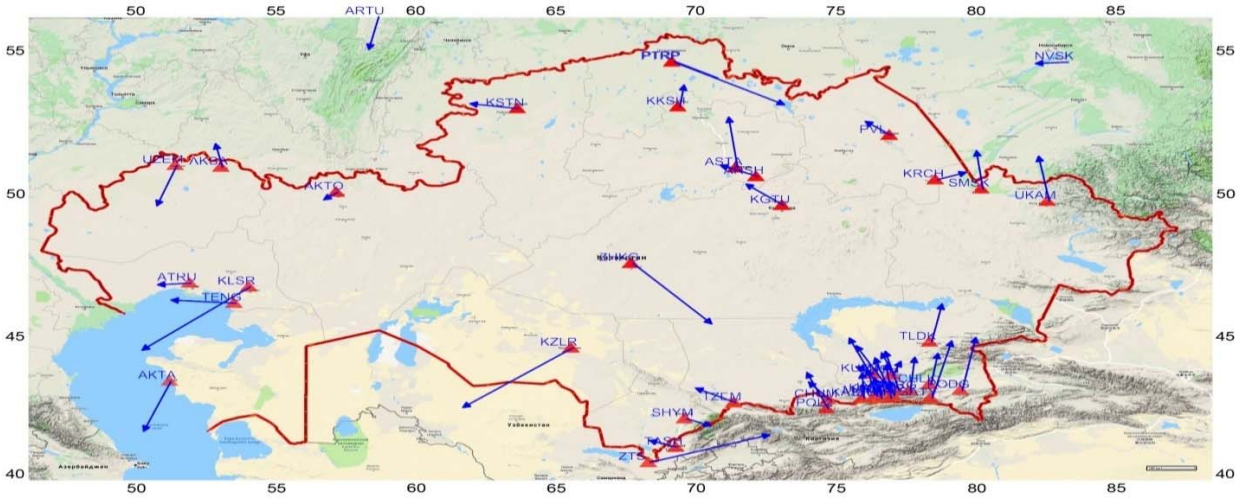

Figure 7– Vectors of horizontal speeds of GPS stations

Twice a year, the geomechanical state of the earth's crust of earthquake-prone areas of Kazakhstan is assessed using satellite monitoring of modern earth surface movements using the following data: seismic data; digital elevation model; digital sole model (Moho); tectonic faults; component of the speed of the earth's surface West-East (meters per year); component of the surface speed of the earth South-North (meters per year); vertical component of speed (meters per year); absolute value of speed (meters per year); parameters of the stress and strain field of the earth's crust.

In addition, data such as:

- administrative boundaries; - settlements; - data on emergency facilities (fire brigades, hospitals, emergency collection points, etc.); - data on hydrology (rivers, lakes, hydro-network); - sea routes and bathymetry of the Caspian Sea; - data on GPS stations of geodynamic monitoring. Thus, under the control of the database management system there are 4 databases for each of the topics, and a database of auxiliary layers:

- firedb - database for monitoring fires and burned out areas;
- geodinamic - database of monitoring of geodynamic displacements;
- oilspills - oil spill monitoring database;
- water - database for flood and flood monitoring;
- auxiliarylayers - a database of auxiliary layers.

Results and its discussions. An emergency space monitoring database management system has been developed. A geospatial database of operational emergency monitoring on the territory of Kazakhstan has been created, including operational data for space monitoring of forest and steppe fires, GPS monitoring of intense movements of the earth's crust, space monitoring of floods and floods, space monitoring of oil pollution of the Caspian Sea. An experimental sample of a web-GIS portal (geoportal) for space

monitoring of emergency situations in the Republic of Kazakhstan has been developed and is undergoing testing.

Further briefly on the main results of each area:

- Geodynamic GPS monitoring of intensive movements of the earth's crust is aimed primarily at solving the following problems: primary processing of satellite information data, special post-processing for operational and short-term forecast of earthquakes and seismic-related processes (landslides, landslides, mudflows) and transmission of monitoring data to control centers in crisis situations.

In the course of solving these problems with the use of new GPS monitoring stations, a new result was obtained for the first time that has predictive value. Based on the results of processing the velocity field, a local anomaly of the displacement velocity to the south of Almaty was identified. No anomaly was previously observed.

Calculations of the crust strength criterion (Coulomb-Mohr) (figure 8) showed the formation of the region of possible destruction of the rock mass due to the achievement of shear (shear) stress of the ultimate tensile strength of the soil.

For stations of the Almaty seismic test site, the errors in determining the velocities are slightly higher than the world ones and amount to ± 0.3 mm / year in plan and ± 1.3 mm / year in the vertical direction.

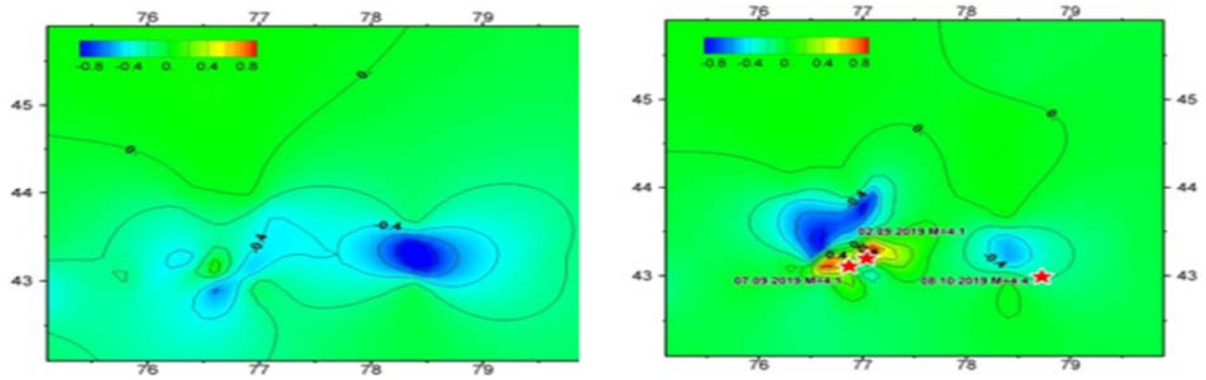

Figure 8 - Strength criterion of the Earth's crust of the Northern Tien Shan according to GPS observations until 2018 (left) and as of July 2019 (right)

- Based on the results of space monitoring of oil spills, a preliminary database of foci of oil pollution in the Kazakhstan part of the Caspian Sea was created using data from radar and optical surveys. The preliminary database contains 1304 scenes received by the SAR Sentinel-1A satellite, as well as 50 and 20 scenes received by the optical Sentinel-2A and LANDSAT-8 satellites, respectively.

Mapping of the main sources of oil pollution in the sea was carried out, in particular: ship routes, wells, oil islands, oil pipeline, oil and gas structures, as well as earthquake epicenters, which consequently affect the eruption of mud volcanoes located on the bottom of the Caspian Sea.

According to the results of monitoring of oil spills on the sea surface from April 1, 2018 to July 31, 2019, the total area of detected oil spills in the Kazakhstani part of the Caspian Sea reached 60.4 km2.

- Methods for monitoring forest and steppe fires and burned out areas have been developed. Preliminary results have been obtained from monitoring active fires and assessing the areas affected by fires according to MODIS data covering the territory of Kazakhstan. According to the results of space monitoring, the database of fire centers and areas affected by fires is continuously being filled. The content, structure and type of an online report on the results of monitoring of fires and burned out areas have been developed for presentation in the form of separate graphs and charts for a selected period of time in the geoportal itself.

Emergency committee facilities have been prepared and digitized, such as fire brigades, fire hydrants, emergency rescue services, hospitals, airspace, operational rescue squad, collection points and fire trains to assess the real danger of fires for settlements and prompt decision-making.

- The data of space flood monitoring were generated for 16 regions of Kazakhstan. The composition of the data includes: two-year series of data from space-based monitoring of floods of various temporal averaging (daily, ten-day and seasonal);

The current state of the geoportal and its unique features:

The current state of the hardware and software implementation and the pilot version of the Geoportal are available at http://igmass.kz/. The geoportal allows solving two main problems - timely electronic exchange of spatial data between interested organizations and companies of different profiles, as well as providing mass access to cartographic emergency monitoring products based on modern information and communication technologies.

In addition, one of the unique capabilities of the system is not only the receipt of the above information, but also the provision of various tools to users to conduct their own analysis and generate reports by constructing graphs and charts based on monitoring results (figure 9).

These tools allow, in particular:

- analyze various spatial information;
- generate specialized reports, including their analysis, refinement and reliability control;
- provide various graphical representations of information to ensure the convenience of its analysis;
- carry out processing and analysis of satellite information (including for assessing areas covered by fire using satellite data of various spatial resolutions);
- provide the ability to analyze historical information, including making convenient comparisons with operational information.

Thus, the system provides users with the opportunity to obtain a sufficiently large amount of information of a high level of processing and means for its analysis.

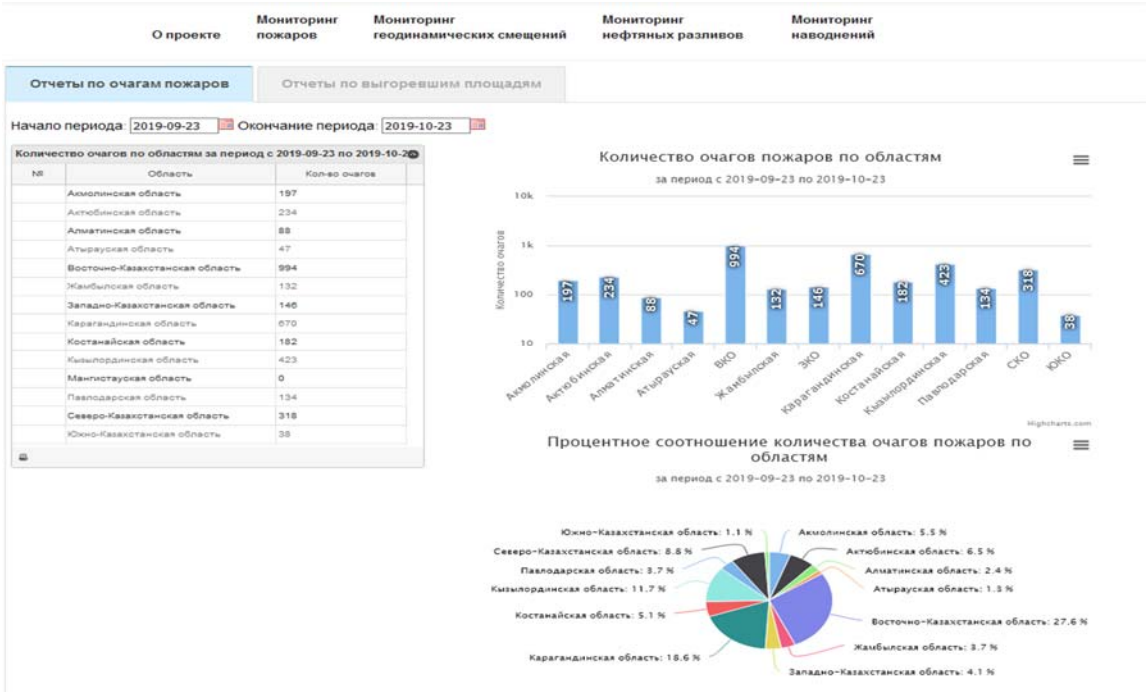

Figure 9 - An example of displaying a web portal for generating a report of fire outbreaks

When analyzing the dynamics of the situation for any particular time period, the user downloads all or selectively available information for a certain period. Such an analysis may be accompanied by appropriate tabular and other information characterizing the development of the situation for the selected period. The analytical unit also generates overview information for decades, months and years, which is available to users. Similarly, work is carried out with cartographic and analytical information when analyzing the development of the situation over a long period.

Conclusion. The created geoportal of geospatial data for operational monitoring of emergencies in Kazakhstan, including operational data for space monitoring of forest and steppe fires, GPS monitoring of intense movements of the earth's crust, space monitoring of floods, space monitoring of oil pollution of the Caspian Sea and operational coverage of these data on the geoportal with the possibility access from

anywhere in the world will allow you to timely respond and reduce critical damage in human life, flora, fauna and even completely prevented.

These works are carried out with financial support by the CS MES RK, in the framework of the scientific and technical program O.0782 “Development of a multi-purpose aerospace forecast monitoring system (MAKSM), as well as the creation on its basis of services for the comprehensive presentation of emergency and natural-generated emergency information in conjunction with semantic and geospatial data”.

Ж. Ш. Жантаев, С. М. Нуракынов, С.В. Гаврук,
Б.А.Искаков, Н.К. Сыдық, А. А. Мерекеев

Ионосфера институты, «ҰҒЗТО» АҚ, Алматы, Қазақстан;

ГЕОПОРАТАЛ ҚҰРУ ЖӘНЕ ОНЫҢ ҚР АУМАҒЫНДА ТАБИҒИ ЖӘНЕ ТЕХНОГЕНДІК СИПАТТАҒЫ ТЖ ЖЕДЕЛ МОНИТОРИНГІНДЕ РӨЛІ

Аннотация. Ғарыштық және ақпараттық технологиялардың дамуымен спутниктік деректердің көмегімен төтенше жағдайлар мониторингі үлкен өзектілікке ие. Әлемдік тәжірибе негізінде ТЖ жою жөніндегі шаралар туралы шешімдер қабылданатын негізгі, ал көбінесе жалғыз ақпарат көзі ғарыштық мониторинг жүйесі болып табылатынын куәландырады. ТЖ режимінде жеделдікке басты көңіл бөлінгендіктен, тек тиісті органдарды ғана емес, сонымен қатар еліміздің қарапайым тұрғындарын да дер кезінде хабардар ету қажет. Өкінішке орай, қазіргі уақытта бірнеше бағыт бойынша деректер бар бірыңғай жүйе жоқ. Осыған байланысты, аса өткір тұрған табиғи және техногендік апаттар бойынша өзекті ақпаратты қамтитын бірыңғай геопортал құрудың аса қажеттілігі өздігінен пайда болады. ЖҚЗ мен ГАЖ жаңа жетістіктерін пайдалана отырып, құрылған төтенше жағдайлар ғарыштық мониторингінің тұтас және көп бейінді жүйесінің баламасы Қазақстанда ғана емес, бүкіл Орта Азияда да жоқ.

Бұл мақалада ғарыш мониторингі жүйесі, оның құрамы және ғарыш мониторинг жүйесінің ресурстары мен жұмыс нәтижелеріне қашықтықтан қол жеткізу жүйесі мен сервистерінің базалық элементтерінің функционалдық сұлбасы қарастырылады. Авторлар OGC спецификациясына сәйкес келетін негізгі бағдарламалық компоненттерге жалпыланған сипаттама береді: Операциялық жүйе, деректер қорын басқару жүйесі (ДҚБЖ), веб-сервер, бағдарламалау тілі, GDAL кітапханасы, картографиялық материалдарды көрсетуге арналған web-интерфейс. Сондай-ақ, мыналар сипатталады: спутниктік деректерді жинаудың кіші жүйесі; өңдеу және интерпретациядау қолмен жүзеге асырылатын деректерді интерпретациялау блогы және барлығы автоматтандырылған суреттерді өңдеу блогы; жүйені ақпараттық қамтамасыз ету құрамы, оның форматтары мен көздері, жаңарту жиілігі, мониторинг деректерін интеграциялау және тарату.

Шикі деректерді алудан бастап төтенше жағдайлардың бірнеше түрлері бойынша деректерді гепорталға жүктегенге дейін ғарыштық мониторинг жұмыстарының барлық циклі сипатталады. Басым бағыт ретінде төрт бағыт таңдап алынды: орман және дала өрттерінің жедел ғарыштық мониторингі; жер қыртысының қарқынды қозғалыстарының GPS мониторингі; қар жамылғысының, су тасқыны мен су басу қаупінің ғарыштық мониторингі; Каспий теңізі акваториясының мұнай өнімдерімен ластануының ғарыштық мониторингі.

Орман және дала өрттерінің мониторингі үш негізгі міндеттен тұрады. Бірінші, температуралық аномалиялардың жедел мониторингі. Бұл рәсім тәулігіне екі рет, ЖҚЗ деректерін алғаннан кейін 0,5-1 сағат ішінде орындалады. Екінші, өртенген аудандардың карталарын құру - жедел режимде төмен шешімді ЖҚЗ мәліметтерінен тәулігіне екі рет, егжей-тегжейлі түрде, орташа шешімді мәліметтерден жеті күн сайын орындалады. Үшіншіден, жергілікті жердің (өсімдік жамылғысы, топырақ ылғалдылығы, көлбеулік, жел, беткей экспозициясы, трассаға, елді мекенге және өрт гидрантына дейінгі қашықтық) және метеодеректерді ескере отырып өрт қауіптілік тәуекелін модельдеу және бағалау.

Тасқын судың өтуіне және қар жамылғысының түсуіне ғарыштық мониторинг үш деңгейде жүргізілуі мүмкін. Бірінші деңгейде тәулігіне екі рет төмен шешімді спутниктік деректер бойынша қар және мұз жамылғысының жылжуына талдау жүргізіледі. Екінші деңгейде су басу аймақтарын карталау үшін орташа шешімді деректер тартылады. Үшінші деңгейде, жағдайды талдау қажет болған жағдайда, аса қиын жағдайларда жоғары және аса жоғары шешімді оптикалық және радарлық ЖҚЗ деректері пайдаланылады. Сондай-ақ, су басу кезеңінде қажеттілігіне қарай ірі су тасқындарының дамуын модельдеу және болжау жасалады.

Мұнай ластануының ғарыштық мониторингі 01 наурыз-31 желтоқсан аралығында жүргізіледі. Спутниктік деректерді өңдегеннен кейін біз - су бетінің температуралық деректерін ескере отырып, Каспий теңізі акваториясының мұнаймен ластану картасын, су бетіндегі желдің жылдамдығы мен бағытын, теңіз акваториясындағы мұнаймен ластанудың негізгі көздерінің карта –сызбасын, атап айтқанда: кемелер трассаларын, сондай-ақ жер сілкінісінің эпицентрлерін деректерді алған сәттен бастап 0.5-1 сағат ішінде 3 тәулікте 1 рет аламыз.

Жер бетінің геодинамикалық жылжуын есептеу үшін дәлдігі жоғары спутниктік навигация желісінің деректері пайдаланылады. Қазақстан аумағында 49 перманентті GPS станциясының деректерін өңдегеннен кейін,

оның ішінде - 19 TRIMBLE станциясы, 20 LEICA станциясы, Алматы сейсмополигонының аумағында 10 станция тоқсанына бір рет Қазақстан аумағындағы GPS станцияларының ығысу жылдамдығының картасы (вектор, жылдамдық өрісі) есептелінеді. Жылына екі рет Қазақстанның сейсмикалық қауіпті аумағының жер қыртысының геомеханикалық жай-күйіне мынадай деректерді пайдалана отырып, жер бетінің қазіргі заманғы қозғалыстарының спутниктік мониторингінің деректері бойынша бағалау жүргізіледі: сейсмикалық деректер; рельефтің сандық моделі; табанның сандық моделі (Мохо); тектоникалық сынықтар; Батыс-Шығыс жер беті жылдамдығының компоненті (жылына метр); Оңтүстік-Солтүстік жер беті жылдамдығының компоненті (жылына метр); жылдамдықтың тік компоненті (жылына метр); жылдамдықтың абсолюттік шамасы (жылына метр); жер қыртысының кернеуі және деформациясы.

Бұдан басқа, жүйенің бірегей мүмкіндіктерінің бірі жоғарыда аталған ақпаратты алу ғана емес, сонымен қатар пайдаланушыларға мониторинг нәтижелері бойынша Графиктер мен диаграммаларды құру арқылы жеке талдау жүргізуге және есептерді қалыптастыруға мүмкіндік беретін түрлі құралдарды ұсыну болып табылады.

Түйін сөздер: Геопортал, ТЖ ғарыштан бақылау, ЖҚБ, ГАЖ, геодинамика, өрт, су тасқыны, мұнай төгілулері.

Ж. Ш. Жантаев, С. М. Нуракынов, С.В. Гаврук, Б.А. Искаков, Н.К. Сыдык, А.А. Мерекеев

Институт ионосферы АО «НЦКИТ», Алматы, Казахстан;

СОЗДАНИЕ ГЕОПОРТАЛА И ЕГО РОЛЬ В ОПЕРАТИВНОМ МОНИТОРИНГЕ ЧС ПРИРОДНОГО И ТЕХНОГЕННОГО ХАРАКТЕРА НА ТЕРРИТОРИИ РК

Аннотация. С развитием космических и информационных технологий мониторинг чрезвычайных ситуаций с помощью спутниковых данных набирает огромную актуальность. Мировой опыт свидетельствует, что основным, а зачастую и единственным источником информации, на основе которой принимаются решения о мерах по ликвидации ЧС, являются системы космического мониторинга. И так как в режиме ЧС основной упор делается на оперативность, необходимо учитывать и своевременное оповещение не только соответствующих органов, но и простых жителей нашей страны. Но, к сожалению, на данный момент не существует единой системы с данными по нескольким направлениям. В связи с этим, крайняя необходимость создания единого геопортала, который содержал бы актуальную информацию по ряду наиболее остро стоящим природным и техногенным катастрофам зарождается само по себе. Аналогов созданной цельной и многопрофильной системы космического мониторинга чрезвычайных ситуаций с использованием новейших достижений ДЗЗ и ГИС нет не только в Казахстане, но и во всей Средней Азии.

В данной статье рассматривается система космического мониторинга, его состав и функциональная схема базовых элементов системы и сервисов удаленного доступа к ресурсам и результатам работы системы космического мониторинга. Авторы дают обобщенную характеристику основным программным компонентам подходящим спецификациям OGC: операционная система, система управления базами данных (СУБД), веб-сервер, язык программирования, библиотека GDAL, web-интерфейс для отображения картографических материалов. Также описываются: подсистема сбора спутниковых данных; блок интерпретаций данных, где осуществляется обработка и интерпретация вручную и блок обработки снимков, где все автоматизировано; состав информационного обеспечения системы, его форматы и источники, частота обновления, интеграция и распространения данных мониторинга.

Описывается весь цикл работ космического мониторинга от получения сырых данных до загрузки на геопортал данных по нескольким видам чрезвычайных ситуаций. В качестве приоритетных было выбрано четыре направления: оперативный космический мониторинг лесных и степных пожаров; GPS мониторинг интенсивных подвижек земной коры; космический мониторинг снежного покрова, наводнений и паводков; космический мониторинг загрязнения нефтепродуктами акватории Каспийского моря.

Мониторинг лесных и степных пожаров состоит из трех основных задач. Первое, оперативный мониторинг температурных аномалий. Это процедура выполняется два раза в сутки за 0,5-1 часа после получения данных ДЗЗ. Второе, построение карт выгоревших площадей - в оперативном режиме выполняется два раза в сутки из данных ДЗЗ низкого разрешения, в детальном раз в семь дней из данных среднего разрешения. Третье, моделирование и оценки риска пожароопасности с учетом характеристик местности (растительный покров, влажность почвы, наклонность, ветер, экспозиция склона, дистанция до трассы, населенного пункта и пожарного гидранта) и метеоданных.

Космический мониторинг прохождения паводковых вод и схода снежного покрова может проводиться в три уровня. На первом уровне два раза в сутки проводится анализ схода снежного и ледяного покрова по спутниковым данным низкого разрешения. На втором уровне привлекаются данные среднего разрешения для картирования зон затопления. На третьем уровне при необходимости анализа ситуации в особо критических случаях используются оптические и радарные ДДЗ высокого и сверхвысокого разрешения. Также, в период затопления по мере необходимости делается моделирование и прогноз развития крупных наводнений.

Космический мониторинг нефтяных загрязнений проводится в период 01 марта по 31 декабря. После обработки спутниковых данных получаем - карту нефтяного загрязнения акваторий Каспийского моря с учетом температурных данных водной поверхности, скорости и направление приводного ветра, карты – схемы основных источников нефтяного загрязнения в акватории моря, в частности: трасс судов, а также эпицентры землетрясений 1 раз в 3 сутки за 0.5-1 часа с момента получения данных.

Для расчета геодинамических смещений поверхности используются данные сети высокоточной спутниковой навигации. После обработки данных 49 перманентных GPS станций на территории Казахстана, в том числе - 19 станций TRIMBLE, 20 станций LEICA, 10 станций на территории Алматинского сейсмополигона один раз в квартал высчитывается карта скорости смещений GPS станций территории Казахстана (вектор, поле скоростей). Два раза в год проводится оценка геомеханического состояния земной коры сейсмоопасных территории Казахстана по данным спутникового мониторинга современных движений земной поверхности с использованием следующих данных: сейсмические данные; цифровая модель рельефа; цифровая модель подошвы (Мохо); тектонические разломы; компонента скорости поверхности земли Запад-Восток (метры в год); компонента скорости поверхности земли Юг-Север (метры в год); вертикальная компонента скорости (метры в год); абсолютная величина скорости (метры в год); параметры поля напряжений и деформаций земной коры.

Кроме того, одной из уникальных возможностей системы является не только получение перечисленной выше информации, но и предоставление пользователям различных инструментов, позволяющих проводить собственный анализ и формировать отчеты с помощью построения графиков и диаграмм по результатам мониторинга.

Ключевые слова: Геопортал, космический мониторинг ЧС, ДЗЗ, ГИС, геодинамика, пожары, наводнение, нефтеразливы.

Information about authors:

Zhantayev Zhu.Sha., Institute of Ionosphere, JSC NCSRT, Almaty, Kazakhstan, Director, Doctor of Geological and Mineralogical Sciences, Corresponding member of NAS RK; admion1@mail.ru; https://orcid.org/0000-0002-9189-9546;

Nurakynov S.M., Institute of Ionosphere, JSC NCSRT, Almaty, Kazakhstan, head of the Cartography and GIS Laboratory, PhD doctor student; nurakynov@gmail.com; https://orcid.org/0000-0001-9735-7820;

Gavruk S.V., Institute of Ionosphere, JSC NCSRT, Almaty, Kazakhstan, head of the sector, mjdagot@gmail.com;

Iskakov B.A. Institute of Ionosphere, JSC NCSRT, Almaty, Kazakhstan, head of the department of Geodynamics, berikiskakov@gmail.com;

Sydyk N.K. Institute of Ionosphere, JSC NCSRT, Almaty, Kazakhstan, head of the Cartography and GIS sector, PhD doctor student; nurmahambet.s@gmail.com; https://orcid.org/0000-0003-1429-2393;

Merekeyev A.A. Institute of Ionosphere, JSC NCSRT, Almaty, Kazakhstan, engineer, aiba__99@mail.ru; https://orcid.org/0000-0002-9227-4695

REFERENCES

[1] Kondratiev K.Ya., Shumakov F.E. The physical basis of space monitoring of water bodies in the visible and near infrared zones of the spectrum // Earth exploration from space. 1990. №6. P. 44-48 (in Russian).

[2] Lopes S., Gonzales F., Llop R., Cuevas M. An evaluation of the utility of NOAA-AVHRR images for monitoring forest fire risk in Spain // International Journal of Remote Sensing. 1991. Vol. 12. P. 1841-1851.

[3] Usage of web servers [Electronic resource] / Q-Success. https://w3techs.com/technologies/overview/web_server/all

[4] Portal Development Guide // BEA WebLogic Portal. BEA Systems, Inc., 2008. 38 p.

[5] Shashi Sh., Sanjay Ch. Fundamentals of spatial databases. Moscow:, 2004. 336 p (in Russian).

[6] Debian. The universal operating system [Electronic resource] / Software in the Public Interest, Inc. https://www.debian.org/. загл. с экрана.

[7] PostGIS [Electronic resource] / Spatial and Geographic objects for PostgreSQL PostGis. https://postgis.net/documentation/

[8] Smith L. What PostgreSQL has over other open source SQL databases: Part I. [Electronic resource] / Compose, an IBM Company. https://www.compose.com/articles/what-postgresql-has-over-other-open-source-sql-databases/

[9] Apache HTTP Server [Electronic resource] / The Apache Software Foundation. https://httpd.apache.org/

[10] Python [Electronic resource] / Python Software Foundation. https://www.python.org/

[11] Open layers [Electronic resource] / CC BY 3.0. https://openlayers.org.

[12] GDAL [Electronic resource] / Frank Warmerdam, Even Rouault, and others. https://gdal.org/

[13] Arkhipkin O.P., Sagatdinova G.N., Assessment of the potential development of floods based on the analysis of long-term time series of remote sensing data // Modern problems of remote sensing of the Earth from space. 2014. T. 11. №4. P.127-136 (in Russian).

[14] Kostianoy A.G., Kosarev A.N. The Caspian Sea Environment: The Handbook of Environmental Chemistry / ed. Hutzinger O. V. 5: Water Pollution. Pt. P. / volume eds. Kostianoy A.G., Kosarev A.N. Springer, 2005. 271 p.

[15] Izrael Yu.A., Tsiban A.V. Anthropogenic Ocean Ecology. M.: Flint: Nauka, 2009. 529 p (in Russian).

NEWS
OF THENATIONAL ACADEMY OF SCIENCES OF THE REPUBLIC OF KAZAKHSTAN
PHYSICO-MATHEMATICAL SERIES
ISSN 1991-346X **https://doi.org/10.32014/2020.2518-1726.54**
Volume 3, Number 331 (2020), 202 – 208

УДК 524.1; 551.521.64

V.P. Antonova, S.V. Kryukov, V.Yu. Lutsenko, A.M. Malimbayev

«Institute of Ionosphere» JSC «NCSRT», Almaty, Kazakhstan.
E-mail: valanta@rambler.ru, cosmoserg@mail.ru, unclegoering@gmail.com,
nanozavr@mail.ru, valanta@rambler.ru

VARIATIONS OF LOW ENERGY NEUTRONS AND EARTH'S SEISMOACTIVITY

Abstract. The results of the study of variations in the intensity of slow neutrons at the high-altitude Tien-Shan cosmic ray station (3340 m above sea level, 20 km from Almaty) are presented. The effect of cosmic and geophysical events on the flux of thermal and epithermal neutrons was successively analyzed. The comparison was made with well-known variations of high-energy neutrons of galactic origin recorded by the 18NM64 monitor. Like the 18NM64 neutron monitor, the installation for detecting thermal and epithermal neutrons is located near the Zailiysky fault of the earth's crust.

It has been established that, in the absence of seismic activity, the variations of thermal neutrons on the earth's surface are of the same nature as the high-energy neutrons recorded by the monitor 18NM64. However, during the activation of seismic activity, the frequent breakdown of the correlation between the intensity of thermal and high-energy neutrons was noted. The cause of this phenomenon is the additional thermal neutron flux of the lithospheric origin, which appears under these conditions. It is shown that the amplitude of the additional thermal neutron flux from the Earth's crust is equal to 5-7% of the background level.

A difference was found also in the spectral composition of variations of slow and high-energy neutrons in the range ($2\cdot10^{-7} \div 2\cdot10^{-6}$) Hz. Variations, due to the gravitational influence of the moon, are present throughout the 12-year period of research of thermal neutrons. The amplitude and its dynamics were determined. The analysis of our catalog of earthquakes in the vicinity of Almaty with an intensity of ≥ 3 points showed that ~ 65÷70% of these events occurred during the full moon or new moon.

Key words: cosmic rays, variations of thermal and of high-energy neutrons, seismic activity, earthquakes.

Introduction. Active study of near-Earth space using data on the registration of the intensity of the neutron component of cosmic rays began in sixties of the last century after the International Geophysical Year, 1957-1958. An international network of ground-based standard neutron monitors was organized mainly on the basis of proportional counters, the gas filling of which includes boron trifluoride enriched with boron isotope ^{10}B. The counting efficiency is determined by the probability of neutron capture by boron nuclei. It is maximum for neutrons of thermal energies. However, low-energy neutrons are more susceptible to the influence of the surrounding geophysical environment. Since neutron monitors were designed to study outer space outside the Earth's atmosphere, the counters are surrounded by polyethylene to reflect thermal and slow down fast neutrons, and lead is used to increase the counting rate due to local neutron generation. The high-mountain Tien-Shan neutron monitor 18NM64 (3340 m above sea level) has been included in the international network since 1973 and registers high-energy neutrons (above 200 MeV) of galactic origin with high statistical accuracy, counting rate ~$5\cdot10^6$ imp/hour. By now, variations in the intensity of high-energy neutrons and their sources are quite well studied.

Thermal neutron measurements have long been episodic in nature. The interest in measuring thermal neutrons increased after the detection of their bursts in the Pamir and Tien Shan during the extreme gravitational impact on the Earth's crust from the Moon and the Sun (new moon, full moon, solar eclipses) [1-3]. It was supposed that the earth's crust, undergoing mechanical action, displaces the stocks of

radioactive gases of radon isotopes. In the process of radioactive decay, alpha particles are formed that interact with the nuclei of the elements of the earth's crust and air with the formation of neutrons. An experimental confirmation of the existence of variations in the background thermal neutron flux associated with lunar periods was also presented by the authors of [4].

The stationary installation for detecting thermal and epithermal neutrons at the high-altitude Tien-Shan cosmic rays station was created and put into operation in November 2006. Like the 18NM64 neutron monitor, it is located in a seismically active region near a fracture of the earth's crust. Studies of variations in the intensity of thermal neutrons have shown the promise of their use for the diagnosis and prediction of earthquakes in seismically active regions [5].

Experimental complex for detecting thermal and epithermal neutrons

The detector of thermal neutrons (DTN) is composed of two modules. Either module includes six proportional counters filled with the mixture of helium-3 gases and argon. One module (DTN1) is installed in one the building with 18NM64 standard neutron monitor; the second module (DTN2), 10 m from the building in a light plywood container. The modules are fed separately and are independent. The principled difference between thermal neutron detectors and the neutron monitor is the absence of the lead and the absorber, that reflects thermal and slows down fast neutrons**.** Thermal neutron detection efficiency ~ 60%. The counting speed of the module installed inside the building is ~ $6.8 \cdot 10^4$ imp / h, and the external ~ $4.9 \cdot 10^4$ imp / h, the time resolution is 10 seconds.

The effect of atmospheric and interplanetary disturbances on the intensity of thermal neutrons

Placing the thermal neutron detectors beside with the neutron monitor, 18NM64, made it possible to compare changes in the thermal neutron flux with well-studied variations of high-energy neutrons, caused by atmospheric and interplanetary sources. The study showed that regardless of the energy of the recorded neutrons, all detectors react in the same way to changes in atmospheric pressure; an increase in pressure leads to a decrease in the counting rate of both high-energy neutrons and thermal neutrons, figure 1 (left panel). A decrease in pressure leads to the opposite effect in the neutron intensity. High correlation coefficients (K = 0.97 for detectors inside the building and K = 0.84 for the external module, DTN2) with the neutron monitor, the similarity and amplitude of the response to changes in atmospheric pressure made it possible to draw the conclusion about the atmospheric origin of the recorded neutrons. This conclusion makes it possible to use the barometric formula for the correction of high-energy neutrons also for neutrons of thermal and epithermal energies.

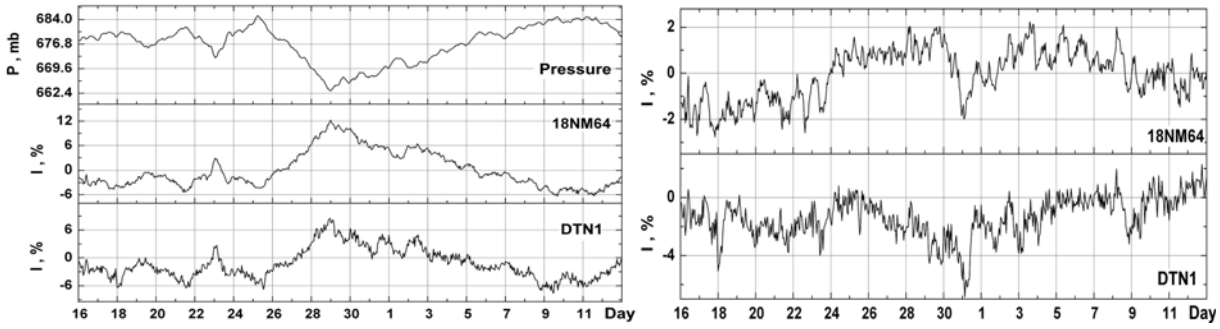

Figure 1 − Values of atmospheric pressure, the intensity of high-energy and the thermal neutrons (left panel - without pressure correction, right panel - with correction), March - April, 2015

Also, regardless of the energy of detected neutrons, all detectors react in the same way to disturbances in the interplanetary space caused by the coronal masses ejection (CME). It is known, that the ejection of solar plasma with the frozen-in magnetic field forms a shock wave in interplanetary space, which acts like a giant piston, "sweeping out" galactic cosmic rays and causing magnetic storms on Earth. Ground neutron monitors at this time register a decrease in the intensity of cosmic rays (Forbush-effect) or changes in intensity caused by a geomagnetic storm, figure 1(right panel).

The effect of activation of seismic processes on the intensity of thermal neutrons

The presented results in the previous section confirm the conclusion about the genetic connection of thermal neutrons with high-energy neutrons of galactic origin in seismically calm conditions [3]. However, during the activation of seismic processes, the synchronism of variations in the intensity of thermal neutrons and high-energy ones is broken, figure 2. The moment of the main shock of the earthquake is marked by the vertical line.

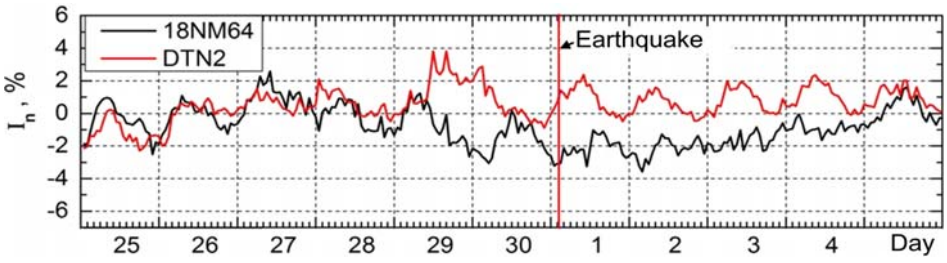

Figure 2 − Variations of thermal and high-energy neutrons, April - May 2011

Almaty is surrounded by a number of potential sources of strong earthquakes, therefore, the diagnosis and forecast of seismic activity will always be relevant for residents of the city and its environs. The study of the measured geophysical parameters was conducted during periods of activation of seismic processes in order to identify earthquake precursors. The catalog of seismic events for analysis included 32 earthquakes perceptible in Almaty with an intensity of ≥ 3 b. When compiling the catalog, the information presented on the website of the Institute of Geophysical Research, National Nuclear Center, IGR NNC RK (http://www.kndc.kz) was used.

Variations of atmospheric and interplanetary origin in the intensity of thermal neutrons are excluded by simple mathematical transformations, considering that they are similar to variations of high-energy neutrons. Figure 3 presents the calculation results for three periods accompanied by earthquakes. There are no low-frequency trends or daily variations, but a significant increase in the thermal neutron flux on the eve of the earthquake or immediately after it is obvious. It was found that ~ 60% of earthquakes in Almaty with the intensity of ≥ 3b during the period 2007-2018 were accompanied by the increase in the intensity of thermal neutrons, but on the eve of earthquakes of such events ~ 25-30%. It is also obvious that the lithosphere is the source of the additional flux of thermal neutrons during the activation of seismic processes. The amplitude of the additional thermal neutron flux of the lithospheric origin is equal to 5-7% of the background level. Sometimes it reaches values of 10-12%. The conclusion of authors [3, 5] about the possibility of using thermal neutron registration for the diagnosis and prediction of earthquakes is confirmed. However, a necessary condition for this is the synchronous registration of high-energy neutrons.

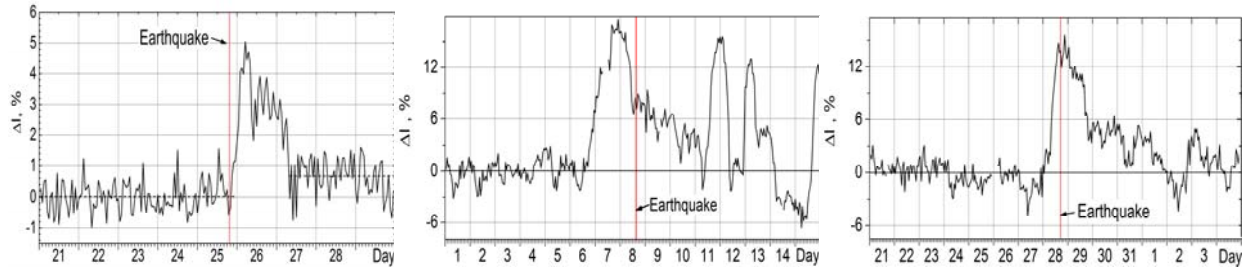

Figure 3 − Variations of thermal neutrons intensity of lithospheric origin during seismic activity 25.12.2006, 08.04.2009 and 28.01.2013

The gravitational effect of the moon on the intensity of thermal neutrons

The identify of periodic variations of thermal neutrons was carried out by spectral analysis using the Blackman-Tukey method in low-frequency ranges ($2 \cdot 10^{-7} \div 2 \cdot 10^{-6}$) Hz and ($7 \cdot 10^{-6} \div 7 \cdot 10^{-5}$) Hz. [6]. It is in these ranges that the spectrum of the most well-known variations of high-energy neutrons of galactic

origin is located: daily, 27-day. The daily variation is well stands out both in the intensity of high-energy neutrons and in the intensity of thermal neutrons. The spectral analysis of periodic variations of thermal and high-energy neutrons showed the difference in the distribution of spectral estimates in the low-frequency range ($2 \cdot 10^{-7} \div 2 \cdot 10^{-6}$) Hz. In this range, the 27-day variation is a known spectral component in the intensity of high-energy cosmic rays of galactic origin. However, we did not find this periodicity either in the intensity of high-energy neutrons or in thermal neutrons during the 24th cycle of solar activity, 2009—2018. Its absence is due to the extremely low solar activity of only 24 cycles.

The stable spectral peak is detected in the intensity of thermal neutrons at a frequency corresponding to the period of 29.5 days (synodic, lunar month) throughout the entire 12-year period of research of thermal neutrons, Figure 4. This variation is due to the gravitational influence of the moon on neutrons of lithospheric origin. The difference in the total annual paths of the Moon and the Sun, reduced to the same time, gives the duration of the average synodic revolution of the Moon, or lunar month, of 29.531 days, during which the Moon returns to its previous position relative of the Sun.

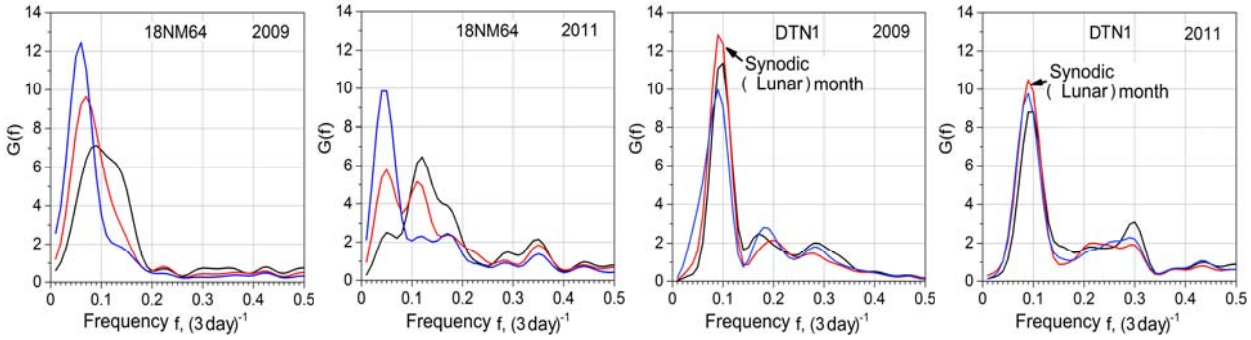

Figure 4 – Power spectra of variations of high-energy (18NM64) and thermal neutrons (DTN) in the range ($2 \cdot 10^{-7} \div 2 \cdot 10^{-6}$) Hz

In the intensity of high-energy neutrons, this variation is not detected throughout the study period, which indicates an additional, internal source of thermal neutrons (lithosphere). The stability of the spectral peaks was tested using three low frequency filters of different lengths. In the power spectra of variations of thermal neutrons, the spectral peak corresponding to the synodic month is stable, which confirms its reliability, in contrast to low-frequency peaks in the spectra of variations of high-energy neutrons.

The method of complex signal demodulation was applied to determine the amplitude of the lunar variation with the period of 29.5 days in the intensity of thermal neutrons [7]. It varies within +/- 0.9% of the average with an apparent semi-annual periodicity during the entire research period. The results of calculations for three years are presented in the figure 5.

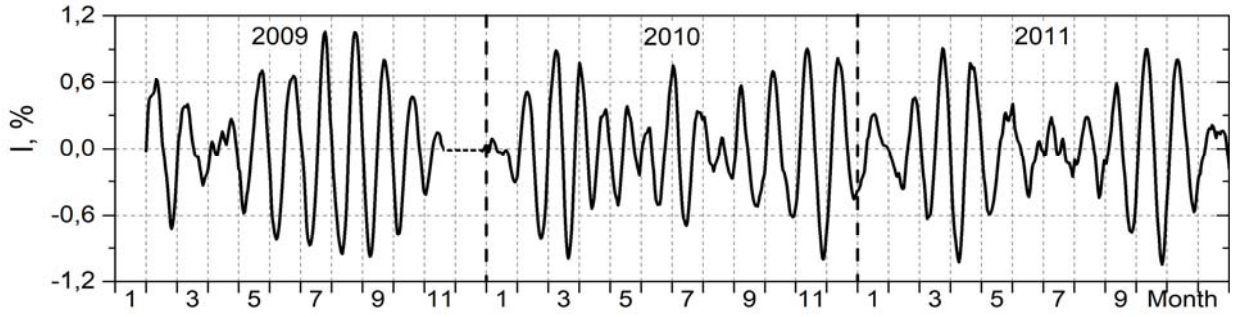

Figure 5 – Temporal scan of the periodicity of 29.5 days of thermal neutrons intensity for 2009-2011

The analysis of our catalog of earthquakes in the vicinity of Almaty with an intensity of ≥ 3 points showed that ~ 65÷70% of these events occurred during the full moon or new moon (+/- 1 ÷ 2 days). The correlation between bursts of thermal neutrons, the phases of the moon and seismic activity was

previously noted by the staff of the Research Institute of Nuclear Physics, Moscow State University in the Pacific seismic ring [8].

Conclusions. The study of variations in the intensity of thermal (epithermal) neutrons at the high-altitude station of the Tien Shan, located near the fault of the earth's crust, showed that this geophysical parameter can be used in predicting earthquakes. However, the necessary condition for this is the synchronous registration of high-energy neutrons to highlight variations of lithospheric origin. It is recommended that the forecasting also take into account the amplification of the gravitational effect of the moon during full moons and new moons.

The work was carried out in accordance with RBP-008 "Development of space technologies for monitoring and forecasting natural resources, technogenic environmental changes, creation of space technology and ground-based space infrastructure, research of long-distance and near-space objects" under the theme «Development of methods for the diagnosis and prediction of geoactiv events based on measurements of the parameters of the ionosphere, mesosphere, atmospheric electric field and thermal neutrons» (2018-2020), registration number (RN) 0118PK00798.

В.П. Антонова, С.В. Крюков, В.Ю. Луценко, А.М. Малимбаев

ЕЖШС «Ионосфера институты» «ҰҒЗТО» АҚ, Алматы, Қазақстан

АЗ ЭНЕРГИЯЛЫ НЕЙТРОНДАРДЫҢ ВАРИАЦИЯЛАРЫ ЖӘНЕ ЖЕРДІҢ СЕЙСМИКАЛЫҚ БЕЛСЕНДІЛІГІ

Аннотация. 2006 жылы қарашасында биіктіктегі ғарыштық сәулелік станцияда жылу термиялық және эпитермиялық нейтрондарды анықтауға арналған стационарлық қондырғы жасалып, пайдалануға берілді. 18NM64 нейтронды мониторы, жоғары энергиялы нейтрондар сияқты, ол Солтүстік Тянь-Шань тауларында (теңіз деңгейінен 3340 м биіктікте, Алматыдан 20 км) Заилийский жарылысының жанында сейсмикалық белсенді жерде орналасқан. Жылу нейтронының детекторлары мен 18NM64 нейтронды мониторының арасындағы негізгі айырмашылық қорғаныс пен сіңіргіш заттың болмауы болып табылады, ол жылуды бейнелейді және галактикалық шығу тегі тез нейтрондарды баяулатады. Термиялық нейтрондардың қарқындылығының өзгеруін зерттеу олардың сейсмикалық белсенді аймақтардағы жер сілкіністерін диагностикалау және болжау үшін пайдаланылатындығын көрсетті. Бұл мақалада ғарыштық және геофизикалық бұзылу көздерінің термиялық және эпитермиялық нейтрондар ағынына әсерін дәйекті талдау нәтижелері келтірілген.

18NM64 нейтронды монитордың жанында жылу нейтрондық детекторларын орналастыру жылу нейтрон ағынының өзгеруін атмосфералық және планетааралық көздер әсерінен пайда болған жоғары энергиялы нейтрондардың өзгерулерімен салыстыруға мүмкіндік берді. Зерттеу көрсеткендей, тіркелген нейтрондардың энергиясына қарамастан, барлық детекторлар атмосфералық қысымның өзгеруіне бірдей жауап береді. Сонымен қатар, барлық детекторлар тәждік массаның шығарылуынан (CME) туындаған планетааралық кеңістіктегі бұзылуларға бірдей жауап береді. Жылу нейтронының детекторлық мәліметтерінің нейтронды монитордың деректерімен жоғары корреляция коэффициенттері тіркелген нейтрондардың атмосфералық шығу тегі туралы қорытынды жасауға мүмкіндік берді. Зерттеу нәтижелері жылу нейтрондарының галактикалық шығу тегі жоғары энергетикалық нейтрондармен сейсмикалық тыныштық жағдайында генетикалық байланысы туралы қорытындыны растады.

Алайда, сейсмикалық процестердің активтенуімен жылу және жоғары энергиялы нейтрондардың қарқындылығындағы вариациялардың синхронизмі бұзылатындығы анықталды. Жылу нейтрондарының интенсивтілігіндегі атмосфералық және планетааралық шығу өзгерістері қарапайым энергетикалық нейтрондардың өзгеруіне ұқсас болғандықтан қарапайым математикалық қайта құрулармен жойылады.

Жер сілкінісінен кейінгі үш кезеңдегі есептеу нәтижелері келтірілген. Төмен жиіліктегі трендтер немесе тәуліктік ауытқулар жоқ, бірақ жер сілкінісі қарсаңында немесе ол пайда болғаннан кейін жылу нейтрондарының ағынының едәуір артуы. 2007-2018 жылдар аралығында Алматыдағы жер сілкінісінің ~ 60% болатындығы ≥ 3b белгілі болды, жылу нейтрондарының қарқындылығының артқы деңгейден 5-7% - ға артуымен қатар жүрді, және осындай оқиғалардың жер сілкінісі қарсаңында ~ 25-30%. Сондай-ақ, литосфера сейсмикалық процестердің активтенуі кезінде қосымша жылу нейтрондық ағынының көзі болып табылады.

Жылулық нейтрондардың мерзімді өзгерістері төмен жиілік диапазонында ($2\cdot10^{-7} \div 2\cdot10^{-6}$) Гц және ($7\cdot10^{-6} \div 7\cdot10^{-5}$) Гц -де Блэкман-Тукей спектрлік талдауы арқылы анықталды. Жылу және жоғары энергиялы нейтрондардың периодты өзгерулерінің спектрлік анализі спектрлік бағалардың таралуындағы

айырмашылықты көрсетті. ($2\cdot10^{-7} \div 2\cdot10^{-6}$) Гц. Термиялық нейтрондарды зерттеудің 12 жылдық кезеңі ішінде 29,5 күн (синодтық, айлық) кезеңге сәйкес келетін жиіліктегі жылу нейтрондарының интенсивтілігінің өзгеруінен тұрақты спектрлік шың анықталды. Бұл өзгеріс айдың литосфералық нейтрондарға гравитациялық әсеріне байланысты. Жоғары энергиялы нейтрондардың қарқындылығында бұл өзгеріс бөлінбейді. Кешенді сигналды демодуляция әдісі 29,5 тәулік кезеңі бар айдың өзгеру амплитудасын және оның динамикасын анықтау үшін қолданылды. Алматы маңында орналасқан жер сілкінісі каталогының талдауы ≥ 3 балға дейін, ~ 65-70% толық ай немесе жаңа ай кезінде болғанын көрсетті.

Сонымен, Тянь-Шань биіктіктегі станциясында жылу және эпитемальды нейтрондардың қарқындылығындағы вариацияларды зерттеу бұл геофизикалық параметрді жер сілкінісін болжауда қолдануға болатындығын көрсетті. Алайда, литосфералық шығу тегі вариациясын есептеу үшін жоғары энергиялы нейтрондарды синхронды тіркеу бұл үшін қажетті шарт болып табылады. Болжамда сонымен қатар толық ай және жаңа ай кезінде айдың гравитациялық әсерін ескеру ұсынылады.

Түйін сөздер: ғарыштық сәулелер, жылу және жоғары энергетикалық нейтрондардың вариациялары, сейсмикалық белсенділік, жер сілкінісі.

В.П. Антонова, С.В. Крюков, В.Ю. Луценко, А.М. Малимбаев

ДТОО «Институт ионосферы» АО «НЦКИТ», Алматы, Казахстан

ВАРИАЦИИ НЕЙТРОНОВ НИЗКИХ ЭНЕРГИЙ И СЕЙСМОАКТИВНОСТЬ ЗЕМЛИ

Аннотация. Стационарная установка для регистрации тепловых и эпитепловых нейтронов на высокогорной станции космических лучей была создана и введена в эксплуатацию в ноябре 2006 года. Как и нейтронный монитор 18HM64, регистрирующий высокоэнергичные нейтроны, она расположена в сейсмически активном районе вблизи Заилийского разлома земной коры в горах Северного Тянь-Шаня (3340 м над уровнем моря, 20 км от Алматы). Принципиальная разница между детекторами тепловых нейтронов и нейтронным монитором 18NM64 заключается в отсутствии свинца и поглотителя, который отражает тепловые и замедляет быстрые нейтроны галактического происхождения. Исследования вариаций интенсивности тепловых нейтронов показали перспективность их использования для диагностики и прогнозирования землетрясений в сейсмически активных регионах. В данной статье представлены результаты последовательного анализа влияния космических и геофизических источников возмущений на поток тепловых и эпитепловых нейтронов.

Размещение детекторов тепловых нейтронов рядом с нейтронным монитором 18NM64 позволило сравнивать изменения потока тепловых нейтронов с хорошо изученными вариациями нейтронов высокой энергии, вызванными атмосферными и межпланетными источниками. Исследование показало, что независимо от энергии регистрируемых нейтронов все детекторы одинаково реагируют на изменения атмосферного давления. Кроме того, все детекторы одинаково реагируют на возмущения в межпланетном пространстве, вызванные выбросом корональных масс (CME). Высокие коэффициенты корреляции данных детектора тепловых нейтронов с данными нейтронного монитора позволили сделать вывод об атмосферном происхождении зарегистрированных нейтронов. Результаты исследования подтвердили вывод о генетической связи тепловых нейтронов с высокоэнергетическими нейтронами галактического происхождения в сейсмически спокойных условиях.

Однако было обнаружено, что при активизации сейсмических процессов синхронность вариаций интенсивности тепловых и высокоэнергетических нейтронов нарушается. Вариации атмосферного и межпланетного происхождения в интенсивности тепловых нейтронов исключаются простыми математическими преобразованиями, учитывая, что они аналогичны вариациям нейтронов высоких энергий.

Представлены результаты расчета для трех периодов, сопровождаемых землетрясениями. Нет низкочастотных трендов или суточных колебаний, но значительное увеличение потока тепловых нейтронов накануне землетрясения или сразу после него становится очевидным. Выяснилось, что ~ 60% землетрясений в Алматы с интенсивностью ≥ 3b в период 2007-2018 гг. сопровождались увеличением интенсивности тепловых нетронов на 5-7% от уровня фона, а накануне землетрясений таких событий ~ 25-30%. Также очевидно, что литосфера является источником дополнительного потока тепловых нейтронов при активации сейсмических процессов.

Выявление периодических вариаций тепловых нейтронов проводилось методом спектрального анализа Блэкмана-Тьюки в низкочастотных диапазонах ($2\cdot10^{-7} \div 2\cdot10^{-6}$) Гц и ($7\cdot10^{-6} \div 7\cdot10^{-5}$) Гц. Спектральный анализ периодических вариаций тепловых и высокоэнергетических нейтронов показал различие в распределении спектральных оценок в диапазоне. ($2\cdot10^{-7} \div 2\cdot10^{-6}$) Гц. Стабильный спектральный пик выявлен в вариациях

интенсивности тепловых нейтронов на частоте, соответствующей периоду 29,5 дня (синодический, лунный месяц) в течение всего 12-летнего периода исследования тепловых нейтронов. Эта вариация обусловлена гравитационным воздействием Луны на нейтроны литосферного происхождения. В интенсивности нейтронов высокой энергии эта вариация не выделяется. Методом комплексной демодуляции сигнала была определена амплитуда лунной вариации с периодом 29,5 суток и ее динамика. Анализ нашего каталога землетрясений в окрестностях Алматы с интенсивностью ≥ 3 балла показал, что ~ 65 ÷ 70% этих событий произошло в полнолуние или новолуние.

Таким образом, исследование вариаций интенсивности тепловых и эпитепловых нейтронов на высокогорной станции Тянь-Шаня показало, что этот геофизический параметр может быть использован при прогнозировании землетрясений. Однако необходимым условием для этого является синхронная регистрация нейтронов высоких энергий для выделения вариаций литосферного происхождения. Рекомендуется, чтобы при прогнозировании также учитывался гравитационный эффект Луны во время полнолуния и новолуния.

Ключевые слова: космические лучи, вариации тепловых и высокоэнергетических нейтронов, сейсмическая активность, землетрясения.

Information about authors:

Antonova Valentina Pavlovna, PhD. Phys.-mat. sciences, Head of laboratory, «Institute of Ionosphere» JSC «NCSRT», Almaty, valanta@rambler.ru, https://orcid.org/0000-0002-1865-4868;

Kryukov Sergey Viktorovich, Senior researcher, «Institute of Ionosphere» JSC «NCSRT», Almaty, cosmoserg@mail.ru, https://orcid.org/0000-0002-1413-7433;

Lutsenko Vadim Yurievich, PhD student, Head of sector, «Institute of Ionosphere» JSC «NCSRT», Almaty, unclegoering@gmail.com, https://orcid.org/0000-0002-0416-6724;

Malimbayev Andrey Maratovich, PhD student, Leading researcher, «Institute of Ionosphere» JSC «NCSRT», Almaty, nanozavr@mail.ru, https://orcid.org/0000-0002-3507-913X

REFERENCES

[1] Volodichev NN, Kuzhevskii BM, Nechaev OIu, Panasiuk MI, Shavrin PI (1977) Origination of neutron intensity bursts during new and full Moon. Space exploration [Kosmicheskie issledovaniya] Vol. 35, №2, P. 144-154 (in Russ.).

[2] Volodichev NN, Zakharov VA, Kuzhevskij BM, Nechaev OYu, Podorolski AN, Chubenko AP, Shepetov AL, Antonova VP (2001) The flows of neutrons of space radiation and from terrestrial crust. Proceedings of 27th ICRC, Hamburg, Germany. P. 4204-4207.

[3] Antonova VP, Volodichev NN, Kryukov SV, Chubenko AP, Shchepetov AL (2009) Results of Detecting Thermal Neutrons at Tien Shan High Altitude Station. Geomagnetism and Aeronomy, Vol. 49, №6, P. 761-767.

[4] Alekseenko VV, Jappuev DD, Kozyarivsky VA, Kujaev AU, Kuzminov VV, Mikhailova OI, Stenkin YuV (2007) Analysis of variations in the flux of thermal neutrons at an altitude of 1700 m above sea level. News of the RAS, Physical Series [Izvestuya RAN, Seriya Fizicheskaya] Vol. 71, №7, P. 1075-1078 (in Russ.).

[5] Antonova VP, Kryukov SV, Lucenko VYu, Chubenko AP (2016) Effects of earthquakes in variations of thermal neutrons intensity at the high altitude station of Northern Tien-Shan. News of NAS RK. Series of physico-mathematical, Vol. 3, №4 (307), P. 20-26. ISSN 1991-346X

[6] Jenkins G, Watts D (1971) Spectral analysis and its applications. Mir, Moscow, USSR (in Russ.).

[7] Privalinsky VE, Panchenkov VA, Asarina EYu. (1992) Hydrological Time Series Models. Gidrometeoizdat, Russia (in Russ.).

[8] Volodichev NN, Sigaeva EA (2017) Neutrons from the Earth's surface due to lunar and solar tides, and Earth's seismicity. Bulletin of Moscow University. Series 3. PHYSICS. ASTRONOMY [Vestnik MGU Seriya 3. Fizika. Astronomiya] №6, P. 94-98 (in Russ.).

NEWS
OF THENATIONAL ACADEMY OF SCIENCES OF THE REPUBLIC OF KAZAKHSTAN
PHYSICO-MATHEMATICAL SERIES
ISSN 1991-346X **https://doi.org/10.32014/2020.2518-1726.55**
Volume 3, Number 331 (2020), 209 – 216

УДК 550.383

G.I. Gordiyenko, A.F. Yakovets, Yu.G. Litvinov

«Institute of Ionosphere» JSC «NCSRT», Almaty, Kazakhstan,
ggordiyenko@mail.ru, artyak40@mail.ru, yurii-litvinov@mail.ru

LONG - TERM VARIATIONS IN THE F- AND D-REGIONS OF IONOSPHERE

Abstract. The long-term changes in the near-noon, diurnal, and midnight critical frequencies of the ionosphere F2 layer (foF2) and near-noon minimum reflection frequencies (fmin) were studied using ground-based vertical radio sounding of the ionosphere at Alma-Ata station [43.25N, 76.92E] for the period 1957-2017. The data on solar and geomagnetic activity were used as factors affecting the state of the ionosphere.

It was taken into account that the minimum reflection frequency depends both on the absorption of the probe signal in the lower ionosphere, and on the noise level and technical characteristics of the ionosonde. Therefore, it seems problematic to estimate the absolute value of signal absorption in this way. However, as a qualitative characteristic, as an indicator of the absorption level of the probe signal, the parameter fmin can be used.

Arithmetic average values of median foF2 for near noon (10-14 LT), near midnight (23-01 LT) hours and average diurnal values for this period of ionosphere observation are considered as initial data. The variability of the lower ionosphere was studied using fmin data for daylight hours. The monthly average values of the solar radio emission flux F10.7 and the Ap index are considered as characteristics of solar and geomagnetic activity. The geomagnetic (Ap) indexes, the near-noon, near-midnight, diurnal averaged foF2, and near-noon fmin variations are found to be in strong dependence from the solar activity; all of them show a dominant pattern of variation with a period of ~34-36 years and linear negative trend. The correlation coefficient between the foF2 and F10.7 long-term variations is very high, up to 0. 99 that permit us to believe that the solar activity can be considered to be the main driver for the long-term variations in the ionospheric F2-region.

The geomagnetic (Ap) index, the near-noon, near-midnight, daily averaged foF2, and near-noon fmin variations are found to be in strong dependence from solar activity; all of them show a dominant pattern of variation with a period of ~34-36 years and linear negative trend. The correlation coefficient between the foF2 and F10.7 long-term variations is very high, up to 0. 99, that permits us to believe that the solar activity can be considered as a main driver for the long-term variations in the ionospheric F2-region.

The long-term course of fmin is similar to those found in F10.7, Ap, and foF2, i.e. the periodicity of 34-36 years is also evident in the fmin variations. However, in contrast to the F2-layer parameters, the fmin variation clear demonstrates an upward (positive) linear trend that is opposite in sign to the trend found in F10.7. This means relatively high sensitivity of the fmin values to the solar activity changes and significant influence of other trend drivers on them, one of which is the possible impact of anthropogenic factors on the state of the lower ionosphere.

Key words: midlatitude ionosphere; upper and lower ionosphere; D-region, F2-region, long-term trends.

Introduction. In our previous work we investigated the long-term variations in the near-noon (10-14 LT) critical frequency of the ionospheric F2-layer (foF2) measured at the mid-latitude station Alma-Ata [43.25N, 76.92E] over the period from 1957 to 2012 [1]. The purpose of this paper is to provide further analyses of the F2-layer variations and study long-term trends (a long-term linear change) in the near-noon, near-midnight and daily averaged F2-layer critical frequencies measured at the Alma-Ata station in more extended time period, from 1957 to 2017 including the period of very deep minimum in solar activity observed in 2008-2009. In addition to the F2-layer parameters the minimum frequency of

reflection fmin is also used as a climatic characteristic of the upper atmosphere/low ionosphere (D region) to do the trend analyses in the ionospheric absorption. The fmin value depends, apart from the absorption of radio waves in the ionosphere, on technical characteristics of ionosondes that does not give us any opportunity to use this ionosphere parameter to determine the absolute values of the absorption of radio waves. However, as a qualitative characteristic, as an indicator of absorption of radio waves, the fmin value is widely used ([2-3] and references therein).

For the present trend analyses, monthly median foF2 and fmin values routinely measured at the Alma-Ata station have been used. The arithmetic means of the foF2 values at the near-noon (10-14 LT), near-midnight (23-01 LT) hours, and daily means foF2 are calculated for the analyses, the fmin values are taken only for the near-noon hours: $foF2_{10\text{-}14}$, $foF2_{23\text{-}01}$, $foF2_{av}$, and $fmin_{11\text{-}13}$ correspondingly. The monthly mean solar flux F10.7 and geomagnetic index Ap are also used as the indexes for solar and geomagnetic activities (available at htt://ww.swpc.noaa.gov) to illustrate their long-term variations.

Description of the data, and observation results *Trends in the ionospheric F-region.* As an example, median mean values $foF2_{10\text{-}14}$, $foF2_{23\text{-}01}$, $foF2_{d.av}$ together with the corresponding data of solar and geomagnetic activity is shown in figure 1a-e. The dots represent observed data, the thick lines show the fitting curves. It should be also noted, the statistical processing of the ionospheric data series requires their continuity that is not always possible because of different reasons (ionosonde repair and other technical problems).

The regression dependences between the selected ionospheric parameters and F10.7 (figure 1f-h) have been analyzed to define the missing data. Thick lines represent the linear regression lines for these data; dashed lines correspond to the polynomial functions of the second degree that better fit the given F2-layer parameters ($R^2_{polinomial}>R^2_{linear}$) where R^2 is the coefficient of determination that provides a measure of how well the least-square curve fits the observational data, r is the correlation coefficient. Assuming the second-order polynomial dependence with F10.7 the missing foF2 values have been defined from the regression equations to fill available gaps in the data sets. Two things are evident in the figure, firstly the variations of all parameters are strictly modulated by cyclic 11-year variations of solar activity and secondly the foF2 data are much scattered relatively to the smoothed lines that can be attributed to various sources other than solar activity, including planetary waves and seasonal variations. As an example, the great part of seasonal variations is evident in Figure 1e where large deviations of the $foF2_{23\text{-}01}$ values from the smoothed line is caused by the fact that summer nighttime foF2 values are much higher than winter ones. Since this intraseasonal variability has to be taken into consideration in the trend analyses, annual averages of the parameters considered were calculated. Figure 2a-e demonstrates temporal variations of the calculated annual averages (denoted by symbol*) of the $F10.7^*$, Ap^* indexes, and the F2-layer parameters ($foF2^*_{10\text{-}14}$, $foF2^*_{23\text{-}01}$, and $foF2^*_{av}$) for whole period of observations; variations of the ionospheric parameters with $F10.7^*$ are presented in Figure 2f-h.

The main feature of the variations is their similarity (figure 2a-e) and close connection between the ionospheric parameters and solar activity (figure 2f-h). The coefficients of determination R^2 (the coefficients R2 and derived regression equations are shown in the figure fields) are found to be very high, from 0.97 to 0.99 it means that from 97% to 99% of the annual foF2 variations can be explained by their relationship with the 11-year cycle of solar activity.

According to our previous work [1], the 11-year (132 months) running mean values of the annual averages of the ionospheric parameters ($foF2^*_{10\text{-}14}(132)$, $foF2^*_{23\text{-}01}(132)$, and $foF2^*_{av}(132)$ were calculated to obtained an independent picture of long-term trends in the upper ionosphere; the 11-year smoothing technique was also applied to the F10.7 and Ap data sets ($F10.7^*(132)$, $Ap^*(132)$); Figure 3 presents these calculated values and shows that geomagnetic activity is strongly controlled by the solar activity, both show a dominant pattern of variations with the period ~34-36 years that is also reflected in all ionospheric parameters considered.

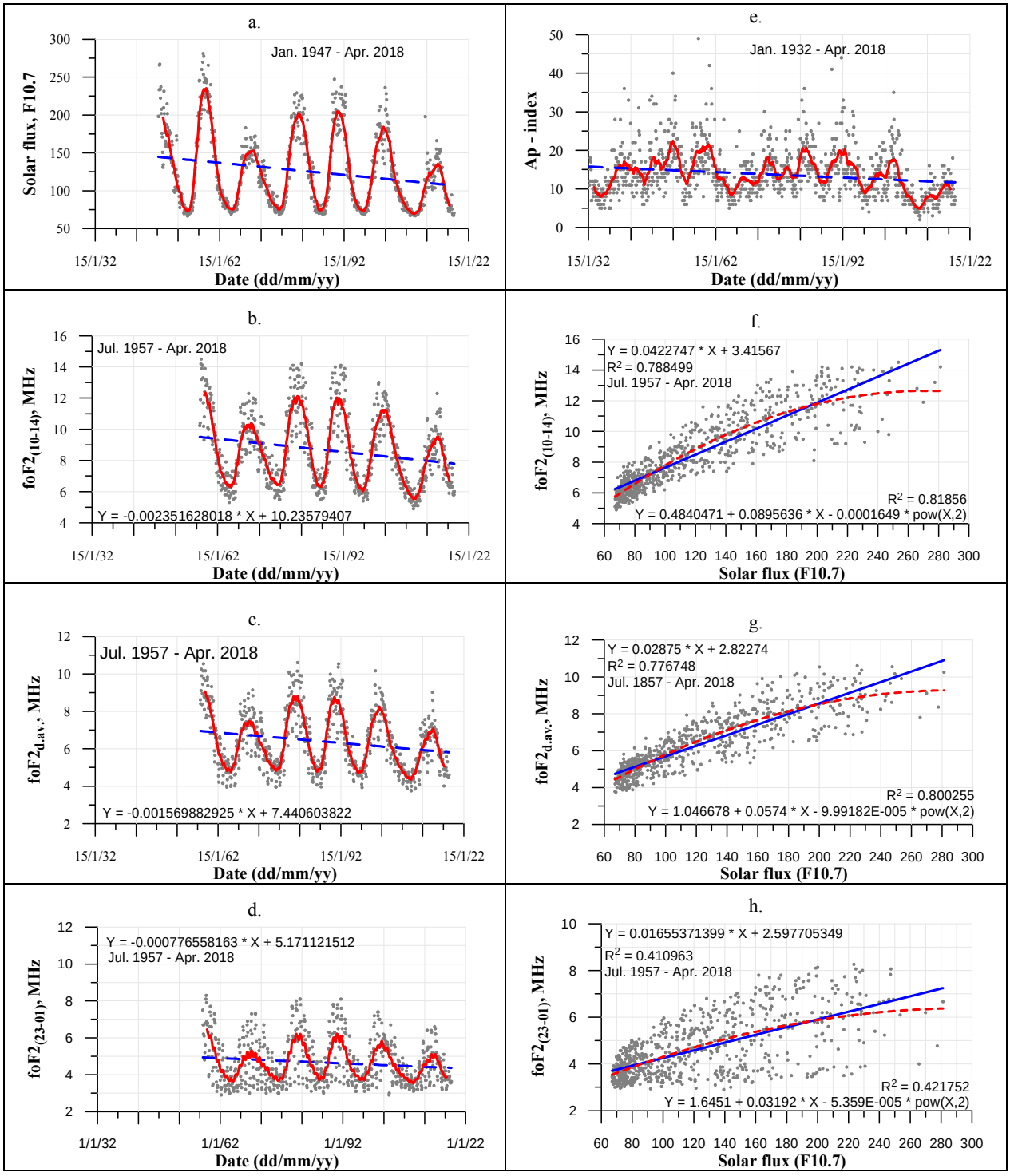

Figure 1 - The long-term variations of the near-noon(b), daily mean (c) and near-midnight (d) monthly median foF2 values in Alma-Ata [43.25^{0}N, 76.92^{0}E] in 1957-2017 together with the corresponding variations of solar flux F10.7 (a) and Ap index (c); solid dots – measured data, thick lines show the fitting lines, dashed lines – linear fits. Monthly median near-noon (f), daily mean (g), and near-midnight (h) foF2 values versus monthly mean F10.7; thick lines represent the linear regression lines for these data, dashed lines correspond to the polynomial functions of the second degree

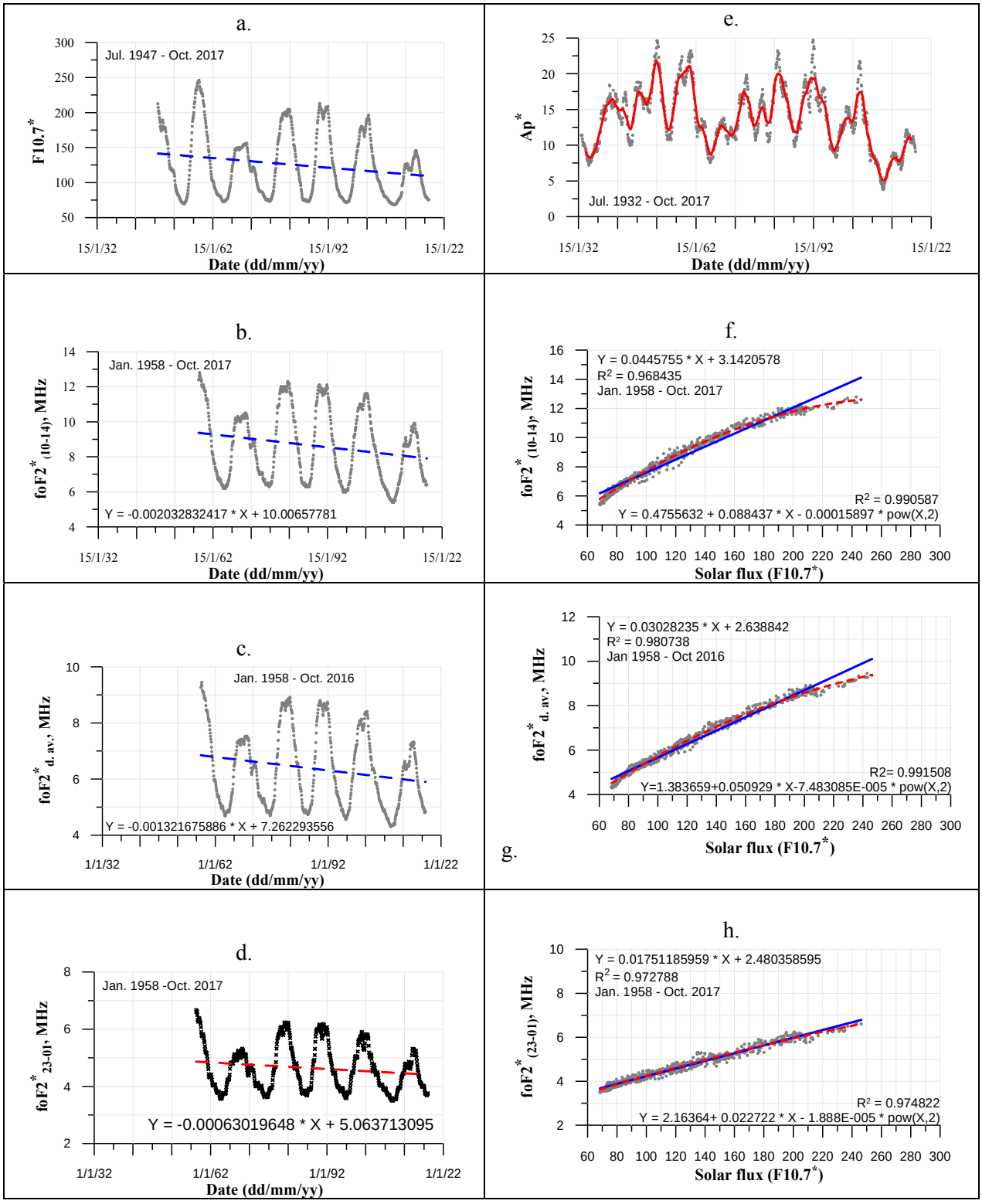

Figure 2 - As the Figure 1 but the annual averages of the F10.7, Ap, and foF2 values.

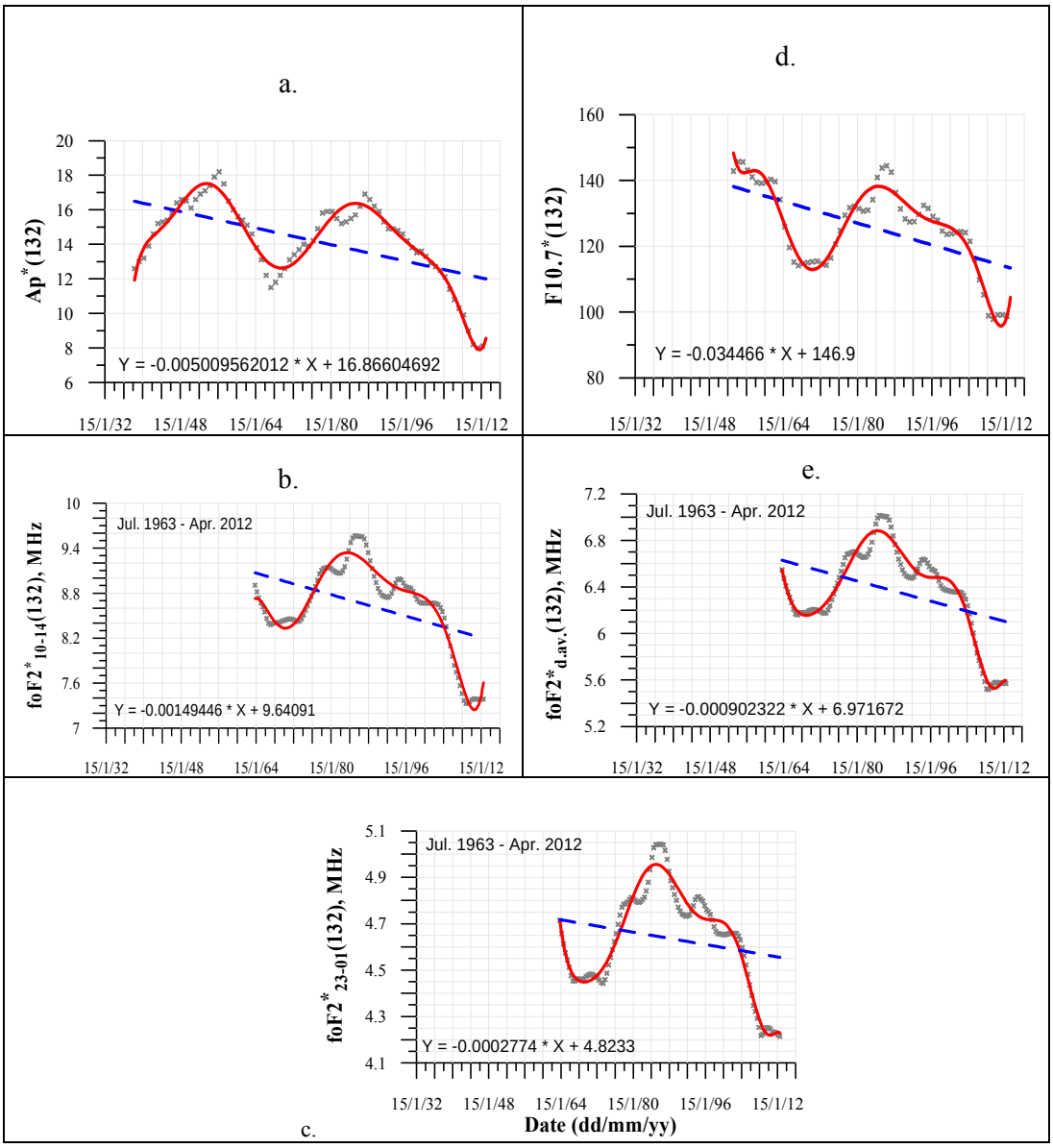

Figure 3 - The 132-month smoothed values of the annual averages of the ionospheric F2-layer parameters, F10.7, and Ap.

This period is slightly differs from our earlier finding [1] where the period was estimated to be in a range of 30-32 years. The extended data sets used in the study reveal the period more clearly. It should be mentioned that similar period (31-32 years) has been found in all the solar terrestrial parameters ([4-6], and references therein) and was interpreted as the 35-year Brutcher climatic periodicity. Note, the negative trend (dashed line), the lowering in the F2-layer critical frequency, is also seen in figure 3. The long-term trends found in different ionospheric characteristics (figures 1-3) are given in table.

Table

#	Parameter	Trend, MHz/year	Parameter	Trend, MHz/year	Parameter	Trend, MHz/year
1	$foF2_{10\text{-}14}$(med)	-0.02822	$foF2^{*}_{10\text{-}14}$	-0.02439	$foF2^{*}_{10\text{-}14}$ (132)	-0.01758
2	$foF2_{d.av}$ (med)	-0.01884	$foF2^{*}_{d.av}$	-0.01586	$foF2^{*}_{d.av}$ (132)	-0.01077
3	$foF2_{23\text{-}01}$ (med)	-0.00932	$foF2^{*}_{23\text{-}01}$	-0.00756	$foF2^{*}_{23\text{-}01}$ (132)	-0.00364

The regression dependences of $foF2^*_{10\text{-}14}(132)$, $foF2^*_{23\text{-}01}(132)$, $foF2^*_{d.av}(132)$ on $F10.7^*(132)$ were studied for the period 1963-2012 (the 11-year smoothing technique that was applied to the foF2* data sets reduced the available period for study to between 1963 and 2012), the coefficients of determination (R^2) were found to be 0.96, 0.98, and 0.90 for near-noon, daily averaged and near-midnight data correspondingly figure 4a.

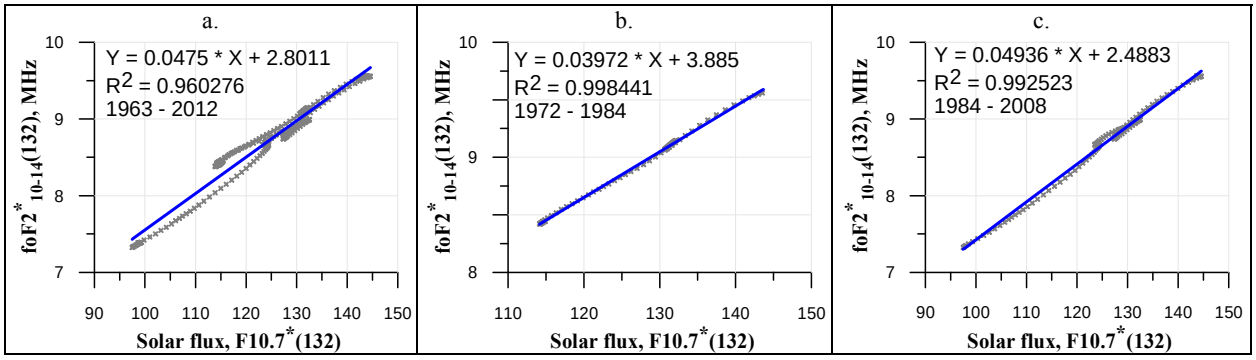

Figure 4 - The regression dependence between $foF2^*(132)$ and $F10.7^*(132)$
for the periods 1963-2012, (a), 1972-1984 (b) and 1984-2008 (c)

However, a combination of two groups of points was evident in figure 4 (upper panel) that assumed some different dependence between the parameters on different phases of the 34-36-years cycle (the period 1972-1984, and 1984-2008), when the $foF2^*(132)$ values increase to their maximum and then decrease to their minimum values. Examples of the regression dependences between $foF2^*(132)$ and $F10.7^*(132)$ for the two time periods are shown in figure 4a,b. It is distinctly seen in both cases that 99% of the variations in the ionospheric parameters can be explained by linear dependence between them and solar activity. So, the solar activity can be considered to be the main driver for the long-term variations in the ionospheric F2-region.

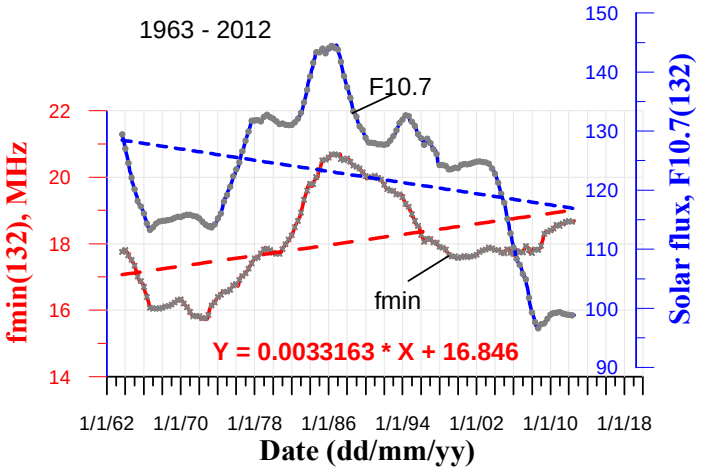

Figure 5 - The 132-month smoothed values of fmin and F10.7
where dashed lines represent their linear trends for the whole measuring interval

Trends in the D-region. A similar analysis, as that carried out for foF2, has been carried out for the fmin data observed at the Alma-Ata station in the years 1957-2017. As it has been already mentioned, the ionospheric parameter fmin is used as a qualitative characteristic of the ionospheric absorption in the D-region, and our interest "is there any trend in the fmin data, and if "yes" what is its sign?" For this purpose, we use the monthly median fmin values for near-noon interval of local time averaging the data over three hours, from 11:00 LT to 13:00 LT. Then, the fmin data were smoothed using the 11-year running mean smoothing to suppress effects of the 11-year solar cycle and obtain a picture of long-term variation in them. Figure 5 shows the fmin(132) and F10.7(132) variation together with the regression

lines (dashed lines) and demonstrates that the long-time course of fmin(132) is similar to those found for F10.7 and foF2 (figures 1-3) in the event that the periodicity of 34-36 years is also evident in the fmin(132) variation which is found in variations of the F2-layer parameters. However, figure 5 clear illustrates a stable upward (positive) trend in fmin(132) values opposite in sign to the trends observed in variations F10.7 and foF2. It means relative high sensitivity of the fmin values to the solar activity changes and significant influence of other trend drivers on them that is very possible the impact of anthropogenic factors on the state of the lower ionosphere.

Conclusion. The F2-layer critical frequency (foF2) and lowest frequency (fmin) observed at the mid-latitude ionospheric station Alma-Ata [43.25N, 76.92E] in the period 1957-2017 were used to study long-term trends in the upper (F2-layer) and lower (D-region) ionosphere.

The geomagnetic indexes (Ap), the near-noon, near-midnight, daily averaged foF2 are found to be in strong dependence from the solar activity; all of them show a dominant pattern of variation with a period of ~34-36 years and linear negative trend.

The trend magnitudes are found to be of the same order independently of the fact whether the solar activity effects in the data sets are smoothed or not; the trends are statistically significant and lie within of -0.018 to -0.028, -0.011 to -0.019, -0.0036 to -0.0093 MHz/year for near-noon, daily averaged and near-midnight values correspondingly.

The long-term course of fmin is similar to those found in F10.7, Ap, and foF2, i.e. the periodicity of ~34-36 years is also evident in the fmin variation. However, in contrast to the F2-layer parameters, the fmin variation clear demonstrates an upward (positive) linear trend that is opposite in sign to the trend found in the F10.7. This means relatively high sensitivity of the fmin values to the solar activity changes and significant influence of other trend drivers on them, one of which is the possible impact of anthropogenic factors on the state of the lower ionosphere.

The work was carried out with accordance Grant № AP05131261of Ministry of Education and Science RK.

А.Ф. Яковец, Г.И. Гордиенко, Ю.Г. Литвинов

ЕЖШС «Ионосфера институты» «ҰҒЗТО» АҚ, Алматы, Қазақстан

ИОНОСФЕРАНЫҢ F ЖӘНЕ D АЙМАҒЫНДАҒЫ ҰЗАҚ МЕРЗІМДІ ВАРИАЦИЯЛАРЫ

Аннотация. Алматы станциясындағы ионосфераның жер үсті тік радиозондауының деректері бойынша F2 Ионосфера қабатының (foF2) және жер маңындағы ең төменгі шағылысу жиіліктерінің (fmin) ұзақ мерзімді өзгерістері зерттелді [43.25 N, 76.92 E] 1957-2017 жж.

Сонымен қатар, ең аз шағылысу жиілігі төменгі ионосферада зондирлеуші сигналдың жұтылуына да, шу деңгейі мен ионозондтың техникалық сипаттамаларына да байланысты. Сондықтан сигналдың жұтылуының абсолюттік мәнін осындай жолмен бағалау проблемалы болып табылады. Алайда, қолшатыр сигналының жұту деңгейінің индикаторы ретінде сапалы сипаттама ретінде fmin параметрін пайдалануға болады.

Бастапқы деректер ретінде fof2 медиандық fof2 (10-14 LT), терек жанындағы (23-01 LT) сағат арифметикалық орташа мәндері және ионосфераның бақылауының қаралып отырған кезеңіндегі орташа тәуліктік мәндері қарастырылды. Төменгі ионосфераның өзгергіштігі күндізгі сағат үшін fmin деректерін пайдалану арқылы зерттелген. Күн радиосәулелендіру ағынының орташа айлық мәндері F10. 7 және Ap индексі күн және геомагниттік белсенділіктің сипаттамалары ретінде рассматрен.

Күн және геомагниттік белсенділігі бойынша деректер ионосфераның жағдайына әсер ететін факторлар ретінде тартылды. Ионосфера аймағының F2 параметрлері, сондай-ақ Ap геомагниттік белсенділіктің индексі T ≈ 35 жыл мерзімділігін және сызықтық теріс трендін анықтай отырып, күн белсенділігіне қатаң тәуелділікті сезінеді. FoF2 және F10.7 ұзақ мерзімді вариация арасындағы детерминация коэффициенттері 0.99 мәндеріне жетеді, бұл күн белсенділігі Ионосфера аймағының F2 ұзақ мерзімді өзгергіштігінің негізгі драйвері болып табылады деп болжайды.

Бұл нәтиже бір жағынан күн белсенділігіне жоғары тәуелділікті, екінші жағынан басқа факторлардың төменгі ионосфераның жағдайына, антропогендік факторларға әсерін болжайды.

Түйін сөздер: орташалықты ионосфера; жоғарғы және төменгі ионосфера; D-облыс; F2-облыс; ұзақ мерзімді трендтер.

А.Ф. Яковец, Г.И. Гордиенко, Ю.Г. Литвинов

ДТОО «Институт ионосферы» АО «НЦКИТ», Алматы, Казахстан

ДОЛГОВРЕМЕННЫЕ ВАРИАЦИИ В ОБЛАСТИ F И D ИОНОСФЕРЫ

Аннотация. Исследованы долговременные изменения околополуденных, среднесуточных и полуночных критических частот слоя F2 ионосферы (foF2) и околополуденных минимальных частот отражения (fmin) по данным наземного вертикального радиозондирования ионосферы на станции Алма-Ата [43.25N, 76.92E] за период 1957-2017 гг.

Принималось во внимание, что минимальная частота отражения зависит как от поглощения зондирующего сигнала в нижней ионосфере, так и от уровня шумов и технических характеристик ионозонда. Поэтому оценить абсолютное значение поглощения сигнала таким способом представляется проблематичным. Однако, как качественная характеристика, как индикатор уровня поглощения зондирующего сигнала, параметр fmin можно использовать.

В качестве исходных данных рассмотрены арифметически средние значения медианных foF2 для околополуденных (10-14 LT), околополуночных (23-01 LT) часов и среднесуточные значения за рассматриваемый период наблюдений ионосферы. Изменчивость нижней ионосферы исследована с использованием данных fmin для дневных часов. Среднемесячные значения потока радиоизлучения Солнца F10.7 и индекс Ap рассматрены как характеристики солнечной и геомагнитной активности.

Привлекались данные по солнечной и геомагнитной активности как факторы, оказывающие влияние на состояние ионосферы. Получено, что параметры F2 области ионосферы, а также индекс геомагнитной активности Ap испытывают строгую зависимость от солнечной активности, обнаруживая периодичность T ≈ 35 лет и линейный отрицательный тренд. Коэффициенты детерминации взаимосвязи долгопериодных вариаций foF2 и F10.7 достигают значений 0.99, это предполагает, что солнечная активность является основным драйвером долговременной изменчивости F2 области ионосферы.

Значения fmin, обнаруживая подобно параметрам F2 области ионосферы ~35-летнюю периодичность, демонстрируют положительный тренд в наблюдаемый период 1957-2017 гг. Данный результат предполагает с одной стороны высокую зависимость от солнечной активности, с другой стороны влияние других факторов на состояние нижней ионосферы, возможно факторов антропогенных.

Ключевые слова: среднеширотная ионосфера; верхняя и нижняя ионосфера; D-область; F2-область; долговременные тренды.

Information about authors:

Gordienko Galina Ivanovna, Ph.D. mat. Sciences, ANS, Institute of the Ionosphere, JSC "NCSCIT", Almaty, ggordienko@mail.ru. 1) The author made a significant contribution to the research concept, obtaining data and interpretation, 2) the author wrote the first version of the article 3) the author approved the final version of the article before submitting it for publication. https://orcid.org/0000-0002-9337-206X;

Yakovets Arthur Fedorovich, Ph.D. mat. Sciences, VNS, Institute of the Ionosphere, JSC "NTSKIT", Almaty, artyak40@mail.ru. 1) The author made a significant contribution to the research concept, data analysis and interpretation, 2) the author wrote the first version of the article, 3) the author approved the final version of the article before submitting it for publication. https://orcid.org/0000-0002-3374-9507;

Litvinov Yuri Georgievich, Ph.D. mat. Sci., SSS, Institute of the Ionosphere, NCSCIT JSC, Almaty, yurii-litvinov@mail.ru. 1) The author made a significant contribution to obtaining the data and their analysis, 2) the author made a critical review of the article for important intellectual content, 3) the author approved the final version of the article before submitting it for publication. https://orcid.org/0000-0002-0600-0517

REFERENCES

[1] Gordiyenko G. I., Vodyannikov V. V., Yakovets A. F. and Litvinov Yu. G. (2014), Earth Planets and Space, 66 (125), 1-6, http://www.earth-planets-space.com/content/66/1/125.

[2] Lauter E. A., Entzian G. Winter anomaly 1980/81 as an example of stratomesospheric coupling//Phys. Solariterr. 1982. Vol. 18. P. 83-90.

[3] Kokourov V. D. Minimum frequency of reflections as a climatic characteristic of the upper atmosphere// Geomagnetism and Aeronomy. 2003. Vol. 43(2). P.274-276 (in Russian).

[4] Clúa de Gonzalez A. L, Gonzalez W. D, Dutra S. L. G., Tsurutani B. T. Periodic variation in the geomagnetic activity: a study based on the Ap index//J Geophys. Res. 1993. Vol. 98. P. 9215.

[5] Echer E., Rigozo N. R., Nordemann D. J. R., and Vieira L. E. A. (2004). Prediction of solar activity on the basis of spectral characteristics of sunspot number//Annales Geophysicae. 2004. Vol.22. P. 2239-2243.

[6] Prabhakaran Nayar S. R. Periodicities in solar activity and their signature in the terrestrial environment//IL WS WORKSHOP, GOA, February 19-24. 2006. P.1-9.

NEWS
OF THENATIONAL ACADEMY OF SCIENCES OF THE REPUBLIC OF KAZAKHSTAN
PHYSICO-MATHEMATICAL SERIES
ISSN 1991-346X **https://doi.org/10.32014/2020.2518-1726.56**
Volume 3, Number 331 (2020), 217 – 224

МРНТИ 89.57.35
УДК 550.34; 528.88

Zh.Sh. Zhantayev, A.Zh. Bibosinov, B.A. Iskakov, A.G. Fremd

SLLP "Institute of Ionosphere" JSC «NCSRT»Almaty, Kazakhstan

GEOSPATIAL MODELING AS A METHOD FOR FORECASTING OIL-PROSPECTIVE HORIZONS IN THE SECTION OF THE EARTH`S CRUST

Abstract. Modern ideas about the formation of hydrocarbon deposits are based on the results of experimental and theoretical studies of the dynamics of the lithosphere. They are based on the established facts of “instability of fluid systems in the sedimentary cover and basement, as well as migration of fluids through permeable zones resulting from changing stresses in the earth's crust. It follows from this that the geological environment is nonequilibrium. Forces of external action and thermodynamic conditions inside the crust contribute to the extrusion of fluids from the lower horizons to the upper and ensure their movement through the zones of decompression to the places of unloading, which are often fracture zones limited by fluid resistances. And this means that the centers of unloading are not static, but replenished and the process of formation of deposits is essentially geodynamic.

Thus, one of the factors for successfully predicting the oil prospectivity of the study area is the detection and analysis of the morphological features of the weakened zones, which are usually not only faults, but also horizons, which are layers that differ from the host rocks by a relatively high coefficient of porosity and fracture and can serve collectors. As well as adjacent multidirectional formations, essentially representing subvertical channels providing the flow of hydrocarbons into the reservoir.

On the other hand, it is of interest to visualize the section of the geological environment from the standpoint of geomechanical permeability, an indicator of which can be the distribution of the horizontal component of the low lithostatic pressure.

Visualization of the distribution of the stresses that are responsible for possible horizontal fluid movements allows us to differentiate the section from the standpoint of the geometry and intensity of the weakened zones and the possible migration routes of fluids, including hydrocarbons, associated with them.

Obviously, such model constructions will make it possible to draw non-trivial conclusions about the nature of the known reservoir and use this methodological approach in predicting the locations of other possible hydrocarbon accumulations.

In the present work, using the example of a well-known hydrocarbon field, we consider the methodology and the results of parametric modeling of the geological environment – creating a three-dimensional image of the distribution of decompression zones and stress-strain state (SSS) parameters using data previously performed on this area of seismic studies using the common depth point method (MOGT) ..

Presentation of seismic data in the decompression parameters, reinforced by the SSS parameters, makes it possible to obtain a “formalized” section and thereby increase the efficiency of geophysical surveys both at the search stage and at the stage of exploitation of hydrocarbon deposits.

Keywords: density inhomogeneities, hydrocarbons, fluid dynamics.

The search for hydrocarbon deposits both in Kazakhstan and abroad is, as a rule, a traditional set of methods and technologies that allows for a comprehensive analysis of the results obtained using data from geological and geophysical studies, ending with recommendations for drilling exploratory wells.

Among geophysical methods, gravel and seismic exploration are usually dominant. The implementation of the traditional research complex is a very time-consuming and cost-intensive process, the payback of which is justified "under the conditions of exploration of large and medium anticlinal oil

and gas bearing structures located at shallow depths" [1]. This is explained by a rather high percentage of "dry" wells with a high cost of drilling itself. Therefore, the use of a well-known set of methods when searching for deposits located at great depths should be approached with some caution.

Consequently, the methods of direct prospecting ground-space observations are unfortunately not a source of complete and unconditional geospatial information about the presence and location of possible hydrocarbon deposits in a geological section. And to fill this gap by reducing the ambiguity of the results obtained, largely succeeds by the method of mechanical and mathematical modeling of the geological environment [2, 3].

Using the data on the distribution of the elastic characteristics of the geological environment, borrowed from the results of seismic observations, the method allows you to develop spatial parametric models of the distribution of density inhomogeneities and values of the parameters of the stress-strain state in the geological space of the study area, regardless of the depth of the proposed reservoir.

In the development of models, the following stages can be distinguished:

Stage 1. Creation of spatial models for the distribution of zones of decompression.

The construction of such models can be used at the search stage, since they allow us to identify, in the context of the studied structure, the areas of decompression, with which the real spatial position and morphology of possible reservoirs, as well as those structural elements of the deep structure that can serve as supply channels, canals migration or areas of possible accumulation of hydrocarbons.

Stage 2. Construction of a spatial model of the geological section in the parameters of the SSS.

The mechanical and mathematical modeling of the geological environment involves the calculation of a set of parameters of the stress-strain state (SSS) with spatial reference of the calculated values. The distribution of the latter in the geological space can be used in solving a wide range of applied problems. Including when performing geodynamic zoning of territories and determining areas of latent energy concentration, identifying areas of increased permeability and assessing the directions of possible fluid movement, etc.

Stage 3. Development of complex parametric models.

The construction of complex models is aimed at performing an analysis of the correspondence of the decompression distribution with the distributions of SSS parameters in the studied block of the earth's crust. In particular, the identification of areas of reduced pressure is one of the main conditions for the movement of fluids in the geological environment. Therefore, it seems important to establish their spatial position and link with the distribution of decompression zones, which, by definition, can be collectors, as well as serve as channels for their migration.

Stage 4. Analysis of intermediate results.

An analysis of the distributions of density inhomogeneities and the anomalous values of the SSS parameters in the volume of the geological environment allows you to:

1. Get a visual spatial representation of the properties of the geological environment and identify new structural forms.

2. A clear idea of the morphology of productive horizons provides the basis for the design of well locations and allows conclusions to be drawn regarding the possible location of new deposits.

The applied methodology was previously tested on the basis of regional seismic observations and showed good convergence of the established decompression zones with the known hydrocarbon deposits of the Caspian region. The main provisions of the proposed methodology are given in [3,4,5].

Below are the results illustrating the above steps of the technology. They are based on 3D seismic data using the OGT method, obtained on the area of the Botahan hydrocarbon field.

The object of this study is a layer of the earth's crust with a thickness of ~ 3.5 km, including well-known ones. productive to hydrocarbons, suprasalt horizons, localized in the depth interval 1.2-1.4 km from the earth's surface.

It is obvious (figure 1A) that the section of the Botahan structure is a complex geological object in which density inhomogeneities are present in an implicit form. An attempt to isolate them showed (figure 1 B, C, D) that in the section there are relatively disaggregated layers localized at the same depths as the productive horizons identified by the MOGT seismic data. These layers are laterally sustained in depth (figure 1 C) and represent a ragged surface with a complex relief. But in general, ~ 2/3 of the area is relatively homogeneous, with the exception of those sections that reflect the position of the faults

established earlier. Fault zones are relatively more permeable than productive horizons. It should be noted that the relative decompression of the fault zones when viewed from above (figure 1, D) is clearly lower than when viewed from below (figure 1, E). The last figure also clearly shows a horseshoe-shaped region of increased permeability, apparently adjacent to a dome-shaped structure.

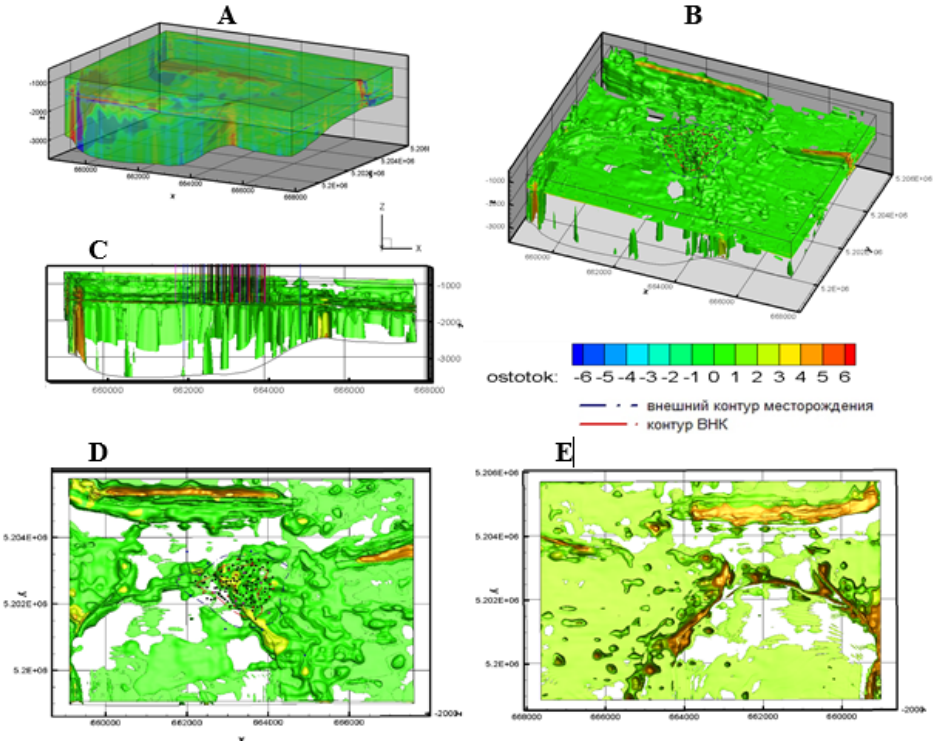

Figure 1 - Projections of the spatial position of decompression zones in a section Botany structures. A - summary section; B-3D projection of the productive horizon; C- side view in the direction of ZV (vertical lines - the position of the wells); D- top view; E- bottom view (mirror image)

From the description of the results illustrated in figure 1, it follows that all the established areas of decompression are interconnected and form a single fluid dynamic system of the Botahan field.

The abnormal values of the SSS parameters carry direct information about the features of the physical state of the geological environment. It was established that the distribution of the identified areas is not chaotic, but is confined to the position of the faults and the contour associated with the boundary of the host rocks, which has a dome-shaped structure. These elements of the geological structure are associated with the lowest possible average pressure values. At the same time, in the section there are areas of a slight decrease in average pressure, which indicates heterogeneity and increased permeability of the medium as a whole.

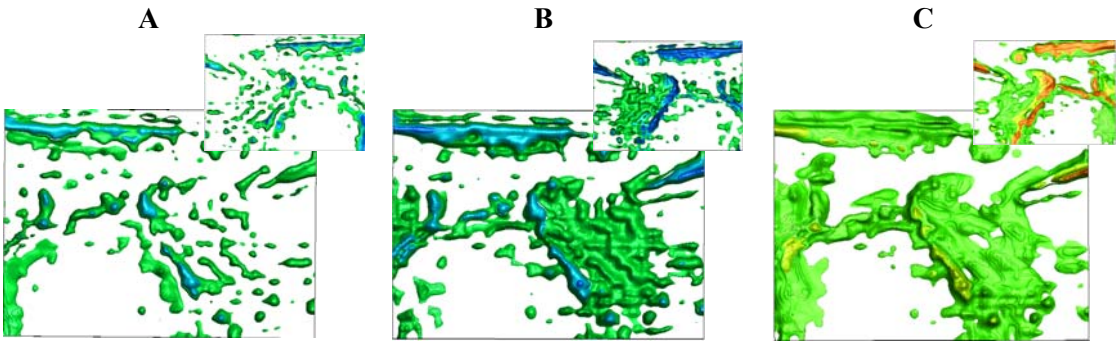

Figure 2 - Distribution of anomalous values of the SSS parameters (in Pa 105): A– average pressure; B - vertical pressure; C is the intensity of shear stresses. On each of the distributions, values of 20, 60 and 100 are shown. In the upper right corner Shows a bottom view (mirror image and 180 ° rotation)

A similar, but more contrasting picture of the distributions is observed in the analysis of anomalous values of vertical pressure and shear stress intensity. It is obvious that concentrated and relatively more significant accumulations of potential strain energy are associated precisely with weakened structural elements of the geological section. And relatively smaller - with adjacent sections. A comparison of the distributions presented in an integrated form (figure 2) suggests that the anomalous values of the parameters of the stress-strain state (SSS) can be used to identify areas of increased permeability and energy saturation of the geological environment, which is an integral part of geodynamic zoning.

The same properties of the geological environment must be taken into account when conducting prospecting for oil and gas. An analysis of the spatial distribution of the anomalous values of the SSS parameters showed that the intensity of permeability and energy saturation of the medium increase with depth, which is clearly seen in the color saturation of the structural elements of the same name in the inset (upper right corner) of figure 2.

As already noted, the identification of areas of low pressure is one of the main conditions for the movement of fluids in the geological environment. Therefore, it seems important to establish the spatial correlation of the position of the anomalous values of the SSS parameters and to link the decompression zones, which by definition can be collectors, and also serve as channels for their migration.

Obviously, the spatial overlap of the distributions of the compared parameters revealed their full agreement, indicating that in the decompression zones there are objective geodynamic conditions for the movement of fluid flows. Moreover, the intensity of the anomalous values increases with depth, thereby providing the necessary pressure drop for squeezing the fluids from the bottom up (figure 3 C, D).

Finally, the distribution of abnormal values of the intensity of tangential stresses characterizing the energy saturation of the geological environment shows that in the vertical zones of increased permeability, which are faults and a horseshoe-shaped region of the junction of the dome-shaped structure with host rocks, the largest reserves of potential energy accumulated during deformation are concentrated (figure 4). Moreover, areas of increased concentration of torsion (shear) energy with depth occupy a significantly larger area (figure 4B), which suggests that the largest reserves of latent shear energy are concentrated in the lower part of the studied volume of the geological environment

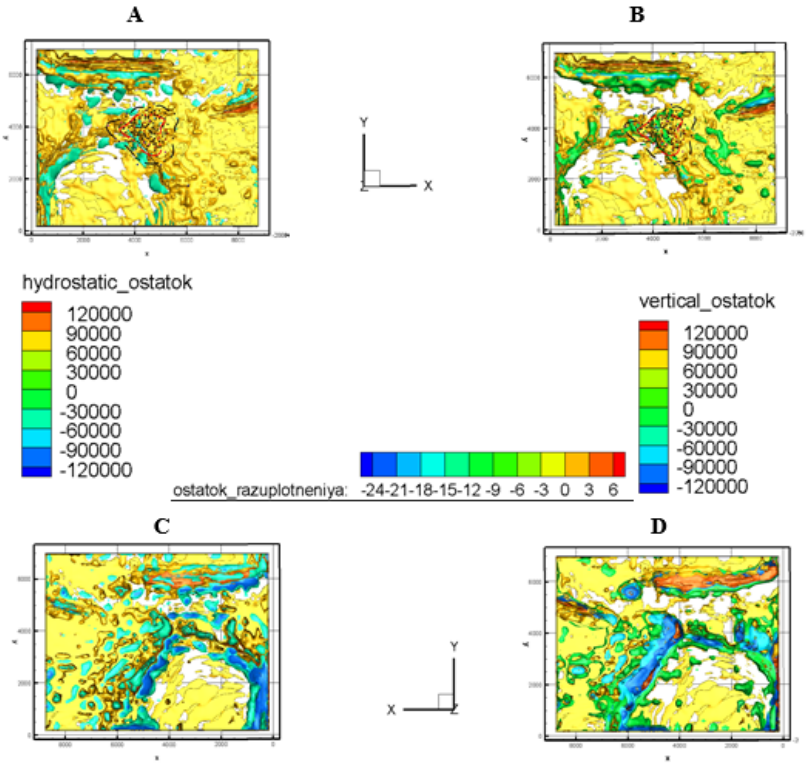

Figure 3 - Vertical projections of distributions relatively low values of hydrostatic (A, C) and vertical (B, D) pressures in combined with the distribution of decompression values. A, B – view from above. C, D - bottom view (projection is rotated 180º)

Three-dimensional parametric visualization of productive horizons in combination with geological and geophysical data allows us to use the proposed methodological approach to seismic data to identify oil-prospective structures, as well as to select the location of exploration wells.

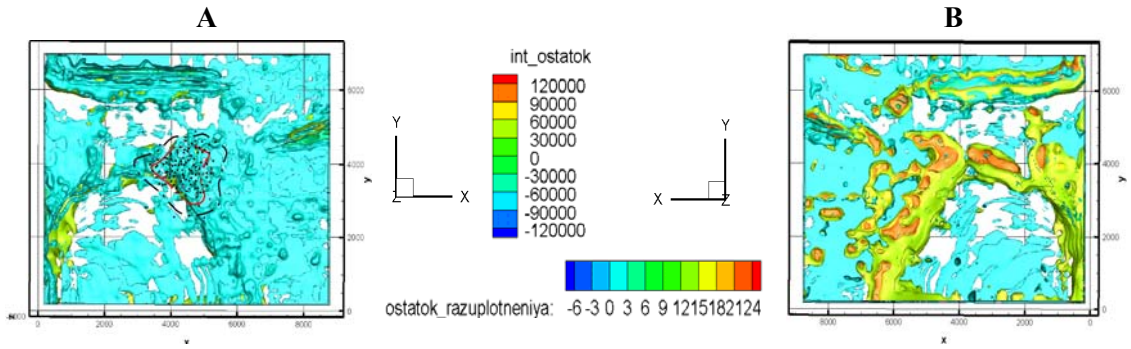

Figure 4 - Vertical projections of relatively low distribution values of intensity of tangential stresses in combination with distribution of decompression values.
A - top view. B - bottom view (projection is rotated 180º)

Development of models for the distribution of zones of possible directivity of fluid flows.

To obtain an objective idea of the distribution in the context of the values of stresses responsible for the fluid permeability and directivity of fluid flows, it is necessary to exclude stresses due to vertical pressure from the calculations. The latter will allow visualizing the distribution of only those stresses that are responsible for possible horizontal mass movements and differentiating the section from the standpoint of the geometry and intensity of the weakened zones and the possible migration routes of fluids, including hydrocarbons, associated with them.

Obviously, such model constructions will make it possible to draw non-trivial conclusions about the nature of the known reservoir and use this methodological approach in predicting the locations of other possible hydrocarbon accumulations.

Confirmation of the foregoing is figure 5, illustrating the spatial distribution of the horizontal component values of the zones of reduced pressure. Obviously, the areas of reduced pressure, displayed in shades of light yellow and green colors, having a funnel shape, are fan-shaped diverging normalized values of their intensity, rising from the lower part of the section and flattening in the upper one. These areas can be interpreted as channels of possible migration through which fluids enter their places of accumulation.

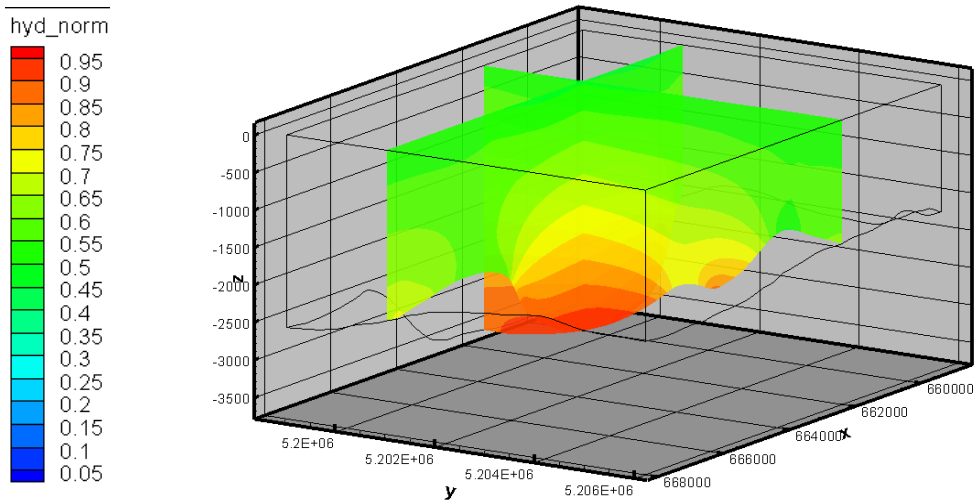

Figure 5 - Spatial projections of vertostatic pressure in the context of the Botahan structureical sections of the distribution of values the horizontal component of lith

A comprehensive interpretation of the obtained distributions and the data of geological and geophysical studies will help to identify the places of possible accumulation of hydrocarbons.

Thus, the distribution of the SSS parameters in the geological half-space can be used in solving a wide range of applied problems. Including when performing geodynamic zoning of territories and determining areas of latent energy concentration, identifying areas of increased permeability and assessing the directions of possible fluid movement, etc.

An analysis of the distributions of the values of the decompression parameters and the SSS in the volume of the geological environment of the Botahan field made it possible to draw several important methodological conclusions of an applied nature.

1. The proposed methodology for the analysis of seismic data allows you to get a visual spatial representation of the properties of the geological environment. In particular, in the area of the Botahan field, a new zone of increased permeability has been established adjacent to the deposit.

2. A clear idea of the morphology of productive horizons provides the basis for the design of wells and allows us to draw conclusions about the possible location of new deposits.

3. The proposed methodology can be used as one of the stages of the search and exploration of hydrocarbon deposits in the projected areas in order to identify productive horizons in the context of the earth's crust.

As a general conclusion, we can say that the presentation of seismic data in decompression parameters reinforced by the SSS parameters allows one to obtain a clear spatial image of the geological environment section and thereby increase the efficiency of geophysical studies both at the search stage and at the stage of exploitation of hydrocarbon deposits.

This work was carried out according to RBP-002 “Applied scientific research in the field of space activity” under the theme “To develop technologies for ground-space monitoring observations of the development of geodynamic processes in the territory of the Caspian region and forecasting hydrocarbon deposits”.

Ж. Ш. Жантаев, А. Ж. Бибосинов, Б. А. Искаков, А. Г. Фремд

«Ионосфера Институты» ЕЖШС «ҰҒЗТО» АҚ, Алматы, Қазақстан

ЖЕР ҚЫРТЫСЫНЫҢ ҚИМАСЫНДА МҰНАЙ-ПЕРСПЕКТИВТІ ГОРИЗОНТТАРДЫ БОЛЖАУ ҮШІН ГЕОКЕҢІСТІКТІК МОДЕЛЬДЕУ ӘДІСІН ПАЙДАЛАНУ

Аннотация. Көмірсутек кен орындарын қалыптастыру туралы қазіргі идеялар литосфера динамикасын эксперименттік және теориялық зерттеулердің нәтижелеріне негізделген. Олар «шөгінді жамылғы мен жертөледегі сұйықтық жүйелерінің тұрақсыздығы», сондай-ақ жер қыртысының кернеулерінің өзгеруі салдарынан сұйықтықтың өткізгіш аймақтар арқылы ауысуы фактілеріне негізделген. Осыдан геологиялық орта тепе-теңдікке жатпайтыны белгілі болады. Сыртқы әсер етуші күштер және жер қыртысының ішіндегі термодинамикалық жағдайлар сұйықтықтың төменгі горизонттан жоғарғыға қарай ағып кетуіне ықпал етеді және олардың көбінесе сұйықтыққа төзімділігімен шектелген сыну аймақтары болып табылатын түсіру орындарына түсетін жерлерге түсуін қамтамасыз етеді. Бұл дегеніміз, түсіру орталықтары тұрақты емес, бірақ толықтырылған және кен орындарын қалыптастыру процесі геодинамикалық сипатқа ие.

Осылайша, зерттеу аймағының мұнай перспективасын сәтті болжаудың факторларының бірі әлсіреген аймақтардың морфологиялық ерекшеліктерін анықтау және талдау болып табылады, олар әдетте тек бұзылулар ғана емес, сонымен қатар горизонттардың негізгі жыныстардан салыстырмалы түрде жоғары кеуектілік және сыну коэффициентімен ерекшеленетін және қызмет ете алатын қабаттары болып табылады. жинаушылар. Мұнымен қатар іргелес көп бағытты формациялар, олар коллекторға көмірсутектердің ағынын қамтамасыз ететін субтвертативті арналарды білдіреді.

Екінші жағынан, геомеханикалық өткізгіштік тұрғысынан геологиялық ортаның бөлігін визуализация қызықтырады, оның көрсеткіші төменгі литостатикалық қысымның көлденең компонентінің таралуы болуы мүмкін.

Сұйықтықтың мүмкін горизонтальды қозғалысына жауап беретін кернеулердің таралуын визуализация бөлімді геометрия мен әлсіреген аймақтардың қарқындылығынан және сұйықтықтардың, соның ішінде олармен байланысты көмірсутектердің көші-қон бағыттарынан бөлуге мүмкіндік береді.

Мұндай модельдік конструкциялар белгілі резервуардың табиғаты туралы тривиальды емес тұжырым жасауға және осы әдіс тәсілін көмірсутектердің басқа ықтимал жинақталатын жерлерін болжауда қолдануға мүмкіндік беретіні анық.

Осы жұмыста, белгілі көмірсутек кен орны мысалын қолдана отырып, геологиялық ортаны параметрлік модельдеудің әдістемесі мен нәтижелерін қарастырамыз - жалпы тереңдік нүктесінің әдісін (MOGT) қолдана отырып, сейсмикалық зерттеулердің осы аймағында бұрын жасалған деректерді пайдалана отырып, декомпрессионды аймақтардың таралуы мен кернеуленген-деформацияланған күйінің (КДС) параметрлерінің үш өлшемді бейнесін жасау.

КДС параметрлерімен күшейтілген декомпрессия параметрлерінде сейсмикалық мәліметтерді ұсыну «формаланған» бөлім алуға мүмкіндік береді және сол арқылы іздеу сатысында да, көмірсутек кен орындарын пайдалану сатысында да геофизикалық зерттеулердің тиімділігін арттырады.

Түйін сөздер: біртекті емес тығыздық, көмірсутектер, флюидодинамика.

Ж.Ш. Жантаев, А.Ж. Бибосинов, Б.А. Искаков, А.Г. Фремд

ДТОО «Институт Ионосферы» АО «НЦКИТ», г. Алматы, Казахстан

ГЕОПРОСТРАНСТВЕННОЕ МОДЕЛИРОВАНИЕ КАК МЕТОД ПРОГНОЗИРОВАНИЯ НЕФТЕПЕРСПЕКТИВНЫХ ГОРИЗОНТОВ В РАЗРЕЗЕ ЗЕМНОЙ КОРЫ

Аннотация. Современные представления о формировании месторождений углеводородов базируются на результатах экспериментальных и теоретических исследований динамики литосферы. В их основе лежат установленные факты «нестабильности флюидных систем в осадочном чехле и фундаменте, а также миграции флюидов по проницаемым зонам, возникающим в результате меняющихся напряжений в земной коре». Из этого следует, что геологическая среда неравновесна. Силы внешнего воздействия и термодинамические условия внутри коры способствуют выдавливанию флюидов из нижних горизонтов в верхние и обеспечивают их передвижение по зонам разуплотнения до мест разгрузки, в качестве которых часто выступают приразломные зоны, ограниченные флюидоупорами. А это значит, что очаги разгрузки являются не статичными, но пополняемыми и процесс формирования месторождений по существу геодинамический.

Таким образом, одним из факторов успешного прогноза нефтеперспективности исследуемой территории является обнаружение и анализ морфологических особенностей ослабленных зон, в качестве которых обычно выступают не только разломы, но и горизонты, представляющие собой слои, отличающиеся от вмещающих пород относительно высоким коэффициентом пористости и трещиноватости и могущие служить коллекторами. А также смежные с ними разнонаправленные образования, по существу, представляющие собой субвертикальные каналы, обеспечивающие поступление углеводородов в коллектор.

С другой стороны, представляет интерес визуализация разреза геологической среды с позиций геомеханической проницаемости, индикатором которой могут служить распределения значений горизонтальной составляющей пониженного литостатического давления.

Визуализация распределения тех напряжений, которые ответственны за возможные горизонтальные перемещения флюидов позволяет дифференцировать разрез с позиций геометрии и интенсивности ослабленных зон и связанных с ними возможных путей миграции флюидов, в том числе углеводородов.

Очевидно, что такие модельные построения позволят сделать нетривиальные выводы о природе известной залежи и использовать этот методический подход в прогнозе мест других возможных скоплений углеводородов.

В предлагаемой работе на примере известного месторождения углеводородов рассмотрены методика и результаты параметрического моделирования геологической среды – создания трёхмерного образа распределения зон разуплотнения и параметров напряжённо-деформированного состояния (НДС) с использованием данных, ранее выполненных на этой площади сейсмических исследований методом общей глубинной точки (МОГТ).

Представление данных сейсмических исследований в параметрах разуплотнения, усиленных параметрами НДС позволяет получить «офизиченный» разрез и тем самым повысить эффективность геофизических исследований как на стадии поиска, так и на этапе эксплуатации месторождений углеводородов.

Ключевые слова: плотностные неоднородности, углеводороды, флюидодинамика.

Information about authors:

Fremd A.G., SLLP "Institute of Ionosphere", head of the laboratory, candidate of physical and mathematical sciences, afremd@list.ru, https://orcid.org/0000-0002-4323-454X;

Zhantayev Zh.Sh., SLLP "Institute of Ionosphere", director, doctor of physical and mathematical sciences, admion1@mail.ru;

Bibosynov A.Zh., JSC «NCSRT»**,** deputy chairman of the board, PhD doctor**,** bibossinov@gmail.com;

Iskakov B.A., SLLP "Institute of Ionosphere", head of geodynamics department, berikiskakov@gmail.com

FEFERENCES

[1] Zhukov V.T., Lazarev G.E., Lomonosov M.N., Thevensky Yu.I., Khvostov V.V. Current trends in development of oil and gas exploration methods, Neftegaz.RU, 2009.

[2] Zhantaev J.Sh., Fremd A.G., Iskakov B.A., Bibosinov A.Zh., Құрmanov B.K. Patent "Method for predicting hydrocarbon deposits" No. 30013; declared 05/16/2014; publ. 09/30/2016, Bull. No. 12. 8s.

[3] Zhantaev J.Sh., Fremd A.G., Bibosinov A.Zh. Innovative patent of the Republic of Kazakhstan for the invention: “A method for predicting hydrocarbon deposits”, (11) 26632. (21) 2012 / 0073.1 on the application of 01.16.2012.

[4] Zhantayev Zh.Sh, Bibosynov A.Zh., Daurenbek K.A., Iskakov B.A., Ivanchukova A.V., Fremd A.G. “Using the distribution of velocity inhomogeneities in the development of the geodynamic justification of a system of тregional GPS observations in Caspian region ”, report at the international scientific conference -“ Independent Kazakhstan: 20 years of the development of space research ”, Almaty 2011.

[5] Zhantayev Zh.Sh., Fremd A.G., Bibosinov A.Zh, Ivanchukova A.V.,. Iskakov B.A. “Distribution of decompression zones in the upper part of the crustal section as a criterion for identifying oil-promising territories of the Caspian region” Sat. “Geological science of independent Kazakhstan. Achievements and prospects. Almaty 2011, p. 291-300.

NEWS
OF THENATIONAL ACADEMY OF SCIENCES OF THE REPUBLIC OF KAZAKHSTAN
PHYSICO-MATHEMATICAL SERIES
ISSN 1991-346X **https://doi.org/10.32014/2020.2518-1726.57**
Volume 3, Number 331 (2020), 225 – 230

МРНТИ 89.57.35
УДК 550.34; 528.88

Zh.Sh. Zhantayev A.G. Fremd, B.A. Iskakov

SLLP "Institute of Ionosphere" JSC «NCSRT», Almaty, Kazakhstan

GROUND-SPACE METHODS FOR FORECASTING DEEP OIL-PERSPECTIVE HORIZONS

Abstract. The search for hydrocarbon deposits is a multifactorial task, which at present cannot be successfully solved on the basis of data from only one method. And for its solution, as a rule, a set of data is obtained, obtained both by ground means and remote, providing an objective picture of the structure of the sedimentary cover based on high information density without significant time and financial costs

The paper considers modern methodological approaches used in the practice of prospecting for oil and gas, which give an objective idea of the criteria on the basis of which a geostructural image of a section of the geological environment is created.

The resulting complex of terrestrial and remote data is aimed at clarifying the structure of the zones of possible oil and gas accumulation and identifying the most promising hydrocarbon traps within them. The main attention is paid to the identification of local structures of various types and discontinuous disturbances. It is the structural aspect, that is, the identification of discontinuous faults of various ranks and the determination of their parameters – strike, direction of fall and kinematics – that is most significant for determining the directions and choosing the methodology for oil and gas prospecting works in each specific area.

The use of thermal range images with the construction of maps of surface temperatures and thermal anomalies based on them, taking into account the influence of the atmosphere, weather conditions, and geological features of the region under study, makes it possible to more efficiently identify productive structures and the most active faults at the present stage. Isolation of such objects makes it possible to concentrate on them seismic exploration and drilling, and thereby reduce the cost and significantly increase the reliability of forecasting and search operations carried out by traditional methods (geology, geophysics, geochemistry).

Among them, in particular, is deep seismic exploration using the common depth point method, which allows to identify migration channels and fluid supports - structural elements that indicate the possible productivity of certain horizons. Nevertheless, despite the leading role of seismic exploration, interpretation of its data at great depths should be approached with some caution due to the high percentage of “dry” wells and the high cost of drilling itself.

.Along with the existing ones, it is proposed and justified the use of the method of parametric 3D modeling of a geological section, which allows creating a visual spatial image of the distribution of oil prospective horizons. The method is verified on data from known deposits and showed good convergence of results.

The results obtained are of interest to subsoil users and organizations planning to search for deposits in oil-spitting regions.

Keywords: density inhomogeneities, hydrocarbons, fluid dynamics.

Despite the successes in the development of technologies for the development of new, practically inexhaustible, energy sources, currently traditional energy sources are at the peak of their demand.

According to experts, by 2040 a 30% increase in demand for energy is predicted, which significantly exceeds current consumption [1].

At the 66-th session of the UN General Assembly in 2011, the President of Kazakhstan, N.A. Nazarbayev, in his report emphasized the need to develop scenario forecasts and a global energy-ecological strategy for the future, which is objectively understandable. Indeed, even without taking into account population growth, the size of the global economy should increase by at least 2 times by 2040, which in turn will require affordable and reliable sources of energy.

And although Kazakhstan belongs to the states with excess energy resources, and it is able to export oil, gas, coal, uranium, without prejudice to its domestic needs, but nevertheless, it also needs to plan to increase natural energy sources, which include hydrocarbons.

Today, Kazakhstan is one of the key exporters of hydrocarbons for the global economy. As of 2013, according to BP Statistical Review of World Energy 2013, Kazakhstan ranked twelfth in the world in terms of proven oil reserves. A significant part of them is located in the Caspian oil and gas basin. However, their additional exploration and further industrial development are complicated[1]:

• low geological exploration of the subsoil;

• the location of a significant part of resources in subsalt horizons located at depths of the order of 5 and more than thousand meters, which increases the capital costs of investors by an order of magnitude.

So, from 202 open oil and gas fields, with estimated recoverable resources of oil in the amount of 7.8 billion tons, and natural gas - 7.1 trillion cubic meters, the vast majority of them are associated with subsalt horizons [2]. This circumstance, against the background of increasing growth rates of production volumes, negatively affected the level of growth in the balance of hydrocarbon reserves. Already, beginning in mid-1995, there was a deficit in replenishment of balance sheet resources, which in the future may pose a real threat to the economic security of Kazakhstan [2].

Therefore, at the KAZENERGY forum held in 2013, Kazakhstan presented a project to create the Eurasia international oil consortium, which is aimed at exploring the deep deposits of the Caspian Depression. According to foreign geologists, the main hydrocarbon reserves, amounting to about 40-50 billion tons of standard fuel, are in the Caspian basin, with 90% of them located at depths of more than 7 km. According to the President of the Society of Petroleum Geologists B.M. According to the results of the work, Kuandykova “will identify new promising areas and objects for exploration, which will make it possible by 2030–2050 to double the existing recoverable reserves of hydrocarbons (hydrocarbons) [3].

According to Akhmet Timurziev, one of the supporters of the concept of the inorganic origin of oil and the author of the Deep Oil project, turning the country's heat and energy complex (FEC) to deep hydrocarbon resources will minimize the cost of replenishing the resource base and stabilize the growth of oil production, including due to its extraction in the territories of the "old regions", which undoubtedly is a cost-effective alternative to the development of new territories.

Forecasting methods for deep oil-bearing horizons.

The search for hydrocarbon deposits both in Kazakhstan and abroad is, as a rule, a traditional set of methods and technologies that allows for a comprehensive analysis of the results obtained using data from geological and geophysical surveys and ending with recommendations for drilling exploratory wells.

Among the geophysical methods, as a rule, gravity and seismic exploration dominate. The implementation of the traditional research complex is a very time-consuming and cost-intensive process, the payback of which is justified "under the conditions of exploration of large and medium anticline oil and gas bearing structures located at shallow depths" [4]. This is explained by a rather high percentage of “dry” wells with a high cost of drilling itself. Therefore, the use of a well-known set of methods when searching for deposits located at great depths should be approached with some caution.

At the same time, deep seismic exploration using the common depth point method (MOGT) allows us to obtain new data on the structure of the earth's crust, indicating its connection with the structure and oil content of the sedimentary cover. These data, obtained along the Tatsays geotraverse, which crossed the entire Volga-Ural province, allowed V.A. Trofimov set “new criteria for the interpretation of seismic data, which, combined with the results of other methods, make it possible to assess the prospects of large tectonic elements, small sections and local objects, as well as to purposefully determine the prospects for deep-seated horizons” [7, 8, 9]. Apparently, the identification of migration channels and possible fluid backlash, which together can serve as a search sign of a reservoir provided that fluids come from below, up to the level of the upper mantle, are among these “criteria”. Another search feature is the presence of dynamic anomalies under each of the known studied deposits - “subvertical or steeply inclined disturbed zones, which probably display the desired oil supply channels, or, more correctly, oil and gas supply channels”. In the works of R.M. Bembel et al. [10], they are called subvertical zones of destruction, having linear dimensions with a width of several hundred meters to several kilometers. Interestingly, no such “dry” wells were identified in the area of such zones.

Thus, based on regional seismic studies, it was found that each hydrocarbon field has its own main fluid supply channel displayed on the seismic sections in the form of a subvertical disturbed zone and, possibly, secondary channels.

The implemented approach to the interpretation of seismic data allowed the author to identify a gigantic positive structure at levels of 7–11 km, which, according to search criteria already established, suggests the presence of a large hydrocarbon field at this depth and recommends drilling of a parametric well [7].

Along with methods based on ground-based observations, in recent years, the emphasis on prospecting for mineral deposits (MPI) and, in particular, hydrocarbons has shifted towards methods using data from remote sensing of the Earth's surface (ERS).

The attractiveness of remote sensing methods in the study of oil and gas regions is due to the possibility of obtaining an objective picture of the structure of sedimentary cover without significant time and material costs. The geospatial information obtained in this way allows us to establish the spectral images of objects due to the deep migration of hydrocarbon fluids and heat and mass transfer of deep matter, leading to changes in soils, soils, and vegetation located on the surface of the study area. The integral effect of these factors is expressed in anomalies associated with both a change in the stress-strain state of the earth's crust and fluid-geodynamic processes, which are detected in space images [11, 12].

Thus, the remote sensing methods at the search stage make it possible to identify promising geological structures and thereby specify the directions of ground research.

In the analysis of space images, much attention is paid to structural and morphological methods. Among the latter, there is a large group of geomorphological methods that use maps and spectrozonal satellite imagery data of various scales, aimed at identifying possible search features - features of the phototone of the soil and vegetation, the presence of ring structures, lineaments, and other features of the relief and landscape as a whole. Unfortunately, the results of applying these methods do not allow us to draw unambiguous conclusions even for predicting shallow structures.

Against this background, the method is distinguished, which is called the structural method, focused not so much on identifying direct deciphering signs as on detecting indirect ones, which make it possible to establish some quantitative characteristics of the desired deposits, regardless of the depth of their occurrence. The method is implemented in the form of a software complex that has “no analogues in world practice”, which, according to its authors, allows one to conduct scientific analysis, predict the location and establish various parameters of oil and gas deposits and other objects of the geological environment, including those located at great depths, right down to up to 20-25 km ”[4, 5].

It is based on the discovery [6], which allowed its author to solve the inverse problem of determining the depth and localization of a buried deposit up to determining its thickness with an accuracy comparable to the accuracy of seismic methods. The error of definitions on average is 3-5% of the depth of the analyzed surface, and "the success of exploratory drilling exceeds 75%." At the same time, the cost of forecasting work in relation to the traditional technology of searches is (0.3-0.4)% [Structometric analysis and search of minerals, http://www.magnolia.com.ru/files/anomalies.gif].

The final product of the application of this technology is the recommendations for well placement provided in the form of cartographic materials, as well as 3D and 2D probabilistic models of the geological section. Obviously, the use of this technology due to its “limited” verification and practical use is not indisputable, but from the point of view of cost and timelines it can be very attractive.

The method of geospatial modeling of the section of the geological environment.

Unfortunately, direct search methods for ground-space observations are not a source of complete and unconditional geospatial information about the presence and location of possible hydrocarbon deposits in the geological section. And to fill this gap, reducing the ambiguity of the results obtained, is largely succeeded by the method of mechanical-mathematical modeling of the geological environment [13, 14].

Using the data on the distribution of the elastic characteristics of the geological environment, borrowed from the results of seismic observations, the method allows you to develop spatial parametric models of the distribution of density inhomogeneities and values of the parameters of the stress-strain state in the geological half-space of the study area, regardless of the depth of the proposed reservoir.

In solving this problem, the following stages can be distinguished:

Stage 1. Creation of spatial models for the distribution of zones of decompression.

The construction of such models can be used at the search stage, since they allow us to identify, in the context of the studied structure, the areas of decompression, which may be associated with the actual spatial position and morphology of possible reservoirs, as well as those elements of the deep structure that can serve as supply channels, migration channels or areas of potential hydrocarbon accumulation.

Stage 2. Construction of a spatial model of the geological section in the parameters of the SSS.

The mechanical and mathematical modeling of the geological environment involves the calculation of a set of parameters of the stress-strain state (SSS) with spatial reference of the calculated values. The distribution of the latter in the geological space can be used in solving a wide range of applied problems. Including when performing geodynamic zoning of territories and determining areas of latent energy concentration, identifying areas of increased permeability and assessing the directions of possible fluid movement, etc.

Stage 3. Development of complex parametric models.

The construction of complex models is aimed at identifying the degree of correspondence of the distribution of decompression zones with the distribution of the values of the SSS parameters in the studied block of the earth's crust. In particular, the identification of areas of reduced pressure is one of the main conditions for the movement of fluids in the geological environment. Therefore, it seems important to establish their spatial position and link with the distribution of decompression zones, which, by definition, can be collectors, as well as serve as channels for their migration.

An analysis of the distributions of density inhomogeneities and the anomalous values of the SSS parameters in the volume of the geological environment allows you to:

1. Get a visual spatial representation of the properties of the geological environment and identify new structural forms.

2. To give a visual representation of the morphology of productive horizons, which is the basis for the design of wells and allows you to draw conclusions about the possible location of new deposits.

The proposed methodology can be used as one of the stages of the search and exploration of hydrocarbon deposits in the projected areas in order to identify productive horizons in the context of the earth's crust.

The developed method was verified on the materials of several fields of the Northern Caspian and showed good convergence with the data of downhole observations in terms of the correspondence of the levels allocated and the actual productive horizons [15].

The method allows to establish the presence of hydrocarbon migration channels and to study their spatial structure. Thus, in the presence of information on possible fluid backings, it is possible to draw predictive conclusions about the location of the reservoir.

As a general conclusion, we can say that the presentation of seismic data in decompression parameters reinforced by the SSS parameters allows to obtain a clear spatial image of the geological environment section and thereby increase the efficiency of geophysical studies both at the search stage and at the stage of exploitation of hydrocarbon deposits.

This work was carried out according to RBP-002 “Applied scientific research in the field of space activity” under the theme “To develop technologies for ground-space monitoring observations of the development of geodynamic processes in the territory of the Caspian region and forecasting hydrocarbon deposits”.

Ж.Ш. Жантаев, А.Г. Фремд, Б.А. Искаков

«Ионосфера Институты» ЕЖШС «ҰҒЗТО» АҚ, Алматы, Қазақстан

ЖЕРДІҢ ТЕРЕҢ ҚАБАТТАРЫНДАҒЫ МҰНАЙ-ПЕРСПЕКТИВТІ АЙМАҚТАРДЫ АНЫҚТАУҒА АРНАЛҒАН ЖЕР-ҒАРЫШТЫҚ ӘДІСТЕРІ

Аннотация. Көмірсутек шикізатын іздеу - көп факторлы міндет, қазіргі уақытта оны тек бір әдіс негізінде ғана сәтті шешу мүмкін емес. Оны шешу үшін, әдетте, уақыттың және қаржылық шығындарсыз ақпараттың жоғары тығыздығына негізделген шөгінді жамылғының құрылымының объективті көрінісін беретін жер үсті және қашықтықтан алынған мәліметтер жиынтығы алынады.

Мақалада мұнай мен газды барлау тәжірибесінде қолданылатын қазіргі заманғы әдіснамалық тәсілдер қарастырылған, олардың негізінде геологиялық орта бөлігінің геоструктуралық бейнесі жасалынған өлшемдер туралы объективті түсінік берілген.

Алынған жер үсті және қашықтағы мәліметтер кешені мұнай мен газдың ықтимал жинақталу аймақтарының құрылымын анықтауға және олардың ішіндегі ең перспективті көмірсутек тұзақтарын анықтауға бағытталған. Негізгі назар әр түрлі типтегі және тоқтаусыз бұзылулардағы жергілікті құрылымдарды анықтауға аударылады. Бұл құрылымдық аспект, яғни әр түрлі қатардағы тоқтаусыз ақауларды анықтау және олардың параметрлерін анықтау - соққы, құлау бағыты мен кинематика бағыттарды анықтау және әр нақты ауданда мұнай мен газды барлау әдістемесін таңдау үшін маңызды болып табылады.

Зерттелетін аймақтың атмосферасын, ауа-райының жағдайын және геологиялық ерекшеліктерін ескере отырып, жер бетіндегі температура карталарын және оларға негізделген жылу аномалияларының карталарын салумен жылу диапазонының суреттерін пайдалану өндірістік құрылымдарды және қазіргі кезеңдегі ең белсенді кемшіліктерді тиімді анықтауға мүмкіндік береді. Мұндай объектілерді оқшаулау оларға сейсмикалық барлау мен бұрғылауға шоғырлануға мүмкіндік береді, осылайша өзіндік құнын төмендетеді және дәстүрлі әдістермен (геология, геофизика, геохимия) жүргізілетін болжау және іздеу жұмыстарының сенімділігін айтарлықтай арттырады.

Олардың ішінде, атап айтқанда, көші-қон каналдары мен сұйықтық тіректерін - белгілі горизонттардың мүмкін өнімділігін көрсететін құрылымдық элементтерді анықтауға мүмкіндік беретін тереңдіктің жалпы әдісін қолдана отырып, терең сейсмикалық барлау бар. Сейсмикалық барлаудың жетекші рөліне қарамастан, оның деректерін үлкен тереңдікте түсіндіруге «құрғақ» ұңғымалардың жоғары пайызы және бұрғылаудың өзіндік құны жоғары болғандықтан өте сақтықпен қарау керек.Мақалада іздеу көмірсутегі кен орындарының орналасқан үлкен тереңдікте. Сонымен қатар, қолданыстағы шешімдерімен ұсынылады және негізделеді әдісін қолдану, параметрлік 3D-модельдеу геологиялық қимасын, мүмкіндік беретін жасау көрнекі кеңістіктік бейнесі бөлу нефтеперспективных горизонттардың. Әдісі верифицирован осы атақты кен орындарын және жақсы жинақталуы нәтижелері. Алынған нәтижелер қызығушылық үшін жер қойнауын пайдаланушылар мен тол.

Түйін сөздер: біртекті емес тығыздық, көмірсутектер, флюидодинамика.

Ж.Ш. Жантаев, А.Г. Фремд, Б.А. Искаков

ДТОО «Институт Ионосферы» АО «НЦКИТ», Алматы, Казахстан

НАЗЕМНО-КОСМИЧЕСКИЕ МЕТОДЫ ПРОГНОЗИРОВАНИЯ ГЛУБОКОЗАЛЕГАЮЩИХ НЕФТЕПЕРСПЕКТИВНЫХ ГОРИЗОНТОВ

Аннотация. Поиск месторождений углеводородов - это многофакторная задача, которая в настоящее время не может быть успешно решена на основе данных исключительно одного метода. И для её решения, как правило, используется набор данных, полученных как наземными средствами, так и дистанционными, обеспечивающими получение объективной картины строения осадочного чехла на основе высокой плотности информации без значительных временных и финансовых затрат.

В работе рассмотрены современные методические подходы, используемые в практике поисковых работ на нефть и газ, дающие объективное представление о критериях, на основании которых и создаётся геоструктурный образ разреза геологической среды.

Получаемый в результате комплекс наземных и дистанционных данных направлен на уточнение строения зон возможного нефтегазонакопления и выделения в их пределах наиболее перспективных ловушек углеводородов. Основное внимание уделяется выявлению локальных структур различного типа и разрывных нарушений. Именно структурный аспект, то есть выделение разрывных нарушений различного ранга и определение их параметров – простирания, направление падения и кинематики является наиболее весомым для определения направлений и выбора методики нефтегазопоисковых работ на каждом конкретном участке.

Использование снимков теплового диапазона с построением по ним карт температур поверхности и тепловых аномалий с учетом влияния атмосферы, погодных условий и геологических особенностей исследуемого региона позволяет с большей эффективностью выявлять продуктивные структуры и наиболее активные на современном этапе разрывные нарушения. Выделение подобных объектов позволяет сосредоточить на них сейсморазведочные работы и бурение, а этим сократить стоимость и значительно повысить достоверность прогнозно-поисковых работ, проводимых традиционными методами (геология, геофизика, геохимия).

К их числу, в частности, относится глубинная сейсморазведка методом общей глубинной точки, позволяющая выявлять миграционные каналы и флюидоупоры, - элементы строения, указывающие на возможную продуктивность тех или иных горизонтов. Тем не менее, несмотря на ведущую роль сейсморазведки, к интерпретации её данных на больших глубинах следует подходить с известной осторожностью из-за высокого процента «сухих» скважин и высокой стоимости собственно бурения.

Наряду с существующими решениями, предлагается и обосновывается использование метода параметрического 3D моделирования геологического разреза, позволяющего создать наглядный пространственный

образ распределения нефтеперспективных горизонтов. Метод верифицирован на данных известных месторождений и показал хорошую сходимость результатов.

Полученные результаты представляют интерес для недропользователей и организаций планирующих поиски месторождений в нефтеперспективных регионах.

Ключевые слова: плотностные неоднородности, углеводороды, флюидодинамика.

Information about authors:

Fremd A.G., SLLP "Institute of Ionosphere", head of the laboratory, candidate of physical and mathematical sciences, e-mail: afremd@list.ru;

Zhantayev Zh.Sh., SLLP "Institute of Ionosphere", director, doctor of physical and mathematical sciences, e-mail: admion1@mail.ru;

Iskakov B.A., SLLP "Institute of Ionosphere", head of geodynamics department, e-mail: berikiskakov@gmail.com

ORCID 0000-0002-4323-454X

REFERENCES

[1 Zakharov A, Hovakimyan M. Trends in the development of world energy. World and National Economy, edition MGIMO-MFA of Russia No. 1 (32), 2015. “Oil and gas in Kazakhstan” No. 2, 2000 GEOLOGY. Deep privileges KAZAKHSTAN No. 5, 2015.

[2] Zhukov V.T., Lazarev G.E., Lomonosov M.N., Thevensky Yu.I., Khvostov V.V. Current development trends oil and gas exploration methods, Neftegaz.RU, 2009

[3] Zhukov V.T., Lazarev G.E., Thevensky Yu.I. Comprehensive analysis and forecast of hydrocarbon deposits and environmental characteristics according to aerospace characteristics according to aerospace data. -M. 1997 .-- 6 p.

[4] Thevensky Yu.I. Small ring structures of loose deposits of the earth's crust / Scientific discovery. OTP Diploma RAS No. 02-d / 02 of October 22, 2002.

[5] Trofimov V.A. New approaches to forecasting the localization of hydrocarbon-promising facilities in deep horizons of the Volga-Ural and West Siberian oil and gas provinces.

[6] Trofimov V.A. Deep seismic surveys of the MOU-OGT at the Tatseyss-2003 geotraverse crossin Volga-Ural oil and gas province // Geotectonics. 2006. No. 4. S. 3-20.

[7] Trofimov V.A. Assessment of the possibility of predicting decompressed zones of the crystalline basement by seismic data // Geological and geophysical modeling in the search for oil and gas. M .: IGiRGI, 1991.S. 126-133.

[8] Bembel R.M., Megeria V.M., Bembel M.R. Geosolitons: the functional system of the Earth, the concept of exploration and Development of hydrocarbon deposits. Tyumen: Vector Beech, 2003.344 s.

[9] Aerospace monitoring of oil and gas facilities. Edited by Academician V. G. Bondur - M .:Scientific World, 2012.555 s.

[10] Bondur V.G. Aerospace methods and technologies for monitoring oil and gas territories and objects oil and gas complex // Earth exploration from space. 2010. No. 6. P. 3–17.

[11] Zhantayev Zh.Sh., Fremd A.G., Iskakov B.A., Bibosinov A.Zh., Құрманов B.K. Patent "Prediction Method hydrocarbon deposits "No. 30013; declared 05/16/2014; publ. 09/30/2016, Bull. No. 12. – 8s.

[12] Zhantayev J.Sh., Fremd A.G., Bibosinov A.Zh. Innovative patent of the Republic of Kazakhstan for the invention: "Prediction method hydrocarbon deposits ”, (11) 26632. (21) 2012 / 0073.1 for application dated January 16, 2012.

[13] Zhantayev Zh.Sh., Bibosinov A.Zh., Iskakov B.A., Kurmanov B.K., Fremd A.G. Softening of the upper part of the section and the state of the geological environment of the Botahan hydrocarbon field. Abstracts of reports. VIII Kazakhstan - Russian International Scientific and Practical Conference "Mathematical Modeling in Scientific -technological and environmental problems of the oil and gas industry. Atyrau 2014.S. 53-54

NEWS
OF THENATIONAL ACADEMY OF SCIENCES OF THE REPUBLIC OF KAZAKHSTAN
PHYSICO-MATHEMATICAL SERIES
ISSN 1991-346X **https://doi.org/10.32014/2020.2518-1726.58**
Volume 3, Number 331 (2020), 231 – 238

UDK 550.380
IRSTI 37.15.03

V. M. Somsikov, A. B. Andreev, V. I. Kapytin, S. N. Mukasheva

Institute of the Ionosphere, National Center for Space Research and Technology, Almaty, Kazakhstan.
E-mail: vmsoms@rambler.ru, alexey.andreyev@rambler.ru, kapytinsanct@mail.ru snmukasheva@gmail.com

BEHAVIOR OF ACOUSTIC-GRAVITATIONAL WAVES IN THE MESOSPHERE OVER THE KAZAKHSTAN REGION

Abstract. Kazakhstan has been going on for more than 10 years carried out studies I effects in the mesosphere at the basis of modern optical spectrometer SATI (Spectral airglow the Temperature Imager), which is mounted on a mountain complex of Ionosphere Institute - radiopoligone «Orbita» at an altitude of 2730 m above sea level [43 ° 03'30 " N , 76 ° 58'24 " E]. The results of a continuous series of optical spectrometric observations of variations in the mesosphere between 2010 and 2016. Observations were made in Kazakhstan on the basis of modern optical spectrometer SATI (Spectral airglow Temperature Imager), which is mounted on a mountain complex of Ionosphere Institute - radiopoligone "Orbita" at an altitude of 2730 m above sea level [43 ° 03'30 "N , 76° 58'24 "E]. The spectral analysis of recorded wave disturbances over the entire observation period showed a wavelength distribution characteristic of acoustic-gravitational waves. It has been established that the maximum number of recorded disturbances in the mesosphere is about 100-200 km long, a noticeable separate peak is observed for wavelengths of about 350-400 km. The directions of propagation of acoustic-gravitational waves have a seasonal dependence. The western maximum in the distribution directions is observed in all seasons. The south-south-western maximum is observed mainly in winter and autumn. East-north-east has a maximum value in the spring-summer months.

Keywords: mesosphere, atmosphere, acoustic-gravitational waves.

1. Introduction. The most difficult to study area of the atmosphere is the mesosphere, lying between the lower atmosphere and ionospheric altitudes at altitudes from 40-50 to 80-90 km. The composition of the mesosphere, its temperature regime, and the chemical and dynamic processes occurring in it are increasingly of interest to geophysicists in connection with the sensitivity of this atmospheric region to variations in solar activity, chemistry of meteor metals, changes in the Earth's climate and long-term anthropogenic effects [1-3].

At present, the role of acoustic-gravitational waves (AGW) in the transfer of energy from the troposphere to the mesosphere and lower thermosphere is actively and is being investigated : changes in the ebbs and flows in the ionosphere [4], ozone variations in the upper mesosphere [4] associated with the sudden warming of the stratosphere [5-6], as well as AGW in the thermosphere and ionosphere, associated with tropical cyclones [7-8]. Work is underway to create and improve three-dimensional global models of the mesosphere and thermosphere, taking into account long-term ground-based and satellite measurements of helio-geophysical parameters [9-15].

Kazakhstan has been going on for more than 10 years carried out studies I effects in the mesosphere at the basis of modern optical spectrometer SATI (Spectral airglow the Temperature Imager), which is mounted on a mountain complex of Ionosphere Institute - radiopoligone «Orbita» at an altitude of 2730 m above sea level [43 ° 03'30 " N , 76 ° 58'24 " E] [16 -17].

This paper presents the results of a continuous series of optical spectrometric observations for the period of more than 6 years in 2010 and 2016, since in order to identify statistically significant patterns in the behavior of the AGW at altitudes mesosphere during periods of solar activity and increased seismic activity.

2. Optical research in the field of the mesosphere

The SATI instrument employs a spectral method for detecting hydroxyl intrinsic thermal radiation in a maximum emission layer located at an altitude of approximately 87 km at night [18-21]. The temperature in the mesosphere is determined by comparing the measured emission spectrum of OH (6-2) hydroxyl bands at a wavelength of 836 nm with model spectra calculated for different vibrational-rotational temperatures of hydroxyl molecules. The registration of atmospheric hydroxyl radiation was carried out from spatially separated sections of the night sky - on a horizontal ring with a diameter of about 100 km and a width of 14-16 km (figure 1).

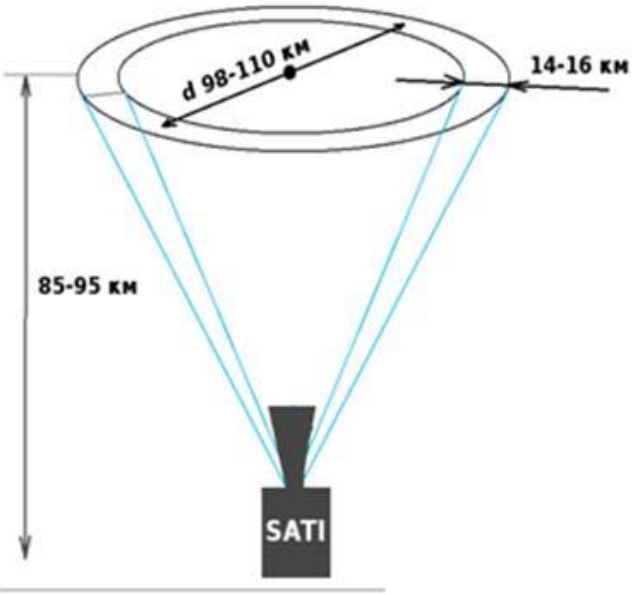

Figure 1 – Scheme of operation of the SATI spectrometer

The device operates in a regular automatic mode. The exposure time of the spectrometer is 1 minute. The average temperature in the mesosphere was monitored at night, and AGW was recorded. It determines the direction of propagation of the wave, its speed, the oscillation period and amplitude as well.

3. Methods for processing experimental SATI data

To identify statistically significant patterns in the behavior of AGW at mesopausal altitudes during periods of solar activity and increased seismic activity, data from continuous series of optical observations for a period of more than 6 years from 2010 to 2016 were processed.

As the primary data processing, the spectral images of the SATI instrument are recalculated into the values of temperature and night sky emission of the mesosphere region. Figures 2 and 3 shown the examples of the results of processing data from optical temperature measurements. The average values of temperature and hydroxyl emission over night for each month for 6 months for each month are shown in Figure 3. As a result of the initial processing of data for 6 years of measurements at SATI from 2010 to 2016, a tendency to decreases values of the maximum mesosphere temperature was found, at an altitude of 87 km, it has a maximum in November-December.

In order to determine the behavior of moving wave disturbances in the mesosphere, the necessary software was created to process SATI data using a modified Fourier transform algorithm known as the co-phase technique [22]. This software allows you to automatically detect moving wave disturbances, determine the propagation direction, wave period, propagation velocity and wavelength from optical SATI measurements (temperature and hydroxyl emission). Using these programs, the results of SATI measurements for the period from 2010 to 2016 were processed.

The temperature values are shown after removal of the constant component and harmonics with periods of more than 90 minutes. So, for a given night of measurements, the main wave mode is a

horizontally propagating wave perturbation moving in a southeast direction. During 6 hours of observation, the direction of propagation changed by no more than 30 degrees, the wave speed is 140-160 km/h, the oscillation period is 40-50 minutes, and the wavelength is defined as 90-130 km.

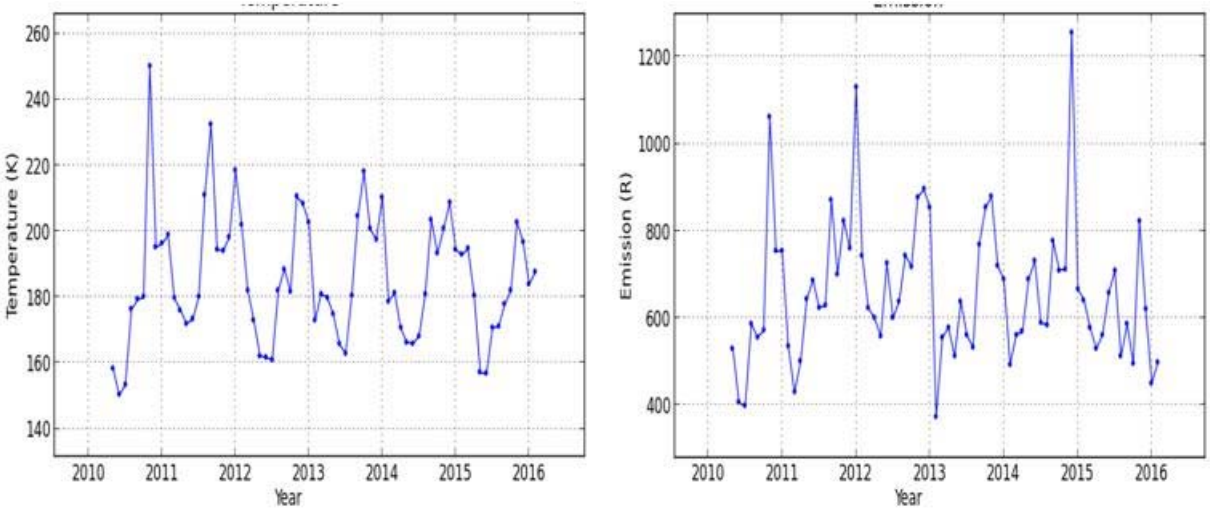

a) hydroxyl temperature b) emission of hydroxyl radiation

Figure 2 – Monthly average values of temperature and emission of hydroxyl radiation at an altitude of 87 km

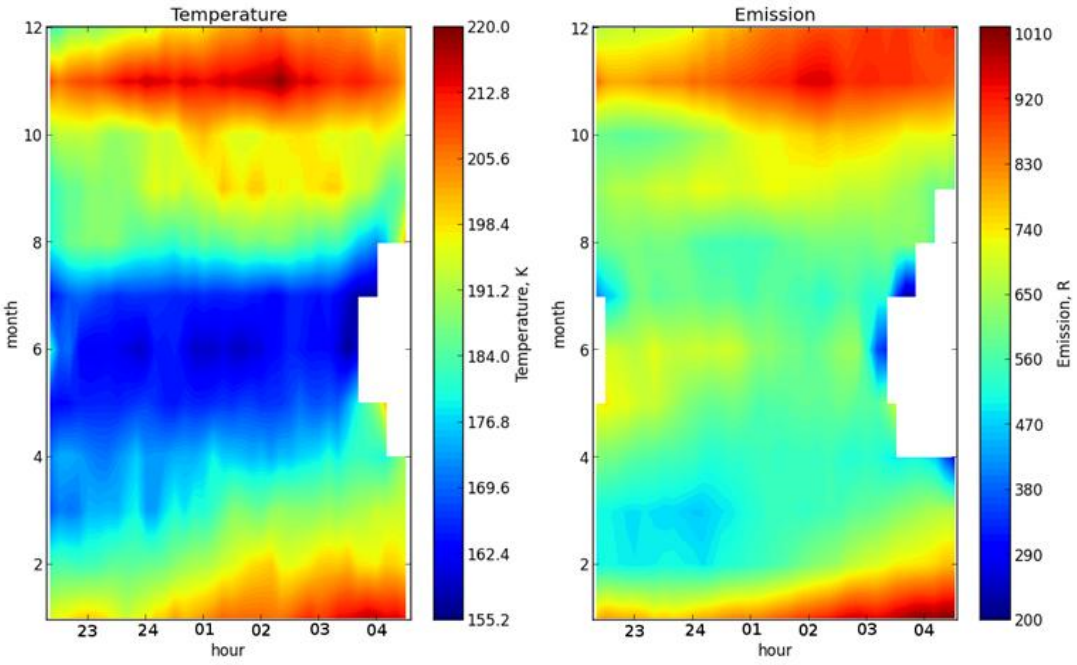

a) temperature values b) hydroxyl emission values

Figure 3 – The values of temperature and hydroxyl emission depending on the time of year and time of day

Figure 4 shown the typical during action registration AGW night on May 11 2010. The ordinate shows the sectors on the ring from which SATI registers night sky radiation.

An analysis of the recorded wave disturbances over the entire observation period showed a wavelength distribution characteristic of the AGW (figure 5). As follows from figure 5, the maximum number of recorded disturbances in the mesosphere has a length of about 100-200 km. There was also a noticeable separate peak for wavelengths of about 350-400 km.

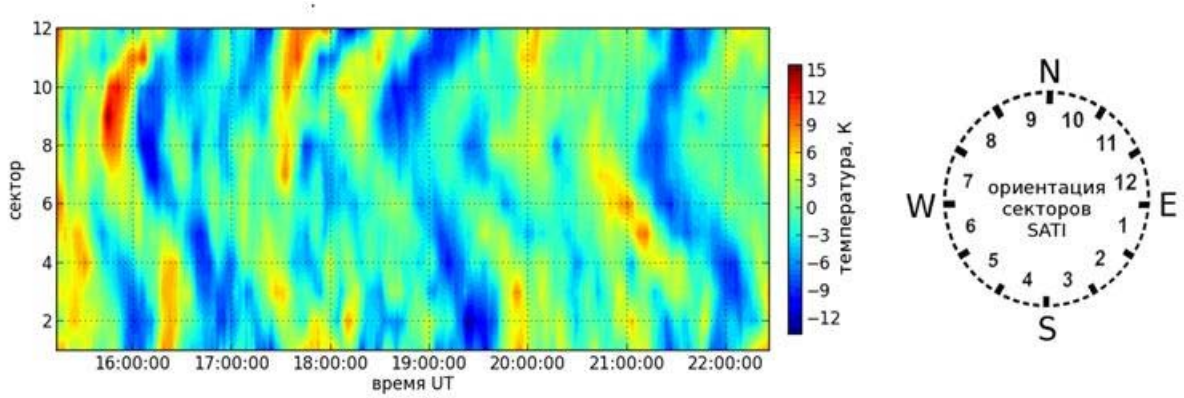

Figure 4 – Wave structure of hydroxyl temperature, values for various points on the plane of the «ring» with a diameter of ≈ 100 km during the night, according to observations at SATI 05/11/2010

To highlight the background features of the behavior of AGW in the mesosphere according to SATI, the entire period of observation data for 5 years (2010-2015) broke by seasons. Figure 6 shows the distribution for the AGW along the direction of propagation for the different seasons, clear, that the direction of propagation AGW have a seasonal dependency, especially perturbation moving east and west direction. One can distinguish the western and south-south-western and east-north-eastern maxima. The western maximum in the distribution directions is observed in all seasons. The south-south-west maximum is observed mainly only in winter and autumn. East-north-east, on the contrary, has a maximum value in the spring and summer months, although it is present in all seasons. In general, most waves have a western direction in winter and an eastern direction in summer. The characteristics of wave perturbations obtained in this way can be considered observable regularly, over 5 years of measurements at SATI.

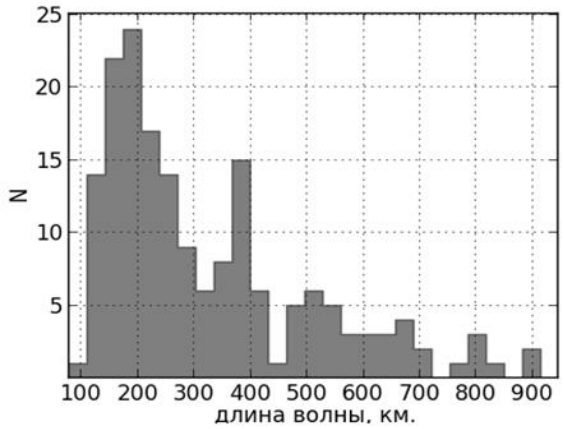

Figure 5 – Distribution of horizontal wavelengths of moving acoustic-gravitational waves in the mesosphere according to SATI for 5 years

To highlight the background features of the behavior of AGW in the mesosphere according to SATI, the entire period of observation data for 5 years (2010-2015) broke by seasons. Figure 6 shows the distribution for the AGW along the direction of propagation for the different seasons, clear, that the direction of propagation AGW have a seasonal dependency, especially perturbation moving east and west direction. One can distinguish the western and south-south-western and east-north-eastern maxima. The western maximum in the distribution directions is observed in all seasons. The south-south-west maximum is observed mainly only in winter and autumn. East-north-east, on the contrary, has a maximum value in the spring and summer months, although it is present in all seasons. In general, most waves have a western direction in winter and an eastern direction in summer. The characteristics of wave perturbations obtained in this way can be considered observable regularly, over 5 years of measurements at SATI.

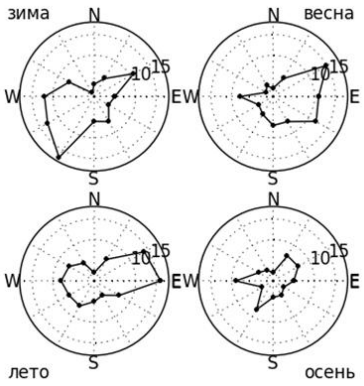

Figure 6 – Seasonal dependence of the directions of propagation of wave disturbances over 5 years

5. Conclusion. Solutions to the problems of the relationship of dynamic processes in the atmosphere with dynamic processes on Earth, prediction of catastrophic phenomena according to observations of variations in atmospheric parameters are extremely effective and relevant around the world. Therefore, they are developing intensively in all countries. Current global trends in the prediction of catastrophic geophysical events, including earthquakes, suggest the use of new methods for monitoring geophysical fields, a high degree of automation of the collection of recorded geophysical parameters and an operational analysis of the results.

Our studies in this direction allowed us to develop: the latest methods, algorithms and programs for solving problems of studying physical processes on Earth, including catastrophic events, based on an analysis of atmospheric wave disturbances in the acoustic-gravitational waves range according to data on variations in the glow of the sky at heights of the mesosphere connected. In particular, based on the results of these observations, algorithms have been created for calculating the efficiency of generation of acoustic-gravitational waves from specific ground-based sources of their propagation into the upper atmosphere, taking into account the specifics of the Almaty region.

To study the relationship between perturbations generated at the Earth's surface and perturbations at the ionospheric altitudes of spacecraft spans, data on variations in the mesosphere are needed. For these purposes, we use the latest equipment for recording optical radiation of oxygen and hydroxyl. The data obtained using this equipment make it possible to compose a general picture of dynamic processes in the atmosphere during various geophysical phenomena.

The work was performed according to the project PH 0118PK00798 in the framework of the target scientific and technical program O.0799.

В. М. Сомсиков, А. Б. Андреев, В. И. Капытин, С. Н. Мукашева

Ионосфера институты, Ұлттық ғарыштық зерттеулер мен
технологиялар орталығы, Алматы, Қазақстан

**АКУСТИКА-ГРАВИТАЦИЯЛЫҚ ТОЛҚЫНДАР ТӘРТІБІ
ҚАЗАҚСТАН ӨҢІРІНЕН МЕЗОСФЕРА САЛАСЫНДА**

Аннотация. Мезосфераның құрамы, оның температуралық режимі, онда болып жатқан химиялық және динамикалық процестер осы атмосфералық аймақтың күн белсенділігінің вариациясына, метеорлық металдар химиясына, Жер климатының өзгеруіне және ұзақ мерзімді антропогендік әсерге сезімталдығына байланысты геофизиктерді көбірек қызықтырады.

Қазіргі уақытта тропосферадан мезосфераға және төменгі термосфераға энергия тасымалындағы акустико-гравитациялық толқындардың рөлі белсенді зерттеледі: ионосферадағы құймалар мен төгінділердің өзгеруі, стратосфераның кенеттен жылынуымен байланысты жоғарғы мезосферадағы озонның вариациясы, сондай-ақ тропикалық циклондармен байланысты термосферадағы және ионосферадағы акустико-гравитациялық толқындар. Мезосфера мен термосфераның үш өлшемді жаһандық модельдерін жасау және жетілдіру бойынша жұмыстар жүргізілуде.

Қазақстанда 10 жылдан астам уақыт бойы мезосфера саласында SATI (Spectral Airglow Temperature Imager) заманауи оптикалық спектрометрі негізінде әсерлерді зерттеу жұмыстары жүргізілуде, ол Ионосфера институтының биік таулы кешенінде – теңіз деңгейінен 2730 м биіктікте орналасқан «Орбита» радиополигонында [43°03'30"N, 76°58'24"E].

Осы жұмыста мезосфера биіктігіндегі акустико-гравитациялық толқындардың мінез-құлқындағы статистикалық маңызды заңдылықтарды анықтау мақсатында 2010 жылдан 2016 жылға дейін 6 жыл аралығындағы оптикалық спектрометриялық бақылаулардың үздіксіз қатарының нәтижелері келтірілген.

Деректерді бастапқы өңдеу ретінде SATI құралының спектрлік бейнелері мезосфера аймағындағы түнгі аспанның температурасы мен эмиссиясының мәндеріне қайта есептелген. Деректерді бастапқы өңдеу нәтижесінде SATI-де 2010 жылдан 2016 жылға дейін өлшеудің 6 жылы ішінде мезосфераның ең жоғары температурасының мәнін 87 км биіктікте азайту үрдісі белгіленген,бұл ретте ол қараша-желтоқсанда максимумға ие.

Осы бағытта біз орындаған зерттеулер мыналарды жасауға мүмкіндік берді: жердегі физикалық процестерді зерттеу бойынша міндеттерді шешуге арналған жаңа әдістер, алгоритмдер мен бағдарламалар, апатты оқиғаларды қоса алғанда, байланысты мезосфераның биіктігіндегі аспанды жару вариациясының деректері бойынша акустико-гравитациялық толқындар диапазонында атмосфераның толқындық толқуын талдау негізінде. Атап айтқанда, осы бақылаулардың нәтижелері бойынша Алматы өңірінің ерекшелігін ескере отырып, оларды атмосфераның жоғарғы қабаттарына таратудың нақты жер үсті көздерінен акустика-гравитациялық толқындарды генерациялау тиімділігін есептеу алгоритмдері жасалды.

Мезосферадағы қозғалатын толқындық ауытқулардың мінез-құлқын анықтау мақсатында, co-phase техникасы ретінде белгілі Фурье түрлендірудің модификацияланған алгоритмі көмегімен SATI деректерін өңдеуге мүмкіндік беретін қажетті бағдарламалық қамтамасыз ету жасалды. Бұл бағдарламалық қамтамасыз ету қозғалатын толқындық ауытқуларды автоматты түрде анықтауға, таралу бағытын, толқын кезеңі, таралу жылдамдығын және SATI оптикалық өлшемдерінің деректері бойынша толқын ұзындығын анықтауға мүмкіндік береді (температура мәні және гидроксил эмиссиясы). Тіркелген толқындық ауытқуларды талдау барлық бақылау кезеңінде акустика-гравитациялық толқындарға тән толқын ұзындығы бойынша бөлуді көрсетті. Мезосферадағы тіркелген наразылықтардың ең көп саны шамамен 100-200 км, толқын ұзындығы үшін шамамен 350-400 км байқалады.

SATI деректері бойынша мезосферадағы акустико-гравитациялық толқындардың жүріс-тұрысының фондық ерекшеліктерін бөлу үшін осы бақылаулардың барлық кезеңі 5 жыл (2010-2015 жж.) маусым бойынша бөлінген. Тіркелген акустика-гравитациялық толқындардың әртүрлі маусымдарға таралу бағыты бойынша бөлінуі зерттелді, акустика-гравитациялық толқындардың таралу бағыттары маусымдық тәуелділікке ие екенін көрсетті, әсіресе бұл шығыс және батыс бағытта қозғалатын ауытқуларға қатысты. Батыс және оңтүстік-оңтүстік-батыс және шығыс-солтүстік-шығыс максимумдарды бөліп көрсетуге болады. Батыс таралу бағыттарында барлық маусымда байқалады. Оңтүстік-оңтүстік-батыс максимум негізінен қыста және күзде ғана байқалады. Шығыс-солтүстік-шығыс керісінше, көктемгі-жазғы айларда, бірақ барлық Маусымда бар. Жалпы алғанда, толқындардың көпшілігі қыста батыс, ал жазда Шығыс бағыты бар. Осылайша алынған толқындық ауытқулардың сипаттамалары 5 жыл бойы SATI-де тұрақты бақыланады деп санауға болады.

Түйін сөздер: мезосфера, атмосфера, акустика-гравитациялық толқын.

В. М. Сомсиков, А. Б. Андреев, В. И. Капытин, С. Н. Мукашева

Институт ионосферы, Национальный центр космических исследований
и технологий, Алматы, Казахстан

ПОВЕДЕНИЕ АКУСТИКО-ГРАВИТАЦИОННЫХ ВОЛН В ОБЛАСТИ МЕЗОСФЕРЫ НАД КАЗАХСТАНСКИМ РЕГИОНОМ

Аннотация. Наиболее сложной для изучения областью атмосферы является мезосфера, лежащая между нижней атмосферой и ионосферными высотами на высотах от 40-50 до 80-90 км. Состав мезосферы, ее температурный режим, происходящие в ней химические и динамические процессы, все больше интересуют геофизиков в связи чувствительностью этой атмосферной области к вариациям солнечной активности, химии метеорных металлов, изменениям климата Земли и долгосрочному антропогенному воздействию.

В настоящее время активно исследуется роль акустико-гравитационных волн в переносе энергии из тропосферы в мезосферу и нижнюю термосферу: изменение приливов и отливов в ионосфере, вариации озона в верхней мезосфере, связанные с внезапным потеплением стратосферы, а также акустико-гравитационные волны в термосфере и ионосфере, связанные с тропическими циклонами. Проводятся

работы по созданию и совершенствованию трехмерных глобальных моделей мезосферы и термосферы с учетом многолетних наземных и спутниковых измерений гелио-геофизических параметров.

В Казахстане уже более 10 лет выполняются исследования эффектов в области мезосферы на базе современного оптического спектрометра SATI (Spectral Airglow Temperature Imager), который установлен на высокогорном комплексе Института ионосферы – радиополигоне «Орбита» на высоте 2730 м над уровнем моря [43°03'30"N, 76°58'24"E].

В настоящей работе приведены результаты непрерывных рядов оптических спектрометрических наблюдений за период более 6 лет с 2010 г. по 2016 г., с целью выявления статистически значимых закономерностей в поведении акустико-гравитационных волн на высотах мезосферы.

В качестве первичной обработки данных спектральные изображения инструмента SATI пересчитаны в значения температуры и эмиссии ночного неба области мезосферы. В результате первичной обработки данных за 6 лет измерений на SATI с 2010 по 2016 г. установлена тенденция уменьшения значений максимальной температуры мезосферы на высоте 87 км, при этом она имеет максимум в ноябре-декабре.

Выполненные нами исследования в данном направлении позволили разработать: новейшие методы, алгоритмы и программы для решения задач по исследованию физических процессов на Земле, включая катастрофические события, на основе анализа волновых возмущений атмосферы в диапазоне акустико-гравитационных волн по данным вариаций свечения неба на высотах мезосферы связанных. В частности, по результатам этих наблюдений созданы алгоритмы расчета эффективности генерации акустико-гравитационных волн от конкретных наземных источников их распространения в верхние слои атмосферы с учетом специфики Алматинского региона.

С целью определения поведения перемещающихся волновых возмущений в мезосфере, было создано необходимое программное обеспечение, позволяющее обрабатывать данные SATI с помощью модифицированного алгоритма преобразования Фурье, известного как техника *co-phase*. Это программное обеспечение позволяет автоматически выявлять перемещающиеся волновые возмущения, определять направление распространения, период волны, скорость распространения и длину волны по данным оптических измерений SATI (значений температуры и эмиссии гидроксила). С помощью данных программ были обработаны результаты измерений SATI за период с 2010 г. по 2016 г. Анализ зарегистрированных волновых возмущений за весь период наблюдения показал распределение по длинам волн, характерное для акустико-гравитационных волн. Показано, что максимальное количество зарегистрированных возмущений в мезосфере имеет длину около 100-200 км, наблюдается заметный отдельный пик для длин волн около 350-400 км.

Для выделения фоновых особенностей поведения акустико-гравитационных волн в мезосфере по данным SATI, весь период данных наблюдений за 5 лет (2010-2015 гг.) разбивался по сезонам. Изучено распределение зарегистрированных акустико-гравитационных волн по направлению распространения для разных сезонов, показало, что направления распространения акустико-гравитационных волн имеют сезонную зависимость, особенно это касается возмущений, двигающихся в восточном и западном направлении. Можно выделить западный и юго-юго-западный и восточно-северо-восточный максимумы. Западный максимум в направлениях распространения наблюдается во все сезоны. Юго-юго-западный максимум наблюдается в основном только зимой и осенью. Восточно-северо-восточный наоборот, имеет максимальную величину в весенне-летние месяцы, хотя и присутствует во все сезоны. В целом большинство волн имеют зимой западное, а летом восточное направление. Полученные таким образом характеристики волновых возмущений можно считать наблюдающимися регулярно, на протяжении 5 лет измерений на SATI.

Ключевые слова: мезосфера, атмосфера, акустико-гравитационная волна.

Information about authors:

Somsikov Vyacheslav Mikhailovich, Institute of the Ionosphere, National Center for Space Research and Technology, doctor of physical and mathematical Sciences, Professor, vmsoms@rambler.ru, https://orcid.org/0000-0003-1005-9367;

Andreev Alexey Borisovich, Institute of the Ionosphere, National Center for Space Research and Technology, PhD-student, alexey.andreyev@rambler.ru, orcid.org/0000-0001-7914-5496;

Kapytin Vitaly Iosifovich, Institute of the Ionosphere, National Center for Space Research and Technology, PhD-student, kapytinsanct@mail.ru, orcid.org/0000-0002-2001-9847;

Mukasheva Saule Nurmukhambetova, Institute of the Ionosphere, National Center for Space Research and Technology, Candidate of Physical and Mathematical Sciences, snmukasheva@gmail.com, https://orcid.org/0000-0002-1609-4430

REFERENCES

[1] Smith, A. K., Pedatella, N. M., Marsh, D. R., & Matsuo, T. (2017) On the dynamical control of the mesosphere-lower thermosphere by the lower and middle atmosphere, Journal of The Atmospheric Sciences, 74:933-947. DOI:10.1175/JAS-D-16-0226.1

[2] John M. C. Plane, Wuhu Feng, Erin C. M. (2015) The Mesosphere and Metals: Chemistry and Changes, Chemical Reviews Chem. Rev., 115:4497-4541. DOI: 10.1021/cr500501m

[3] Minasyants G.S., Minasyants T.M., Vdovichenko V.D., Bibossinov A. G. (2019) Properties of ultraviolet emission at development of solar flares, News of the National Academy of sciences of the Republic of Kazakhstan, 3 (325):56-64. DOI.org/10.32014/2019.2518-1726.24

[4] Goncharenko, L. P., Chau J. L., Liu H.-L., Coster A. J. (2010) Unexpected connections between the stratosphere and ionosphere, Geophys. Res. Lett., 37:L10101. DOI:10.1029/2010GL043125.

[4] Smith, A. K., López-Puertas M., García-Comas M., Tukiainen S. (2009) SABER observations of mesospheric ozone during NH late winter 2002–2009, Geophys. Res. Lett., 36:L23804. DOI:10.1029/2009GL040942.

[5] Hagan M. E., Forbes J. M. (2002) Migrating and nonmigrating diurnal tides in the middle and upper atmosphere excited by tropospheric latent heat release, J. Geophys. Res., 107:4754. DOI:10.1029/2001JD001236.

[6] Immel T. J., Sagawa E. , England S. L., Henderson S. B. , Hagan M. E. , Mende S. B. , Frey H. U. , Swenson C. M., Paxton L. J. (2006) Control of equatorial ionospheric morphology by atmospheric tides, Geophys. Res. Lett., 33:L15108. DOI:10.1029/2006GL026161.

[7] Nicolls M. J., Vadas S. L., Aponte N., Sulzer M. P. (2014) Horizontal wave parameters of daytime thermospheric gravitywaves and E region neutral winds over Puerto Rico, J. Geophys. Res. Space Phys., 119:575-600. DOI:10.1002/2013JA018988.

[8] Bishop R., Aponte N., Earle G. D., Sulzer M., Larsen M., Peng G. (2006) Arecibo observations of ionospheric perturbations associated with the passage of Tropical Storm Odette, J. Geophys. Res., 111:A11320. DOI:10.1029/2006JA011668.

[9] Underwood E. (2018) Toward more realistic modeling of the mesosphere, Journal of Geophysical Research: Atmospheres, 99, DOI.org/10.1029/2018EO096603.

[10] Siskind D. E., Sassi F., Randall C. E., Harvey V. L., Hervig M. E., Bailey S. M. (2015) Is a high-altitude meteorological analysis necessary to simulate thermosphere–stratosphere coupling? Geophys. Res. Lett., 42:8225-8230. DOI:10.1002/2015GL065838.

[11] Pedatella N. M., Raeder K., Anderson J. L, Liu H.-L. (2014) Ensemble data assimilation in the Whole Atmosphere Community Climate Model, J. Geophys. Res. Atmos., 119:9793-9809. DOI:10.1002/2014JD021776.

[12] Marsh D. R., Mills M. E., Kinnison D. E., Lamarque J.-F., Calvo N., Polvani L. M. (2013) Climate change from 1850 to 2005 simulated in CESM1(WACCM), J. Climate, 26:7372-7391. DOI:10.1175/JCLI-D-12-00558.1.

[13] Jin H., Miyoshi Y., Pancheva D., Mukhtarov P., Fujiwara H., Shinagawa H. (2012) Response of migrating tides to the stratospheric sudden warming in 2009 and their effects on the ionosphere studied by a whole atmosphere–ionosphere model GAIA with COSMIC and TIMED/SABER observations.

[14] Ren S., Polavarapu S., Beagley S. R, Nezlin Y., Rochon Y. J. (2011) The impact of gravity wave drag on mesospheric analyses of the 2006 stratospheric major warming, J. Geophys. Res., 116:D19116. DOI:10.1029/2011JD015943.

[15] Liu H.-L., Sassi F., Garcia R. (2009) Error growth in a whole atmosphere climatemodel, J. Atmos. Sci., 66:173-186. DOI:10.1175/2008JAS2825.1.

[16] Pertsev N. N., Andreev A. B., Merzlyakov E. G., Perminov V. I. (2013) Mesospheric-thermospheric manifestations of stratospheric warming: joint use of satellite and ground measurements, Modern problems of remote sensing of the Earth from Space, 10(1): 93-100.

[17] Somsikov V. M., Andreev A. B., Kopytin V. I. (2017) Regularities of behavior of variations of dynamic parameters of the atmosphere during periods of activation of seismic processes in the background. Ground-space monitoring of dynamics of geospheres, Proceedings of the ionosphere Institute 2017, 2:108-122 (in Russ.).

[18] Sargoytchev S.I., Brown S, Solheim B.H., Cho Y.M, Shepherd G.G., López-González M.J. (2004) Spectral airglow temperature imager SATI: A ground-based instruments for the monitoring of mesosphere temperature, Applied optics, 43:30-37.

[19] Aushev V.M., Fedulina I.N., Gordienko G.I., López-González M.J., Pogoreltsev A.I., Ryazapova S.Sh., Shepherd M.G. (2006) Effects in the mesosphere and ionosphere observed at northern midlatitudes, Journal of Planetary and Space Science, 54:559-571.

[20] Semenov A. I., Bakanas V. V., Perminov V. I., Zheleznov Yu. a., Khomich V. Yu. (2002) radiation Spectrum of the earth's night upper atmosphere in the near-infrared region, Geomagnetism and Aeronomy, 42(3): 407-414. (in Russ.).

[21] Shepherd G. (2002) Spectral Imaging of the Atmosphere, International Geophysics Series Academic, 82:54-62.

[22] Hernan A., Montes K., Eric S. (1971) Posmentier. Co-Phase Analysis of Atmospheric Wave Data, Geophys. J. Res., 26:271-278.

ПАМЯТИ ВЫДАЮЩЕГОСЯ УЧЕНОГО, ДОКТОРА ФИЗИКО-МАТЕМАТИЧЕСКИХ НАУК ЛОКТИОНОВА АЛЬБЕРТА АЛЕКСЕЕВИЧА

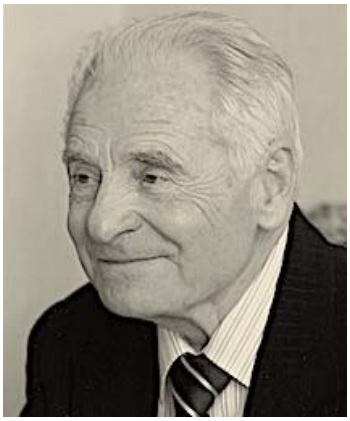

22 декабря 2019 г. на 87-м году ушел из жизни главный научный сотрудник Лаборатории физики космических лучей физико-технического института, доктор физико-математических наук Локтионов Альберт Алексеевич.

Альберт Алексеевич родился 24 декабря 1932 года в Москве. Отец, Локтионов Алексей Кириллович, погиб на фронте в 1944 году. Мать, Локтионова Нина Алексеевна, кандидат технических наук, инженер-металлург, работала в Москве во Всесоюзном институте авиационных материалов. Альберта Алексеевича с самого раннего детства растили бабушка, Мазилкина Варвара Ивановна, и ее муж, Авдевнин Павел Дмитриевич, которые к 1936 году обосновались в городе Алма-Ата.

После школы Альберт Алексеевич поступил на физико-математический факультет КазГУ им. Кирова. С отличием окончив университет в 1955 г., поступил на работу в Физико-технический институт АН КазССР.

Начало научной деятельности в 50-60 годах совпало с созданием Института Ядерной Физики и городка Алатау, куда приезжали молодые ученые с семьями со всего Советского союза. Вместе с молодыми сотрудниками Альберт Алексеевич с женой и коллегой Холмецкой Анной Васильевной, с которой вместе прошли по жизни более 60 лет, стоял у истоков развития физики элементарных частиц в Казахстане. Своим участием в первых строительных субботниках на голом пустыре они буквально заложили основы и будущего института, и научных исследований. Много сил и времени посвящали детям, благоустройству садиков, школы, организации спортивных площадок и пионерского лагеря, посадкам зеленых аллей, по сей день украшающих улицы нашего городка. По прошествии времени стало очевидным, что благодаря многогранным талантам, упорному труду и целеустремленности этому поколению удалось создать удивительно плодотворный микроклимат, когда коллеги по работе становились добрыми соседями и друзьями.

Решение сложных и актуальных проблем физики частиц требовало не только большого интеллектуального напряжения, но огромных капиталовложений, неподъемных для одного института или даже страны. В рамках международного партнерства А.А. Локтионов успешно работал с группами московских институтов, таких как ФИАН, ИТЭФ, МГУ, а также Серпуховский ИФВЭ и Лаборатория физики высоких энергий ОИЯИ Дубна, где размещались самые мощные ускорительные установки того времени. Казахстанские ученые при поддержке государственных комитетов страны получали передовые вычислительные машины для анализа экспериментальных данных, что дало мощный толчок развитию вычислительной техники. Одним из пионеров этого направления стал Альберт Алексеевич. В результате, им была разработана и получена новая физическая интерпретация эволюции множественных процессов в анализе проблем происходящих при взаимодействии взаимодействия ядер высоких энергий.

Более 60 лет он занимался научными исследованиями, сначала как МНС, СНС, затем - руководитель лаборатории электронной вычислительной техники, руководитель лаборатории вычислительной физики, руководитель группы физики нелинейных процессов. По стилю работы его всегда отличали глубокая тщательность, порядочность и ответственность в интерпретации и представлении научных результатов.

Значительными вехами в научной карьере стали защиты сначала кандидатской диссертации по тематике космических лучей, а в 1995 году - докторской диссертации в ученом совете ОИЯИ по специальностям 01.04.16 - физика ядра и элементарных частиц и 05.13.16 - применение вычислительной техники и математических методов в научных исследованиях. Основная специализация в области физики кварков и адронных процессов, создание эффективных математических моделей и программных продуктов позволили решить актуальные задачи фундаментальных исследований. Большая часть научных результатов отражена в десятках публикаций в рецензируемых журналах: https://inspirehep.net/author/profile/A.A.Loktionov.1

Люди, тесно работавшие с Альбертом Алексеевичем, отмечали его исключительную преданность науке. Это качество заметно проявилось в тяжелый период дезинтеграции и развала экономики периода 90-х. В отсутствие центрального финансирования для выживания в исследовательских группах помимо глубоких

профессиональных знаний требовались эрудиция и кругозор для переориентации направлений, настойчивость в поисках и оформлении грантов и участие сразу в нескольких проектах. На базе ранее разработанных средств и методов многомерного извлечения знаний, Альберту Алексеевичу удалось получить качественно новые результаты при решении широкого спектра актуальных научных и технологических проблем. Так, установление корреляций между интенсивностью космических лучей и состоянием геодинамической обстановки заложило основу разработки нового индикатора краткосрочного прогноза землетрясений, дополняющего комплекс традиционных сейсмических, геохимических и других систем. Многомерный анализ данных дистанционного зондирования Земли в оптическом и инфракрасном диапазонах позволил получить новые структурно-прогнозные приложения в сельскохозяйственных и геологических задачах.

С 1963 года Альберт Алексеевич вел также педагогическую работу на физическом факультете Казахского государственного университета им. Кирова, читал спецкурсы по математической статистике и методам планирования экстремальных экспериментов. Многие дипломники и аспиранты набирались опыта под его руководством.

В последние годы Альберт Алексеевич сконцентрировался на изучении проблем эволюции модели возбужденного файерболла во взаимодействиях ионов высоких энергий с атомными ядрами. Новые результаты по исследованиям сильных флуктуаций начальных условий для взаимодействий легких, средних и тяжелых ядер он представил на наиболее влиятельной в этой области конференции «XXIV Quark Matter», (18-24 мая 2014 г., Дармштадт).

В результате сотрудничества, объединенными усилиями ОИЯИ, ИФВЭ (Серпухов) и ИФВЭ (Алма-Ата) была успешно решена серьезная проблема компьютерной независимости при обработке оцифрованной ядерно-физической фильмовой информации, получаемой различными детекторами. Этот результат обеспечил новый уровень выполнения исследований по физике высоких энергий в ОИЯИ и странах-участницах. На следующем этапе, при подготовке к проведению анализа экспериментальных данных с помощью автоматизированных измерительных устройств, были развиты передовые методы теории статистических решений, обеспечивающие эффективное распознавание отдельных треков в событии.

Для расширения традиционного и успешного сотрудничества Казахстана с ОИЯИ в области ядерной физики и физики высоких энергий Альберт Алексеевич предложил рассмотреть вопросы участия казахстанских специалистов и студентов в перспективном мега-проекте ОИЯИ NICA - Nuclotron-based Ion Collider fAcility, – theor.jinr.ru/twiki-cgi/view/NICA/webHome. В результате им была создана коллаборационная группа «BM@N Experiment at the NICA».

Альберт Алексеевич активно участвовал в работе комитетов, научных советов и сообществ как Ученый совет Физико-технического института МОН РК, Объединенный диссертационный совет ОД 53.12.01 при Институте математики МОН РК, Эксперт-рецензент серии международных конференций - International Conference on Information Technologies, Systems and Applications - CITSA, 2004 – 2010 гг.

Искренне жаль, что ушел из жизни удивительно хороший человек, активности которого позавидовали бы многие, даже молодые! До последних дней он поддерживал самые современные исследования, осваивал самые современные методы, был в курсе всего нового в области его интересов. Проведенные научные работы Альберта Алексеевича несомненно будут оценены специалистами и последователями. Он навсегда останется в памяти коллег, учеников и всех тех, кто был сопричастен совместному научному творчеству.

До последнего времени он вел активную научную работу, его яркая творческая жизнь оборвалась внезапно, не позволив реализовать новые научные идеи и замыслы.

Вечная память Альберту Алексеевичу, а членам его семьи – жизни, всегда и во всем достойной громкой чести.

От имени коллектива Физико-технического института
Директор Института, к.ф.-м.н. Серикканов А.С.
Академик НАН РК Мукашев Б.Н.,
Профессор Садыков Т.Х.,
к.ф.м.н. Мухамедшина Д.М.

МАЗМҰНЫ

Қазақстандағы астрофизикалық зерттеулер

Геодинамика және күн-жер байланысы

Ғалымды еске алу

СОДЕРЖАНИЕ

Астрофизические исследования в Казахстане

Геодинамика и солнечно-земные связи

Памяти ученого

CONTENTS

Astrophysical research in Kazakhstan

Geodynamics and solar-terrestrial relations

Memory of the scientist

Publication Ethics and Publication Malpractice
in the journals of the National Academy of Sciences of the Republic of Kazakhstan

For information on Ethics in publishing and Ethical guidelines for journal publication see **http://www.elsevier.com/publishingethics** and **http://www.elsevier.com/journal-authors/ethics**.

Submission of an article to the National Academy of Sciences of the Republic of Kazakhstan implies that the described work has not been published previously (except in the form of an abstract or as part of a published lecture or academic thesis or as an electronic preprint, see **http://www.elsevier.com/postingpolicy**), that it is not under consideration for publication elsewhere, that its publication is approved by all authors and tacitly or explicitly by the responsible authorities where the work was carried out, and that, if accepted, it will not be published elsewhere in the same form, in English or in any other language, including electronically without the written consent of the copyright-holder. In particular, translations into English of papers already published in another language are not accepted.

No other forms of scientific misconduct are allowed, such as plagiarism, falsification, fraudulent data, incorrect interpretation of other works, incorrect citations, etc. The National Academy of Sciences of the Republic of Kazakhstan follows the Code of Conduct of the Committee on Publication Ethics (COPE), and follows the COPE Flowcharts for Resolving Cases of Suspected Misconduct (**http://publicationethics.org/files/u2/New_Code.pdf**). To verify originality, your article may be checked by the Cross Check originality detection service **http://www.elsevier.com/editors/plagdetect**.

The authors are obliged to participate in peer review process and be ready to provide corrections, clarifications, retractions and apologies when needed. All authors of a paper should have significantly contributed to the research.

The reviewers should provide objective judgments and should point out relevant published works which are not yet cited. Reviewed articles should be treated confidentially. The reviewers will be chosen in such a way that there is no conflict of interests with respect to the research, the authors and/or the research funders.

The editors have complete responsibility and authority to reject or accept a paper, and they will only accept a paper when reasonably certain. They will preserve anonymity of reviewers and promote publication of corrections, clarifications, retractions and apologies when needed. The acceptance of a paper automatically implies the copyright transfer to the National Academy of Sciences of the Republic of Kazakhstan.

The Editorial Board of the National Academy of Sciences of the Republic of Kazakhstan will monitor and safeguard publishing ethics.

(Правила оформления статьи для публикации в журнале смотреть на сайтах:

www:nauka-nanrk.kz

http://physics-mathematics.kz/index.php/en/archive

ISSN 2518-1726 (Online), ISSN 1991-346X (Print)

Редакторы: *М. С. Ахметова, Г. Б. Халидуллаева, Д. С. Аленов*
Верстка на компьютере *А.М. Кульгинбаевой*

Подписано в печать 08.06.2020.
Формат 60x881/8. Бумага офсетная. Печать – ризограф.
15 п.л. Тираж 300. Заказ 3.

Национальная академия наук РК
050010, Алматы, ул. Шевченко, 28, т. 272-13-18, 272-13-19